Mitochondrial Dysfunction in the Pathogenesis of Osteoporosis

Daniel Hipps
05001238
Doctor of Philosophy submission March 2021
Institute of Neuroscience

Supervisors:
Professor Sir Doug Turnbull
Professor David Deehan

Acknowledgments

I would like to thank and acknowledge all the support and patience of my wife Libby and the ongoing support from my parents.

I would also like to thank my supervisors, Professor Sir Doug Turnbull and Professor David Deehan.

With a special mention to Doctor Oliver Russell for his frequent help and advice and Doctor Conor Lawless for his help with the statistics

Finally, the members of the Mitochondrial Research Group, the Bio-Imaging facility and Flow Cytometry facility who have all assisted me with this research.

Abstract

Osteoporosis is a skeletal disease, characterised by reduced bone mass and altered microarchitecture, with subsequent loss of strength, increased fragility and risk of fragility fractures. Hip fractures alone cost the NHS £2 billion per year and have associated high morbidity and mortality. The pathogenesis of falling bone mineral density, ultimately leading to a diagnosis of osteoporosis is incompletely understood but the disease is currently thought to be multifactorial.

Humans are known to accumulate mitochondrial mutations with age and mounting evidence suggests that this may be intrinsic to changes in phenotype with advancing age and pathogenesis of age-related disease. Mitochondrial mutations have been shown to occur from the age of 30 years in tissues such as colon, which interestingly correlates with commencement of decline in bone mineral density.

This work has demonstrated the presence of mitochondrial DNA mutations in individual human stem cells and respiratory chain deficiency in human osteoblasts for the first time using novel techniques including single-cell PCR, flow cytometry and imaging mass cytometry.

Work with the Polg$^{mut/mut}$ mouse model which acquire mitochondrial mutations at an enhanced rate, has demonstrated significantly higher levels of osteoblast respiratory chain deficiency compared to age matched wild type controls. This was associated with significantly reduced osteoblast population densities, reduced bone formation and increased osteoclast activity.

Through these novel techniques, this work has demonstrated that underlying mitochondrial pathology directly affects mesenchymal stem cells and osteoblast potentially contributing to osteoporosis which will lead the way for development of new treatment modalities.

Daniel Hipps

A5001238

Table of Contents

Table of Contents 1

Glossary of terms 9

Chapter 1 - Introduction 11

1.1 Introduction 11

1.2 Bone 13

1.2.1 Embryological development of bone 13

1.2.2 The structure of bone 15

1.2.2.1 Woven bone 17

1.2.2.2 Lamellar Bone – Cortical and Cancellous bone 17

1.2.2.3 Bone Marrow 18

1.2.3 Cell lines related to bone 19

1.2.3.1 Mesenchymal stem cells 19

1.2.3.2 Osteoblasts 20

1.2.3.2 Osteocytes 24

1.2.3.3 Osteoclasts 25

1.2.4 Bone homeostasis 28

1.2.4.1 Parathyroid hormone and calcitonin 28

1.3 Current Theories in Osteoporosis pathology 30

1.3.1 Genetic factors in Osteoporosis 30

1.3.1.1 Type 1 Collagen genetic defects: 30

1.3.1.2 Oestrogen receptor 1 31

1.3.1.3 Lipoprotein receptor related protein 5 31

1.3.1.4 Sclerostin 32

1.3.1.5 Transforming growth factor β1 32

1.3.2 Hormonal 33

1.3.2.1 Sex Hormones 33

1.3.2.2 Glucocorticoids 34

1.3.2.3 Insulin 35

1.3.3 Metabolic 35

1.3.3.1 Vitamin D Deficiency 35

1.3.3.2 Metabolic acidosis 36

1.4 Mitochondria 37

1.4.1 Mitochondrial Genetics 37
1.4.1.1 Mitochondrial Genome 37
1.4.2 Mitochondrial Structure 38
1.4.3 Mitochondrial Function 38
1.4.3.1 Oxidative Phosphorylation and Mitochondrial respiratory chain proteins 38
1.4.3.2 Complex I: NADH: Ubiquinone Oxidase 39
1.4.3.3 Complex II: Succinate: Ubiquinone Oxidoreductase Dehydrogenase 40
1.4.3.4 Complex III: Ubiquinol cytochrome c oxidoreductase 40
1.4.3.5 Complex IV: Cytochrome c Oxidase - COX 40
1.4.3.6 Complex V: ATP synthase 40
1.4.3.7 Mitochondrial apoptosis 41
1.4.3.8 Calcium homeostasis 42
1.4.4 Mitochondrial replication 42
1.4.4.1 Transcription 42
1.4.4.2 Translation 43
1.4.4.3 Replication 43
1.4.4.4 Heteroplasmy and Clonal Expansion 44
1.4.6 Mitochondrial Ageing 44
1.4.7 Mitochondria and Osteoporosis. 46
1.4.7.1 The $PolgA^{mut}/PolgA^{mut}$ Mouse 47
1.4.7.2 Sod2 – mitochondrial superoxide dismutase 2 mouse model. 49
1.4.7.3 Tfam Mouse Model 49
1.4.7.4 HTRA2/OMI mouse model 50
1.5 Aims 51
1.5.1 Overview 51
Chapter 2 - Materials and Methods 52
2.1 Reagents, equipment, solutions and consumables: 52
2.1.1 Equipment 52
Flow cytometry 52
Tissue culture and immunohistochemistry 52
2.1.2 Reagents 53
2.1.2.1 Cell Culture 53
2.1.2.2 Immunohistochemistry 54
2.1.2.3 PCR 55

2.1.2.4 Tissue Preparation 56
2.1.3 Chemicals 56
2.1.4 Solutions 58
2.1.4 Consumables 59
2.1.4.1 Equipment Consumables 59
2.1.4.2 Tissue culture consumables 60
2.2 Software 60
2.3 Ethics and Patient cohort 61
2.3.1 Ethics 61
2.3.2 Control paediatric patients 61
2.3.3.1 Paediatric bone samples 61
2.3.2.2 Paediatric cell line samples from anterior cruciate ligament surgery 61
2.3.2 Adult patient samples 61
2.4 Sample preparation 63
2.4.1 Decalcification protocol 63
2.4.2 Bone Marrow preparation 63
2.4.2.1 Lymphoprep protocol 63
2.4.2.2 Mesenchymal Stem Cell separation 64
2.5 Histochemistry 66
2.5.1 Haematoxylin and eosin 66
2.5.2 3,3'-Diaminobenzidine (DAB) staining 66
2.6 Immunofluorescence 68
2.6.1 Quadruple immunofluorescence Assay 68
2.6.2 High throughput immunofluorescent assay 70
2.6.3 Imaris and Spotfire image analysis 71
2.7 DNA extraction and lysis 72
2.8 PCR and sequencing 72
2.8.1 Long-range PCR methods and optimisation 72
2.8.2 Agarose gel electrophoresis 74
2.8.3 DNA purification and quantification 74
2.8.3.1 Purification 74
2.8.3.2 Quantification – Illumina MiSeq 74
2.9 Flow cytometry 76
2.9.1 Symphony A5 and FACSCanto II systems 79
2.9.2 BD FACS Aria III Cell Sorter 79

2.10 Imaging Mass Cytometry 80
2.10.1 Hyperion and Helios Mass Cytometry systems 80
2.10.2 Antibody conjugation 83
2.10.3 Conjugation testing and results 83
2.11 Cell Culture 84
2.11.1 MSC isolation 84
2.11.2 Differentiation 85
2.11.3 Osteogenic media 85
Chapter 3 - Mitochondrial DNA mutations in mesenchymal stem cells and clonal expansion. 87
3.1 Introduction: 87
3.1.1 Mitochondrial DNA mutation formation and clonal expansion 87
3.2 Aims of investigation 89
3.3 Methodology and Results 89
3.3.1 Patient Cohort 89
3.3.2 Methods Development 91
3.3.2.1 Mesenchymal stem cell separation. 91
3.3.2.2 Red cell lysis buffer 91
3.3.2.3 Lymphoprep bone marrow preparation 92
3.3.2.4 Flow cytometry 92
3.3.2.5 PCR protocol development 93
3.3.2.6 Ion Torrent quantification and library prep 100
3.3.2.7 Sequencing Trial 102
3.3.2.8 Changing to the Illumina MiSeq sequencer from the Ion Torrent sequencer 103
3.3.3 Final Methods 104
3.4 Results 105
3.4.1 MiSeq results of a 78-year-old patient – proof of concept and analysis pathway using MiSeq and analysis pipeline. 105
3.4.2 Comparison of mitochondrial DNA mutation load with increasing age: Final MiSeq sequencing output. 108
3.4.2.1 Overall trends and combined results. 108
3.5 Discussion: 119
3.5.1 Limitations 122
3.5.2 Future work 123
3.6 Conclusion: 123
3.7 Appendix: Individual patient sample data set 124

3.7.1 Data for the patient “Hip 1” 124
3.7.2 Data for the patient “Hip 2” 127
3.7.3 Data for the patient “Hip 3” 131
3.7.4 Data for the patient “Hip 4” 135
3.7.5 Data for the patient “Hip 6” 140
Individual SNPs greater than 50% heteroplasmy 141
3.7.6 Data for the patient “Hip 7” 146
3.7.7 Data for the patient “Hip 8” 151
3.7.8 Data for the patient “Hip 9” 154
3.7.9 Data for the patient “Hip 10” 157
3.7.10 Data for the patient “Hip 11” 161
3.7.11 Data for the patient “Hip 12” 164
3.7.12 Data for the patient “Hip 13” 169
3.7.13 Data for the patient “Femur 1” 173
Chapter 4 - High throughput screening to identify mitochondrial respiratory chain protein deficiencies 177
4.1 Introduction 177
4.1.1 Accumulation of respiratory chain protein deficiencies 179
4.2 Aims of this investigation 180
4.3 Methods: Development of a high throughput assay for assessing mitochondrial protein deficiencies 181
4.3.1 Patient Cohort. 181
4.3.2 Flow cytometry assay; preliminary methods development and results. 182
4.3.2.1 Antibody selection 182
4.3.2.2 Fixation trials 185
4.3.2.3 Permeabilisation buffer and process. 187
4.3.2.4 Blocking Agents and Washes 190
4.3.2.4 Wash number and technique optimisation 192
4.3.2.5 Antibody Titration 193
4.3.3 Further Optimisation of the flow cytometry assay 194
4.3.3.1 Cell types 195
4.3.3.2 Further Antibody optimisation 197
4.3.3.3 Confocal microscopy and the development of the flow cytometry assay. 198
4.3.3.4 Further Permeabilisation buffer optimisation 199
4.4 High throughput imaging on the CellDiscoverer7 203

4.4.1 Fixation 204
4.4.2 Permeabilisation 206
4.4.3 Antibody optimisation; biotin amplification and blockade. 207
4.4.4 Cell sorting and imaging 211
4.4.5 Further antibody optimisation and validation. 216
4.4.5.1 Human Muscle sections 216
4.4.5.2 Wildtype and Deficient cell lines – ND4 vs NDUFB8 antibodies 218
4.5 Final optimised assay for high throughput screening 221
4.5.1 Assay 221
4.5.2 Testing the Assay 222
4.6 Results 223
4.6.1 Flow cytometry sorting of MSCs 223
4.6.2 Impact of freeze-thaw cycles on cells. 226
4.6.3 The effect of flow cytometry on cell viability. 227
4.6.4 Utilising a fresh sample 227
4.6.5 Fresh sample results. 232
4.7 Discussion 234
4.7.1 Conclusion 236
4.7.2 Future work 236
Chapter 5 - Imaging Mass Cytometry 237
5.1 Introduction 237
5.2 Aims of experiment 238
5.3 Methods Development 238
5.3.1 Immunofluorescence protocol for detecting mitochondrial deficiency in osteoblasts. 238
5.3.2 Fixation and Decalcification protocol 239
5.3.3 Imaging and analysis 240
5.3.4 Hyperion Imaging Mass Cytometry 246
5.3.4.1 Hyperion Antibodies 246
5.3.4.2 Antibody conjugation 247
5.3.4.3 Antibody Panel Design 248
5.3.4.4 3,3’-Diaminobenzidine (DAB) staining 250
5.3.4.5 Mass cytometry protocol development. 253
5.3.4.6 Optimisation with Histocyte control sections and osteosarcoma mouse models. 253
5.3.4.7 Optimisation using human bone marrow lesions 257

5.3.5 Final samples 259
5.3.5.1 MCD Viewer 261
5.3.5.2 Cell profiler 262
5.3.5.3 Fiji and QuPath analysis 262
5.3.5.4 Bone Marrow Lesion Results 264
5.3.5.4 Mitocyto 268
5.3.5.5 Nikon Elements and Volocity. 268
5.4 Results 271
5.4.1 Final experiment results and analysis using Volocity, and R based algorithms. 271
5.4.1.1 Data for the patient “Hip 1” 273
5.4.1.2 Data for the patient “Hip 2” 274
5.4.1.3 Data for the patient “Hip 3” 275
5.4.1.4 Data for the patient “Hip 4” 276
5.4.1.5 Data for the patient “Hip 5” 277
5.4.1.6 Data for the patient “Hip 6” 278
5.4.1.7 Data for the patient “Hip 7” 279
5.4.1.8 Data for the patient “Hip 8” 280
5.4.1.9 Data for the patient “Hip 9” 281
5.4.1.10 Data for the patient “Hip 10” 282
5.4.1.11 Data for the patient “Femur 1” 283
5.4.1.12 Data for the patient “Paediatric 1” 284
5.4.1.13 Data for the patient “Paediatric 2” 285
5.4.1.14 Results Summary 286
5.5 Discussion 288
5.6 Conclusion 290
5.7 Appendix 294
Chapter 6 Final discussion and conclusion 295
6.1 Current understanding of osteoporosis 295
6.2 Summary of results and further discussion 296
6.2.1 Results summary evidence of the role mitochondrial pathology plays in osteoporosis. 296
6.2.2 The effect of mitochondria pathology on mesenchymal stem cell functions 297
6.2.3 Mitochondrial respiratory chain deficiency in Osteoblasts. 298
6.2.4 Future Work 299
6.3 Final conclusion 300

List of Figures..... 303

List of tables..... 311

References:..... 312

Glossary of terms

ACL	anterior cruciate ligament
ADP	adenosine diphosphate
ALP	alkaline phosphatase
ATP	adenosine triphosphate
BMD	bone mineral density
BMP	bone morphogenic protein
CD	cluster differentiation
COX	cyclooxygenase
CyToF	cytometry by time of flight
DAB	3,3'-Diaminobenzidine
EDTA	ethylenediaminetetraacetic acid
FACS	fluorescence-activated cell sorting
FADH	flavin adenine dinucleotide (FAD) + hydrogen
FBS	fetal bovine serum
FGF	fibroblast growth factor
HSP	heavy strand promoter
IGF	insulin growth factor
IHC	immunohistochemistry
IL	interleukin
IMC	imaging mass cytometry
LSP	light strand promoter
M-CSF	macrophage colony-stimulating factor
MSCs	mesenchymal stem cells
MTCO1	Mitochondrially Encoded Cytochrome C Oxidase I
MTCO2	Mitochondrially Encoded Cytochrome C Oxidase II
MTCO3	Mitochondrially Encoded Cytochrome C Oxidase III
NADH	nicotinamide adenine dinucleotide (NAD) + hydrogen
NDUFB8	NADH dehydrogenase [ubiquinone] 1 beta subcomplex subunit 8
NGS	normal goat serum
OPG	osteoprotegerin
OSCP	oligomycin sensitivity conferral protein

OXPHOS	oxidative phosphorylation
PBS	phosphate buffered saline
PBST	phosphate buffered saline with tween
PCR	polymerase chain reaction
PFA	paraformaldehyde
PTH	parathyroid hormone
RANKL	receptor activator of nuclear factor kappa-B ligand
RBC	red cell lysis
ROI	region of interest
ROS	reactive oxygen species
SDHA	succinate dehydrogenase complex flavoprotein subunit A
SIFT	sorting intolerant from tolerant
SNP	single nucleotide polymorphism
SOST	sclerostin
TAE	Tris-acetate-EDTA
TBS	tris buffered saline
TBST	tris buffered saline with tween
TCA	tricarboxylic acid cycle
TFAM	mitochondrial transcription factor A
TGF	transforming growth factor
TNF	tumour necrosis factor
TOM	translocases of the out mitochondrial membrane
TRAP	tartrate-resistant acid phosphatase
UV	ultraviolet
VDAC	voltage-dependent anion channels

Chapter 1 - Introduction

1.1 Introduction

Osteoporosis is defined as a skeletal disease, which is characterised by reduced bone mass and microarchitecture, with subsequent loss of strength that predisposes to fragility and risk of fractures (1). The World Health Organisation defines osteoporosis as a bone mineral density (BMD) score of less than -2.5 standard deviations from a young population of the same sex, osteopenia reduced bone mass is defined as having a BMD score between -1 and -2.5 (2). Bone mass peaks in early adulthood, followed by a slow decline with bone mineral density falling consistently as a feature of advancing age (3). This deterioration in bone microarchitecture with increasing porosity and reduced mineralisation levels affects men and women universally and leads to an inherent weakening of the bone and increased risk of fracture with age (4, 5).

Osteoporosis is part of the ageing population paradigm and therefore is set to increase over the coming years. Recently published data (2014) in developed industrialised countries has estimated prevalence ranging from 9-38 % of women and 1-8 % of men. In these countries, osteoporosis affects up to 49 million individuals (6). In the US alone it is estimated 16.8 million (54%) of post-menopausal women are osteopenic and 9.4 million (30%) are osteoporotic (7).

Fragility fractures associated with osteoporosis cause significant morbidity, mortality and huge costs to healthcare economies worldwide (8-10). The lifetime risk of hip fracture in the white American population is 6% for males and 17.5% for females. The cumulative incidence rises to 17% for men and 33% of women by the age of 90 taking into account life expectancy (11). Hip fracture alone costs the NHS £2 billion per year and is associated with a high 30-day and 1-year mortality. UK National Hip Fracture database reports 7.1% at 30 days although this was previously 10.7% in 2007 (12).
The pathogenesis of falling bone mineral density, ultimately leading to a diagnosis of osteoporosis is incompletely understood but the disease is currently thought to be multifactorial in nature (3, 13, 14). In general terms, however, age-related osteoporosis is thought to occur because the amount of bone removed by the process of osteoclastic bone resorption is not matched by the amount of new bone formed by osteoblasts (15-17).

The formation of new bone is highly energy dependent and the osteoblasts sole function for their three-month lifespan is to produce bone (18). They require a sufficient amount of ATP to fuel this process adequately. It has been shown in human colon that mitochondrial dysfunction and

respiratory chain defects are evident in colonic crypts by the approximate age of 30 (19). This also correlates with the approximate age that bone homeostasis begins to fail and bone mineral density levels begin to decline in men and women (3).

Humans are known to accumulate mitochondrial mutations with age (20, 21) and mounting evidence suggests that this may indeed be the overarching cause intrinsic to the changing phenotype in advancing age and age-related diseases seen in various tissues (22-24). A direct link between mitochondrial dysfunction and falling bone mineral density has never been established but mitochondrial DNA mutations may play a role in the pathogenesis of osteoporosis.

1.2 Bone

Bone can take a number of different shapes and forms and these are related to different sub-structures. There is lamellar and mature bone and also cortical and cancellous. There is also another form of bone related to pathology and trauma; woven bone which has a more random structure, increased turnover and osteocytes numbers. It is inherently weaker than lamellar bone.

The cortical bone which makes up 80% of the skeleton, which in an adult consists of 206 bones consisting of Haversian systems or organised osteons. These osteons are connected by Volkmann canals which contain arterioles, venules, capillaries and nerves. Between each osteon is interstitial lamellae or layers of mineralised matrix which have been laid down. These layers of bone are what give cortical bone its strength when compared to cancellous or trabecular bone. Nutrition is supplied via the Volkmann canals and capillaries (25). Bone serves a number of different functions (26):

- Mechanical support of soft tissues
- Levers for muscle action
- Protection of the central nervous system
- Storage and release of calcium and other ions
- Housing and support of haematopoiesis

1.2.1 Embryological development of bone

Bone is formed from the mesoderm germ layer except in the cranium where the neural crest also contributes. The mesoderm layer is also responsible for other connective tissue development including cartilage and skeletal muscle.

Bone is formed by either intramembranous ossification in the case of the clavicle, skull and facial bones or in the case of the long bones' endochondral ossification. Endochondral ossification occurs where $Prx1^{+}$ progenitor mesoderm cells condense and proliferate to create a limb bud. The cells at this primary ossification enter a chondrogenic differentiation pathway controlled by the expression Sox9. Sox9 expression drives this differentiation of condensation of cells into chondrocytes and acts at each stage of chondrocyte differentiation (27, 28). These differentiating cells express increased levels of Col10a1 as the transcription factor Runx2 drives these chondrocytes to become hypertrophic (28) forming a bone collar and vascularisation of the cartilage template takes place. This neovascularisation is a result of vascular endothelial growth factor released by the hypertrophic chondrocytes.

With the creation of a blood supply come haemopoietic stem cells which give rise to osteoclasts. These osteoclasts remove the cartilage template creating space for Osx1+ pre-osteoblasts to populate and grow. (29). These Osx1^{+} cells are stimulated by adjacent hypertrophic chondrocytes causing perichondrocyte differentiation (28).

A longitudinal growth axis is created along with the two growth plates or physis which play a part in bone growth until skeletal maturity. Periosteal growth occurs perpendicular to these growth plates and the numbers of osteoblast and osteoclast cells expand to gradually replace the cartilage matrix with bone matrix. Further secondary ossification centres occur near to the epiphysis of the long bones. At the physis or growth plate, hypertrophic chondrocytes, proliferation of osteoblasts and mineralisation lead to continuing growth until the end of puberty.

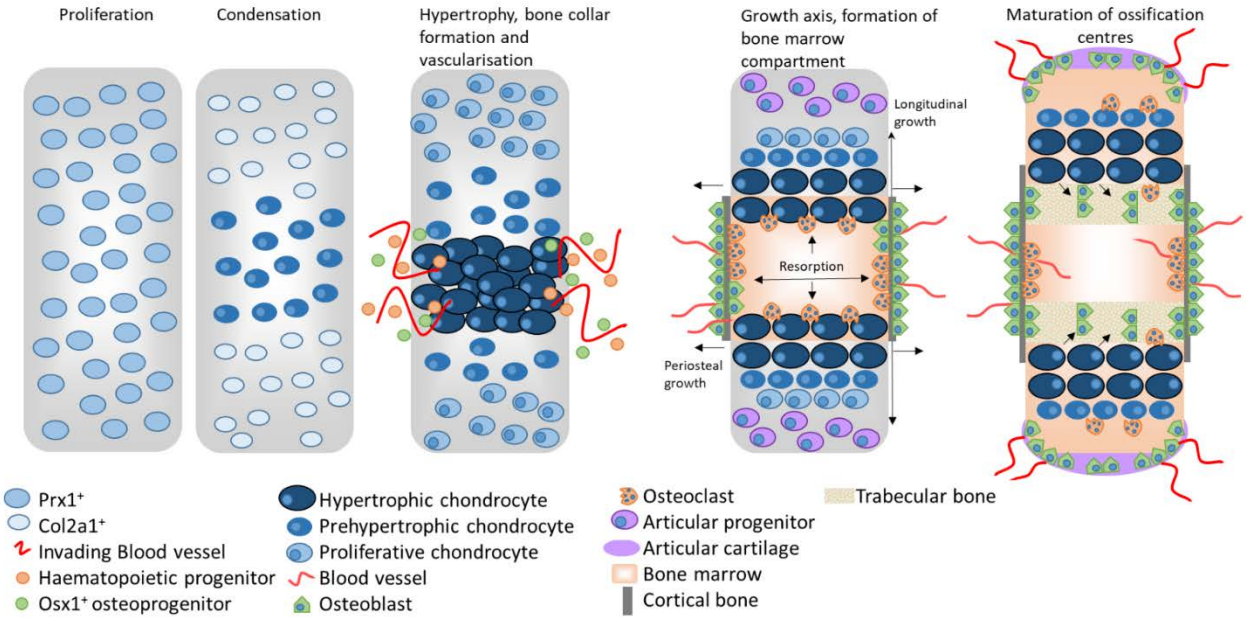

Figure 1 Endochondral ossification adapted from Salazar et al., (29).

Intramembranous ossification differs in the formation of bone, where the condensation of mesenchymal stem cells occur, these cells differentiate directly into osteoblasts to form bone (28). There are a number of signalling pathways associated with the control of bone development; Indian hedgehog plays a role in chondrocyte proliferation, differentiation and osteoblasts differentiation. It also interacts with parathyroid-related protein in a feedback loop to control chondrocyte hypertrophy.

Fibroblast growth factor signalling also has an effect upon proliferating chondrocytes rates and differentiation as do the bone morphogenic protein family (28).

1.2.2 The structure of bone

The structure of bone varies dependent on its function including structural support, protection and storage of cells and mineral ion homeostasis (30). Typically, it is composed of the mineralised bone matrix which is laid down by osteoblasts. The structure of bone can be considered at varying levels of scale and maturity. The mature lamellar bone structure can be considered on various levels of scale (30). Immature woven bone, however, differs in both function and structural composition than that of mature bone.

- Macroscopically mature bone can be divided in to cortical and cancellous and typically consists of a cortical bone cylinder surrounding a porous cancellous interior.
- The microstructure of cortical bone from 10-500µm is made up of the Haversian system, osteons and single trabecular.
- Below 10 µm are the lamellae
- The nanostructure of bone is made up of collagen fibres and hydroxyapatite crystals

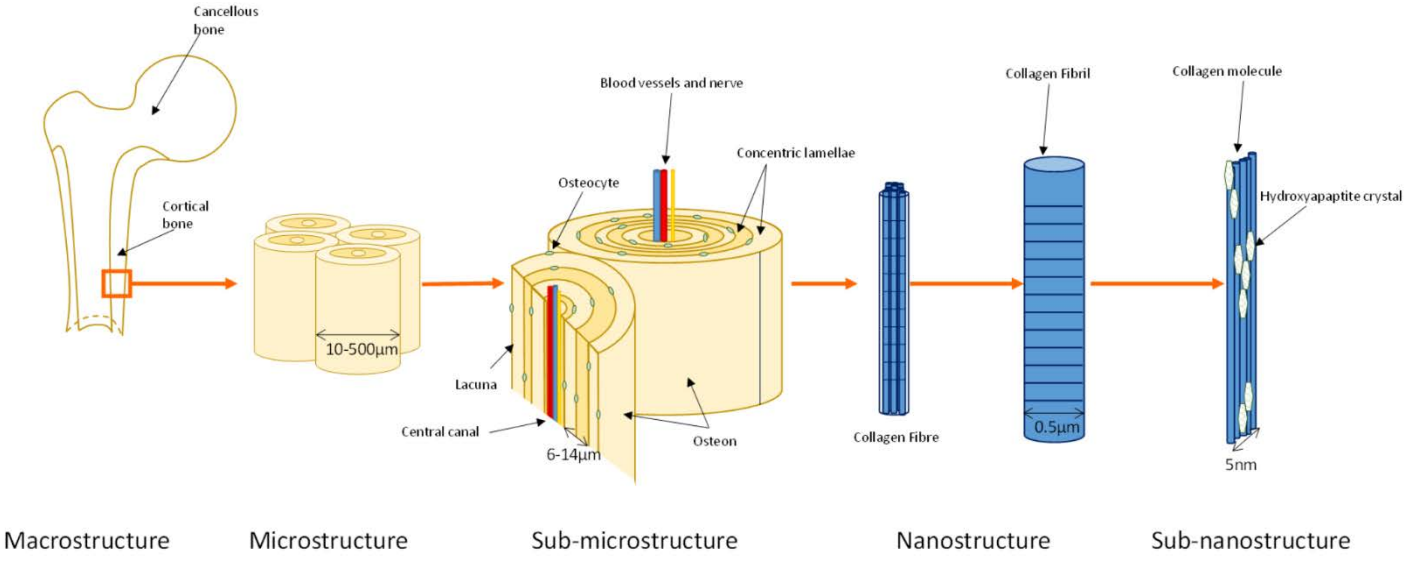

Figure 2 The structure and substructure of bone adapted from Rho et al., (30).

The fundamental building blocks of bone are the mineralised bone matrix which consists of hydroxyapatite crystals ($Ca_5(PO_4,CO_3)_3(OH)$), collagen fibres and non-collagenous proteins. The hydroxyapatite crystals are plate-shaped and dispersed among the gaps between the collagen fibres

(31). The average size of these plate-shaped crystals is 50x25nm and 2-3nm thick(32). The non-collagenous proteins are made up of phosphoproteins such as osteopontin, sialoprotein, osteonectin and Osteocalcin. These proteins may contribute to the regulation of crystal shape and deposition and also may function as a mineral ion reservoir for storage of Calcium and phosphate (30).
The most abundant component of the matrix is the collagen fibres, these are typically type I although there is type III, IV and VI present. The collagen molecules are secreted by the osteoblasts and form a triple helix made up of two α1 and one α2 polypeptide (33). The molecules are grouped together to create a fibril. The fibrils are typically 300nm long and 1.23nm wide, when grouped together they create a fibre, along with water and hydroxyapatite they make up the fundamental building blocks of bone.

The collagen fibres are grouped together to create lamellae which are typically 3-7µm thick (34). The orientation of the collagen fibres within the lamellae can either be parallel to the axis of the bone or perpendicular, this helicoidal structure was described by Giraud-Guille as a twisted plywood arrangement (35). These lamellae concentrically wrap around a central canal to form an osteon or Haversian system, this Haversian system is roughly 200-250µm in diameter and lie parallel to the long axis of the bone and make up the core component of bone microarchitecture. There are interconnecting canals between osteons; Volkmann's canals. Between the lamellar sheets are osteocytes, differentiated from osteoblasts they are concerned with bone homeostasis. They reside in lacuna which are connected and allows the relay of signalling molecules and nutrients via the canaliculi (36). Normal non-pathological bone can be either mature and lamellar in microscopic appearance or immature and woven. Lamellar bone makes up the core component of normal cortical and trabecular bone.

1.2.2.1 Woven bone

Woven bone on the other hand differs to that of lamellar bone in the arrangement of the mineralised collagen fibres. The collagen fibres within the woven bone are varying lengths and disorganised in their arrangement. This is in contrast to lamellar bone which is stress orientated. Osteocytes are also different been more rounded than elongated and fusiform as in cortical bone (37).

Woven bone exists as part of fracture repair. It is rapidly formed by osteoblasts by a process of endochondral ossification, remodelling then takes place and it is eventually replaced with lamellar bone. It also occurs at the primary spongiosa at the metaphysis during bone growth prior to remodelling (25, 38). It can also occur in relation to malignancy.

1.2.2.2 Lamellar Bone – Cortical and Cancellous bone

The organised microstructure and Haversian systems of lamellar bone give it strength and rigidity, and this can be related to its function. Lamellar bone can be either cortical or can be cancellous. Cortical bone and can be found in diaphyseal regions such as the femoral shaft and make the hard outer casing surrounding a softer cancellous interior. It gives the majority of the strength and rigidity to the skeleton. Cancellous, on the other hand, is found more in the metaphyseal regions and is more elastic than cortical bone. It is made up of connected trabecular struts with porous holes between which are filled with bone marrow. The trabecular struts are made up of flattened sheets of osteons which make up a honeycomb arrangement with each trabecular aligned along the lines of stress. Within the internals of the honeycomb is the bone marrow. The condition of this honeycomb arrangement peaks in early adulthood along with bone mass. This is followed by a slow decline with bone mineral density falling consistently as a feature of advancing age (3). This deterioration in bone microarchitecture with increasing porosity and reduced mineralisation levels affects men and women universally and leads to osteoporosis and an inherent weakening of the bone and increased risk of fracture with age (4, 5).

1.2.2.3 Bone Marrow

Bone marrow lies within cancellous bone and houses mesenchymal and haematopoietic stem cell (HSCs) populations and their progeny as well as adipose cells and stromal cells. Haematopoietic stem cells give rise to three core components (39):

- Myelopoietic cells
- Erythropoietic cells
- Thrombocytes (platelets)

These, in turn, differentiate into erythrocytes and the cells of the immune/lymphatic system among others. Haematopoietic stem cells have the lifelong clonal capacity to generate all blood cell lineages. They tend to be located along the endosteal lining of the bone or near to the endothelium of the penetrating capillaries or sinusoids (40). The stromal cells contain mesenchymal stem cells (MSCs) and their progeny, there are also connective tissue cells in the form of fibroblasts and endothelial cells. Mesenchymal stem cells can differentiate into osteoblasts, chondrocytes, adipocytes and myocyte cells.

1.2.3 Cell lines related to bone

There are three main cells concerned with bone homeostasis:

- Osteoblasts – derived from MSCs
- Osteoclasts – derived from HSCs
- Osteocytes – terminally differentiated from osteoblasts

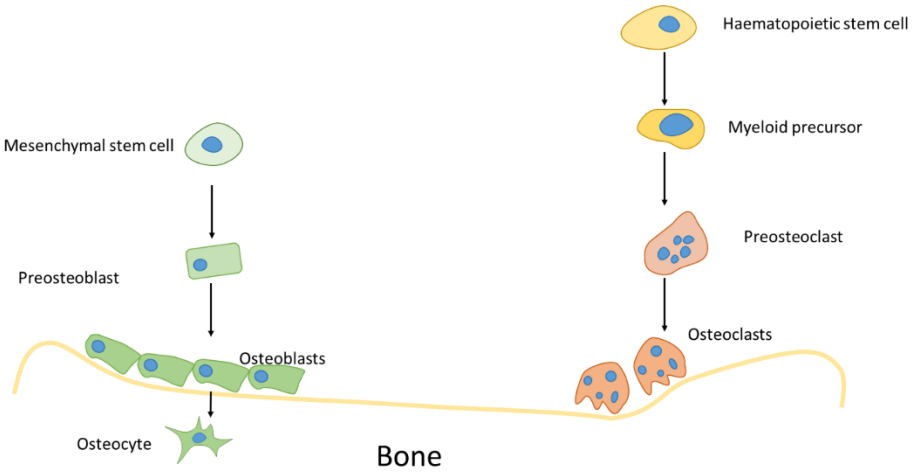

Figure 3 Differentiation of osteoblasts, osteoclast and their precursors.

1.2.3.1 Mesenchymal stem cells

Mesenchymal stem cells (MSCs) or marrow stromal cells as they are also known makeup 0.01% of the bone marrow cell population (41). They provide support to haematopoiesis through manipulation and control of the structural support and local microenvironment within the bone marrow. This environment contains regulatory growth proteins and encourages cell-cell and cell extra-cellular matrix interaction (42). They also have the ability to expand into a number of different cell lineages including those related to bone, cartilage, tendons, skeletal and smooth muscle and neural cells (43-46). The cytokine expression profile of MSCs is not identified in isolation but takes aspects of the progeny cell lines. It is however negative for the haematopoietic stem cell markers CD45, CD34 and CD14. There is also a strong expression of CD44 (47). Further identifying factors can be seen in *Table 1*. They can be harvested from bone marrow aspirates and manipulated *in vitro* to differentiate into a number of different cell lines including osteoblasts. The osteogenic differentiation capacity, surface marker and expression profile of MSCs have also been shown to be the same *in-vivo* and *ex-vivo* following expansion (48).

Marker Type	Designation
Specific Antigens	SH2,SH3,SH4, STRO-1, α-smooth muscle actin, MAB1740
Cytokines and growth factors	Interleukins: 1α, 6, 7, 8, 11, 12, 14 and 15, LIF, SCF, Flt-3 ligand, GM-CSF, G-CSF, M-CSF
Cytokine and growth factor receptors	IL-1R, IL-3R, IL-4R, IL-6R, IL-7R, LIFR, SCFR, G-CSFR, IFNγR, TNFIR, TNFIIR, TGFβIR,TGFβIIR, BFGFR, PDGFR, EGFR
Adhesion molecules	Integrins: αvβ3, αvβ5, Integrin chains: α1, α2, α3, α4, α5, αv, β1, β3, β4, ICAM-1, ICAM-2, VCAM-1, ALCAM-1, LFA-3, L-selectin, endologin, CD44
Extracellular matrix	Collagen type I, III, IV, V, and VI, Fibronectin, laminin, Hyaluronan, proteoglycans

Table 1 Main Characteristics of mesenchymal stem cells: Expression of Specific Antigens, Cytokine Receptors, Adhesion Molecules, and Production of Cytokines and Matrix Molecules (47).

1.2.3.2 Osteoblasts

As highlighted above osteoblasts are a derivative of MSCs. They are single nucleated cells and columnar in appearance. Their primary function is the secretion of the mineralised bone matrix. They secrete type I collagen along with the proteins osteocalcin and osteopontin. They also produce hydroxyapatite which is incorporated into the collagen framework to produce the mineralised matrix which gives bone its' structure and function. Pre-osteoblast stromal cells also influence osteoclast differentiation and osteoclastogenesis through the RANK receptor and RANK ligand (Receptor Activator of Nuclear Factor kappa-B ligand) as well as M-CSF and OPG (Osteoprotegerin).

RANK-L is a member of the TNF superfamily and causes differentiation of osteoclast progenitors, its action is blocked by OPG (49). The expression and release of RANK-L from osteoblasts and pre-osteoblasts are inhibited by testosterone and oestrogen and as a result, inhibit osteoclastogenesis and bone resorption (49).

OPG is a glycoprotein and also a member of the TNF superfamily. In mouse studies overexpression of OPG leads to osteopetrosis and an increase in bone mineral density. The action of OPG is to negatively regulate osteoclast maturation (50). It is expressed primarily by osteoblasts but also epithelial cells including those of the gastrointestinal tract, lung, breast and skin (51, 52) as well vascular endothelial cells, B-cells and dendritic cells (53). The expression of OPG is regulated through the Wnt/β-catenin signalling pathway, vitamin D_3, IL-1β, TNFα and oestrogens.

1.2.3.2.1 Osteoblast differentiation

There have been a number of papers linking mitochondrial dysfunction and MSCs differentiation anomalies. Kato et al., reviewed a patient with Leigh syndrome, a syndrome which is caused by mitochondrial dysfunction related to mitochondrial mutations.

Samples taken from this patient were associated with reduced osteoblastic differentiation potential. Mitochondria have an important role and function in the differentiation of MSCs and embryonic stem cells (54). During MSC differentiation to osteoblasts, mitochondrial activity is increased with concurrent increases in respiratory chain complex enzymes (55).

Differentiation of osteoblasts from MSCs is controlled by a number of protein signalling pathways. Runx2 (runt-related transcription factor 2) is a transcription factor and regulator at the intersection of many differentiation control pathways. It has been shown to bind to the Osteocalcin promoter and be present in osteoblast progenitors as well at osteoblast differentiation (41).

Expression of Runx2 and other factors along with osteoblast differentiation are controlled by multiple pathways including the Bone Morphogenic Protein (BMP), Wnt and Notch pathways:

BMP is a member of the transforming growth factor-β cytokine superfamily. There are two BMP receptors (BMPR-I and II). Once BMP binds these receptors this causes phosphorylation of Smad proteins which in turn translocate to the nucleus as transcription factors including Runx2 (56).

The Wnt family of secreted glycolipoproteins are directly linked to cell proliferation, polarity and cell fate at embryogenesis (57). The Wnt signalling pathway is important in the regulation of bone remodelling, homeostasis, differentiation of osteoblasts and maintenance of bone mineral density. The Wnt pathways can be classified as canonical signalling through β-catenin or non-canonical which is not reliant on β-catenin. Wnt binds the transmembrane receptor – Frizzled in combination with the Lipoprotein receptor related protein 5 (LRP5), this leads to β-catenin accumulating and this then leads to transcription factor activation *see Figure 5*. The non-canonical pathway also acts via the Frizzled receptor but requires other co-receptors. As highlighted in 1.3.1.3 mutations in LRP5 can lead to high bone mineral density (BMD) (58, 59)as well as decreased BMD and osteoporosis (60). Murine studies have also shown defects in β-catenin leads to osteoporosis (61).

Wnt signalling role in osteoblastogenesis is conflicting Bennett et al., found canonical signalling via Wnt 10b or GSK3 inhibition promotes osteoblastogenesis (62) However other studies have shown that canonical Wnt signalling sustains MSCs in a proliferative and undifferentiated lifecycle compared with the non-canonical which leads to osteoblastogenesis (63).

Intracellular calcium is reported to activate the Wnt/ β-catenin pathway and subsequent osteoblast differentiation. Lower levels of intracellular calcium were found in samples with mitochondrial disease these also had lower levels of osteoblasts than the control cohort (54).

Notch protein, a transmembrane receptor is also important in the differentiation pathway of MSCs to osteoblasts. Notch protein interacts with the membrane bound ligands Delta or Jagged and this leads to activation of transcription factors leading to improved osteoblastogenesis, however, notch may not increase osteogenesis (41).

All three of the above pathways target Runx2 which lead to osteoblast differentiation genes been activated, the hedgehog and fibroblast growth factor family proteins have also been implicated. Again it has been suggested that the hedgehog proteins act through Runx2 to cause osteoblastogenesis (64). Of the hedgehog proteins, the Indian hedgehog and Sonic hedgehog proteins have been shown to have a role in osteoblastogenesis. They bind the surface receptor Patched which then stops patched-mediated suppression of the transmembrane protein Smoothened. This leads to activation of intracellular signalling and the stabilisation of the Gli2 transcription factor. Gli2 then leads to transcription of Gli1 and Hh genes (65).

Fibroblast growth factors (FGF) stimulate the differentiation of multiple cell lines including pre-osteoblasts. FGF may modulate Runx2 and so have an impact upon osteoblastogenesis. FGF has been shown to increase osteoblast generation in conjunction with BMP-2 in murine studies (66). However, it has also been shown to antagonise Wnt-mediated osteogenesis (41).

Overall osteoblastogenesis is under a complex array of pathways which act centrally through the Runx2 transcription factor.

1.2.3.2.2 Osteoblast Markers

Osteoblasts are derived from MSCs and as a result share a pool of surface markers and genes *(Table 1*) with other cells of this lineage. However, there are 3 independent proteins activating Runx2 as highlighted above which is a crucial component in a number of pathways leading to osteoblast differentiation. Osterix and Osteocalcin are also unique factors related to osteoblasts.

Osterix or transcription factor Sp7 is expressed in pre-osteoblasts which express Runx2 and type I collagen. It leads to the development of pre-osteoblasts into osteoblasts and subsequent bone formation both by intramembranous and endochondral ossification with abnormalities in mineralisation occurring in its absence. (67). Sp7 also inhibits chondrocyte differentiation (68) and mutations have been associated with osteogenesis imperfecta and osteoporosis (69).

Osteocalcin is a non-collagenous protein secreted solely by osteoblasts and strongly expressed by mature osteoblasts it accounts for 10-20% of the non-collagenous proteins within the bone (70). It is a 49-amino-acid peptide that is secreted into the bone matrix and the blood as an uncarboxylated form (71). As well as its primary role concerned with bone homeostasis it also has a hormonal role acting on beta cells within the pancreas to release more insulin and adipose cells to release adiponectin increasing insulin sensitivity (72).

Osteocalcin levels during bone development are low but increase with the onset of puberty and increased mineralisation (73), levels can also be increased in relation to increased bone turnover and conditions associated with this such as primary and secondary hyperparathyroidism, hyperthyroidism, or acromegaly. Conditions where there is a decreased rate of bone formation such as hypothyroidism, hypoparathyroidism, and glucocorticoid-treated patients, are associated with low levels (74).

Osteocalcin undergoes post-translational modification where glutamic acid residues are carboxylated to form γ-carboxyglutamic acid residues. The glutamic acid residues are vitamin K dependent and have a high affinity for calcium ions (75) although loss and gain experiments have not found any purpose of the glutamic acid residues in osteoblast driven mineralisation of the extracellular protein matrix (76, 77).

Ducy et al., also found that Osteocalcin knock out mice developed increased cortical and cancellous bone with increased bone mineral density. However, mice also deficient in Osteocalcin were shown

to have abnormal larger hydroxyapatite crystals and decreased levels of mineralisation (78). It is suggested that Osteocalcin has a role in regulating bone mineralisation and maturation although the exact role is not clear (73).

1.2.3.2.3 Osteoblast function and bone mineralisation

Osteoblasts, as highlighted above, are differentiated from MSCs prior to this terminal differentiation they are pre-osteoblasts. Once terminally differentiated osteoblasts appear as cuboidal cells lying along layers of immature osteoid. Integrins, connexins and cadherins tightly bind the osteoblasts to one another and to the surface of the bone (79). During the proliferative phase, they also acquire alkaline phosphatase activity, something pre osteoblasts do not possess. They also possess increased endoplasmic reticulum, Golgi apparatus and mitochondria in comparison to other cells. This is to account for their increased metabolic activity and syntheses and secretion of the matrix (25).

They take on two forms those which are more metabolically active lining the bone surfaces at the endosteal and periosteal membranes and those less active which maintain ion balance and are entrapped within the resting regions.

The two main functions of osteoblasts are to regulate osteoclast differentiation and activity as highlighted above and to form bone. Osteoblasts secrete both collagen and non-collagenous proteins as part of the mineralisation process. Type I collagen molecules are secreted becoming triple helixes and then fibrils which make up fibres. The fibrils are impregnated with hydroxyapatite crystals. These crystals are transported from the osteoblasts in alkaline phosphatase-rich vesicles (80). As the crystals enlarge the vesicles rupture. The crystals become interspersed with the collagen fibrils and continue to grow (81, 82). Mitochondrial calcium plays an important role in mineralisation and supplies the calcium for the vesicles (80, 82).

1.2.3.2 Osteocytes

Some of the osteoblasts become trapped within the newly formed matrix which they deposit around them, this triggers a terminal differentiation process and they become osteocytes (25).
Osteocytes have a role in bone maintenance. They have a high nuclear to cytoplasm ratio and project cytoplasmic process along the canaliculi to create a network to communicate and allow the exchange of molecules. They have a minimal role in mineralised matrix production but have a more significant role in ion (calcium and phosphorous) homeostasis. Calcium storage is stimulated by calcitonin and

inhibited by parathyroid hormone as part of the calcium maintenance. They also secrete sclerostin which has a negative effect on osteoblast activity (25).

1.2.3.3 Osteoclasts

Osteoclasts are multinucleated cells from haematopoietic stem cell lineage. They are aggregations of giant cells and their primary function is to resorb bone. This can be part of a pathological or normal homeostatic process. The activation and process of osteoclastogenesis is covered in 1.2.3.2
Unlike the cuboidal osteoblast, the multinucleated osteoclasts possess a ruffled brush border with the cell membrane infolding to increase the surface area for bone resorption. Integrin $\alpha_v\beta_3$ and other anchoring proteins bind to the bone surface sealing the space below the osteoclast (83). Hydrogen ions produced via the activity of carbonic anhydrase cause the pH to reduce which increase the solubility of the hydroxyapatite crystals (25). The organic matrix is removed through enzymatic activity of cathepsin K and TRAP (tartrate-resistant acid phosphatase). Cathepsin K is a lysosomal cysteine protease able to break down collagen. TRAP or tartrate-resistant acid phosphatase is a synthesised glycosylate monomeric metalloproteinase released by osteoclasts. It causes dephosphorylation of some the proteins of the mineralised matrix including osteopontin and bone sialoprotein (84). These proteins bind osteoclasts and inhibit osteoclast activity when in phosphorylated form. It is highly expressed in osteoclasts but not exclusive to osteoclasts and is expressed by macrophages and other cells elsewhere in the body.

The resorption of bone is an energy-dependent process, ATP is needed for this process and in particular to drive the proton pump for secretion of acid. Osteoclasts like osteoblasts have increased mitochondrial mass and activity and this has been shown to increase from haematopoietic stem cells lines through to pre-osteoclasts and final differentiation into osteoclasts (85, 86). The complex I deficient mouse model used by Jin et al., (87) based upon an essential deletion of the Ndufs4 sub unit led to a phenotype showing systemic inflammation and osteopetrosis. Normal mitochondrial function supresses macrophage activation and inflammation and so promote osteoclast differentiation leading to bone resorption. The complex I deficiency also saw a drive towards glycolysis from, fatty acid oxidation. The creation of fatty and lactic acids as a consequence also further decreases osteoclast differentiation with monocyte precursors shifting to a macrophage lineage. RANK and FMS receptor expression within the bone marrow was also downgraded compared with wild type mice. Fatty acid generation has also previously been shown to inhibit osteoclastogenesis (88).

Further links have been established with mitochondrial dysfunction and osteoclastogenesis. Peroxisome proliferator–activated receptor-γ coactivator 1β (PGC-1β) coded for by Ppargc1b, has been shown to have in-vitro and in-vivo murine effects. PGC-1β was induced during osteoclast differentiation by cAMP response element binding protein as a result of reactive oxygen species. Impairment of Ppargc1b transcription led to inhibited in-vitro decreased osteoclast differentiation. Ishii et al. also established that mitochondrial biogenesis orchestrated by PGC-1β, together with iron uptake mediated through transferrin receptor 1 to supply mitochondrial respiratory proteins, as a fundamental pathway linked to osteoclast activation and resultant reduced bone resorption (89).

ROS (reactive oxygen species), which are produced by mitochondria as a by-product of the electron transport chain, during normal respiration as well as in times of oxidative stress. Generation of mitochondrial ROS increases under hypoxic conditions, ischaemia and reperfusion injuries, chemical stressing and drug treatment as well as other pathological conditions (90). These ROS have also been shown to be a driving factor in osteoclastogenesis. Osteoclasts have been shown to produce ROS (91-93) and also be activated by them (94, 95). Ha et al. showed that the addition of antioxidants to culture caused reduced osteoclast formation by 30% in culture. Antioxidants were shown to affect both RANKL and M-CSF activity and subsequent osteoclastogenesis and subsequent osteoclast survival. ROS production induced by RANKL participate within the RANK signalling cascade (96). Again Srinivasan et al., showed that inducing mitochondrial respiratory stress of macrophages led to retrograde signalling and tartrate-resistant acid phosphatase cells. The introduction of antioxidants again reduced the level of RANKL induced osteoclastogenesis (90).

The mitochondrial apoptotic pathway has also been shown to be active in osteoclasts. Following removal of stromal cells there is an increase in hydrogen peroxide concentrations leading to hydroxyl free radical generation and activation of cytochrome c, this leads to formation of apoptosome and activation of caspse-3-like and caspase-9 (86). The Fas receptor and Fas ligand have also been implicated in apoptosis in osteoclasts. Fas is up regulated during osteoclast differentiation and the activation leads to mitochondrial release of cytochrome c. Mice with Fas defects were found to have an increased number of osteoclasts leading to decreased bone mineral density, bone volume, trabecular thickness (97).

Bisphosphonates which are used to treat osteoporosis cause osteoclast apoptosis, they have a high affinity for mineralised tissue localising their effects to bone (98). They function by generating a toxic

analogue of adenosine triphosphate which targets the mitochondria and induce apoptosis. Nitrogen bisphosphonates work via a different mechanism; farnesyl diphosphate synthase in the cholesterol biosynthetic pathway is inhibited suppressing geranylgeranylation which is a process required for osteoclastic bone resorption (99). Geranylgeranylation is a post translational modification of proteins where the addition of one or two lipophilic geranylgeranyl isoprene units are added. It is a form of prenylation and thought to act as a membrane anchor for proteins (100).

Mitochondrial calcium storage is also implicated in normal osteoclast function. Experiments involving rat femurs have shown increased calcium granulations within the mitochondria at the brushed border of the osteoclast compared to those elsewhere in the cell (101). The resorbed calcium would have the potential to lead to an intracellular concentrations increasing and triggering of apoptotic pathways (102).

1.2.4 Bone homeostasis

Bone is under a constant cycle of turnover mediated by osteoclastic resorption and new mineralisation by osteoblasts. Although osteoclastic resorption is followed by osteoblast mineralisation no clear evidence has linked the two processes, but current evidence suggests multiple factors play a role. IGF and TGFβ may be released in resorption stimulating osteoblast activity. Equally, factors deposited by osteoclasts have been linked to osteoblast activity. Humoral factors such as parathyroid hormone and prostaglandin E cause an increase in resorption and mineralisation respectively. There is also the interaction between osteoblasts and osteoclastogenesis as highlighted earlier. Mechanical factors also have a role in bone remodelling (26). There are many influences on skeletal homeostasis as can be seen in *Figure 4*.

This constant cycle of bone turnover is at its peak during childhood which explains their ability to remodel after fracture quicker than adults. There is a slow decline in formation compared to resorption until the age of 30 following this point resorption takes precedent (3). The estimated bone turnover for adults is 4% for cortical bone and 25% for trabecular bone per year (103).

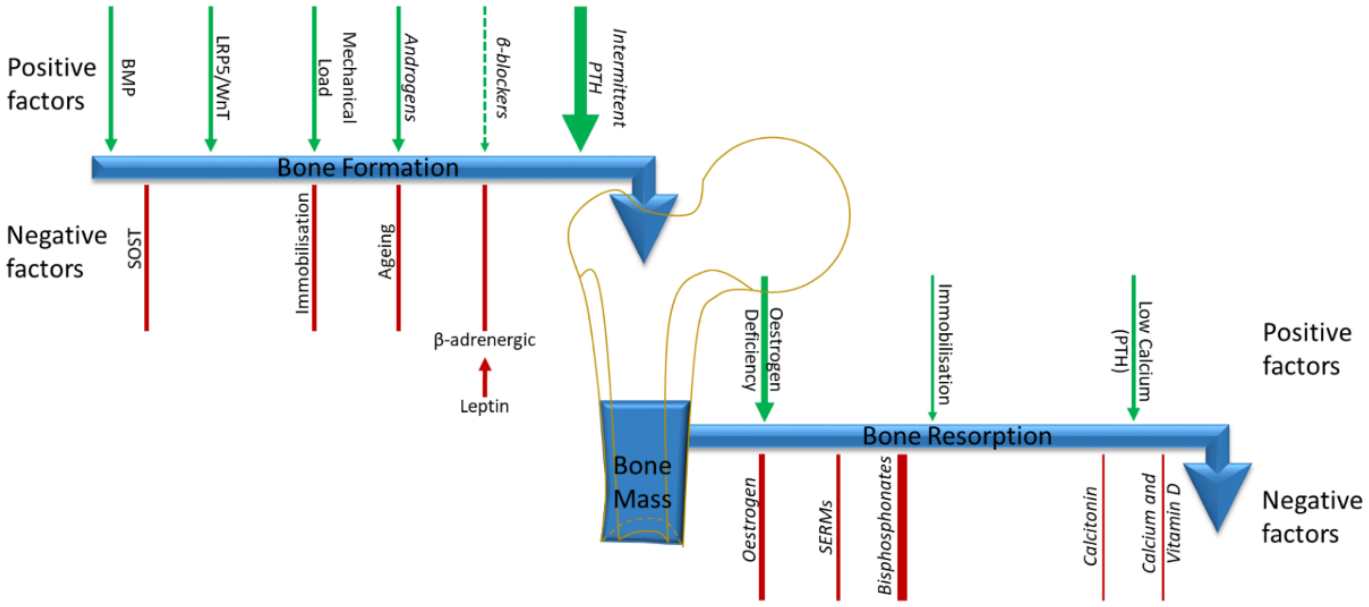

Figure 4 Skeletal homeostasis and bone mass. Negative factors on resorption and formation are shown in red whereas positive factors are shown in green. Pharmacological factors are marked in italics. The relative impact, where known, is represented by the thickness of the arrows. Solid lines are current therapies and dotted lines putative ones. Abbreviations: BMP, bone morphogenetic protein(s); SOST, sclerostin; LRP5, low-density lipoprotein (LDL)-receptor-related protein 5; PTH, parathyroid hormone; SERM, selective oestrogen-receptor modulator. Adapted from (104).

1.2.4.1 Parathyroid hormone and calcitonin

Parathyroid hormone is secreted by the chief cells of the parathyroid gland in response to low serum calcium. Parathyroid hormone (PTH) acts upon the parathyroid hormone 1 receptors found in the

kidneys and bone. It also acts on the parathyroid hormone 2 receptor, which is present in the central nervous system, pancreas and testes.

In bone, the action of PTH is to increase bone resorption and indirectly osteoclast activity. Osteoclast activity is increased by way of osteoclastogenesis. To do this PTH binds to osteoblasts increasing expression of RANK-L and down-regulating the expression of OPG (*see 1.2.3.2)* this action increases the pool of mature osteoclasts and subsequently leads to the breakdown of mineralised matrix releasing calcium into the bloodstream (105). PTH also acts upon the kidneys leading to increased calcium reabsorption. In the gastrointestinal tract, it leads to the activation of vitamin D (25-hydroxycholecalciferol to 1,25-dihydroxycholecalciferol) which also increase calcium absorption in the gastrointestinal tract gut (106).

Calcitonin is produced by the parafollicular cells of the thyroid and antagonises PTH by raising serum calcium. Calcitonin is released in response to raised serum calcium and also gastrin and pentagastrin (107). Calcitonin inhibits osteoclastic activity there is no evidence suggesting an effect upon osteoblasts or bone formation. Osteoclasts have a large number of calcitonin receptors through which calcitonin acts to inhibit osteoclast activity and reduce bone resorption and the release of calcium into the serum (108). Calcitonin receptors can also be found on mononuclear osteoclast precursors as well as in the kidney and brain.

A number of other factors related to bone homeostasis in terms of hormonal and metabolic components are discussed in 1.3

1.3 Current Theories in Osteoporosis pathology

Osteoporosis can be age-related referred to as primary osteoporosis or secondary related to other medical conditions or side effects of pharmacological agents (Table 2). Osteoporosis is essentially a result of the imbalance between osteoclastic resorption and osteoblast bone formation. Intrinsic factors that determine the risk of osteoporosis and fractures include ageing in addition to genetic, hormonal and metabolic factors (109).

Causes of Secondary Osteoporosis in Premenopausal Women

Pharmacologic or toxic treatment	Malnutrition or malabsorption
Glucocorticoids	Anorexia nervosa
Antiepileptic Medication	Inflammatory intestinal disease
Aromatase inhibitors	Coeliac disease
Heparin	Intestinal resection
Alcohol	Chronic inflammatory disease (rheumatoid arthritis, SLE, etc.)
LHRH analogues	Liver Disease
Endocrine Diseases	Osteogenesis imperfecta
Hypogonadism	Transplant patients (solid organs and bone marrow)
Hyperthyroidism	HIV infection
Cushing's disease	Haemochromatosis
Growth Hormone deficiency	Idiopathic osteoporosis
Panhypopituitarism	Osteoporosis associated with pregnancy
Hyperparathyroidism	Systemic macrocytosis

Table 2: Causes of Secondary Osteoporosis in Premenopausal Women (110).

1.3.1 Genetic factors in Osteoporosis

Genetic factors in osteoporosis and reduced of bone mineral density in have been estimated to be present in 50 to 85% of patients, whereas fracture heritability has ranged from 25 to 68% (111, 112). Current evidence suggests that hereditary bone loss is under polygenic control. Although evidence suggests only 4-5% of the genetic variation in BMD can be accounted for by alleles which are associated with BMD (113).

1.3.1.1 Type 1 Collagen genetic defects:

Type 1 collagen makes up a major component of bone. The collagen fibrils act as a scaffold upon which hydroxyapatite crystals are laid down upon. The mineralisation of the collagen fibrils, water

content and their orientation relate to the strength of the bone. The proportions of collagen fibrils, hydroxyapatite and water vary depending on location and type of bone (114).

Type 1 collagen is encoded by the *COL1A1* and *COL1A2* genes that code for the α1 and α2 protein chains of type 1 collagen respectively. These genes have been extensively researched in relation to osteoporotic fractures. Polymorphisms at the Sp1 binding site have been reported to be associated with susceptibility to osteoporotic fractures. The polymorphism causes an imbalance in the α1 and α2 protein chains with over transcription of the COL1A1 gene and abnormality in bone mineralisation (115). Bone cores from G/T heterozygotes have significantly reduced bone strength ex-vivo than those from G/G homozygotes and are less well mineralized (116, 117)

1.3.1.2 Oestrogen receptor 1

Oestrogen has a significant role in osteoporosis and there is a clear decline in bone mineral density associated with the menopause. Oestrogen receptor 1 (ESR1) polymorphisms contribute to osteoporosis and fragility fractures but the exact mechanism of their action is unclear (113).

1.3.1.3 Lipoprotein receptor related protein 5

Lipoprotein receptor related protein 5 (LRP5) was first discovered in association with the LRP5 loss of function mutations in osteoporosis pseudoglioma syndrome a recessive disorder characterised by low bone mass and abnormal eye vasculature (118). In contrast, patients with the autosomal dominant high bone mass disease with an LRP5 missense gain of function mutation have high bone mineral density. This mutation causes the LRP5 receptor to become resistant to binding by sclerostin. Mutations in the *SOST* gene that encodes for sclerostin cause high bone mass disorders. From this, it has been deduced that the LRP5 complex plays a role in bone mass regulation via osteoblast proliferation whereas *SOST* which is expressed by osteocytes negatively regulate bone mass and antagonise LRP5 (119).

The LRP5 protein is a binding site for the Wnt pathway. The Wnt family of secreted glycolipoproteins are directly linked to cell proliferation, polarity and cell fate at embryogenesis (57). The Wnt signalling pathway is important in the regulation of bone remodelling, homeostasis, differentiation of osteoblasts and maintenance of bone mineral density. The Wnt protein signal functions by regulating the amount of transcriptional co-activator β-catenin that controls key developmental gene expression programs (119). The role of LRP5 and Wnt proteins in osteoporosis has meant that Wnt antagonists have become targets for potential therapeutics in osteoporosis (120).

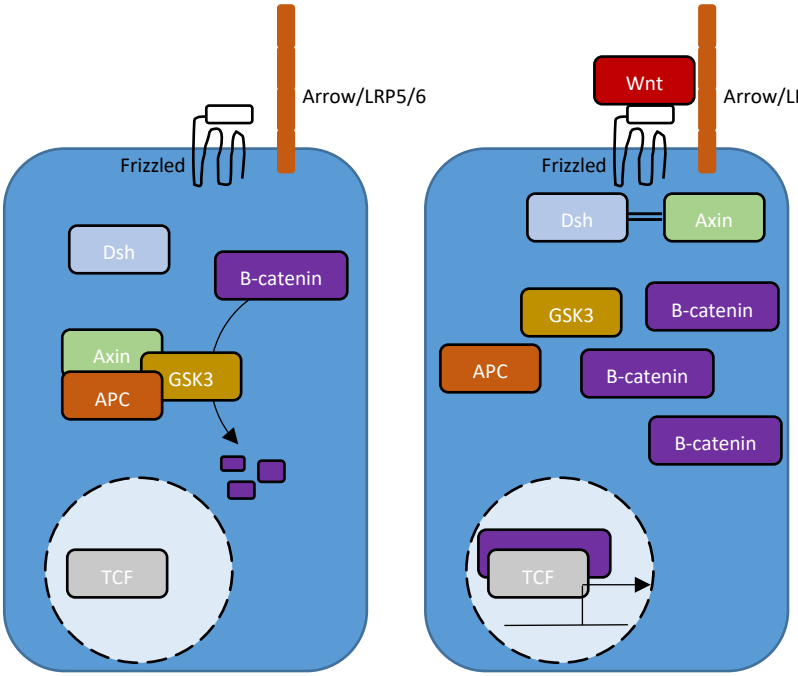

Figure 5 The Wnt Pathway (57) The frizzled/LRP5 complex is bound by the Wnt protein. This induces a signal to intracellular proteins preventing the breakdown of ß-catenin. An abundance ß-catenin within the cell and nucleus interacts with transcription factors and the activation of certain genes targeted by the Wnt signalling pathway.

1.3.1.4 Sclerostin

As highlighted, sclerostin is encoded by the *SOST* gene, is produced almost only by osteocytes, and antagonise the Wnt proteins from binding. Inactivation of sclerostin by mutations prevent this antagonistic effect and lead to high or increased BMD. This effect has been utilised as a treatment for osteoporosis in the form of monoclonal anti-sclerostin antibodies (121).

1.3.1.5 Transforming growth factor β1

Transforming growth factor β1 (TGF- β1), is thought to act as a coupling factor between bone formation and resorption. It is not thought to contribute significantly to the genetic regulation of bone mineral density (113). However, a recent meta-analysis showed that polymorphisms (TGF-β1 T869C and TGF-β1 T29C) are correlated with postmenopausal osteoporosis (PMOP) risk. This risk was associated with an Asian population rather than Caucasian population (122).

1.3.2 Hormonal

1.3.2.1 Sex Hormones

Oestrogen and testosterone have established roles in bone homeostasis. Testosterone contributes to longitudinal and positional bone growth whereas oestrogen is more important in the maintenance of trabecular volume and bone strength (123). Something, which declines with osteoporosis.

Androgen and oestrogen receptors are expressed in osteoblast and osteocytes but also epiphyseal chondrocytes and growth plate cartilage cells, (124). In vitro studies have shown that both testosterone and oestrogen contribute to increase BMD by inhibiting osteoclast proliferation and activity. This action is thought to be through the RANK ligand of osteoblasts and RANK receptor of the osteoclasts. Sex hormones also appear to inhibit interleukin (IL)-1α, -6 and tumour necrosis factor (TNF) –α which may activate the RANK/RANKL receptor (125) see *Figure 6*.

Males have a higher bone mass than females but men with hypogonadism either primary or secondary also have reduced bone mineral density (49). However, the androgen levels are better preserved than oestrogen levels in females and this provides a relative maintained higher bone mass than women.

Following the menopause and natural decline in androgens for males, there is increased osteoclastic activity due to increasing RANKL expression in marrow cells (126). Consequently, osteoclastic activity exceeds osteoblastic activity and there is a loss of bone mineral density.

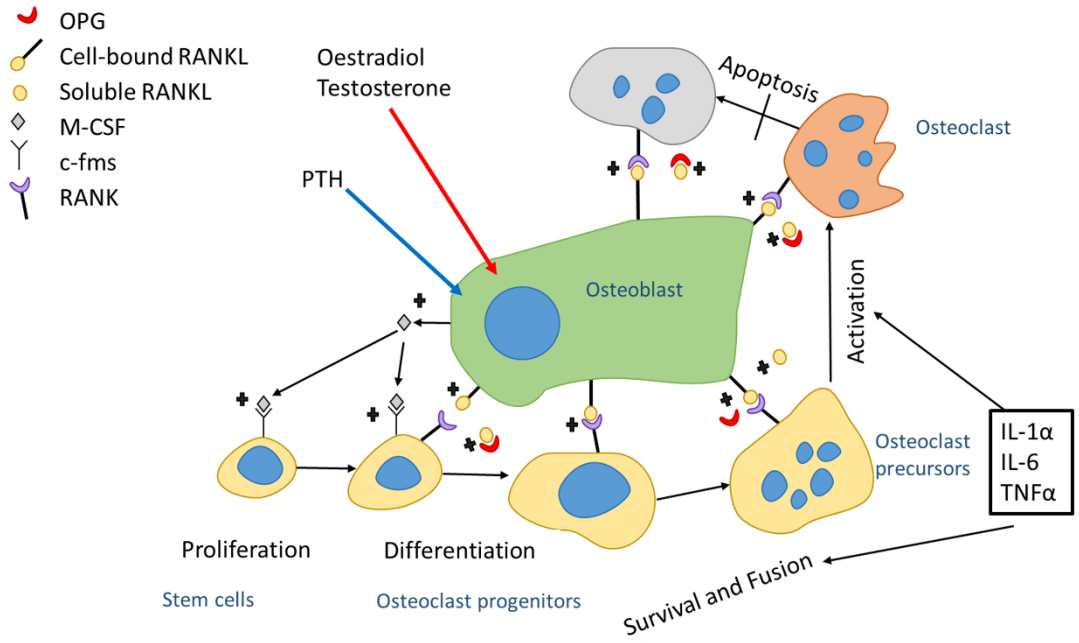

Figure 6: Osteoclast proliferation and differentiation are under the control of cytokines such as macrophage colony stimulating factor (mCSF) binding to the Macrophage colony-stimulating factor 1 receptor (c-fms) and Receptor activator of nuclear factor Kappa-B ligand (RANKL). The RANK receptor on osteoclasts is bound by RANKL secreted from osteoblasts or bound to the osteoblast cell membrane. RANKL expression is inhibited by the sex hormones oestradiol and testosterone; in contrast, parathyroid hormone (PTH) increases RANK expression. Interleukins 1 and 6 as well as tissue necrosis factor IL-1α, IL-6 and TNFα also play a role in osteoclast differentiation (49).

1.3.2.2 Glucocorticoids

Glucocorticoids represent probably the most common cause of secondary osteoporosis (127). Glucocorticoids cause decreased absorption of calcium from the gut and increased excretion from the kidneys leading to increased levels of parathyroid hormone and osteoclastic action leading to bone mineral density loss. Glucocorticoids also have a negative influence on osteoblast populations and also result in reduced bone formation (127). Glucocorticoid levels are known to increase naturally with age (128). These increasing levels of endogenous glucocorticoid contribute to the pathogenesis of osteoporosis and age.

Glucocorticoids directly affect osteoblasts via the Wnt signalling pathway. Wnt signalling pathways are regulated by secreted antagonists including dickkopf (Dkk) (129). Glucocorticoids enhance the expression of dickkopf-1 (Dkk-1) in human osteoblasts (130). Glucocorticoids, therefore, suppress the canonical Wnt signal and suppress the differentiation and development of osteoblasts (130).

1.3.2.3 Insulin

Osteoporosis poses significant risks to patients with diabetes. Women with type 1 diabetes were 12 times more likely to report hip fractures whereas women with type 2 diabetes had a 1.7 times increase compared to normal (131).

Type 1 diabetics (T1DM) have higher rates of bone resorption and turnover due to the effects of secondary hypoparathyroidism, hypomagnesaemia and lower levels of circulating vitamin D. Small vessel disease is as a complication of diabetes is also thought to contribute to the development of osteoporosis (131). Obesity and Type 2 diabetes (T2DM) are closely related. In males excess adipose tissue leads to increased aromatase activity and increased conversion of testosterone to oestradiol, these raised oestradiol levels lead to relative protection from osteoporosis (132).

Impaired fracture healing has been observed clinically as well as in vitro cell culture studies in patients with T1DM and T2DM. Such in vitro studies showed that raised circulating insulin levels lead to increased urinary calcium excretion. Advanced glycation of end products may also contribute to poor bone strength and fragility (133).

1.3.3 Metabolic

1.3.3.1 Vitamin D Deficiency

Vitamin D deficiency has been associated with osteoporosis it has also been utilised as a treatment regime (134). Vitamin D is derived from two sources in humans; UV-B radiation from sunlight exposure and dietary intake (135). Ergocalciferol or VitD2 is present in plant matter following the irradiation of ergosterol (134). Cholecalciferol or VitD3 is created by irradiation of 7-dehydrocholesterol in the human epidermis and also found in oily fish and supplements (135). Vitamin D levels impact on bone homeostasis by way of deregulation of calcium homeostasis with increased levels of parathyroid hormone. Its' role along with parathyroid hormone is to essentially increase calcium transport within the intestine, bone and kidneys. Raised calcium levels have negative feedback on the parathyroid gland. Reduced parathyroid hormone leads to less bone resorption by osteoclasts. Adequate supplies of vitamin D in the form of 1,25-(OH)2D aid in the maintenance of adequate serum calcium without excessive bone resorption (134).

A review published by the European Society for Clinical and Economic Aspects of Osteoporosis and Osteoarthritis demonstrated that patients with a serum 25-hydroxyvitamin D (25-(OH)D) levels <50 nmol/L have increased bone turnover, bone loss, and possibly mineralisation defects compared with

patients with levels >50 nmol/L. These findings also correlated with an increased risk of fragility fractures (136). They also suggest that patients with below 50 nmol/L should be given prophylactic supplementation to reduce fracture risk.

1.3.3.2 Metabolic acidosis

In the normal subject, a balance exists between endogenous acid production and renal excretion. If excretion capacity decreases or acid production increases there is an excess of acid leading to release of alkali calcium salts in bone (137). It is suggested that calcium is either dissolved from bone mineral directly or through the stimulation of cell-mediated bone resorption in response to metabolic acidosis (138). This has been shown conclusively in a rat model. Rats exposed to metabolic acidosis for two weeks had increased rates of bone resorption and decreased bone formation compared to controls over the same period (138).

The ongoing release of alkali from bone leads to hypercalciuria and hypophosphataemia due to an increase-filtered load and decreased renal reabsorption. This utilisation of alkali and loss of calcium from the body leads to a loss of bone mineral density (139). This loss of bone mineral density leads to the development of osteoporosis.

1.4 Mitochondria

1.4.1 Mitochondrial Genetics

The most widely accepted hypothesis regarding mitochondrial origin is one of endosymbiosis and a defining event in the evolution of eukaryotic cells (140). Mitochondrial DNA has been traced back to members of the rickettsial subdivision of the α-Proteobacteria.

1.4.1.1 Mitochondrial Genome

Mitochondrial DNA has the same fundamental role in all eukaryotic cells. In humans, it is made up 16,569 base pairs and is composed of a double-stranded cytosine-rich light (L) and guanine-rich heavy (H) strands in a circular configuration *Figure 7* (21). Human mitochondrial DNA harbours 37 genes. These genes encode for 13 polypeptide complexes, which make up components of the respiratory chain complexes. They also encode two ribosomal RNAs for mitochondrial transcription and 22 transfer RNAs. All the other proteins required for mitochondrial function and the oxidative phosphorylation pathway are encoded within nuclear DNA (141).

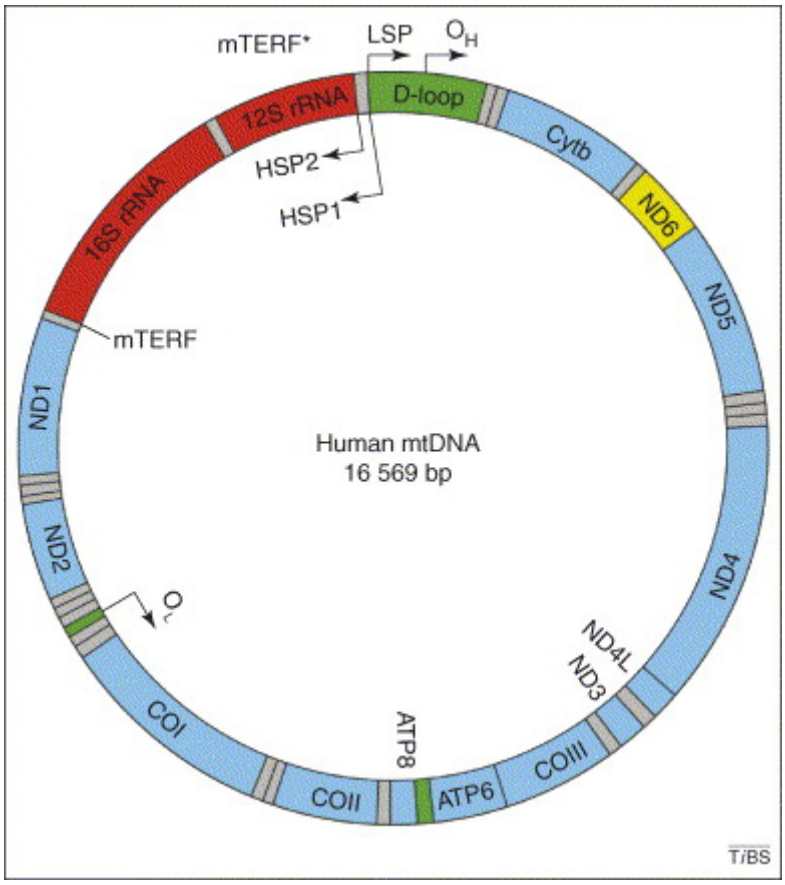

Figure 7 Schematic representation of the human mtDNA genome, the genome codes for 13 proteins, 22 tRNAs and 2 rRNAs are mapped. The two strands of the mtDNA are designated heavy and light (142).

1.4.2 Mitochondrial Structure

Some of the first organelles viewed under electron microscopy were mitochondria. Sjostrand's model contained inner and outer membranes (143) whereas Palade's model which depicts the double membrane and internal folding or cristae mitochondriales which have become accepted today (144). In Palade's model, there are two internal compartments the intermembrane space and the matrix within the internal membrane (145). Within the matrix, multiple copies of the mitochondrial DNA are located (144). The outer membrane is composed of a phospholipid bilayer with many pores to allow the exchange of the metabolic intermediates and nucleotides between the cytoplasm and mitochondrial matrix (146). It allows passage of molecules up to 5,000 Daltons permeated by voltage-dependent anion channels (VDAC) (147). The inner membrane is composed of approximately 70% protein and 30% lipids (148). The inner membrane houses the proteins of the oxidative phosphorylation pathway responsible for the generation of energy for cellular function and metabolism (149).

1.4.3 Mitochondrial Function

One of the mitochondria's main function is to provide biological energy by oxidation of the products of the Krebs cycle and fatty acid oxidation, this process is known as oxidative phosphorylation. Whilst this is the mitochondria's most important role, it also has a role in apoptosis, calcium homeostasis, a role in hormone production and ammonia detoxification.

1.4.3.1 Oxidative Phosphorylation and Mitochondrial respiratory chain proteins

Five complexes make up the oxidative phosphorylation system they are located on the inner membrane of the mitochondria:

- NADH: Ubiquinone Oxidoreductase (Complex I)
- Succinate: Ubiquinone Oxidoreductase (Complex II)
- Ubiquinol: Cytochrome c Oxidoreductase (Complex III)
- Ferrocytochrome c: Oxygen Oxidoreductase (Complex IV)
- ATP Synthase (Complex V)

Complexes I-IV, ubiquinone and cytochrome c make up the respiratory chain (148) *Figure 8*. During oxidative phosphorylation, there is a flow of electrons from electron donors to receiver molecules. As these electrons are transferred, there is a release of energy and this energy is used to transport protons across the inner mitochondrial membrane creating a potential pH and electrical gradient.

The final stage of the electron transport chain is ATP synthase this enzyme generates ATP from ADP in a phosphorylation reaction using the energy created by the proton flow, this process is known as chemiosmosis. As a by-product reactive oxygen species are generated, the superoxide and peroxide anions $O_2^{-\cdot}$ and $O_2^{2-\cdot}$. As highlighted earlier, mouse models with a superoxide dismutase deficiency were shown to have premature osteoporosis compared to wild types.

Control of oxidative phosphorylation can be split into three domains (150):

- Availability of reducing components NADH and FADH.
- Availability of the components for ATP synthesis (ADP and Pi)
- Availability of oxygen to form water at the cytochrome c oxidase enzyme.

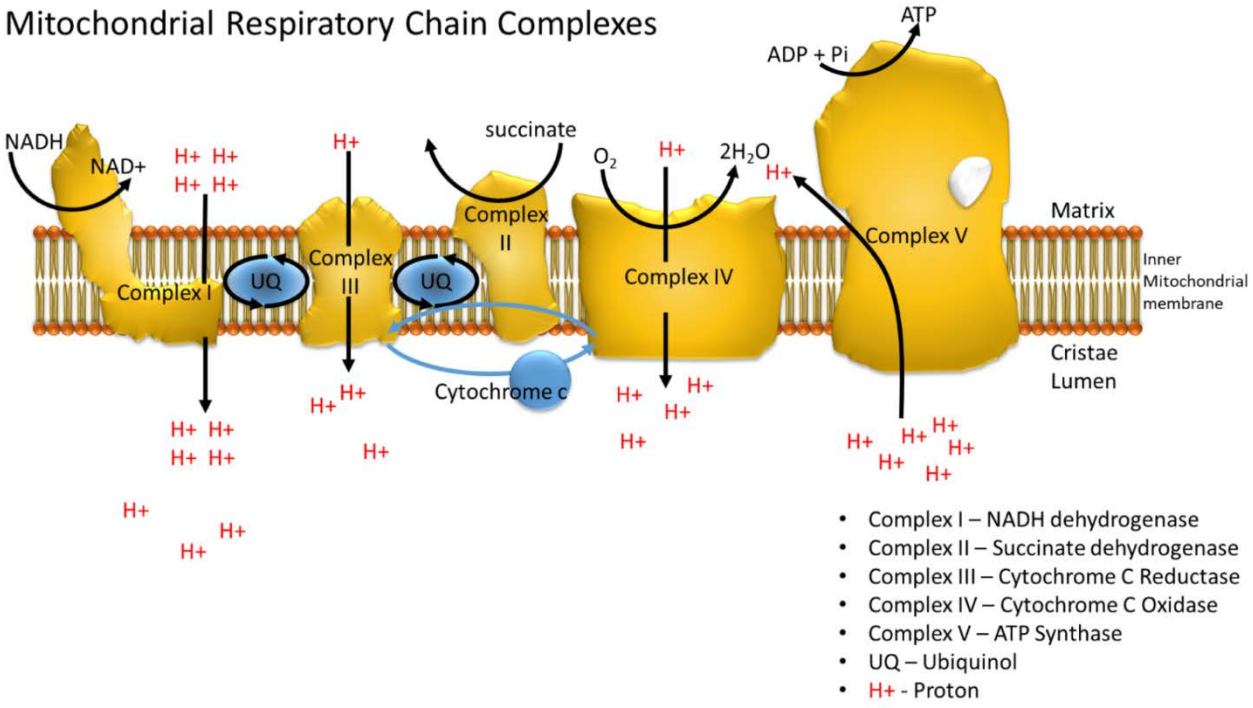

Figure 8 the oxidative phosphorylation pathway of the Mitochondrial Respiratory Chain. NADH is utilised as a product of the Krebs Cycle, serial redox reactions generate a proton gradient which can be used to convert ADP to ATP and biological energy (151).

1.4.3.2 Complex I: NADH: Ubiquinone Oxidase

Complex I is the largest of the 5 complexes and is composed of 45 different subunits of which 7 are coded for by mtDNA (152). It is an L shape structure which straddles the inner mitochondrial membrane with the vertical limb extending out of the inner membrane. It is further classified into three functional molecules consisting of the N, Q and P module (153).

Functionally it acts as the entry point of the electron transport chain, facilitating the transfer of two electrons between NADH and ubiquinone in lieu of the transfer of four protons across the membrane (153). The electrons removed from NADH by the N module are transferred by Iron sulphur clusters embedded within the Q module (154). Whereas the P module embedded within the membrane functions as a proton pump to drive the movement of protons into the intermembrane space (155).

1.4.3.3 Complex II: Succinate: Ubiquinone Oxidoreductase Dehydrogenase

Complex II is significantly smaller than complex I only 124kDa compared to Complex I which is in excess of 1000kDa. It is constructed from just four nuclear encoded subunits, the A and B subunits lie within the matrix of the mitochondria whereas C and D are embedded within the inner mitochondrial membrane(149, 156).

It is the second entry point of electrons into the electron transport chain but plays no role in the transport of protons across the inner mitochondrial membrane. Electron transport is facilitated by the oxidation of succinate to fumarate forming $FADH_2$ which is the utilised within the TCA cycle (149). The transfer of electrons B subunit again acting via iron sulphur clusters.

1.4.3.4 Complex III: Ubiquinol cytochrome c oxidoreductase

Complex III consists of 11 subunits all of these units, except cytochrome b, are encoded by the nuclear DNA. It is embedded within the inner mitochondrial membrane. Functionally it transfers electrons from ubiquinol to cytochrome c allowing the release of two protons in to the inter membrane space (157).

1.4.3.5 Complex IV: Cytochrome c Oxidase - COX

Complex IV is made up of 14 subunits of which 3 are encoded by mitochondrial DNA; MTCO1, MTCO2 and MTCO3 (158). It is the final complex of the electron transport chains where electrons are removed from cytochrome c as it is oxidised and transferred to molecular oxygen which combines with two protons and reduces to form water. Four protons are also transferred across the inner mitochondrial membrane (159).

1.4.3.6 Complex V: ATP synthase

ATP synthase is the final step in generating ATP. It is made up of two distinct segments and 15 different subunits of which two are encoded by the mitochondrial genome. The F0 segment lies within the inner mitochondrial membrane whereas the F1 segment lies externally within the matrix

space(155). Whilst the F1 segment is made up of three alternating α and β subunits with further γ, δ and ε subunits. The F0 segments consists of a c-ring comprising of the a, b, d, F6 subunits as well as oligomycin sensitivity-conferring protein.

Functionally, Complex V causes the phosphorylation of ADP to ATP. This is caused by protons being driven through the F_0 segment by the electrochemical gradient. This movement of protons causes a 360° rotation of the complex and it is this rotation which provides the energy to convert ADP to ATP in the F_1 segment. Three ATP molecules are generated for the transfer of 8 protons during the rotational movement. ATP synthases can reverse the process by hydrolysing ATP and restoring mitochondrial membrane potential by the movement of protons (160).

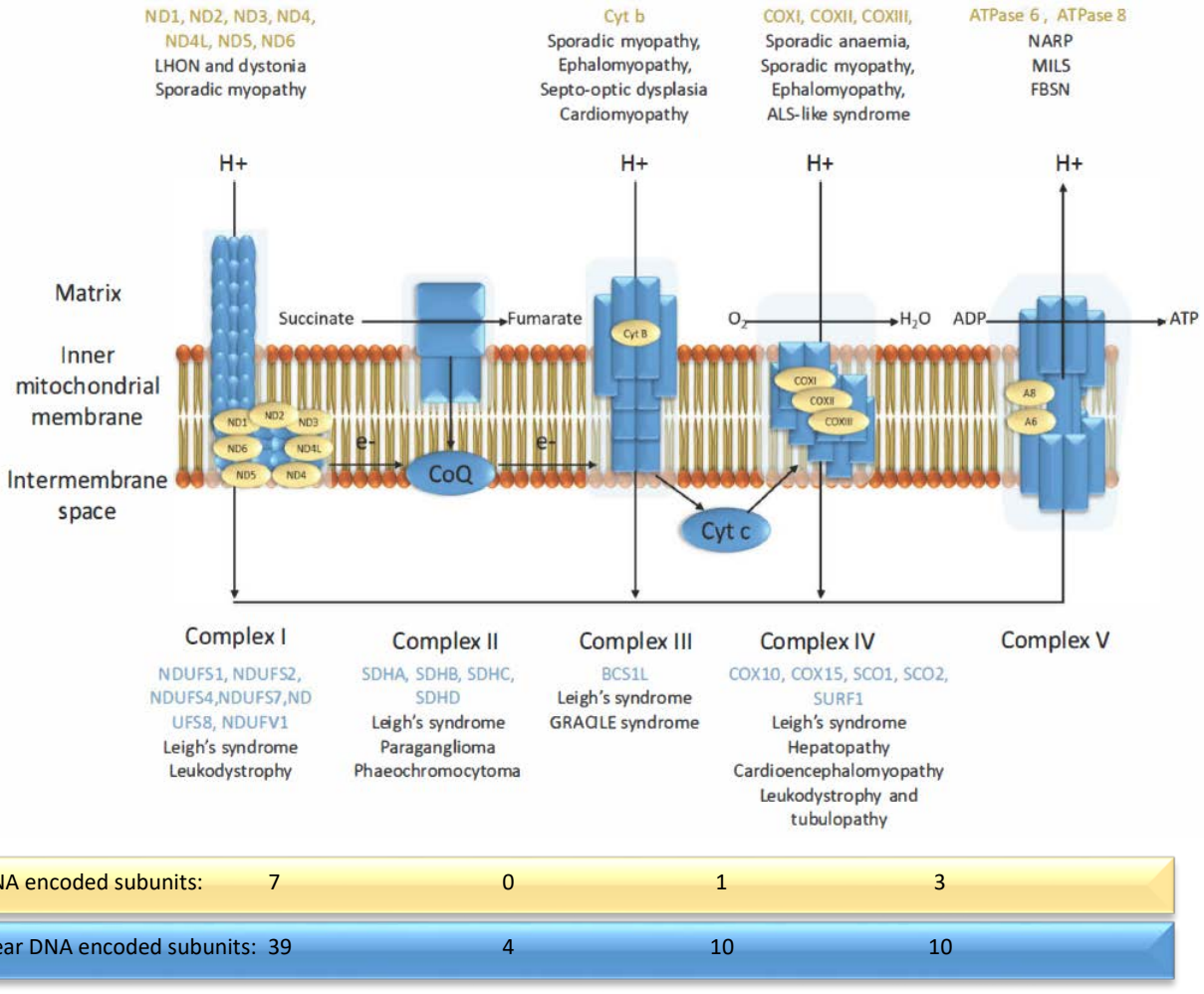

Figure 9 Disorders associated with mutations in the proteins of the respiratory chain. (mitochondrial DNA encoded proteins (yellow) Nuclear DNA encoded proteins (blue) (161).

1.4.3.7 Mitochondrial apoptosis

Programmed cell death or apoptosis is a mitochondrial controlled process in the mammalian cell (147). The release of intramembranous proteins from the mitochondria into the cytosol of the cell

occurs as a response to apoptotic stimuli. Apoptosis can occur in a caspase-dependent manner through cytochrome c, the serine protease Omi/HtrA2 and Secondary Mitochondrial Activator of Caspases (SMAC), or in a caspase-independent manner through apoptosis-inducing factor AIF and endonuclease G. The Bcl-2 family of proteins regulates apoptosis, promoting and inhibiting the permeabilisation of the mitochondrial membrane in response to apoptotic stimuli and as a consequence programmed cell death (147).

1.4.3.8 Calcium homeostasis

Mitochondria play a role in the maintenance of calcium balance within the cell. They have the ability to uptake, store and excrete Ca^{2+} ions in response to changing Ca^{2+} concentrations within the cell. Normal balance is maintained by the endoplasmic reticulum however if this balance is disturbed mitochondria are able to respond to maintain normal levels of Ca^{2+}, the Ca^{2+} uniporter within the mitochondrial membrane is activated and drives calcium into the mitochondria (162, 163).
Under normal physiological conditions, calcium signalling leads to mitochondrial ATP production and feedback on cytoplasmic signalling. In cases where there is an excess of calcium ions within the cell cytoplasm the mitochondrial permeability transition pore opens leads to an influx of calcium. This leads to mitochondrial inner membrane reorganisation, mitochondrial swelling and outer membrane permeabilisation (162). Outer membrane disruption can lead to the release of apoptotic factors from the intramembranous space and into the cytoplasm (164).

1.4.4 Mitochondrial replication

Transcription, translation and replication of mtDNA require nuclear-encoded enzymes and proteins that need to be transported into the mitochondria. In order for transcription to take place in humans mitochondrial DNA-directed RNA polymerase (POLRMT) and mitochondrial transcription factor A or TFAM are required along with one of the mitochondrial transcription factor B variants TFB1M and TFB2M (142).

1.4.4.1 Transcription

Initiation of transcription is not fully understood but is unable to take place without the presence of TFAM. It is thought TFAM may alter mtDNA structure by binding to and unwinding promoter regions facilitating transcription (165). The promoter regions of mitochondrial DNA are contained within the D-loop. TFAM has a greater affinity for the light strand promoter and enhances L-strand transcription to a greater extent than the heavy strand.

There is one light strand promoter (LSP) and two heavy strand promoters (HSP) *(Figure 7)*. Heavy strand transcription starts at nucleotide position 561 within the HSP whereas light strand transcription starts at position 407 of the LSP. These two transcription sites are functionally independent of one another (166). A further second transcription initiation site for the heavy strand is situated adjacent to the gene for the 12s rRNA at nucleotides position 638.

Once transcription is initiated at the LSP the L-strand can be transcribed as a single polycistronic RNA precursor this is then processed to 1 mRNA and 8 of the tRNAs (167). The H-strand may be transcribed as one single RNA but a more complex model was suggested by Attardi et al (168). In this model, it is suggested that the H-strand transcription occurs at different rates at the two different promoter sites. Transcription starting at the first promoter site is more frequent and finishes at the 16s rRNA gene and is responsible for the majority of the rRNA species whereas transcription from the second promoter site occurs less frequently but represents almost the entire H-strand and all the corresponding mRNAs and most of the tRNAs (166). The MTERF (mitochondrial transcription termination factor) family of proteins regulate the termination of transcription.

1.4.4.2 Translation

Mitoribosomes are formed from the mitochondrial ribosomal RNAs (16s and 12s) with nuclear-encoded ribosomal proteins. Mitochondrial tRNA species are much smaller than nuclear species and are charged with the corresponding amino acids by the nuclear-encoded amino-acyl tRNA synthetases (142). The mitochondrial ribosomes and amino-acyl tRNA complexes along with the nuclear elongation (EFG1, EFG2, EFTs and EFTu) and initiation factors (IF2 and IF3) lead to the synthesis of the 13 polypeptides of the OXPHOS system (169).

1.4.4.3 Replication

Mitochondrial replication and repair are reliant on mtDNA polymerase (Pol-γ). Mt DNA Polymerase has a proofreading activity in addition to its 5'→3' polymerase activity. Mt DNA polymerase has intrinsic 3'→5' exonuclease activity, which is highly mispair-specific. This ensures accurate replication of mtDNA (170). Initiation of replication is thought to be linked to mitochondrial transcription and primers are located within the D-loop region of the mitochondrial genome (171). The origin of H-strand replication is located downstream of the LSP in the D-loop region. Replication begins at this point once replication passes the L-strand origin, which is 2/3 of the genome distance from the H-strand site, and then the L-strand is replicated. The L-strand proceeds in the opposite direction to the H-strand (166).

Despite the proofreading action of mtDNA polymerase, the mitochondrial genome mutation rate is much higher than the nuclear DNA, 10-17 times higher (21). This was previously attributed to the proximity of mitochondrial DNA to the free oxygen species generated in the OXPHOS pathway as highlighted earlier but now it appears unclear for this enhanced mutation rate.

1.4.4.4 Heteroplasmy and Clonal Expansion

Homoplasmy and heteroplasmy concerning mitochondria relate to the mtDNA genome and mitochondria within each cell. In homoplasmy, all the mitochondrial genomes are identical within the cell. During mitosis, the mitochondria within the cell are randomly separated and so any mutated mtDNA copies are randomly separated. This creates a different mutation load within the daughter cells. Leading to variable disease expression within a cell and a threshold effect at which the mutation load leads to an altered phenotype. The majority of mitochondrial DNA mutations do not affect all mitochondria within a cell and so are heteroplasmic (24). The threshold for heteroplasmic mutations is in the range of 60-90% (21).

In post-mitotic tissue-preferential amplification of mtDNA mutations occur leading to high levels of mutations (172). This preferential amplification is thought to be due a number theories such as random genetic drift aided by relaxed replication of the mitochondrial genome (173). Alternatively the proposal by De Grey et al., would suggest that mitochondria with poorer respiratory chain function undergo less lysosomal degradation because there is less self-inflicted free radical damage and so they accumulate with in the cell (174). A similar theory is also proposed by Yoneda et al., (175).

Kowald et al., suggest that a negative feedback loop is responsible between transcription and replication in relation to a surplus of an intracellular product (176). There is also the perinuclear niche theory proposed by Vincent et al., this would suggest that mtDNA deletions expand around the nuclear region causing increased biogenesis and then progression of heteroplasmic change and to exceed threshold levels (177). A review of the proposed theories by Lawless et al., does not clarify which theory is indeed responsible and further work is still required (178).

1.4.6 Mitochondrial Ageing

Previously mitochondrial ageing was thought to be due to repetitive oxidative damage occurring due to reactive oxygen species generated in the respiratory chain causing damage to macromolecules especially mtDNA(179). This led to further respiratory chain protein dysfunction and further

generation of oxidative species coupled with defective mitochondrial respiration and ultimately determines an organism's lifespan by way of mitochondrial dysfunction (180). Point mutation and deletions in mitochondrial DNA are known to accumulate in humans as well as other animals (181). These mutations affect different tissues at different levels and are known to affect the brain (182), skeletal muscle (183) and heart (184).

These mutations have been observed in mouse models, which represent an ageing phenotype. The $PolgA^{mut}/PolgA^{mut}$ mouse model was based on mutations within mtDNA polymerase gamma. mtDNA polymerase (Pol-γ) is the only polymerase which acts upon mitochondrial DNA, as a result, is only found in the mitochondria (185). In the absence of any other DNA polymerases, it is known that Pol-γ is responsible for the replication and repair of mitochondrial DNA (186).

This model demonstrated the presence of mutant mitochondrial proteins within the respiratory chain leading to defective oxygen and ATP metabolism although no increase in reactive oxygen species (186). Along with the other mouse models discussed below this goes against the previous theory of ageing proposed in 1955 by Denham Harman and the updated theory of Alexeyev et al. which attributed repetitive oxidative damage to the longevity of an organism (179, 187).
Recent evidence suggests that although these point mutations occur with age they can also be inherited at the time of fertilisation (188). The effect of these mutations is dependent on where they occur and the level of heteroplasmy. The majority of point mtDNA mutations do not affect all mitochondria within a cell and so are heteroplasmic (24). The threshold for heteroplasmic mutations to cause phenotype effect is in the range of 60-90% (21). With clonal expansion and accumulation of these mutations with age within cells, they contribute to the ageing phenotype and OXPHOS dysfunction seen (173).

Reactive oxygen species are thought to play much less of a role in mitochondrial mutations and ageing than previously thought. Mitochondrial transcription factor A or Tfam packages the DNA into nucleoids which make them less prone to reactive oxygen species damage (189) and the levels of reactive species are much lower than previously thought 0.1% compared with 1-2% (190). Along with point mutations mtDNA is also prone to large-scale deletions and these are known to increase with age (191). A mouse model has shown that the accumulation of these deletions leads to age-related OXPHOS dysfunction in certain cell lines (192).

Overall, mitochondrial deletions and point mutations accumulated with age lead to respiratory chain dysfunction and reduced OXPHOS capacity contributing to an ageing phenotype.

1.4.7 Mitochondria and Osteoporosis.

Reduced bone mineral density has been associated with mitochondrial disease by association rather than clear cause and effect. Gandhi et al., conducted a retrospective review of mitochondrial patients and demonstrated a high number of risk factors related to poor bone health in mitochondrial patients(193). These included diabetes, vitamin D deficiency, chronic diseases including hepatic, renal, endocrine – hypogonadisms, adrenal and parathyroid dysfunction.

One fifth of the cohort had renal tubular acidosis and as highlighted in 1.3.3.2 metabolic acidosis is an osteoporosis risk factor. Seventeen percent were vitamin deficient associated with gastrointestinal issues or renal insufficiency. There was also the effect of polypharmacy including glucocorticoids and anti-epileptics to be accounted for (193).

Whilst there is not a clear link between mitochondrial pathology and the cause of osteoporosis in humans there have been various mitochondrial mutated mouse models, which have shown an association and observational finding of mitochondrial dysfunction and (24, 181, 194-196). The study by Guo et al., found significant associations of single nucleotide polymorphisms in NADH dehydrogenase 2 and cytochrome b genes although the correlation and relation to osteoporosis are unclear (197). One suggested link had been in relation to impaired respiratory chain function leading to an increase in lactic acid production and stimulation of osteoclast activity and bone resorption (195). As highlighted in 1.3.3.2 metabolic acidosis does contribute to osteoporosis.

Mitochondria are the main source of ATP and as a by-product ROS, these have been linked to oxidative stress induced osteoblast damage and dysfunction (198, 199). High levels of hydrogen peroxide within osteoblasts have been shown to trigger apoptosis of osteoblasts and inhibited osteoblastogenesis (200) (128). Conversely, hydrogen peroxide build-up has a positive effect on osteoclastogenesis and is required for osteoclast maturation. Excessive hydrogen peroxide inactivates the forkhead box O transcription factors which along with oestrogen promote osteoblastogenesis (201).

Oxidised cholesterol or oxysterols can also modulate bone formation and resorption. Oxysterols are generated from the cholesterol by the p450 enzyme, which is located in the endoplasmic reticulum

and mitochondria. oxysterol 20(S)-hydroxycholesterol, in combination with either the 22(S) or 22(R) versions cause an increase of osteoblast and alkaline phosphatase activity as well as Osteocalcin gene expression and mineralisation (202). In contrast, other oxysterols such as cholestan-3 β,5 α,6 β-triol inhibit osteoblastogenesis (203).

1.4.7.1 The PolgA^{mut}/PolgA^{mut} Mouse

The PolgA^{mut}/PolgA^{mut} mitochondrial mutator mouse possesses a defective version of mitochondrial DNA polymerase and consequently accumulates mitochondrial DNA mutations at 3-5 times the rate of wild-type mice. This leads to a premature ageing phenotype including cardiomyopathy, sarcopenia and osteoporosis as well as a reduced lifespan of around 12 months (181). The PolgA^{mut}/PolgA^{mut} mouse reflects the ageing phenotype seen in humans where mtDNA mutations accumulate with age to high levels in certain tissues (204).

The PolgA^{mut}/PolgA^{mut} mouse model showed a clear reduction in whole-body bone mineral density at 40 weeks with marked kyphosis. Further analysis of dissected femurs showed a clear reduction in bone mineral density at 40 weeks and x-ray densitometry revealed changes in body composition with the development of osteoporosis (181).

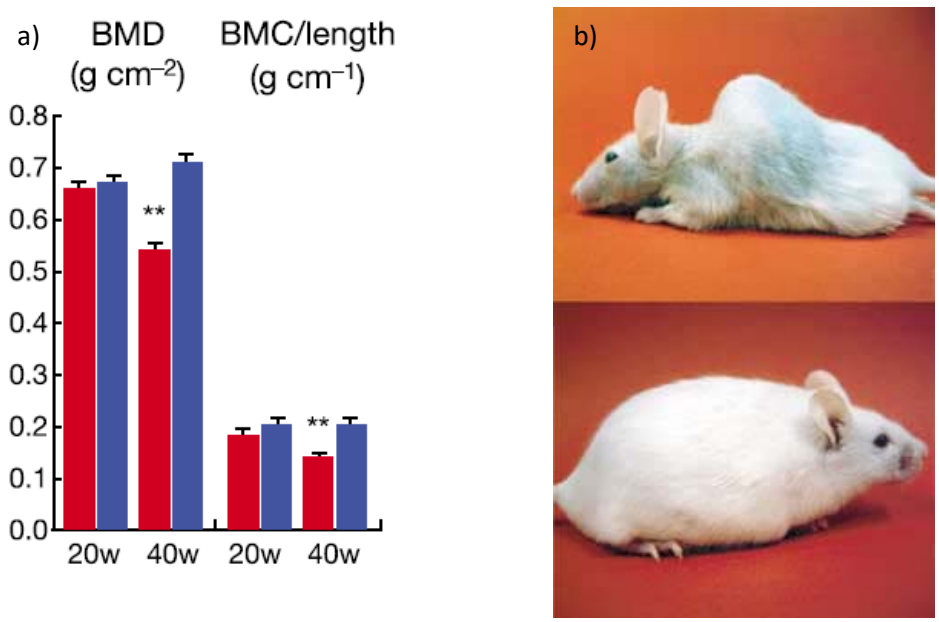

Figure 10 a) Bone mineral density and bone mineral content measured by X-ray densitometry of dissected femur from PolgA^{mut}/PolgA^{mut} mice (red bars) and wild-type mice (blue bars) at 20 weeks and 40 weeks old. b) The Ageing-related phenotype seen in PolgA^{mut}/PolgA^{mut} mice (181).

The PolgA^{mut}/PolgA^{mut} mouse model has been used in Newcastle to demonstrate a clear link between the pathogenesis of osteoporosis and mitochondrial DNA. The published main findings were (205, 206):

1. Significant reductions were found in bone density by 7 months in female mice and by 11 months in male mice compared to age and sex-matched wild-type mice.
2. Reduced osteoblast populations in the PolgA^{mut}/PolgA^{mut} with increases in osteoclast numbers and bone resorbing activity.
3. PolgA^{mut}/PolgA^{mut} mice exhibited a respiratory deficiency in terms of expression of complex I and complex IV proteins in osteoblasts (205). *See Figure 11.*
4. Accumulated mtDNA mutations are associated with decreased oxidative phosphorylation, with osteoblasts harvested from PolgA^{mut}/PolgA^{mut} mice showing significantly lower baseline levels of oxygen consumption for ATP production and significantly reduced spare and maximal respiratory capacities.
5. Using osteoblasts differentiated from mesenchymal stem cells harvested from bone marrow, a strong correlation with mitochondrial respiratory chain dysfunction, impairment of mineralised bone formation by osteoblasts in vitro and the accelerated development of osteoporosis was seen. Falling levels of bone formation observed in PolgA^{mut}/PolgA^{mut} cell lines with advancing age were consistent with declining bone density levels observed on micro-CT scan data.

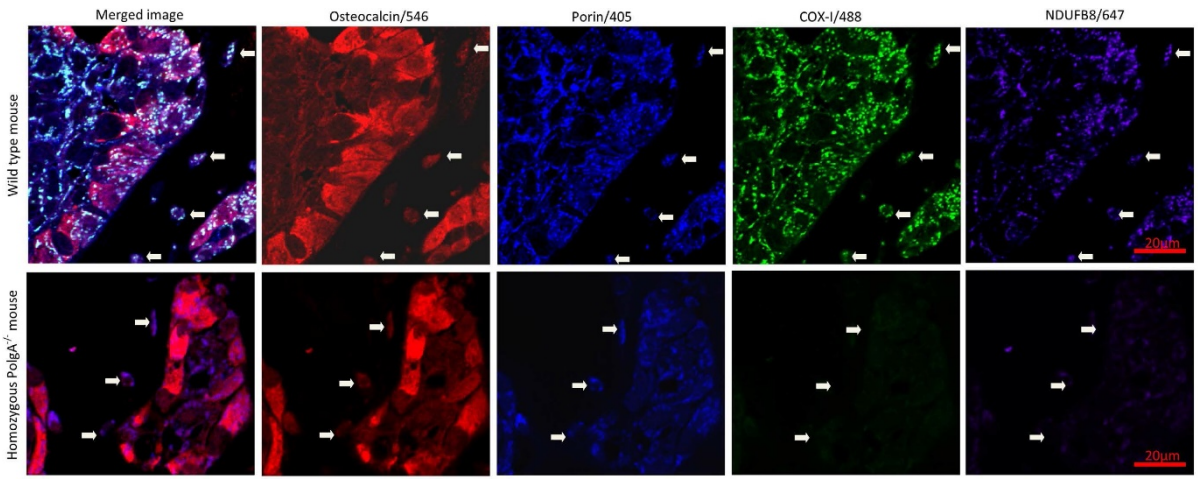

Figure 11 Quadruple immunofluorescence assay of mouse femur, 90x magnification Osteoblasts targeted with an antibody to Osteocalcin. PolgA^{mut}/PolgA^{mut} mouse in comparison with age-matched wild-type control mice top row, NDUFB8 (Complex I) and COX-I (Complex IV) mitochondrial respiratory chain deficiencies are seen at 11 months in PolgA^{mut}/PolgA^{mut} (lower row) relative to mitochondrial mass (porin) (205).

1.4.7.2 Sod2 – mitochondrial superoxide dismutase 2 mouse model.

Osteocytes are mature osteoblasts that become embedded in the secreted bone matrix. Osteocytes represent around 95% of bone cells that are distributed throughout the bone matrix with a network of lacunae and canaliculi. The dendritic processes within the canaliculi allow communication with other cells (207). They have been shown to secrete soluble factors which have an influence on bone and other tissues (207). Osteocytes also influence osteoblast and osteoclast activity and are crucial for bone homeostasis. The number of viable osteocytes decreases with age from 88% at 10–29 years of age to 58% at 70–89 years of age (208, 209). Reactive oxygen species (ROS) have been linked with causing oxidative damage and bone ageing in both humans and animals (210-213). The anion superoxide (O_2^--) is generated during mitochondrial respiration as part of the respiratory chain pathway. Superoxide dismutase 2 is distributed throughout the mitochondria and metabolises O_2^- to H_2O_2. Sod2 deficiency has been reported to lead to oxidative damage to tissues. Kobayashi et al. developed a mouse model to look at mitochondrial superoxide dismutase 2 deficiency in osteocytes and the impact on age-related osteoporosis.

Similar to ageing bone a lack of Sod2 resulted in enhanced O_2^- production. Analysis demonstrated marked bone loss similar to age-dependent loss, disorganisation of the canalicular network and decreased number of live osteocytes. Sod2 deficiency also suppressed bone formation by upregulation of sclerostin and RANKL. This model demonstrated that mitochondrial superoxide induced in osteocytes by Sod2 deficiency mirrored age-related bone loss and alter bone metabolism via deregulation of RANKL and sclerostin expression (109).

1.4.7.3 Tfam Mouse Model

Mitochondrial transcription factor A or Tfam is a nuclear-encoded protein which binds upstream of heavy and light chain promoters of mitochondrial DNA and promotes transcription of mitochondrial DNA (214). Tfam plays a regulatory role in the maintenance and replication of mtDNA in mammals. It is required for transcription and initiation of mtDNA promoters, dysfunction in protein transcription leads to respiratory chain deficiency (215, 216).

Mice with a Tfam knockout have been created and used for analysis of mitochondrial pathology. Tfam gene knockout heterozygous mice were found to have around 50% reduction in Tfam transcripts and protein, with a 34% reduction in mtDNA copy number in tissues investigated (214). Miyazaki et al. (217) investigated the effect of Tfam deficiency on osteoclast survival and bone resorption. They found in Tfam knockout heterozygous mice that osteoclasts had increased bone

resorbing activity, reduced intracellular ATP levels and an increased rate of apoptosis. They concluded that ATP depletion leads to osteoclastic bone resorption. Mitochondrial dysfunction is known to occur with age and ATP depletion may, therefore, play a role in the pathogenesis of osteoporosis.

1.4.7.4 HTRA2/OMI mouse model

HTRA2/OMI is serine protease which functions independent of ATP. It is located on the intermembrane space in the mitochondria the proposed function of this protease is one of protein quality control. In the model mutant mitochondria appear to be relatively protected from mitophagy Transgenic *htra2*^{mnd2} mice were shown to have a premature ageing profile which included osteoporosis among other pathologies. Significant increases in clonally expanded mtDNA deletions were present. The exact cause and effect of HTRA2 deletions are speculated but believed to be related to disassembly of the respiratory chain complexes with advancing age and the generation of ROS. They speculate that the cardiac cells with mitochondrial deficiencies are unable to meet metabolic demands leading to premature death (218). As highlighted earlier osteoblasts contain a high level of mitochondria and bone formation is a metabolically demanding action. In the same way, the cardiomyocytes are unable to function adequately the same may be true of the osteoblasts compromising bone formation and leading to premature osteoporosis.

1.5 Aims

In view of the relevance of the PolgA^{mut}/PolgA^{mut} mouse model work undertaken at Newcastle University into osteoporosis and mitochondrial mutations the aims of this research are:

1. To establish if mitochondrial DNA (mtDNA) mutations are present within human mesenchymal stem cells and osteoblasts
2. Establish that if there are mtDNA mutations do they cause subsequent mitochondrial respiratory chain deficiency and contribute to the pathogenesis of osteoporosis in humans.

1.5.1 Overview

I propose to advance this work with novel research into the effects of mitochondrial mutations and consequent respiratory chain dysfunction on the function of human osteoblasts. The work by Dobson et al., (205) would serve as a starting point using very similar techniques to those already employed in the PolgA^{mut}/PolgA^{mut} mouse model.

The basis of this work would involve extracting bone marrow at the time of orthopaedic elective and trauma surgery. The research will focus on two different patient cohorts aged <30 and >70 as patient participation allows, these groups will provide samples in order to test the hypotheses by correlating the results of the below techniques with age in the patient cohort.

1. Sequencing individual mesenchymal stem cells for evidence of mtDNA mutations and clonal expansion.
2. Analysing individual mesenchymal stem cells for evidence of respiratory chain protein deficiency.
3. Determining if osteoblasts with impaired expression of mitochondrial respiratory chain proteins are detected in bone with human ageing and determine if this is due to clonally expanded mtDNA mutations.

Chapter 2 - Materials and Methods

2.1 Reagents, equipment, solutions and consumables:

2.1.1 Equipment

Microscopes

Nikon Instruments A1 Confocal Laser Microscope

Nikon Instruments Eclipse Ti-E inverted Microscope

Olympus BX51 Microscope TF

Zeiss Axio-observer LSM800/SDI Microscope

Zeiss Celldiscoverer 7 Microscope

Flow cytometry

BD Accuri C6 flow cytometer

BD FACSAria III Cell Sorter

BD FACSCanto II Analyser

BD FACSymphony A5 Analyser and plate reader

Fluidigm Helios Mass Spectrometer

Fluidigm Hyperion Imaging System

Tissue culture and immunohistochemistry

Contained Air Solutions Tripass 2 – Class 2 Microbiological Safety Cabinet

Eppendorf Centrifuge 5418

Grant Sub Aqua Pro water bath

Heraeus Megafuge 8 Centrifuge

Integra Vacusafe

Panasonic CO2 Incubator MCO-170AIC

Thermo Fisher Microm HM325

PCR

Aligent 2100 Bioanalyzer

Applied Biosystems Veriti 96 well thermal Cycler

Astec UV hood

Cleaver Scientific MP- 250V electrophoresis power supply

Illumina MiSeq Sequencer

Invitrogen E-Gel™ iBase™ unit and E-Gel™ Safe Imager™ transilluminator combo kit

Invitrogen MagnaRack™ Magnetic Separation Rack

Qubit Fluorometer

Thermo Fisher Ion Chef System Sequencer

Miscellaneous Laboratory equipment

Bio-Rad ChemiDoc MP Imaging System

Eppendorf ThermoMixer C

Freezing container, Nalgene® Mr Frosty

Genlab MINO/6 Oven

Grant Dry Block Thermostat

Jenway 3510 pH Meter

Ohaus Adventurer Precision Balance

Scientific Industries Vortex-Genie 2

Stuart Orbital Shaker SSL1

Stuart Roller Mixer SRT9

Stuart See-saw Rocker SSL4

Stuart SB Tube Rotator

2.1.2 Reagents

2.1.2.1 Cell Culture

Alpha Minimum Essential Media *(22571-038)*	Gibco
Dulbecco's Modified Eagle's Medium *(31885-049)*	Gibco
Iscove's Modified Dulbecco's Medium + GlutaMax–I *(31980-022)*	Gibco
RPMI-1640 Medium, with sodium bicarbonate *(R0883)*	Sigma Aldrich
Antibiotic-antimycotic *(15240062)*	Gibco
Gentamicin (50 mg/mL) *(15750037)*	Gibco
Penicillin Streptomycin *(15140-1480)*	Gibco

Trypan Blue solution *(t8154)*	Sigma Aldrich
TrypLE Express (1x) Stable Trypsin Replacement Enzyme *(12605-010)*	Gibco
2-Phospho-L-ascorbic acid trisodium salt *(49752-10g)*	Sigma Aldrich
Beta- glycerophosphate disodium salt hydrate *(G9422)*	Sigma Aldrich
Dexamethasone powder 25mg *(D4902-25MG)*	Sigma Aldrich
Fetal bovine serum	Gibco
L-Glutamine *(25030-024)*	Gibco
Minimum Essential Medium Non-Essential Amino Acids *(M7145-100ml)*	Sigma Aldrich
Sodium L-ascorbate *(A4034)*	Sigma Aldrich
Sodium Pyruvate (100mM) *(11360-070)*	Gibco

2.1.2.2 Immunohistochemistry

Avidin/Biotin blocking kit *(sp-2001)*	Vector
DPX Mountant *(06522)*	Sigma Aldrich
Eosin	Cell Path
Ethanol	Merck
Haematoxylin	TCS Biosciences Ltd.
Histoclear	National Diagnostics
Hydrochloric Acid	VWR
Hydrophobic Pen (*Z377821)*	Sigma Aldrich
Methanol	Merck
Normal Goat Serum (NGS)	Sigma Aldrich
Prolong gold	Life Technologies

2.1.2.2.1 Primary antibodies

Anti-cathepsin K IgG goat anti-rabbit (sc-30056)	Santa-Cruz
Anti-MTCO1/Complex IV IgG2a goat anti-mouse (abl4705)	Abcam
Anti-NDUFB8/Complex I IgGl goat anti-mouse (abll0242)	Abcam

Anti-Osteocalcin IgG goat anti-rabbit (sc-30045)	Santa-Cruz
Anti-VDACl/porin IgG2b goat anti-mouse (abl4734)	Abcam

2.1.2.2.2 Primary Conjugated antibodies

Anti-TOMM20 Alexa Fluor 594 *(ab210665)*	Abcam
Anti-MTCO2 Alexa Fluor 647 *ab200525)*	Abcam

2.1.2.2.3 Secondary antibodies

Alexa 488 IgG2a goat anti-mouse	Life Technologies
Alexa 546 IgG goat anti-rabbit	Life Technologies
Alexa 647 streptavidin conjugated	Life Technologies
Biotinylated goat anti-mouse IgGl	Jackson/Stratech
Dylight 405 IgG2b goat anti-mouse	Jackson/Stratech
Anti-rabbit Alexa Fluor 405nm	Life Technologies
Anti-mouse IgG Alexa Fluor 488nm	Life Technologies
Anti-mouse IgG2a Alexa Fluor 488nm	Life Technologies
Anti-mouse IgG2b Alexa Fluor 546nm	Life Technologies
Anti-mouse IgG1 Alexa Fluor 647nm	Life Technologies
Streptavidin Alexa Fluor 647nm	Life Technologies
Anti-mouse IgG1 biotin	Life Technologies

2.1.2.2.4 CyToF antibody consumables

MAXPAR X8 antibody labelling kit	Fluidigm
Intercalator	Fluidigm

2.1.2.3 PCR

AMPure XP *(A63881)*	Beckman Coulter
E-Gel™ SizeSelect™ 2% Agarose Gel	Invitrogen
GoTaq Long PCR Master Mix *(M4021)*	Promega
Ion Xpress™ Plus Fragment Library Kit *(4471269)*	Thermo Fisher Scientific

Ion Xpress™ Barcode Adapters 1-16 Kit *(4471250)*	Thermo Fisher Scientific
Low TE buffer *(602-1155-01)*	Thermo Fisher Scientific
Nuclease free water	Ambion
Primers	Eurofinns
Proteinase K Solution	Fisher Scientific
Qubit dsDNA HS Assay Kit *(Q32851)*	Invitrogen

2.1.2.4 Tissue Preparation

DNASE I 100 MG *(11284932001)*	Sigma Aldrich
Iso-pentane *(158941)*	Merck
Liquid nitrogen	BOC
Lymphoprep *(07851)*	Stem Cell Technologies
MSC phenotyping kit *(*130-095-198*)*	Miltenyi Biotec

2.1.3 Chemicals

16% Formaldehyde solution Methanol Free *(F017/3)*	TAAB Laboratories
Acetic acid	VWR
Alizarin red S (A5533)	Sigma Aldrich
Ammonium hydroxide (28% NH3)	Sigma Aldrich
Dimethyl sulfoxide *(D4540)*	Sigma Aldrich
Dulbecco's Phosphate Buffered Saline *(14190-144)*	Sigma Aldrich
Dulbecco's Phosphate Buffered Saline with ca and mg *(D8662-1L)*	Sigma Aldrich
Fast blue RR salt *(FO5OO)*	Sigma Aldrich
Formcial-2000 *(1314)*	Statlab
Glycine *(G7126)*	Sigma Aldrich
N,N-Dimethylformamide *(D4551)*	Sigma Aldrich
Naphthol AS-MX phosphate disodium *(N5OOO)*	Sigma Aldrich
Paraformaldehyde solution 4% in PBS *(sc281692)*	Santa Cruz Biotechnology
RBC Lysis Buffer *(00-4333-57)*	Affymetrix EBioscience

Sodium Chloride *(S7653)*	Sigma Aldrich
Sodium Azide *(S2002)*	Sigma Aldrich
Tetra-ethylene diamine tetra-acetic acid, dehydrate *(15700)*	Affymetrix
Triton X-100 *(X100)*	Sigma Aldrich
Trizma Base *(T1503)*	Sigma Aldrich
Tween20 *(p1379-500ml)*	Sigma Aldrich

2.1.4 Solutions

5x Tris Buffered Saline +/- Tween

- 2l dH_2O
- 121g Trizma Base
- 90g Sodium chloride
- Concentrated HCl
- +/- Tween20 5mls

Alizarin Red Stain 2% pH4.3

- 100mls dH_2O
- 2g Alizarin red

Alkaline Phosphatase Stain

- 100mls TBS
- l0mg naphthol AS-MX phosphate disodium
- 0.2mls *N,N*- Dimethylformamide
- 60mg fast blue RR salt

Ammonia Solution 0.25M

- 4.8mls of NH_4OH
- 500mls dH_2O

DNA loading buffer

- 0.25% (w/v) Bromophenol blue
- 0.25% (w/v) Xylene Cyanol
- 30% (v/v) Glycerol

DNA electrophoresis gel buffer (1L)

- 100 ml 10x TAE (0.4 M Tris-acetate, 10 mM EDTA, pH 8.3)
- 900ml Nanopure water
- SYBR Safe DNA Gel Stain 4µl/100mls Thermo Fisher

DNA electrophoresis gel running (1L)

- 100 ml 10x TAE (0.4 M Tris-acetate, 10 mM EDTA, pH 8.3)
- 900ml Nanopure water

Single cell lysis buffer (500µl)

- 250 µl 1% Tween 20
- 50 µl 0.5M TrisHCl pH 8.5
- 195 µl dH_2O
- 5 µl proteinase K

Phosphate Buffered Saline *(BR0014G)* Oxoid

- 1 tablet/100mls dH_2O

2.1.4 Consumables

2.1.4.1 Equipment Consumables

0.2ml Thin-walled PCR tubes	Starlab
0.5ml Thin-walled PCR tubes	Starlab
3.0 ml Graduated Pasteur Pipette (Sterile), Ind. Wrapped *(E1414-0311)*	Starlab
96 Well semi-skirted Plate, with raiser rim	Starlab
Aerosol resistant pipette tips	Starlab
Coverslips	Starlab
Falcon Round-Bottom Tubes 5ml *(352003)*	BD Bioscience
Eppendorf Lobind 1.5ml tubes	Sigma Aldrich
Eppendorf tubes (0.6ml, 1.5ml, 2.0ml)	Starlab
Falcon Tubes (15ml and 50ml)	BD
Gilson pipette (P2, P10, P20, P100, P200, P1000)	Anachem
Gloves	Starlab
Qubit assay Tubes *(q32856)*	Invitrogen
Weigh boats	VWR

X-tra clipped corner slides	Leica

2.1.4.2 Tissue culture consumables

6 and 12 well plates	Greiner Bio-One
Cellstar T25 flask	Greiner Bio-One
Cellstar T75 flask	Greiner Bio-One
Falcon Cell Strainer 70µm	Fisher Scientific
Stericup filter unit	Merck Millipore
ViewPlate 96 well glass bottomed plate	Perkins Elmer
Partec CellTrics 50µm filter *(04-004-2327)*	Wolflabs

2.2 Software

Bitplane - Imaris, v.8.4

Microsoft Office

Nikon - NIS-Elements

TIBCO – Spotfire and Columbus

Volocity

Zeiss - Zen system

2.3 Ethics and Patient cohort

2.3.1 Ethics

Ethical approval for the collection of paediatric samples was via the Great North Biobank, application number (*GNB-012).*

Ethical approval for use of adult human samples was gained as an adjunct to the Newcastle Bone and Joint Biobank – *(REC reference 14/NE/1212, IRAS project ID 166522)*. Newcastle University reference *8741/2016.*

2.3.2 Control paediatric patients

2.3.3.1 Paediatric bone samples

Paediatric bone samples were taken from a variety of orthopaedic operations. In these operations there was removal of bone which would have otherwise been discarded but instead was collected. These included a range of osteotomies among other procedures. Bone marrow samples were also taken when appropriate tissue was gained.

2.3.2.2 Paediatric cell line samples from anterior cruciate ligament surgery

Anterior cruciate ligament surgery involves access the bone marrow cavity and removing a core of bone to allow passage of the ligament reconstruction, in these instances bone and marrow were also collected. The quality of the marrow was disrupted by the irrigation fluid used during the procedure however it was possible to culture cell lines from the samples gained to create young control cell lines for use in comparison to adult samples.

2.3.2 Adult patient samples

Bone and bone marrow samples were taken at the time of routine arthroplasty procedures including total hip and total knee replacements. Like in the case of the paediatric samples all tissue was surplus to the operative requirements and was otherwise due to be discarded at the time of surgery.

Sample	Age (years)	Sex	Surgery	Date of Surgery	Indication	Co-morbidities	Osteoporotic preventive/causative medication
Hip 1	53	F	Total hip replacement	16/01/2019	Osteoarthritis	hypertension	Omeprazole/lisinopril
Hip 2	84	F	Total hip replacement	12/03/2019	Osteoarthritis	ischaemic heart disease, type II diabetes mellitus, asthma, hypertension, peripheral neuropathy, venothromboembolism, vitamin D deficiency, B12 and folate deficiency	Atorvastatin, Metformin, Warfarin
Hip 3	88	F	Total hip replacement	13/03/2019	Osteoarthritis	type II diabetes mellitus, chronic kidney disease, atrial fibrillation, diverticular disease, hypertension	Furosemide, Atorvastatin
Hip 4	83	F	Total hip replacement	01/04/2019	Failed Fixation	hypothyroid, hypertension, osteoarthritis	Calcichew d3,cholecalciferoll, furosemide, levothyroxine, risedronate
Hip 5	66	F	Total hip replacement	02/04/2019	Osteoarthritis	hypothyroid, raised cholesterol, hypertension,	Lansoprazole, Levothyroxine, losartan, simvastatin
Hip 6	45	F	Total hip replacement	02/04/2019	Osteoarthritis		
Hip 7	82	M	Total hip replacement	03/04/2019	Osteoarthritis	chronic obstructive pulmonary disease, gastro-oesophageal reflux disease, iron-deficiency anaemia	Omeprazole, steroid inhalers - tiotropium, fluticasone, Seretide
Hip 8	74	F	Total hip replacement	11/04/2019	Osteoarthritis	atrial fibrillation, pulmonary hypertension, iron-deficiency anaemia	Omeprazole, Bisoprolol, Rivaroxaban
Hip 9	64	M	Total hip replacement	11/04/2019	Osteoarthritis	chronic kidney disease, type II diabetes mellitus	Dialysis, Atorvastatin, Diltiazem, Furosemide,
Hip 10	62	M	Total hip replacement	02/05/2019	Osteoarthritis	type II diabetes mellitus, hypertension	Lisinopril, metformin atorvastatin, Adalat
Hip 11	61	F	Total hip replacement	24/11/2017	Osteoarthritis	hypertension	Propranolol, Venlafaxine
Hip 12	78	F	Total hip replacement	24/11/2017	Osteoarthritis	hypertension	
Hip 13	25	M	Total hip replacement	09/03/2017	Post traumatic acetabular fracture non-union		
Hip 14	72	F	Hemiarthroplasty of the hip	20/11/2019	Trauma – fractured neck of femur	chronic kidney disease, type II diabetes mellitus, hypertension, hypothyroidism, vitamin D deficiency	Atorvastatin, propranolol, doxazosin, thyroxine, risendronate, cholecalciferol.
Femur 1	22	M	Intramedullary nail and bone graft	27/03/2019	Leg length discrepancy after trauma		
ACL 1	14	M	ACL reconstruction	11/08/2017	ACL deficiency		
ACL 2	15	M	ACL reconstruction	11/08/2017	ACL deficiency		
Paediatric 1	13	M	Excision of a bone bridge and fat graft	29/11/2018	Physeal injury and growth arrest		
Paediatric 2	1.5	F	Open reduction and pelvic osteotomy	18/04/2019	Developmental dysplasia of the hip		

Table 3: Patient demographics and details from which samples were used in this research.

2.4 Sample preparation

2.4.1 Decalcification protocol

When fresh bone samples were taken, they were trimmed to create 2-5mm thick slices. They were placed in tissue cassettes and fixed in 4% paraformaldehyde (PFA) solution for 72 hours. The volume of PFA used was 20x the volume of the tissue.

Following PFA fixation samples were rinsed in dH_2O once. They were then placed in a solution of 14% tetra-EDTA (Affymetrix) at 4°C on a rocker. The pH of the EDTA solution was adjusted to 7.4 using glacial acetic acid. The decalcification solution was changed three times per week. Samples were left in EDTA for 21 days

Formical-2000 was also used on occasions for rapid tissue preparation. Specimens were fixed and prepared as above. Followed by a wash in dH_2O once. The cassettes were then placed in formical-2000 solution. The volume of solution was twenty times that of the specimen. The specimen was left on the rocker in the cold room for 48 hours before a wash in dH_2O wash.
Samples were then placed in PBS and were processed, embedded and cut on to X-tra clipped corner slides ready for staining.

2.4.2 Bone Marrow preparation

Some of the bone marrow was put directly into culture. This was done by vortexing the sample of bone marrow in tissue culture medium and then incubating as covered in the tissue culture methods.

2.4.2.1 Lymphoprep protocol

The majority of the bone marrow was processed using a density gradient to separate mononuclear cells from red blood cells, plasma and other blood constituents. Bone marrow was first diluted with tissue culture (sterile) PBS at a ratio of 1:4. The product was then passed through a 70µm cell strainer. 15ml of lymphoprep was then added to a falcon tube. 30mls of the filtered marrow PBS mixture was added carefully on top taking care not to mix the two constituents.

The Falcon tube was then spun at 800G for 20 minutes with slow acceleration and deceleration profiles selected on the centrifuge. From the centrifuged tube the mononuclear layer was removed using a sterile Pasteur pipette. This layer was placed into a new 50ml falcon tube which was then topped up with sterile PBS to wash the layer. This falcon tube was then spun again at 500g for 5 minutes.

The cell pellet was then either resuspended in:

1. Freezing media – (10% Dimethyl sulfoxide and FBS) then frozen using a Mr Frosty freezing container at -80°C before long term storage in liquid nitrogen.
2. For overnight storage, pellets were re-suspending in RPMI media overnight at 4°C in the fridge.
3. For flow cytometry, if using the same day, the pellet was resuspended in Ca, Mg PBS. DNAse was added in 10µl steps to break up any clumped cells. A maximum of 50µl was used per 7.5mls of PBS. This solution was filtered using a 50µm celltrics filter into a FACS tube ready for flow cytometry use.

2.4.2.2 Mesenchymal Stem Cell separation

In order to sort MSC cells from bone marrow for culture, the Miltenyi Biotec MSC phenotyping kit was used. This kit is based upon sorting MSCs via positive cell markers for; CD73, CD90, and CD105 and the negative markers CD45, CD34, CD14 and CD20.

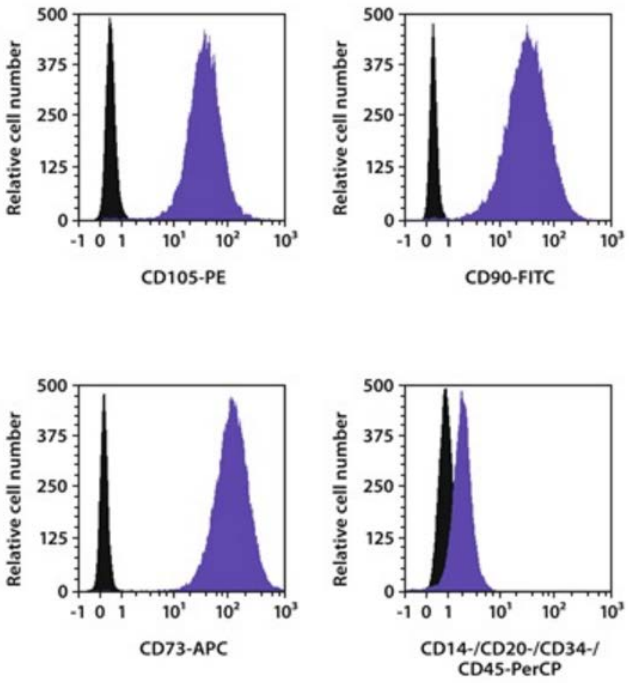

Figure 12 Flow analysis of the CD105-PE positive cells, the CD90-FITC positive cells, CD73-APC positive cells and PerCP positive cells (219).

The lympho-prepped cell suspension was stained as per the Miltenyi Biotec protocol (219), DNAse was added to the cell suspension to reduce clumping of the cells. The suspension was then filtered through a 50µm filter as this yielded a better result than a 30µm filter. Initially, cells were run through the FACS Canto III analyser to clarify successful staining the results can be seen in *Figure 13*. Once the protocol as above was determined they were run on the FACS Aria III Cell Sorter. Cells were

individually sorted into a 96 well PCR plate. Each well of this plate contained 15µl of single cell lysis buffer. Alternatively, the cells were sorted as a pool of cells into a 96 well flat-bottomed tissue culture plate. Each well of this plate contained 100µl of α-MEM media.

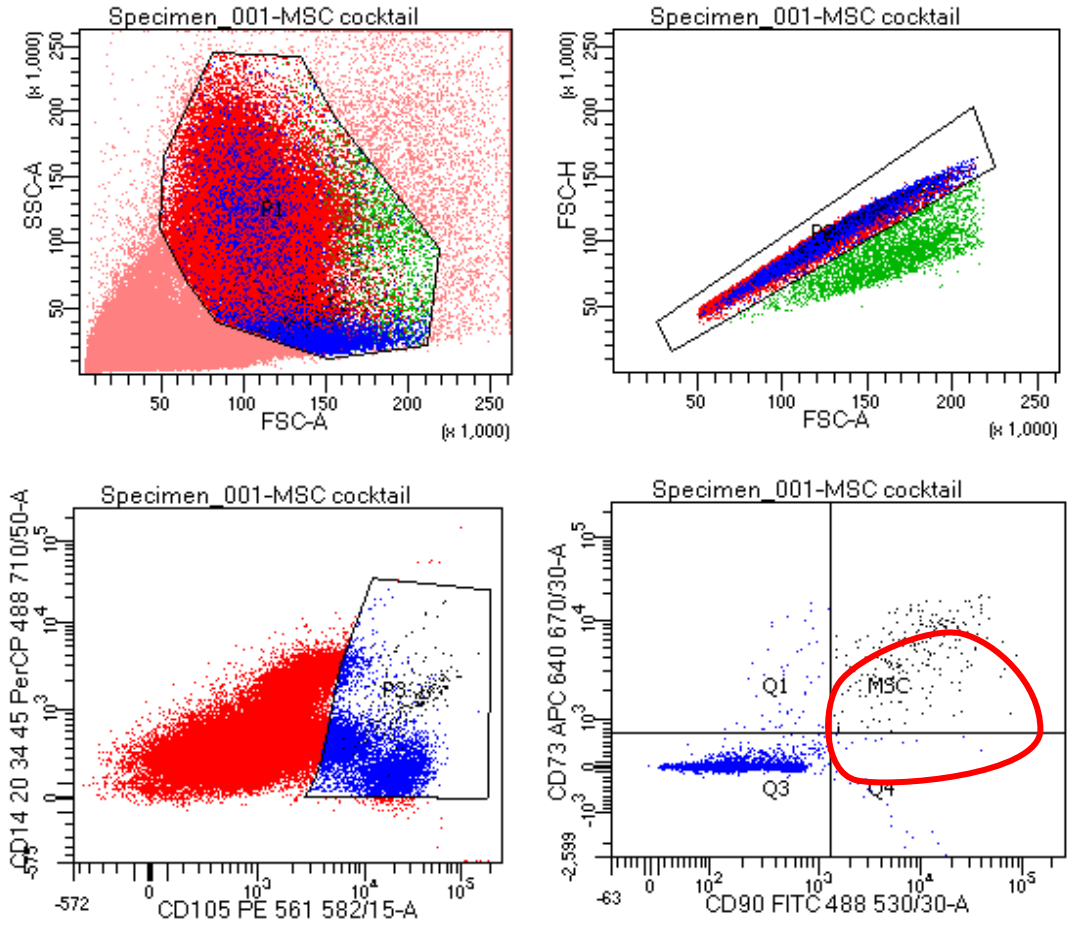

Figure 13 Flow Cytometry Sort of MSCs from fresh bone marrow. The MSC population is circled in red. The MSC population is first defined the side scatter (SSC-A) representing granularity and forward scatter (FSA-A) representing size. Further delineation is then made using positive expression of CD73, CD90, and CD105, and these cells must lack expression of CD34, CD45, and CD14.

2.5 Histochemistry

2.5.1 Haematoxylin and eosin

Cut sections of decalcified bone were then left to air dry on the slides for one week. Sections were first heated to 60°C for 30 minutes followed by deparaffinisation using Histoclear for 5 minutes followed by another 5 minutes in fresh Histoclear. Specimens were then rehydrated using graded alcohol concentrations followed by a dH_2O wash (5 minutes for each stage). Slides were then stained in Haematoxylin for 5 minutes followed by a wash in running tap water for 5 minutes. Slides were then blued in Scott's tap water for 1 minute followed by a 3-minute running tap water wash. Slides were washed in 95% alcohol (10 dips) before counterstaining with eosin for 1 minute.

Slides were then dehydrated through an alcohol gradient followed by 2 clearing stages in histoclear. Slides were then mounted with the appropriate size coverslip using DPX mounting medium.

2.5.2 3,3′-Diaminobenzidine (DAB) staining

Slides were prepared as in the H+E staining steps. Following rehydration endogenous horseradish peroxidase activity was initially blocked using 3% hydrogen peroxide solution in PBS however this led to the loss of sections from the slide and the blocking step was moved to follow primary antibody incubation.

Antigen retrieval was performed by incubating sections in 1mM EDTA pH 8 80°C for 35 minutes followed by a rinse in cold dH_2O. Sections were then encircled using a PAP pen prior to blocking and staining. Block was performed with a 10% NGS PBS solution for 1 hour. 200 µl per section was used. Following block sections were rinsed in dH_2O before Avidin and Biotin block. Slides were first blocked with avidin for 15 minutes followed by 2 PBS washes on the rocker for 5 minutes and then the biotin block again followed by 2 PBS washes. Slides were then stained with the primary antibodies at 1:200 concentration in a humidified chamber at 4°C overnight.

Following incubation, slides were washed in PBS for 7 minutes on the shaker twice. An endogenous peroxidase blocking step was then performed using 0.3% hydrogen peroxide PBS solution which was applied to the slides for 10 minutes followed by 2 PBS washes for 7 minutes.

For mouse-based antibodies the slides were incubated with 1:200 of mouse biotin secondary for 1 hour at room temperature in the humidified chamber followed by 2 7-minute PBS washes before a

secondary incubation with ABC buffer for 30 minutes. After these slides were rinsed three times with PBS. DAB solution was then made up and applied to the slides which were developed for around 10 minutes. This time was variable, and completion was checked under the microscope.

For rabbit-based antibodies the Dako kit was used after the peroxidase blocking step for 30 minutes. After these slides were rinsed three times with PBS. DAB solution was then made up and applied to the slides which were developed for around 10 minutes. This time was variable, and completion was checked under the microscope.

Both the mouse and rabbit antibody slides were then stained with haematoxylin as above before been run through a dehydration gradient and mounted using DPX medium.

2.6 Immunofluorescence

2.6.1 Quadruple immunofluorescence Assay

Previous work by Dobson et al. (205) showed for the first time a link with mitochondrial mutations and OXPHOS dysfunction and osteoblast dysfunction leading to the development of premature osteoporosis in the PolgA^{mut}/PolgA^{mut} mouse model. They demonstrated a respiratory deficiency in terms of expression of complex I and complex IV in osteoblasts from these mice using quadruple immunofluorescence assay.

This same assay was employed to identify mitochondrial complex I and complex IV deficiencies within osteoblasts in human tissue.

Following decalcification and paraffin embedding as described above tissue was cut in 4-micron thick sections and mounted on Leica X-tra clipped glass slides. These slides were then left to air dry for one week.

Dewaxing was performed at 60°C for 30 minutes followed by deparaffinisation using histoclear for 5 minutes followed by another 5 minutes in fresh histoclear. Specimens were then rehydrated using graded alcohol concentrations. The specimens were then immersed in 70% alcohol with 0.25% ammonium chloride at room temperature for 1hr which reduced autofluorescence. Following this, final rehydration in 50% alcohol for 10 minutes was performed.

Antigen retrieval was performed using 1mM tetra EDTA at pH 8.0 at 80°C for 35 minutes before a PBS wash for 5 minutes with agitation. Sections were marked and encircled with a PAP pen then incubated with 10% normal goat serum in PBS block in a humidified container at room temperature for 1 hour. Following this, three PBS washes were performed as above. Avidin/Biotin blocker was then used according to the manufacturer's instructions (Vector Laboratories). Following a final two PBS washes the sections were incubated with the primary antibodies overnight in the dark at 4°C. Monoclonal antibodies were used for respiratory chain complex identification, mitochondrial mass and osteoblast markers. Osteoblast markers were used at a concentration of 1:50 whereas the other antibodies were used at a 1:100 ratio in 10% NGS PBS solution.

Primary antibodies:

- NDUFB8 - NADH dehydrogenase [ubiquinone] 1 beta subcomplex subunit 8. NDUFB8 is an accessory unit of NADH dehydrogenase (ubiquinone), complex 1 of the respiratory chain
- MTCO1 - Mitochondrial Encoded Cytochrome C Oxidase I, Cytochrome C Oxidase I is the main subunit of complex IV of the respiratory chain
- VDAC – Voltage-dependent anion channels are a member of the porin channels and found on the mitochondrial outer membrane. This antibody was used to represent mitochondrial mass
- Osteocalcin – is secreted solely by osteoblasts and was used as a marker of osteoblast cells

Following overnight incubation, cells were washed with PBS three times as previously described. Secondary antibodies were then applied at a 1:200 concentration except to the VDAC secondary which was applied a 1:100 again in a 10% NGS PBS solution.

Secondary antibodies:

- Alexa 488 IgG2A – MTCO1
- Alexa 568 IgG H+L – Osteocalcin
- Jackson Immune, Biotinylated anti–IgG1 – NDUFB8
- Jackson immune, 405 Dylight – VDAC

Following a 2-hour incubation period, the sections were again washed as before with PBS three times. They were then incubated with streptavidin-conjugated Alexa 647 at a concentration of 1:100 again incubated for 2 hours at 4°C in the dark. Finally, sections were mounted using Prolong Gold and kept at -20°C until imaging. Concurrent no primary controls were created at the same time in a similar fashion but only the Osteocalcin primary antibody was applied. Anti-Osteocalcin was replaced with anti-Cathepsin K to identify osteoclasts.

This protocol formed the basis of immunofluorescent methods development and would be utilised and adapted in chapters 4 and 5.

2.6.2 High throughput immunofluorescent assay

This assay is developed in Chapter 4 on the development of the High throughput screening to identify mitochondrial respiratory chain protein deficiencies. MSC cells were sorted on to a Senso 96 well glass bottomed plate using the flow cytometry MSC separation assay. Or MSCs could be cultured directly onto the plate. The media was removed, and the cells were washed once with sterile PBS. They were then fixed with fresh 4% paraformaldehyde (TAAB) 2 minutes. This was followed by three TBST washes. Cells were then permeabilised using a methanol gradient:

- 70% methanol for 5 minutes.
- 95% methanol for 5 minutes.
- 100% methanol for 10 minutes
- 95% methanol for 5 minutes
- 70% methanol for 5 minutes.

Three washes with TBST followed. The cells were then blocked with 10% NGS diluted in TBST with 0.3M glycine for 1 hour. Cells were then ready for primary antibody staining.

Primary antibodies were left to incubate overnight at 4°C on rocker at 30 rpm. Antibodies were diluted in 10% NGS and TBST.

Antibody	**Ig**	**Concentration**
Anti-Rabbit NDUFB8	Rabbit H+L	1:100
Anti-Mouse VDAC1	IgG2b	1:100
Anti-Mouse MTCO1	IgG2a	1:100

Three washes in TBST followed primary staining after which a secondary antibody cocktail diluted in 10% NGS and TBST was used

Antibody	**Concentration**
Anti-Rabbit Alexa 568	1:200
Anti-IgG2b Alexa 647	1:200
Anti-IgG2a Alexa 488	1:200
Dapi	1:1000

Antibodies were incubated with the plate covered with foil (in the dark) for 2 hours at 4°C on rocker at 30 rpm. Three TBST washes followed, and then sterile PBS added to wells. The cells were then ready to be imaged using the Zeiss CD7 microscope at 20x zoom.

2.6.3 Imaris and Spotfire image analysis

Initially, images were taken using a Nikon A1 confocal microscope at a 60× optical magnification with a 1.55× digital magnification applied, using solid-state lasers to provide light at the following wavelengths 405, 488, 568 and 647 nm.

Image analysis was performed on Imaris image analysis software (Bitplane, v.8.4). Using the 405nm channel, the mitochondrial mass was identified in areas positive for the VDAC antibody in cells which were positive for the Osteocalcin antibody (568nm).

The software was then used to measure the average intensity value of these positive areas in the VDAC (405nm), COX-I/MTCO1 (488 nm) and Complex I/NDUFB8 (647 nm) channels. No primary controls were used to calculate background signal intensity for the 405, 488 and 647nm wavelengths in Osteocalcin-positive cells to compare to the stained cells.

As part of methods development image acquisition using a Zeiss Axio-observer LSM800/SDI microscope was favoured. Images taken on this microscope were at varying magnification depending upon the application. This was still based upon using four solid-state lasers to provide light at the following wavelengths 405, 488, 568 and 647 nm.

Images obtained from the Axio-observer were analysed using TIBCO software Columbus and Spotfire. Using Columbus, a pipeline was built for automatic analysis. Cells were identified using a nuclear stain followed cytoplasm identification and segmentation using TOM20 as a marker, this allowed separation of individual cells. A mask was then created from the TOM20 staining and intensity values for Complex I and Complex IV for each cell were gained. Analysis of this pipeline was performed in Spotfire.

2.7 DNA extraction and lysis

DNA was extracted from individual stem cells which had been sorted using flow cytometry as in *2.4.2.2 Mesenchymal Stem Cell separation.* A lysis buffer (Tris-Tween-Proteinase K lysis buffer: 0.5 M Tris-HCl, 0.5% Tween 20, 1% Proteinase K, pH 8.5) was made up in the UV hood. Cells were sorted using flow cytometry into a 96 well plate containing 15µl of buffer per well. The plate was sealed on completion of cell sorting.

Prior to lysis, cells were pulse spun and then incubated at 55°C for three hours, followed by 10 minutes at 95 °C.

The lysates were then placed into labelled individual 0.2ml PCR tubes and stored at -20°C for amplification.

2.8 PCR and sequencing

2.8.1 Long-range PCR methods and optimisation

Long range PCR was utilised to sequence the mitochondrial genome within individual stem cells. The aim was to identify clonally expanded mitochondrial DNA point mutations within individual cells by comparison to a consensus sequence from the same patient. Primer pairs were chosen to amplify the 16kb mitochondrial genome with overlapping regions to ensure full coverage.

Originally 4 pairs of primers (4F-13R, 12F-21R, 20F-28R and 29F-5R) were utilised however results were more consistently gained in terms of successful amplification using 5 pairs of primers. Primers were chosen in reference to the Revised Cambridge Reference sequence as highlighted in *Table 18.*

Initially, TaKaRa LA Taq DNA Polymerase was trialled however successful amplification of the mitochondrial genome was not achieved and there were no clear bands seen on electrophoresis gels. The utilisation of Promega Go Taq Long PCR Master Mix as per the NHS diagnostic laboratory at the Wellcome Trust Centre for Mitochondrial Research improved yields. PCR reactions were typically set up to a total volume of 25µl, this required 1µl of sample DNA, 0.5µl of the upstream and downstream primers (stock concentration 10µM), 11µl of nuclease-free water and 12.5µl of Go Taq. Master mixes were created on these ratios per sample number with the addition of a control DNA sample and a nuclease-free water sample to check for contamination.

Primers were initially used at a 1:50 concentration from stock (10µM) before increasing to a 1:10 concentration. The final primers chosen for the amplification of the mitochondrial genome in mesenchymal stem cells were as follows:

	Primer location in the mitochondrial genome*		
Primer Pair	Forward Primer	Reverse primer	Amplicon size (bp)
D4F:6R	323 - 343	3574 - 3556	3233-3251
6F:13R	3017 - 3036	6944 - 6924	3888-3927
13R:20R	6358 - 6377	10147 - 10128	3751-3789
20F:28R	9607 - 9627	13859 - 13839	4212-4252
28F:D4R	13365 - 13383	771 - 752	3938-3975

Table 4: Numbering based on Anderson et al. Sequence and organization of the human mitochondrial genome (220). and Andrews et al. Reanalysis and revision of the Cambridge reference sequence for human mitochondrial DNA (221) These primers are published in Tuppen et al Brain 2010, 133(10): 2952 (222).

The thermal cycler was initially set up as per the Go Taq protocol (223). This consisted of a 95°C initial denaturation step for two minutes, followed by a denaturation step at 94°C for 30 seconds. Then an annealing/extension step at 65°C for 6 and a half minutes before a final extension step at 72°C. A 2 step stage 2 and 3 step stage 2 were compared as were a range of temperatures (60,61,62,63,64 and 65°C) for the annealing steps. The 2-stage step 2 consisted of 94°C followed by 65°C for 6 and a half minutes. The 3-stage step 2had an additional 2-minute step at 72°C for each cycle.

A 2-step stage 2 with an annealing/extension step of 60°C was selected with some alteration to the times as below. Stage 2 was initially run 32 times before being increased to 40 with improvement in yields.

- Stage 1 - 95°C 2 minutes
- Stage 2 – 94°C 30 seconds, followed by 60°C for 5 minutes (40 cycles)
- Stage 3 – 72 °C final extension 8 minutes followed by 4°C indefinite soak

For consensus samples, the same protocol was used, and the basis of the sample was taken from a pellet of lympho-prepped cells prior to flow cytometry sorting.

2.8.2 Agarose gel electrophoresis

A 1% agarose gel was made up by dissolving 1.5g of standard agarose in 150mls of 1x TAE buffer using a microwave to heat the buffer. 6µl of Syber Safe (4µl/100mls) were added and the gel was poured into a casting tray with an appropriate comb to meet the well requirement (usually 25 wells). The gel was left to set before transfer to an electrophoresis tank filled with 1x TAE buffer.
1µl of loading dye was placed on parafilm and then mixed with 5µl PCR product. The combination was then loaded on to the gel. 5µl of a 1kb DNA ladder (Promega) were also loaded for sizing of products. The gel was electrophoresed at 120 volts for 45 minutes which allowed sufficient time for the PCR products to separate. PCR products were visualised and imaged using the BioRad ChemiDoc.

2.8.3 DNA purification and quantification

2.8.3.1 Purification

PCR amplicons were purified based upon the protocol from Ion Express Plus Fragment Library kit (224). First of all, 30µl of Low TE buffer was added to each sample and the sample transferred to an Eppendorf DNA lo-bind tube. Then 81µl of AMPure XP Reagent beads were added. The 81µl equates to 1.8x the sample volume. In further purification steps, the volume of AMPure beads added would vary to maintain this ratio. The suspension of amplicon and beads were mixed thoroughly before pulse-spin and incubation at room temperature for 5 minutes. Aside. The tubes were then transferred to a magnetic rack for 3 minutes. The supernatant was then carefully removed followed by two freshly made up 70% ethanol 500µl washes taking care not to disturb the pellet. After each addition of alcohol, the tubes were turned at least twice to allow movement of the beads within the tube. After aspiration of the second wash the tubes were pulse spun and placed back in the magnetic rack. Any residual ethanol was removed using a p20 pipette. The tubes were then left to air dry for 3 minutes. Following this the bead pellets were resuspended in 20µl of Low TE buffer and then vortexed for 10 seconds. They were then pulse spun again before been placed back in the magnetic rack for at least a minute or until the solution cleared. The supernatant was then aspirated and transferred to a new Eppendorf DNA lo-bind tube.

2.8.3.2 Quantification – Illumina MiSeq

In preparation for Illumina MiSeq sequencing, samples were first purified as in *2.8.3.1 Purification*. The Qubit dsDNA HS assay kit (Thermofisher) was used in conjunction with Qubit Fluorometer. This was first calibrated using the 2 standards contained within the kit before 2µl of the cleaned up sample was mixed with the 198µl of the combined solution of Qubit dsDNA HS Reagent and dsDNA HS buffer in a Qubit assay tubes as detailed in the Qubit protocol (225). The Qubit Fluorometer

generated a concentration recorded in ng/µl. Once all of the amplicons from each sample were quantified, they were pooled. 2ng of each amplicon was added to a 96 well plate to a total of 10ng for the complete genome. This PCR plate was then sealed and frozen until preparation for sequencing.

Preparation for sequencing for the MiSeq including clean up, barcoding and quantification took place at the Institute of Genetic Medicine at Centre for Life.

2.9 Flow cytometry

A flow cytometer is an instrument which allows the measurement of the physical parameters of particles including cells as well as the constituent content and profiles using fluorescently labelled antibodies (226). A stream of cells is passed into the cytometer and as each cell passes a laser or light source it creates a set of readings that can be detected and converted into a digital signal. This laser creates the readings of forward scatter which represents cell size and side scatter which represents the granularity of the cells.

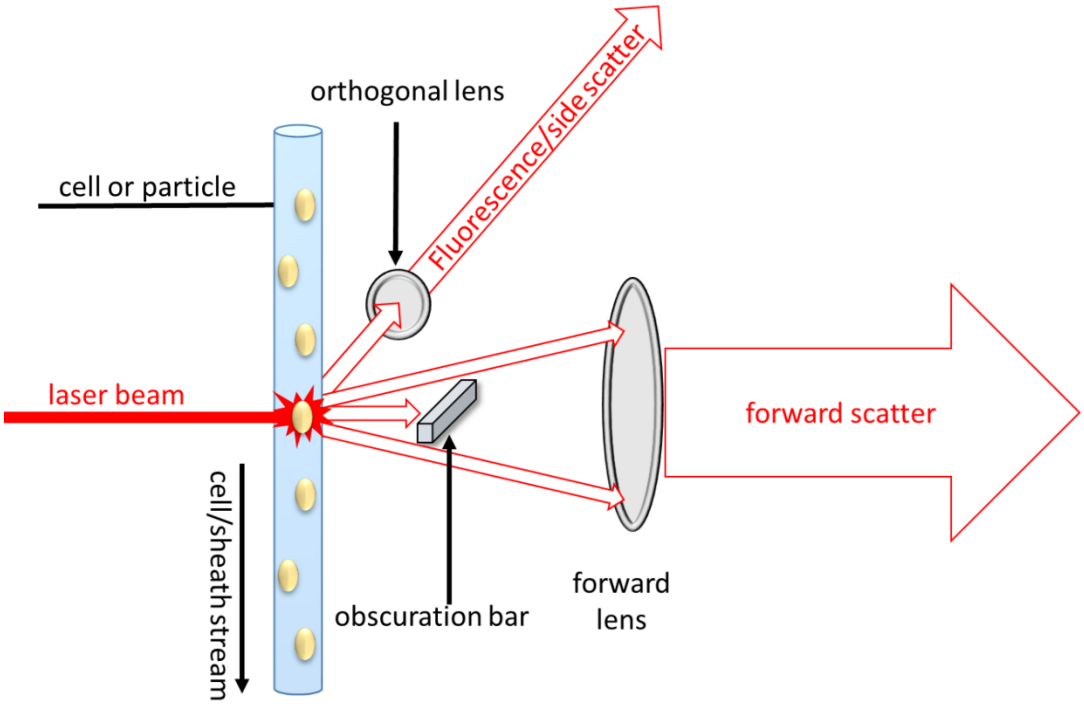

Figure 14 Schematic representation of a flow cytometer, with the laser beam, the sheath stream containing the individual cells, and the lenses for the collection of forward scatter and side scatter/fluorescence all at orthogonal angles to each other. The obscuration bar ensures only light that has hit a particle and been refracted accounts for forward scatter (227).

The use of fluorescent antibodies allows further profiling. When labelled cells are hit with a certain wavelength the fluorescent antibodies will then emit different wavelengths which can again be detected and allow further profiling of the cells. To do this specific wavelength filters and mirrors are required. The number of concurrent antibodies that can be detected is limited similarly to confocal microscopy and is based upon the common lasers used as in *Table 5*.

Laser	Emission wavelengths (nm)
Argon ion	Usually 488, 514, UV(351/363)
Red helium-neon (HeNe)	633
Green helium-neon (HeNe)	543
Krypton ion	Usually 568, 647
Violet diode	408
Blue solid state	488

Table 5 Common lasers used in flow cytometry and their emission profiles (226)

The instrument was first invented in prototype form by Andrew Moldavan in 1934 (228) however it would take many years before it was perfected into its modern-day counterpart (226). The advantage of flow cytometry over conventional light microscopy techniques is the rapid rate of cell analysis up to 5000 per second. However, it requires cells to be in suspension which can be both advantageous and disadvantageous depending on the application.

The use of cytometry would allow a high throughput analysis to be performed without the issues encountered using conventional light microscopy as covered in chapter 4. Flow cytometry was also utilised to separate mesenchymal stem cells from fresh bone marrow using the Miltenyi MSC kit (219). A trial experiment also showed it was able to detect osteocalcin-positive cells from fresh bone marrow. This led to the question: Could flow cytometry be used to identify osteocalcin-positive cells (osteoblasts) and their mitochondrial protein deficiencies in humans as an alternative to quadruple immunofluorescence using confocal microscopy?

Flow cytometry has been used before in relation to mitochondrial study: investigating mitochondrial function by the incorporation of rhodamine 123 in bovine spermatozoa, yeast and other cell lines (229-231), or looking at reactive oxygen species generation and membrane potential (232-234). There is no literature exploring the use of flow cytometry to quantify levels of mitochondrial respiratory chain complex deficiencies as per the quadruple immunofluorescence assay developed by Rocha et al., (235).

The basic protocol was based upon the protocol laid out by Filby et al. 2011 (236). This protocol was optimised using k562 cell lines and fibroblasts. The protocol required these cells to be in suspension

and fixed with a 4% formaldehyde and PBS solution the time for this was variable and is covered in the high throughput results chapter. Fixation could be checked on a flow cytometer with the addition of a detergent (0.1% Triton X-100) which would cause lysis of the cell if not fixed and a changed in the forward scatter/side scatter profile as in *Figure 15.*

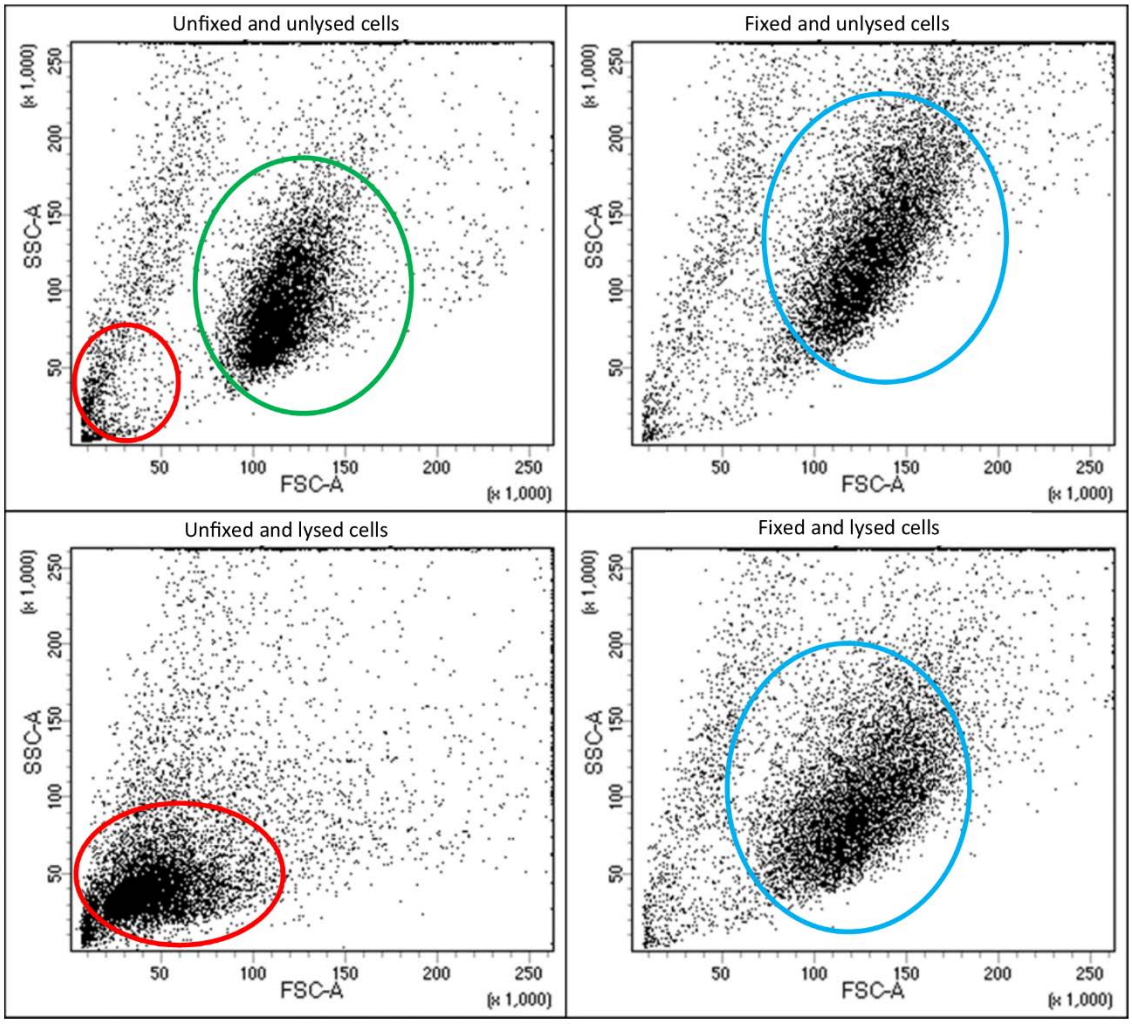

Figure 15 Results of fixation and lysis buffer addition to k562 cells. The dead cells and debris are in the red circle, the unfixed in the green circle and fixed in the blue circle. After the addition of a lysis buffer, there is little change in the blue circle populations compared to the green population which disappears with concurrent change in the dead cell population (red).

Once fixed cells were counted using the BD Accuri C6 flow cytometer. This gave an accurate count of cells per µl and also a visual check of the fixed profile allowing only fixed cells to be counted. Cells were then spun down at 230G for 3 minutes before been re-suspended at 1 x 10^7/ml. Either 5ml round bottom falcon flow tubes were used or a 96 well suspension plate. Cells were stained in 100µl of PBS with 2%FBS at the above density. After fixation cells were washed by spinning down at 230G for 3 minutes, removing the supernatant then re-suspending in PBS with 2% FBS. 2 washes were performed after fixation prior to lysis. To lyse the cells a permeabilisation buffer was added, this was

made up of PBS + 2% FBS + 0.1% Triton X-100. 100µl of this was used to re-suspend the cell pellet and incubated for 5 minutes at room temperature. 100µl of PBS + 2% FBS was added to the cells to end permeabilisation which were then spun down and washed as above. The cells were blocked using a 10% NGS PBS solution for 1 hour at 22°C. The Eppendorf thermomixer was used for this process at 450rpm to ensure the cells stayed in suspension. After this process cells were washed again and then stained for 1-2hrs extending to overnight depending on the antibody, concentrations were also titrated in a solution of PBS and 10% NGS. Following this, the cells were washed 3 times before a secondary antibody was added again incubation period and concentration was titrated. Following these cells were washed twice before analysis on either the BD FACSCanto II Analyser or BD FACSymphony A5 Analyser and plate reader.

2.9.1 Symphony A5 and FACSCanto II systems

The BD Bioscience FACSympony A5 is a cell analyser with the ability to also read plates. It is able to measure up to 50 different characteristics of cells and identify distinct phenotypes in heterogeneous populations. The university machine is configured with 5 lasers 28 different fluorescent detectors. The BD FACSCanto II allows the detection of up to 10 parameters the University machine is set up with 3 different lasers.

2.9.2 BD FACS Aria III Cell Sorter

The BD FACS Aria III Cell Sorter is a flow cytometer setup with the potential of up to six laser wavelengths—633 nm, 561 nm, 488 nm, 445 nm, 405 nm, and 375 nm—and up to 20 detector positions, to measure up to 18 colours simultaneously. This allows the identification of individual cells based upon the phenotype and fluorescently conjugated antibody profile. The cells are then deflected from their path depending on this profile using electrostatic charge. The FACS Aria III was used in the separation of individual MSCs from bone marrow for PCR and high throughput analysis. Cells were individually sorted into a 96 well PCR plate and also pooled into a 96 well flat bottom plate or Ibidi 8 well chamber slide.

2.10 Imaging Mass Cytometry

2.10.1 Hyperion and Helios Mass Cytometry systems

The Helios and Hyperion imaging module system from Fluidigm is the latest generation of CyToF (cytometry by the time of flight) machine. It works on the principle of time of flight mass spectrometry and inductively coupled plasma mass spectrometry (237, 238). Unlike fluorescence microscopy, it is a method for measuring single cell properties much like flow cytometry but instead of relying on the fluorescent spectrum it relies on measuring the time of flight determined by the mass of the molecule/antibody coupled protein. Unlike flow cytometry, it is not bound by the constraints of the fluorescent spectrum and so a great number many more parameters (up to 40) can be measured without signal overlap (239). As it is reliant on mass, not fluorescence there is also no issue with autofluorescence which has been an issue in both the quadruple immune fluorescent assay and the use of flow cytometry.

Mass cytometry antibodies instead of been conjugated to fluorescent probes are attached to isotopically pure heavy metals which then alters the time of flight of the protein and antibody. This alteration can be detected and used to create data similar to that of flow cytometry or reconstructed into an image if using the Hyperion module.

Cells can be treated in a similar fashion to flow cytometry in terms of fixation, permeabilisation and blocking. They are then labelled with heavy metal conjugated antibodies. Once labelled they are passed in a stream through an inductively coupled plasma torch, this vaporises the cells creating an ion cloud which is then passed through a quadrupole. The purpose of this is to remove the low mass ions. Following this, the time-of-flight chamber accelerates ions at a fixed potential with low mass travelling further. The time of flight is measured allowing simultaneous measurement of multiple parameters on cells. This data can be formatted to give a readout similar to that of flow cytometry. A DNA stain is required to categorise cells as there is no other equivalent to forward scatter or side scatter.

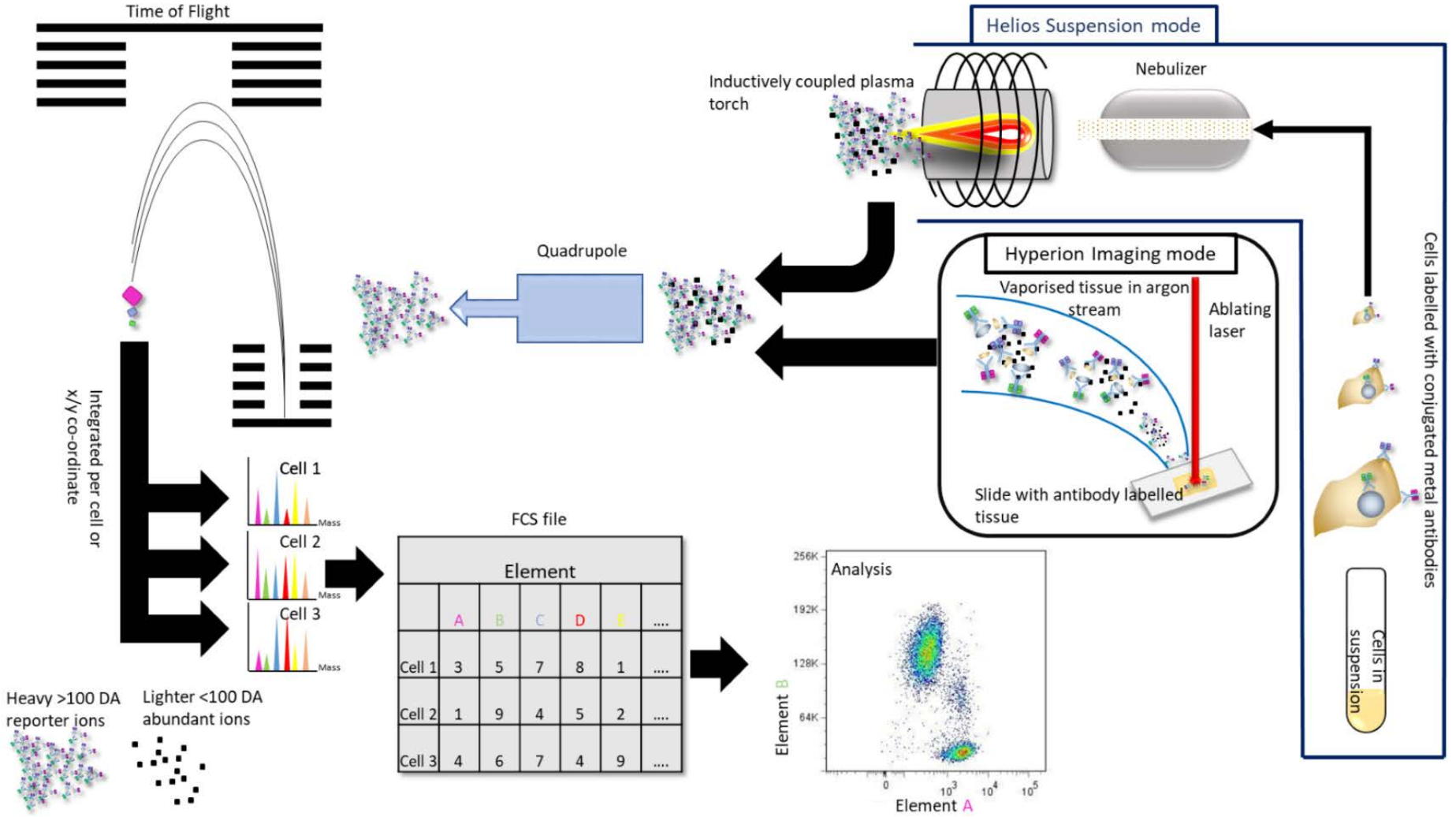

Figure 16 Schematic representation of mass cytometry in suspension (Helios) and imaging modes (Hyperion) based upon Atkuri et al.,(239).

Whilst mass cytometry could be used as an analogue to flow cytometry and there are benefits and drawbacks as highlighted in *Table 6.* One major benefit of mass cytometry is its' use in imaging tissue. Here rather than analysing single cells in suspension a laser is used to ablate the tissue and the ablated tissue enters the mass cytometer in a stream of argon gas as in *Figure 16*. From there on the process is essentially similar but the X/Y coordinates of the laser are recorded, and the data can be used to reconstruct an image. Again, this does not use fluorescence so no autofluorescence or concerns of spectral overlap need to be addressed. The major drawback of this process is time taken to image a section which is significantly slower than microscopy or analysis of cells within a suspension as the laser scans at 1µm at 100-200 Hz (240).

Feature	Flow Cytometry	Mass Cytometry
No. of biomeasures that can be multiplexed	3–18 Parameters	Up to 40 parameters (the instrument is capable of multiplexing 100 biomeasures)
Compensation	Fluorescence compensation absolutely required	No fluorescence-style compensation required. However, correction for isotopic impurities in metal tags and oxides is needed
Status of cells	Both live and fixed cells can be analysed	Cells are required to be fixed prior to analysis
Cell sorting	Yes (in sorters)	No
The efficiency of analysis of injected samples	>95%	30–40% of injected cells are analysed
Speed of acquisition	Up to 60,000 cells/s	Up to 1000 cells/s
High-throughput compatible	Yes (with a 96-well format)	Yes (with a 96-well format)

Table 6 Comparison of mass cytometry and flow cytometry (239).

Mass cytometry, therefore, offers a solution to imaging osteoblasts ex vivo and within bone sections in a similar fashion to Dobson et al., (205) to quantify mitochondrial respiratory chain protein deficiencies and their impact upon osteoblast function. It also would allow analysis of MSCs and any osteoblasts extracted from bone marrow aspirates in suspension.

2.10.2 Antibody conjugation

Whilst there are a number of pre-conjugated antibodies available suitable for mass cytometry the majority of these are not suitable to mitochondrial and osteoblast research, as a result, the panel of antibodies desired had to be conjugated. A conjugation kit is available from Fluidigm and protocol available for the reaction (PRD002) (241). An overview of the process is represented in *Figure 8.*

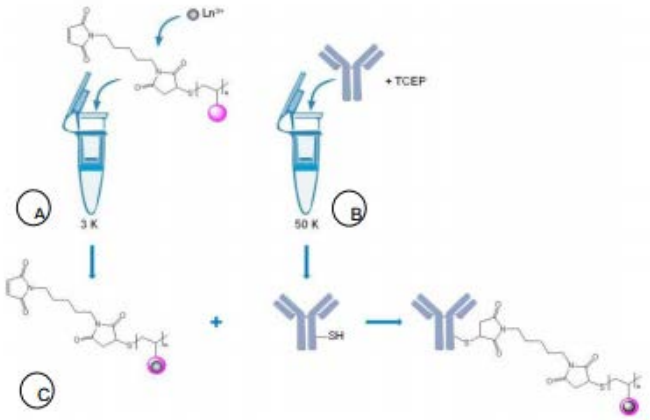

Figure 8 Schematic representation first loading the polymer with lanthanide (A) and partially reducing the antibody (B), then conjugating the antibody with the lanthanide-loaded polymer (C) (31).

2.10.3 Conjugation testing and results

Conjugation testing can then take place using the Helios mass cytometer.

This was done with AbC™ Total Antibody Compensation Bead Kit from ThermoFisher (A10497). First, 1 drop of positive and negative beads are added to a FACS tube then 100µl of PBS and finally 1µl of antibody. The solution is vortexed then incubated at room temperature for 30 minutes. The incubation period is followed by 1 wash steps with the addition 2mls of PBS. The solution is then spun down using a centrifuge at 1000G for 5 minutes. The supernatant is discarded taking care not to disturb the pellet. The beads are then incubated with a positive marker such as cisplatin 2.5µM or iridium 1:500 for 30 minutes at room temp. This is followed by three 2ml dH_2O washes with centrifuge steps as above between. After the final wash step, the supernatant is again discarded, and the beads re-suspended in 200µl of PBS.

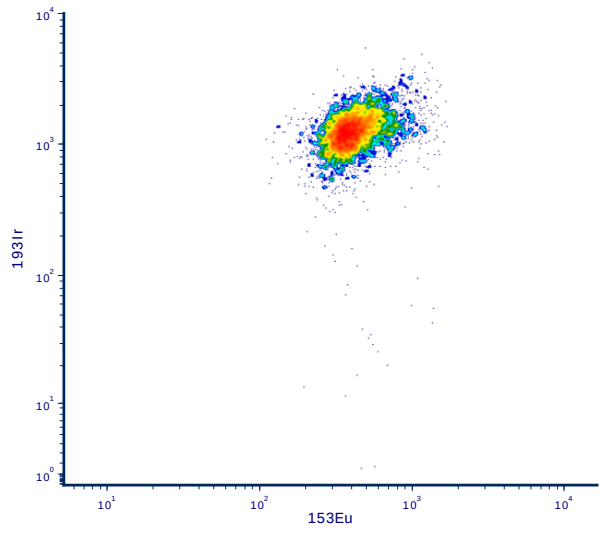

Figure 9 Binding of MT1-MMP antibody conjugated with 153 Europium in comparison to 193 Iridium binding on AbC compensation beads.

2.11 Cell Culture

2.11.1 MSC isolation

Samples of bone were obtained from patients undergoing hip and knee arthroplasty electively. Bone marrow was taken from the femoral canal along with excess cuts of cortical and cancellous bone. Initially, bone chips and marrow were both used as a source of cells for culture. The culture of osteoblasts was based upon the previous mouse model (206).

It is possible to grow osteoblasts from bone chips and from MSC's differentiated into osteoblasts by an osteogenic media. Bone chips taken from the femoral neck provides an excellent source for culture (242). However, this was not always available from the sample population and when used was not as efficient as MSC differentiation. As a result, osteoblasts cultures were derived from differentiated MSC cultures based upon marrow samples.

Marrow samples culture was based upon chapter 7 of Bone Research Protocols (242). For culture αMEM media (Gibco), with 10% of total volume FBS, 0.1% of total volume gentamicin (50 mg/mL concentration), 1% of total volume of Antibiotic-Antimycotic Solution (SIGMA) (10,000 units penicillin, 10 mg streptomycin and 25µg Amphotericin B per mL) was used. Samples of marrow were also taken at the time of anterior cruciate ligament surgery as well as hip and knee arthroplasty.

Marrow samples were transported from a donor at the time of removal to the tissue culture lab. Marrow was then vortexed for 10 seconds with a 1:1 ratio of αMEM media. This was then allowed to stand for 1 minute during which period the fat settled to the top. The fat was removed then the cell

suspension aspirated and inserted into a T75 flask. Fat cell contamination has previously caused issues in the growth of human osteoblasts (243). This process was repeated until a total 25mls of media had been added to the flask.

T75 flasks were then incubated at 37°C. On day one post incubation, non-adherent cells were removed by PBS wash and new media was added. Media was then changed twice weekly until cells became 70-80% confluent. For hip marrow samples, this ranged from 3-14 days whereas knee samples overall took much longer 14-49 days.

2.11.2 Differentiation

Once confluent, cells were passaged to 12 well plates at a density of 50,000 per well. In order to do this, the media was first aspirated followed by a PBS wash. 2mls of the trypsin-EDTA solution was added coating the entire bottom of the flask. The flask was then placed in the incubator at 37°C for five minutes. Following this, the flask was agitated to ensure cells were no longer adherent. 5mls of media were added and aspirated then placed in a 50ml falcon tube. The suspension was then centrifuged at 300g for 5 minutes. The supernatant was discarded, and the cell pellet resuspended in 1ml of media prior to counting. Counting was performed by taking 10µl of re-suspended cell suspension and 10µl of trypan blue. These were mixed and placed into a cellometer counting chamber. A Nexcelom cellometer auto 1000 was used to count.

The cells were then distributed at 50,000/well of a 12 well plate with the remainder frozen. Freezing took place in 1ml aliquots of freezing media. Freezing media consisted of 4.5mls of standard αMEM with 0.5mls of dimethyl sulfoxide. Cells were placed in a “Mr Frosty” freezing container in -80°C freezers before been placed into liquid nitrogen for long-term storage.

The cells that were placed in the 12 wells went into osteogenic media with media changes twice weekly for 21 days. Cells distributed at this density have previously proved to go on to differentiate into osteoblasts and create mineralised bone (113).

2.11.3 Osteogenic media

Osteogenic media is generally based upon DMEM or αMEM but requires supplementation for the differentiation of osteoblasts and production of mineralised matrix. αMEM mimics the protein composition of cells and contains higher concentrations of nucleotides and amino acids than other

media (244). In a direct comparison between DMEM and αMEM, the growth of rat osteoblasts cultures was 2-3 days shorter in αMEM than DMEM (243). DMEM has been found to stimulate more extracellular mineralisation than αMEM but cells grown in αMEM had greater acid phosphatase (Apase) activity (245). This mineralisation has been found to be non-specific mineralisation and other studies suggest αMEM carries a favourable advantage for the growth of osteoblasts and cellular activity (246).

Supplementation tends to be with β-glycerophosphate, Ascorbic acid and dexamethasone although other supplements such as 3-isobutyl-1methylxanthine, HEPES and 1,25 dihydroxy vitamin D3 have been used (243, 245-248). Media was also supplemented with 10% FBS, antibiotics and antifungals as above.

β-glycerophosphate is a hydrolysed product of tissue-nonspecific alkaline phosphatase. In order for bone mineralisation to take place, a source of orthophosphate is required and in-vitro β-glycerophosphate has been used at concentrations varying from 2-10mM. At higher concentrations 5 and 10mM, it was found to causes non-specific mineralisation and reduce cell viability (243, 246). Consequently, a low concentration of 2mM was used in the osteogenic media.

Dexamethasone was first shown to promote osteoblast differentiation in the rat (249) and has been successfully used in osteoblast cultures at varying concentrations (243, 245-248). 10nM was shown to give maximum Apase activity but 100nM concentrations showed increased osteoblastic morphology and mineral deposition (245). As a result, 100mM concentrations were used. Dexamethasone was not used in the previous mouse model and has been shown to have a detrimental effect on mouse osteoblast cultures (246, 250).

Ascorbic Acid is a cofactor for the hydroxylation of proline and lysine residues in collagen (251, 252). It also increases non-collagenous bone matrix protein synthesis and is considered essential to osteoblast culture (253). However ascorbic acid is unstable at 37°C and neutral pH requiring the addition of ascorbic acid daily. An analogue of ascorbic acid L-Ascorbic acid 2 Phosphate (AsAP) has been used in culture and is more stable not requiring daily media change (245). In order to replicate 0.25mM concentrations of ascorbic acid AsAP was tested in various conditions and found 0.05mM to be equivalent, any higher concentration had a detrimental effect on cell growth and matrix deposition (245). Its stability at 37°C and neutral pH also meant media could be changed less frequently. A concentration of 0.05mM of AsAP was used and made fresh for each media change.

Chapter 3 - Mitochondrial DNA mutations in mesenchymal stem cells and clonal expansion.

3.1 Introduction:

With age human tissue has been shown to acquire mitochondrial DNA mutations which lead to defective respiratory chain function (254). Although these mtDNA mutations may be low (<0.1%) compared to total mtDNA, individual cells can contain high levels of individual mutations (255). Once this level of heteroplasmy or mutated mitochondria exceeds the levels of wild type mitochondria, a phenotypic threshold is reached and this leads to defective respiratory chain dysfunction leading to effects upon cellular function (256). The threshold level of heteroplasmy to cause an effect is between 50 and 60% in skeletal muscle (257), although this is dependent upon tissue type and can be anywhere up to 95% dependent on the mutation and cell type or as low as 8% in the case of a dominant mechanism of action disrupting respiratory chain function (258). Instances, where this occurs, are part of the ageing cell profile, where mutations have clonally expanded. Although clonal expansion plays a significant role, individual mutations may exist which in combination with other mutations can also contribute to the pathogenicity.

Clonal expansion is the process to describe the accumulation of a single mutated species of mitochondrial DNA to higher levels than the threshold to cause an effect upon cellular function such as respiratory chain deficiency. Clonally expanded mutations exist in a single cell where the mutation prevalence expands with replication. Mitochondrial mutations can affect the respiratory chain proteins and if reach the phenotypic threshold leads to dysfunction. Mitochondrial mutations affecting respiratory chain proteins in mice have been associated with premature onset osteoporosis (109, 181).

3.1.1 Mitochondrial DNA mutation formation and clonal expansion

The mitochondrial genome is a double-stranded circular genome and codes for 13 of the polypeptides which make up the respiratory chain as well as a further 2 ribosomal RNAs and 22 transfer RNAs. There is also a non-coding control region known as the displacement loop or D-loop. Somatic mitochondrial DNA mutations have been shown to accumulate with age in various tissues including colon, skeletal muscle, myocardium and brain (19, 259-261).

The theory of random genetic drift proposed by Elson et al., (254) was based upon the replication dynamics proposed by Shadel et al. (262) and demonstrated that relaxed replication alone can lead

to marked intracellular drift in post-mitotic tissue leading to a single mutated mitochondrial DNA molecule reaching high levels within a cell due to clonal expansion. This is without offering any selective advantage in terms of replication or phenotypical properties as previous theories such as Wallace et al. had suggested (263). Wallace et al. also hypothesised that mtDNA's proximity to free radicals generated in oxidative phosphorylation was thought to be a causative factor in the generation of mutations (264). Coller et al., (265), proposed a mechanism of random processes to account for the increased incidence of homoplasmic mtDNA mutations found in human tumours. They demonstrated this using a number of computer models and showed that a mtDNA mutation requires around 70 generations to become homoplasmic.

The computer model used by Elson et al. demonstrated that the majority of the mtDNA mutations were occurring before the age of 30, which is also the age at which bone mineral density begins to decline (3). Mutations beyond this point would not have time to accumulate and cause an effect. This is supported by the model by Coller et al., who modelling with an epithelial cell showed that random mutation generation took on average only 70 generations to become homoplasmic and was sufficient to explain the presence of homoplasmic mtDNA mutations found in human tumours (266). Given the length of time for clonally expanded mutations to reach phenotypic threshold it has been suggested that the origin of these mutations would need to take place in early development or even in the maturing oocyte where rapid growth and division of the embryo are taking place (267).

Mitochondrial DNA replication is independent of nuclear replication and again differs as it also lacks the repair mechanism and protective proteins such as histone compared to nuclear DNA (268). Single-cell analysis on skin fibroblasts has shown point mutations to occur at high levels up to 50% in patients over 65 years old (269). Work using colonic epithelium has shown that whilst some mutations exist at embryogenesis and are inherited, there is the presence of pathogenic mutations from early adulthood at low levels and also clonal expansions. These clonal expansions increase dramatically with age and are a significant factor in tissue dysfunction (270). In the case of colonic epithelium, Smith et al., showed age related mtDNA mutations and OXPHOS dysfunction cause metabolic remodelling and in the cases of the $PolgA^{mut}/PolgA^{mut}$ mouse model show a positive environment for the propagation of colonic adenoma and tumour. They also showed significant increases in OXPHOS deficiency and mtDNA mutation load with age and present in normal epithelium as well as with human adenoma or carcinoma within the colon (271).

3.2 Aims of investigation

This investigation aims to identify evidence of mitochondrial DNA mutations in mesenchymal stem cells taken from bone marrow in comparison to a consensus sequence of cells from the same bone marrow sample. The purpose is to clarify whether pathogenic mtDNA mutations exist at high level heteroplasmies. These identified mutations would then be compared to protein deficiencies explored in the high throughput and CyToF chapters. The results of this investigation will be compared to other tissues such as stem cells from the colon where similar experiments have taken place (19).

3.3 Methodology and Results

3.3.1 Patient Cohort

Bone marrow samples were collected at the time of routine orthopaedic surgery often total hip replacement surgery. In the case of total hip surgery, the femoral neck is cut, and the bone marrow was aspirated using a syringe or collected using a curette into a sterile universal container (20mls). Ideally close to the 20mls of bone marrow was taken, although this varied from patient to patient and the scenario in which the bone marrow was collected. For the sample “Femur 1” less bone marrow was collected via syringe due to limited access to the intramedullary cavity, this sample was taken during an intramedullary nailing procedure. The marrow samples were then taken to the laboratory on ice to reduce cellular insult. In addition, bone samples were also collected at the time of surgery from the same patients for use in the Mass Cytometry chapter. Patient demographics, biometrics and information can be seen in *Table 7*. Ethical approval for the collection of paediatric and adult samples was gained via the Great North Biobank, application number (*GNB-012)* and Newcastle Bone and Joint Biobank – *(REC reference 14/NE/1212, IRAS project ID 166522)* respectively.

Table 7 Patients' whose samples were used in the mtDNA sequencing experiments.

Sample	Age (years)	Sex	Surgery	Date of Surgery	Indication	Co-morbidities	Osteoporotic preventive/causative medication
Hip 1	53	F	Total hip replacement	16/01/2019	Osteoarthritis	hypertension	Omeprazole/lisinopril
Hip 2	84	F	Total hip replacement	12/03/2019	Osteoarthritis	ischaemic heart disease, type II diabetes mellitus, asthma, hypertension, peripheral neuropathy, venothromboembolism, vitamin D deficiency, B12 and folate deficiency	Atorvastatin, Metformin, Warfarin
Hip 3	88	F	Total hip replacement	13/03/2019	Osteoarthritis	type II diabetes mellitus, chronic kidney disease, atrial fibrillation, diverticular disease, hypertension	Furosemide, Atorvastatin
Hip 4	83	F	Total hip replacement	01/04/2019	Failed Fixation	hypothyroid, hypertension, osteoarthritis	Calcichew d3,cholecalciferoll, furosemide, levothyroxine, risedronate
Hip 6	45	F	Total hip replacement	02/04/2019	Osteoarthritis		
Hip 7	82	M	Total hip replacement	03/04/2019	Osteoarthritis	chronic obstructive pulmonary disease, gastro-oesophageal reflux disease, iron-deficiency anaemia	Omeprazole, steroid inhalers - tiotropium, fluticasone, Seretide
Hip 8	74	F	Total hip replacement	11/04/2019	Osteoarthritis	atrial fibrillation, pulmonary hypertension, iron-deficiency anaemia	Omeprazole, Bisoprolol, Rivaroxaban
Hip 9	64	M	Total hip replacement	11/04/2019	Osteoarthritis	chronic kidney disease, type II diabetes mellitus	Dialysis, Atorvastatin, Diltiazem, Furosemide,
Hip 10	62	M	Total hip replacement	02/05/2019	Osteoarthritis	type II diabetes mellitus, hypertension	Lisinopril, metformin atorvastatin, Adalat
Hip 11	61	F	Total hip replacement	24/11/2017	Osteoarthritis	hypertension	Propranolol, Venlafaxine
Hip 12	78	F	Total hip replacement	24/11/2017	Osteoarthritis	hypertension	
Hip 13	25	M	Total hip replacement	09/03/2017	Post traumatic acetabular fracture non-union		
Femur 1	22	M	Intramedullary nail and bone graft	27/03/2019	Leg length discrepancy after trauma		

3.3.2 Methods Development

3.3.2.1 Mesenchymal stem cell separation.

Mesenchymal stem cells were first separated using the Miltenyi kit (219); this kit is based upon the findings and criteria defined by Dominici et al., (272). Without using the Miltenyi kit or antibody markers mesenchymal stem cells are classified on culture by their phenotype properties; plastic adherence, spindle shapes, adipogenic, osteogenic, myogenic and chondrogenic potential. The original intended use of the separation assay was for use in culture but as the work developed it was realised that this could be used to isolate individual stem cells on which PCR and subsequent DNA sequencing could be performed.

The issue when extracting MSCs from bone marrow is their frequency is extremely low at 1 per 34000 of the nucleated cell population (273). The use of animal models has also suggested that MSC frequency also declines with age as well as their osteogenic potential. In human study, the decline is not confirmed with varying opinions although these could be dependent on the volume and site of bone marrow aspirates obtained (274). As well as low frequency, the other major issue in the samples collected was the significant contamination of samples with other cell types in particular red blood cells.

3.3.2.2 Red cell lysis buffer

To remove some of this contamination a red cell lysis buffer was used as a pre-emptive step after the collection of samples. 1x RBC lysis buffer from Affymetrix *(00-4333)* was used as per the below published protocol from Affymetrix.

This was done after the filtration of samples with a 100µm cell strainer. 10mls of lysis buffer were added to each 1ml of filtered bone marrow. This mixture was incubated for 10 minutes at room temperature and then the reaction stopped by adding 30mls of PBS. The mixture was then spun at 300g for 5 minutes before fluorescent antibody staining for flow cytometry.

Whilst the Affymetrix assay improved yields in terms of positive cells sorted per number of cells analysed/processed this still was not particularly efficient, with a large number of contaminating cell types of no interest. Further use of the Affymetrix assay demonstrated that the efficacy dropped off.

As a result, 10x red cell buffer was made from scratch using: 80ml ddH_2O, 8.99g NH_4Cl, 40µl 0.5M EDTA pH 8.0. pH was adjusted to 7.3 then the final concentration was made up to 100mls with

ddH_2O. This was then used for red cell lysis: 5mls of RBC buffer was added to a 50ml Falcon tube followed by the bone marrow sample. This was topped up to 50mls total with ddH_2O. The tube was then inverted several times to mix and left at room temperature for 5 minutes. If the solution failed to clear, a further incubation for 5 minutes was performed at 37°C. Following this, the Falcon tube was centrifuged at 300g for 5 minutes and then the pellet was re-suspended in flow buffer for use. Whilst the second more concentrated buffer improved flow analysis results, there remained a degree of contamination with red cells and other cell lines not of interest which decreased the efficiency of the cell sorting process and overall time to sort.

3.3.2.3 Lymphoprep bone marrow preparation

The bone marrow was processed using a density gradient (lymphoprep) to separate mononuclear cells from red blood cells, plasma and other blood constituents. Bone marrow was first diluted with tissue culture (sterile) PBS at a ratio of 1:4. The product was then passed through a 70µm cell strainer. 15ml of lymphoprep was then added to a falcon tube. 30mls of the filtered marrow PBS mixture was added carefully on top taking care not to mix the two constituents.

The Falcon tube was then spun at 800g for 20 minutes with slow acceleration and deceleration profiles selected on the centrifuge. From the centrifuged tube the mononuclear layer was removed using a sterile Pasteur pipette. This layer was placed into a new 50ml falcon tube which was then topped up with sterile PBS to wash the layer. This falcon tube was then spun again at 500g for 5 minutes the cell pellet was then resuspended for flow cytometry in Ca, Mg PBS.

By using the lymphoprep separation step this allowed the removal of a concentrated mononuclear layer and as a result, there was a much higher proportion of MSCs within this layer compared to using just a red cell lysis buffer. The lymphoprep step had two benefits, it removed the fat contamination from the sample and also the red cell contamination. This improving the yield of MSCs from sorting and as a consequence the efficiency of the sort.

3.3.2.4 Flow cytometry

The method for separating stem cells from bone marrow in preparation for PCR is detailed in *2.4.2.2 Mesenchymal Stem Cell separation.* This method was adhered to except for a modification to the antibody fluorophores. The lineage negative markers: CD14, CD20, CD34 and CD45 were conjugated to the FITC fluorophore. The positive markers CD105, CD90 and CD73 were conjugated with PE, APC and Brilliant Violent 421, respectively.

The reason to change the fluorophores from those in the Miltenyi kit is that the above fluorophores are optimally suited to the four-laser setup of the BD FACS Aria III whereas the PerCP and Pe of the original antibodies do share spectral crossover so do not represent the best spectral profile across the four lasers for sorting and excluding cells. The BioLegend antibodies also posed a significant cost reduction compared to the Miltenyi kit.

3.3.2.5 PCR protocol development

Unlike single mutations or PCR/sequencing read errors clonal expansion is easier to demonstrate by virtue of the fact mutations are clonally expanded. When first developing the PCR analysis of stem cells, bone marrow was taken from a 25-year-old (Hip 13), a 61-year-old (Hip 11), a 67-year-old and a 78-year-old (Hip 12). Single-cell sorting was done into a 96 well plate using flow cytometry and the Miltenyi kit MSC sorting kit/assay, this was followed by a lysis step detailed below.

The lysis step consisted of using the 15µl of single-cell lysis buffer per well of a 96 well plate for each sorted cell. The lysis buffer consisted of:

- 250 µl 1% Tween 20
- 50 µl 0.5M Tris-HCl pH 8.5
- 195 µl dH2O
- 5 µl proteinase K

Once the cells were sorted into this buffer using the Aria Fusion cell sorter the plate was sealed and centrifuged at 150g for 1 minute. The plate was then run in the thermo-cycler at 55°C for three hours, followed by 10 minutes at 95 °C. Lysates were then frozen at -20°C.

First attempts to amplify the mitochondrial genome used 2 primer pairs 1F:19R and 19F:1R see *Table 18* for primer details. This initial analysis was done using LA Taq DNA polymerase. This failed to produce any PCR products; further attempts were also made using the primer pairings 5F:29R and 29F:5R before moving to a 3-primer pair setup reducing the amplicon size. The three primer pairs consisted of 1F:13R, 13F:26R and 26F:1R. All these reactions were performed in a 25µl reaction volume on a 3-temperature cycling protocol (Table 8). The denaturation/annealing/extension cycle number was increased from 30 to 35 and the primer concentration increased from 2µM to 10µM as part of the optimisation.

	Temperature	Time	Cycle Count
Initial denaturation	94°C	30 seconds	1
Denaturation	94°C	30 seconds	35
Annealing	58°C	30 seconds	
Extension	68°C	10 Minutes	
Final Extension	72°C	10 Minutes	1
Soak	4°C	Indefinite	1

Table 8: Initial setup of the Thermocycler for long-range PCR.

Using three primer pairs rather than two decreased the amplicon size from ≈8000 base pairs (bp) to ≈6000bp and did improve results. However, positive amplification of the mitochondrial genome on electrophoresis gels was not consistent.

GoTaq long PCR master mix is currently used by the NHS Highly Specialised Service for Rare Mitochondrial Disorders for long-range PCR. GoTaq long PCR master mix has been shown to outperform other polymerases (TaKaRa LA Taq, New England Biolabs: LongAmp® Taq 2X Master Mix, Life Technologies: GeneAmp® XL PCR Kit, Sigma: JumpStart™ AccuTaq™ LA DNA Polymerase Mix) for amplification of a 17.5kb human β-globin target sequence although this is a Promega study (275).

Trial use of the GoTaq long PCR master mix did improve amplicon generation but this was not universal across all of the samples and generation of amplicons representing the complete mitochondrial genome were not possible only fragments.

As a result, the amplicon size was again reduced to around ≈4500bp by using four sets of overlapping primers: 29F:5R, 4F:13R, 12F:21R and 20F:28R the details of which are in the table below and *Figure 17* shows positive amplicon generation on an electrophoresis gel.

Forward Primer	Primer Location in the mitochondrial genome	Reverse Primer	Primer Location in the mitochondrial genome	Amplicon size (bp)
4F	2091-2111	13R	6944-6924	4854
12F	5855-5875	21R	10649-10629	4795
20F	9607-9627	28R	13859-13839	4253
29F	13790-13809	5R	3087-3068	5867

Table 9 Primer details for ≈4500bp amplicons.

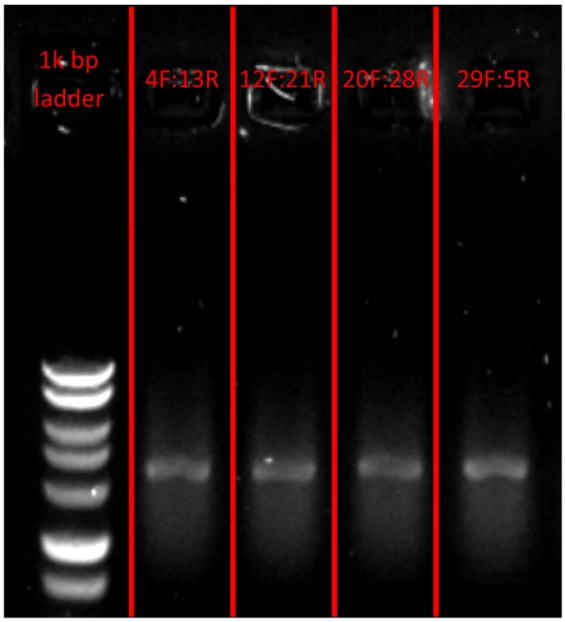

Figure 17 Electrophoresis gel showing positive amplicon products utilising the primers 29F:5R, 4F:13R, 12F:21R and 20F:28R from a single MSC cell from the 25-year-old patient.

The thermal cycler was initially set up as per the Go Taq protocol (223). This consisted of a 95°C initial denaturation step for two minutes, followed by a denaturation step at 94°C for 30 seconds. Then an annealing/extension step at 65°C for 6 and a half minutes before a final extension step at 72°C as in *Table 10*.

	Temperature	Time	Cycle Count
Initial denaturation	95°C	2 minutes	1
Denaturation	94°C	30 seconds	35
Annealing/Extension	65°C	5 minutes	
Final Extension	72°C	8 Minutes	1
Soak	4°C	indefinite	1

Table 10: Initial thermocycler settings for GoTaq master mix.

A 2-step stage 2 and 3 step stage 2 were compared as were a range of temperatures (60-65°C) for the annealing steps. The 2-stage step 2 consisted of 94°C followed by 65°C for 6 and a half minutes. The 3-stage step 2 had an additional 2-minute step at 72°C for each cycle after the 65°C step.

			Temperature	Time	Cycle Count
Stage 1		**Initial denaturation**	95°C	2 minutes	1
Stage 2	**2 steps**	**Denaturation**	94°C	30 seconds	35
		Annealing/extension	60, 61, 62, 63, 64, 65°C	6.5 minutes	
Stage 3		**Final Extension**	72°C	8 Minutes	1
		Soak	4°C	indefinite	

Table 11: 2 stage step 2 setup of the thermocycler for use with GoTaq long PCR master mix.

			Temperature	Time	Cycle Count
Stage 1		**Initial denaturation**	95°C	2 minutes	1
Stage 2	**3 steps**	**Denaturation**	94°C	30 seconds	35
		Annealing	60, 61, 62, 63, 64, 65°C	30 seconds	
		Extension	72°C	2 Minutes	
Stage 3		**Final Extension**	72°C	10 Minutes	1
		Soak	4°C	indefinite	

Table 12 3 stage step 2 setup of the thermocycler for use with GoTaq long PCR master mix.

A 2-step stage 2 with an annealing/extension step of 60°C was selected with some alteration to the times as below. Stage 2 was initially run 35 cycles before being increased to 40 with improvement in yields.

	Temperature	Time	Cycle Count
Initial denaturation	95°C	2 minutes	1
Denaturation	94°C	30 seconds	40
Annealing/extension	60°C	5 minutes	
Final Extension	72°C	10 Minutes	1
Soak	4°C	indefinite	

Table 13 Setup of the thermocycler as used for sample generation for sequencing.

For the majority of the samples, the thermocycler setup as in *Table 13* was suitable. However, where amplification of some products proved difficult a further alteration was made to the protocol and setup. An additional extension step was added, so a three-step stage 2. The setup of the thermocycler is displayed below in *Table 14.*

	Temperature	Time	Cycle Count
Initial denaturation	95°C	2 minutes	1
Denaturation	94°C	30 seconds	40
Annealing	60°C	30seconds	
Extension	65°C	5 minutes	
Final Extension	72°C	10 Minutes	1
Soak	4°C	indefinite	

Table 14 Setup of the thermocycler with the additional annealing/extension step.

With the successful generation of amplicons to represent the mitochondrial genome further single cells were amplified to look to generate a sufficient number to sequence and allow comparison across an age range.

During this process, further alterations to the protocol were made. For more reproducible amplicon generation further reduction in amplicon size by using 5 primer pairs were employed as in Table 15. Although these primer pairs were used for the majority of samples moving 1 primer pair up or down the primer table *(Table 18)* was employed if amplification failed. Changing the primer pairings by 1 position resulted in the generation of amplicons of a similar size with no loss of the genome this effect can be demonstrated in *Figure 18.* New primer stocks were also made up if amplicon generation was failing in the control DNA and across the sample DNA.

Forward Primer	Primer Location in the mitochondrial genome	Reverse Primer	Primer Location in the mitochondrial genome	Amplicon size (bp)
D4F	323 - 343	6R	3574 - 3556	3252
6F	3017 - 3036	13R	6944 - 6924	3928
13F	6358 - 6377	20R	10147 - 10128	3790
20F	9607 - 9627	28R	13859 - 13839	4253
28F	13365 - 13383	D4R	771 - 752	3976

Table 15 Final primer pairings used for the amplification of the mitochondrial genome in single mesenchymal stem cells.

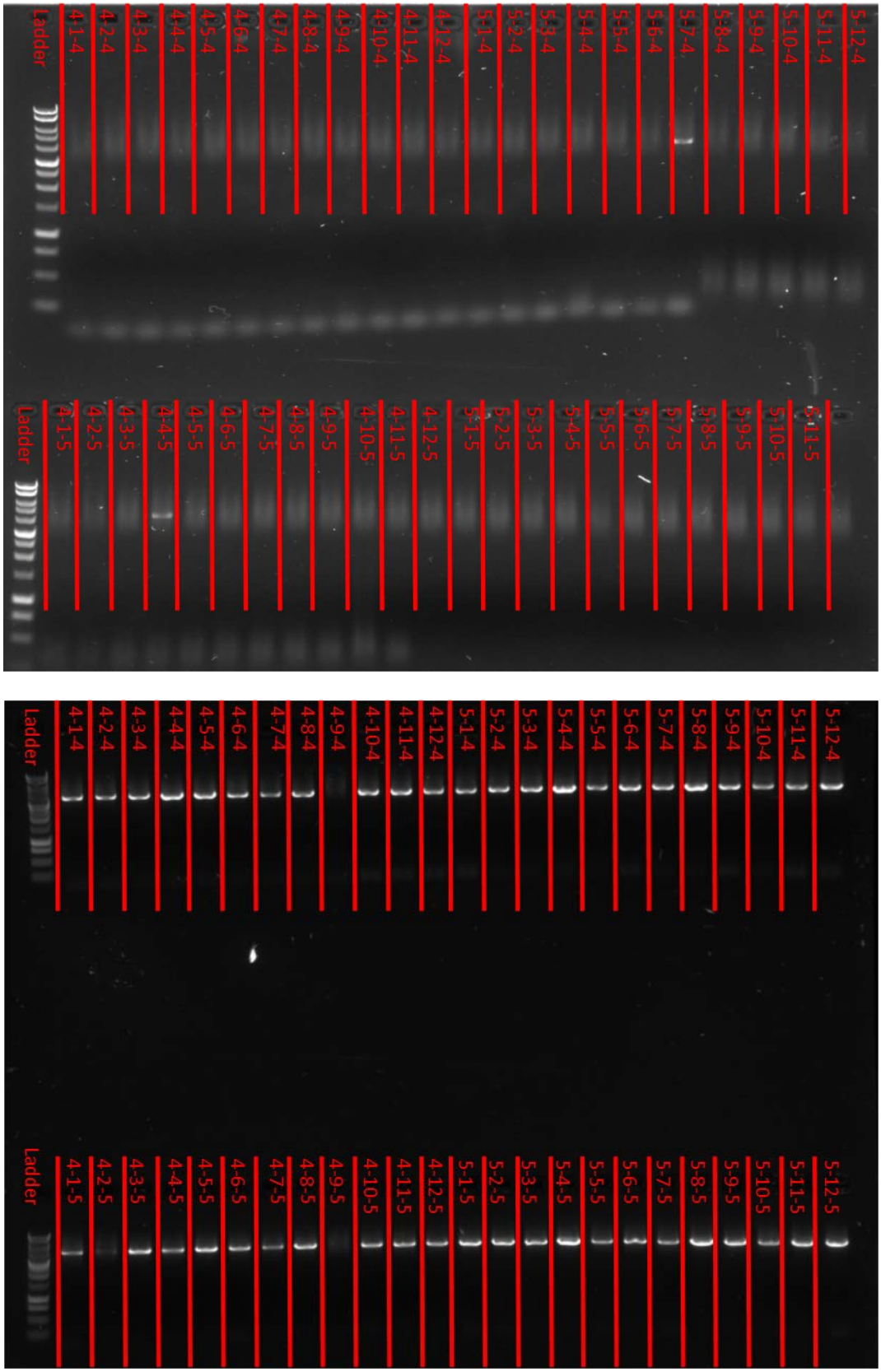

Figure 18 Comparison of using the primers as in Table 7 compared to moving each primer pair by 1 primer set further along the genome as on the reference Table 18. Using the same patients (4 and 5) DNA and cell samples (1-12). Primer pairing changes 20F:28R to 21F:29R (top image) and 28F:D4R to 29F:1R (bottom image).

On completion of the PCR, the products were imaged using the BioRad ChemiDoc in 1% agarose gels using SYBR safe as detailed in *2.8.2* of the materials and methods chapter. In short, this consisted of using 1% agarose in the electrophoresis gel buffer with SYBR safe DNA dye. These were poured into moulds and then once set transferred to an electrophoresis tank with DNA electrophoresis gel running buffer. 5µl of PCR product was mixed with 1µl of DNA loading buffer, the product was then loaded into each well of the gel and compared to a 1kb ladder.

Those amplicons which produced positive when imaged with the ChemiDoc were then cleaned up using AMPure XP reagent beads. The Ampure beads protocol is listed below:

1. First 30µl of low TE buffer was added to the PCR product. Then products were then added to Eppendorf DNA LoBind 1.5ml tubes.
2. The AMPure beads solution was then vortexed thoroughly before use to ensure beads were suspended.
3. Then 81µl (1.8x product volume) of AMPure beads were added to each PCR product and mixed with a pipette 5 or more times. The combined solution was then pulsed span and incubated for 5 minutes.
4. The combined solution was then pulsed span again before transfer to a magnetic rack for at least 3 minutes. Once the solution had cleared the supernatant was removed without disturbing the magnetic bead pellet.
5. The pellet was then washed with 500µl of a freshly prepared 70% ethanol solution (made up with nucleoside free water). After the addition of the alcohol, the LoBind tubes were rotated twice over a 30 second period. The supernatant was then discarded
6. The alcohol washing step was then repeated.
7. Samples were now pulsed, spun and placed back into the magnetic rack. The residual ethanol supernatant was removed with a p20 pipette and the tubes left to air dry for 3 minutes.
8. Following this, the tubes were removed from the rack and 20µl of low TE buffer were added to each tube. Pulse spinning the tubes before mixing of the low TE buffer and beads aided resuspension. This was performed by pipetting the solution and beads multiple times to resuspend the beads fully before vortexing each mixed tube for 10 seconds.
9. The tubes were then pulsed, spun and placed in the magnetic rack for a minute or longer until the solution cleared. This solution was then transferred to new Eppendorf DNA LoBind tubes for quantifying.

3.3.2.6 Ion Torrent quantification and library prep

Once products were purified as detailed in Chapter 2.8.3 , they were quantified. Initially, this was in preparation for using the Ion Torrent sequencer. Following the Ion Express Plus fragment library kit protocol the samples were quantified on an Agilent Bioanalyzer 2100.

The Agilent bioanalyzer sizes and analyses DNA fragments by using a set of micro interconnect channels through which the amplicons are driven based upon size electrophoretically.

The protocol for the DNA 12000 kit was followed to quantify the amplicons of each sample (276). The analyser outputs the size of the fragment, the concentration of the DNA in ng/µl and also the molarity nmol/l. The output of the bioanalyzer can be visualised as below in *Figure 19.*

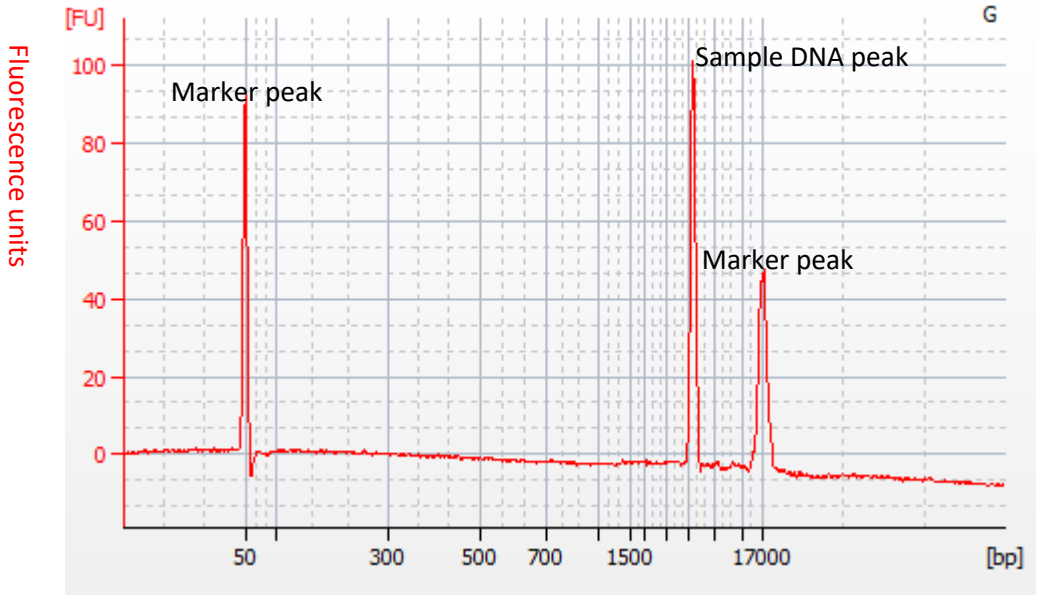

Figure 19 Output from the bioanalyzer demonstrating DNA peak at around 4000bp with the two marker reference peaks at either end of the output.

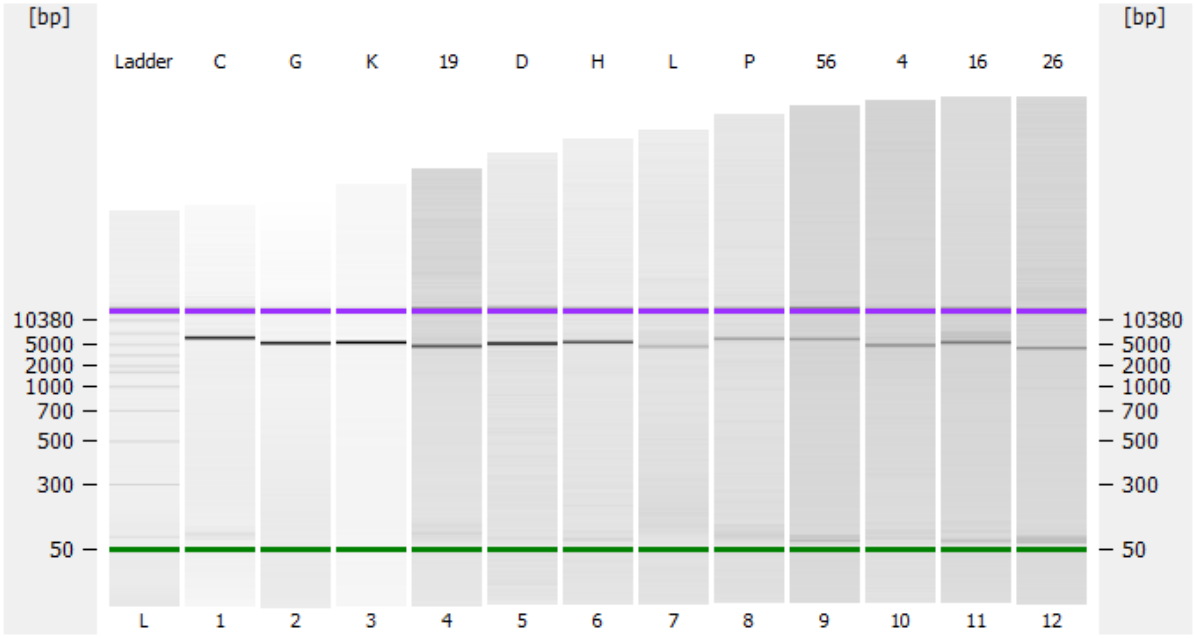

Figure 20 A virtual electrophoresis gel produced by the bioanalyzer. The marker DNA is represented by the purple and green bars with the sample amplicons represented by the black/grey bars in lanes C, G, K,19, D, H, L, P, 56, 4, 16, 26. Again these reside around the 4000bp mark.

Once each of the amplicons for a single MSC had been quantified they were combined into an equimolar solution of 100ng. The pooled amplicons were then fragmented using the Ion Shear Plus kit. This was used as per the protocol in the library preparation protocols from Thermo Fisher Scientific (224). After this, a further purification step using the AMPure XP reagent beads was performed with the only change being that low TE buffer was not added at the start of the step.

After the purification step, the amplicons needed to be labelled with a barcode before sequencing. The Ion Xpress™ Barcode Adapters 1-16 Kit was used for this step and the protocol is again covered in the library preparation protocol (224). A purification step follows the barcoding step. Followed by a size-select step by running the unamplified DNA through a 2% agarose E-Gel and using the E-Gel iBase from Invitrogen.

Once size selected the samples were amplified as per the Thermo Fisher protocol and purified. They were then quantified using the Agilent High sensitivity chip on the Bioanalyzer. The high sensitivity protocol was followed for this step (277). This produced similar graphs to the DNA 12000 kit and again gave the same information in terms of concentration, size and molarity. The samples were then ready to be pooled at the highest possible equimolar concentration in preparation for sequencing. They were stored at -20°C in the intervening time.

3.3.2.7 Sequencing Trial

From the initial protocol design and optimisation 7 samples consisting of the complete mitochondrial genome were compiled ready for sequencing. This was done using the Ion Torrent. This is a next-generation sequencer based in the Wellcome Centre for Mitochondrial Research Newcastle UK. The output of the sequencer was fastq files. These could be uploaded to mtDNA-server. The mtDNA-server is a Hadoop-based server which allows mtDNA next-generation sequencing data processing including sequence alignment, per-base alignment scoring (BAQ), heteroplasmy and contamination detection (278). The mtDNA-server then creates an HTML report including boxplots for heteroplasmy *(Figure 21)*, bar plot for the frequency of heteroplasmy and the locus of heteroplasmic variants *(Figure 22).*

Whilst the data from the mtDNA server output demonstrated the feasibility to sequence individual MSCs. There was no comparison to consensus sequences to give levels of background mutations and delineate haplogroup and other characteristics. The proposed patient number and samples per patient would make use of the bio-analyser and ion torrent methods and protocol not suitable to the larger scale of future experiments.

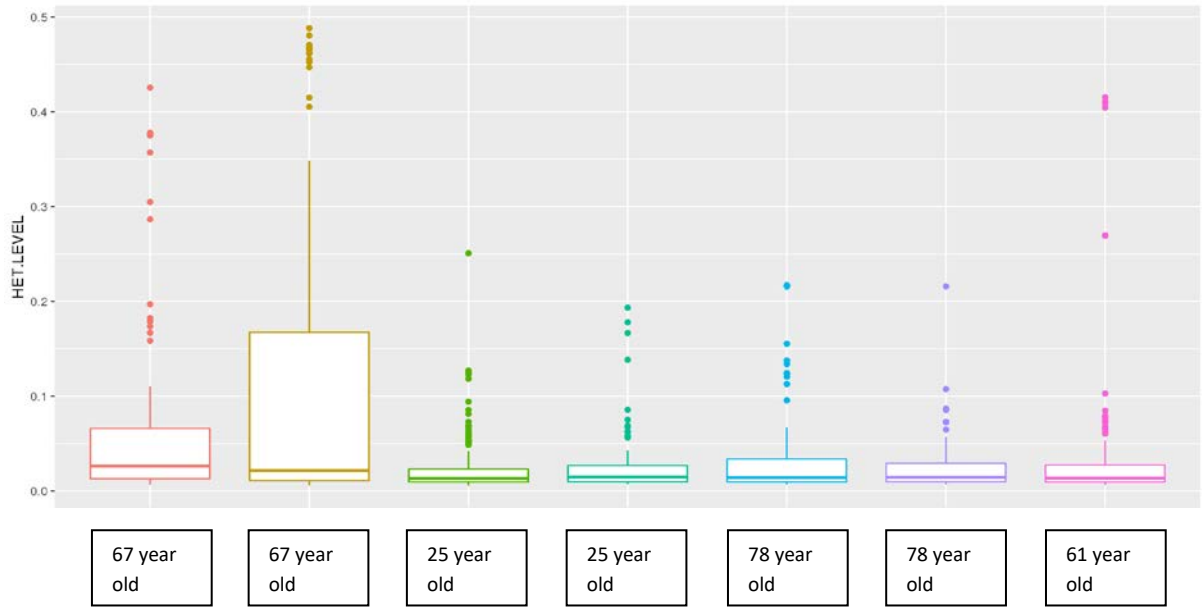

Figure 21 Output from mtDNA server: Heteroplasmy levels for each patient (2 cells per patient except the 61-year-old patient) demonstrated through a boxplot.

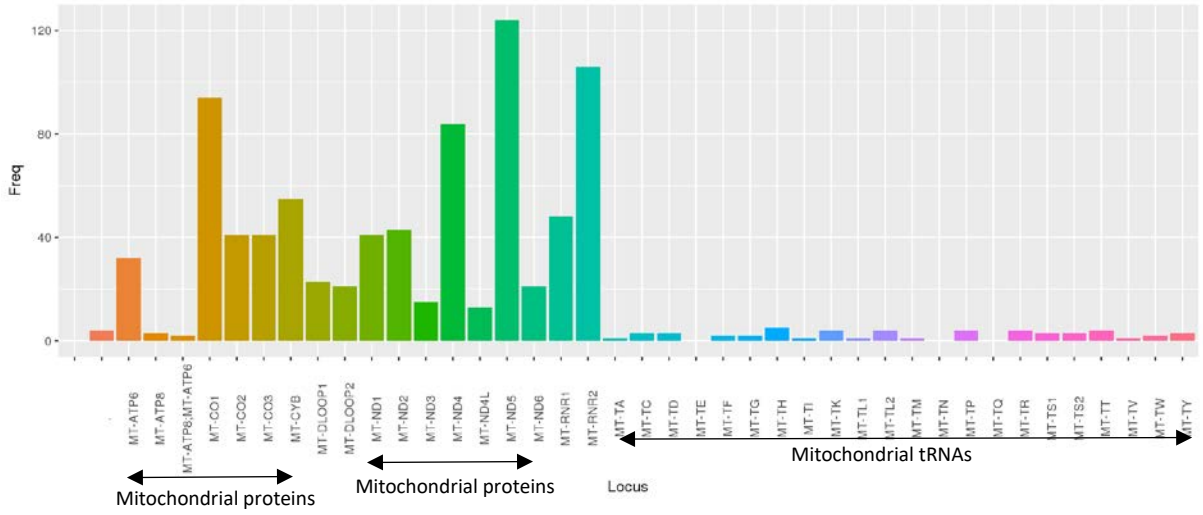

Figure 22 Heteroplasmy per Region across all Samples (Amount of heteroplasmic sites grouped according to their loci on the mitochondrial genome).

3.3.2.8 Changing to the Illumina MiSeq sequencer from the Ion Torrent sequencer

Initial sequencing runs were performed on the Ion Torrent however beyond the preliminary optimisation run the MiSeq was used for sequencing. Both the Illumina MiSeq and Ion Torrent are next-generation sequencers, the direct comparisons are listed in *Table 16*. In summary, the Illumina MiSeq offers a greater depth of coverage across a greater number of samples per run. There is also a decreased error rate in the MiSeq as it performs both forward and reverse paired-end reads of each fragment as opposed to single-end reads of the Ion torrent (279). Combined with the lower rate it is also cheaper per chip used. The Ion Torrent was used as proof of concept but for the numbers of samples to be sequenced in the final experiment the MiSeq was the logical choice to use both in terms of running the individual cells but also in the preparation steps required with quantification of samples done using the Qubit rather than the Aligent Bio-analyser been a much simpler process. Details of quantification using the qubit can be found in 2.6.3.2 Quantification – Illumina MiSeq.

Platform	Illumina MiSeq	Ion Torrent PGM
Instrument Cost*	$128 K	$80 K**
Sequence yield per run	1.5-2Gb	20-50 Mb on 314 chip, 100-200 Mb on 316 chip, 1Gb on 318 chip
Sequencing cost per Gb*	$502	$1000 (318 chip)
Run Time	27 hours***	2 hours
Reported Accuracy	Mostly > Q30	Mostly Q20
Observed Raw Error Rate	0.80 %	1.71 %
Read length	up to 150 bases	~200 bases
Paired reads	Yes	Yes
Insert size	up to 700 bases	up to 250 bases
Typical DNA requirements	50-1000 ng	100-1000 ng

Table 16 Technical specifications of Next Generation Sequencing platforms utilised in Quail et al. 2012 (279)

3.3.3 Final Methods

The final methods are described in the materials and methods chapter. In short, they consisted of:

1. Bone marrow sample gained from patient usually during total hip replacement surgery. This would then be prepared by filtering and then using lymphoprep to create a mononuclear rich
2. Flow cytometry single MSC cell separation using the BioLegend antibodies as an alteration from the Miltenyi protocol but still utilising this protocol.
3. Cell lysis
4. Amplification using the 5-primer pair reaction using a 2-stage cycle on the thermocycler.
5. Purification using AMPure beads
6. Quantification using the Qubit fluorometer
7. Sequencing on the MiSeq

3.4 Results

3.4.1 MiSeq results of a 78-year-old patient – proof of concept and analysis pathway using MiSeq and analysis pipeline.

Following the success of the Ion Torrent sequencing analysis across a range of samples, a run was prepared for the MiSeq sequencer. This was prepared as in the material and methods chapter and as above.

A 78-year-old patient who had undergone a total hip replacement and donated a marrow sample was selected from the available samples, work with colonic crypt stem cells showed increasing of the prevalence of mtDNA mutations with age (19) and so the oldest patient was selected for the next step of optimisation, this is Hip 12 in *Table 7*, 18 single MSCs were successfully amplified to produce full copies of the mitochondrial genome and this, in turn, was compared to 3 consensus sequences from the same patient.

The fastq files were then loaded into the analysis pipeline. This compared the sequencing data to the Cambridge reference sequence, giving a BAM or binary alignment score and also a base pair score indicating the number of reads for each cell's DNA.

From the output of the pipeline direct comparison between the consensus genome and single-cell genomes were performed. Unique heteroplasmies less than 5% were removed along with common ones and the NUMTs (nuclear mitochondrial DNA segments). The heteroplasmy base pair site and mutations were then uploaded to Mitomap/Mitomaster (280) and MitImpact 2(281).
From this data heteroplasmies greater than 30% with non-synonymous changes or tRNA shifts were entered into Mutpred, logging the change in the amino acid at the specific codon location. This was done by comparing to the original paper by Anderson et al.,(155) and output from Mitomap and MitImpact. Mutpred then predicted the likely outcome that this change would cause in terms of pathogenicity. The summary of the results can be seen in *Figure 23.* The Mutpred output of the non-synonymous and tRNA changes are presented in *Table 17*.

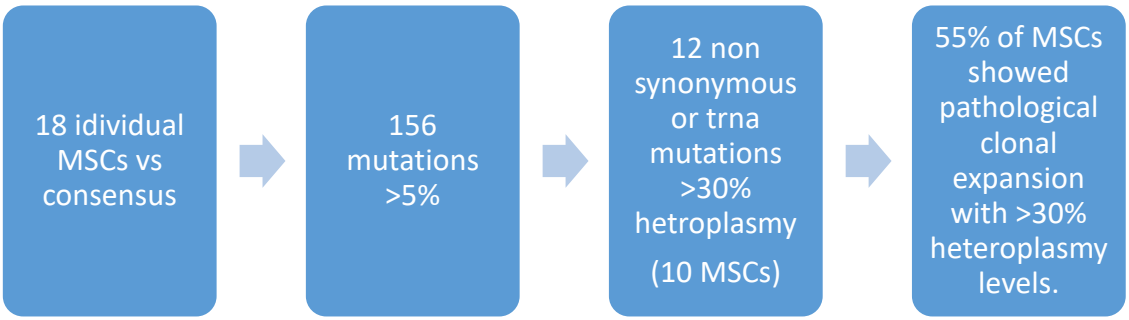

Figure 23 Summary of MiSeq analysis process.

Cell	Mutation	Heteroplasmy Percentage	Amino acid change	Locus	Mutpred prediction top 5 features
Hip 12-3	m.5070A>G	53.56%	Threonine > Alanine	NADH dehydrogenase subunit 2	1. Gain of loop (P = 0.0851) 2. Loss of helix (P = 0.1706) 3. Loss of glycosylation at T201 (P = 0.1714) 4. Loss of catalytic residue at T201 (P = 0.4033) 5. Loss of stability (P = 0.5201)
Hip 12-4	m.10561T>C	42.76%	Leucine > Proline	NADH dehydrogenase subunit 4L	1. Loss of stability (P = 0.0204) 2. Gain of catalytic residue at L31 (P = 0.0239) 3. Gain of disorder (P = 0.0888) 4. Gain of glycosylation at L31 (P = 0.569) 5. Gain of phosphorylation at S29 (P = 0.608)
Hip 12-4	m.5628T>C	44.34%	tRNA	tRNA Alanine	
Hip 12-5	m.10345T>C	49.04%	Isoleucine > Threonine	NADH dehydrogenase subunit 3	1. Loss of stability (P = 0.0014) 2. Gain of catalytic residue at I96 (P = 0.1463) 3. Gain of glycosylation at S91 (P = 0.5825) 4. Loss of phosphorylation at S101 (P = 0.717) 5. Loss of MoRF binding (P = 0.7286)
Hip 12-7	m.10161A>C	33.54%	Threonine > Proline	NADH dehydrogenase subunit 3	1. Gain of catalytic residue at T35 (P = 0.0068) 2. Loss of phosphorylation at T35 (P = 0.0161) 3. Gain of disorder (P = 0.0471) 4. Gain of glycosylation at T35 (P = 0.0486) 5. Loss of ubiquitination at K33 (P = 0.1264)
Hip 12-10	m.8873G>A	31.23%	Glycine > Aspartic Acid	ATP synthase F0 subunit 6	1. Loss of MoRF binding (P = 0.0542) 2. Loss of methylation at R118 (P = 0.0561) 3. Gain of relative solvent accessibility (P = 0.09) 4. Gain of solvent accessibility (P = 0.1376) 5. Loss of catalytic residue at M115 (P = 0.1441)
Hip 12-10	m.8873G>A	31.23%	Glycine > Aspartic Acid	ATP synthase F0 subunit 6	1. Loss of MoRF binding (P = 0.0542) 2. Loss of methylation at R118 (P = 0.0561) 3. Gain of relative solvent accessibility (P = 0.09) 4. Gain of solvent accessibility (P = 0.1376) 5. Loss of catalytic residue at M115 (P = 0.1441)
Hip 12-10	m.4428G>A	30.61%	tRNA	tRNA Glutamine	
Hip 12-11	m.9205T>C	46.26%	Terminalisation > Glutamine	ATP synthase F0 subunit 6	
Hip 12-13	m.13676A>G	89.84%	Asparagine>Serine	NADH dehydrogenase subunit 5	1. Gain of glycosylation at N447 (P = 0.0985) 2. Loss of catalytic residue at N447 (P = 0.1) 3. Gain of helix (P = 0.132) 4. Gain of disorder (P = 0.1367) 5. Loss of loop (P = 0.2897)
Hip 12-16	m.8828A>G	66.04%	Asparagine > Glycine	ATP synthase F0 subunit 6	1. Loss of stability (P = 0.0587) 2. Loss of catalytic residue at N101 (P = 0.1411) 3. Gain of disorder (P = 0.2075) 4. Loss of glycosylation at T96 (P = 0.2608) 5. Loss of helix (P = 0.3949)
Hip 12-17	m.4893A>G	34.97%	Methionine>Valine	NADH dehydrogenase subunit 2	1. Loss of stability (P = 0.0709) 2. Gain of helix (P = 0.2059) 3. Gain of glycosylation at S140 (P = 0.2568) 4. Loss of sheet (P = 0.437) 5. Loss of loop (P = 0.4786)
Hip 12-19	m.5367A>G	78.57%	Threonine > Alanine	NADH dehydrogenase subunit 2	1. Loss of sheet (P = 0.0817) 2. Gain of helix (P = 0.132) 3. Gain of methylation at R295 (P = 0.2551) 4. Loss of stability (P = 0.2717) 5. Loss of catalytic residue at T300 (P = 0.3716)

Table 17 Demonstrating the output from the mutpred scored for the 13 non-synonymous mutations seen in the MSC population compared to the consensus sequence of Hip 12 on the initial MiSeq experiment.

3.4.2 Comparison of mitochondrial DNA mutation load with increasing age: Final MiSeq sequencing output.

3.4.2.1 Overall trends and combined results.

For the final experiment, 13 patients were examined. In total there were 139 cells sequenced and 13 consensus samples. This accounted for over 2.5 million base pairs. In addition, several samples were re-sequenced due to sequence drop off. 2492 mutations were detected across the samples and consensus sequences. Examination of single nucleotide polymorphisms (SNPs) in the cohort showed that 31.94% of all mtDNA mutations were T>C, A>G represented 28.01%, C>T represented 18.62% and G>A 13.88%. The remaining possible polymorphisms (A>C, A>T, C>A, C>G, G>T, G>C, T>A and T>G) were all 2.25% and below.

In terms of quality control as highlighted in individual patients' data sets which can be viewed in the appendix (3.7 Appendix: Individual patient sample data set) a number of the individual cells had poor coverage or sequence error. Typically, this was represented by a large number of sequential d-loop mutations. These samples have been excluded from the further overall analysis. This would leave 121 individual cells and 13 consensus sequences. To account for this in subsequent analysis mutation rates have been calculated per cells analysed.

Of these filtered results the majority of mutations fell below 25% heteroplasmy as can be seen in *Figure 24.* 25% and under mutations accounted for 84.78% of all mutations, greater than 25% but less than or equal to 50% heteroplasmy levels accounted for just 8.17%, greater than 50% and less than or equal to 75% was 2.59% with the remainder greater than 75% making up the final 4.45% of which most were homoplasmic variants.

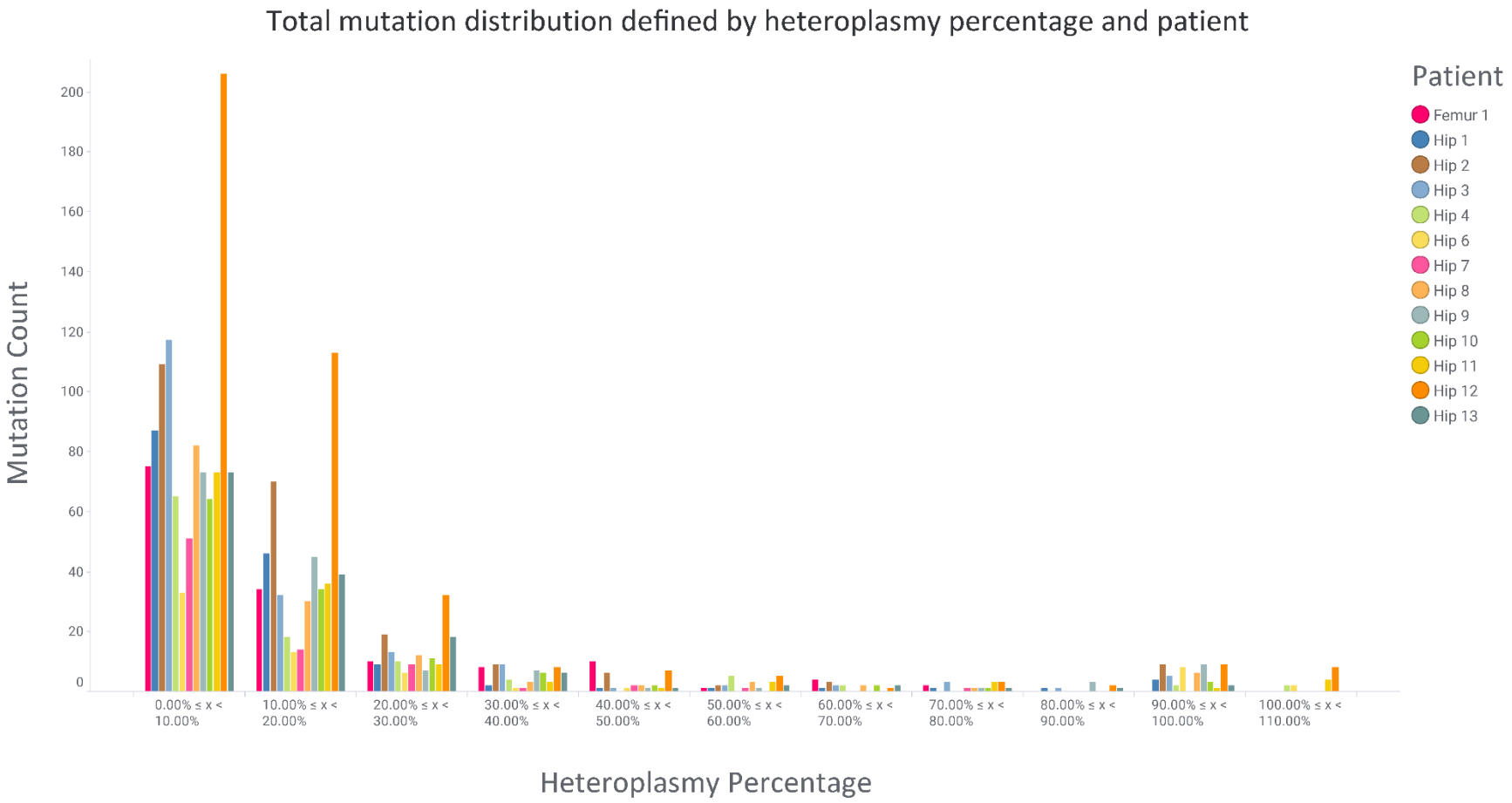

Figure 24 Total mitochondrial DNA mutations distribution by heteroplasmy percentage and patient.

The majority of mutations were missense non-synonymous variants (42.58%), synonymous variants made up 24.91% of the sample. rRNA changes accounted for 14.98%, non-coding SNPs 8.22% and tRNA mutations 7.78%. The remaining 2% of the mutations were made up of stop codon loss/gain, start gain and a stop codon retained. This is demonstrated below in *Figure 25.*

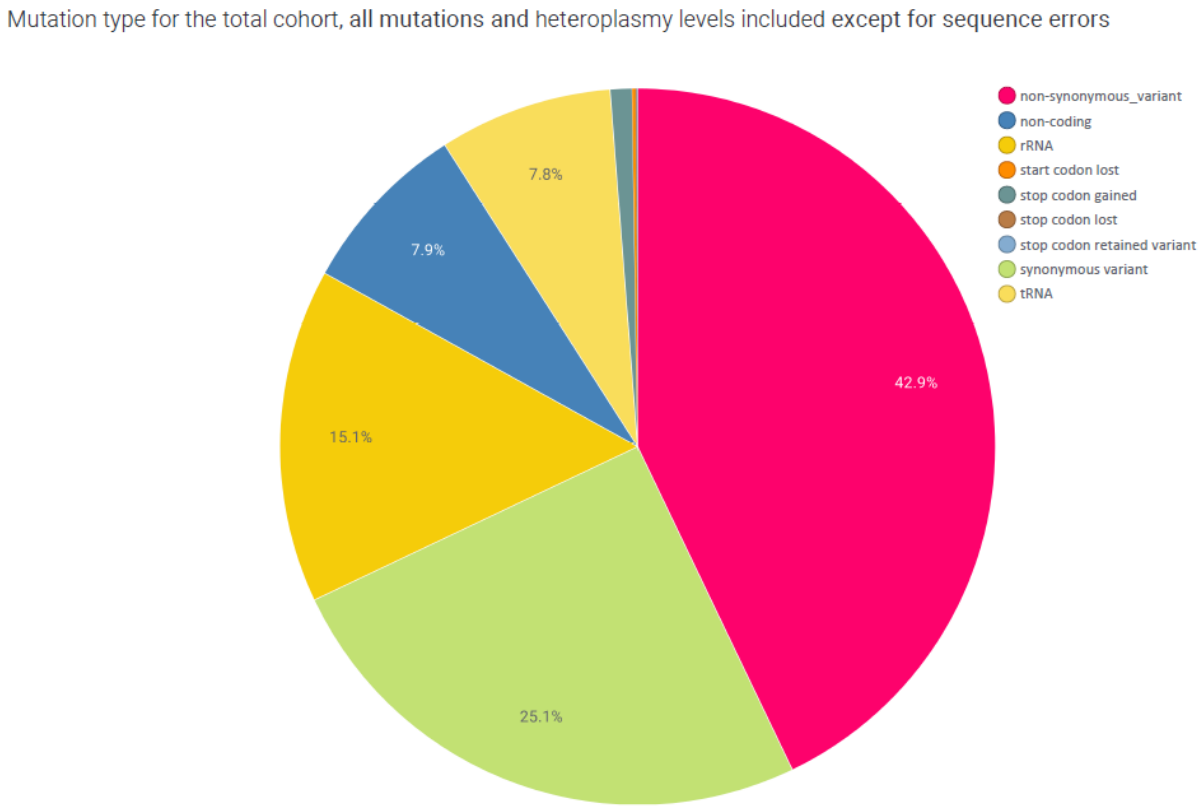

Figure 25 Pie chart demonstrating the mutation type encountered within the patient cohort.

In terms of mutations per gene across the whole patient cohort; tRNA mutations only accounted for a small percentage (7.78%) of total mutations with no clear trend to one tRNA or another. The highest percentage of all the mutations was in the MT-CO1 gene - 12.38%. Total complex IV mutations accounted for 19.63% whereas total complex I mutations accounted for 37.69%. The mitochondrial encoded proteins of the F_0 region (MT-ATP6 and MT-ATP8) account for 4.06%. Ribosomal mutations 12s and 16s were 14.98%. The rest of the mutations were in the non-coding D-Loop region of the mitochondrial genome. This data can be reviewed in *Figure 26*.

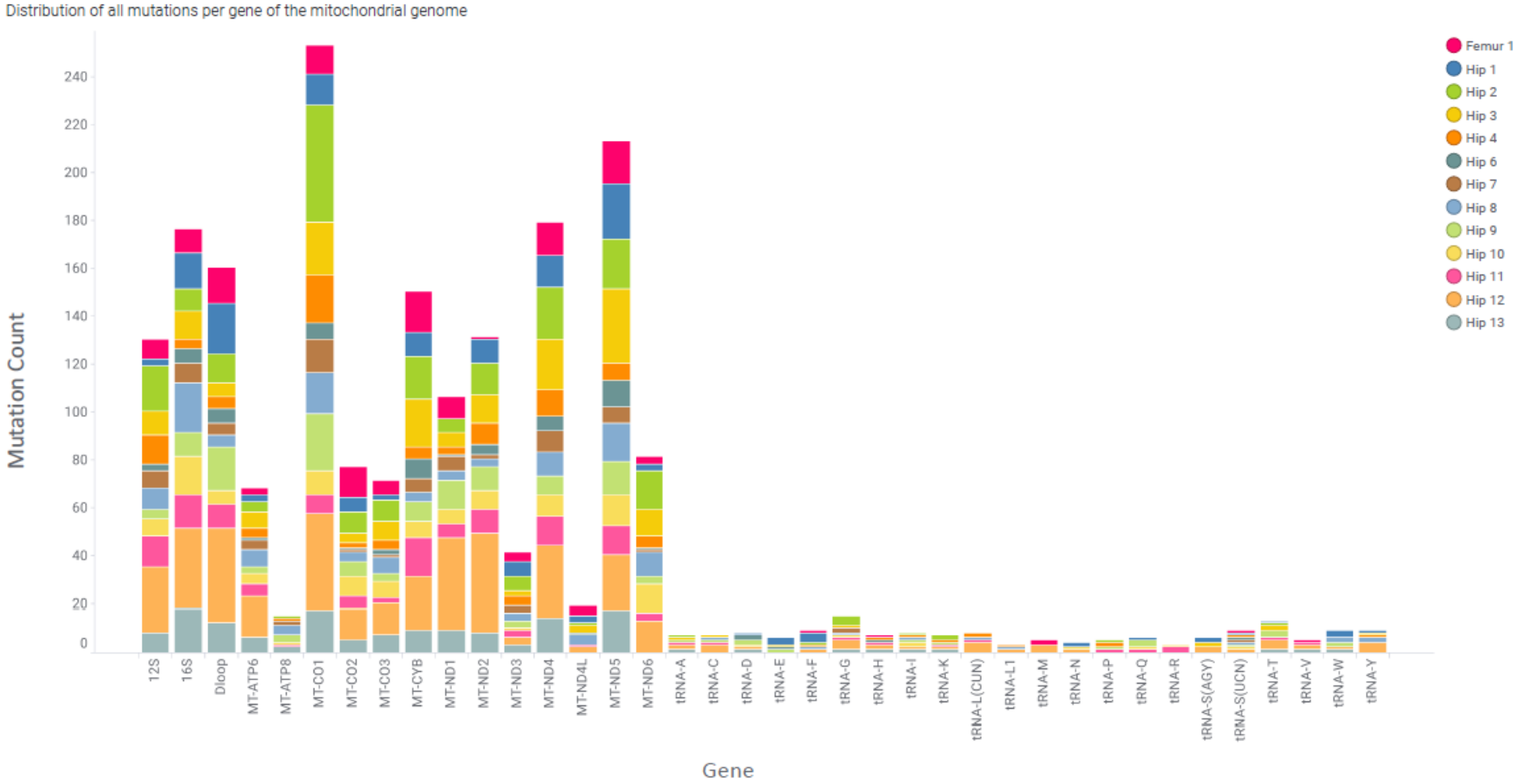

Figure 26 Mutation distribution across the mitochondrial genome for the whole sample group (sequence error cells removed), Further delineation of each gene by patient.

Breaking down the number of average mutations per cell and comparing them to age would account for the need to filter out sequence error cells which had high numbers of d-loop mutations among the error reads and also for the patient “hip 12” from which the pilot data was gained but had 19 cells sequenced as opposed to the 10 cells of the other samples.

As in *Figure 27* I showed the high-level heteroplasmy mutations (greater than 50%) had a relatively constant rate across the age range of under 2 mutations per cell analysed. Mutations per cell with a heteroplasmy of less than or equal to 25% showed a graduated increase with age as did total mutations in synchronisation There were definitive peaks in several patients older than the 2 younger patients.

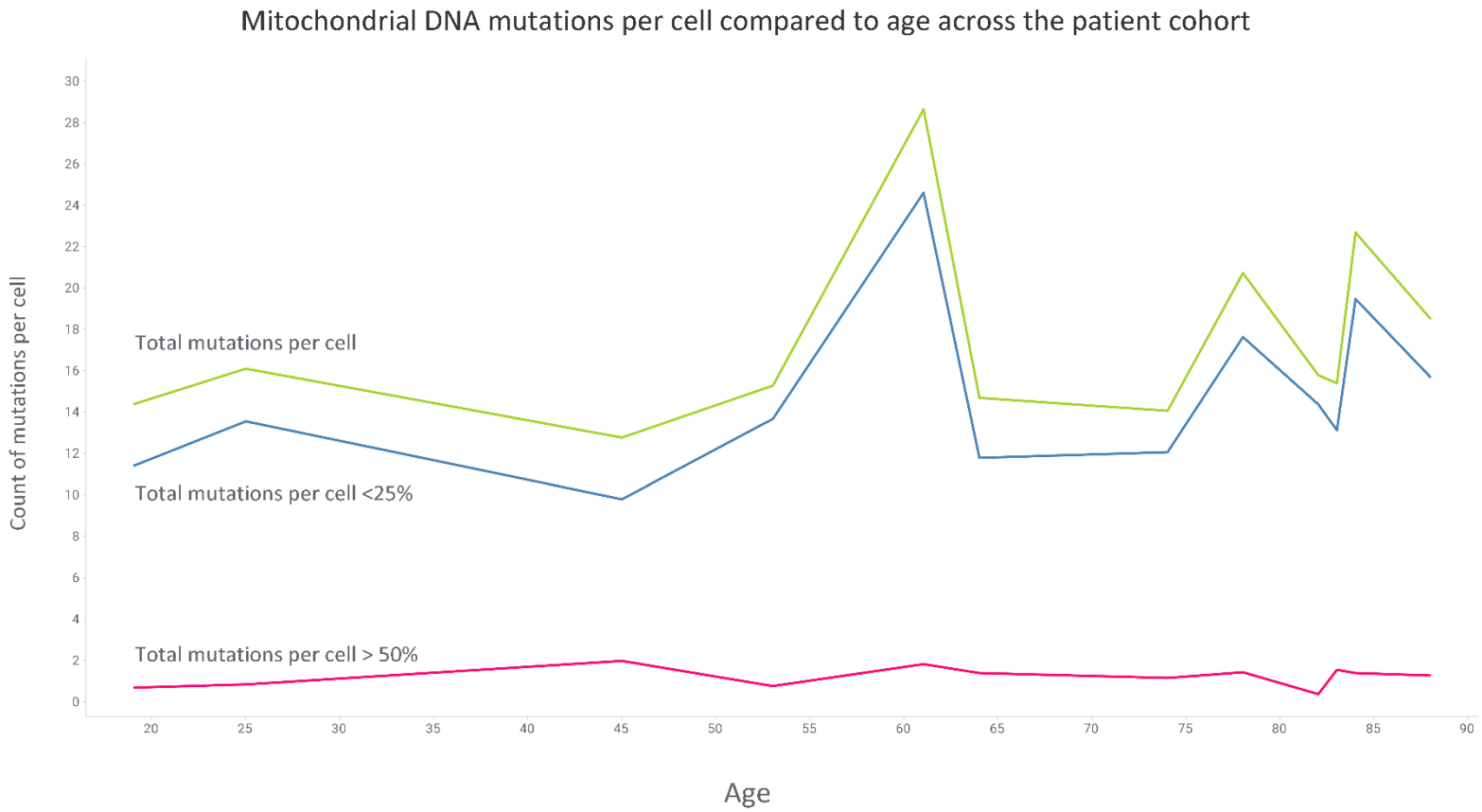

Figure 27 Average mitochondrial DNA mutations per patient per cell comparing age across the patient cohort to mutation rate. Sample split based upon heteroplasmy percentage of each mutation.

The low-level mutation rate appeared to be independent and increase with age much more dramatically than high-level mutations. Certainly, comparing the distribution of mutations per cell across the patients showed an increased and greater spread of distribution in older patients than the younger as in *Figure 28.* Unfortunately, the integrity of this trend is limited by the data set size per patient in terms of the number of cells analysed and the total number of patients analysed.

This is similar in terms of but also in contrast to the previous findings in colonic crypts by Greaves et al.,(282). This showed an increase in mitochondrial mutations with age although the gradient of the trend was steeper and more exponential in nature as opposed to the gradual increase seen in this data set.

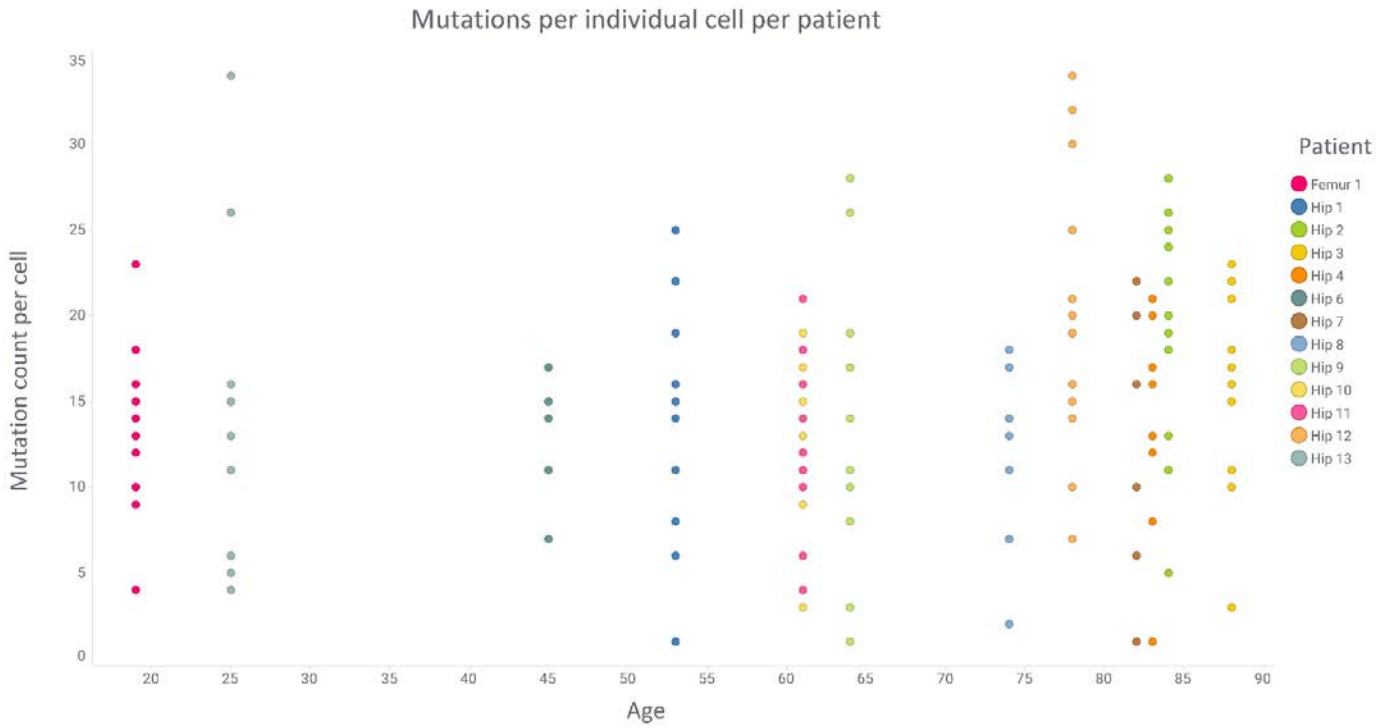

Figure 28 Total Mitochondrial DNA mutations per cell of each patient showing the distribution of mutation counts between individual cells for each patient.

Reviewing the non-synonymous or missense mutations' data in *Figure 29 and Figure 30* graphically demonstrates the SIFT scores recorded for each of the non-synonymous mutations. SIFT scores give a prediction of the likely pathogenic profile of each mutation, predicting whether it will be tolerated or have deleterious effects. (283). Each amino acid substitution is assigned a score of predicted damaging effects, if the score is ≤0.05 this is deemed damaging or deleterious, and tolerated if the score is > 0.05. Further delineation is given if there is "low confidence" within these predictions.

As in *Figure 29* the rate of "tolerated" and "tolerated low confidence" mutations seem relatively stable across the age range. In contrast, "deleterious" mutations show a gradual increase with age as do "deleterious low confidence" which shows a more significant increase. Twenty of the "deleterious" mutations had heteroplasmy levels greater than 25%, the rest were below 25% heteroplasmy and likely occurred during adult life without the length of time required to reach homoplasmic levels via clonal expansion (270). Although one of the mutations seen at 66.10% heteroplasmy was seen in the 19-year-old control patient and presumably is a germline mutation rather than an acquired mutation to reach such levels of heteroplasmy at an early age.

By splitting each patient into individual mutations in *Figure 30* there are more SIFT scored "deleterious low confidence" demonstrated at higher heteroplasmy levels than just the "deleterious". Again, there is some present in both the 25 and 19-year-old controls suggested that these are most likely germline mutations rather than sporadic ones given the time frame to clonally expand to such levels.

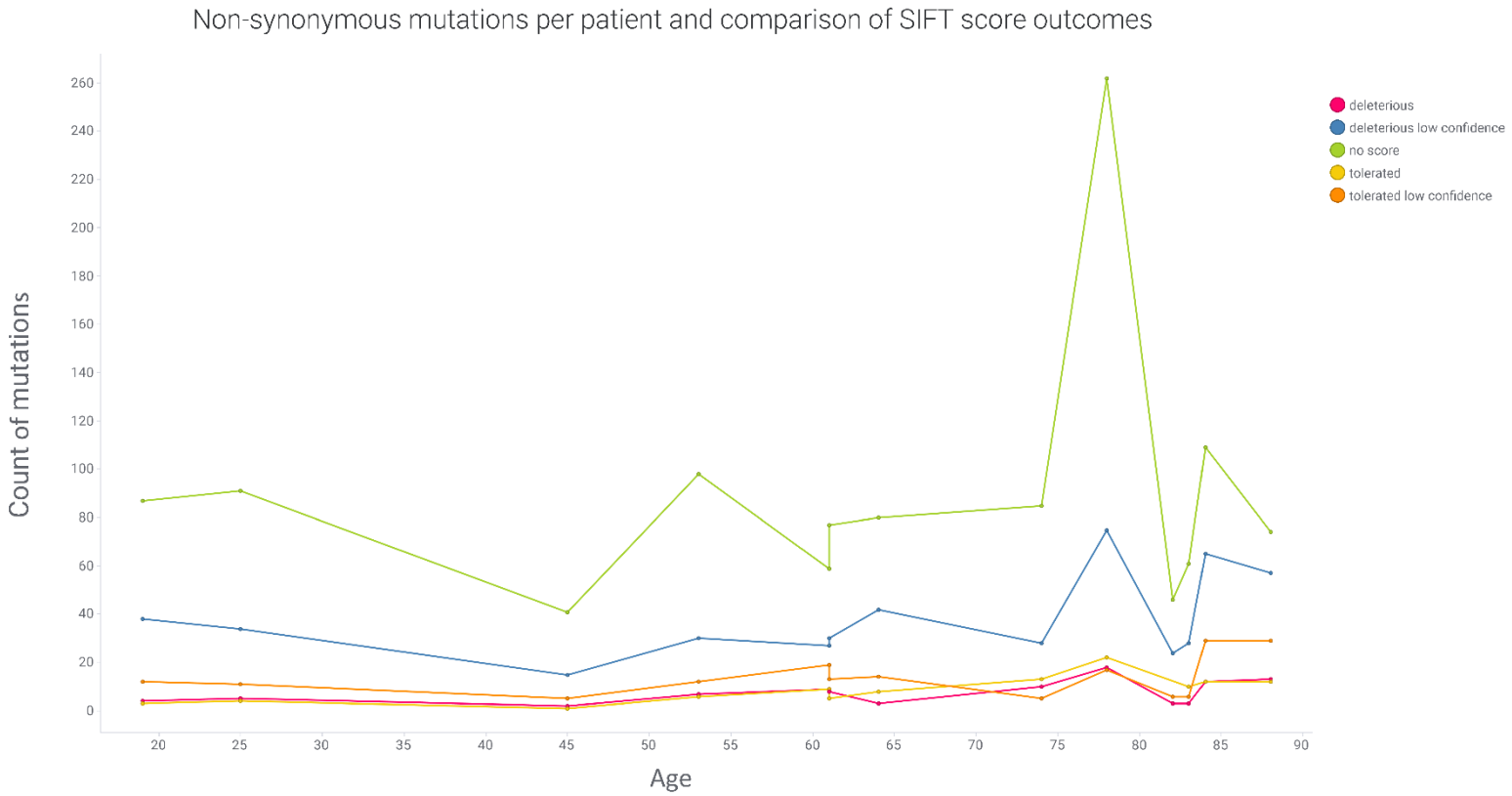

Figure 29 Non-synonymous mutations arranged by SIFT outcome compared to age.

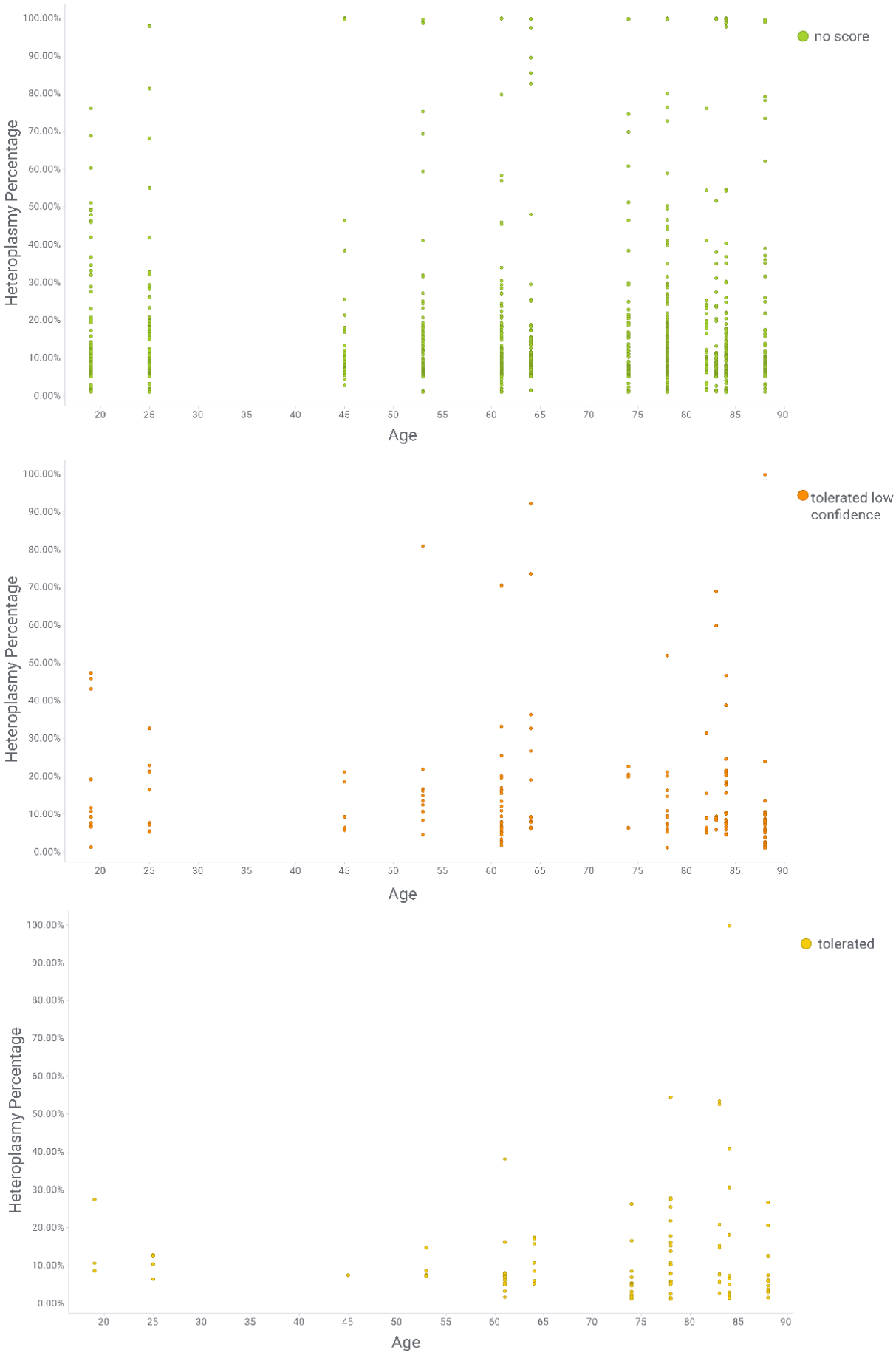
Heteroplasmy Percentage
100.00%
90.00%
80.00%
70.00%
60.00%
50.00%
40.00%
30.00%
20.00%
10.00%
0.00%
20 25 30 35 40 45 50 55 60 65 70 75 80 85 90
Age
no score
tolerated low confidence
tolerated

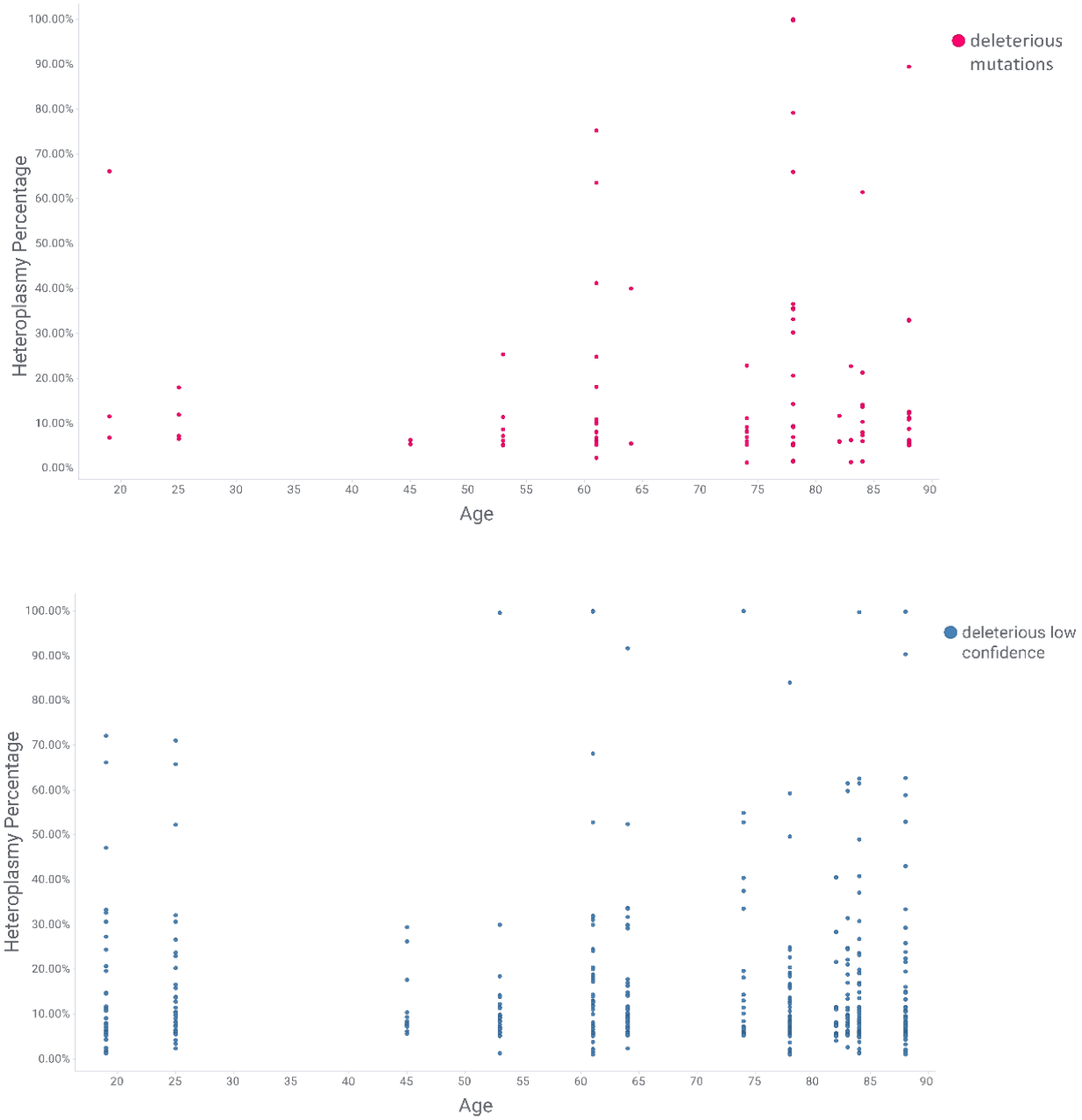

Figure 30 Non-synonymous mutations of each patient - heteroplasmy rates for each mutation defined for each SIFT score category. Data arranged by patients' ages.

3.5 Discussion:

The work by Dobson et al established the presence of mitochondrial deficiency in osteoblasts leading to accelerated bone loss (206). The presence of mitochondrial respiratory chain protein deficiency was seen in osteoblasts which are post-mitotic cells. Work by Taylor, et al (19) has shown the accumulation of mtDNA mutations in colonocytes, also post-mitotic tissues and their subsequent relation to mitochondrial pathology. The work by Greaves et al., (282) showed the presence of mtDNA mutations and respiratory deficiency in colonic stem cells. There has not been any previous work into the genetic nature of the acquired deficiency in osteoblasts and no previous established work in the presence of the precursor cells to osteoblasts and other cell types the mesenchymal stem cell. Establishing if mitochondrial DNA mutations affect MSCs in a similar way to the colonic stem cells was the aim of this investigation.

The purpose of this work was to establish if mitochondrial mutations occur in MSCs and if so, is there a relationship of age-related changes which can be seen in colonic epithelium.

The method developed here for the first-time analyses mesenchymal stem cells in isolation for mitochondrial DNA mutations. It puts forward a pathway and experimental pipeline akin to using the laser microdissection of the colonic epithelium to isolate individual cells and assess individual mitochondrial mutation load.

The issues in extracting mesenchymal stem cells are reliant in gaining access to the bone marrow cavity. Targeting routine orthopaedic surgery allows access to this cavity and subsequent MSC cells. The issue has been that there are only few MSC cells represented in the marrow Mesenchymal stem cells make up 0.01% of the bone marrow cell population (41). The samples can also be contaminated with red blood cells, fat, and saline from the surgical procedure. This leaves the issues of extracting the stem cells.

First, the stem cells must be isolated and concentrated. This becomes even more significant with age as MSC numbers decline and fat contamination increases due to age-related changes in the bone marrow. Simple red cell lysis is not effective enough in concentrating the MSCs, there are still significant numbers of other cells left within the sample as well as fat molecules. Due to the issues encountered in separated MSCs using red cell lysis, lymphoprep offered a much more efficient step. It would concentrate the mononuclear cells, remove the red cells and remove the fat globules. The mononuclear layer had a sufficient density of MSCs to then be separated by flow cytometry. The use of flow cytometry to separate cells could be applied to any cells in solution. However, to make

the sort the most efficient it can be there is a significant advantage to a concentration step as done here. The only alteration of the miltenyi protocol was to optimise the fluorophores for use on the cytometer at the university.

Mesenchymal stem cells were defined based upon the Miltenyi Biotect phenotyping kit markers (219). The criteria that was used was based upon the criteria laid out by Dominici et al., (272). The work by Dominici et al., summarised the Mesenchymal and Tissue Stem Cell Committee of the International Society for Cellular Therapy proposed minimal criteria to define human MSC. This included plastic adherence in standard culture conditions, positive expression of CD105, , CD73 and CD90, with a lack of expression of CD45, CD34, CD14 or CD11b, CD79alpha or CD19 and HLA-DR surface molecules. Whilst retaining the pluripotent differentiation potential with ability to differentiate into osteoblasts, adipocytes and chondroblasts in vitro.

The process of harvesting the stem cells from patients undergoing surgery and subsequent sorting using flow cytometry had significant effects upon cell viability and culturing cells from the sorted population proved difficult and further confirmation of these cells as MSCs by way of differentiation potential could not be demonstrated.

Recent work by Chan et al., (284) defines or multipotent human skeletal stem. There is a question over the exact purity of MSCs, Chan et al., suggest that there are several stem cell groups within this umbrella term. Bone marrow stromal cells or those with the potential to differentiate into osteoblasts, chondroblasts or adipocytes were defined on surface markers. These like the Miltenyi MSC phenotyping kit included; CD90, CD105, CD73 and CD44 (not part of the kit). It was also noted that CD271 and CD146 were identified in cells with higher colony forming ability and multi differentiation lineage.

Chan et al., defined a further subset of stem cells which were positive for CD73, CD164, CD146 and PDPN. These cell were found to have the greatest differentiation potential for osteogenic and chondrogenic lineage cells but no adipogenic potential. These stem cells then became stroma progenitor cells giving rise to osteoprogenitors and chondroprogenitors cells in vitro. Although the “MSC” defined by the CD markers here were accepted by Chan et al., as having osteogenic potential further experiments may wish to pursue the subset of hSCCs with enhanced osteogenic potential as defined by Chan et al.,

One of the issues in analysing the mitochondrial genome of individual cells was the quality of mtDNA extracted. Cells which had made it to through this process of extraction, lymphoprep, potential freeze/thaw and then single-cell separation using flow cytometry were likely to incur damage even if fixed. This led to difficulty in getting 10 cells complete genomes and further the calibre of the amplicons varied significantly. This led both to sequence error, drop of coverage or requirement to repeat analysis of cells or consensus sequences.

Whether taking samples directly without delay or freeze-thaw steps as in the case of the high throughput assay chapter would have a positive impact upon the mtDNA generated by preserving cellular integrity would still need to be assessed in future work.

What the data has shown is that homoplasmic and heteroplasmic mtDNA mutations do exist in MSCs. This complements the findings of Park et al., who compared iPS-MSCs to dental tissue-derived MSCs (285) and did identify some mutations in MSCs although the full mitochondrial genome was not explored in detail. This is the first work to fully explore the mtDNA genome of MSCs. The levels of high heteroplasmies are relatively constant throughout the cohort despite age but there is an increase in the lower-level mutations. This would suggest that the high-level mutations are germline mutations this is in contrast to Greaves et al., (270) who found a significant increase in the high level mutations as opposed to the lower mutation increases seen here. The work by Greaves et al., was in colonocytes which are much more metabolically active and at greater risk of mtDNA mutations from ROS and enhanced turnover. MSCs in contrast only see upregulation of their mitochondria number and respiratory chain proteins as part of the differentiation pathway becoming more metabolically active once terminally differentiated. The lower rates of mutation <25% had a slow but gradual increase across the limited sample with increases in age. Objectively the younger controls also had lower levels of mutation and fewer deleterious mutations than the older samples.

Mutations, as a percentage were most often seen in complex I which is not surprising given that complex, is the most complicated of the complexes in terms of its components and assembly. It is coded for both by nuclear and mitochondrial DNA, consisting of 45 subunits of which 7 are encoded by mtDNA (286). All 7 of these mtDNA coded proteins have reported pathological variants as do 21 of the nuclear-encoded proteins and 10 of the assembly factors (287, 288).

Mitochondrial DNA is prone to mutations with age with *de novo* mutations arising at a rate up to 10x greater than nucleic mutations (289). Mitochondrial DNA encodes for 7 proteins (ND1-6, ND4L) of

complex I, compared to just 3 proteins of complex IV (COI-III). This accounts for 56% of the DNA accounting for complex I compared to 27% of complex IV (290). Not only is there more mtDNA accounting for complex I proteins but age-related mtDNA mutations frequently affect the area between the heavy and light strand origins of replication (291). This frequently affects the ND3, ND4, ND4L and ND5 proteins affecting complex I. Overall mutations affecting complex I are around twice as likely to occur than those affecting complex IV (290). This is comparable to the data from the mesenchymal stem cells as seen here; just 19.63% for complex IV whereas complex I mutations accounted for 37.69%.

3.5.1 Limitations

Clearly, the size of the sample is a limiting factor; unfortunately, by nature of the demographics of patients undergoing routine orthopaedic surgery the option to collect bone marrow from young patients is limited and so the control sample is limited in size. Equally the feasibility to collect a larger sample was limited due to time constraints. With increased sample size hopefully, the graduated changes seen between young and old patients would be amplified. In addition, a larger sample size would allow the stratification of the two populations better than the current population which has some “young” under 25 years old and some “old samples” greater than 60 but then also several samples in between.

One of the major issues, as alluded to and highlighted within individual data, is dropped coverage and sequence error. This is typically caused by the poor integrity of amplicons and the fact individual MSCs mitochondrial DNA is limited in quantity and perhaps quality after the long extraction process. Sequence error was typically generated due to subsequent areas of low coverage and read depth next to areas of high coverage or read depth. There were also areas of generalised low read depth seen in several samples.

The issues in DNA quality may have some relation to frozen storage time. Also, cells were collected in the chronological ordering of their naming except for hip 11,12,13. These samples were collected around 12 months before the rest of the samples and do experience large areas of sequence drop off and subsequently it is possible that the integrity of the cells degrades with time leading to poor sequencing results. As seen in the high throughput chapter direct harvesting of stem cells from the patient to experimental procedures lead to an improved result and it is possible to postulate that this result may carry through to the DNA sequencing results.

The issues in this approach would be at what point to store the samples before sequencing to allow a full plate of samples to be sequenced for the optimal economy of the sequencer. This would need to be examined in future work.

In hindsight although all PCR amplification steps were run with control nuclease free water to check for contamination a further step to confirm the accuracy of the sequencing would have been to split a sample once amplified and purified to see if the same results were gained on each run. This would be a further check of accuracy in addition to reviewing the read depth of each base pair call. Although the volume of DNA gained for sequencing was low further experiments should include this step as a crucial check of sequencing accuracy.

3.5.2 Future work

The clear aim of future work would be to expand the sample size and further optimise DNA extraction and the quality of amplicons produced. A larger sample would clarify the trends seen in this small sample size, improved quality of amplicons would hopefully eliminate read error and also improved read depth and allow mutations to be called at greater confidence.

The method outlined here could also be expanded to any cells that can be suspended in solution. Whilst osteoblasts are lining the bone marrow cavity and preliminary work as part of the flow cytometry assay showed the presence of Osteocalcin positive cells within marrow samples further categorisation, identification and creation of a cytometry panel would need to be implemented and validated to expand this assay to osteoblast mutations. Whilst the examination of daughter cells as done in the cases of colonic crypts (270) would not be possible it would be an important experiment to examine the mutation load seen in MSCs and subsequent progeny be that osteoblasts, chondrocytes, myocytes or adipocytes.

3.6 Conclusion:

This chapter aimed to assess mitochondrial DNA mutation load and if there was a presence within the genome of mesenchymal stem cells and if present, was the mutation rate related to age as with other tissues.

The experiments detailed in this chapter have for the first time quantified the levels of mutation seen in humans MSCs and compared age to the mutation rate. Whilst there are limitations mainly related to sample size and read error due to poor DNA quality, it has shown that MSCs possess mtDNA

mutations and there is an age-related component to increased frequency of mutations seen. This is in keeping with the age-related mitochondrial respiratory chain deficiency model seen in other cells and clarified in the other chapters of this work.

3.7 Appendix: Individual patient sample data set

3.7.1 Data for the patient "Hip 1"

Hip 1 samples were taken from a 53-year-old female patient undergoing a total hip replacement for arthritis.

Coverage

Figure 31 shows the read depth of each base which varied from 0 and single figures to over 12000. There were low values around the overlap of primer pair 1 and primer pair 5 around the 16500 – 700 bp. This was seen universally across the sample cells including the consensus sequence. There is also a significant drop off of Hip 1-6 between 7400 and 10500 bp. Aside from sample 6 and using the read depth cut off of 500 times all other cells mitochondrial genomes coverage was 93% and above.

Figure 31 Coverage graphs for Hip 1 - read depth of each base and 500 read depth threshold demonstrated.

Haplogroup

All cells were K2b1a1a haplogroup. m.73A>G and m.146T>C were commonly missing across the cells but were in the area of low coverage. Due to missing haplogroup markers, all cells were between 91.98% and 98.93% match to K2b1a1a.

Polymorphic variant specific to the patient

Cells 5 and 10 have one SNP present m.146T>C (98.95% and 75.22% heteroplasmy respectively) this lies within the non-coding portion of the mitochondrial genome D-Loop. The single nucleotide polymorphism database (dbSNP (292)) reference for this mutation is rs370482130.

Individual SNPs greater than 50% heteroplasmy.

Mutations are presented in *Figure 32.*

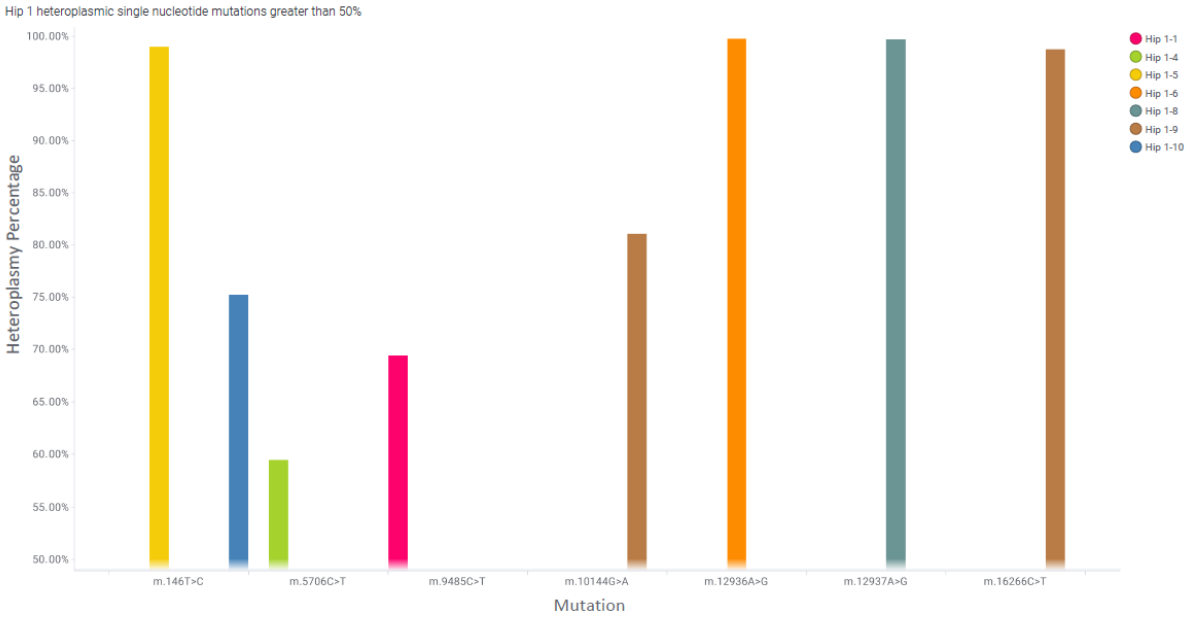

Figure 32 Hip 1 heteroplasmic single nucleotide mutations greater than 50% heteroplasmy.

- Cell 1 has one SNP present: m.9485C>T (69.39% heteroplasmy), causing a synonymous change of the MT-CO3 gene altering the codon ttC/ttT. There is no dbSNP reference number.
- Cell 2 has no SNPs greater than 50%.
- Cell 3 has no SNPs greater than 50%.
- Cell 4 has one SNP present: m.5706C>T (59.39% heteroplasmy) this codes for tRNA asparagine gene with no documented pathological consequences.
- Cell 5 has no further SNPs greater than 50%.
- Cell 6 has a one SNP present: m.12936A>G (99.72%) causing a synonymous change of the MT-ND5 gene altering the codon caA/caG. There is no dbSNP reference number.
- Cell 7 has no SNPs greater than 50%.

- Cell 8 has one SNP present: m.12937T>G (99.63%) causing a non-synonymous change of the MT-ND5 gene. With a change in amino acid from Methionine to Valine. The SIFT score is (283) deleterious low confidence (0.05) effects, the Polyphen score (293) is benign (0.005) (0). The dbSNP reference is rs201612920, and COSMIC (294) reference is COSV62294393.

- Cell 9 has 2 SNPs present: m.10144G>A (81.01%) and m.16266C>T (98.68%).

    - m.10144G>A causes a non-synonymous change of the MT-ND3 gene with a change of the amino acid from Glycine to Aspartate. The SIFT score is "tolerated" (0.47) and Polyphen score "benign" (0.056). There is no dbSNP reference number.

    - m.16266C>T is part of the non-coding D-Loop hypervariable region and has no detrimental effects. The dbSNP reference is rs879098011.

- Cell 10 has no further SNPs greater than 50%.

Across the whole sample of MSCs cells, there were 54 non-synonymous mutations with SIFT or Polyphen scores however the heteroplasmy percentage of these samples aside from the cells above were 29.97% and below. In total there were 153 mutations present across the sample.

3.7.2 Data for the patient "Hip 2"

Hip 2 samples were taken from an 84-year-old female undergoing a total hip replacement for arthritis.

Coverage

As depicted in *Figure 33* there were low values around the overlap of primer pair 1 and primer pair 5 around the 16500 – 700 bp. Hip 2-6 and Hip2-10 also experienced areas of dropped coverage around 1500-3500 bp and 14500-500 bp. Aside from these samples coverage of the mitochondrial genome with a read depth of greater than 500 times was 93.84% and above. (Hip 2-6 – 82.95%, Hip 2-10 79.78%).

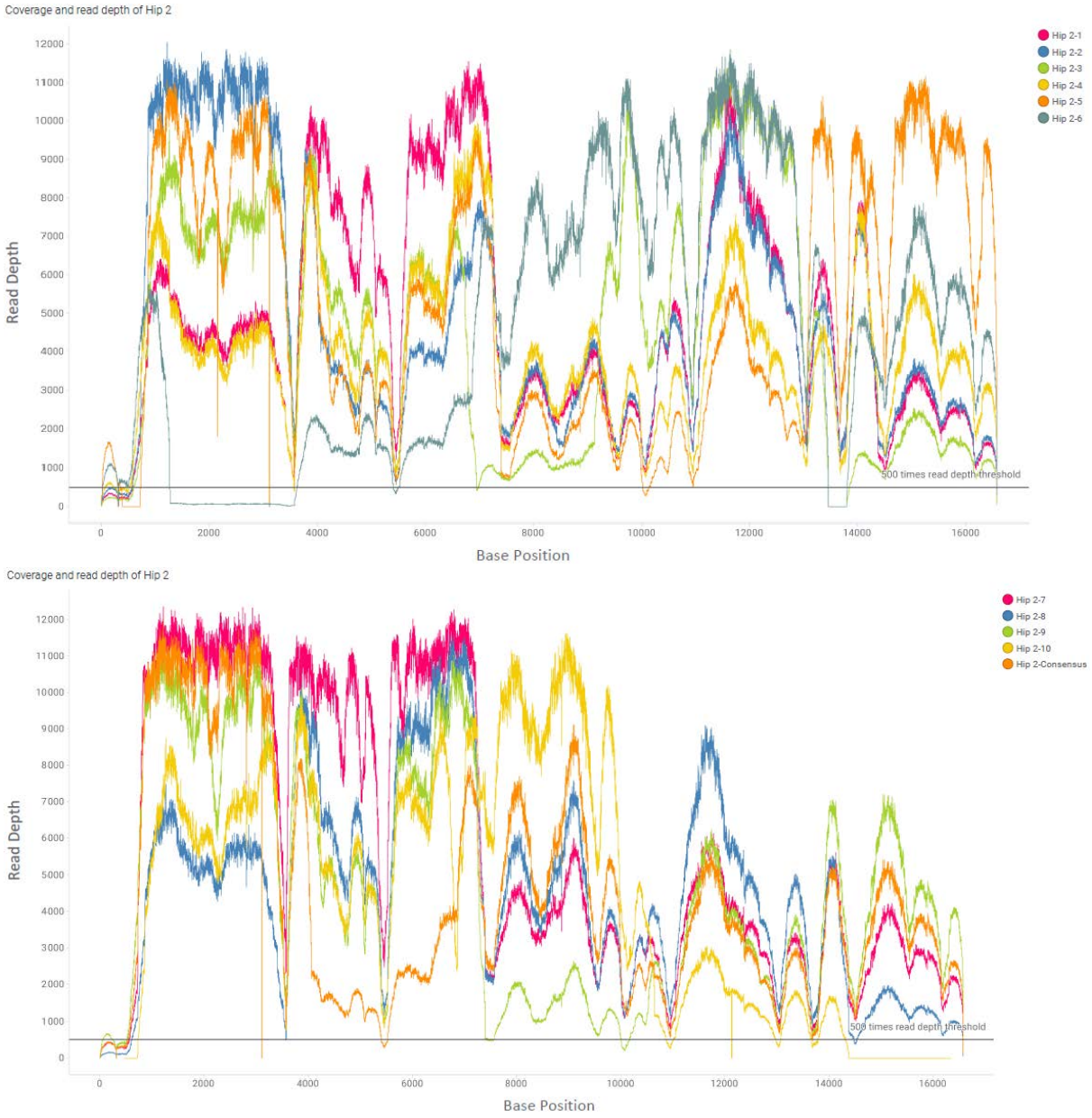

Figure 33 Coverage graphs for Hip 2 - read depth of each base and 500 read depth threshold demonstrated.

Haplogroup

All cells and the consensus sequence were J1b1a1 haplogroup. Due to low coverage and missing haplogroup markers cell 10 was called as J1b1a only. m.73A>G and m.750A>G were commonly missing across most of the cells.

Polymorphic variant specific to the patient

There were 2 polymorphic variants seen in 6 of the cells and the consensus sequence. The first m.6723G>A on the MT-CO1 gene caused a non-synonymous mutation with a change from valine to isoleucine. The SIFT score was tolerated low confidence (1) and Polyphen score was benign (0.127). Heteroplasmy levels were 38.76% and below.

The second polymorphic variant was m.7110T>C on the MT-CO1 gene caused a non-synonymous mutation with a change from tyrosine to histidine. The SIFT score was deleterious low confidence (0.01) and Polyphen score was probably damaging (1). Heteroplasmy levels were 40.77% and below.

Individual SNPs greater than 50% heteroplasmy

Mutations are presented in *Figure 34.*

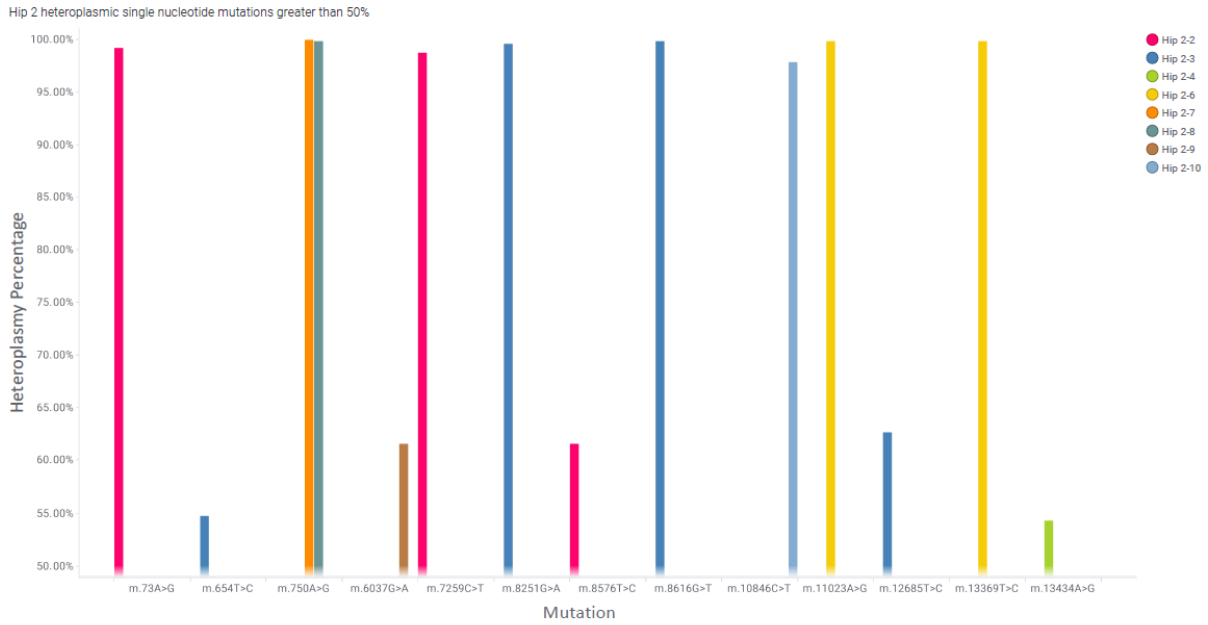

Figure 34 Hip 2 heteroplasmic single nucleotide mutations greater than 50% heteroplasmy.

- Cell 1 has no SNPs greater than 50%.
- Cell 2 has three SNPs present: m.73A>G (99.17%), m.7259C>T (98.73%), m.8576T>C 61.52%).
    - m.73A>G this lies within the non-coding portion of the mitochondrial genome D-Loop. The dbSNP reference for this mutation is rs869183622.
    - m.7259C>T causes a synonymous change within the MT-CO1 gene altering the codon atC to atT. There is no dbSNP reference number.

  - m.8576T>C causes a non-synonymous change of the MT-ATP6 gene with a change of the amino acid from leucine to proline. The SIFT score is deleterious (0) and Polyphen score is probably damaging (0.998). There is no dbSNP reference for this mutation.

- Cell 3 has four SNPs present: m.654T>C (54.73%), m.8251G>A (99.58%), m.8616G>T (99.82%) and m.12685T>C (62.60%).

  - m.654T>C is within RNR1 mitochondrial 12s ribosome gene with no documented deleterious effects.

  - m.8251C>A causes a synonymous change of the MT-CO2 gene altering the codon ggG/ggA the dbSNP reference is rs3021089.

  - m.8616A>T causes a non-synonymous change of the MT-ATP6 gene with a change of the amino acid from leucine to phenylalanine. The SIFT score is tolerated (0.08) whereas the Polyphen score is probably damaging (0.997). The dbSNP reference for this mutation is rs41427749.

  - m.12685T>C T causes a non-synonymous change of the MT-ND5 gene with a change of the amino acid from phenylalanine to leucine. The SIFT score is 0 - deleterious low confidence and Polyphen score 0.995 probably damaging. There is no dbSNP reference.

- Cell 4 has 1 SNP present: m.13434A>G (54.30%) causes a synonymous change of the MT-ND5 gene, altering the codon atA/atG. There is no dbSNP reference number.

- Cell 5 has no SNPs greater than 50%.

- Cell 6 has 2 SNPs: m.11023A>G (99.80%) and m.13369T>C (99.79%).

  - m.11023A>G causes a synonymous change within the MT-ND4 gene with a codon change ccA/ccG. There is no dbSNP reference number.

  - m.13369T>C causes a non-synonymous change within the MT-ND5 gene. This causes an alteration of the amino acid from serine to proline. The SIFT score is 0 - deleterious low confidence and Polyphen score 0.995 probably damaging. There is no dbSNP reference.

- Cell 7 has one SNP: m.750A>G (99.94%) this affects RNR1 mitochondrial 12s ribosome gene with no documented deleterious effects. The dbSNP reference is rs2853518.

- Cell 8 has one SNP: m.750A>G (99.82%) this affects RNR1 mitochondrial 12s ribosome gene with no documented deleterious effects. The dbSNP reference is rs2853518.

- Cell 9 has one SNP: m.6037G>A (61.51%) this is a non-synonymous change affecting the MT-CO1 gene causing an amino acid change of glycine to aspartate. The SIFT score is 0 - deleterious low confidence and Polyphen score 1 probably damaging. There is no dbSNP reference.

- Cell 10 has 1 SNP, m.10846C>T (97.80%) causing a synonymous change within the MT-ND4 gene altering the codon acC/acT. There is no dbSNP reference.

Across the whole sample of MSCs cells, there were 104 non-synonymous mutations with SIFT or Polyphen scores. The heteroplasmy percentage of these samples aside from the above mutations varied from 48.94% to 1.31%. In total there were 212 mutations present across the sample.

3.7.3 Data for the patient "Hip 3"

Hip 3 samples were taken from an 88-year-old female undergoing a total hip replacement for arthritis.

Coverage

As depicted in *Figure 35* there were low values around the overlap of primer pair 1 and primer pair 5 around the 1 – 700 bp. Hip 3-1, 5 and 9 also experienced areas of low coverage around 14500-500 bp. Hip 3-2 has an area of dropped coverage from around 1200-3700 bp. Aside from cell Hip 3-2 and 9, the mitochondrial genome coverage with a read depth of greater than 500 times was 91.57% and above. (cell 2 – 82.55%, cell 9 85.44%).

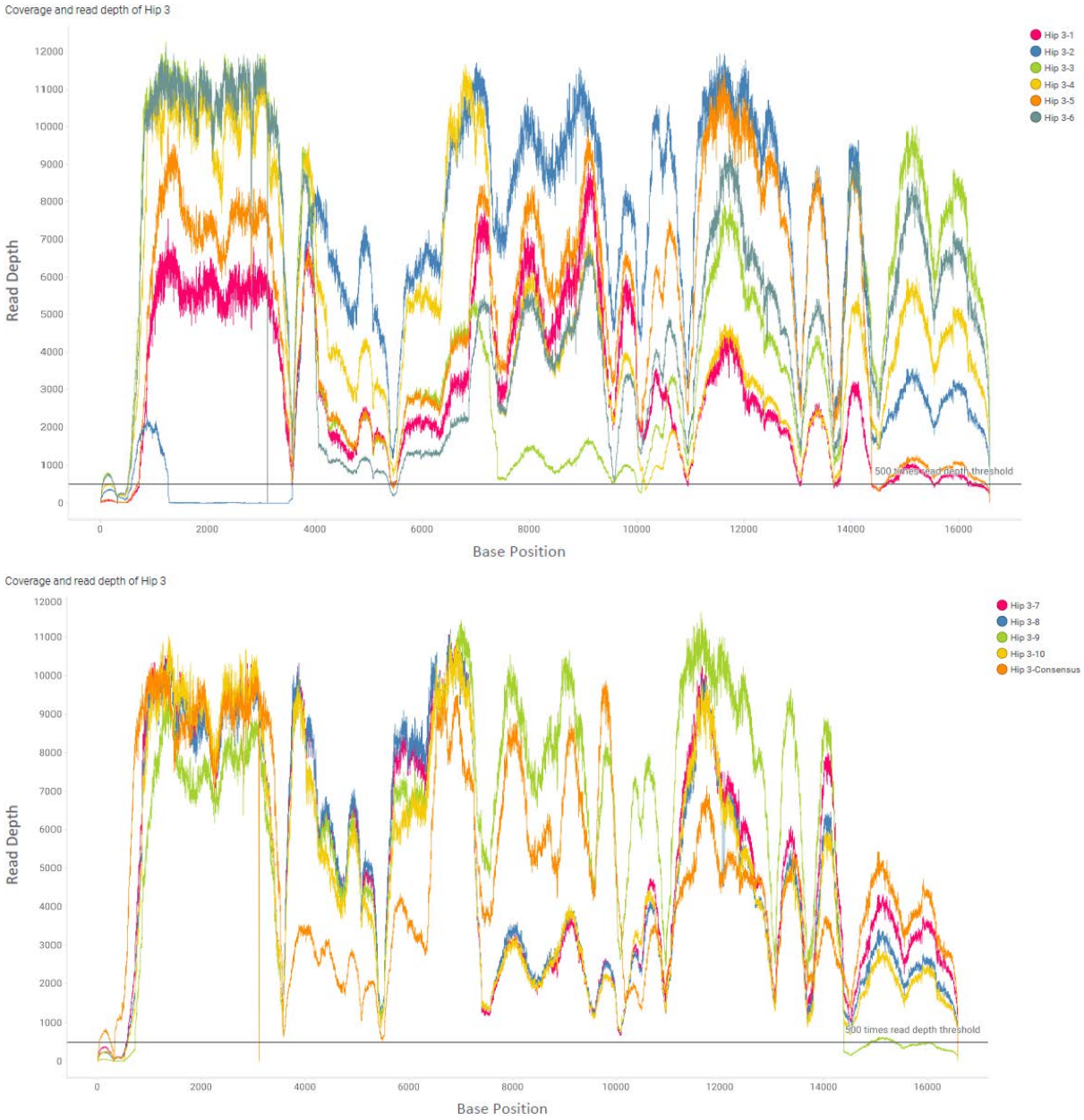

Figure 35 Coverage graphs for Hip 3 - read depth of each base and 500 read depth threshold demonstrated.

Haplogroup

All cells and the consensus sequence were HV0F haplogroup. Except for cell 2, the confidence of this call was >0.8 (cell 2 0.73). Commonly missing haplogroup markers across the cells and consensus were m.228G>A, m.14323T>A and m.15721T>C.

Polymorphic variant specific to the patient

There were no polymorphic variants seen in Hip 3.

Individual SNPs greater than 50% heteroplasmy

Mutations are presented in *Figure 36*

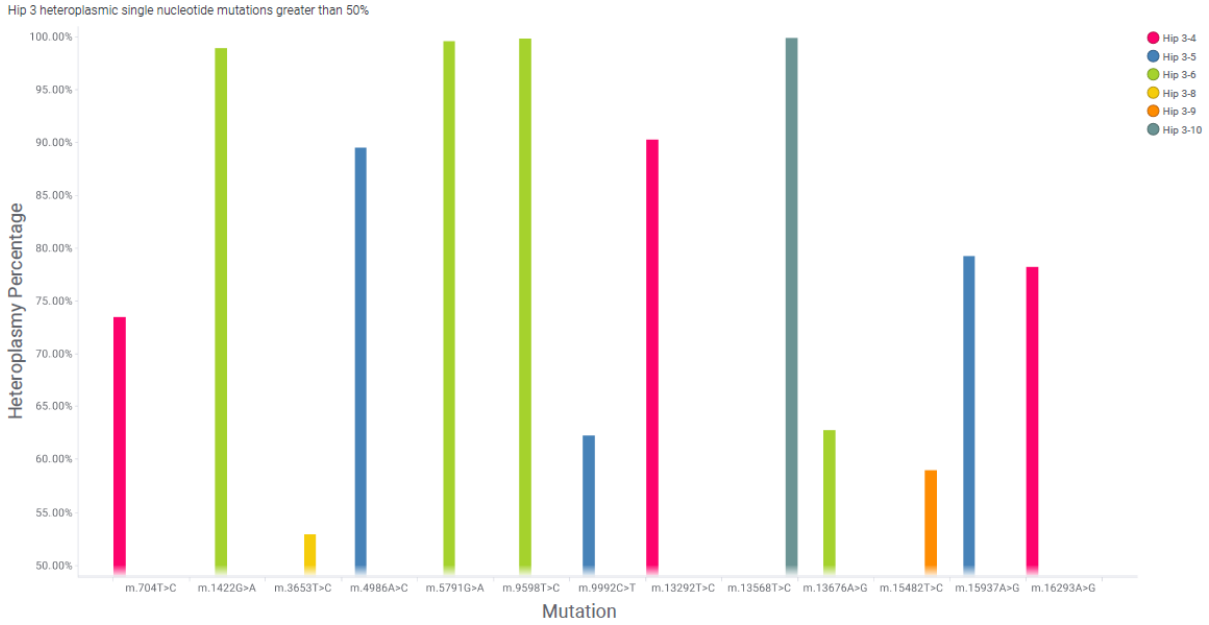

Figure 36 Hip 3 heteroplasmic single nucleotide mutations greater than 50% heteroplasmy.

- Cell 1 has no SNPs greater than 50%.
- Cell 2 has no SNPs greater than 50%.
- Cell 3 has no SNPs greater than 50%.
- Cell 4 has 3 SNPs: m.704T>C (73.41%), m.13292T>C (90.29%) and m.16293A>G (78.20%).
    - m.704T>C this affects RNR1 mitochondrial 12s ribosome gene with no documented deleterious effects. There is no dbSNP reference number.
    - m.13292T>C causes a non-synonymous change of the MT-ND5 gene. This causes a change of the amino acid from isoleucine to threonine. The SIFT score is 0 - deleterious low confidence and Polyphen score 0.99 probably damaging. There is no dbSNP reference number.
    - m.16293C>G is within the non-coding D-Loop hypervariable region and has no detrimental effects. The dbSNP reference is rs878890610.

- Cell 5 has 3 SNPs: m.4986A>C (89.51%), m.9992C>T (62.20%) and m.15937A>G (79.23%).
    - m.4986A>C causes a non-synonymous change of the MT-ND2 gene. This causes a change of the amino acid from threonine to proline. The SIFT score is 0.01 - deleterious and Polyphen score 1 probably damaging. There is no dbSNP reference number.
    - m.9992C>T codes for tRNA glycine and has no detrimental effects documented or dbSNP reference number.
      m.15937A>G codes for tRNA threonine and has no detrimental effects documented or dbSNP reference number.
- Cell 6 has 4 SNPs: m.1422G>A (99.92%) m.5791G>A (99.55%), m.9598T>C (99.86%) and m.13676A>G (62.73%).
    - m.1422G>A this affects RNR1 mitochondrial 12s ribosome gene with no detrimental effects documented or dbSNP reference number.
    - m.5791G>A codes for tRNA cysteine and no detrimental effects documented or dbSNP reference number.
    - m.9598T>C causes a non-synonymous change of the MT-CO3 gene. This causes a change of the amino acid from leucine to proline. The SIFT score is 0 - deleterious low confidence and Polyphen score 0.996 probably damaging. There is no dbSNP reference.
    - m.13676A>G causes a non-synonymous change of the MT-ND5 gene. This causes a change of the amino acid from asparagine to serine. The SIFT score is 0.04 - deleterious low confidence and Polyphen score 0.265 benign. There is a COSMIC - the Catalogue Of Somatic Mutations In Cancer reference (294): COSV62378489 associated with a renal clear cell carcinoma.
- Cell 7 has no SNPs greater than 50%.
- Cell 8 has one SNP: m.3653T>C (62.73%) which causes a non-synonymous change of the MT-ND1 gene. This causes a change of the amino acid from isoleucine to threonine. The SIFT score is 0.03 - deleterious low confidence and Polyphen score 0.54 benign. There is no reference on COSMIC or dbSNP.
- Cell 9 has one SNP: m.15482T>C (58.95%) which causes a non-synonymous change of the MT-CYB gene. This causes a change of the amino acid from isoleucine to threonine. The SIFT score is 0.26 - tolerated low confidence and Polyphen score 0.003 benign. The dbSNP reference is rs1556424592.
- Cell 10 has one SNP: m.13568T>C (99.90%) which causes a non-synonymous change of the MT-ND5 gene. This causes a change of the amino acid from serine to proline. The SIFT score is 0.04 - deleterious low confidence and Polyphen score 0.503 possibly damaging. The dbSNP reference is rs1556424592.

Across the whole sample of MSCs cells, there were 111 non-synonymous mutations with SIFT or Polyphen scores. The heteroplasmy percentage of these samples aside from the above mutations varied from 42.99% to 1.0%. In total there were 185 mutations present across the sample.

3.7.4 Data for the patient "Hip 4"

Hip 4 samples were taken from an 83-year-old female undergoing a total hip replacement for the failure of fixation following a fractured neck of femur.

Coverage

As depicted in *Figure 37* there were low read depths across all of the samples except hip 4-Consensus. Using a 500x read depth cut off coverage was as low as 39.32% in hip 4-7 to a maximum of 79.12% in hip 4-5 and 99.38% in the consensus sample. If the threshold is reduced to >1 read depth, then coverage is 95% and above for all cells but this would introduce noise and potential for reading error.

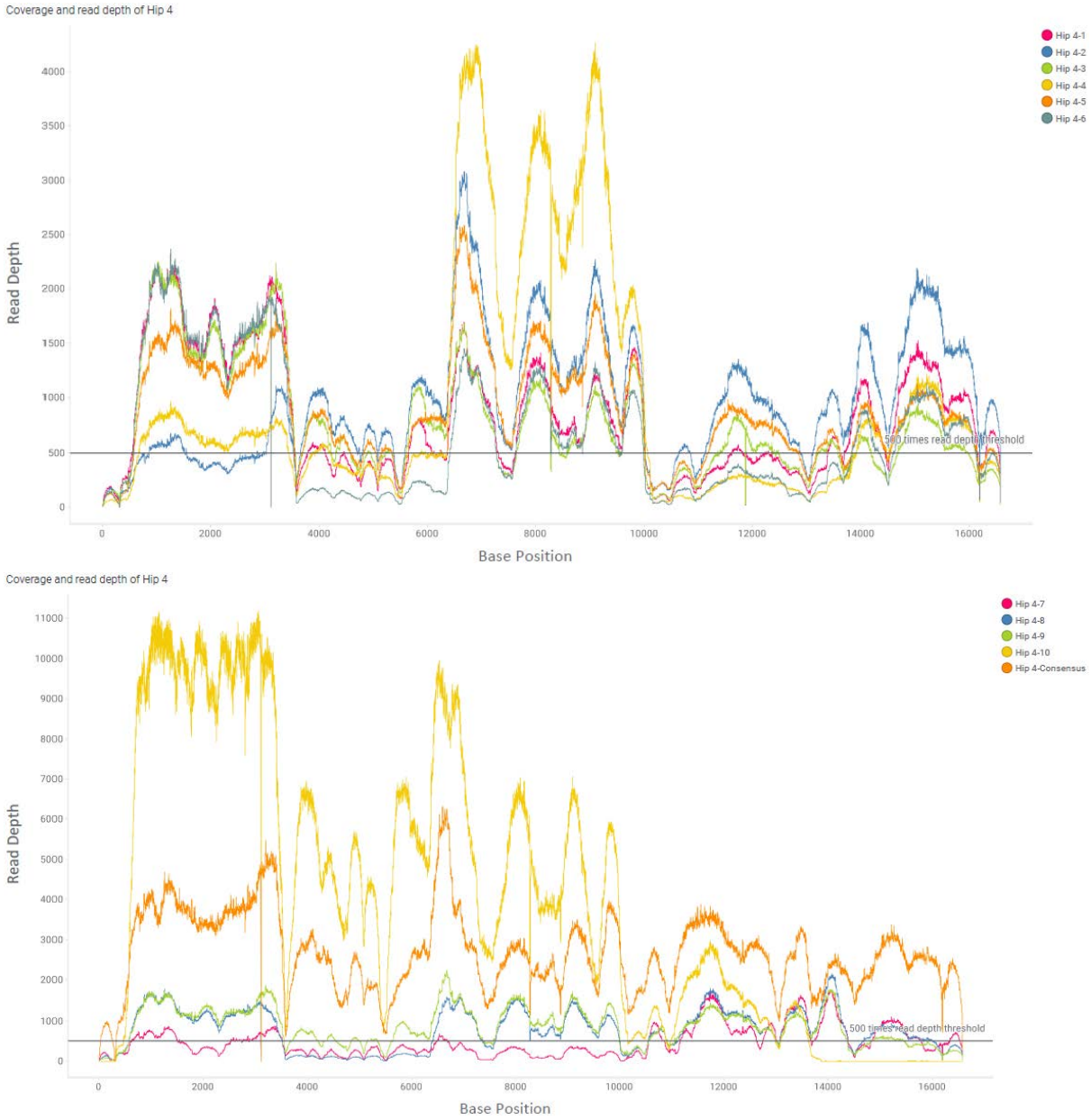

Figure 37 Coverage graphs for Hip 4 - read depth of each base and 500 read depth threshold demonstrated.

Haplogroup

All cells and the consensus sequence were T2 haplogroup. There was a further delineation of some samples (Cells 1, 3, 6, 7, 8 and 10) to T2f3. Due to poor coverage, several haplogroups markers were missing. Markers missing across all samples included m.73A>G and m.750A>G.

Polymorphic variant specific to the patient

There were no polymorphic variants seen in Hip 4.

Individual SNPs greater than 50% heteroplasmy

Mutations are presented in *Figure 38.*

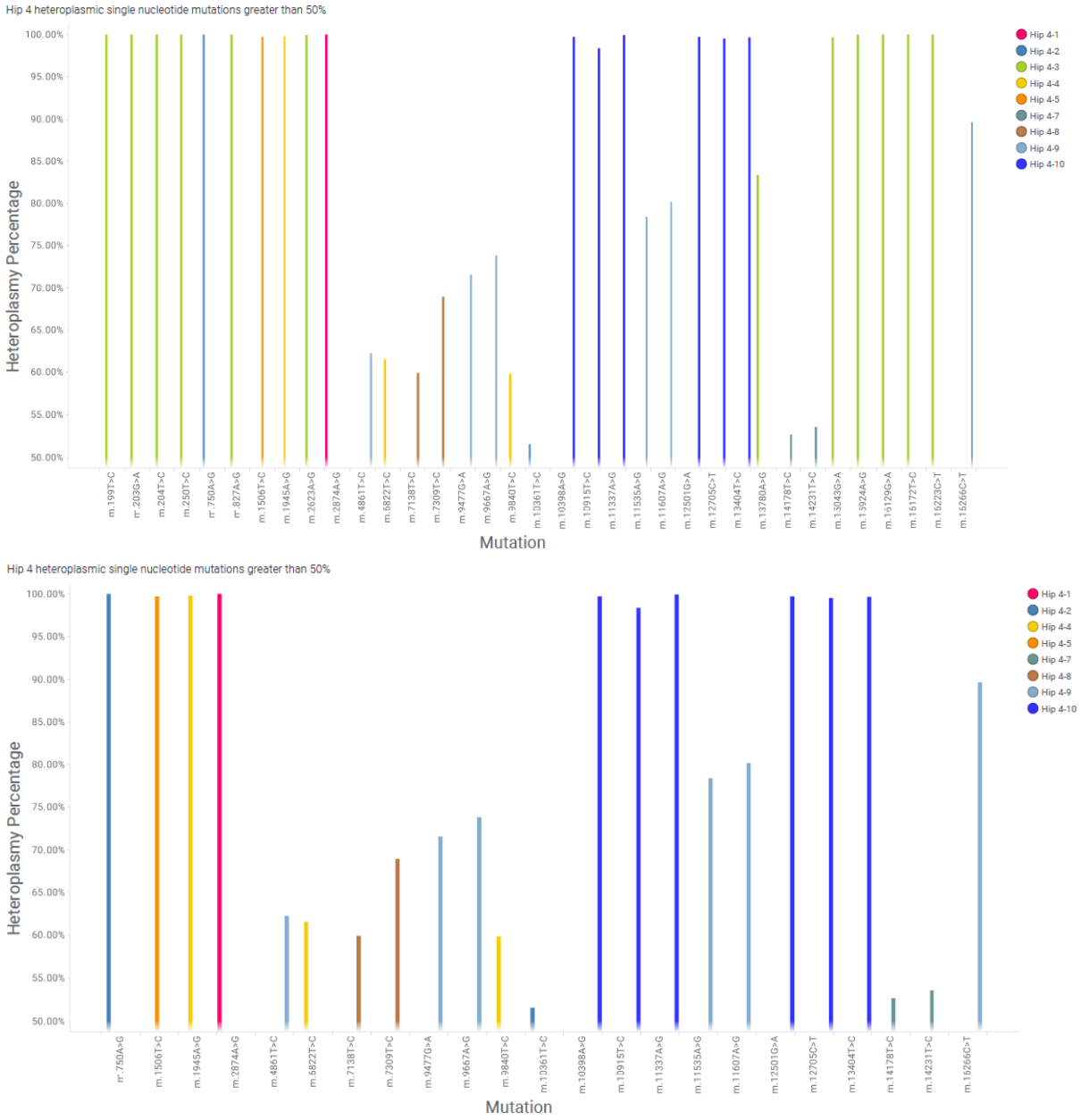

Figure 38 Hip 4 heteroplasmic single nucleotide mutations greater than 50% heteroplasmy. The top graph includes all cells, the bottom graph has cell 3 removed as there was a concern of sequence error.

- Cell 1 has one SNP: m.2874A>G (100%) within the mitochondrial 16s ribosome gene. There are no detrimental effects documented or dbSNP reference number.

- Cell 2 has two SNPs: m.750A>G (100%) and m.10361T>C (51.60%)

    - m.750A>G this affects RNR1 mitochondrial 12s ribosome gene with no documented deleterious effects. The dbSNP reference is rs2853518.

    - m.10361T>C causes a synonymous change of the MT-ND3 gene causing a change in the codon of agT/agC. There is no dbSNP reference number.

- Cell 3 has 12 SNPs the majority of these were homoplasmic in clusters and were not seen elsewhere within the consensus or other cells which brings into question the validity due to low read depth of the data and potential contamination of this sample or sequencing error.

    - m.199T>C, m.203G>A, m.204T>C, m.250T>C, m.16129G>A, m.16172T>C and m.16223C>T were all 100% and lying with the non-coding D-loop region. dbSNP reference numbers were rs72619362, rs1556422396, rs3135032, rs1556422406 rs41534744, rs2853817 and rs2853513 respectively. The read depth was below the threshold (500x) 119-272 for the mutations. The presence of the above mutations calls into question the validity of the below mutations and the likelihood of sequence error.

    - m.827A>G (100%) affects RNR1 mitochondrial 12s ribosome gene with no documented deleterious effects. Read depth was 827. The dbSNP reference is rs28358569

    - m.2623A>G (99.93%) affects rRNA for the mitochondrial 16s ribosome gene with no documented deleterious effects. Read depth was 2623. There is no dbSNP reference number.

    - m.13780A>G (83.38%) is a non-synonymous change affected the MT-ND5 gene. This causes an amino acid change from isoleucine to valine. The SIFT score is 0 - deleterious low confidence and Polyphen score 0.003 benign. The dbSNP reference is rs41358152. Read depth was only 325 times.

    - m.15043G>A (99.64%) is a synonymous change affecting MT-CYB gene. It causes a change in the codon of ggG/ggA. The dbSNP reference is rs193302985 with no associated pathology. Read depth was 843.

    - m.15924A>G (100%) affects the tRNA threonine gene of the mtDNA. The dbSNP reference is rs193303001. Read depth was 502 times.

- Cell 4 has 3 SNPs: m.1945A>G (99.82%), m.6822T>C (61.51%) and m.9840 T>C (59.84%)

    - m.1945A>G affecting the rRNA for the 16s mitochondrial ribosome. The dbSNP is rs1556422585 and there are no documented pathological effects.

  - m.6822T>C causes a non-synonymous change of the MT-CO1 gene. This causes a change of the amino acid from serine to proline. The SIFT score is 0 - deleterious low confidence and Polyphen score 0.988 probably damaging. There is no dbSNP reference.

  - m.9840 T>C causes a non-synonymous change of the MT-CO3 gene. This causes a change of the amino acid from serine to proline. The SIFT score is 0 - deleterious low confidence and Polyphen score 0.99 probably damaging. There is no dbSNP reference.

- Cell 5 has one SNP: m.1506T>C (99.71%) affecting the rRNA for the 12s mitochondrial ribosome. There is no dbSNP and there are no documented pathological effects.

- Cell 6 has no SNPs greater than 50%.

- Cell 7 has 2 SNPs: m.14178T>C (52.70%) and m.14231T>C (53.49%)

  - m.14178T>C causes a non-synonymous change of the MT-ND6 gene. This causes a change of the amino acid from isoleucine to valine. The SIFT score is 0.62 – tolerated and Polyphen score 0.023 benign. The dbSNP reference is rs28357671.

  - m.14231T>C causes a non-synonymous change of the MT-ND6 gene. This causes a change of the amino acid from tyrosine to cysteine. The SIFT score is 0.37 – tolerated whereas the Polyphen score 0.97 – probably damaging. There is no dbSNP reference.

- Cell 8 has 2 SNPs: m.7138T>C (59.90%) and m.7309T>C (68.95%).

  - m.7138T>C causes a non-synonymous change of the MT-CO1 gene. This causes a change of the amino acid from isoleucine to threonine. The SIFT score is 0.12 – tolerated low confidence and the Polyphen score 0.099 - benign. There is no dbSNP reference.

  - m.7309T>C causes a non-synonymous change of the MT-CO1 gene. This causes a change of the amino acid from isoleucine to threonine. The SIFT score is 0.06 - tolerated low confidence and the Polyphen score 0.031 - benign. The dbSNP reference is rs1556423267.

- Cell 9 has 6 SNPs: m.4861T>C (62.23%), m.9477G>A (71.57%), m.9667A>G (73.81%), m.11535A>G (78.36%), and m.11607A>G (80.13%).

  - m.4861T>C causes a non-synonymous change of the MT-ND2 gene. This causes a change of the amino acid from leucine to proline. The SIFT score is 0 - deleterious and the Polyphen score 1 – probably damaging. There is no dbSNP reference.

  - m.9477G>A causes a non-synonymous change of the MT-CO3 gene. This causes a change of the amino acid from valine to isoleucine. The SIFT score is 0.12 – tolerated low confidence and the Polyphen score 0 – probably benign. The dbSNP reference is rs2853825.

  - m.9667A>G causes a non-synonymous change of the MT-CO3 gene. This causes a change of the amino acid from asparagine to serine. The SIFT score is 0.08 – tolerated low confidence and the Polyphen score 0.127 – probably benign. The dbSNP reference rs41482146.

  - m.11535A>G causes a non-synonymous change of the MT-ND4 gene. This causes a change of the amino acid from tyrosine to cysteine. The SIFT score is 0 – deleterious low confidence and the Polyphen score 0.998 - probably damaging. There is no dbSNP reference.

  - m.11607A>G causes a stop gain in the MT-ND4 gene as a consequence there is no SIFT or Polyphen score and no dbSNP reference.

- Cell 10 has 6 SNPs: m.10398A>G (99.70%), m.10915T>C (98.34%) m.11337A>G (99.90%), m.12501G>A (99.72%), m.12705C>T (99.47%) and m.13404T>C (99.63%).

  - m.10398A>G causes a non-synonymous change of the MT-ND3 gene. This causes a change of the amino acid from threonine to alanine. The SIFT score is 1 – tolerated low confidence and the Polyphen score 0 - benign. The dbSNP reference is rs2853826.

  - m.10915T>C causes a synonymous change within the MT-ND4 gene altering the codon tgT/tgC. The dbSNP is rs2857285.

  - m.11337A>G causes a non-synonymous change of the MT-ND4 gene. This causes a change of the amino acid from asparagine to serine. The SIFT score is 0.77 – tolerated low confidence and the Polyphen score 0.017 - benign. There is no dbSNP reference.

  - m.12501G>A, m.12705C>T and m.13404T>C are all synonymous variants of the MT-ND5 gene. The dbSNP references are rs28397767, rs193302956, rs1556424275. m.13404T>C also has a COSMIC reference COSV62293963 associated it with endometrial carcinoma (294).

Across the whole sample of MSCs cells, there were 71 non-synonymous mutations with SIFT or Polyphen scores. The heteroplasmy percentage of these samples aside from the above mutations varied from 31.46% to 1.33%. In total there were 181 mutations present across the sample which reduced to 153 if cell 3 was removed.

3.7.5 Data for the patient "Hip 6"

Hip 6 samples were taken from a 45-year-old female undergoing a total hip replacement osteoarthritis.

Coverage

As depicted in *Figure 39* there were low read depths across a number of the cells with only cells 1 and 3 exceeding 90% coverage at 500 times read depth. Cells 2 and 10 had a coverage of greater than 80%, with the remaining cells sitting between 58-78%. At a read depth of 1 coverage was 97.7% or above but at these low depths, there is a risk of noise and error. In the samples with low coverage, there was no pattern matched to primer pairings but universally low data.

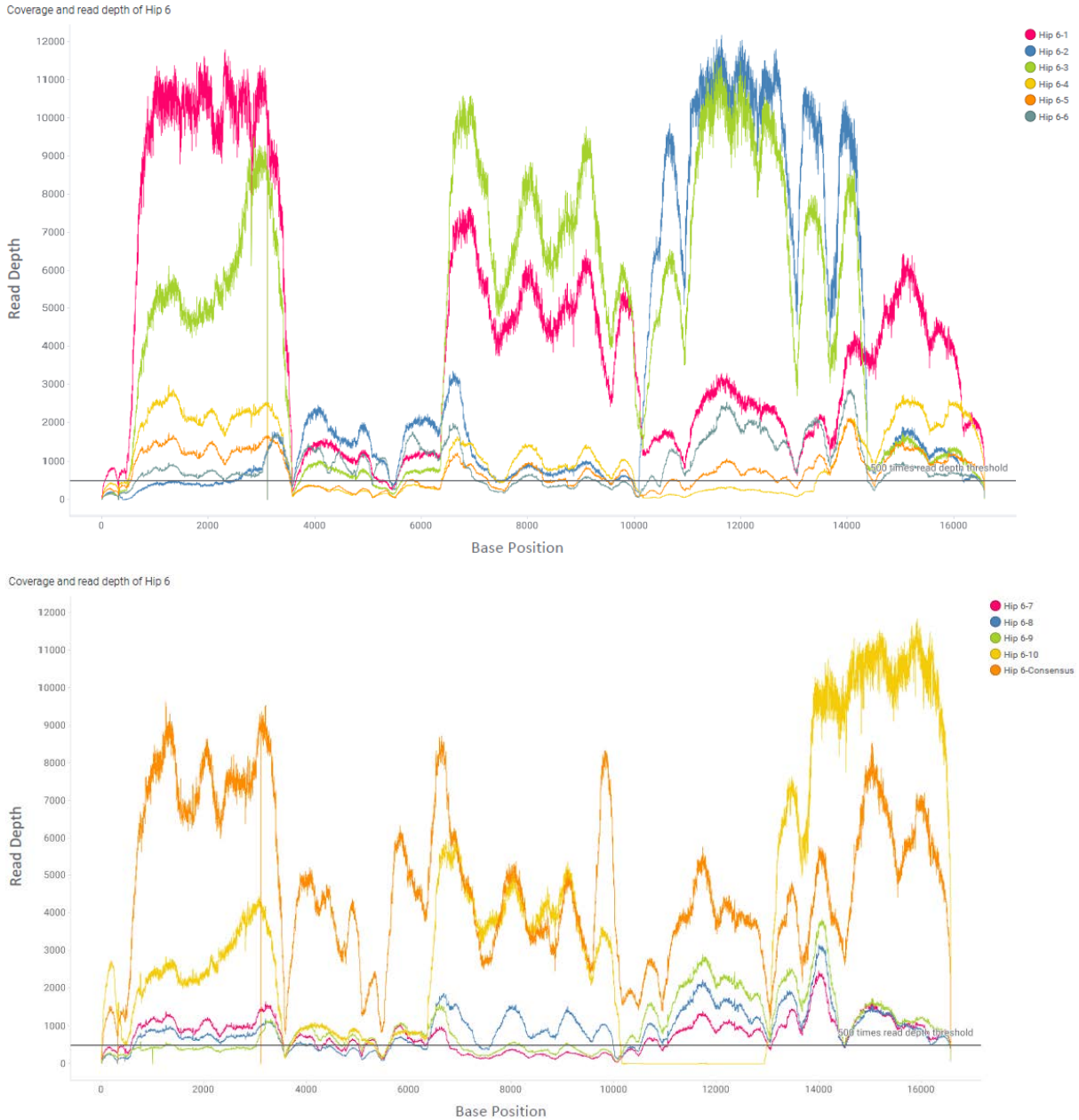

Figure 39 Coverage graphs for Hip 6 - read depth of each base and 500 read depth threshold demonstrated.

Haplogroup

The majority of the cells and the consensus sequence were T2 haplogroup. There was a further delineation of some samples (Cells 1, 4, 6, 7, 8 and the consensus) to T2b3. Due to poor coverage, several haplogroups markers were missing across the samples this led to some cells been called as H13a1 and H2a2 haplogroups (3,10 and then 2 respectively). The difference in these haplogroups has been considered in further analysis.

Polymorphic variant specific to the patient

m.4745A>G a synonymous variant of MT-ND2 causing a codon change caA/caG was present in five of the samples; cells 2,6,7,9 and 10 but was not present in the consensus. Several d-loop mutations were present in multiple samples, but this was thought to be due to sequencing error.

Individual SNPs greater than 50% heteroplasmy

Mutations are presented in *Figure 40.*

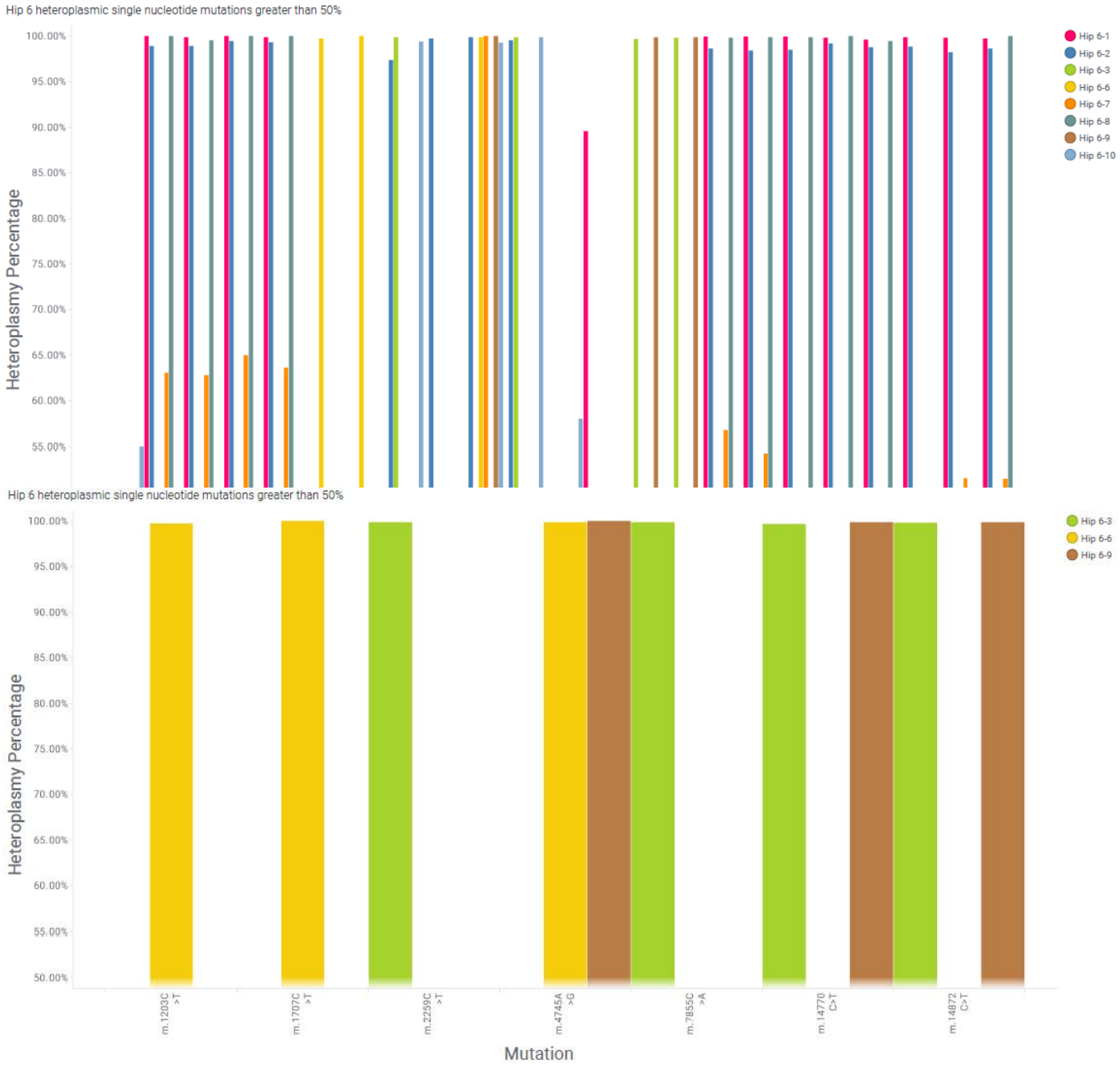

Figure 40 Hip 6 heteroplasmic single nucleotide mutations greater than 50% heteroplasmy. The top graph includes all cells, the bottom graph has cells 1,2,7,8,10 removed as there was a concern of sequence error.

- Cell 1 has 13 SNPs m.199T>C (100%), m.203G>A (99.88%), m.204T>C (100%), m.250T>C (99.86%), m.13780A>G (89.58%), m.15043G>A (99.90%), m.15924A>G (99.92%), m.16129G>A (99.96%), m.16172T>C(99.78%), m.16223C>T (99.60), m.16311T>C (99.85%), m.16362T>C (99.81%), m.16391G>A (99.74%).
    - m.199T>C, m.203G>A, m.204T>C, m.250T>C, m.16129G>A, m.16172T>C, m.16223C>T, m.16311T>C, m.16362T>C and m.16391G>A are all non-coding mutations within the D-Loop. The clustering of these mutations within close regions of the genome and read counts suggest error or contamination of the sample.

  - m.13780A>G causes a non-synonymous change of the MT-ND5 gene. This causes a change of the amino acid from isoleucine to valine. The SIFT score is 0 – deleterious low confidence and the Polyphen score 0.003 - benign. The dbSNP reference is rs41358152.

  - m.15043G>A causes a synonymous change and alteration of the codon ggG to ggA. The dbSNP reference is rs193302985

  - m.15924A>G causes a tRNA tyrosine mutation. The dbSNP reference is rs193303001

- Cell 2 has 15 SNPs m.199T>C (98.91%), m.203G>A (98.89%), m.204T>C (98.89%), m.250T>C (99.32%), m.2259C>T (97.41%), m.4480T>C (99.73%), m.4745A>G (99.87%), m.7855C>A (99.51%), m.15043G>A(98.63%), m.15924A>G (98.44%), m.16129G>A (98.47%), m.16172T>C (99.19%), m.16223C>T (98.78%), m.16311T>C (98.84%), m.16362T>C (98.23%), m.16391G>A (98.65%).

  - m.199T>C, m.203G>A, m.204T>C, m.250T>C, m.16129G>A, m.16172T>C, m.16223C>T, m.16311T>C, m.16362T>C and m.16391G>A are again all non-coding mutations within the D-Loop. The clustering of these mutations within close regions of the genome and read counts suggest error or contamination of the sample.

  - m.2259C>T is within the mitochondrial 16s ribosome gene, the dbSNP reference is rs201336470, there are no reported detrimental effects.

  - m.4480T>C causes a non-synonymous change of the MT-ND2 gene. This causes a change of the amino acid from leucine to proline. The SIFT score is 0.1 – tolerated and the Polyphen score 0.102 - benign. There is no dbSNP reference.

  - m.4745A>G, m.7855C>A and m.15043G>A are all synonymous changes affecting the MT-ND2, MT-CO2, and MT-CYB genes respectively. m.4745A>G has a dbSNP reference of rs1556422896. m.7855C>A has no dbSNP reference but m.15043G>A reference number is rs193302985.

- Cell 3 has 4 SNPs: m.2259C>T (99.87%), m.7855C>A (99.83%), m.14770C>T (99.66%) and m.14872C>T (99.77%).

  - m.2259C>T is within the mitochondrial 16s ribosome gene, the dbSNP reference is rs201336470, there are no reported detrimental effects.

  - m.7855C>A, m.14770C>T and m.14872C>T all cause synonymous changes to the MT-CO2, MT-CYB and MT-CYB genes respectively. The dbSNP reference for m.14770C>T is rs1556424488. m.14872C>T has both a dbSNP reference rs878879194 and a COSMIC reference, COSV62377781. There is no dbSNP reference for m.7855C>A.

- Cell 4 has no SNPs greater than 50%.

- Cell 5 has no SNPs greater than 50%.

- Cell 6 has 3 SNPs: m.1203C>T (99.75%), m.1707C>T (100%) and m.4745A>G (99.86%)
    - m.1203C>T is within the mitochondrial 12s ribosome gene, there are no reported detrimental effects. There is no dbSNP reference.
    - m.1707C>T is within the mitochondrial 16s ribosome gene, there are no reported detrimental effects. There is no dbSNP reference.
    - m.4745A>G causes a synonymous change to the MT-ND2 gene, this alters the codon caA/caG. The dbSNP reference is rs1556422896.
- Cell 7 has 9 SNPs: m.199T>C (63.07%), m.203G>A (62.80%), m.204T>C (64.99%), m.250T>C (63.61%), m.4745A>G (100%), m.15043G>A (56.74%), m.15924A>G (54.31%), m.16362T>C, (51.56%), m.16391G>A (51.51%).
    - m.199T>C, m.203G>A, m.204T>C, m.250T>C, m.16362T>C and m.16391G>A are again all non-coding mutations within the D-Loop. The clustering of these mutations within close regions of the genome and read counts suggest error or contamination of the sample.
    - m.4745A>G and m.15043G>A cause synonymous changes of the MT-ND2 and MT-CYB gene respectively. The dbSNP references are rs1556422896 and rs193302985.
    - m.15924A>G this affects the tRNA threonine gene with no documented pathological consequences.
- Cell 8 has 10 SNPs: m.199T>C (100%), m.203G>A (99.54%), m.204T>C (100%), m.250T>C (100%), m.15043G>A (99.78%), m.15924A>G (99.89%), m.16129G>A(99.85%), m.16172T>C (100%), m.16223C>T (99.43%) and m.16391G>A (100%).
    - m.199T>C, m.203G>A, m.204T>C, m.250T>C, m.16129G>A, m.16172T>C, m.16223C>T and m.16391G>A are again all non-coding mutations within the D-Loop. The clustering of these mutations within close regions of the genome and read counts suggest error or contamination of the sample.
    - m.15043G>A causes synonymous changes in the MT-CYB gene. This causes an alteration of the codon ggG/ggA. The dbSNP reference is rs193302985.
    - m.15924A>G this affects the tRNA threonine gene with no documented pathological consequences. The dbSNP reference is rs193303001.
- Cell 9 has 3 SNPs: m.4745A>G (100%), m.14770C>T (99.83%) and m.14872C>T (99.85%).
    - m.4745A>G causes a synonymous change to the MT-ND2 gene. The dbSNP reference is rs1556422896.
    - m.14770C>T and m.14872C>T causes synonymous changes of the MT-CYB gene. The dbSNP reference for m.14770C>T is rs1556424488 and the dbSNP and COSMIC reference for m.14872C>T are rs878879194 and COSV62377781.

- Cell 10 has 5 SNPs: m.73A>G (54.95%), m.2259C>T (99.37%), m.4745A>G (99.24%), m.7855C>A (99.86%) and m.13680C>T (57.98%).
    - m.73A>G this lies within the non-coding portion of the mitochondrial genome D-Loop. The dbSNP reference for this mutation is rs869183622.
    - m.2259C>T is within the mitochondrial 16s ribosome gene, there are no reported detrimental effects the dbSNP reference is rs201336470.
    - m.4745A>G causes a synonymous change to the MT-ND2 gene. The dbSNP reference is rs1556422896
    - m.7855C>A causes a synonymous change to the MT-CO2 gene, there are detrimental effects documented or a dbSNP reference number.
    - m.13680C>T causes a synonymous change to the MT-ND5 gene. The dbSNP and COSMIC references are rs1556424304, COSV62377776.

Across the whole sample of MSCs cells, there were 56 non-synonymous mutations with SIFT or Polyphen scores. The heteroplasmy percentage of these samples aside from the above mutations varied from 34.95% to 1.08%. In total there were 196 mutations present across the sample. The low counts and pattern of mutations observed in cells 1, 2, 7, 8 and 10 do call into question their validity and potential for contamination and read error.

3.7.6 Data for the patient "Hip 7"

Hip 7 samples were taken from an 82-year-old female undergoing a total hip replacement osteoarthritis.

Coverage

As depicted in *Figure 41* good coverage across the samples with read depths of greater than 500 times for 95% or above of each cell and the consensus data. The only exclusion to this were cells 5 and 6 who had 83% coverage at 500 times or more. Cell 5 had a drop in read depth around 3500-6500 bp whereas cell 6 dropped read depth from around 10000-13500 bp. Lowering the read depth to 250 and the coverage for cells 5 and 6 was 83% and 94% respectively.

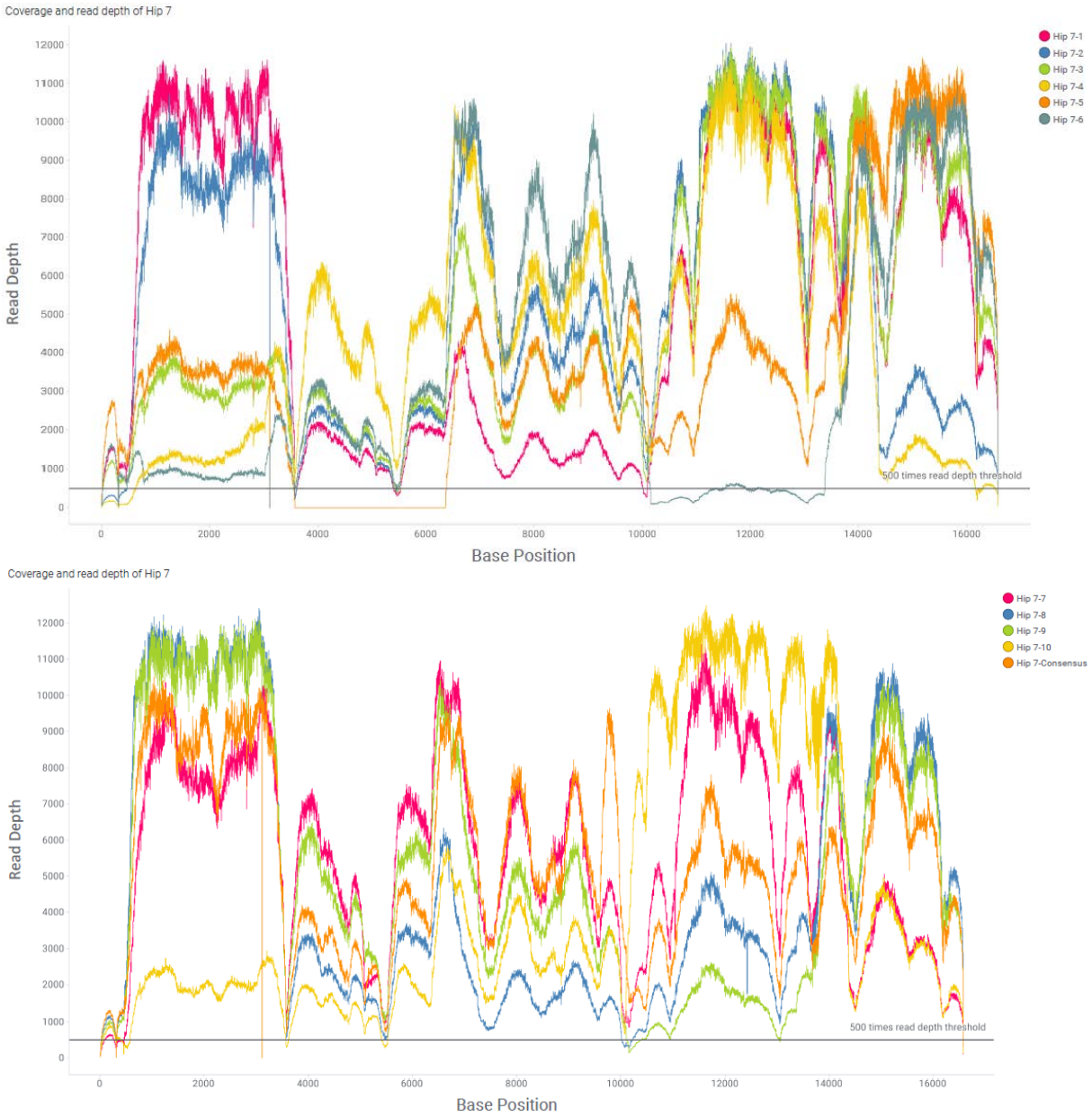

Figure 41 Coverage graphs for Hip 7 - read depth of each base and 500 read depth threshold demonstrated.

Haplogroup

All cells and the consensus sequence were H1a haplogroup. There was a further delineation of some samples (Cells 2, 3, 6, 8 and consensus) to H1a6. Due to poor coverage, the haplogroup marker m.73A>G was missing in almost all the samples. Cell 7 was H1bm haplogroup with a confidence of 0.71 but was missing 5 of the H1a6 haplomarkers.

Polymorphic variant specific to the patient

There were no polymorphic variants seen in Hip 7.

Individual SNPs greater than 50% heteroplasmy

Mutations are presented in *Figure 42*

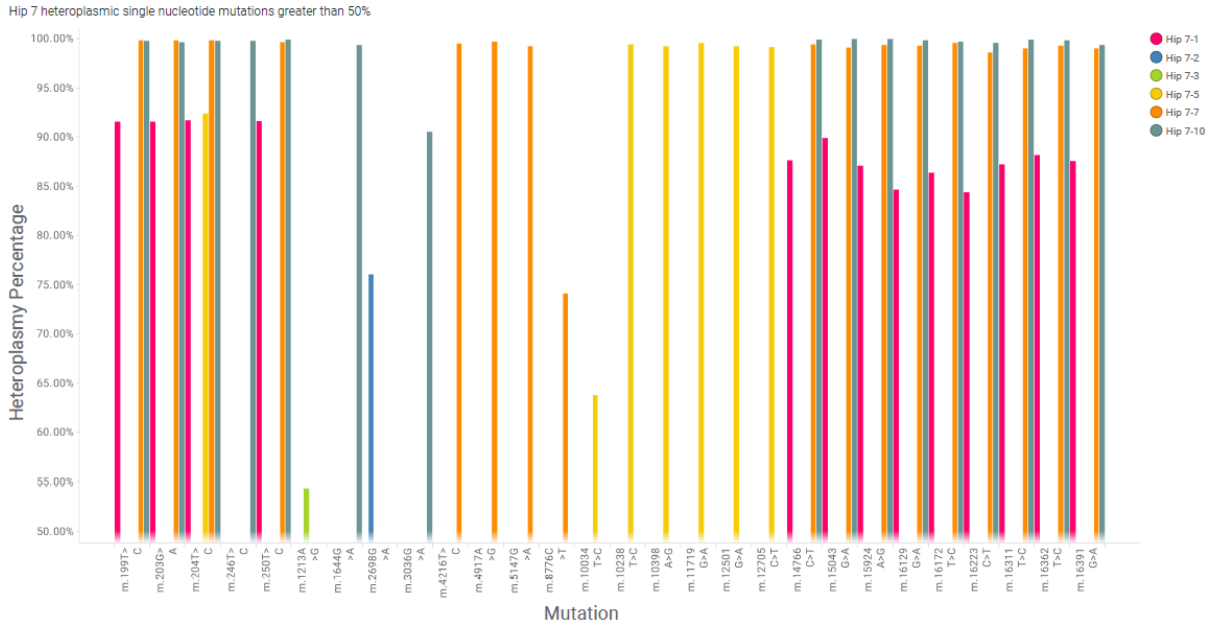

Figure 42 Hip 7 heteroplasmic single nucleotide mutations greater than 50% heteroplasmy.

- Cell 1 has 13 SNPs: m.199T>C (91.57%), m.203G>A (91.55%), m.204T>C (91.71%), m.250T>C (91.62%), m.14766C>T (87.63%), m.15043G>A (89.87%), m.15924A>G (87.07%), m.16129G>A (84.67%), m.16172T>C (86.36%), m.16223C>T (84.37%), m.16311T>C (87.19%), m.16362T>C (88.19%), m.16391G>A (87.54%).
    - m.199T>C, m.203G>A, m.204T>C, m.250T>C, m.16129G>A, m.16172T>C, m.16223C>T, m.16311T>C, m.16362T>C and m.16391G>A are again all non-coding mutations within the D-Loop. The clustering of these mutations within close regions of the genome and read counts suggest error or contamination of the sample.
    - m.14766C>T causes a non-synonymous change of the MT-CYB gene. With a change in amino acid from Threonine to Isoleucine. The associated SIFT score is deleterious low confidence (0.04), the Polyphen score is benign (0.003). The dbSNP reference is rs193302980.
    - m.15043G>A causes a synonymous change of the MT-CYB gene, altering the codon ggG/ggA, the dbSNP reference is rs193302985.

  - m.15924A>G codes for tRNA threonine gene with no documented pathological consequences.

- Cell 2 has one SNP: m.2698G>A (76.02%) within the mitochondrial 16s ribosome gene. There are no detrimental effects documented. Or dbSNP reference number.

- Cell 3 has one SNP: m.1213A>G (54.38%) within the mitochondrial 12s ribosome gene. There are no detrimental effects documented. Or dbSNP reference number.

- Cell 4 has no SNPs greater than 50%.

- Cell 5 has 6 SNPs: m.204T>C (92.37%), m.10034T>C (63.74%), m.10238T>C (99.42%), m.10398A>G (99.21%), m.11719G>A (99.57%), m.12501G>A (99.23%), m.12705C>T (99.12%).

  - m.204T>C is a non-coding mutation within the D-Loop, the dbSNP reference is rs3135032.

  - m.10034T>C codes for tRNA glycine gene with no documented pathological consequences. The dbSNP reference is rs41347846

  - m.10238T>C causes a synonymous change of the MT-ND3 gene altering the codon ggT/ggC the dbSNP reference is rs193302927.

  - m.10398A>G cause a non-synonymous change of the MT-ND3 gene. With a change in amino acid from Threonine to Alanine. The associated SIFT score is tolerated low confidence (1), the Polyphen score is benign (0). The dbSNP reference is rs2853826.

  - m.11719G>A causes a synonymous change of the MT-ND4 gene altering the codon ggG/ggA, the dbSNP reference is rs2853495.

  - m.12501G>A and m.12705C>T both cause a synonymous change of the MT-ND5 gene altering the codon atG/atA and atC/atT respectively. The dbSNP reference for m.12501G>A is rs28397767, the dbSNP and COSMIC reference for m.12705C>T is rs193302956 and COSV62293963.

- Cell 6 has no SNPs greater than 50%.

- Cell 7 has 17 SNPs: m.199T>C (99.84%), m.203G>A (99.84%), m.204T>C (99.84%), m.250T>C (99.63%), m.4216T>C (99.50%), m.4917A>G (99.65%), m.5147G>A (99.18%), m.8776C>T (74.08%), m.14766C>T (99.40%), m.15043G>A (99.03%), m.15924A>G (99.36%), m.16129G>A (99.29%), m.16172T>C (99.58%), m.16223C>T (99.59%), m.16311T>C (99.98%), m.16362T>C (99.30%), m.16391G>A (99.98%).

  - m.199T>C, m.203G>A, m.204T>C, m.250T>C, m.16129G>A, m.16172T>C, m.16223C>T, m.16311T>C, m.16362T>C and m.16391G>A are again all non-coding mutations within the D-Loop. The clustering of these mutations within close regions of the genome and read counts suggest error or contamination of the sample.

  - m.4216T>C cause a non-synonymous change of the MT-ND1 gene. With a change in amino acid from Tyrosine to histidine. The associated SIFT score is tolerated low confidence (1), the Polyphen score is benign (0.006). The dbSNP and COSMIC references are rs1599988 and COSV62293824.

  - m.4917A>G causes a non-synonymous change of the MT-ND2 gene. With a change in amino acid from asparagine to aspartic acid. The associated SIFT score is tolerated (0.09), the Polyphen score is benign (0.06). The dbSNP reference rs28357980.

  - m.5147G>A causes a synonymous change of the MT-ND2 gene altering the codon ggG/ggA, the dbSNP reference is rs2853495

  - m.8776C>T causes a non-synonymous change of the MT-ATP6 gene. With a change in amino acid from leucine to phenylalanine. The associated SIFT score is deleterious (0.01), the Polyphen score is probably damaging (0.997). There is no dbSNP reference.

  - m.14766C>T causes a non-synonymous change of the MT-CYB gene. With a change in amino acid from leucine to phenylalanine. The associated SIFT score is deleterious (0.01), the Polyphen score is probably benign (0.003). The dbSNP reference is rs193302980.

  - m.15043G>A causes a synonymous change of the MT-CYB gene altering the codon ggG/ggA, the dbSNP reference is rs193302985.

  - m.15924A>G codes for tRNA threonine gene with no documented pathological consequences. The dbSNP reference is rs193303001.

- Cell 8 has no SNPs greater than 50%.

- Cell 9 has no SNPs greater than 50%.

- Cell 10 has 15 SNPs: m.199T>C (99.76%), m.203G>A (99.64%), m.204T>C (99.76%), m.246T>C (99.74%), m.250T>C (99.87%), m.1644G>A (99.34%), m.3036G>A (90.53%), m.14766C>T (99.88%), m.15043G>A (99.93%), m.15924A>G (99.96%), m.16129G>A (99.82%), m.16172T>C (99.65%),m.16223C>T (99.52%), m.16311T>C (99.88%), m.16362T>C (99.79%) and m.16391G>A (99.32%).

  - m.199T>C, m.203G>A, m.204T>C, m.246T>C, m.250T>C, m.16129G>A, m.16172T>C, m.16223C>T, m.16311T>C, m.16362T>C and m.16391G>A are again all non-coding mutations within the D-Loop. The clustering of these mutations within close regions of the genome and read counts suggest error or contamination of the sample.

  - m.1644G>A codes for tRNA valine gene with no documented pathological consequences. There is no dbSNP reference.

  - m.3036G>A is within the mitochondrial 16s ribosome gene. There are no detrimental effects documented or dbSNP reference.

- m.14766C>T causes a non-synonymous change of the MT-CYB gene. With a change in amino acid from leucine to phenylalanine. The associated SIFT score is deleterious (0.01), the Polyphen score is probably benign (0.003). The dbSNP reference is rs193302980.
- m.15043G>A causes a synonymous change of the MT-CYB gene altering the codon ggG/ggA, the dbSNP reference is rs193302985.
- m.15924A>G codes for tRNA threonine gene with no documented pathological consequences. The dbSNP reference is rs193303001.

Across the whole sample of MSCs cells, there were 68 non-synonymous mutations with SIFT or Polyphen scores. The heteroplasmy percentage of these samples aside from the above mutations varied from 41.27% to 4.09%. In total there were 206 mutations present across the sample. The low counts and pattern of mutations observed in cells 1,5,7 and 10 do call into question their validity and potential for contamination and read error.

3.7.7 Data for the patient "Hip 8"

Hip 8 samples were taken from a 74-year-old female undergoing a total hip replacement osteoarthritis.

Coverage

As depicted in *Figure 43* there was low coverage across the samples except for cell 2, 4 and the consensus sequence which all had >96% coverage at read depths of greater than 500 times. There was poor read depth around the crossover of primer pairings 5 and 1. Cells 1, 5, 6, 8, 9 and 10 had large areas of low coverage between 3750 to around 10000 bp. Lowering the read depth threshold to 1 all samples except cell 7 (78.84%) were covered at >94%.

Figure 43 Coverage graphs for Hip 8 - read depth of each base and 500 read depth threshold demonstrated.

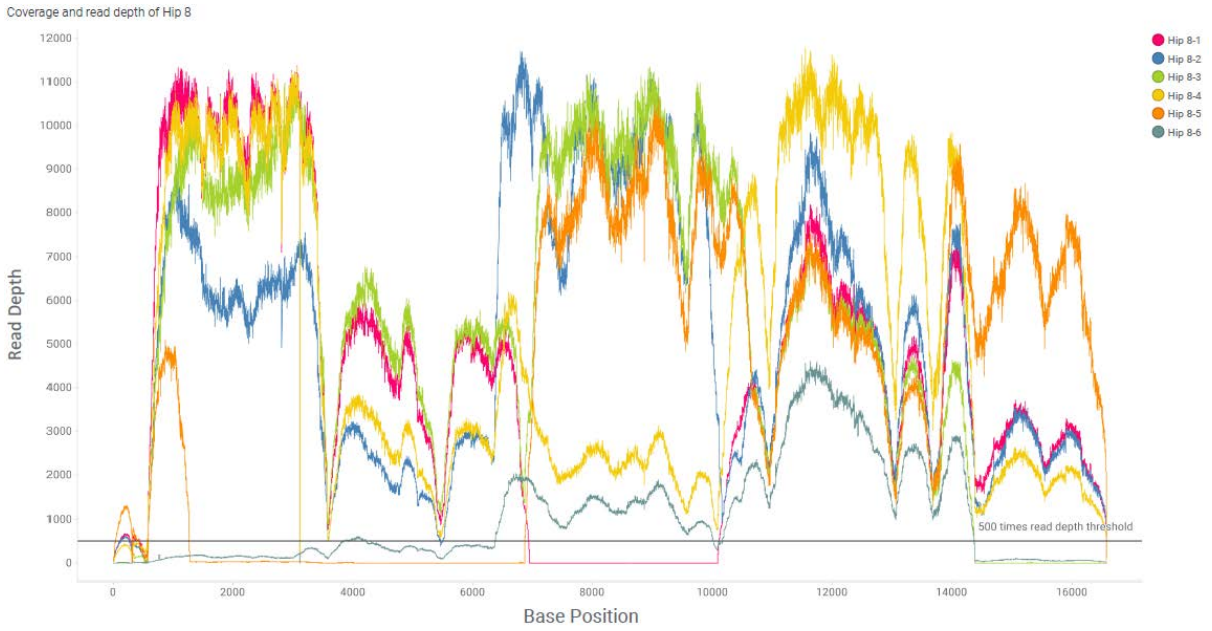

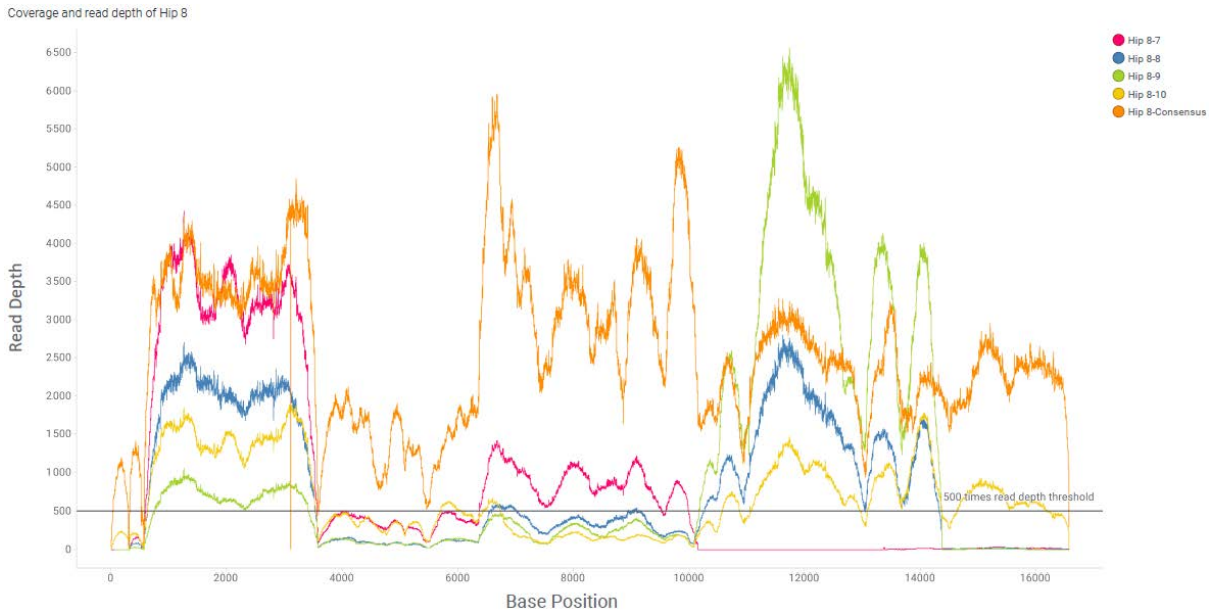

Haplogroup

All cells and the consensus sequence were "I" haplogroup except cell 8 and 9. There was a further delineation of some samples (Cells 1, 2, 4, 5, 10 and consensus) to I3a. Due to poor coverage, the haplogroup marker m.73A>G was missing in almost all the samples. Cells 8 and 9 were labelled as N1a1, they were missing 22 of the 32 haplomarkers of I3a. This was due to poor coverage with no reads of some base pairs or single figures for the majority of the other missing haplomarkers.

Polymorphic variant specific to the patient

There were no polymorphic variants seen in Hip 8. Although there was a mutation of the 16s ribosome gene - m.1719G>T which was seen at near homoplasmic levels in cells 1,2,3 and 4.

Individual SNPs greater than 50% heteroplasmy

Mutations are presented in *Figure 40*.

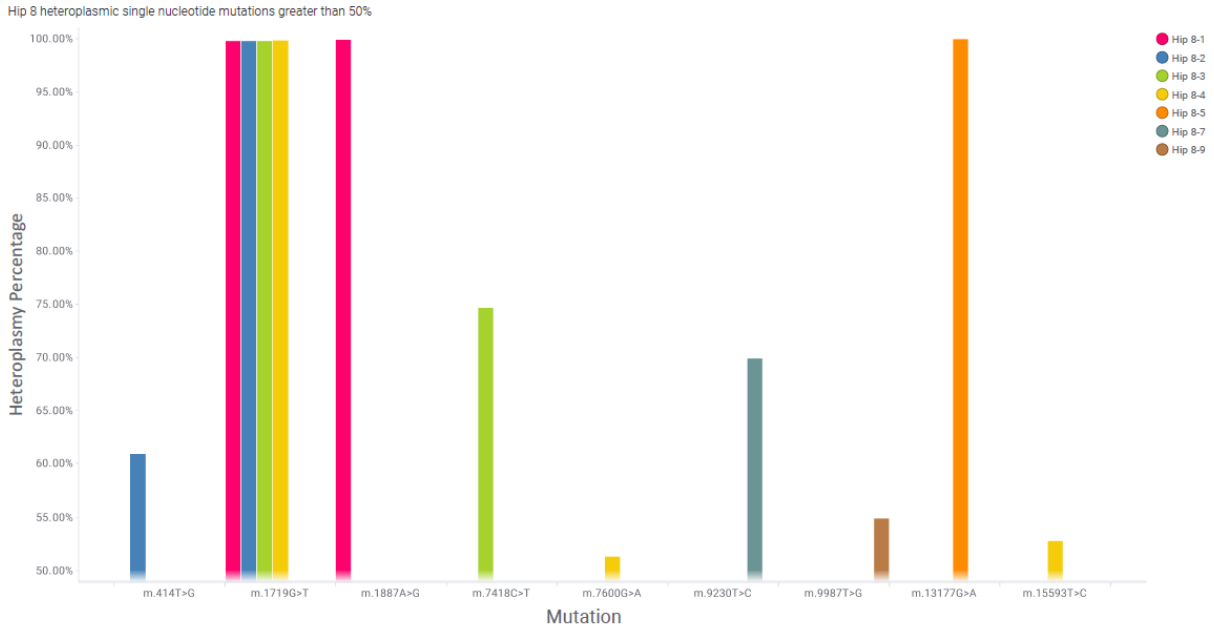

Figure 44 Hip 8 heteroplasmic single nucleotide mutations greater than 50% heteroplasmy.

- Cell 1 has 2 SNPs: m.1719G>T (99.74%), m.1887A>G (99.90%), both lie within the mitochondrial 16s ribosome gene. There are no detrimental effects documented or dbSNP reference numbers.
- Cell 2 has 2 SNPs: m.414T>G (60.86%) and m.1719G>T (99.73%).
    - m.414T>G is a non-coding mutation within the D-Loop. There is no dbSNP reference number.
    - m.1719G>T lies within the mitochondrial 16s ribosome gene. There are no detrimental effects documented and no dbSNP reference number.
- Cell 3 has 2 SNPs: m.1719G>T (99.75%) and m.7418C>T (74.59%).

  - m.1719G>T lies within the mitochondrial 16s ribosome gene. There are no detrimental effects documented. There is no dbSNP reference number.
  - m.7418C>T causes a synonymous change of the MT-CO1 gene altering the codon ttC/ttT, there is no dbSNP reference

- Cell 4 has 3 SNPs: m.1719G>T (99.79%), m.7600G>A (51.28%), m.15593T>C (52.79%).
  - m.1719G>T lies within the mitochondrial 16s ribosome gene. There are no detrimental effects documented. There is no dbSNP reference number.
  - m.7600G>A causes a synonymous change of the MT-CO2 gene altering the codon gcG/gcA, the dbSNP reference is rs386829010.
  - m.15593T>C causes a non-synonymous change of the MT-CYB gene. With a change in amino acid from serine to proline. The associated SIFT score is deleterious low confidence (0), the Polyphen score is probably damaging (0.996). There is no dbSNP reference.
- Cell 5 has 1 SNP: m.13177G>A (99.94%) this causes a non-synonymous change of the MT-ND5 gene. With a change in amino acid from serine to proline. The associated SIFT score is deleterious low confidence (0), the Polyphen score is probably damaging (0.996). There is no dbSNP reference.
- Cell 6 has no SNPs greater than 50%.
- Cell 7 has 1 SNP: m.9230T>C (69.84%) causes a synonymous change of the MT-CO3 gene altering the codon taT/taC, the dbSNP reference is rs879058558.
- Cell 8 has no SNPs greater than 50%.
- Cell 9 has 1 SNP: m.9987T>G (54.87%) this causes a non-synonymous change of the MT-CO3 gene. With a change in amino acid from serine to alanine. The associated SIFT score is deleterious low confidence (0), the Polyphen score is possibly damaging (0.831). There is no dbSNP reference.
- Cell 10 has no SNPs greater than 50%.

Across the whole sample of MSCs cells, there were 56 non-synonymous mutations with SIFT or Polyphen scores. The heteroplasmy percentage of these samples aside from the above mutations varied from 40.42% to 1.24%. In total there were 141 mutations present across the sample.

3.7.8 Data for the patient "Hip 9"

Hip 9 samples were taken from a 64-year-old male undergoing a total hip replacement osteoarthritis.

Coverage

As depicted in *Figure 45* coverage was good across the samples with >94% coverage at read depths of greater than 500 times seen in all samples except cell 3 which was 88.06%. There were the usual lower read depths around the crossover of primer pairs 1 and 5.

Figure 45 Coverage graphs for Hip 9 - read depth of each base and 500 read depth threshold demonstrated.

Haplogroup

All cells and the consensus sequence were U5a1b1d haplogroup with a confidence of 0.86 or more.

Polymorphic variant specific to the patient

There were no polymorphic variants seen in Hip 9. Although there was a mutation of the 12s ribosome gene - m.750A>G which was seen at near homoplasmic levels in cells 3,4,5 and 6. It was not seen in the consensus sequence. The dbSNP reference is rs2853518.

Individual SNPs greater than 50% heteroplasmy

Mutations are presented in *Figure 46.*

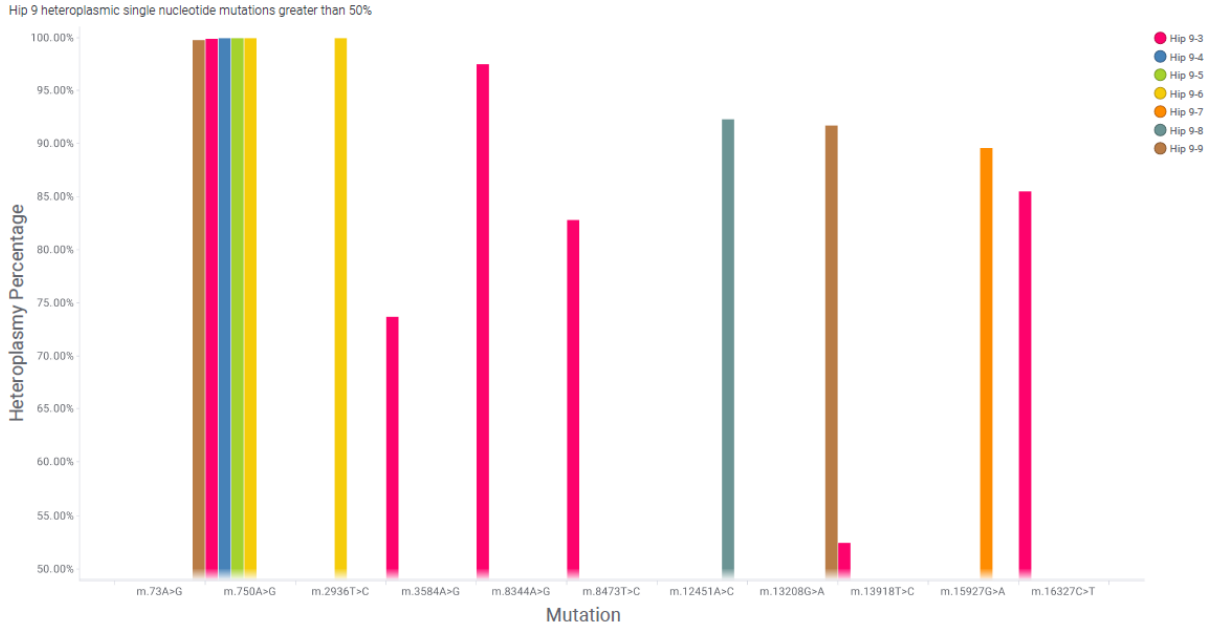

Figure 46 Hip 9 heteroplasmic single nucleotide mutations greater than 50% heteroplasmy.

- Cell 1 has no SNPs greater than 50%.
- Cell 2 has no SNPs greater than 50%.
- Cell 3 has 6 SNPs: m.750A>G (99.82%), m.3584A>G (73.66%), m.8344A>G (97.49%), m.8473T>C (82.74%), m.13918T>C (52.45%), m.16327C>T (85.47%).
    - m.750A>G lies within the mitochondrial 12s ribosome gene. There are no detrimental effects documented. The dbSNP reference is rs2853518.
    - m.3584A>G causes a non-synonymous change of the MT-ND1 gene. With a change in amino acid from asparagine to serine. The associated SIFT score is tolerated low confidence (0.12), the Polyphen score is benign (0.009). There is no dbSNP reference.
    - m.8344A>G) this affects the tRNA lysine with no documented pathological consequences. The dbSNP reference is rs118192098.
    - m.8473T>C causes a synonymous change of the MT-ATP8 gene altering the codon ccT/ccC, the dbSNP reference is rs386829037.

  - m.13918T>C causes a non-synonymous change of the MT-ND5 gene. With a change in amino acid from phenylalanine to leucine. The associated SIFT score is deleterious low confidence (0), the Polyphen score is probably damaging (0.99). There is no dbSNP reference.

  - m.16327C>T is a non-coding mutation within the D-Loop. The dbSNP reference is rs41355449.

- Cell 4 has 1 SNP: m.750A>G (99.91%), this lies within the mitochondrial 12s ribosome gene. There are no detrimental effects documented. The dbSNP reference is rs2853518.

- Cell 5 has 1 SNP: m.750A>G (99.88%), this lies within the mitochondrial 12s ribosome gene. There are no detrimental effects documented. The dbSNP reference is rs2853518.

- Cell 6 has 2 SNPs: m.750A>G (99.90%), m.2936T>C (99.89%).

  - m.750A>G (99.88%), this lies within the mitochondrial 12s ribosome gene. There are no detrimental effects documented. The dbSNP reference is rs2853518.

  - m.2936T>C this lies within the mitochondrial 16s ribosome gene. There are no detrimental effects documented. There is no dbSNP reference.

- Cell 7 has 1 SNP: m.15927G>A (89.54%) this affects the tRNA threonine with no documented pathological consequences. The dbSNP reference is rs193303002.

- Cell 8 has 1 SNP: m.12451A>C (92.26%) this causes a non-synonymous change of the MT-ND5 gene. With a change in amino acid from isoleucine to leucine. The associated SIFT score is tolerated low confidence (0.06), the Polyphen score is benign (0.022). There is no dbSNP reference.

- Cell 9 has 2 SNPs: m.73A>G (99.71%), m.13208G>A (91.70%).

  - m.73A>G is a non-coding mutation within the D-Loop. The dbSNP reference is rs869183622.

  - m.13208G>A this causes a non-synonymous change of the MT-ND5 gene. With a change in amino acid from cysteine to tyrosine. The associated SIFT score is deleterious low confidence (0), the Polyphen score is probably damaging (0.998). There is no dbSNP reference, but the COSMIC reference is COSV99053427.

- Cell 10 has no SNPs greater than 50%.

Across the whole sample of MSCs cells, there were 67 non-synonymous mutations with SIFT or Polyphen scores. The heteroplasmy percentage of these samples aside from the above mutations varied from 39.94% to 2.34%. In total there were 147 mutations present across the sample.

3.7.9 Data for the patient "Hip 10"

Hip 10 samples were taken from a 62-year-old male undergoing a total hip replacement osteoarthritis.

Coverage

As depicted in *Figure 47* coverage was good across the samples with >95% coverage at read depths of greater than 500 times seen in all samples except cell 1 (88.49%), cell 5 (88.68%), cell 6 (77.81%), cell 9 (78.44%) and cell 10 (66.01%). Reducing read depth to 1, then coverage in all cells was >94% of the mitochondrial genome. There were the usual lower read depths around the crossover of primer pairs 1 and 5. Cell 16 had reduced coverage from around 10750 to 13000 bp, cell 10 had reduced coverage from around 7500 to 10500 bp and 14000 to 750 bp.

Figure 47 Coverage graphs for Hip 10 - read depth of each base and 500 read depth threshold demonstrated.

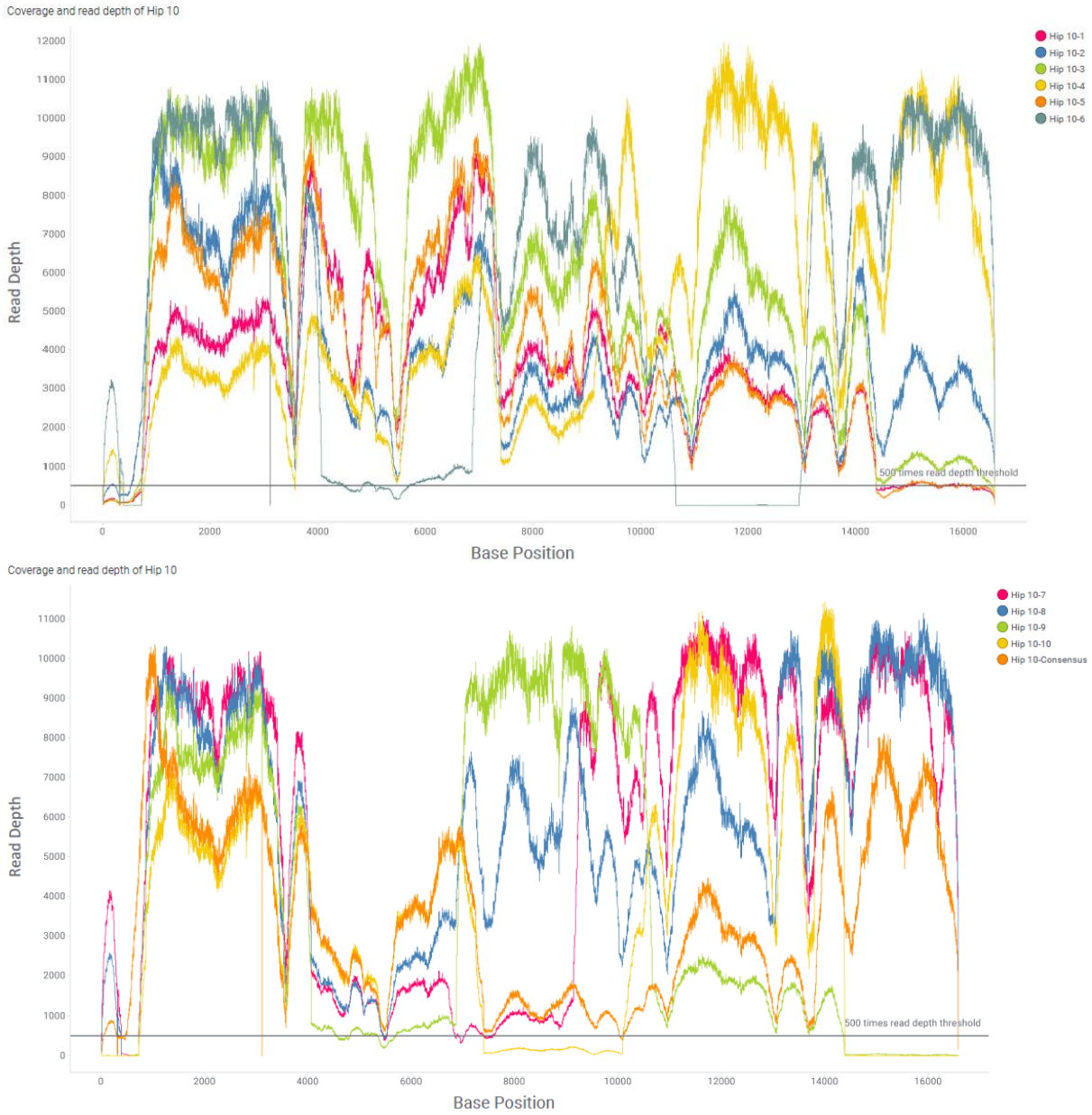

Haplogroup

All cells and the consensus sequence were HV haplogroup with a confidence of 0.69 or more. The lowest confidence rank was seen in cell 10 due to low coverage. Only cell 7 was I1a1e, this was missing 2 of the 8 haplogroup markers. 750G was missing in all cells except cell 9 and the consensus. 263G was affected by low or no read depth in cells 5, 9 and 10.

Polymorphic variant specific to the patient

There were no polymorphic variants seen in Hip 10. Although there was a mutation of the MT-ND6 gene - m.14360C>A which was seen at varying levels of heteroplasmy (1.66% - 8.15%) in cells 1,2,3,5 9 and 10. It was not seen in the consensus sequence. It was a non-synonymous change resulting in an amino acid change from tryptophan to leucine There is no dbSNP reference.

Individual SNPs greater than 50% heteroplasmy

Mutations are presented in *Figure 48.*

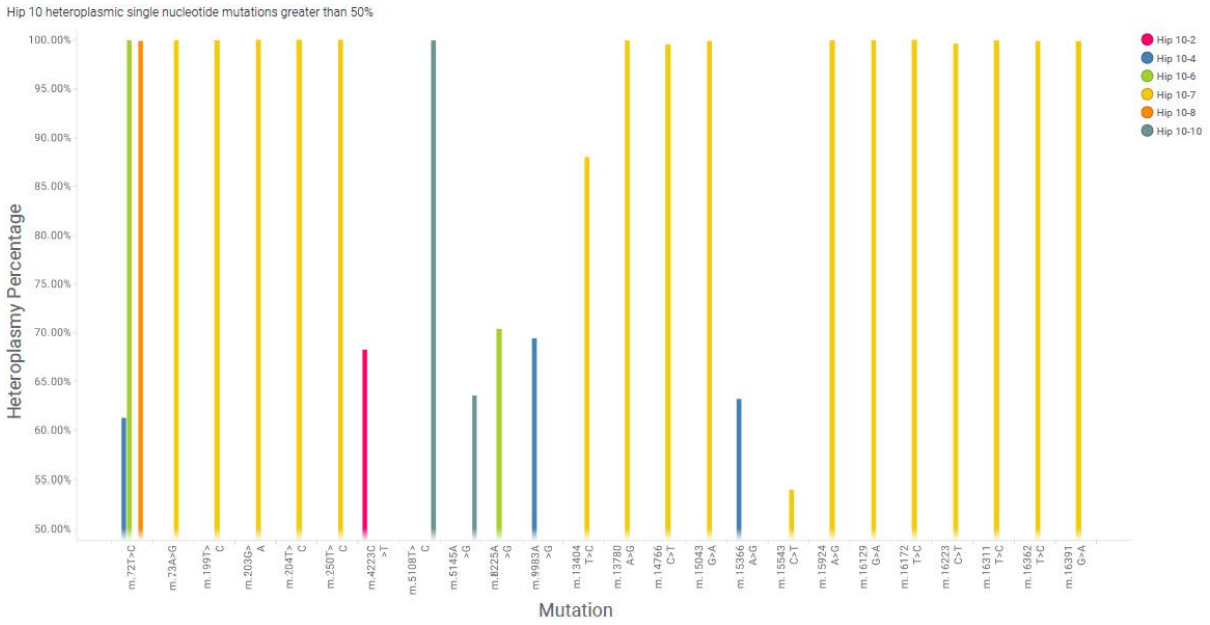

Figure 48 Hip 10 heteroplasmic single nucleotide mutations greater than 50% heteroplasmy.

- Cell 1 has no SNPs greater than 50%.
- Cell 2 has 1 SNP: m.4223C>T (68.20%) this causes a non-synonymous change of the MT-ND1 gene. With a change in amino acid from serine to phenylalanine. The associated SIFT score is deleterious low confidence (0), the Polyphen score is probably damaging (0.842). The dbSNP reference is rs9629043.
- Cell 3 has no SNPs greater than 50%.
- Cell 4 has 3 SNPs: m.72T>C (61.27%), m.9983A>G (69.40%) and m.15366A>G (63.18%).
    - m.72T>C is part of the non-coding D-Loop hypervariable region and has no detrimental effects. The dbSNP reference is rs879158303.

- m.9983A>G causes a synonymous change of the MT-CO3 gene altering the codon tgA/tgG, there is no dbSNP reference.

- m.15366A>G this causes a non-synonymous change of the MT-CYB gene. With a change in amino acid from asparagine to serine. The associated SIFT score is deleterious low confidence (0), the Polyphen score is probably damaging (0.842). There is no dbSNP reference.

- Cell 5 has no SNPs greater than 50%.

- Cell 6 has 2 SNPs: m.72T>C (99.91%) and m.8225A>G (70.36%).

  - m.72T>C is part of the non-coding D-Loop hypervariable region and has no detrimental effects. The dbSNP reference is rs879158303.

  - m.8225A>G this causes a non-synonymous change of the MT-CO2 gene. With a change in amino acid from isoleucine to valine. The associated SIFT score is tolerated low confidence (1), the Polyphen score is probably damaging (0.943). There is no dbSNP reference.

- Cell 7 has 13 SNPs: m.73A>G (99.93%), m.199T>C (99.95%), m.203G>A (99.97%), m.204T>C (99.97%), m.250T>C (100.00%), m.13404T>C (88.00%), m.13780A>G (99.91%),m.14766C>T (99.50%), m.15043G>A (99.86%), m.15543C>T (54.02%), m.15924A>G (99.96%), m.16129G>A (99.95%), m.16172T>C (99.97%), m.16223C>T (99.62%), m.16311T>C (99.93%), m.16362T>C (99.85%) and m.16391G>A (99.85%).

  - m.73A>G, m.199T>C, m.203G>A, m.204T>C, m.250T>C, m.16129G>A, m.16172T>C, m.16223C>T, m.16311T>C, m.16362T>C and m.16391G>A. are again all non-coding mutations within the D-Loop. The clustering of these mutations within close regions of the genome and read counts suggest error or contamination of the sample.

  - m.13404T>C causes a synonymous change of the MT-ND5 gene altering the codon atT/atC, the dbSNP reference is rs1556424275.

  - m.13780A>G this causes a non-synonymous change of the MT-ND5 gene. With a change in amino acid from isoleucine to valine. The associated SIFT score is deleterious low confidence (0), the Polyphen score is benign (0.003). The dbSNP reference is rs41358152.

  - m.14766C>T causes a non-synonymous change of the MT-CYB gene. With a change in amino acid from threonine to isoleucine. The associated SIFT score is deleterious low confidence (0.04), the Polyphen score is benign (0.003). The dbSNP reference is rs193302980.

  - m.15043G>A causes a synonymous change of the MT-CYB gene altering the codon ggG/ggA, the dbSNP reference is rs193302985.

  - m.15543C>T causes a non-synonymous change of the MT-CYB gene. With a change in amino acid from proline to leucine. The associated SIFT score is deleterious low

confidence (0.02), the Polyphen score is probably damaging (0.999). There is no dbSNP reference.

  - m.15924A>G codes for tRNA threonine gene with no documented pathological consequences. The dbSNP reference is rs193303001.

- Cell 8 has 1 SNP: m.72T>C (99.84%) this is part of the non-coding D-Loop hypervariable region and has no detrimental effects. The dbSNP reference is rs879158303.
- Cell 9 has no SNPs greater than 50%.
- Cell 10 has 2 SNPs: m.5108T>C (99.94%) and m.5145A>G (63.55%)
  - m.5108T>C causes a synonymous change of the MT-ND2 gene altering the codon acT/aaC, the dbSNP reference is rs386419948.
  - m.5145A>G causes a non-synonymous change of the MT-ND2 gene. With a change in amino acid from threonine to alanine. The associated SIFT score is deleterious (0.03), the Polyphen score is probably damaging (0.998). There is no dbSNP reference.

Across the whole sample of MSCs cells, there were 83 non-synonymous mutations with SIFT or Polyphen scores. The heteroplasmy percentage of these samples aside from the above mutations varied from 38.10%% to 1.66%. In total there were 193 mutations present across the sample.

3.7.10 Data for the patient "Hip 11"

Hip 11 samples were taken from a 61-year-old female undergoing a total hip replacement osteoarthritis.

Coverage

As depicted in *Figure 49* coverage was generally lower across this sample set compared to others using a threshold of 500 times read depth coverage varied from 54.52% across the 91.09% excluding the consensus. Cells 6, 7 and 8 were lower than the others.

Figure 49 Coverage graphs for Hip 11 - read depth of each base and 500 read depth threshold demonstrated.

Haplogroup

All cells and the consensus sequence were K1a4a1a2a haplogroup with a confidence of 0.89 or more except for cell 7 which had low coverage and confidence of 0.79. The haplomarkers 750G and 16093C were missing across all cells and the consensus sequence.

Polymorphic variant specific to the patient

There were no polymorphic variants seen in Hip 11.

Individual SNPs greater than 50% heteroplasmy

Mutations are presented in *Figure 50.*

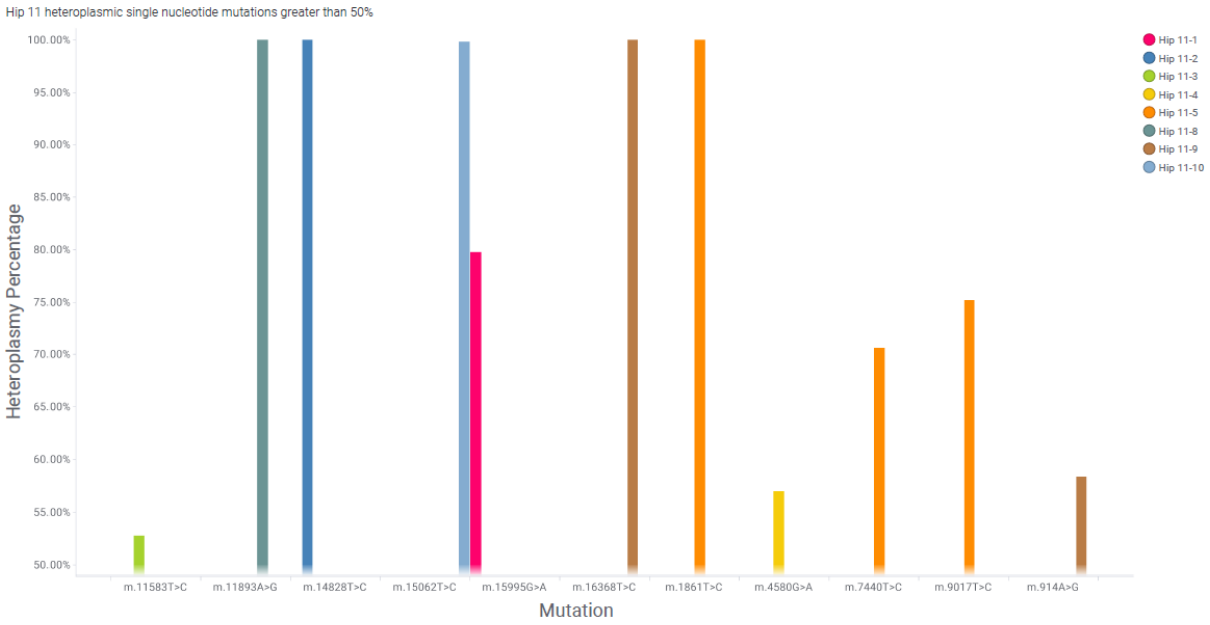

Figure 50 Hip 11 heteroplasmic single nucleotide mutations greater than 50% heteroplasmy.

- Cell 1 has 1 SNP: m.15995G>A (79.74%) this codes for tRNA proline gene with no documented pathological consequences or dbSNP reference.
- Cell 2 has 1 SNP: m.14828T>C (100%) this causes a non-synonymous change of the MT-CYB gene. With a change in amino acid from serine to proline. The associated SIFT score is deleterious low confidence (0), the Polyphen score is probably damaging (0.983). There is no dbSNP reference.
- Cell 3 has 1 SNP: m.11583T>C (52.79%) this cause a non-synonymous change of the MT-ND4 gene. With a change in amino acid from isoleucine to threonine. The associated SIFT score is deleterious low confidence (0.04), the Polyphen score is probably damaging (0.98). There is no dbSNP reference.
- Cell 4 has 1 SNP: m.4580G>A (57.02%) this causes a synonymous change of the MT-ND2 gene altering the codon atG/atA, the dbSNP reference is rs28357975.
- Cell 5 has 3 SNPs: m.1861T>C (100%), m.7440T>C (70.60%) and m.9017T>C (75.19%).

  - m.1861T>C is within the mitochondrial 16s ribosome gene, there is no dbSNP reference, there are no reported detrimental effects.
  - m.7440T>C causes a non-synonymous change of the MT-CO1 gene. With a change in amino acid from serine to proline. The associated SIFT score is tolerated low confidence (0.05), the Polyphen score is benign (0.03). There is no dbSNP reference.
  - m.9017T>C causes a non-synonymous change of the MT-ATP6 gene. With a change in amino acid from isoleucine to threonine. The associated SIFT score deleterious (0), the Polyphen score is probably damaging (0.98). There is no dbSNP reference.

- Cell 6 has no SNPs greater than 50%.
- Cell 7 has no SNPs greater than 50%.
- Cell 8 has 1 SNP: m.11893A>G (100%) this causes a synonymous change of the MT-ND4 gene altering the codon gaA/gaG, the dbSNP reference is rs878934321.
- Cell 9 has 2 SNPs: m.914A>G (58.33%) and m.16368T>C (100%).
  - m.914A>G is within the mitochondrial 12s ribosome gene, there is no dbSNP reference, there are no reported detrimental effects.
  - m.16368T>C this lies within the non-coding portion of the mitochondrial genome D-loop. The dbSNP reference for this mutation is rs1556424875.
- Cell 10 has 1 SNP: m.15062T>C (99.82%) this C causes a non-synonymous change of the MT-CYB gene. With a change in amino acid from serine to proline. The associated SIFT score is deleterious low confidence (0), the Polyphen score is probably damaging (0.998). There is no dbSNP reference.

Across the whole sample of MSCs cells, there were 56 non-synonymous mutations with SIFT or Polyphen scores. The heteroplasmy percentage of these samples aside from the above mutations varied from 41.25% to 1.06%. In total there were 133 mutations present across the sample.

3.7.11 Data for the patient "Hip 12"

Hip 12 samples were taken from a 78-year-old female undergoing a total hip replacement osteoarthritis. This was originally part of the pilot investigation and as a consequence more cells were analysed (19 plus consensus).

Coverage

Coverage across the sample varied considerably using the 500 times read depth threshold cells 6, 8, 10, 11, 14, 15, 18 and 19 all had poor coverage below 65%, in particular, cells 8, 10 and 11 were particularly poor. Areas of poor coverage were around 10000 to 13500 bp. Although some samples just ran low read depth globally reducing the read depth threshold improved coverage significantly if only a read depth of 1 was used the majority of samples were 92% coverage.

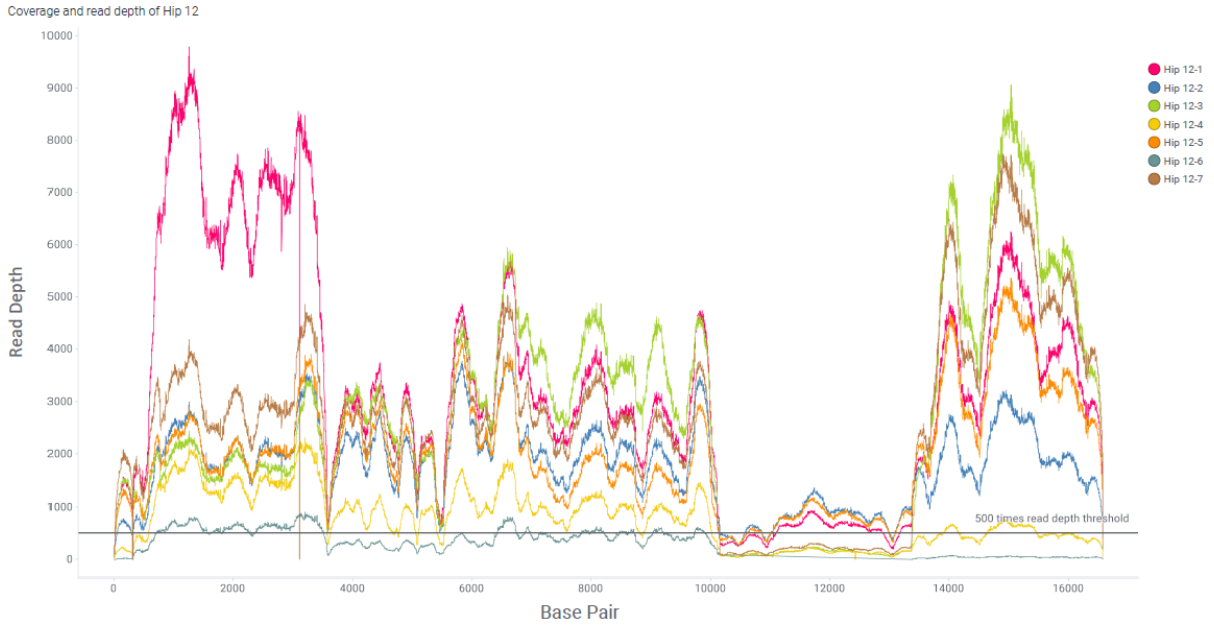

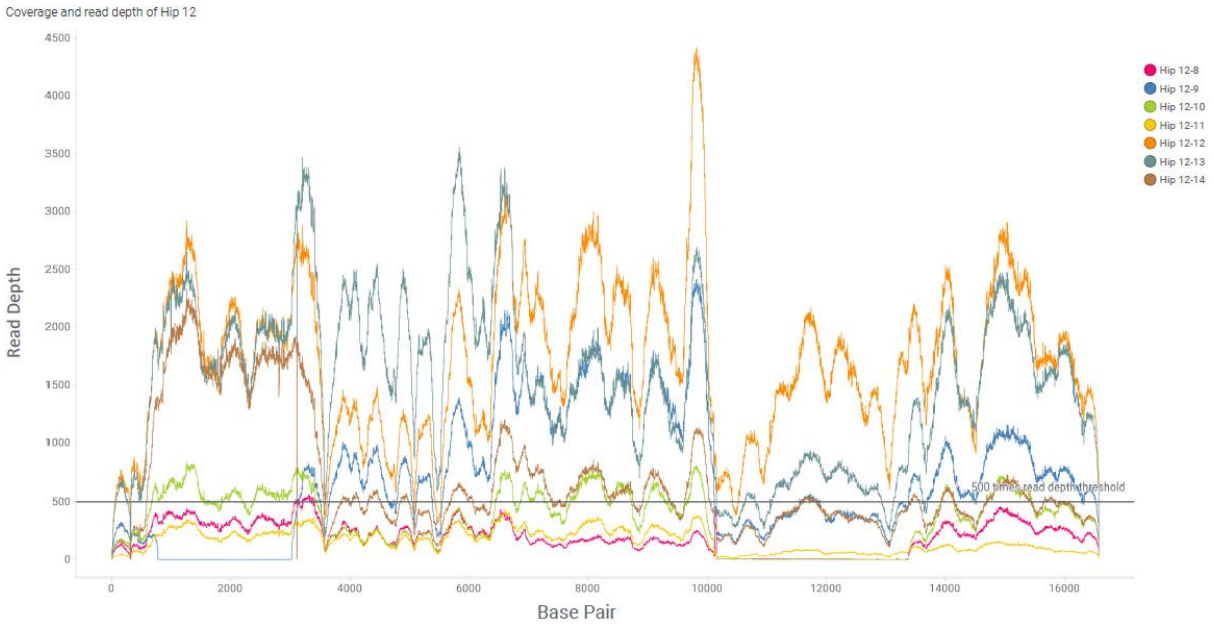

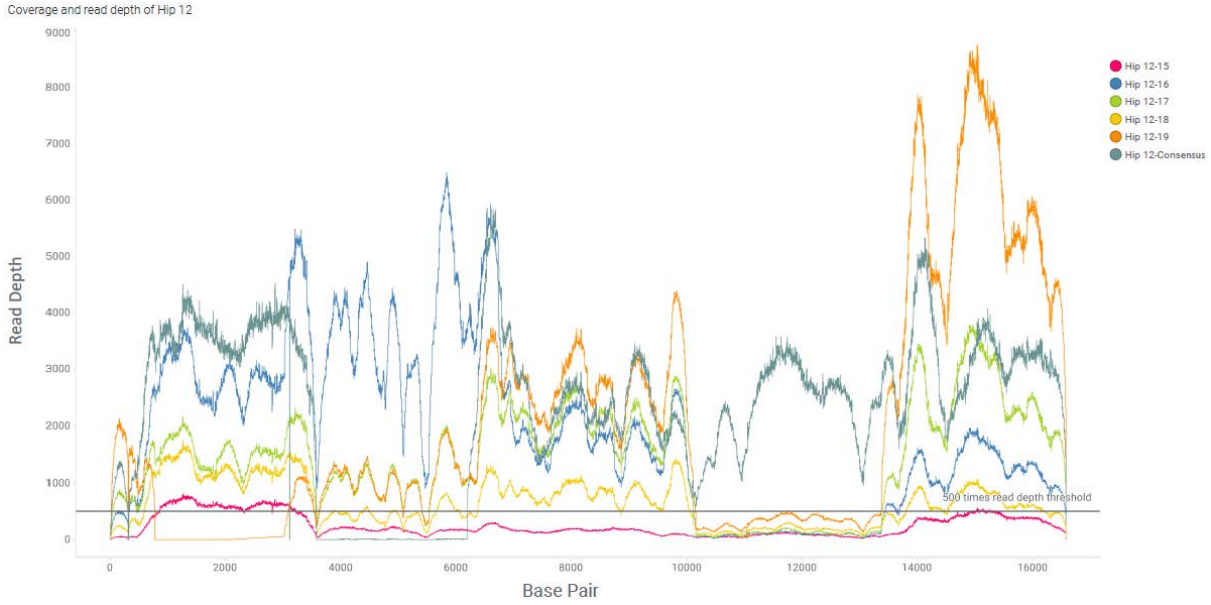

Figure 51 Coverage graphs for Hip 12 - read depth of each base and 500 read depth threshold demonstrated.

Haplogroup

All cells were haplogroup H, all but cell 11 (H) and 19 (H2a2) were H1 and all but cell 6 were H1a3a. Cell 6, 11 and 19 had low read depth and were missing the majority of haplomarkers, read depth of the haplomarkers was in tens rather than hundreds or thousands. 73G was missing almost universally but this was due to the process of duplicate eradication within the analysis pipeline.

Polymorphic variant specific to the patient

There were no polymorphic variants seen in Hip 12. Although there was a mutation of the MT-ND2 gene - m.4769A>G which was seen at essentially homoplasmic levels (1.66% - 8.15%) 13 of the cells. It was not seen in the consensus sequence. It was a synonymous change resulting in a codon change of atA/atG. The dbSNP reference is rs3021086.

Individual SNPs greater than 50% heteroplasmy

Mutations are presented in *Figure 52*

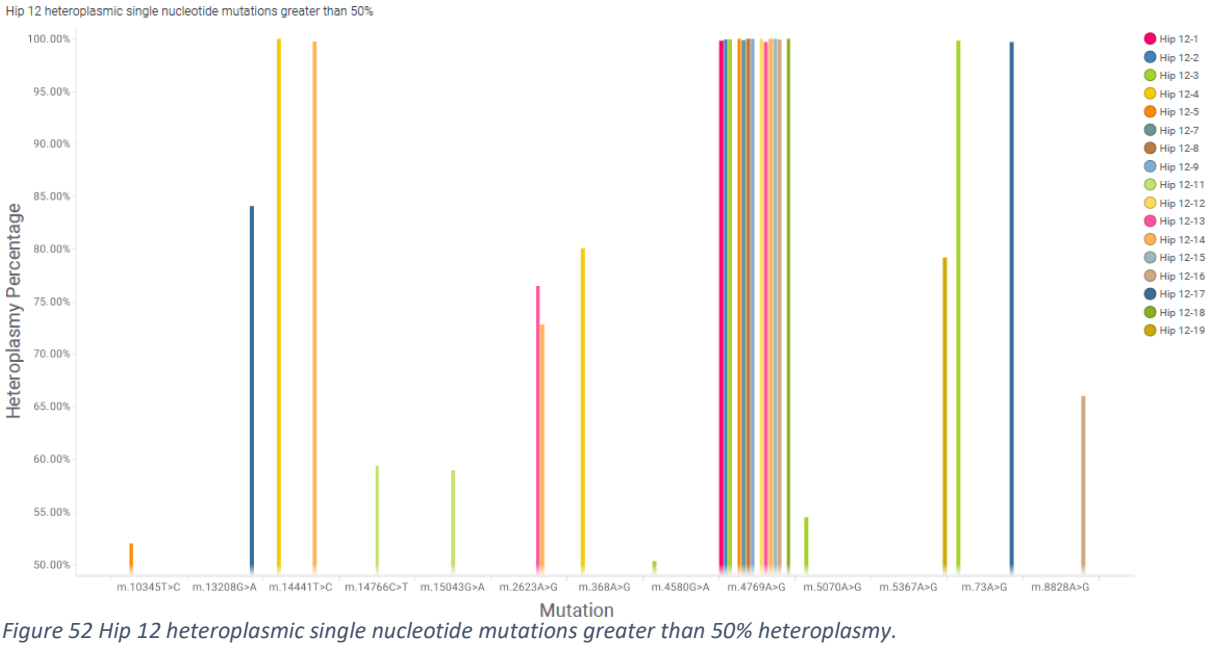

Figure 52 Hip 12 heteroplasmic single nucleotide mutations greater than 50% heteroplasmy.

- Cell 1 has 1 SNP: m.4769A>G (99.79%) this causes a synonymous change of the MT-ND2 gene altering the codon atA/atG, the dbSNP reference is rs3021086.
- Cell 2 has 1 SNP: m.4769A>G (99.91%) this causes a synonymous change of the MT-ND2 gene altering the codon atA/atG, the dbSNP reference is rs3021086.
- Cell 3 has 4 SNPs: m.73A>G (99.82%), m.4580G>A (50.34%), m.4769A>G (99.95%) and m.5070A>G (54.48%)
    - m.73A>G this lies within the non-coding portion of the mitochondrial genome D-Loop. The dbSNP reference for this mutation is rs869183622.
    - m.4580G>A this causes a synonymous change of the MT-ND2 gene altering the codon atG/atA, the dbSNP reference is rs28357975.
    - m.4769A>G this causes a synonymous change of the MT-ND2 gene altering the codon atA/atG, the dbSNP reference is rs3021086.
    - m.5070A>G this causes a non-synonymous change of the MT-ND2 gene. With a change in amino acid from threonine to alanine. The associated SIFT score is tolerated (0.09), the Polyphen score is benign (0.094). There is no dbSNP reference.
- Cell 4 has 2 SNPs: m.368A>G (80.05%) and m.14441T>C (100%)
    - m.368A>G this lies within the non-coding portion of the mitochondrial genome D-Loop. There is no dbSNP reference.
    - m.14441T>C this causes a non-synonymous change of the MT-ND6 gene. With a change in amino acid from tyrosine to cysteine. The associated SIFT score is

deleterious (0) the Polyphen score probably damaging (0.983) There is no dbSNP reference.

- Cell 5 has 2 SNPs: m.4769A>G (100%) and m.10345T>C (52.00%)
    - m.4769A>G this causes a synonymous change of the MT-ND2 gene altering the codon atA/atG, the dbSNP reference is rs3021086.
    - m.10345T>C this causes a non-synonymous change of the MT-ND3 gene. With a change in amino acid from isoleucine to threonine. The associated SIFT score is tolerated low confidence (0.09) the Polyphen score is benign (0.006). The dbSNP reference is rs201397417.
- Cell 6 has no SNPs greater than 50%.
- Cell 7 has 1 SNP: m.4769A>G (99.88%) this causes a synonymous change of the MT-ND2 gene altering the codon atA/atG, the dbSNP reference is rs3021086.
- Cell 8 has 1 SNP: m.4769A>G (100%) this causes a synonymous change of the MT-ND2 gene altering the codon atA/atG, the dbSNP reference is rs3021086.
- Cell 9 has one SNP: m.4769A>G (100%) this causes a synonymous change of the MT-ND2 gene altering the codon atA/atG, the dbSNP reference is rs3021086.
- Cell 10 has no SNPs greater than 50%.
- Cell 11 has 2 SNPs: m.14766C>T (59.31%) and m.15043G>A (58.87%).
    - m.14766C>T causes a non-synonymous change of the MT-CYB gene. With a change in amino acid from threonine to isoleucine. The associated SIFT score is deleterious low confidence (0.04) the Polyphen score is benign (0.003). The dbSNP reference is rs193302980
    - m.15043G>A causes a synonymous change of the MT-CYB gene altering the codon ggG/ggA, the dbSNP reference is rs3021086.
- Cell 12 has 1 SNP: m.4769A>G (100%) this causes a synonymous change of the MT-ND2 gene altering the codon atA/atG, the dbSNP reference is rs3021086.
- Cell 13 has 2 SNPs: m.2623A>G (76.43%) and m.4769A>G (99.70%).
    - m.2623A>G within the mitochondrial 16s ribosome gene. There are no detrimental effects documented and no dbSNP reference number.
    - m.4769A>G this causes a synonymous change of the MT-ND2 gene altering the codon atA/atG, the dbSNP reference is rs3021086.
- Cell 14 has 3 SNPs: m.2623A>G (72.76%), m.4769A>G (100%) and m.14441T>C (99.72%).

  - m.2623A>G within the mitochondrial 16s ribosome gene. There are no detrimental effects documented and no dbSNP reference number.

  - m.4769A>G this causes a synonymous change of the MT-ND2 gene altering the codon atA/atG, the dbSNP reference is rs3021086.

  - m.14441T>C causes a non-synonymous change of the MT-ND6 gene. With a change in amino acid from tyrosine to cysteine. The associated SIFT score is deleterious (0) the Polyphen score probably damaging (0.983) There is no dbSNP reference.

- Cell 15 has 1 SNP: m.4769A>G (100%) this causes a synonymous change of the MT-ND2 gene altering the codon atA/atG, the dbSNP reference is rs3021086.

- Cell 16 has 2 SNPs: m.4769A>G (99.91%) and m.8828A>G (65.97%).

  - m.4769A>G this causes a synonymous change of the MT-ND2 gene altering the codon atA/atG, the dbSNP reference is rs3021086.

  - m.8828A>G causes a non-synonymous change of the MT-ATP6 gene. With a change in amino acid from asparagine to serine. The associated SIFT score is deleterious (0.01) the Polyphen score probably damaging (0.988) There is no dbSNP reference.

- Cell 17 has 2 SNPs: m.73A>G (99.70%) and m.13208G>A (84.06%).

  - m.73A>G this lies within the non-coding portion of the mitochondrial genome D-Loop. The dbSNP reference for this mutation is rs869183622.

  - m.13208G>A causes a non-synonymous change of the MT-NT5 gene. With a change in amino acid from cysteine to tyrosine. The associated SIFT score is deleterious low confidence (0) the Polyphen score probably damaging (0.998) There is no dbSNP reference but there is a cosmic reference COSV99053427.

- Cell 18 has 1 SNP: m.4769A>G (100%) this causes a synonymous change of the MT-ND2 gene altering the codon atA/atG, the dbSNP reference is rs3021086.

- Cell 19 has 1 SNP: m.5367A>G (79.17%) this causes a non-synonymous change of the MT-ND2 gene. With a change in amino acid from threonine to alanine. The associated SIFT score is deleterious (0.02) the Polyphen score possibly damaging (0.448) There is no dbSNP reference.

Across the whole sample of MSCs cells, there were 132 non-synonymous mutations with SIFT or Polyphen scores. The heteroplasmy percentage of these samples aside from the above mutations varied from 49.60% to 1.00%. In total there were 395 mutations present across the sample of 19 MSC cells. m.4769A>G could be considered a polymorphic variant and was present in 13 of the 19 cells, with poor coverage most likely to account for the absence in the remaining cells.

3.7.12 Data for the patient "Hip 13"

Hip 13 samples were taken from a 25-year-old male who was undergoing a total hip replacement premature osteoarthritis due to a significant acetabular fracture sustained previously.

Coverage

Using the 500 times read depth threshold coverage varied between 54.48% to 82.25% except for the consensus sequence which had a read depth off 99.79%. Reducing the threshold to 250 times or 1-time improved coverage except in samples 1, 2, and 11 which had areas of drop off in comparison to the other cells. There were drops in read depth and coverage around the 10,000 to 16000 bp mark and also at the cross over of primer pairings 1 and 5 around 16569 to 750. This can be demonstrated in *Figure 53.*

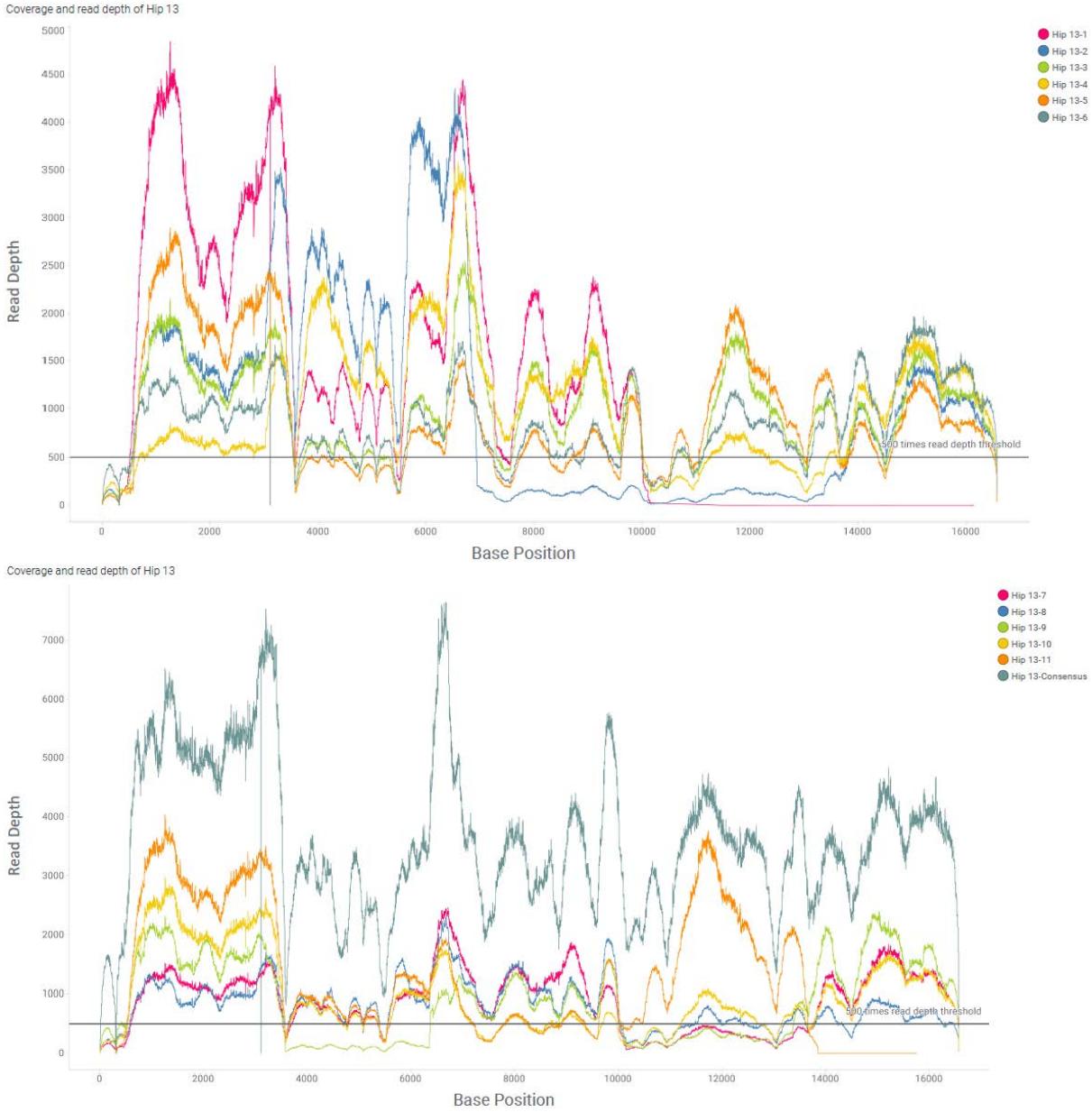

Figure 53 Coverage graphs for Hip 13 - read depth of each base and 500 read depth threshold demonstrated.

Haplogroup

All cells and the consensus sequence were H3g1b with a confidence of 0.5811 (low coverage in cell 11) or above. The only exception to this is cell 9 which was H2a2 and was missing 9 of the 12 haplogroup markers for H3g1b.

Polymorphic variant specific to the patient

There were no polymorphic variants seen in Hip 12.

Individual SNPs greater than 50% heteroplasmy

Mutations are presented in *Figure 54.*

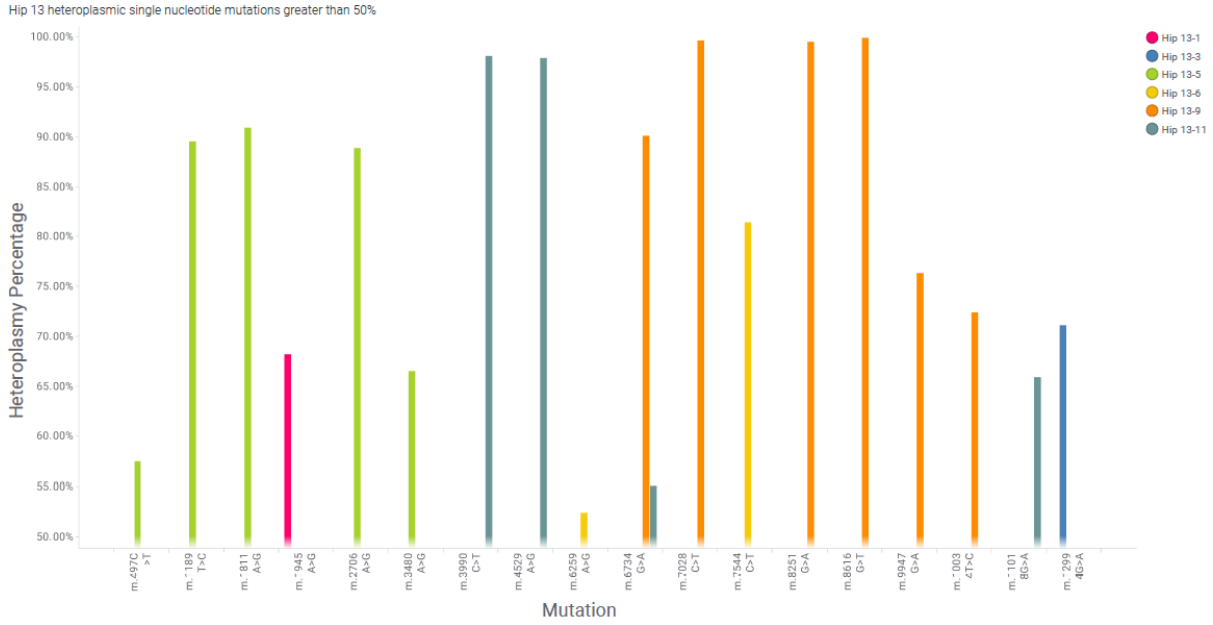

Figure 54 Hip 13 heteroplasmic single nucleotide mutations greater than 50% heteroplasmy.

- Cell 1 had 1 SNP: m.1945A>G (68.14%) lying within the mitochondrial 16s ribosome gene. There are no detrimental effects documented. The dbSNP reference is rs1556422585
- Cell 2 has no SNPs greater than 50%.
- Cell 3 has 1 SNP: m.12994G>A (71.05%), this causes a non-synonymous change of the MT-NT5 gene. With a change in amino acid from alanine to threonine. The associated SIFT score is deleterious low confidence (0) the Polyphen score probably damaging (0.998) There is no dbSNP reference.
- Cell 4 has no SNPs greater than 50%.
- Cell 5 has 5 SNPs: m.497C>T (57.47%), m.1189T>C (89.49%), m.1811A>G (90.90%), m.2706A>G (88.84%) and m.3480A>G (66.47%).
    - m.497C>T is part of the non-coding D-Loop hypervariable region and has no detrimental effects. The dbSNP reference is rs28660704
    - m.1189T>C affects RNR1 mitochondrial 12s ribosome gene with no documented deleterious effects. The dbSNP reference is rs28358571.

  - m.1811A>G and m.2706A>G lie within the mitochondrial 16s ribosome gene there is no pathological effects document. The dbSNP references are rs28358576 and rs2854128 respectively.

  - m.3480A>G causes a synonymous change of the MT-ND1 gene altering the codon aaA/aaG, the dbSNP reference rs28358584.

- Cell 6 has 2 SNPs: m.6259A>G (52.35%) and m.7544C>T (81.36%

  - m.6259A>G causes a non-synonymous change of the MT-CO1 gene. With a change in amino acid from glutamic acid to glycine. The associated SIFT score is deleterious low confidence (0.02) the Polyphen score probably damaging (0.996) There is no dbSNP reference.

  - m.7544C>T codes for tRNA aspartic acid and has no detrimental effects documented. There is no dbSNP reference.

- Cell 7 has no SNPs greater than 50%.

- Cell 8 has no SNPs greater than 50%.

- Cell 9 has 6 SNPs: m.6734G>A (90.03%), m.7028C>T (99.61%), m.8251G>A (99.50%), m.8616G>T (99.89%), m.9947G>A (76.32%), and m.10034T>C (72.35%).

  - m.6734G>A and m.7028C>T cause a synonymous change of the MT-CO1 gene altering the codons atG/aTA and ggC/gcT respectively. The dbSNP reference numbers are rs41413745 and rs2015062.

  - m.8251G>A causes a synonymous change of the MT-CO2 gene altering the codon ggG/ggA, the dbSNP reference rs3021089.

  - m.8616G>T causes a non-synonymous change of the MT-ATP6 gene. With a change in amino acid from leucine to phenylalanine. The associated SIFT score is tolerated (0.08) the Polyphen score probably damaging (0.997) The dbSNP reference is rs41427749.

  - m.9947G>A causes a synonymous change of the MT-CO3 gene altering the codon gtG/gtA, the dbSNP reference rs370688668.

  - m.10034T>C codes for tRNA glycine and has no detrimental effects documented. The dbSNP reference is rs41347846.

- Cell 10 has no SNPs greater than 50%.

- Cell 11 has 4 SNPs: m.3990C>T (98.03%), m.4529A>G (97.84%), m.6734G>A (55.08%) and m.11018G>A (65.83%).

  - m.3990C>T causes a synonymous change of the MT-ND1 gene altering the codon taC/taT, the dbSNP reference rs878853005.

- m.4529A>G causes a synonymous change of the MT-ND2 gene altering the codon acA/acG, there is no dbSNP reference.
- m.6734G>A causes a synonymous change of the MT-CO1 gene altering the codon atG/atA, the dbSNP reference rs41413745.
- m.11018G>A causes a non-synonymous change of the MT-ATP6 gene. With a change in amino acid from glutamic acid to lysine. The associated SIFT score is deleterious low confidence (0.01) the Polyphen score probably damaging (0.988) The is no dbSNP reference.

Across the whole sample of MSCs cells, there were 71 non-synonymous mutations with SIFT or Polyphen scores. The heteroplasmy percentage of these samples aside from the above mutations varied from 39.58% to 1.06%. In total there were 193 mutations present across the sample of 11 MSC cells.

3.7.13 Data for the patient "Femur 1"

Femur 1 samples were taken from a 22-year-old male having an intramedullary nailing procedure to address a leg length discrepancy.

Coverage

Using the 500 times read depth threshold coverage varied between 51.58% to 83.49% except for the consensus sequence which had a read depth off 99.84%. Reducing the threshold to 250 times improved coverage. There were drops in read depth and coverage around the 3500 to 6500 and also 10,000 to 14000 bp mark and also at the cross over of primer pairings 1 and 5 around 16569 to 750. Cell 4 and 10 also had dropped or low coverage around 7500 and 9500 bp. This is demonstrated in *Figure 55.*

Figure 55 Coverage graphs for Femur 1 - read depth of each base and 500 read depth threshold demonstrated.

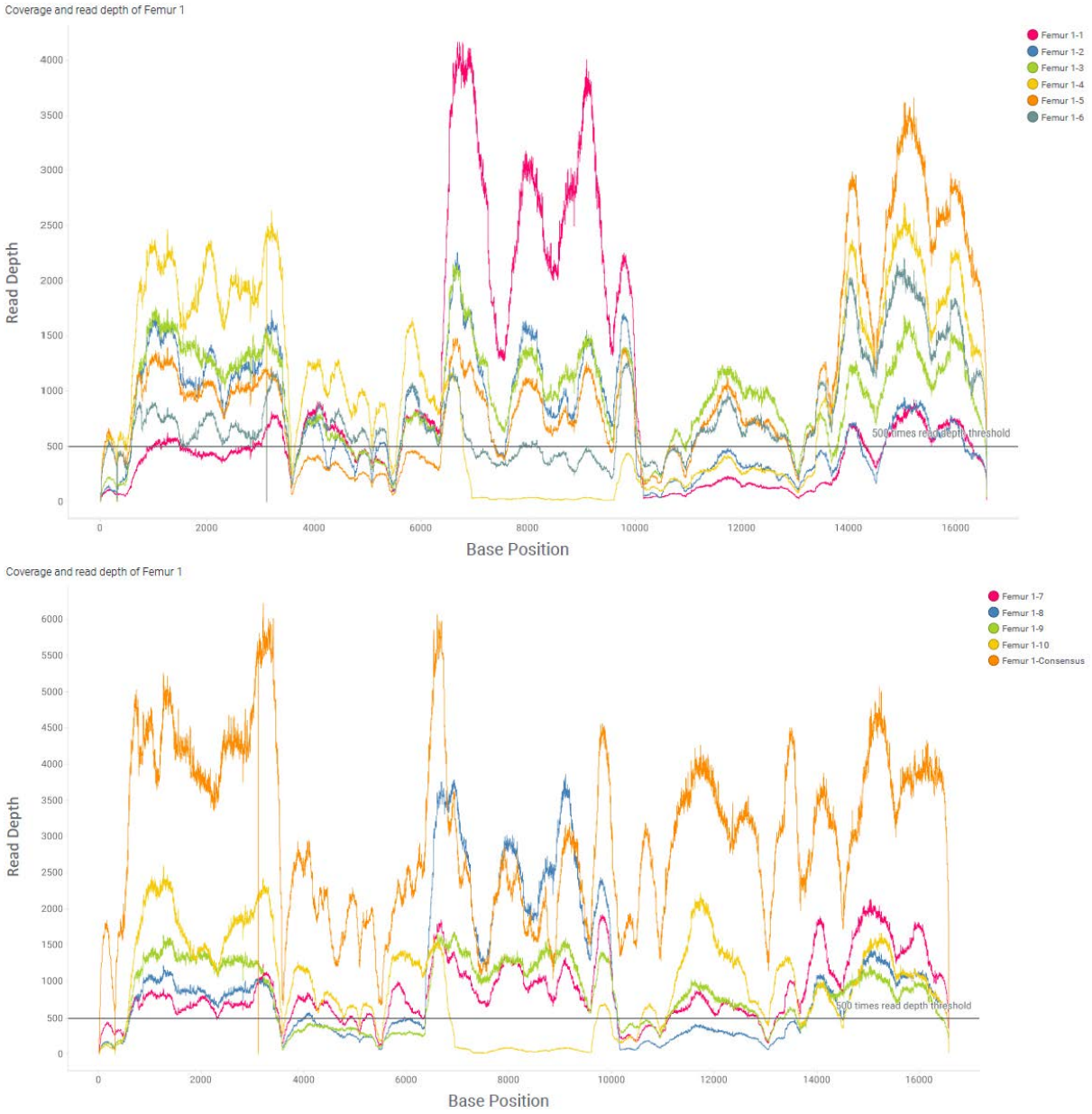

Haplogroup

All cells and the consensus sequence were H2a1 with confidence of 0.7252 or greater. There was a further delineation of all but cells 10 and 4 (low coverage) to the haplogroup H2a1g the confidence of this was 0.6865 in cell 2 to 1 in the consensus. 750G was missing in all but the consensus sequence.

Polymorphic variant specific to the patient

There were no polymorphic variants seen in Femur 1.

Individual SNPs greater than 50% heteroplasmy

Mutations are presented in *Figure 56.*

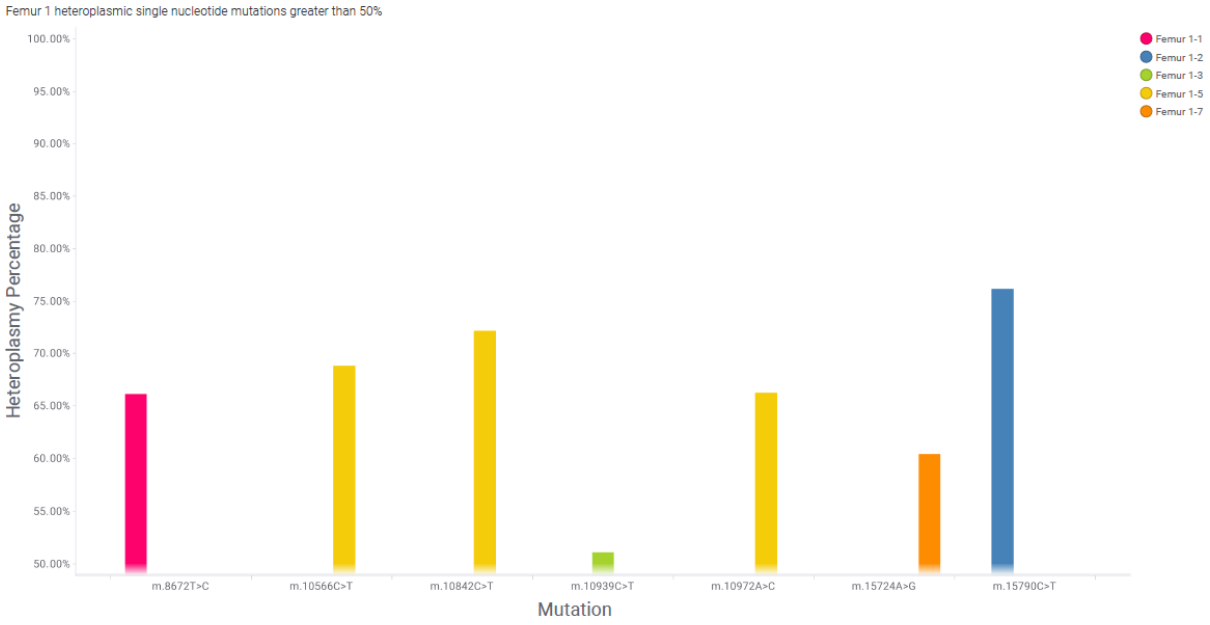

Figure 56 Femur 1 heteroplasmic single nucleotide mutations greater than 50% heteroplasmy.

- Cell 1 had 1 SNP: m.8672T>C (66.10%) this causes a non-synonymous change of the MT-ATP6 gene. With a change in amino acid from leucine to proline. The associated SIFT score is deleterious (0) the Polyphen score probably damaging (0.998) There is no dbSNP reference.
- Cell 2 has 1 SNP: m.15790C>T (76.11%) this causes a synonymous change of the MT-CYB gene altering the codon aaC/aaT, the dbSNP reference rs879063269.
- Cell 3 has 1 SNP: m.10939C>T (51.08%) this causes a synonymous change of the MT-ND4 gene altering the codon ccC/ccT, there is no dbSNP reference.
- Cell 4 has no SNPs greater than 50%.
- Cell 5 has 3 SNPs: m.10566C>T (68.80%), m.10842C>T (72.12%) and m.10972A>C (66.20%).
    - m.10566C>T causes a synonymous change of the MT-ND4L gene altering the codon Cta/Tta, there is no dbSNP reference.
    - m.10842C>T causes a non-synonymous change of the MT-ND4 gene. With a change in amino acid from threonine to isoleucine. The associated SIFT score is deleterious

low confidence (0.02) the Polyphen score probably damaging (0.997) There is no dbSNP reference.

    - m.10972A>C causes a non-synonymous change of the MT-ND4 gene. With a change in amino acid from tryptophan to cysteine. The associated SIFT score is deleterious low confidence (0) the Polyphen score probably damaging (0.997) There is no dbSNP reference.

- Cell 6 has no SNPs greater than 50%.
- Cell 7 has 1 SNP: m.15724A>G (60.33%) this causes a synonymous change of the MT-CYB gene altering the codon tgA/tgG, there is no dbSNP reference.
- Cell 8 has no SNPs greater than 50%.
- Cell 9 has no SNPs greater than 50%.
- Cell 10 has no SNPs greater than 50%.

Across the whole sample of MSCs cells, there were 57 non-synonymous mutations with SIFT or Polyphen scores. The heteroplasmy percentage of these samples aside from the above mutations varied from 47,34% to 1.26%. In total there were 144 mutations present across the sample of 10 MSC cells.

Table 18 Primers for PCR amplification of the mitochondrial genome. Numbering based on Anderson et al. Sequence and organization of the human mitochondrial genome (220). and Andrews et al. Reanalysis and revision of the Cambridge reference sequence for human mitochondrial DNA (221) These primers are published in Tuppen et al Brain 2010, 133(10): 2952 (222).

Primer pair	Primer location in the mitochondrial genome		Amplicon size (bp)
	Forward primer	Reverse primer	
1	721 - 740	1268 - 1248	548
2	1157 - 1177	1709 - 1689	553
3	1650 - 1671	2193 - 2175	544
4	2091 - 2111	2644 - 2625	536
5	2549 - 2569	3087 - 3068	539
6	3017 - 3036	3574 - 3556	558
7	3505 - 3524	4057 - 4037	553
8	3965 - 3984	4577 - 4556	613
9	4518 - 4537	5003 - 4983	486
10	4932 - 4952	5481 - 5462	550
11	5367 - 5386	5924 - 5906	558
12	5855 - 5875	6430 - 6410	576
13	6358 - 6377	6944 - 6924	587
14	6863 - 6882	7396 - 7376	534
15	7272 - 7293	7791 - 7773	520
16	7713 - 7723	8301 - 8283	589
17	8196 - 8215	8740 - 8720	545
18	8656 - 8676	9201 - 9183	546
19	9127 - 9146	9661 - 9641	535
20	9607 - 9627	10147 - 10128	541
21	10085 - 10104	10649 - 10629	565
22	10534 - 10553	11109 - 11089	576
23	11010 - 11030	11605 - 11586	596
24	11541 - 11561	12054 - 12034	514
25	11977 - 11997	12545 - 12527	569
26	12478 - 12498	13009 - 12991	532
27	12940 - 12959	13453 - 13435	514
28	13365 - 13383	13859 - 13839	495
29	13790 - 13809	14374 - 14356	585
30	14317 - 14341	14857 - 14838	540
31	14797 - 14815	15368 - 15349	572
32	15295 - 15315	15896 - 15877	602
D1	15758 - 15777	019 - 001	831
D2	16223 - 16244	129 - 110	476
D3	16548 - 16569	389 - 370	412
D4	323 - 343	771 - 752	449

Chapter 4 - High throughput screening to identify mitochondrial respiratory chain protein deficiencies.

4.1 Introduction

The development of high throughput and high content screen using flow cytometry to measure protein deficiencies within the respiratory chain of mesenchymal stem cells' mitochondria has not yet been reported in the literature.

The use of flow cytometry in high content screening allows a quantitative platform for the measurement of fluorescence and as a consequence high content characterisation of drug compound effects upon single cells. Gasparetto et al., first described high content flow cytometry in 2004 (295). Gasparetto et al., investigated the augmentation of anti-lymphoma activity of rituximab. Flow cytometry use has perhaps been limited due to the difficult task in preparing patient samples compared to cultured cell lines which can be grown on plates quickly and easily. The time efficiency in comparison to conventional high content screens utilising flow cytometry has limited its use. Typically it has been used more in small scale research (296). However, there have been recent advances utilising flow cytometry with autosamplers and peristaltic pumps such as the Hypercyt (297), Intellicyt and IQue Screener that allow high throughput screening using flow cytometry (298-300). The BD Symphony system at the Flow Cytometry Facility, Newcastle University also allows such screening to take place on a smaller scale and is equipped with a plate autosampler.

Flow cytometry had been utilised in the PCR chapters and also initially as a method of extracting MSC cells for culture. This led to the question could flow cytometry be used as a method to provide rapid instant analysis of mitochondrial protein deficiencies over a large number of cells.
There have been a number of previous methods utilised to detect mitochondrial protein deficiencies in situ as opposed to homogenised tissue. Analysis of deficiency still remains difficult due to the varying heteroplasmy levels seen within individual cells and across the tissue. Previous methods include the use of COX – cytochrome c oxidase and SDH – succinate dehydrogenase histochemistry which analysed complex II and IV deficiencies. This was performed on human muscle fibres and this proved a significant assay to demonstrate deficiency however only 100 fibres per patient were analysed (301). Could flow cytometry provide a method to analyse cell numbers in the thousands?

More recently quadruple immunofluorescence has been used to look at protein deficiencies across complex I and complex IV of the respiratory chain. Previously there was no validated histochemistry

based assay to look at complex I deficiencies which are frequently involved in mitochondrial pathology (235). The method devised by Rocha et al., utilised immunofluorescent labelled antibodies to analyse mitochondrial protein deficiencies using confocal microscopy, again in this study only 100 myofibers per patient (235), were analysed.

This assay has been further adapted by Dobson et al., (205). Here the PolgA^{mut}/PolgA^{mut} mouse model mouse was used to investigate the role of mitochondrial mutations on osteoporosis this again relied upon immunofluorescence and confocal microscopy and analysed 100 cells per sample.
Current analysis techniques within the Wellcome Centre for Mitochondrial Research for analysing tissue in situ without disruption of the architecture are based largely on the COX/SDH assay and quadruple immunofluorescent assay, they are time consuming in preparation and analysis. The use of flow cytometry would combine the equivalent of the acquisition and measurement steps of these assays in to one single streamlined process. It would also allow the analysis of single cells in suspension as opposed to the above techniques which are tissue based.

High throughput screens are typically used by the pharmaceutical industry in drug discovery allowing rapid analysis of cells and conducting multiple experiments and measurement parameters (302). The results of experiments lead to rapid feedback and influence upon drug design and testing. Typically, they take place on cells within plates. High throughput screens are often combined with high content screening in the form of fluorescent microscopy or flow cytometry (303).

High content screening is defined as the automation of high-content cell biological investigation of arrayed cells (304). It can take over multiple steps in an experiment including sample preparation, image acquisition, archiving, processing and analysis.

The assays of Dobson and Rocha using confocal light microscopy techniques are restricted to small scale studies in terms of cell numbers however these small-scale techniques play a crucial role in planning a high content assay. Flow cytometry in contrast to these assays or a homogenised tissue assay would allow the analysis of a high volume of single cells in a short amount of time. It would give instant analysis by way of measuring the individual fluorescent profile of each cell similar to that of using confocal microscopy in the quadruple immunofluorescence assays of Rocha and Dobson (205, 235) but not confined by the same time restrictions or potential autofluorescence of extracellular matrix and proteins.

High throughput assays have been utilised previously on a number of occasions using a range of techniques to look at mitochondrial characteristics before. Huang et al., (305) used a high throughput assay based upon fluorescence to track mitochondrial membrane potential in the development of an assay which could be used in drug screening.

Maitra et al., developed a high throughput sequencing microarray for mitochondrial mutation detection using PCR and looking at detecting mitochondrial mutations in patients with pancreatic and bladder cancer (306).

4.1.1 Accumulation of respiratory chain protein deficiencies

Human mitochondrial DNA has a mutation rate of 10-20 times that of the nuclear DNA most likely due to failures of the proofreading mechanisms (307). The genome encodes two ribosomal RNAs, 22 transfer RNAs for protein synthesis, and the 13 polypeptides(155). Mutations can directly affect the subunits of the respiratory chain proteins coded for by mtDNA or if the rRNA or tRNA acquire mutations these can also have an effect. Subunits and proteins from the nuclear-encoded genome can also generate mutations and collectively with the mtDNA mutations the disorders characterised by these mutations are known as mitochondrial encephalomyopathies due to the common involvement of the brain and skeletal muscle, the prevalence of these related disorders is around 10-15 per 100,000. (161).

Direct mutations affecting the complex I and rarely complex II proteins have been linked to a number of disorders such as Leigh's syndrome (308-310). Defects in complex III and IV have been related to mutations affecting ancillary proteins (311, 312). Complex III mutations have been linked to poor exercise tolerance and also effecting the activity of complex I in human studies (313, 314). Complex IV mutations in the 3 genes encode by mtDNA (MTCO1, MTCO2, MTCO3) have been associated with symptoms ranging from muscle cramps (315) to exercise intolerance, lactic acidosis, proximal myopathy and encephalopathy (316). MtDNA mutations affecting complex IV have also been associated with neurological effects including epilepsy, hearing loss, ataxia and mental retardation (317, 318). Complex V has two mitochondrial encoded proteins; ATPase 6 and ATPase 8. Mutations associated with the *MTATP6* gene have been associated with neurological complications including neuropathy, ataxia and retinitis pigmentosa, it can also cause Leigh syndrome and has a cardiac phenotype . Mutations in the *MTATP8,* the gene for ATPase 8 have been linked to cardiac hypertrophy and neurological sequalae (319).

Deficiencies in the proteins of the electron transport chain have been demonstrated using a number of techniques as discussed above and have been shown to be acquired with age due to clonal expansion in colonic crypts by the approximate age of 30 (19, 320). As well as other tissue types including cardiomyocytes (184), skeletal muscle(321) and various neuronal cell types (322, 323) and the liver (324). Although so far accumulation of mutations and respiratory chain dysfunction in bone has only been demonstrated in mouse models (205).

4.2 Aims of this investigation

This work aimed to assess levels of respiratory chain protein deficiency in particular that of complex I and Complex IV in mesenchymal stem cells and cells of an osteoblast lineage using a high throughput or high content screening method.

4.3 Methods: Development of a high throughput assay for assessing mitochondrial protein deficiencies.

4.3.1 Patient Cohort.

The majority of the patient cohort as in chapter 2 was used for the final experiment in some cases there was not enough marrow for both sequencing and high throughput work. Immortalised fibroblast (Wild-type and Complex I deficient) (325) and K562 cell lines (326) were also used along with a paediatric control cell line derived from a patient undergoing anterior cruciate ligament reconstruction (ACL 2) and from a 25-year-old patient (Hip 13). See *Table 19* for individual patient details.

Sample	Age	Sex	Surgery	Indication	Co-morbidities
Hip 1	53	f	Total hip replacement	Osteoarthritis	hypertension
Hip 2	84	f	Total hip replacement	Osteoarthritis	ischaemic heart disease, type II diabetes Mellitus, asthma, hypertension, peripheral neuropathy, venothromboembolism, vitamin D deficiency, B12 and folate deficiency
Hip 3	88	f	Total hip replacement	Osteoarthritis	type II diabetes mellitus, chronic kidney disease, atrial fibrillation, diverticular disease, hypertension
Hip 5	66	f	Total hip replacement	Osteoarthritis	hypothyroid, raised cholesterol, hypertension,
Hip 6	45	f	Total hip replacement	Osteoarthritis	
Hip 7	82	m	Total hip replacement	Osteoarthritis	chronic obstructive pulmonary disease, gastro-oesophageal reflux disease, iron-deficient anaemia
Hip 8	74	f	Total hip replacement	Osteoarthritis	atrial fibrillation, pulmonary hypertension, iron-deficient anaemia
Hip 9	64	m	Total hip replacement	Osteoarthritis	chronic kidney disease, type II diabetes mellitus
Hip 10	62	m	Total hip replacement	Osteoarthritis	type II diabetes mellitus, hypertension
Hip 11	61	f	Total hip replacement	Osteoarthritis	hypertension
Hip 13	25	m	Total hip replacement	Post-traumatic acetabular fracture non-union	
Hip 14	72	f	Hip hemiarthroplasty	Trauma – fractured neck of the femur	chronic kidney disease, type II diabetes mellitus, hypertension, hypothyroidism, vitamin D deficiency
Femur 1	22	m	Intramedullary nail and bone graft	Leg length discrepancy after trauma	
ACL 2	15	m	Anterior cruciate ligament reconstruction	Anterior cruciate ligament deficiency	

Table 19 Demographics and details of patients' whose samples were used in the high throughput assay.

4.3.2 Flow cytometry assay; preliminary methods development and results.

A flow cytometer allows the measurement of the physical parameters of cells in terms of size measured by forward scatter and granularity measured by side scatter. It is also possible to measure and detect the surface markers and constituent content of the cells using fluorescently labelled antibodies (226). Furthermore, flow cytometry is the analysis of single cells in suspension. Analysing the cellular component of bone marrow in suspension, in particular mesenchymal stem cells, would potentially remove the issues encountered with auto-fluorescence when imaging osteoblasts in situ further details of this can be found in Chapter 5.3.3. It would also allow a much larger number of cells to be analysed. Mesenchymal stem cells are the precursor cells to pre osteoblast and subsequent osteoblasts they are located within the bone marrow and are available to collect routinely from bone marrow samples and aspirates. Any mitochondrial protein deficiencies seen in MSCs have the potential to translate into osteoblasts and would be compared to the sequencing data of Chapter 4 and osteoblast protein deficiency data in Chapter 5 using cytometry by time of flight.

Initially, the permeabilisation and staining protocol developed by Filby et al., (236) was utilised. Development of the protocol then followed, all steps were based upon this protocol until alteration as detailed.

4.3.2.1 Antibody selection

The aim of this investigation was to replicate the results of Rocha et al., and Dobson et al., using confocal microscopy. Regarding this as a starting point antibodies were selected to target mitochondrial mass, complex I and complex IV measurement. TOM20 was initially used as an alternative to VDAC.

TOM20 is a component of the TOM complex (translocases of the outer mitochondrial membrane) the TOM complex works in synergy with the TIM complexes (translocases of the inner mitochondrial membrane. The TOM complex has multiple functions including the recognition of mitochondrial targeting signals and acceptance of mitochondrial proteins. The TOM complex allows the passage of mitochondrial proteins across the hydrophobic outer mitochondrial membrane. TOM20, TOM37, TOM70, and TOM72 are redundant receptor proteins whereas TOM40 and TOM22 make up the protein-conducting channel (327). Due to initial antibody pairings in terms of conjugations and secondaries TOM20 was selected over VDAC.

VDAC or the voltage-dependent anion channel controls the passage of adenine nucleotides, Ca^{2+} and other metabolites in and out of the mitochondria. It is predominantly located on the outer mitochondrial membrane (328). $VDAC_1$ is the most abundant protein on mitochondrial outer membrane. There are also 2 other isoforms $VDAC_2$ and $VDAC_3$ (329).

TFAM (mitochondrial transcription factor A) has a role in stabilising the mitochondrial DNA through nucleoid formation and regulates the mitochondrial DNA copy number. Overexpression of TFAM leads to increased levels of mitochondrial DNA(330). One thousand TFAM proteins are present for each mtDNA molecule ad it has been associated and correlated with mtDNA copy number and mitochondrial function (331).

NDUFB8 (NADH dehydrogenase [ubiquinone] 1 beta subcomplex subunit 8) is part of the 1 beta subcomplex which makes up complex I. It has been used as an antibody target by Rocha et al.,(235). It is located on the inner mitochondrial membrane and coded for by chromosome 10 (332).

MTCO1 or cytochrome c oxidase subunit 1 (COX I) and MTCO2 or cytochrome c oxidase subunit 2 (COX II) are a components of complex IV and are encoded by mitochondrial DNA (161).
They are located on the inner mitochondrial membrane and functions as part of complex IV concerned with the transfer of electrons from cytochrome c to a dioxygen molecule converting this molecule to water and leading to the transfer of a further four protons across the mitochondrial membrane prior to the conversion of ADP to ATP and Complex V (159).

4.3.2.1.2 Antibodies and antibody conjugation

As this assay was designed to replicate the equivalent of the quadruple immunofluorescent microscopy the selection of antibodies is highlighted in 4.3.2.1 Antibody selection. To reduce the time period of the protocol and ease of the protocol conjugated antibodies were used as in *Table 20*. Although the quadruple immunofluorescent assay uses mouse monoclonal antibodies some of the conjugated antibodies were rabbit monoclonals.

Antibody	Code	Conc - mg/ml	Vol	Fluorescent molecule	Species and type
NDUFB8	ab192878	0.292	100ul	Not available	RabMab IgG
ISO Rabbit - IgG	ab172730	1.646	200ug		RabMab IgG
APC/Cy7 Conjugation Kit	ab102859				
TOM20	ab210665	0.5	100ul	594	RabMab IgG
MTCO2	ab200525	0.5	100ul	647	RabMab IgG
ISO Rabbit - IgG 647	ab199093	0.5	100ul	647	RabMab IgG
TFAM IgG2b	ab198308	0.5	100ul	488	MsMab IgG2b
Mouse IgG2b K Iso Control	53-4732-80 ebioscience	0.5	50	488	MsMab IgG2b

Table 20 Antibody summary table: RabMab – Rabbit monoclonal antibodies, MsMab – mouse monoclonal antibodies.

The NDUFB8 antibody supplied by Abcam did not have a fluorescent molecule attached and therefore had to be conjugated. A rabbit IgG was also used as an isotype control for the NDUFB8, further isotype fluorescent antibodies were used for controls and measurement of background non-specific binding.

The NDUFB8 and rabbit isotype were conjugated using the APC/Cy7 conjugation kit from Abcam (333). First, a modifier is added to the NDUFB8 or isotype antibody (1µl per 10µl). This mixture is then used to resuspend the lyophilised fluorescent material and incubated for 30 minutes minimum at room temperature in the dark. A quencher is then added after 3 hours again at a ratio of 1µl per 10µl of antibody. The conjugated antibody can then be stored in the fridge. A graphical representation of this is seen in *Figure 57.*

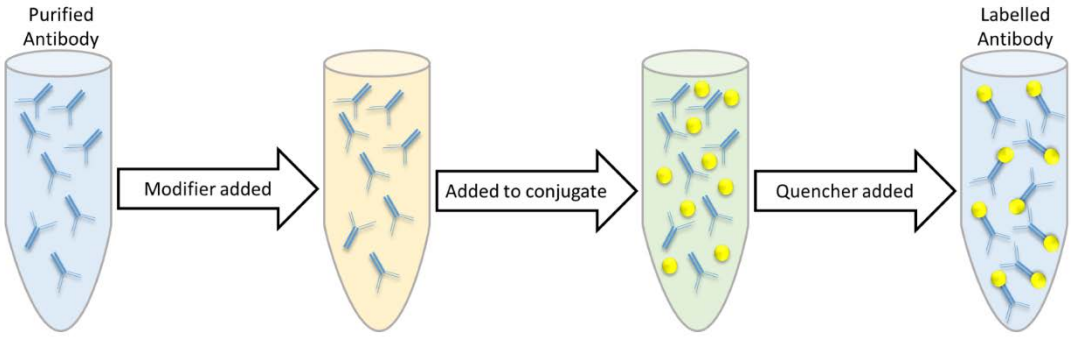

Figure 57 Cartoon representation of the antibody conjugation process with a fluorescent label (yellow circle) (333).

4.3.2.2 Fixation trials

4.3.2.2.1 Fixative

First fixation methods were checked to determine which fixation agent and the time frame were best to retain cell morphology. Different brands of paraformaldehyde were used; paraformaldehyde solution 4% in PBS (ChemCruz sc-281692), 16% formaldehyde solution (Thermo 28908) and 16% formaldehyde solution (TAAB laboratories F017/3). The 16% solutions were diluted to 4% with PBS. Fixation was then checked on K562 cell lines in comparison to live cells using the BD Accuri™ C6 Plus flow cytometer. Triton X-100 was added after fixation and fixation was checked again at 1 minute and 5 minutes for any change in cell morphology.

4.3.2.2.2 Fixation Results

Fixation results are shown in *Figure 58;* in the live cells graph the forward scatter (FSC-A: a measure of size) and the side scatter (SSC-A a measure of granularity) show a clear population circled within the red dashed area. This population is maintained in the populations fixed using Thermo, ChemCruz and TAAB PFA. It also is maintained after the addition of a detergent Triton X-100. This causes lysis of the cell membrane and where the cells were not fixed as in the live cell graph. Cell apoptosis is seen by the increased in small and granular components on the graph. In the fixed cells the populations remain relatively stable with the comparable morphology in terms of forward and side scatter profiles. Those cells fixed with TAAB PFA retained their profile to a greater degree than those fixed with the Thermo and ChemCruz products. Diluted TAAB PFA in PBS was used at a concentration of 4% in the development of a protocol for mitochondrial protein staining and flow cytometry.

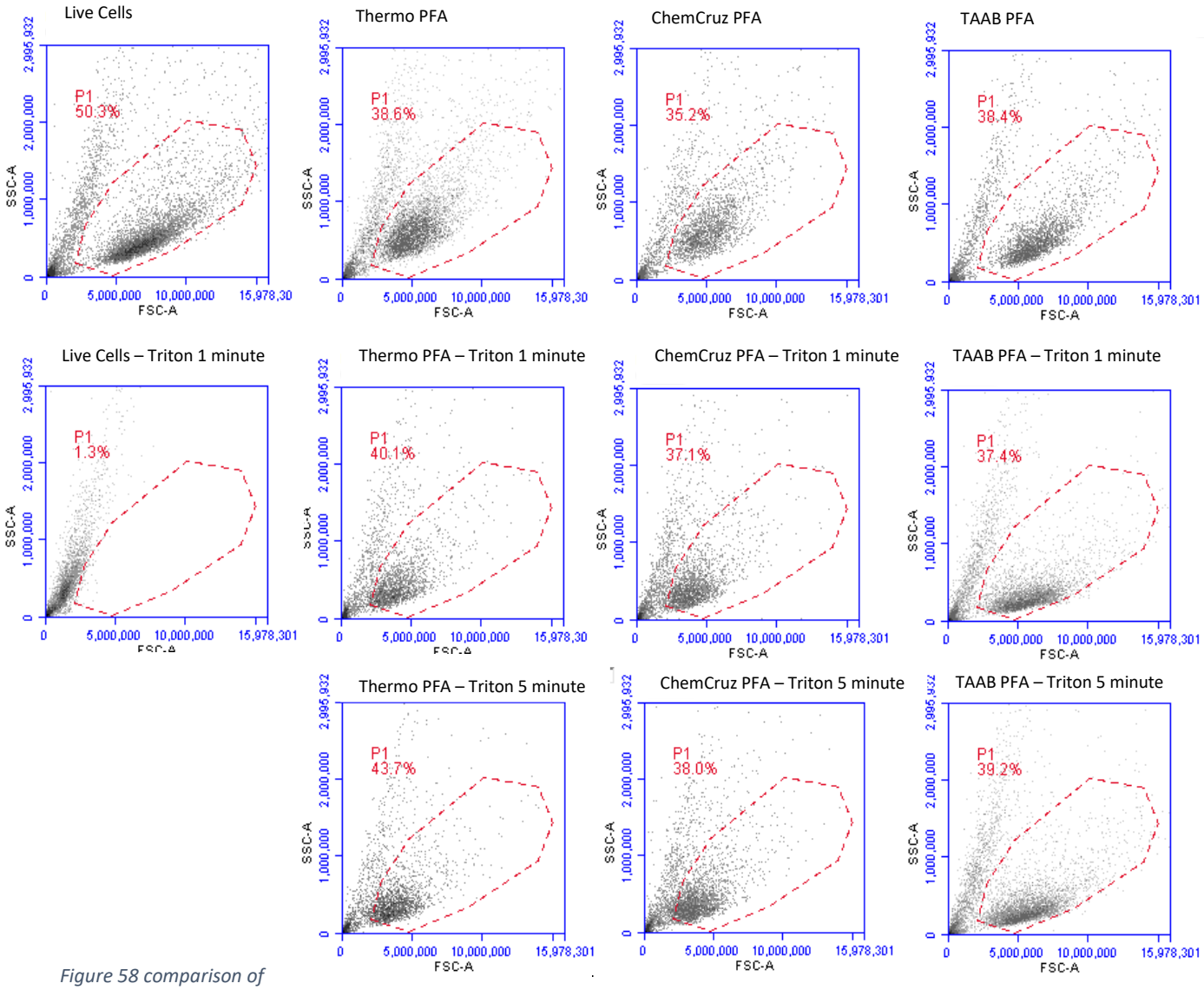

Figure 58 comparison of fixation buffers using K562 cell line as a control population. K562 cell line shown from left to right in PBS, Thermo PFA 4%, ChemCruz PFA 4% and TAAB PFA 4%. The TOP ROW compares FSC and SSC cellular profile before the addition of the permeabilisation agent Triton X-100. The MIDDLE ROW shows the cellular profile after 1 minute of exposure to Triton X-100 and the BOTTOM ROW shows the profile after 5 minutes of Triton X-100 exposure.

4.3.2.2.3 Fixation Time

Fixation time was also checked; 20 minutes, 40 minutes and 60 minutes fixation times were checked using TAAB PFA solution. Fluorescent intensity was then measured using the MTCO2 antibody and Isotype control conjugated to an Alexa 647 fluorophore from Abcam (ab200525). The results in Table 21 show that increasing fixation time had a positive effect on improving the levels of true antibody (MTCO2) binding and signal compared to the non-specific binding of the isotype. Moving forward cells were fixed for 1 hour using TAAB 4% PFA solution on an agitating thermomixer to ensure adequate mixing for 1 hour at room temperature. This correlates with a protocol optimised by Filby et al., (236) which also used fixation times of one hour at room temperature. High levels of non-specific binding were seen across the fixation trials however further development of the protocol would aim to address this.

		Antibody Concentration								
		1:50	1:100	1:200	1:400	1:800	1:1600	1:3200	1:6400	Average factor difference
20-minute fixation	MTCO2 antibody	5213.00	3123.17	1714.88	1092.95	696.14	484.36	400.58	268.37	
	Isotype antibody	6301.00	3865.94	2109.12	1358.58	1558.67	464.18	673.06	362.75	
	Factor MTCO2 vs Isotype control	0.83	0.81	0.81	0.80	0.45	1.04	0.60	0.74	0.76
40-minute fixation	MTCO2 antibody	4752.00	3634.48	2049.33	1369.56	818.01	570.95	569.31	277.60	
	Isotype antibody	6569.00	3950.03	1751.50	1286.81	890.03	665.79	517.15	343.25	
	Factor MTCO2 vs Isotype control	0.72	0.92	1.17	1.06	0.92	0.86	1.10	0.81	0.95
60-minute fixation	MTCO2 antibody	5325.00	2140.08	1052.66	603.77	367.49	284.12	278.76	214.26	
	Isotype antibody	5480.00	1555.82	832.66	896.51	680.18	308.43	244.86	198.42	
	Factor MTCO2 vs Isotype control	0.97	1.38	1.26	0.67	0.54	0.92	1.14	1.08	1.00

Table 21 Results of varying fixation time using TAAB 4% PFA solution on the MTCO2 fluorescent intensity, although specific binding was poor.

4.3.2.3 Permeabilisation buffer and process.

After the optimal conditions for fixation had been determined the permeabilisation step needed to be optimised. The protocol by Filby et al., (236), suggested a 0.1% Triton X-100 with 2% FBS in a PBS solution with an incubation period of 5 minutes. Conventionally the Mitochondrial Research Group have used a 0.5% Tween 20 solution in PBS or TBS as a permeabilisation agent, leaving samples in this permeabilisation agent for staining with antibodies compared to removing it as in the case of Filby et al., (236).

I compared the use of these permeabilisation buffers and the effect suspending in the buffer had upon the fluorescent profile of MTCO2 antibody from Abcam conjugated with an Alexa 647 fluorophore. All cells were treated the same and blocked for 1 hour using a 10% normal goat serum

solution after permeabilisation. This was either in PBS or a permeabilising buffer dependent on the sample.

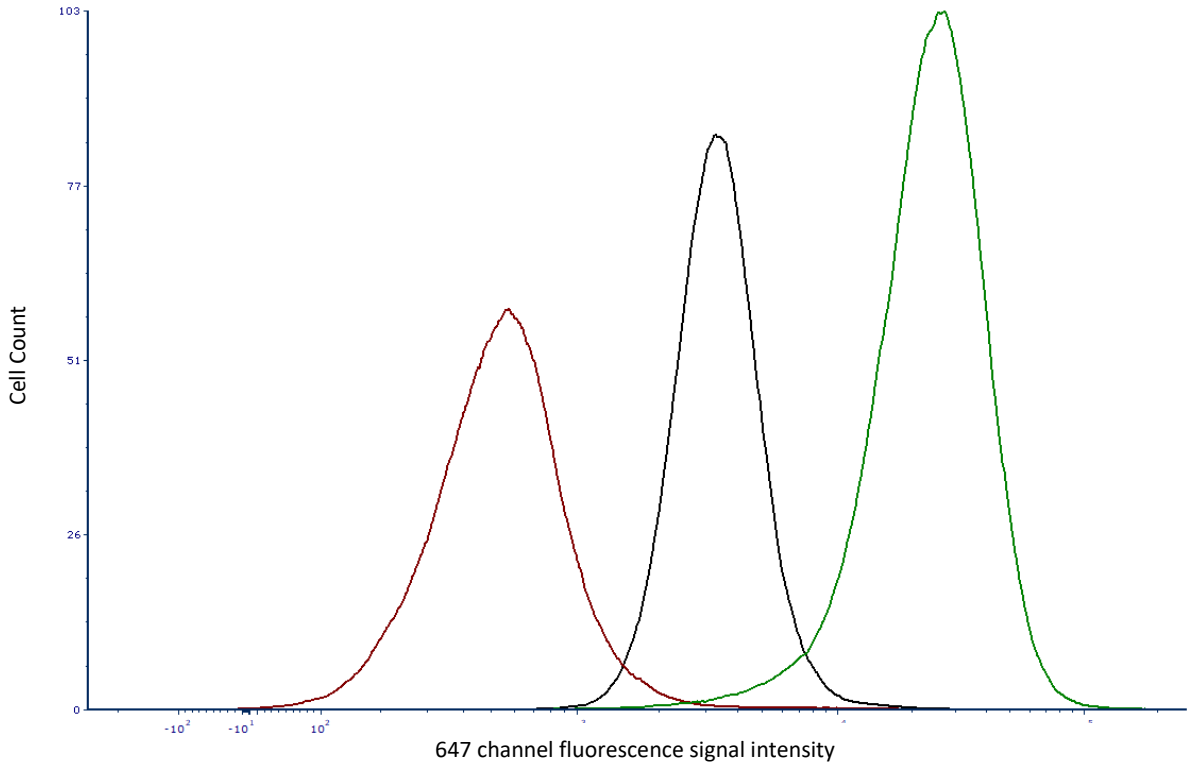

PERMABILISATION AGENT	
TRITON PERMEABILISATION: STAYED IN PBS SOLUTION	504.93
TRITON PERMEABILISATION: STAYED IN TRITON SOLUTION	2819.94
TWEEN 20 PERMEABILISATION: STAYED IN TWEEN 20 SOLUTION	20086.21

Figure 59 Flow cytometry output represented by fluorescent signal intensity profile of the K562 cells in different permeabilisation buffers and stained with the MTCO2 antibody conjugated to Alexa 647.

In *Figure 59* it can be seen that cells left within the permeabilisation buffers had the greatest fluorescent signal intensity. 0.5% Tween 20 in TBS (Tris-buffered saline) (TBST) gave the best fluorescent profile and values. Tween 20 TBS was then compared to Tween 20 PBS (phosphate buffered saline) solution utilising the same antibodies, blocking/fixation/permeabilisation and staining protocol. The results as below in
Table 22 show improved levels of differentiation between isotype controls and MTCO2 antibody fluorescent intensities. Following these results, Tween 20 PBS (PBST) solutions were utilised moving forward as a permeabilisation buffer, with the cells remaining within the 0.5% Tween 20 solution for staining with antibodies and incubation.

Antibody, concentration, permeabilisation and staining buffer	Fluorescence Arithmetic Mean	Factor difference
MTCO2 antibody 1:50 concentration in PBST	24500.23	3.304
Isotype control antibody 1:50 concentration in PBST	7415.02	
MTCO2 antibody 1:50 concentration in TBST	32494.72	2.311
Isotype control antibody 1:50 concentration in TBST	14060.05	
MTCO2 antibody 1:100 concentration in PBST	17041.2	2.771
Isotype control antibody 1:100 concentration in PBST	6150.29	
MTCO2 antibody 1:100 concentration in TBST	21066.66	1.244
Isotype control antibody 1:100 concentration in TBST	16928.55	
MTCO2 antibody 1:200 concentration in PBST	10734.55	2.457
Isotype control antibody 1:200 concentration in PBST	4369.32	
MTCO2 antibody 1:200 concentration in TBST	17511.25	2.253
Isotype control antibody 1:200 concentration in TBST	7773.24	

Table 22 Tween 20 PBS vs Tween 20 TBS as a permeabilisation and staining buffer demonstrating the difference in signal intensity between the isotype control and MTCO2 antibody at different concentrations.

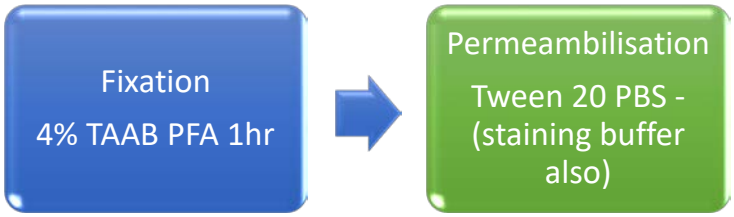

Figure 60 Protocol development summary.

4.3.2.4 Blocking Agents and Washes

Initially, 10% normal goat serum (NGS) was used as a blocking agent as per the previous quadruple immunofluorescent protocol. To improve differentiation between isotype controls and antibodies different blocking regimes and times were trialled.

First, the length of time was trialled as in *Table 23*. A 10 % NGS block was used in PBST solution for 30 minutes, 60 and 90. Increasing the blocking time had a slight positive effect on differentiating the non-specific signal from a background signal with 60-minute block times giving best results.

Antibody and blocking regime	Fluorescence Arithmetic Mean	Factor Difference
MTCO2 antibody blocked for 30 minutes	13702.49	
Isotype control antibody blocked for 30 minutes	10877.87	1.26
MTCO2 antibody blocked for 60 minutes	16356.39	
Isotype control antibody blocked for 60 minutes	12668.24	1.29
MTCO2 antibody blocked for 90 minutes	15419.33	
Isotype control antibody blocked for 90 minutes	12720.06	1.21

Table 23 Duration of blocking step using 10% NGS solution on non-specific binding MTCO2 vs Isotype control.

With non-specific binding still remaining high other agents were trialled. Human IgG (sigma I4506) was trialled as this had been utilised in the flow cytometry facility before with limited incubation times. Human IgG is the most abundant subtype of serum immunoglobulins and the non-specific binding of IgG would be utilised to block the non-specific binding that was occurring with the isotype control. This did show improvement particularly using it for short incubation periods as detailed in *Table 24*. The recommended protocol which was used was 1 µg of block per 100000 cells for 15 minutes with no wash step between block and staining. Increasing length of block had a detrimental affect upon specific binding of the MTCO2 antibody to the cells.

Antibody and blocking regime	Fluorescence Arithmetic Mean	Factor Difference
MTCO2 antibody blocked for 15 minutes	22860.99	2.277
Isotype control antibody blocked for 15 minutes	10041.78	
MTCO2 antibody blocked for 30 minutes	22583.69	1.706
Isotype control antibody blocked for 30 minutes	13236	
MTCO2 antibody blocked for 60 minutes	20266.24	1.569
Isotype control antibody blocked for 60 minutes	12918.51	

Table 24 Human IgG block duration using MTCO2 antibody and Isotype Control and the effect on non-specific binding.

Human BD Fc Block was also trialled (BD Bioscience 564219) as per BD protocol. Fc receptors are part of the immune system and can be the causes of nonspecific binding and false positive staining. Both the IgG block and Fc block target the IgG receptors and reduce non-specific binding

	Fluorescence Arithmetic Mean	Factor Difference
Human BD Fc Receptor Block MTCO2 antibody	14800.46	1.752
Human BD Fc Receptor Block Isotype control	8446.43	

Table 25 Results of using BD Fc receptor block on signal intensity using the MTCO2 antibody and isotype control conjugated to the Alexa Fluor 647 molecule.

Abcam also advocates the use of glycine as part of the blocking buffer. Glycine will bind free aldehyde groups from fixation which would otherwise bind primary and secondary antibodies and be a source of high background fluorescent signal (334).

As a result of positive intial tests using the Fc receptor block and Human IgG blocking agents, a direct comparison of blocking regimes was undertaken with 10% NGS, 10% BSA (bovine serum albumin), Human BD Fc block and human IgG all with the recommended 0.3M glycine as well as 0.3M glycine alone as in *Table 26 and Figure 61.*

Block type	Fluorescence Arithmetic Mean	Factor
BD FC block MTCO2 antibody	13761.68	1.883995
BD FC block 647 isotype	7304.52	
10% BSA MTCO2 antibody	14012.77	0.954366
10% BSA 647 isotype	14682.81	
Human IgG block MTCO2 antibody	12963.62	2.321603
Human IgG block 647 isotype	5583.91	
10% NGS antibody	6173.97	2.021575
10% NGS 647 isotype	3054.04	
no block just 0.3M glycine MTCO2 antibody	17879.23	1.397566
no block just 0.3M glycine 647 isotype	12793.12	

Table 26 Results of variable blocking agents on a non-specific binding fluorescent signal when using the MTCO2 antibody and isotype control.

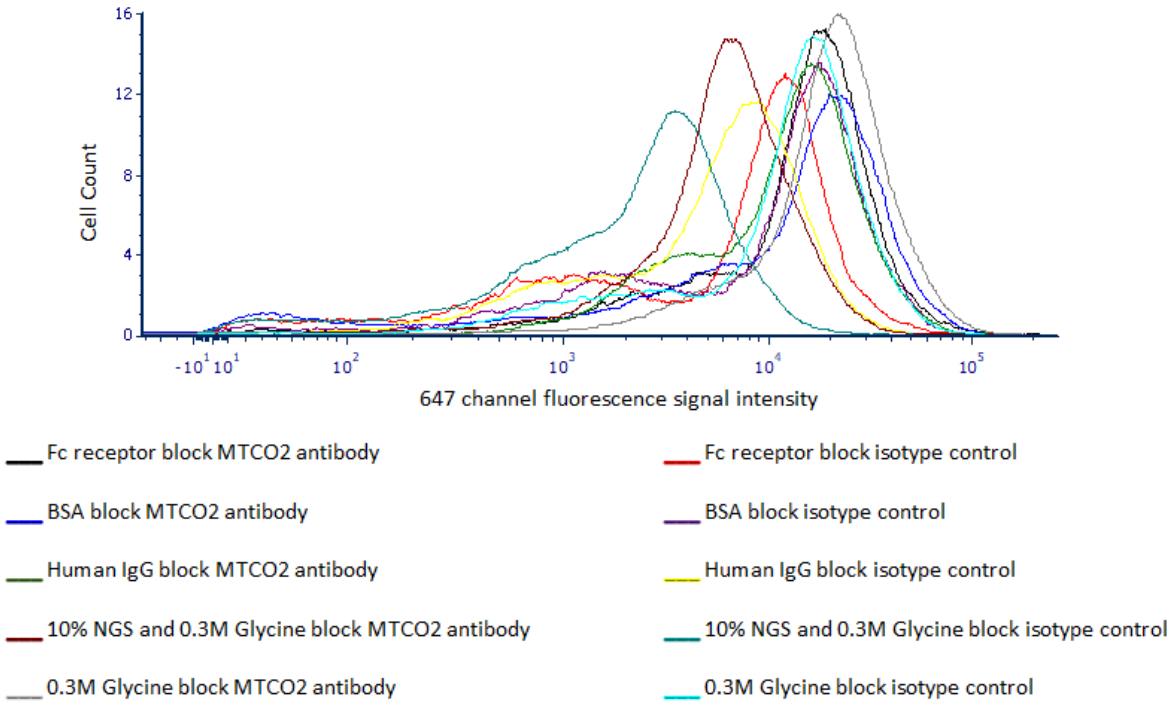

Figure 61 blocking buffer optimisation using K562 cells and MTCO2 antibody and isotype control conjugated with the Alexa 647 fluorophore. Each line represents the signal intensity of the cells analysed using the BD symphony flow cytometer in comparison to each blocking agent. The data is also shown in table 26.

From the results of this experiment, it is clear that BSA did not have any blocking effect and was worse than just 0.3M glycine in PBST alone. The human IgG and 10% NGS with glycine gave the best results and would be utilised moving forward. There was still significant signal from the isotype antibody binding indicating non-specific binding levels were high.

4.3.2.4 Wash number and technique optimisation

Wash number was also increased in terms of duration (10 to 20 minutes), number (3 to 5) and volume (100µl to 150 µl). Increasing washes to 20 minutes utilising the Eppendorf thermomixer at room temperature and 500rpm, as well as the volume and a total number of washes, had a small beneficial effect upon improving the non-specific binding signal. However, despite the use of the Eppendorf thermomixer there was still clumping of cells when left for extended periods of time as in the case of antibody incubation. Further mechanical aids to maintaining a suspension were trialled. A Stuart Roller Mixer SRT9 was utilised but the volumes the cells were suspended in did not allow adequate mixing and pelleting still occurred. Using a Stuart SB Tube Rotator improved results in terms of cell pelleting as did changing from standard Eppendorf 1.5ml tubes to 1.5ml Eppendorf

Lobind tubes which had been utilised in PCR amplicon preparation. Using these tubes and a rotator prevented pelleting which should lead to improved staining and wash steps.

4.3.2.5 Antibody Titration

Antibody titration was undertaken across the range of antibodies by setting up serial dilution plates each with 100,000 cells per well in 100µl of the buffer. Antibodies were matched in terms of concentration expressed in mg/ml so that this was consistent between each antibody and then serial dilution was performed from a 1:50 concentration through to a 1:51200 as in *Figure 62.* 1:50 concentrations of NDUFB8 worked well as did utilising a 1:200 concentration of the other antibodies.

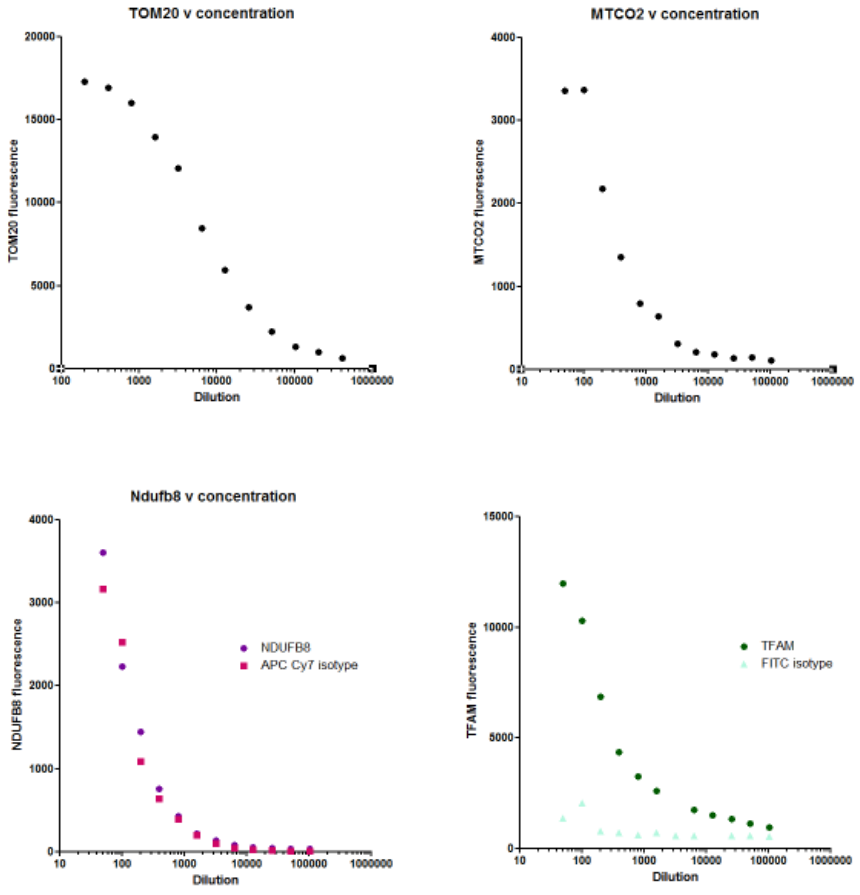

Figure 62 Antibody titration in K562 cells using the TOM20, MTCO2, NDUFB8 and TFAM conjugate antibodies and isotypes.

4.3.3 Further Optimisation of the flow cytometry assay

The protocol at this point in development is summarised in *Table 27 and Figure 63.*

.

1	50mls of K562 cells removed and centrifuged at 300G for 5 minutes
2	wash x2 in PBS and centrifuged at 300G for 5 minutes
3	Fixation 4% TAAB PFA for 1 hour
4	wash x2 in PBS and centrifuged at 300G for 5 minutes
5	Block and permeabilisation using 10% NGS in 0.1% Tween 20 PBS with 0.3M glycine 1 hour
6	Overnight incubation with antibodies in 10% NGS in 0.1% Tween 20 PBS on rotator or rocker if plates used
7	wash x5 for 20 minutes on a rotator (orbital shaker if plates) in PBS and centrifuged at 300G for 5 minutes
8	Final suspension in PBS for flow cytometry utilising BD Symphony A5

Table 27 Initial flow cytometry protocol for measuring mitochondrial respiratory chain protein deficiencies.

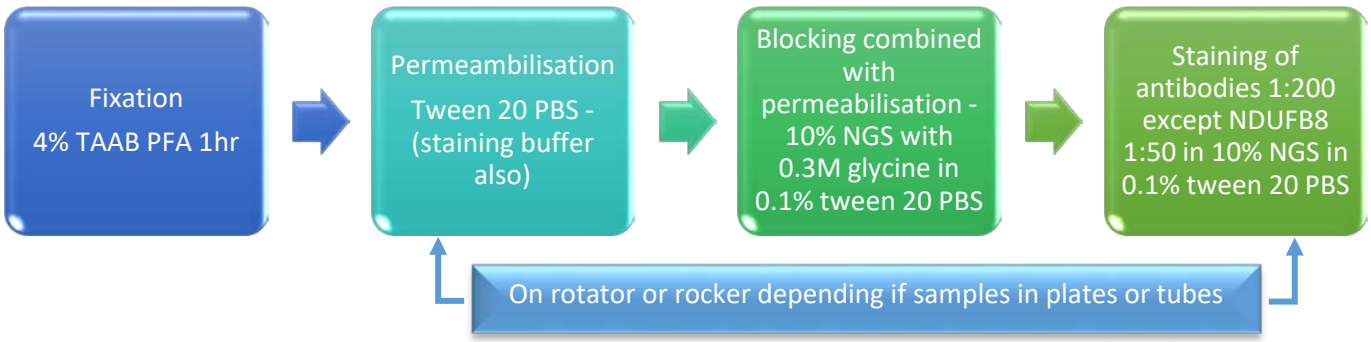

Figure 63 Updated protocol development summary.

One element that could account for this was different the F/P ratio between the MTCO2 and isotype antibodies. The F/P ratio is the average apparent number of fluorochrome molecules conjugated per primary antibody although this was excluded by information from the supplier - Abcam. The MTCO2 antibody had an F/P ratio of 4.2 vs the isotype which was 4. A further isotype (ab199093) for the MTCO2 fluorophore (Alexa 647) was purchased but further testing revealed no significant difference between batches and equally still poor differentiation between true binding and non-specific which would not allow sensitive detection of deficiency as in *Figure 64.*

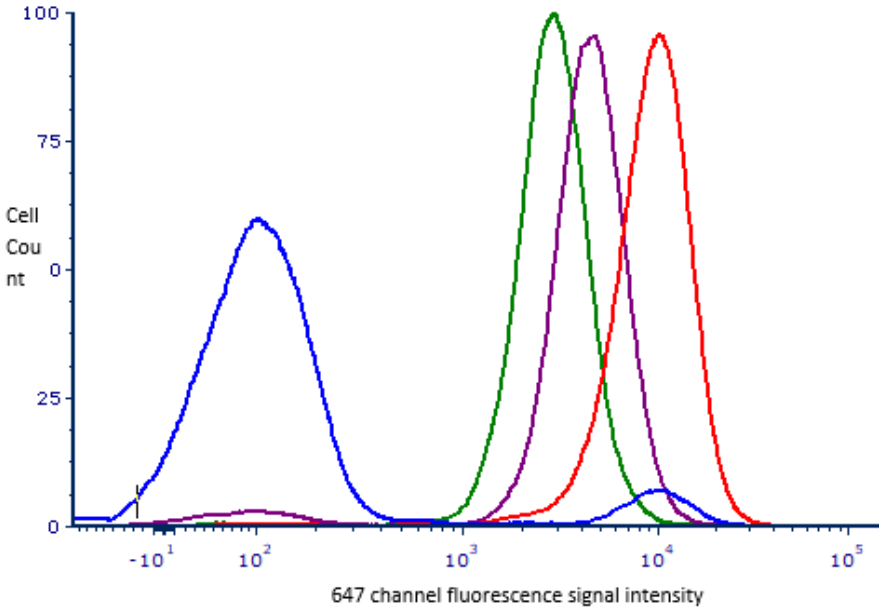

Sample	Arithmetic Mean fluorescent signal intensity
Unstained Cells	672.93
647 Isotype Control - Old Batch	2510.54
647 Isotype Control - New Batch	3733.76
MTCO2 Antibody Alexa 647	8159.86

Figure 64 the comparison of signal intensity profiles of K562 cells passed through the BD symphony flow cytometer. Isotype antibody control batches and MTCO2 antibody conjugated to Alexa 647.

4.3.3.1 Cell types

To assess antibody sensitivity in detecting deficiency a wild type fibroblast and complex 1 cell line (222) were expanded in order to analyse deficiencies against a known control. As in *Figure* 65 there was improved differentiation of the true and non-specific signals seen in both the Tfam and NDUFB8 antibody. There was also a decrease in the complex I signal seen in the deficient cell line as expected. With Tfam values comparable suggest a similar levels of DNA copy number and indication of mitochondrial function.

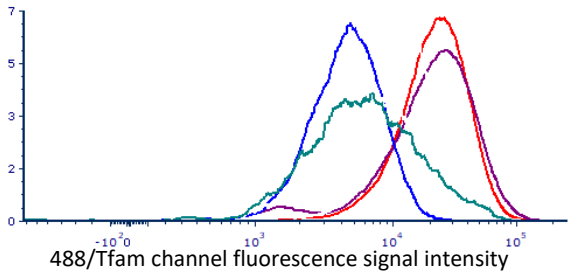

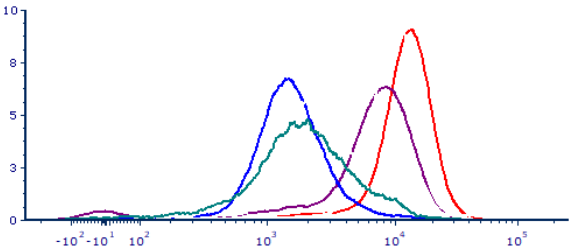

Sample	Arithmetic Mean	Factor difference compared to isotype	Factor difference between wildtype and complex I deficient cells
Complex I deficient fibroblast - 488 Tfam isotype control	7665.72		
Complex I deficient fibroblast - Tfam antibody	21001.91	2.74	
Wildtype fibroblast - 488 Tfam isotype control	4547.37		
Wildtype fibroblast - Tfam antibody	20189.70	4.44	0.96
Complex I deficient fibroblast -APC/Cy7 NDUFB8 isotype control	2264.38		
Complex I deficient fibroblast - NDUFB8 antibody	6380.17	2.82	
Wildtype fibroblast - APC/Cy7 NDUFB8 isotype control	1619.45		
Wildtype fibroblast - NDUFB8 antibody	10731.36	6.63	1.68

Figure 65 Mean signal intensity values for Tfam and NDUFB8 compared to isotype controls for the complex I deficient fibroblasts and wild type non-complex I deficient fibroblasts.

Expanding these results to the full profile of antibodies created mixed results between experiments with inconsistencies seen in the fluorescent profiles gained. MTCO2 antibody signal vs the non-specific signal remained poor throughout. The highest factors of differentiation were seen in the TOM20 antibody vs isotype but were not consistently repeatable.

4.3.3.2 Further Antibody optimisation

Due to the inconsistencies in the staining of antibodies and fluorescent profiles given a primary antibody and secondary antibody incubation step was to be used rather than the conjugated antibodies as in the prior experiments, this also would hopefully improve the antibody fluorescent signal over the non-specific background by use of a secondary antibody amplifying the signal intensity levels of specific binding. This would directly mirror the basis of the assay, the quadruple immunofluorescence protocol by Rocha et al., (235).

Primary antibodies were incubated overnight at 4°C in the dark within a solution of 10% NGS 0.1% Tween 20 PBS with 0.3M glycine overnight as prior. This was followed by wash steps and then the fluorescent secondary antibodies were stained the following day for 2hrs in the dark at 4°C before multiple washes in preparation for flow cytometry. Fluorochromes were also moved to suit the laser profile of the BD A5 symphony flow cytometer as well.

- Tfam was used in combination with a secondary Alexa 405 antibody
- TOM20 was used in combination with a secondary Alexa 488 antibody
- NDUFB8 was used in combination with a secondary Alexa 546 antibody
- MTCO2 was used in combination with a secondary Alexa 647 antibody

Antibody	Arithmetic Mean	Factor Difference
MTCO2	3215.6	3.98
MTCO2 iso	808.37	
NDUFB8	15203.74	1.51
NDUFB8 iso	10067.51	
Tfam	3283.39	5.16
Tfam iso	636.4	
TOM20	12207.05	6.66
TOM20 iso	1834.24	

Table 28 Mean signal intensity values of K562 cells using primary secondary antibody incubation steps on the BD symphony flow cytometer.

The Tfam antibody performance in comparison to the previous conjugated antibody was not as good so it was elected to continue to use the conjugated antibody. Results remained inconsistent in terms of the antibody fluorescent profiles in comparison to isotypes with wide variability in the fluorescent signal strength and factor differences between experiments. Further titrations of primary antibodies were done, and the signal was found to be best for NDUFB8 at 1:50, MTCO2 1:200 and TOM20 1:1600. The blocking optimisation was again repeated, using the primary-secondary antibody

combination blocking in 10% NGS TBST with 0.3M glycine was found to give the best results over the use of Tween 20 and PBS or the addition/use of Fc receptor block or human IgG. The Tfam antibody in comparison to the other antibodies was a monoclonal antibody so only had monovalent affinity recognising only a single epitope of the antigen. The polyclonal antibodies recognise multiple epitopes which increase the risk of cross-reactivity, there is also more batch-to-batch variability as they are not produced from hybridoma clone cell lines. Given the performance of the Tfam antibody been significantly better than the polyclonal NDUFB8, MTCO1 and TOM20 a move to monoclonal variants of these antibodies was made.

4.3.3.3 Confocal microscopy and the development of the flow cytometry assay.

In the absence of antibody and results consistency it was clear the initial optimisation of the protocol used by Filby et al., (236) was not suitable for the staining of mitochondrial antibody targets. The most significant drawback of flow cytometry is that the cells are not imaged and as a consequence detecting what is true specific staining and what is non-specific background is based upon the fluorescent profiles of each antibody vs their isotype and the assumption that this staining is specific. With wide variability seen despite the repetition of experiments, confocal microscopy was used to investigate what exactly the antibodies were binding to. Initially, imaging was done using the Nikon Instruments A1 Confocal Laser Microscope. Below in *Figure 66* shows the nonspecific nature of the NDUFB8 staining with the non-specific binding of the antibody within the cell and high background fluorescence. In comparison to the TOM20 staining, there is clear punctate staining around the nuclear region typical of mitochondrial staining, whereas the NDUFB8 and MTCO1 the staining is non-specific and straddles the nuclear region. Increased laser power and gain were required to demonstrate a signal which suggests an absence of specific binding and non-specific binding and trapping of the Alexa Fluor secondary within the cell and particularly the nuclear region.

With the absence of specific staining within the mitochondria but mitochondrial mass staining present further trials of permeabilisation agents were trialled to see if there was an issue surrounding mitochondrial membrane permeabilisation.

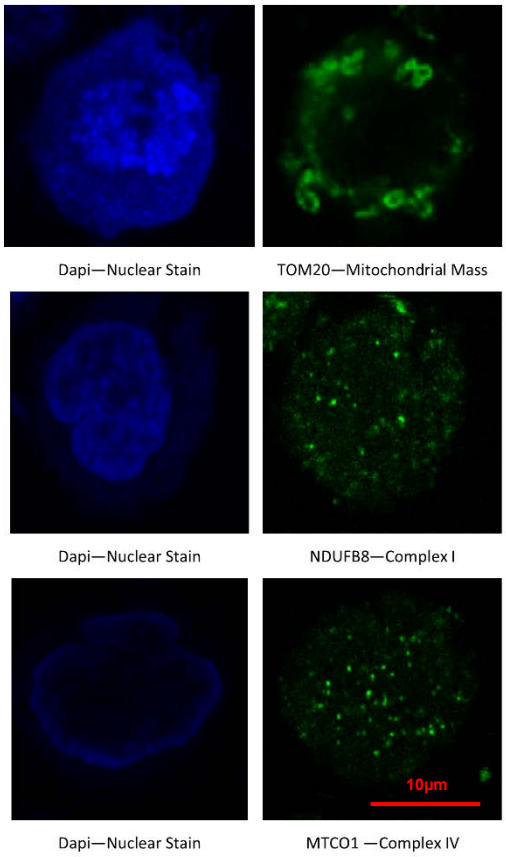

Figure 66 Non-specific staining of K562 cells comparing TOM20 specific mitochondrial punctate staining with NDUFB8 and MTCO1 non-specific staining within the nucleus and cell. All antibodies bound with an Alexa Fluor 488 secondary antibody 60x zoom on Nikon TIE confocal microscope.

4.3.3.4 Further Permeabilisation buffer optimisation

Perfingolysin is a permeabilization agent used in the Agilent Seahorse mitochondrial stress assay where the mitochondrial membrane is permeabilised. This was utilised for 5 minutes at a 1:10,000 concentration. However, when the cells were tested on the BD symphony A5 cytometer it was clear that the perfingo had caused lysis of the cells despite fixation and the characteristic cluster of events was seen near the origin of the axis on both the side and forward scatter as indicated within the red area on *Figure 67.*

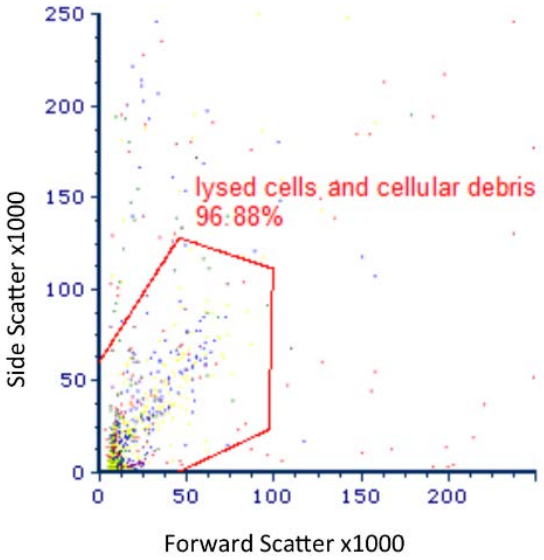

Figure 67 Flow cytometry result of using perfingo lysis agent, the gated area in red demonstrates lysed cells and cellular debris.

Digitonin was trialled as a permeabilisation agent, this has been used in a number of studies investigating mitochondrial function with good effect (335-337). An additional permeabilisation step was added to incorporate the use of digitonin and a concentration of 0.01% in PBS for 2 minutes on ice following the permeabilisation with Tween 20. Although there was some improved staining on confocal microscopy it was not universal or reliable with areas of positive and absent staining in the control line of cells.

Use of Tween 20 was not permeabilising the mitochondrial membrane reliably to allow the staining of the respiratory chain whereas harsher buffers were causing lysis of the cell or loss of the TOM20 signal due to membrane damage. Digitonin did offer some improvement but this was not consistent *see Figure 68*. Reducing the length of time of a 0.1% Triton X-100 solution did not improve results with still poor factor differentiation and overlapping of spectral profiles of the antibody and isotype. Further reviewing of the literature can be summarised in *Table 29*.

A review of different permeabilisation agents for minimising damage to cells for use in flow cytometry also concluded that 0.2% Tween 20 for 30 minutes gave the best conditions although this was in relation to the detection of intracellular RNA. However, it also recognises that no single permeabilisation agent is optimal for all antigens or cells. (338).

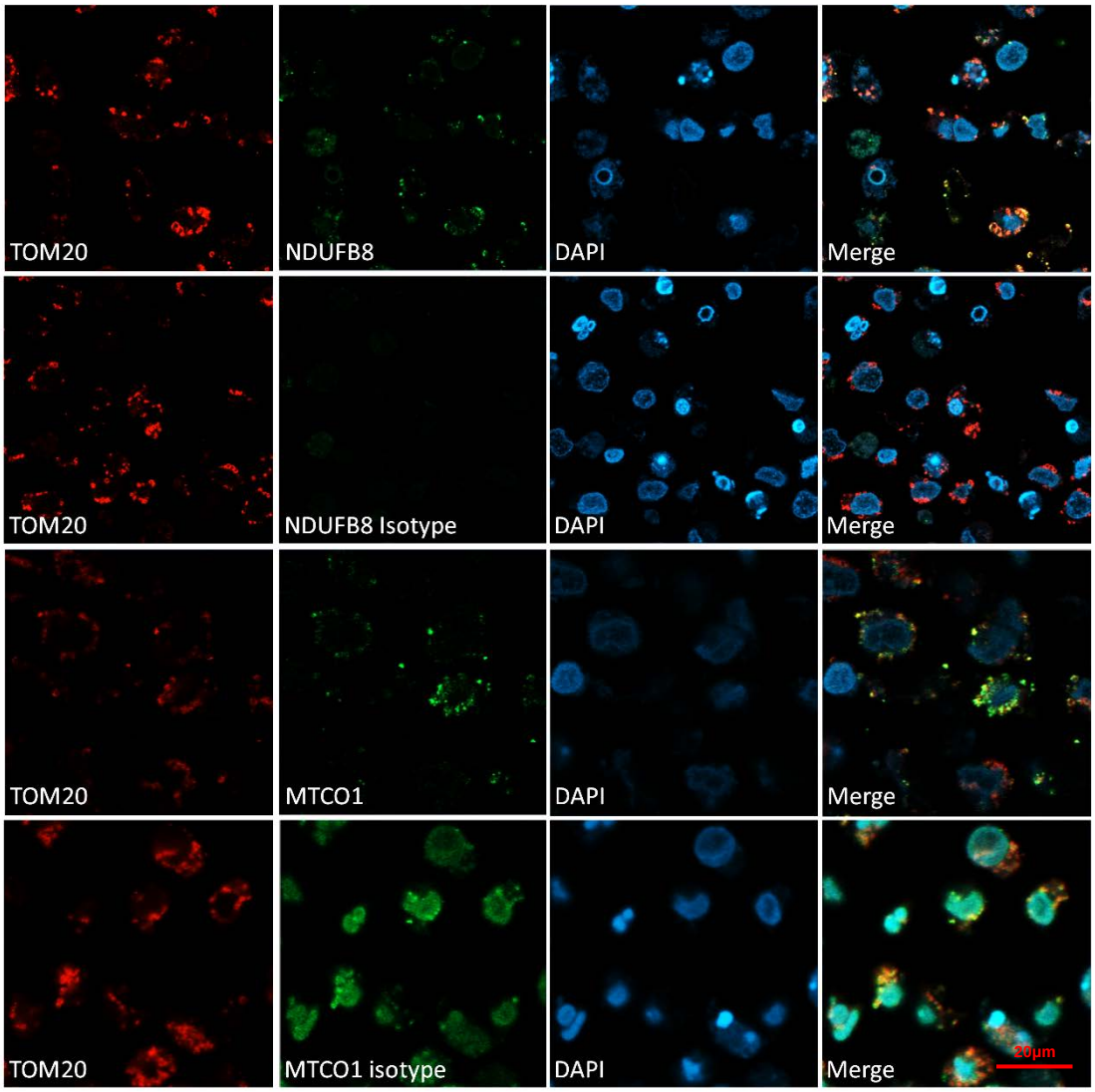

Figure 68 Immunofluorescent images using the Zeiss LMS8000 Airyscanner at 20x magnification demonstrating the variable improvement when using a digitonin step to improve K562 permeabilisation and mitochondrial staining.

	Grünewald et al.,(339)	Hanson et al., (340)	Filby et al., (236)	Murphy et al., (341)	Russell et al., (342)	Rocha et al., (235)	Schmid et al., (343)
Fixation agent	4%PFA	4%PFA	2% PFA	4%PFA	4%PFA	4% PFA	0.25% PFA
Fixation Time (minutes)	10	20	60 (minimum)	10	30	3	60
Fixation temperature (°C)	10	RT	RT	4	Chilled	RT	4
Permeabilisation Agent	1% Tween 20 20 TBS	0.1% Triton X-100	0.1% Triton X-100	1% Tween 20 TBS	1% Tween 20 TBS	Methanol gradient	0.2% Tween 20 PBS
Permeabilisation Time	60	10	5	10	60		15
Permeabilisation Temperature	RT	RT	RT	RT	RT	RT	37
Extra permeabilisation steps				Graduated methanol gradient: • 70% 10 minutes, • 95% with 0.3% H_2O_2 10 minutes, • 100% 20 minutes, followed by rehydration		Graduated methanol gradient: • 70% 10 minutes, • 95% 10 minutes, • 100% 20 minutes, • rehydration 95% methanol 10 minutes, • 70% for 10 minutes.	

Table 29 Summary table of permeabilisation and fixation methods for assessing mitochondria protein targets using immunohistochemistry.

Review of immunocytochemical methods and protocols (344) favoured the use of non-ionic detergents such as Tween 20 and Triton X-100. It also advocated the use of 0.1M glycine to bind any free aldehyde groups left from fixation. However, saponin permeabilisation was not effective on cholesterol poor membranes such as the mitochondrial membrane and so was not considered for use.

Of note regarding fixation, it was suggested fixation has a role in false-negative results by crosslinking cellular elements to mask antigen-binding sites. It was also noted that tight fixation made the interior of the nucleus and mitochondria inaccessible (344). Prolonged fixation could account for the limited success in reliably staining the mitochondrial proteins – NDUFB8 and MTCO1 in the assay. The assays in *Table 29* particularly concerned with mitochondrial staining used either a Tween 20 and/or a methanol gradient for permeabilisation steps. This would be reviewed in the ongoing development of the assay.

4.4 High throughput imaging on the CellDiscoverer7

This high throughput assay was designed to be used with samples of bone marrow. These samples are finite in terms of one per patient with no chance for further samples to be gained. The issues encountered using flow cytometry did not make it feasible to use for a high throughput screening technique. Developing the assay had given unpredictable results with no clear pattern in terms of distinguishing true staining and false-positive staining.

The CellDiscoverer 7 (CD7) microscope by Zeiss allows fast high quality automated imaging of cells with in built automatic focus and calibration steps. It allows the rapid analysis of whole wells in comparison to conventional laser confocal microscopes whilst still retaining adequate cell quality to allow an analysis of mitochondrial protein deficiencies.

Use of the CD7 would allow rapid assessment of a large number of cells achieving the aims of this assay in analysing a large number of MSCs from patients. The CD7 is paired with the Columbus software package from Perkin Elmer. The Columbus system allows the automated analysis and storage of a high volume of images from high content screening instruments.

The availability of the CD7 paired with the Columbus software package meant that high content imaging was now a feasible option to allow the rapid analysis of cells as with using flow cytometry but with the benefit of images, allowing staining profiles to be checked, improved and an assay to be developed.

4.4.1 Fixation

Fixation had been in 4% PFA for 1 hour in the majority of experiments with varying results. In light of the risk of tight fixation preventing access to the mitochondrial membrane, the fixation time was reduced to 5 and 10 minutes and the concentration also reduced to 2%.

Other than this step the blocking and permeabilisation steps were carried out in 0.5% Tween 20 in TBS with 10% NGS and 0.3M glycine. All staining was done in 0.5% Tween 20 in TBS with 10% NGS. Washes between steps were done with 0.5% Tween 20 in TBS. Alteration of the fixation significantly improved the staining of the mitochondrial proteins NDUFB8 and MTCO1 in the K562 cell line. There is clear co-localisation with the mitochondrial mass marker TOM20 as can be seen in terms of the images gained as in *Figure 69* K562 cells stained with NDUFB8, MTCO1, TOM20 and DAPI following a 10 minute and 5-minute fixation step using the Zeiss Axio-observer LSM800/SDI Microscope at 63x magnification.

A direct comparison was made between the TAAB PFA and Chemcruz PFA. This was done over 5,10 and 20 minutes and at a concentration of 2 and 4% using the control fibroblast line. The reduced time of 5 minutes utilising the TAAB PFA at either 4% or 2% gave equally good comparable results in terms of distinguishing mitochondrial mass. However, there was no staining or co-localisation of MTCO1 or NDUFB8. Increasing the times of fixation and using the chemcruz PFA also led to an increase in background autofluorescence and non-specific binding. A further trial of alternate antibodies was tried: GRIM 19 (complex I) COX4 and MTCO2 antibodies were all used but also did not co-localise to the TOM20 antibody.

Figure 69 K562 cells stained with NDUFB8, MTCO1, TOM20 and DAPI following a 10 minute and 5-minute fixation step using the Zeiss Axio-observer LSM800/SDI Microscope at 63x magnification

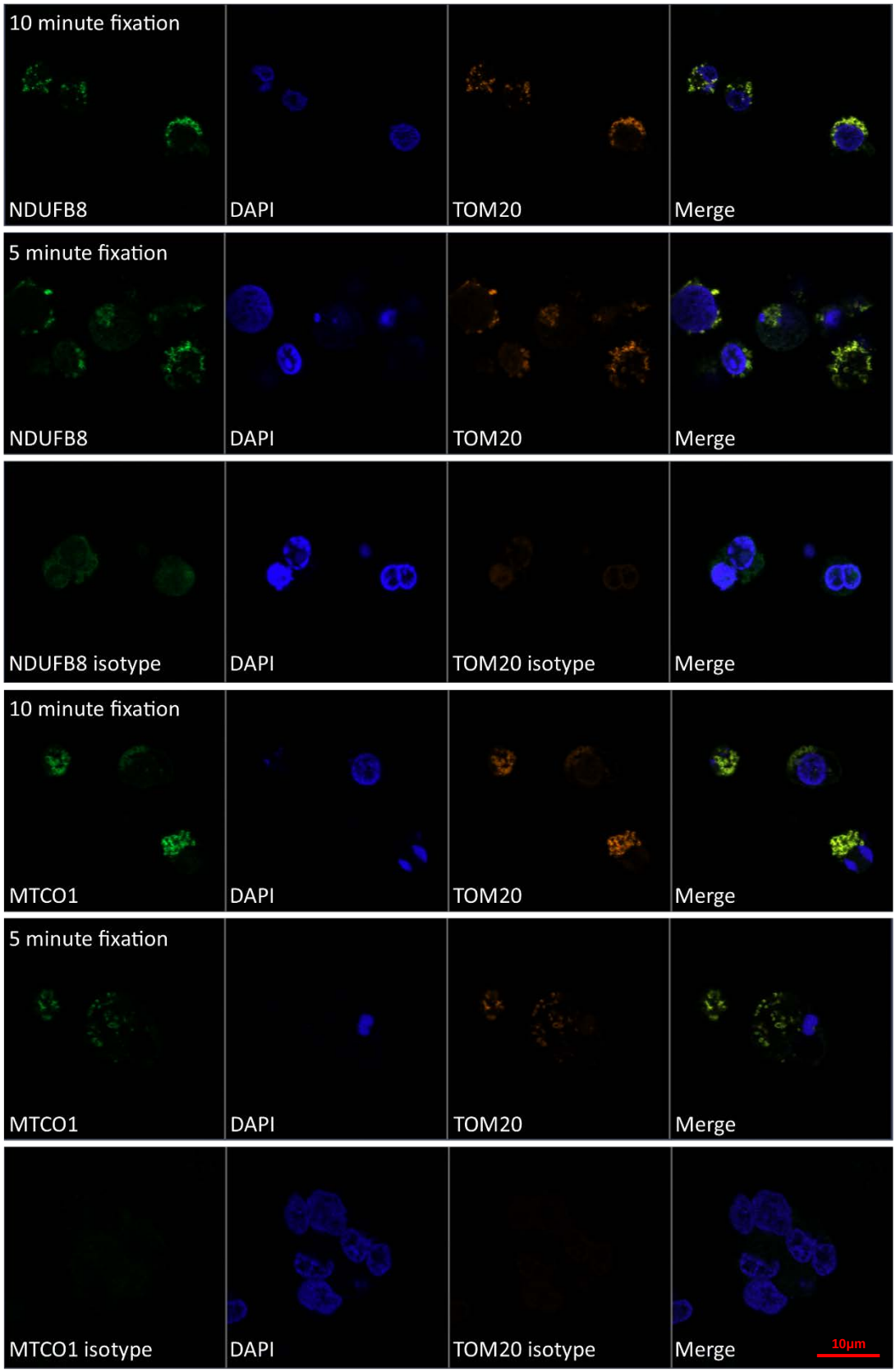

4.4.2 Permeabilisation

Despite the assay working well utilising the Tween 20 permeabilisation in the K562 cell line, there was little to no staining of the mitochondrial proteins of complex I and complex IV in the fibroblasts.

With limited success in using detergent/surfactant-based permeabilisation agents a methanol gradient was used as in Rocha et al., (235). The times were reduced by half; following fixation in 2% TAAB PFA for 5 minutes the cells were washed twice in PBS, 70% methanol was then added for 5 minutes followed by 95% for 5 minutes and finally 100% for 10 minutes. The process was then reversed so 95% for 5 minutes followed by 70% for five minutes. The cells were then washed three times with 0.5% Tween 20 TBS before blocking in a 10% NGS 0.3M glycine 0.5% tween 20 tbs solution.

This method improved the visualisation of complex IV with clear co-localisation between TOM20 and the MTCO1, a titration gradient was performed and screening of the NDUFB8, NDUFB4, GRIM19, MTCO2 and COXIV antibody was done (1:100, 1:200, 1:400, 1;800, 1:1600). The co-localisation of complex I was poor, and the background non-specific binding was high as in *Figure 70*.

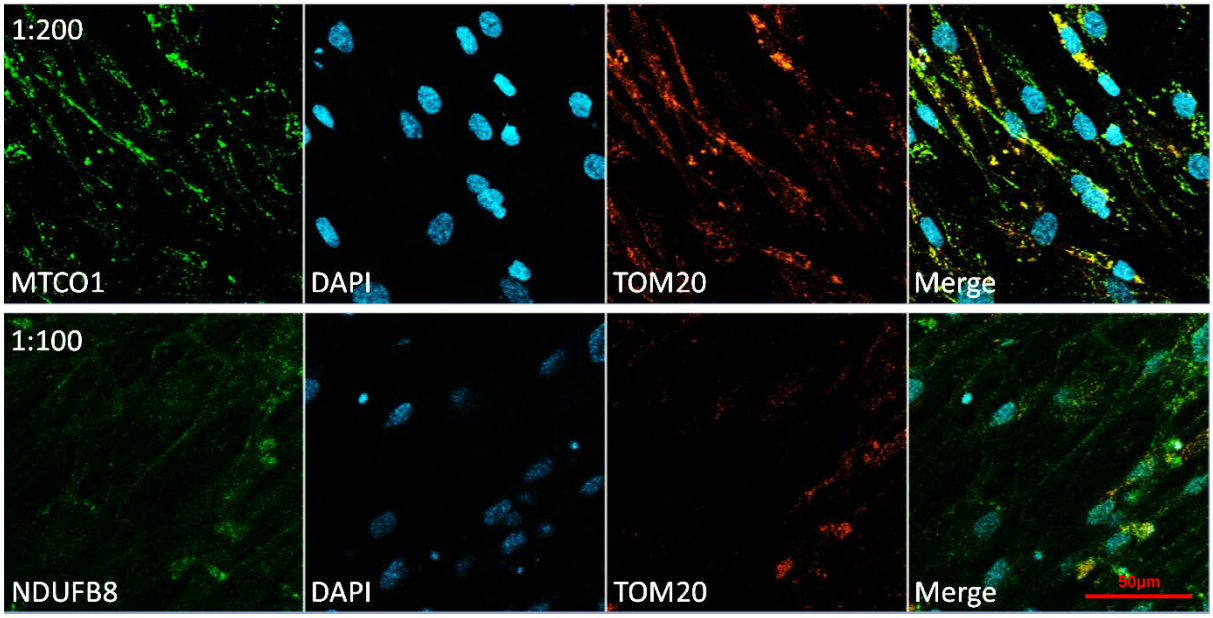

Figure 70 Permeabilisation of the wildtype control fibroblast cell line using a methanol gradient. Complex I, Complex IV and mitochondrial mass visualised using confocal microscopy (Zeiss Axio-observer LSM800 20x lens).

4.4.3 Antibody optimisation; biotin amplification and blockade.

One way to amplify the signal of the complex I antibodies would be to use a biotin secondary followed by a streptavidin-conjugated fluorophore. Biotin is the water-soluble B7 vitamin and is involved in a wide range of metabolic processes within the cell. It has a very strong affinity for avidin and streptavidin which is produced by *Streptomyces avidinii*. Labelled streptavidin can be used to amplify the signal of proteins expressed at low levels by allowing more fluorescent molecules to be bound to the antigen by way of amplification as in *Figure 71*.

Using streptavidin over an avidin tertiary antibody has higher specificity as it lacks carbohydrate moieties (the carbohydrate component of immunoglobulins). It also has higher tissue penetration as it is a smaller complex. The staining process is also simpler (345).

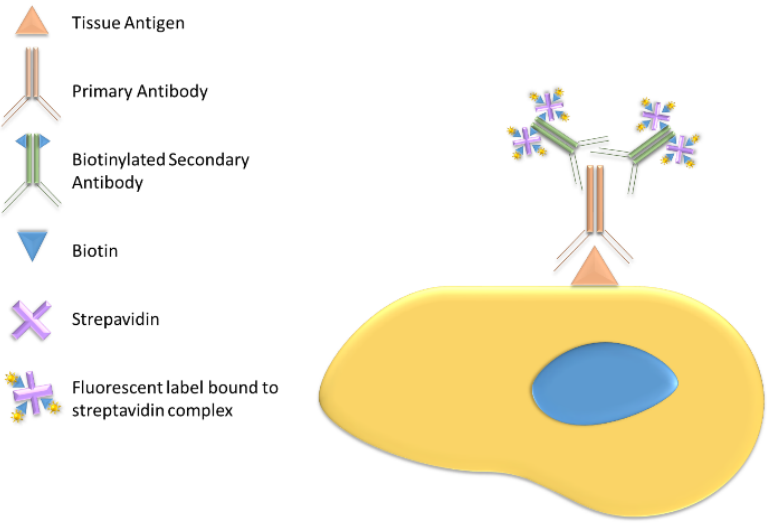

Figure 71 Schematic representation of the use of biotinylated secondary antibodies and streptavidin signal amplification.

When using biotinylated antibodies, it is important to block endogenous biotin which can be responsible for high background signal and non-specific binding by the tertiary streptavidin complex. Blocking of endogenous biotin was done with the Avidin/Biotin blocking kit from Vector. Following the blocking step with 10%NGS 0.3M glycine in TBST, a wash took place using TBST. The avidin was then applied for 15 minutes at room temperature followed by two TBST washes. The biotin was then applied for 15 minutes followed by two TBST washes. The primary antibodies were then incubated in 10%NGS TBST at 4°C overnight on the rocker. Three TBST washes followed, then the secondary antibodies including the biotinylated IgG1 were incubated for 2 hours at 4°C on the rocker. Three further TBST washes followed before the final incubation with the streptavidin Alexa fluor 647 conjugate for 2 hours at 4°C on the rocker. Three final washes with TBST were done, the cells were then ready for imaging.

In *Figure 72* the signal intensity is improved on the NDUFB8 antibody but there is still a high background or noise to specific signal ratio. Differentiation of the specific signal to the background is poor which would make detecting deficiency difficult. Increasing the length of time of the avidin and biotin block to 30 minutes each did not improve the blocking effect. However, doubling the avidin/biotin blocking steps showed significant improvement in the staining of the complex I with NDUFB8 with clear co-localisation with the TOM20 antibody and no detrimental effect upon on the MTCO1 complex IV staining.

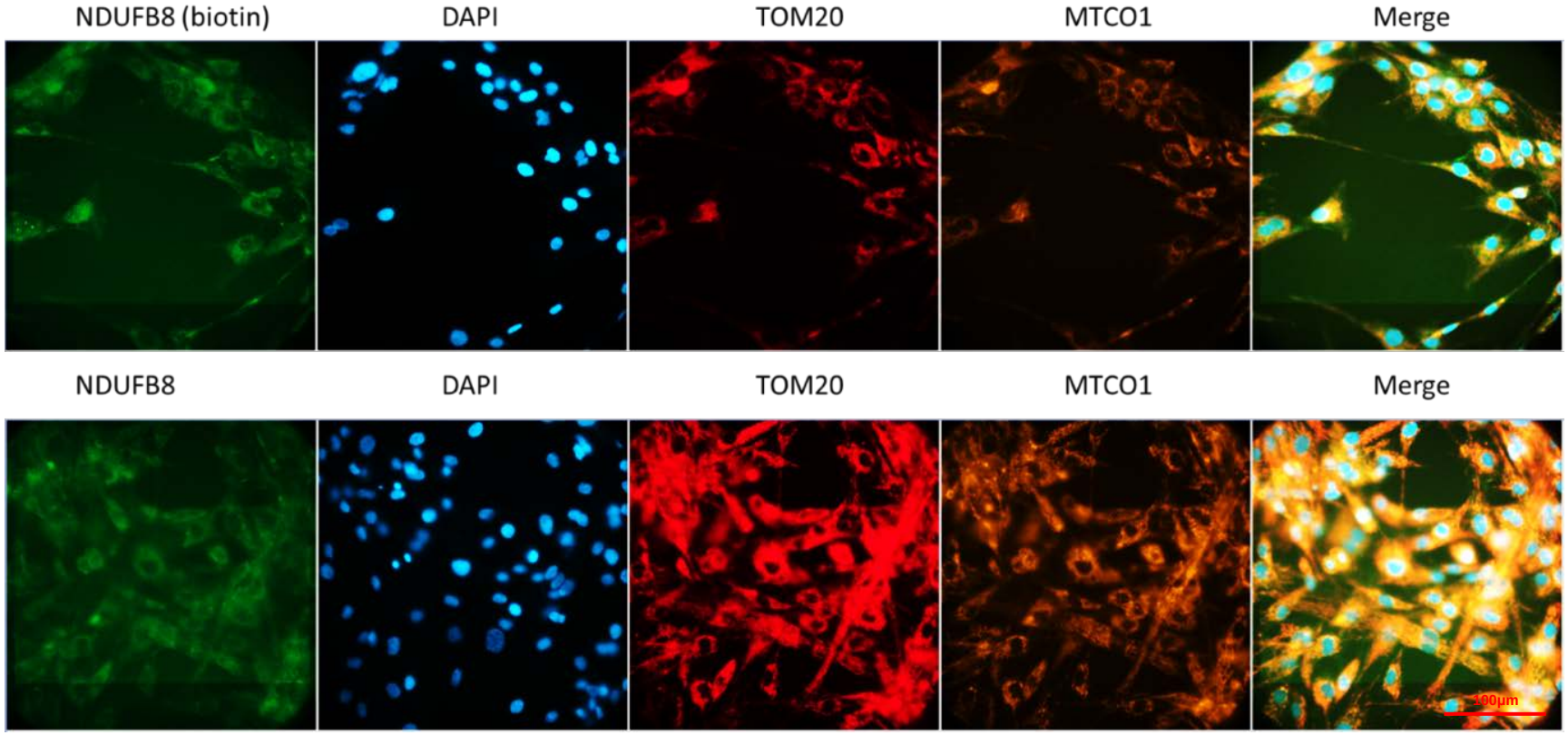

Figure 72 Quadruple immunofluorescence staining of TOM20, MTCO1, DAPI and NDUFB8 using a biotinylated secondary and standard fluorescent secondary antibody. CD7 microscope at 20x magnification.

Antibody titration was performed and 1:200 primary and secondary antibody concentrations for MTCO1 and NDUFB8 was found to be best, the TOM20 signal was strong and as such a concentration of 1:800 of the primary provided sufficient signal for suitable staining *Figure 73* shows the effect of double biotin blocking steps on NDUFB8 staining in fibroblasts.

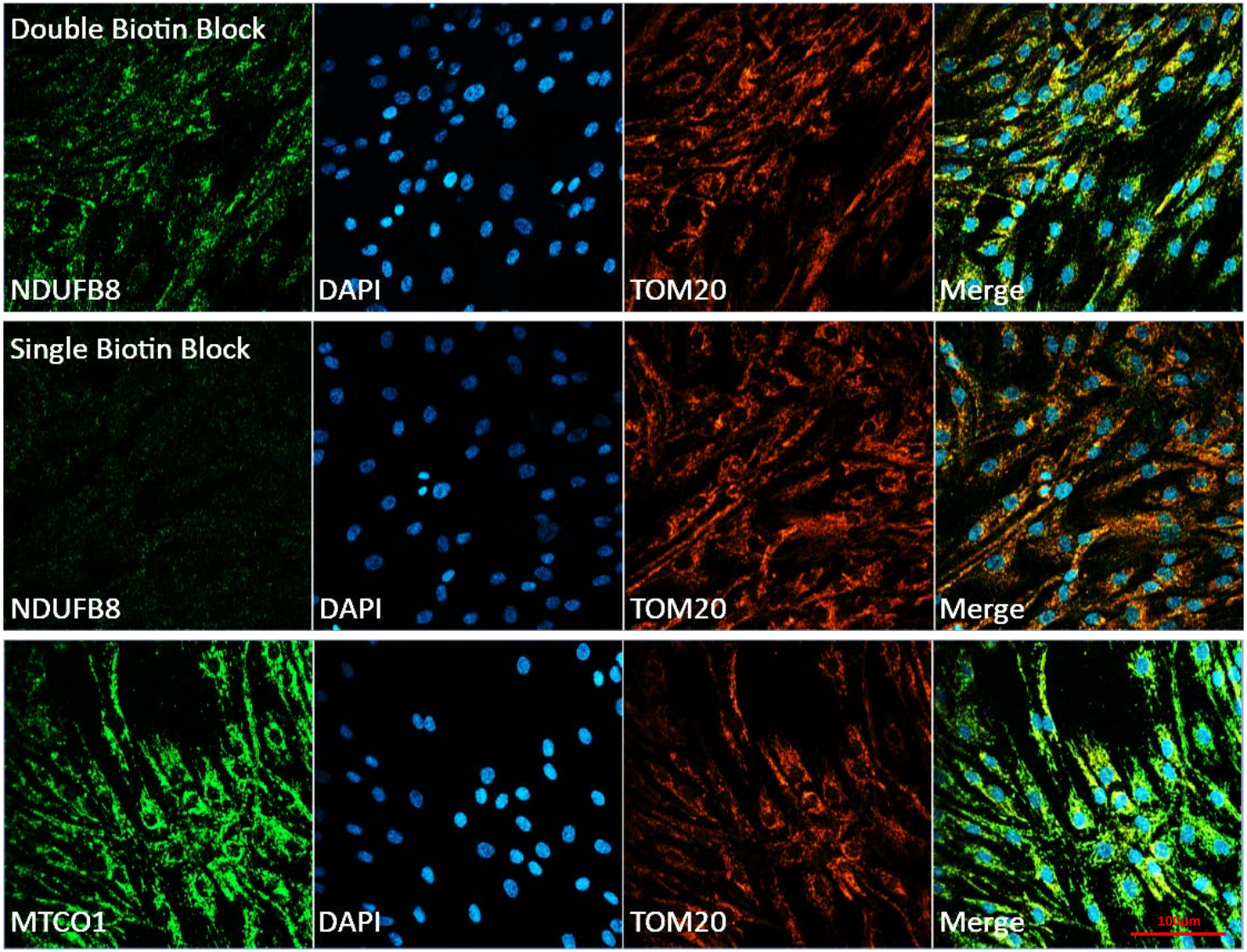

Figure 73 Immunofluorescence images taken using the Zeiss Axio-observer LSM800 confocal microscope to image wild type fibroblasts after a single and double biotin blocking regime CD7 microscope at 20x magnification.

4.4.4 Cell sorting and imaging

With the assay working well on culture cell lines it would need to be tested on MSCs from patients. Sorting these cells allows assessment of MSCs *ex-vivo* and not affected by any aspect of culture. Cells would be sorted using the same assay as detailed in the material and methods chapter. Initially, they were sorted into Perkins Elmer 96 well glass-bottomed plates and Greiner Bio-One 384 well glass-bottomed plates. Cells were then left to bed down over 48hrs before imaging. As can be seen in *Figure 74* the 1000 cells sorted remained in the 96 well plates. Using a 96 well plate it is possible to aspirate and performing the staining protocol by only touching the pipette at the edge of the well. This is not possible in the 384 well and there is a risk of aspiration or dispersion of cells to the periphery which doesn't allow adequate numbers to be analysed.

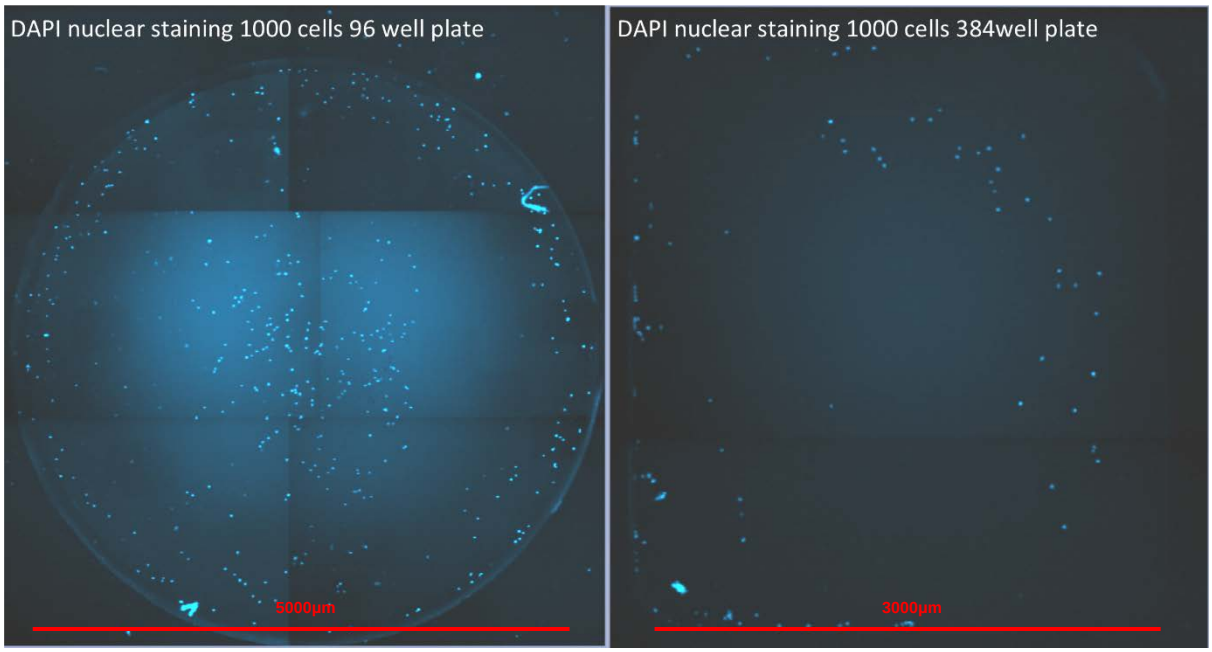

Figure 74 Overview tiled images using the Zeiss CD7 microscope at 5x magnification showing 1000 cells (DAPI staining) sorted into a 96 and 384 well plate.

Initial optimisation sorts were done using the control fibroblast cell line. In the first instance, these cells were simply trypsinised washed and passed through the Aria III fusion flow cytometry sorter to see the impact on survival and staining. Whilst there were some cells which did not survive after sorting the majority did and this allowed satisfactory staining using the above-optimised protocol.

Figure 75 Quadruple immunofluorescence assay of fibroblasts after cell sorting using the CD7 microscope at 20x magnification.

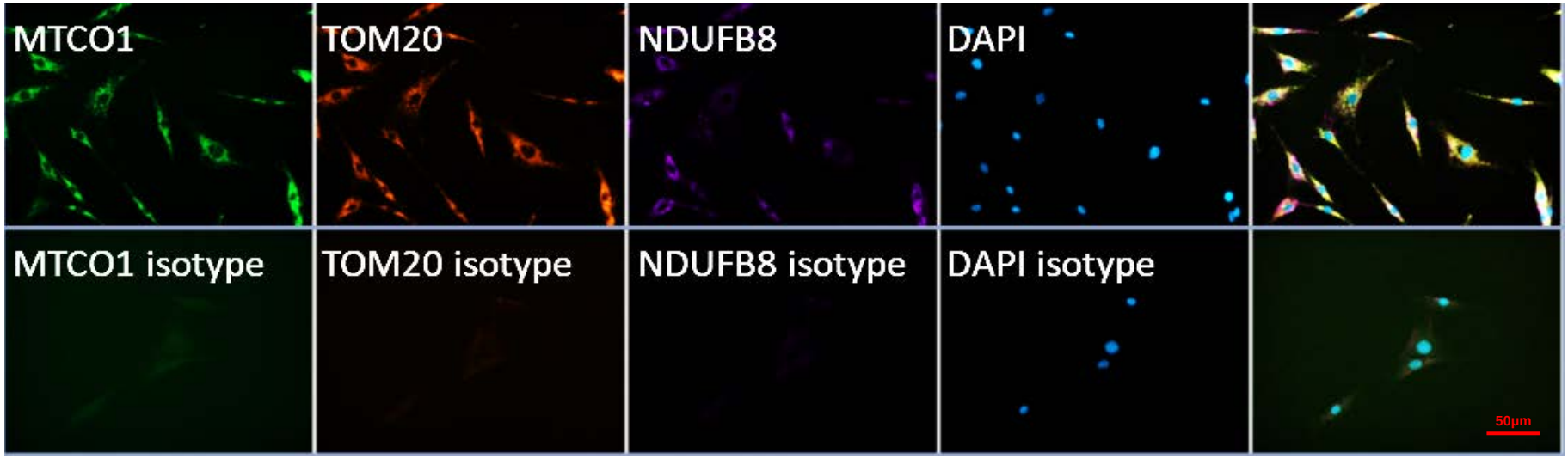

Following successful completion of this further cell sorting was done on a cultured MSC cell line derived from a patient. Here cells were sorted using the MSC sorting protocol into wells and then stained as per the immunofluorescent protocol. The staining profile was the same as that of the previously optimised protocol. There was no crossover from the background staining of the flow cytometry antibodies. However, the flow cytometry sorting antibodies did cause issues as detailed below.

The positive MSC flow cytometry sorting antibodies (CD105, CD90 and CD73) are all mouse IgG1. When the immunofluorescence protocol was trialled on the sorted cells with the flow cytometry antibodies bound to their membrane there was background signal affecting the TOM20 and NDUFB8 channels. This was due to the biotinylated secondary and tertiary antibodies used for the NDUFB8 antibody also IgG1 binding to the flow cytometry antibodies as in *Figure 76.*

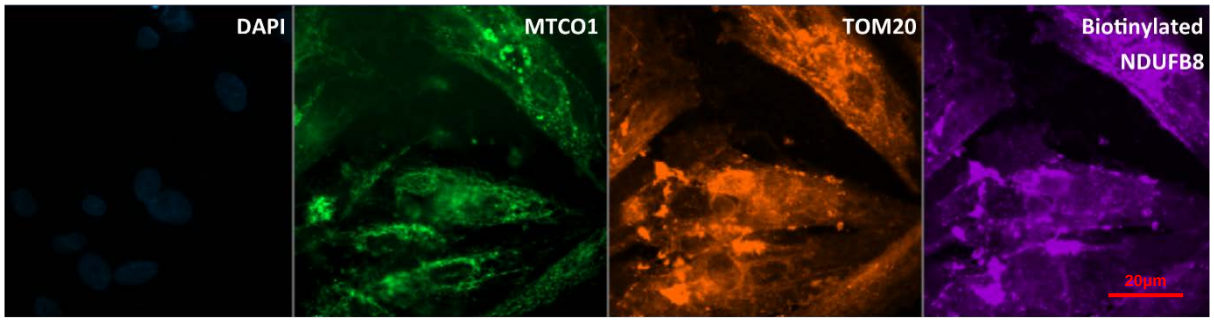

Figure 76 Non-specific binding seen in the TOM20 and NDUFB8 channels caused by non-specific binding of secondary antibodies to the flow cytometry sorting antibodies.

To combat this an IgG1 block was trialled after biotin block in the protocol. To do this an Alexa Fluor 750 anti-mouse IgG antibody was incubated for 2hrs at 4°C followed by 3 TBST washes. The blocking capacity was then checked using a 488 IgG1 anti-mouse antibody. The 488 antibodies also disrupted the 488-channel signal of the MTCO1 antibody.

There was still some residual background signal due to the binding of the flow sorting antibodies with the immunofluorescent antibodies. An alternative panel of antibodies using NDUFB8 rabbit polyclonal antibody, VDAC1 mouse IgG2b was used in place of TOM20 as only an anti-rabbit IgG or anti-mouse IgG2a clone were available, and this would interfere with other antibody signals. The MTCO1 mouse IgG2a primary antibodies were utilised as this was unaffected. A secondary panel of biotinylated anti-rabbit IgG Alexa Fluor 647, anti-mouse Alexa Fluor 488 IgG2a and anti-mouse Alexa Fluor 546 IgG2b was also used. With no IgG1 the non-specific background from the flow cytometry antibodies was not an issue as can be seen in *Figure 77*.

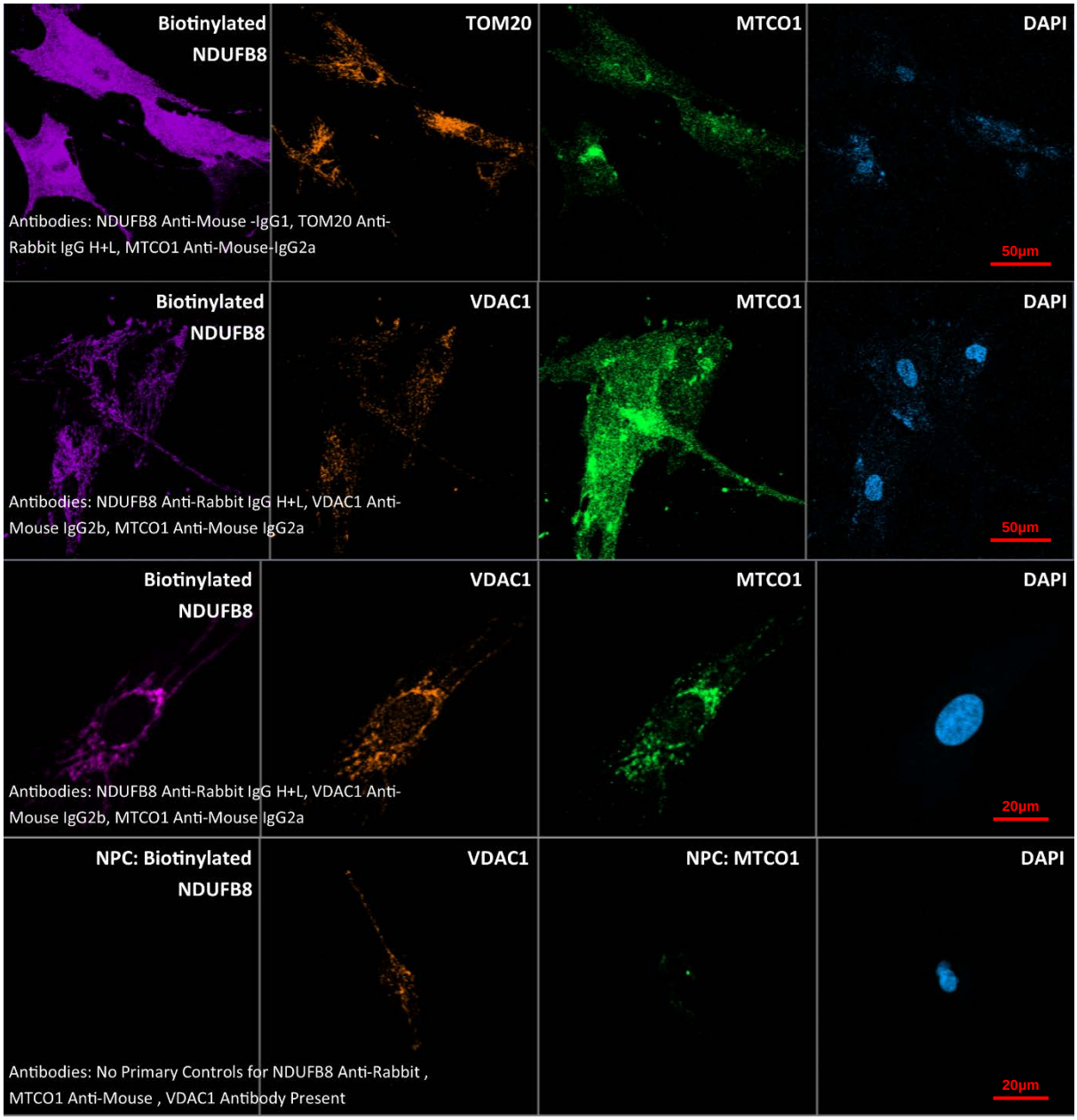

Figure 77 Comparison of antibody staining profile on flow cytometry sorted MSCs, Top row - original antibody panel with extra Alexa Fluor 750 followed by Alexa Fluor 488, Second-row altered panel of antibodies with prior IgG1 488 antibody block, the third-row alternative panel of antibodies without block, fourth row no primary controls for the alternative panel of antibodies.

The strength of the rabbit NDUFB8 signal was found to be sufficient without the use of biotin amplification. This amplification leads to more non-specific staining within the mitochondria and the results were not as clear. The comparative staining with the biotinylated mouse antibody at the same optical settings revealed poor staining and little signal in comparison to the anti-rabbit NDUFB8 as in *Figure 78*. Removing the requirement of biotin amplification and the biotin blocking steps improved the time of the assay and levels of non-specific binding and signal.

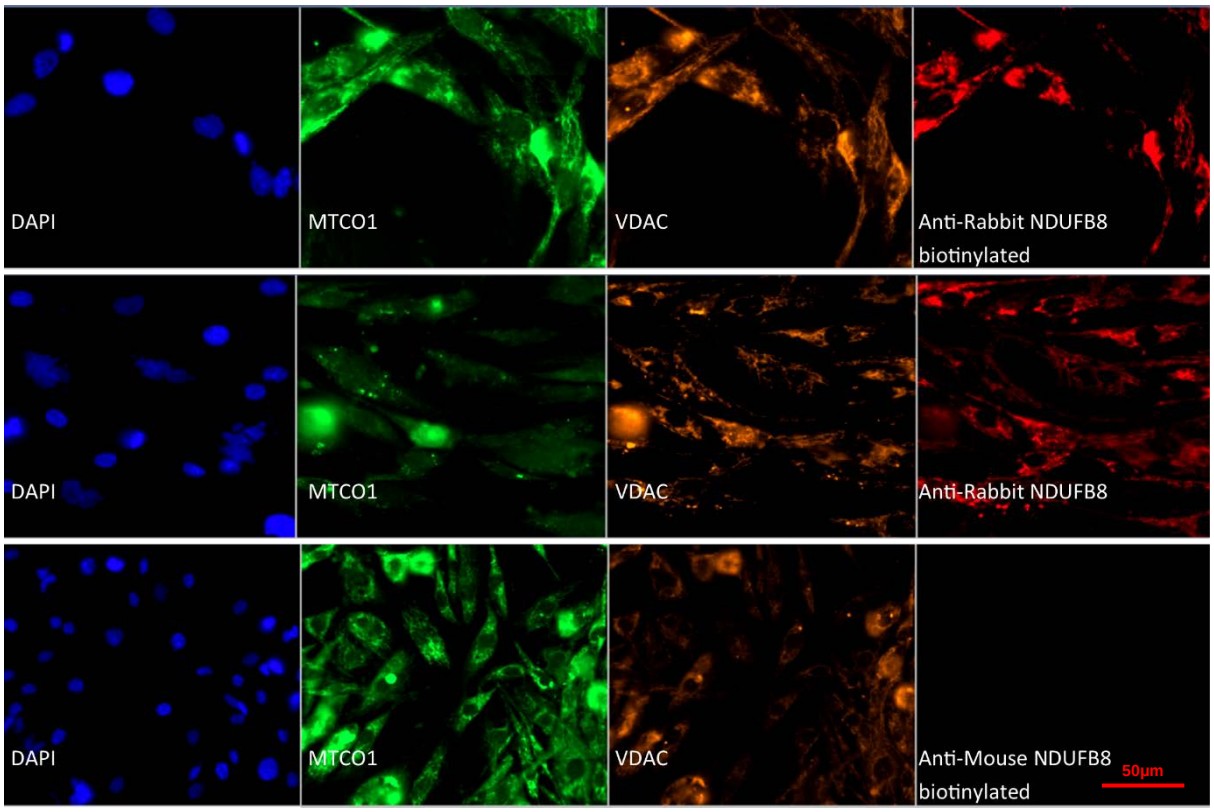

Figure 78 Immunofluorescent imaging at 20x magnification using the CD7 microscope on wildtype fibroblasts demonstrating biotinylated rabbit and mouse NDUFB8 signal vs rabbit NDUFB8 signal.

4.4.5 Further antibody optimisation and validation.

4.4.5.1 Human Muscle sections

Unlike the anti-mouse NDUFB8 antibody which has been validated in muscle and bone (205, 235) the rabbit NDUFB8 has not been used in a quadruple immunofluorescent assay in this way and the only published use has been for western blotting (346).

In order to validate the NDUFB8 antibody direct comparison was made using mouse muscle and comparative staining of the same fibres on serial sections. In order to do this the assay by Rocha et al., (235) was utilised. Both sections were stained with biotin followed by secondary antibodies and compared to VDAC1 staining.

After staining the sections were imaged using the cd7 microscope. Using the Zen 2.5 lite software each individual fibre was isolated and compared to the same fibre on the next serial section for complex one deficiency and direct comparison between the anti-rabbit and anti-mouse NDUFB8 antibodies.

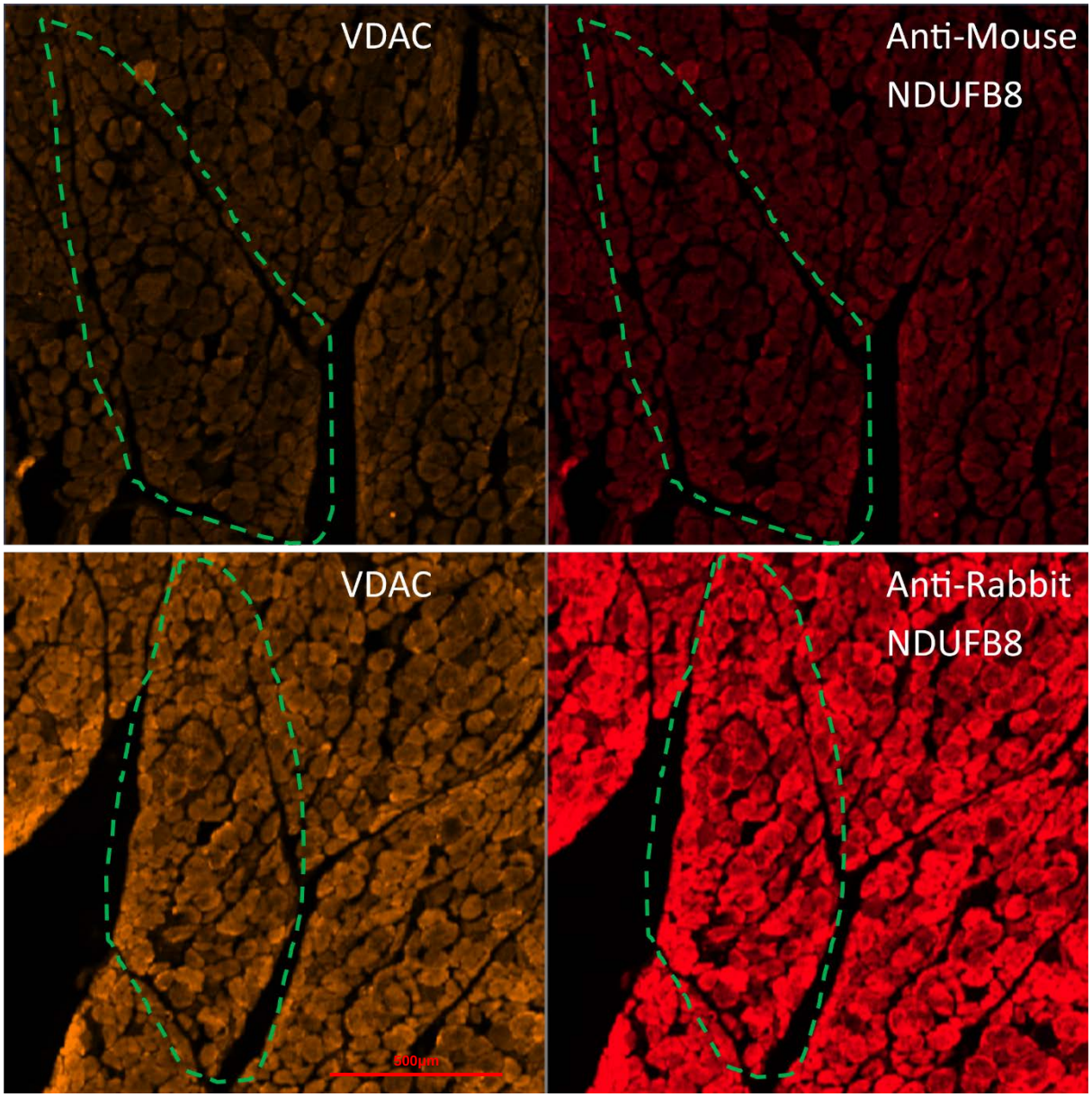

Figure 79 Human muscle viewed at 20x magnification using the CD7 microscope. Serial sections comparing biotinylated anti-mouse NDUFB8 and biotinylated anti-rabbit NDUFB8. Serial section areas marked by the green dashed line. Within this area, each individual fibre was analysed.

Intensity measurements made from Zen lite software were then transferred into the TIBCO Spotfire software. The results of these can be seen below in *Figure 80.* The biotinylated signal of the anti-rabbit again was far more intense than the anti-mouse NDUFB8 and subjectively the images visually demonstrated deficiency better than the use of anti-mouse. There was some correlation of those deficient fibres on serial sections between the two antibodies however there was a large proportion of fibres classed as deficient on their NDUFB8/VDAC ratio using the anti-mouse NDUFB8 that were not using the anti-rabbit NDUFB8. The signal from the biotinylated anti-rabbit NDUFB8 was too bright and was masking these deficient fibres as had been found when using the biotinylated NDUFB8 on the wildtype fibroblasts.

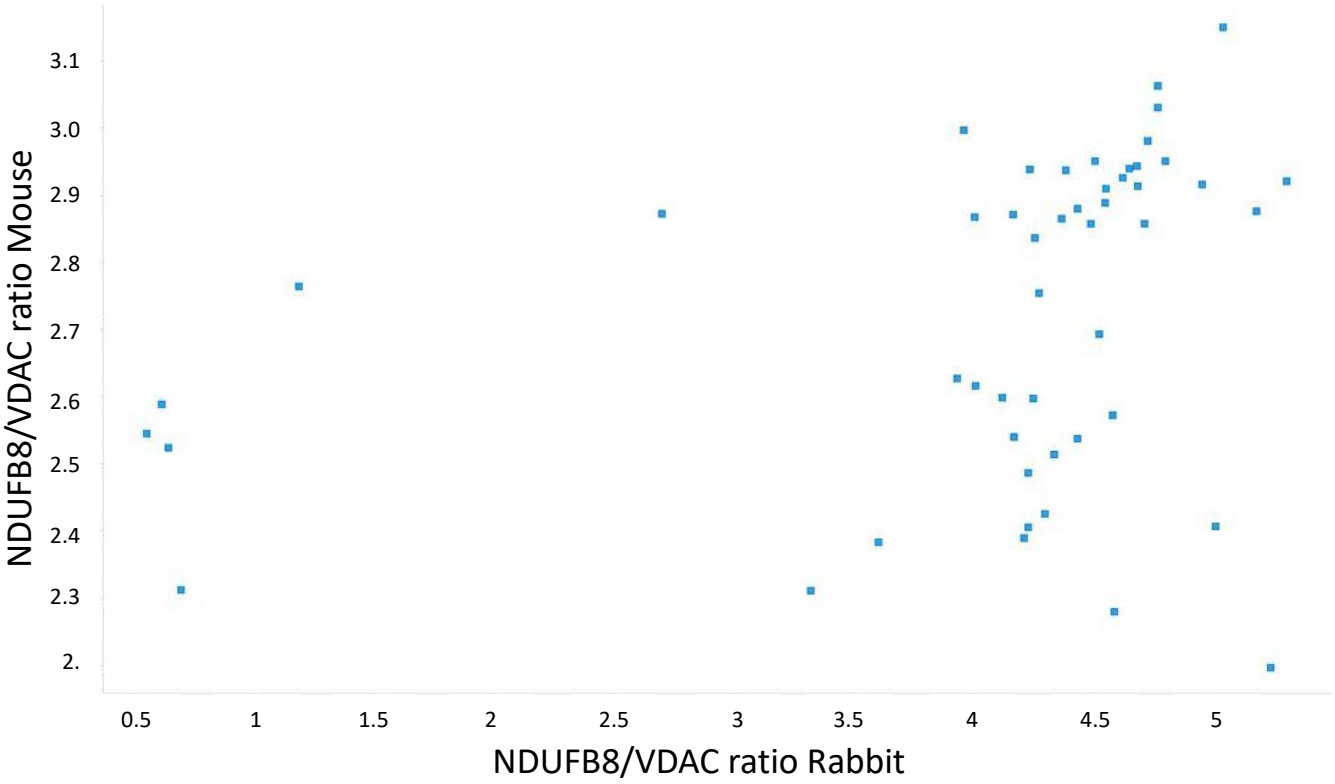

Figure 80 Demonstrating the ratio of NDUFB8 and VDAC signals for individual human muscle fibres. Comparison of Anti-Rabbit NDUFB8 and Anti-Mouse NDUFB8.

4.4.5.2 Wildtype and Deficient cell lines – ND4 vs NDUFB8 antibodies

With the validation of the antibody using the human muscle sections inconclusive, further validation was performed by using the ND4 and anti-rabbit NDUFB8 antibodies on wildtype and complex I deficient fibroblasts.

Complex I deficient and wildtype fibroblasts were grown up in T75s they were then seeded at a density of 10,000 per well in a 96 well senso plate. After 24 hours the staining protocol was initiated; the protocol used is outlined in *4.5 Final optimised assay for high throughput screening.* The ND4 antibody is anti-mouse IgG2a antibody and as a result, this replaced the MTCO1 antibody for this experiment. Both the anti-rabbit NDUFB8 and ND4 were bound with Alexa 488 and Alexa 647 respectively, VDAC was bound with the Alexa 546 antibody.

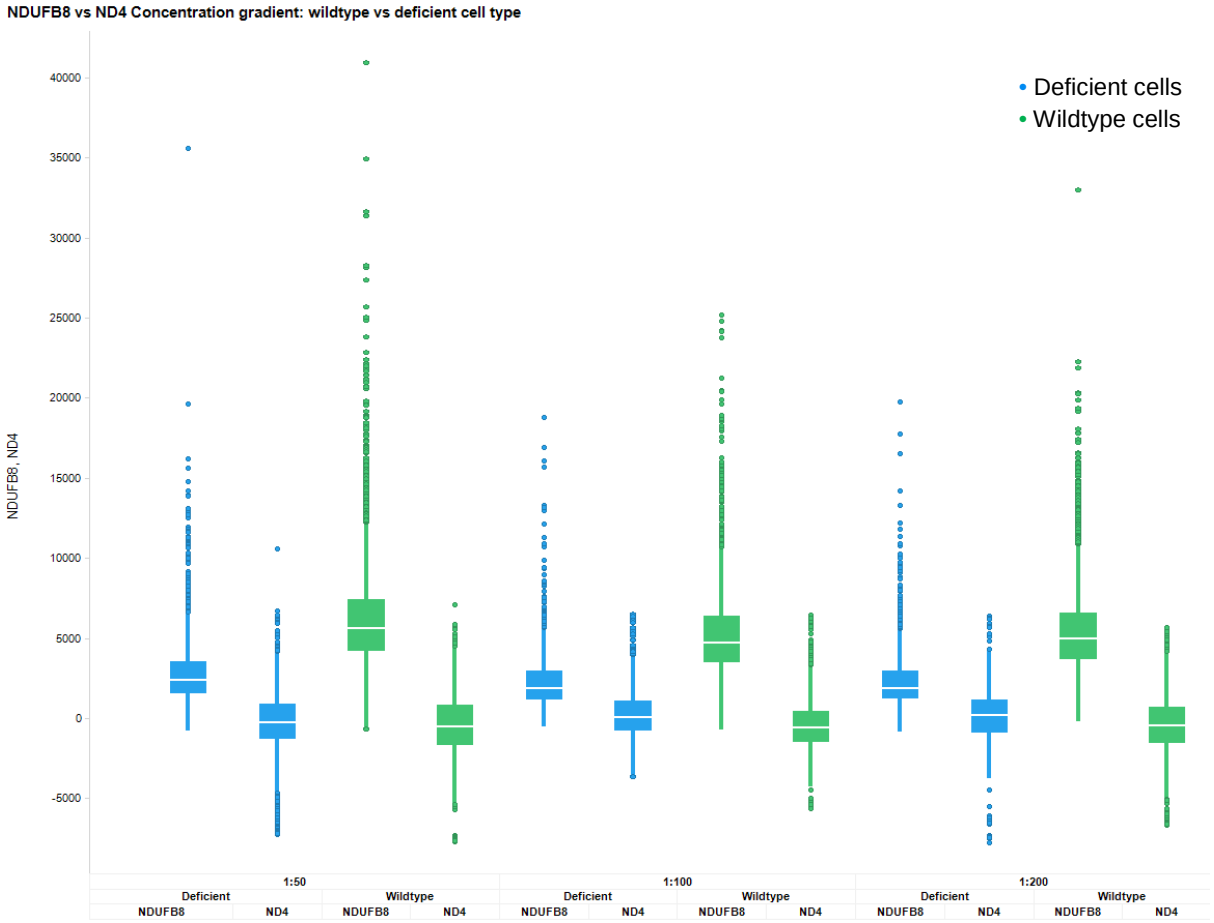

Figure 81 Direct comparison of anti-rabbit NDUFB8 and ND4 antibodies on wild type and deficient fibroblasts.

Whilst the NDUFB8 demonstrated significant differences the ND4 antibody did not highlight deficiency and very little difference from the background signal or non-specific binding as demonstrated in *Figure 82*.

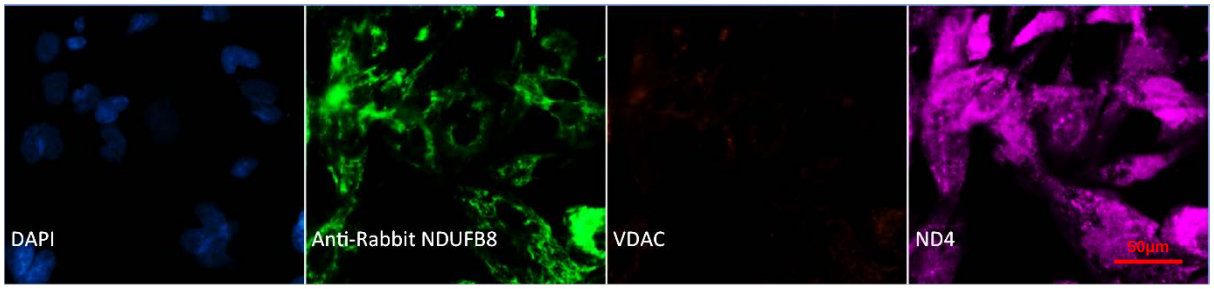

Figure 82 20x image of wildtype fibroblasts taken on CD7 microscope. The comparison of the clear punctate (typical) mitochondrial staining can be seen in clear comparison to the high levels of background seen in the ND4 antibody.

Utilising the wildtype and deficient fibroblasts it was possible to demonstrate deficiency between the two cell types using the NDUFB8 anti-rabbit antibody.

A comparison was also made between the NDUFB8 biotinylated and unbiotinylated signals. As demonstrated in *Figure 83*. The biotinylation step amplified the signal in both the deficient and wildtype fibroblasts but the distribution remained the same. As a result, the extra steps to biotinylate the antibodies and potential for more non-specific background it was elected to use unbiotinylated antibodies.

Complex I vs VDAC: Biotinylated vs non biotinylated rabbit NDUFB8 anti-rabbit on wildtype and deficient fibroblasts

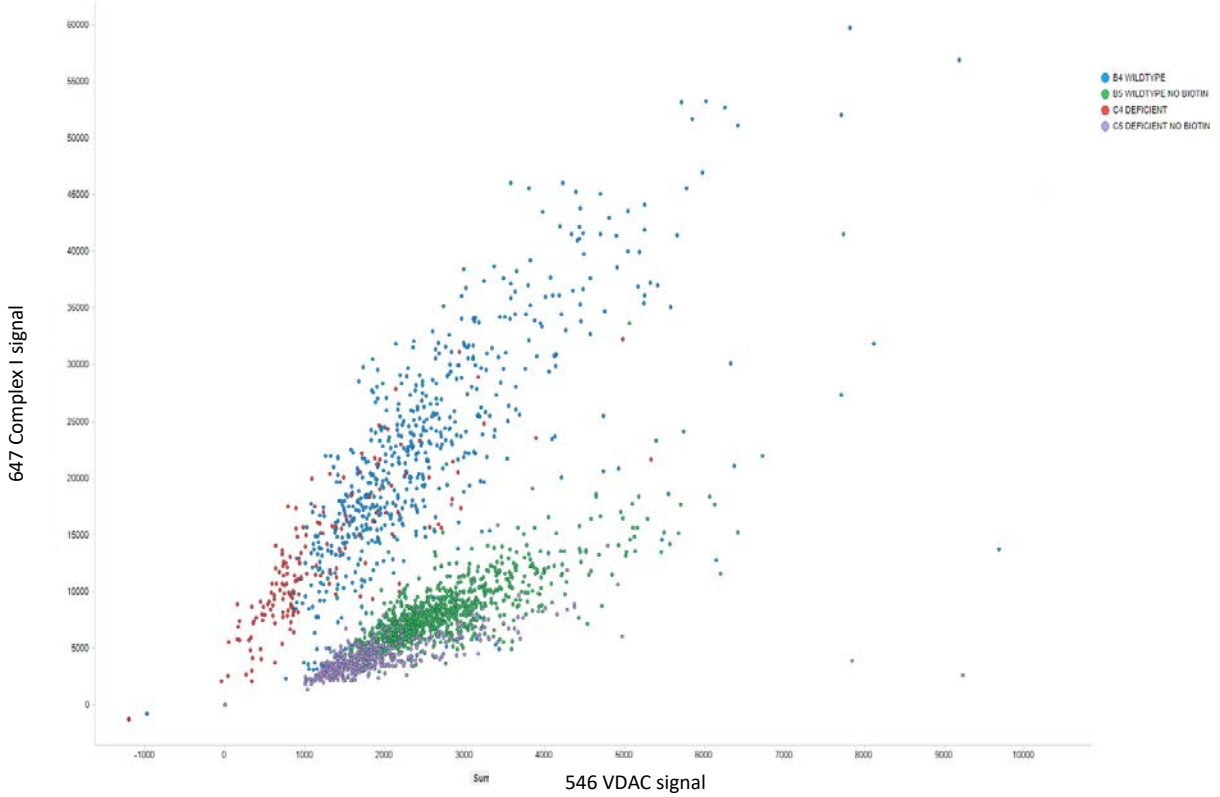

Figure 83 Comparison of biotinylated and unbiotinylated anti-rabbit NDUFB8 and VDAC signal using wildtype and deficient cell lines.

4.5 Final optimised assay for high throughput screening

4.5.1 Assay

1. Cells either sorted on to or cultured in 96 well Senso plate (glass bottom).
2. Media removed from cells and washes x1 with sterile PBS.
3. Fix with fresh 4% paraformaldehyde (TAAB) 2 minutes.
4. Washes x3 TBST.
5. Permeabilisation using methanol gradient:

   70% methanol for 5 minutes.

   95% methanol for 5 minutes.

   100% methanol for 10 minutes.

   95% methanol for 5 minutes.

   70% methanol for 5 minutes.
6. Washes x3 TBST.
7. Protein block 10% NGS diluted in TBST with 0.3M glycine 1 hour.
8. Stain with primary antibodies overnight at 4°C on rocker at 30 rpm. Antibodies diluted in 10% NGS and TBST.

Antibody	**Ig**	**Concentration**
Anti-Rabbit NDUFB8	Rabbit H+L	1:100
Anti-Mouse VDAC1	IgG2b	1:100
Anti-Mouse MTCO1	IgG2a	1:100

9. Washes x3 TBST.
10. Secondary antibody cocktail diluted in 10% NGS and TBST.

Antibody	**Concentration**
Anti-Rabbit Alexa 568	1:200
Anti-IgG2b Alexa 647	1:200
Anti-IgG2a Alexa 488	1:200
Dapi	1:1000

    Antibodies incubated with plate covered with foil (in the dark) for 2 hours at 4°C on rocker at 30 rpm.
11. Washes x3 TBST.
12. Sterile PBS added to wells and wells then imaged using the CD7 microscope at 20x zoom.

4.5.2 Testing the Assay

The assay as a complete process from sorting cells using flow cytometry through to the immunofluorescent assay as laid out above was tested on cultured cells from the 25-year-old male patient. These cells had been grown from marrow samples and were expanded in a t75. Once confluent the cells were trypsinized, washed and stained with MSC markers for sorting via flow cytometry.

Following sorting into a 96 well plate the cells were allowed to bed down on to the plate for 24 hours before running the immunofluorescent assay. The images of this successful test can be seen below in *Figure 84.*

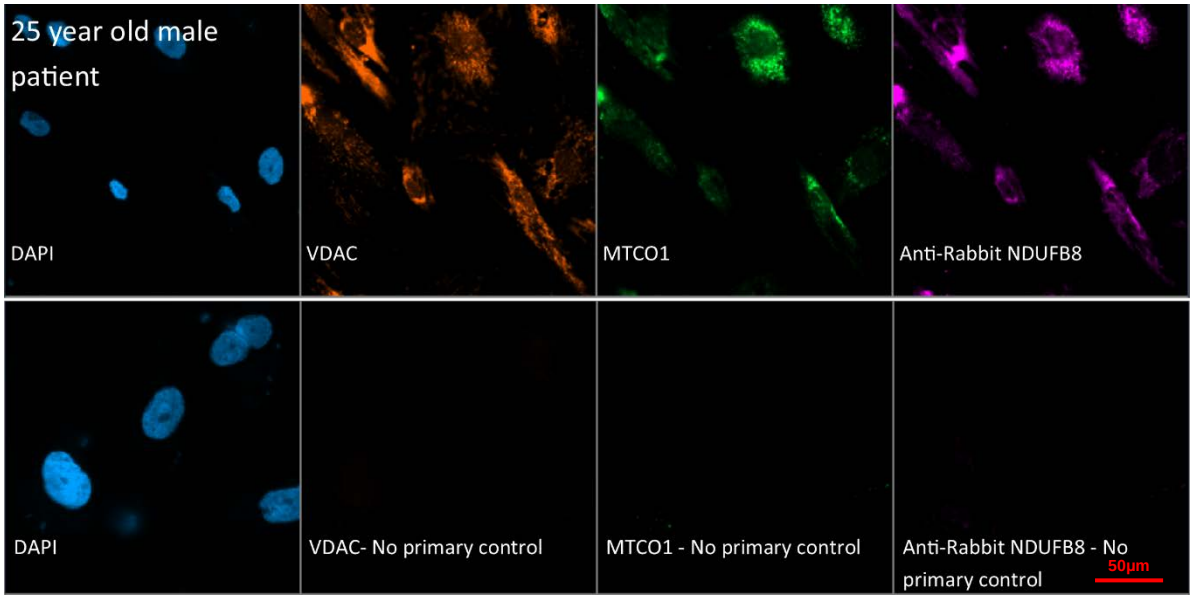

Figure 84 Final test of combined flow cytometry sorting assay and immunofluorescence assay on cultured MSCs from 25-year-old male patient.

4.6 Results

4.6.1 Flow cytometry sorting of MSCs

Frozen lymphoprep samples from the patients detailed in *Table 19* (Hip 1-14) were selected and prepared:

1. Vials were thawed in a water bath at 37°C, then pipetted dropwise into a universal with 5mls of warmed αMEM media.
2. Samples were then spun at 500g for 5 minutes, the supernatant was then aspirated, and the cell pellet was resuspended in 5mls of warmed αMEM media and spun again before suspension in Ca^{2+}, Mg^{2+}, PBS. DNAse was added at this step to aid suspension if cells were clumped. An incubation period of 10-15 mins with DNAse was allowed. Usually, 10-15µl were required added in 5µl increments.
3. Cells were then stained using the MSC sorting protocol *2.4.2.2 Mesenchymal Stem Cell separation.*

After this cells were sorted using the BD FACSAria Fusion flow cytometer on to 96 well senso plates containing αMEM and allowed to bed down for 24hours. The defrosting and staining were done as a staged process to limit times out of media and defrosting across the sample.

The results of the sorting can be seen in *Figure 85.* The initial aim of the sorting process was to get 1000 cells per well. However as in the PCR chapter the number of cells sorted, and time taken to sort those cells varied from sample to sample. Objectively the older patients had a reduced density of MSCs per sample sorted this would also correlate with findings in the literature (347).

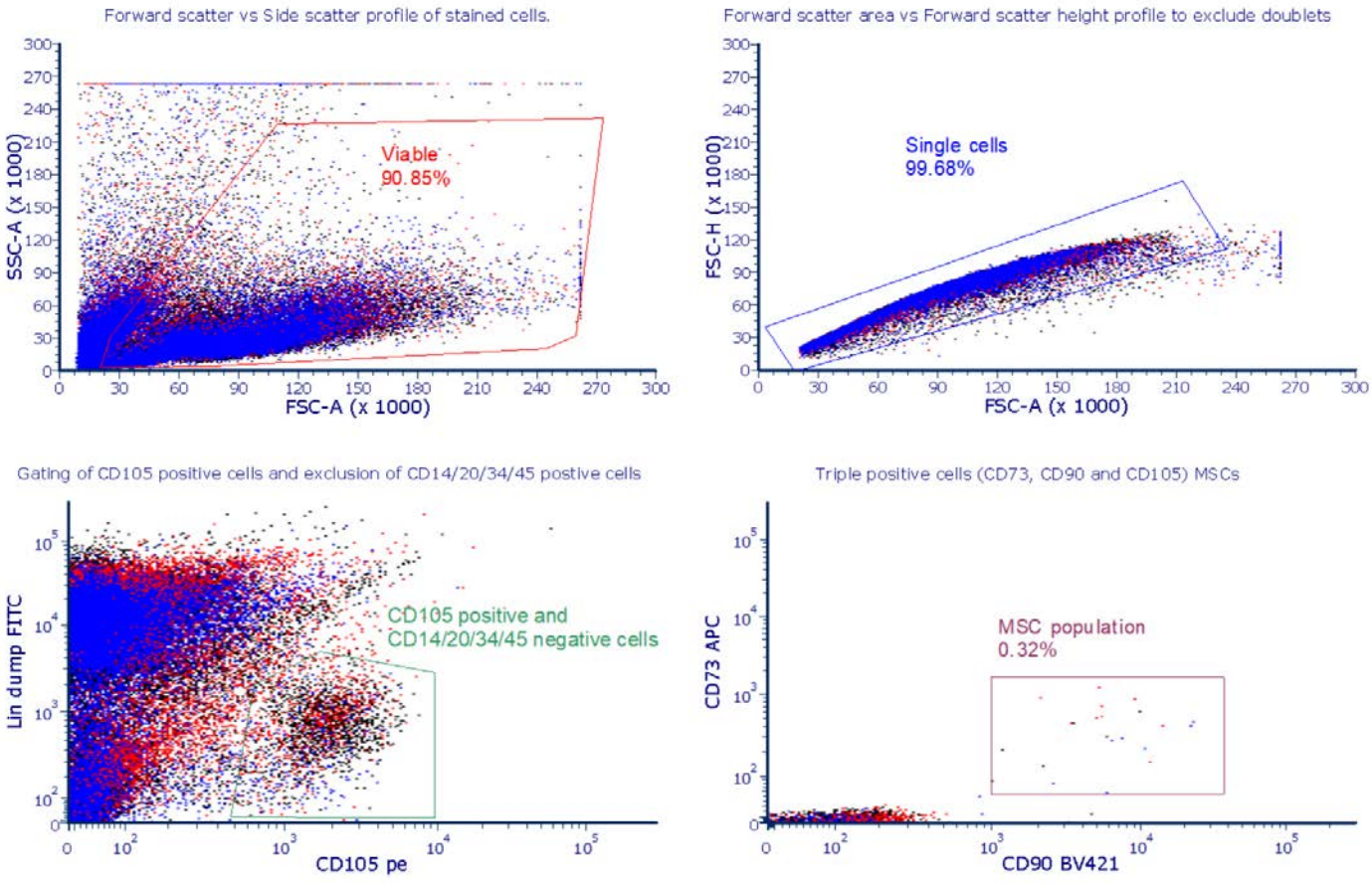

Figure 85 Schematic representation of the sorting process using the BD FACSAria fusion sorter: TOP LEFT cells are sorted on the basis of side and forward scatter dead cells and debris are eliminated. These cells then pass to the TOP RIGHT where cells are sorted using forward scatter height and area, cells joined together are excluded. The sorted single cells are then analysed on the BOTTOM LEFT graph, cells are sorted based on antibodies conjugated with fluorophores: cells positive for CD105 and negative for 14/20/34/45 selected and processed on the BOTTOM RIGHT graph which selects only those cells positive for CD73 and CD90. The sorter then sorts single live cells which are positive for CD73/90/105 and negative for CD14/20/34/45 on to the 96 well plates.

The initial sort resulted in relatively poor sorting results *(see Table 30)*, this was likely due to the thawing process, the incubation processes and the time taken to sort resulting in some samples spending more time in PBS at 4°C awaiting sorter availability after going through the protocol. This resulted in greater cell death and although "live cells" were sorted on to the plate apoptotic pathways had most likely been initiated leading to cell death and upon staining and imaging, no viable cells were present or available to analyse.

	Number of cells sorted	
	First sort	Second Sort
Femur 1	301	
Hip 1	183	
Hip 2	139	
Hip 3	121	
Hip 5	46	244
Hip 6	30	
Hip 7	15	
Hip 8	45	1300
Hip 9	33	668
Hip 10	105	
Hip 11	317	
Hip 13	434	

Table 30 Results of MSC cell sorting on BD FACSAria Fusion.

Due to the poor results, the sorting step was repeated the following day as samples allowed. On this occasion, only a small number of samples were processed rather than batch and then sorted immediately after the staining protocol had finished. On this occasion the results were more promising in terms of cell numbers, however, after allowing the cells to bed down for 24hrs and completing the mitochondrial protein assay there were no viable cells to image or analyse when viewed using the Zeiss Axio-observer LSM800/SDI Microscope or Zeiss Celldiscoverer 7 Microscope.

A further repeat run was performed, and, on this occasion, samples were all processed in an individual manner, this limited the time of defrosting, processing and subsequent time to flow cytometry sorting. The results of this sort can be seen in *Table 31.* Although this individual preparation method improved the yields of cells, with improvement seen from the first sorting results, the end results were the same and no cells survived to be imaged using the CD7 microscope.

	Cells sorted
Femur 1	168
Hip 1	575
Hip 2	198
Hip 8	167
Hip 9	1000
Hip 9	1000
Hip 13	437

Table 31 Further sorting results of MSCs using the BD FACSAria Fusion.

4.6.2 Impact of freeze-thaw cycles on cells.

The impact of freezing cells after the lymphoprep step and then subsequent thawing causes significant injury to the cell lines and lead to apoptosis in many cases. The yields of cells from the MSCs sorting step were subjectively reduced from when cells were sorted fresh and objectively when cells were isolated from cultured MSCs, however, in this case, the density of MSCs is significantly greater and not a straightforward comparison with the isolated mononuclear cells from the lymphoprep step.

Work in human embryonic stem cells using conventional freezing methods with slow cooling protocols and cryoprotectant (10% DMSO) as employed after the lymphoprep separation of cells showed that on returning cells to 37 °C there was an increase in cell death compared with keeping cells at 4°C (348). This would explain the results showing cells sorted as “viable” on flow cytometry but dying when on the plate. Both the cytometer and plate were run at 37°C which was presumed would enhance cell viability.

Specifically in relation to MSCs most collection processes and freezing protocols relate to the *ex-vivo* expansion of cell cultures prior to freezing steps, here yields and the impact of the freeze-thaw process was less of a significance (349). However, Chatzistamatiou et al., (350) compared various methods of MSC collection and freezing of cells taken from Wharton’s Jelly. Cells, which were frozen in the tissue, had very poor results in terms of frozen yields compared to cells taken from fresh tissue.

Results were also extremely poor in those cells which were extracted using enzymatic digestion and then were frozen. After 1 month of freezing no cells were viable. This was thought to be due to the prolonged and successive stresses of enzymatic digestion and freezing. The conclusion of this paper

found optimum MSC viability and collection was found to be by processing cells and expanding populations prior to cryopreservation (350).

Unfortunately utilising this method was not possible as part of the protocol for analysing mitochondrial defects. Varying division rates dependent on mitochondrial defects could not be guaranteed between cells and could lead to dilution of cells with mitochondrial defects.

4.6.3 The effect of flow cytometry on cell viability.

Flow cytometry whilst an efficient method to identify and sort rare subpopulations does have some drawbacks. Cells must, of course, be in suspension, they are then subject to pressure effects, potentially passing through undersize nozzles creating stress which can lead to cell death (351). Cells which are too large for the nozzle can affect the stream and lead to fanning; where the stream is unstable and leads to a spray at a variety of angles and not necessarily into the collection vessel. Utilising larger nozzles can also reduce the pressure at which cells run at which again can improve viability as can running cells at a lower rate as this reduces the shear forces upon the cells (352). Other factors which may affect viability relate to the sample storage pre-sort – viability can be improved by sorting at an optimum temperature for the cells however when the cells are in suspension and waiting to be sorted there is no incubation which may lead to a decrease in the viability of the cells (353).

Once in the cytometer and stream, there is a risk to cells as they are exposed to radiation across the visible light spectrum and ultraviolet spectrum which can cause damage and change (354). Flow cytometry sorting has also been shown to have harmful effects upon certain cell lines and viability was found to be compromised in a human monocytic cell line (355).

4.6.4 Utilising a fresh sample

The factors affecting cell viability in terms of flow cytometry sorting are potentially slightly modifiable but inherently flow cytometry sorting remains a significant stressor to cell survival. An easier modification of the protocol would be to use fresh samples. This would remove the freeze/thaw cycles and damage to cells and compromising effect upon cell viability and survival.

Ideally, the patient selected would be a young patient as MSC density is higher in these samples (356, 357). However, due to timings and logistics, a 72-year-old female undergoing a hip hemiarthroplasty

for a fractured neck of the femur with an abbreviated mental test score of 10 was deemed suitable to consent and to take samples.

Samples were collected as per normal procedure at the time of femoral preparation. They were then taken straight to the lab and mixed with sterile PBS as per the *lymphoprep protocol 2.4.2.1.* After this step, the cell pellet was resuspended in PBS and stained for 1 hour with the MSC sorting antibodies. This was followed by a wash step; the cells were then sorted into a 96 well plate containing media at 37°C. After sorting the cells were spun at 150g for 1 minute. They were then placed in the incubator and allowed to bed down for 24 hours.

After this point, the cells were then stained using the optimised protocol. In addition to the patient samples, a wildtype and deficient fibroblast line were used again as above as means of controls. In total 1000 of the patient cells were sorted into one well and a further 50 as no primary controls were also sorted. The images and results can be seen below. These were taken with the Zeiss CD7 Celldiscoverer microscope for analysis and also the Zeiss Axio-observer LSM800 microscope for higher quality images *see Figure 87 and Figure 88.* In terms of locating the cells, the CD7 was used in overview mode using the DAPI nuclear stain to identify cells *see Figure 86*. These positions once identified as cells rather than debris were then imaged at 40x. The same settings were used to image areas of the wildtype and deficient fibroblast cell lines in tile mode as in Figure 87.

Figure 86 Overview scan results showing single sorted MSC cells as well as cellular debris in a single well of a 96 well plate - taken with the Zeiss CD7 Celldiscoverer microscope at 2.5x.

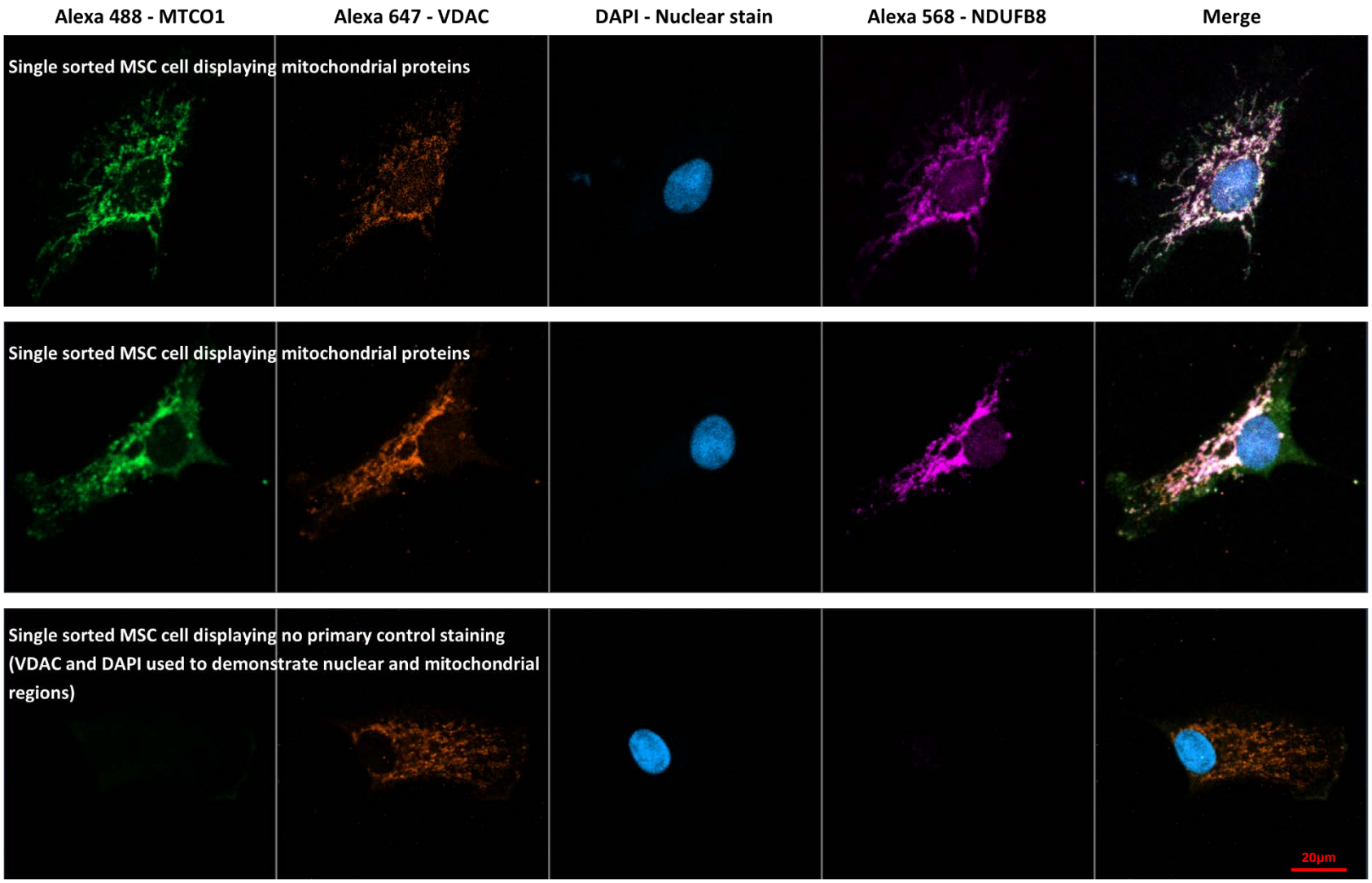

Figure 87 Images of single sorted MSCs taken at 40x using the Zeiss Axio-observer LSM800. Top two rows depict MSCs, and the bottom row show a no primary control cell stained with only VDAC and DAPI primaries.

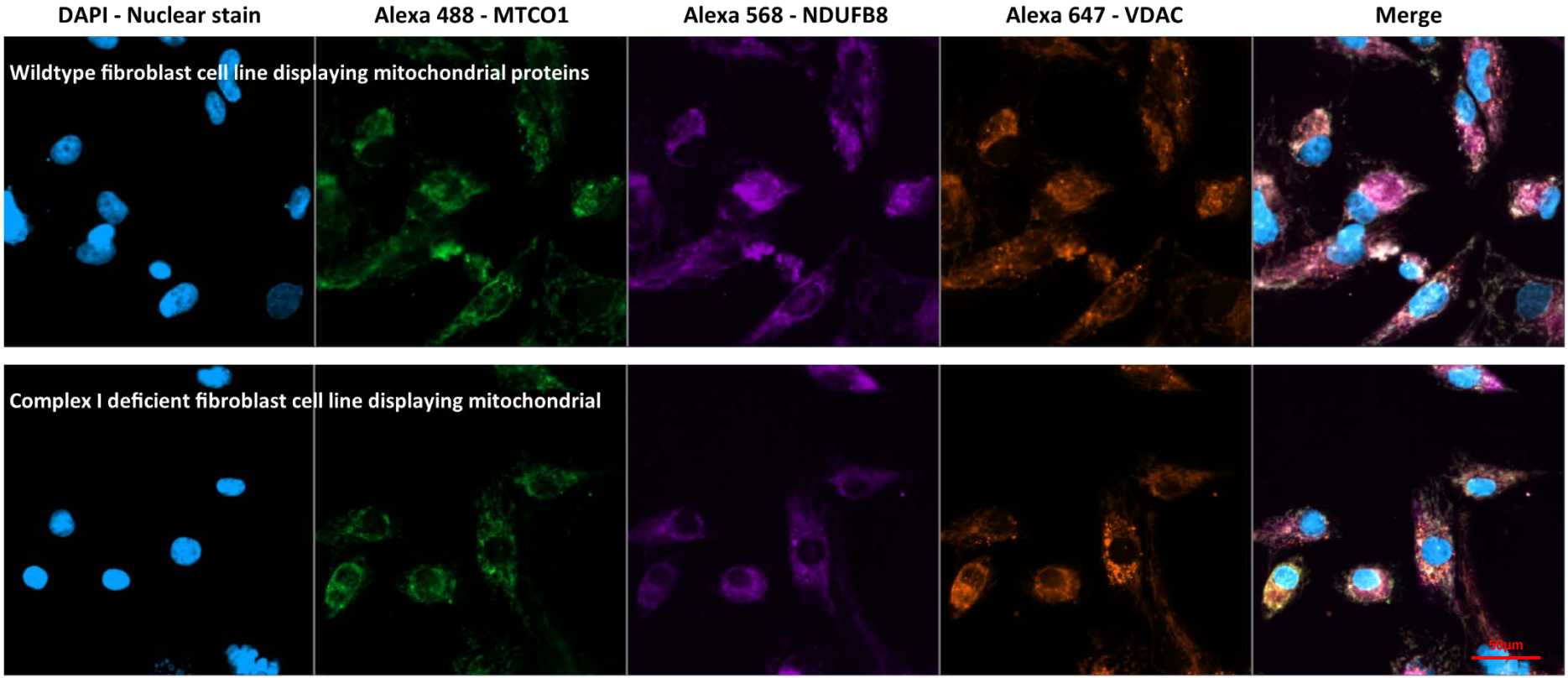

Figure 88 Images of wildtype and complex I deficient fibroblasts used as controls at the same time as the MSC experiment as seen in figure 87.

4.6.5 Fresh sample results.

By utilising a fresh sample, it was possible to analyse 88 cells for mitochondrial protein deficiencies by measuring signal intensities of fluorescent secondary antibodies bound to VDAC, NDUFB8 and MTCO1. The results of this analysis are seen below. This can be compared to the values of the wildtype and complex I deficient fibroblast cell lines.

Utilising the python programming language and R code linear regression was performed based upon correction for mitochondrial mass. Cells which were not within the 95% predictive intervals are highlighted in *Figure 89* Linear regression model showing VDAC mean values compare to complex I and complex IV mean values. MSCs which lie outside the 95% predictive intervals are highlighted. . There is a collection of deficient cells which lie outside the confidence intervals of both complex I and IV (MSCs 8, 20, 32), whereas the MSCs 11 and 39 are only deficient in complex I and IV respectively.

Complex IV deficiency (cytochrome c oxidase) in colonic crypts for patients in the 70th decade varied from 1.70% to 27.90% (19) this would correlate with the values seen here where a value of 4.55% of mesenchymal stem cells had complex IV deficiency. In the paper by Taylor et al., 2003 they modelled the data from the research demonstrating a mean percentage increase in cytochrome c oxidase deficiency crypts with advancing age. Complex I deficiency has also been demonstrated in motor neurones by Rygiel et al., (358). In the cohort of patients studied (70-99 years) complex I deficiency was around 10%.

Whilst these increases and trends cannot be demonstrated on one patient alone, the values found in the 72-year-old patient do correlate with the model by Taylor et al., and Rygiel et al. In an ideal scenario, the experiment would have been performed upon all of the original patient cohort with matched PCR and CyToF data. However, the effects of freeze/thawing the cells and storage at -80°C impacted on viability and prevented this.

This experiment and assay does prove that it is possible to take individual stem cells from a patient and demonstrate individual cell respiratory chain deficiency, but the assay has significant effects upon cell viability.

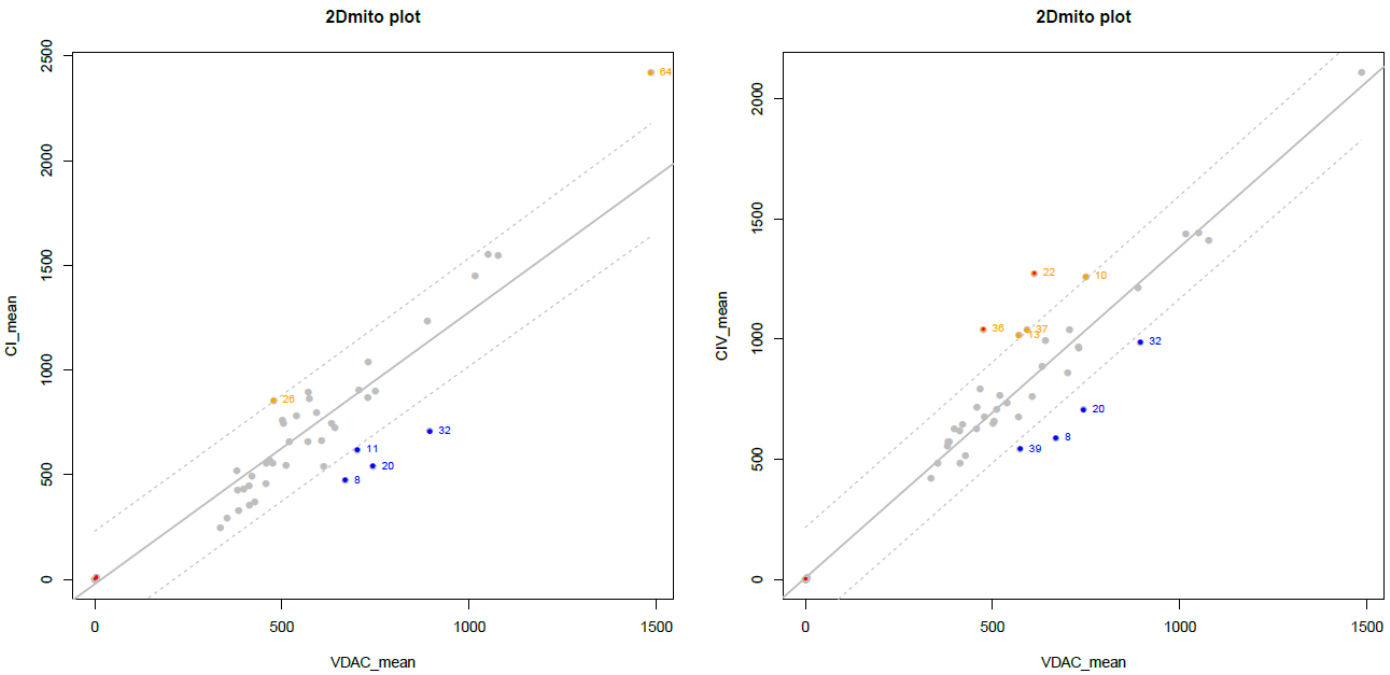

Figure 89 Linear regression model showing VDAC mean values compare to complex I and complex IV mean values. MSCs which lie outside the 95% predictive intervals are highlighted.

Figure 90 Results of the complex 1 deficient fibroblasts clearly demonstrating a deficient population in red for complex 1

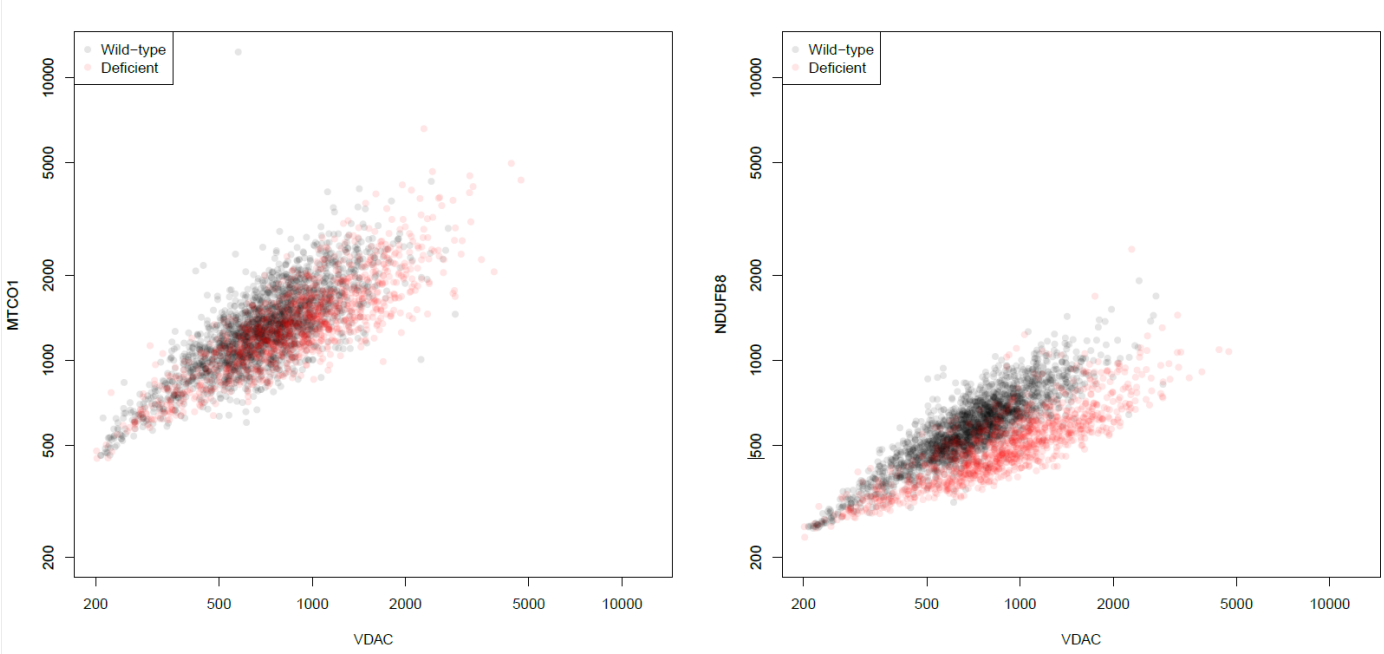

NDUFB8 signal compared to the similar distribution of complex 4 (MTCO1) when compared to the wildtype fibroblasts.

4.7 Discussion

Accumulation of somatic mitochondrial DNA mutations occurs with increasing age (19) mitochondrial DNA is also prone to large-scale deletions and these are also known to increase with age (191). A mouse model has shown that the accumulation of these deletions leads to age-related OXPHOS dysfunction in certain cell lines (192). There has been no documented evidence of mitochondrial deficiency in MSCs only evidence of mitochondrial respiratory chain protein deficiencies in their progeny cells - osteoblasts in mice (205). Attempts to repeat the work of Dobson et al., resulted in high levels of autofluorescence and detection of osteoblasts proved difficult with only osteocytes available for reliable identification due to location within the cortical bone and their shape. This led to the development of an alternative assay and experiment. Autofluorescence in bone is a well-documented issue (359-362). Bone mainly contains type 1 collagen fibres. Type 1 collagen fibres were shown to emit luminescence between 400nm-700nm of the electromagnetic spectrum (361) the most intense luminescence is seen when collagen is hit with ultraviolet wavelength light (362). The secondary antibodies utilised in the assay by Dobson et al., were conjugated to Alexa Fluor 405, 488, 546 and 647nm these all correlate with the emission spectra of collagen 400-700nm.

Autofluorescence is also dependent on mineralisation levels (360), which decline with osteoporosis, However newer osteons and younger bone which has rapid turnover have lower autofluorescence than aged bone which tends to accumulate autofluorescence near the central canal (362). Osteoblasts themselves also exhibit autofluorescence further compounding the problem (363). These multiple factors meant that conventional fluorescence-based microscopy of tissue samples was not appropriate. As a result, single MSCs were analysed independently to avoid the issues around the mineralised matrix causing autofluorescence.

The development of this assay has gone through numerous phases which underlines the difficulty to analyse MSCs from patients without the distortion of expanding their numbers through culture. As highlighted previously MSCs are a rare cell type and one that declines with age (356, 357). The isolation processes and preparation of cells for the staining and mitochondrial analysis protocol all cause damage and or the loss of MSCs from the analysis pool.

The first steps taken were to use flow cytometry this would isolate the single MSCs and potentially osteoblasts from the bone marrow and remove the auto fluorescent properties that are present in bone sections. The difficulty in utilising flow cytometry was the variability in results and ultimately flow cytometry gives no visual representation of staining. Autofluorescence and background staining

most likely contributed to varying results despite altering the assay and taking steps to reduce this. Without imaging, it was clear that the staining of cells could not be trusted or optimised, and a technique first had to be developed based on imaging.

Use of the Zeiss Celldiscover 7 microscope would allow rapid acquisition of images and steps taken in the optimisation of the flow cytometry assay could be employed here. Ultimately however the issues encountered in the fibroblasts utilised and ultimately the MSCs would be of antibody choice. The rabbit species NDUFB8 has not been utilised in published work for immunofluorescence and is not one used in the group, but this gave much-improved differentiation and imaging in comparison to the mouse monoclonal antibody, which took a lot of optimisation and extra steps to improve results.

With an optimised assay for mitochondrial protein analysis, the end results relied on the survival of cells. As alluded to the freezing and thawing of cells in combination with the flow cytometry sorting assay had significant effects on cell viability with only 8.8% of sorted cells surviving and allowing analysis.

However, despite the shortcomings of cells surviving the MSC isolation step the work in this chapter confirms that it is possible to take single MSCs from patients and analyse these for mitochondrial protein deficiencies. This experiment must be done under strict conditions to prevent loss of cells and reduced cell viability with freeze/thaw and storage of cells ultimately resulting in lowered viability and cell depth before completion of the experiment.

Unfortunately, the collection of samples over a period of months did not allow synchronous experiments to take place so bone marrow samples were frozen and stored to be analysed at the same time. This process caused damage to the cells which combined with the harsh effects of flow cytometry and or the mitochondrial staining protocol led to the death of these cells, ultimately preventing analysis of the cohort of patients used in the other chapter's results.

Steps to tackle this for future experiments could rely on control cell lines as used in the *Mitochondrial Diagnostic* laboratory service at Newcastle University. It is not feasible to process or collect all samples at the same time and so benchmarking each individual test against a control is the necessary step that would be required to demonstrate deficiency levels across an age varied population and ultimately see if the results of mitochondrial respiratory chain deficiency correlate with those changes found in other cell lines as well as mesenchymal stem cells.

4.7.1 Conclusion

The completion of this experiment and body of work leading to the development of the assay has demonstrated the ability to detect mitochondrial deficiency in MSCs as detailed above. It would be plausible and possible to complete this assay across a range of patients and age groups to see if the results corroborate the evidence found by Taylor et al., and Rygiel et al., supporting the mitochondrial theory of age-related respiratory chain deficiencies occurring.

Importantly this assay has also demonstrated a detectable difference in the fibroblast control cell lines using a rabbit monoclonal antibody. Previous work as highlighted in this chapter has found distinguishing complex I deficiency between wildtype and deficient cells poor. This has been tried across a number of primary antibodies, secondary antibodies and experimental conditions. The control fibroblast cell lines are easy to expand in culture and readily available. They can be utilised in conjunction with the staining protocol and antibodies developed in this chapter in drug and treatment development.

4.7.2 Future work

Ultimately the question remains to be answered, do MSCs accumulate mitochondrial protein deficiencies with age? Therefore, the logical step would be to repeat the now optimised assay across an age range of patients against benchmark cells to ensure the reliability of the test. There is also likely room to improve the assay further and optimise the yield of viable MSCs by altering the time from *in-vivo* collection to sorting into culture medium and plate and the temperatures at which this occurs.

Work in the other chapters will investigate the patient cohort for evidence of mitochondrial DNA mutations in the MSC population as well as analysing osteoblasts ex-vivo using time of flight cytometry to quantify mitochondrial respiratory chain protein deficiencies.

Chapter 5 - Imaging Mass Cytometry

5.1 Introduction

Flow cytometry emerged in the 1960s and development occurred over the following decades to expand the number of channels that could be measured to five or more simultaneously (364) although the number of parameters that could be measured was limited. Mass cytometry or CyToF – cytometry by time of flight, on the other hand, is a method for measuring single-cell properties much like flow cytometry but instead of relying on the fluorescent spectrum, it relies on measuring the time of flight determined by the mass of the molecule/antibody coupled protein. Unlike flow cytometry, it is not bound by the constraints of the fluorescent spectrum and so a great number many more parameters (up to 45) can be measured without signal overlap (239). Mass cytometry is reliant on the use of stable non-radioactive isotopes of rare earth metals typically lanthanide metals which are coupled to antibodies instead of fluorescent probes. These probes are detailed in 5.3.4.2 Antibody conjugation. It can measure up to 1000 individual cells per second and sample preparation is similar to conventional flow cytometry (365).

Instead of passing a stream of cells across a laser and detector setup as in flow cytometry, mass cytometry uses an inductively coupled plasma torch to vaporise the sample creating a cloud of elemental ions these ions are passed through a quadrupole to filter out low molecular weight ions and then the relative abundance of each ion is measured and quantified to correlate with the antibody target (365).

Importantly as CyToF is reliant on mass, not fluorescence there is no issue with autofluorescence (366), autofluorescence has been an issue in both the quadruple immunofluorescent assay and the use of flow cytometry, it is important to note that it is still possible for signal spill over into adjacent channels. It also doesn't require compensation like flow cytometry. However, there are increased costs and loss of cells during sample preparation, it is also relatively slower than flow cytometry in terms of cell throughput (366).

Mass cytometry has been conventionally used in improving the understanding of the lymphoid system and immunology to look at 25 parameters of cells which are in suspension (367). Experiments such as this have increased the recognition of the diversity and complexity of cellular networks allowing the categorisation of cell subpopulations, hierarchies, and developmental pathways (368). Giesen et al., (369) combined mass cytometry with a high-resolution laser to ablate breast tissue in place of the inductively coupled plasma torch. This ablated and vaporised tissue was then treated

much the same as the vaporised cells used in suspension mass cytometry by passing into the cytometer in a plume of inert gasses. The X and Y coordinates of each laser ablation spot were recorded and then these parameters combined with the antibody measurement profiles to reconstruct an image. These images have a resolution comparable to light microscopy but have the high content of mass cytometry (370).

5.2 Aims of experiment

This investigation aimed to analyse osteoblast *ex-vivo* within samples of bone preserving the tissue architecture. These results will then be compared to the mutation load identified on PCR experiments, bone formation capability of differentiated osteoblasts, MSC complex I and IV mutation load and patient demographics.

5.3 Methods Development

5.3.1 Immunofluorescence protocol for detecting mitochondrial deficiency in osteoblasts.

Initially, this investigation aimed to identify osteoblasts ex vivo in tissue sections in humans as done in the assay by Dobson et al., (205). Samples were gained from hip and knee arthroplasty and then decalcified as per *2.4.1 in chapter 2.* Quadruple immunofluorescent staining was then carried out upon these slides following the protocol by Dobson et al., this protocol had been optimised to take into account the autofluorescence encountered when imaging bone with confocal microscopy. Issues, however, were encountered in identifying osteoblasts and mitochondrial deficiency.
Some of these were related to sampling location and also the collection method of the samples. Initial samples were taken from the template cuts off total knee replacement surgery. This was abnormal diseased arthritic bone with subchondral sclerosis and limited marrow or osteoblast activity. Other sections of bone were taken from the femoral neck at the time of total hip surgery. To gain access to this area an oscillating saw is used to remove the femoral head. It is hypothesised that thermal necrosis and damage associated with the saw was disrupting tissue architecture and making imaging more challenging than the previous mouse work where whole femurs could be fixed, decalcified and embedded on slides to be cut with the microtome. Thermal necrosis has been shown to have a significant effect up to 0.74mm from the cutting surface but this was dependent on the speed and force applied when using the saw. Necrosis was evident by disruption of architecture and empty lacuna (371). When getting the femoral neck samples a preliminary cut to remove the femoral head was made and then a definitive cut for the prosthesis. This leaves a wedge of bone around 5 millimetres or more in thickness. The sawn surfaces would be at risk of thermal and mechanical damage but by using sections cut deeper and towards the middle of the tissue this was avoided. No

primary controls staining only for Osteocalcin are demonstrated below in *Figure 91*. A section near the surface shows disruption of architecture and empty lacuna in comparison to the deeper section with clearly marker osteocytes.

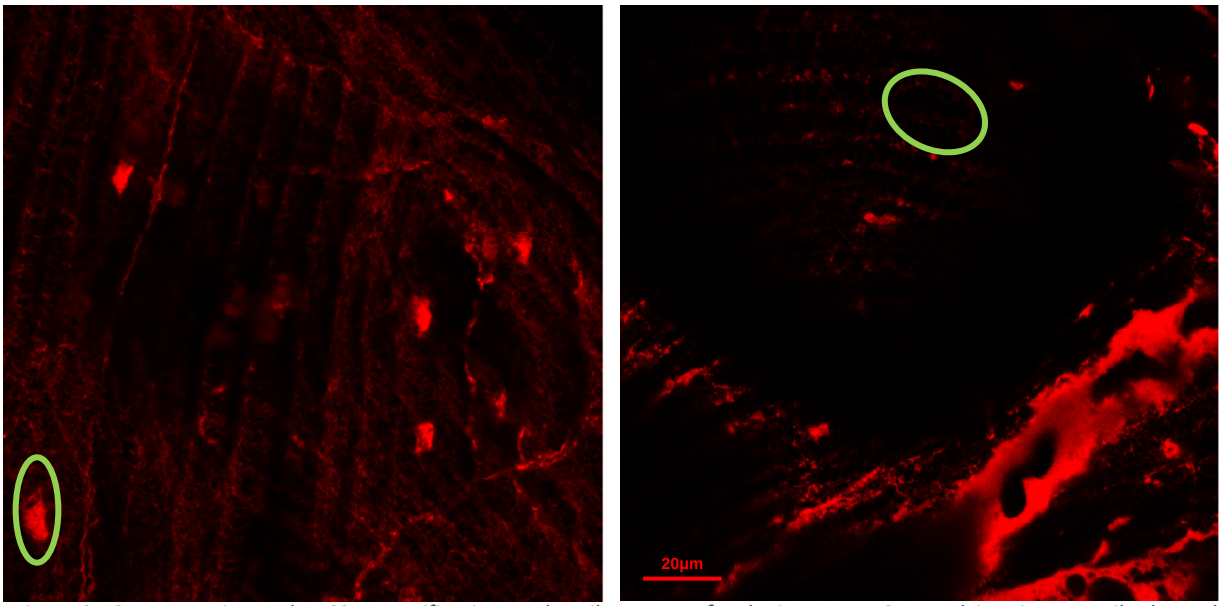

Figure 91 Osteocytes imaged at 60x magnification on the Nikon TIE confocal microscope. Osteocalcin primary antibody used with Alexa 546 secondary. On the left-hand image taken from deeper within the section osteocytes within lacuna are visible as marked in the green oval. The trabecular lines are also clearer whereas on the right-hand image taken from the surface of the tissue section there are empty lacuna (green oval) and disruption of the tissue architecture with discontinuity between the trabecular lines.

5.3.2 Fixation and Decalcification protocol

Once samples were trimmed and placed in tissue cassettes, samples were fixed in 4% PFA for 72 hours followed by a dH_2O wash. Afterwards, decalcification took place; decalcification of bone can be performed via immersion, sonication, microwave, ion-exchange or electrolysis. For this research, I used an immersion technique. Several solutions can be used for immersion decal see *Table 32*. In this research Formical 2000 and 14%, tetra EDTA buffered to pH 7.4 was used. The Formical 2000 protocol was based on the manufacturer's guidelines and the EDTA protocol was based on the handout from the National Society for Histotechnology Annual Symposium 2011 on processing bone (372). Optimisation of the decalcification process had taken place in the mouse model and is detailed in the paper by Dobson et al., (205). The EDTA method was found to give the best results in terms of auto-fluorescence and preservation of the structure.

Formical 2000 solutions were kept at room temperature for 24 hours, whereas EDTA solutions were kept in the fridge at 4°C on a rocker and the solution was changed for fresh on Mondays, Wednesdays and Fridays for 21 days. Following these samples were washed with distilled water and taken for paraffin embedding. In the literature, EDTA was found to preserve the architecture of the

bone best whilst giving the best immunohistochemistry results (373). Formical/formic acid decalcification gives a quicker decalcification but causes increased autofluorescence(372). It was used for the accelerated decalcification initially at the expense of increased autofluorescence.

Immersion Method	
Type of decalcification solution	Total number of days for decalcification
Surgipath I (formic & Formaldehyde)	9
22% Formic acid/10% Sodium Citrate	13
Cal-Rite (formic & Formaldehyde)	9
4% Formic acid/4% Hydrochloric acid	13
50% Rapid Decalcifier (HCl)	4
25% Rapid Decalcifier (HCl)	2
Surgipath II (HCl/EDTA)	4
Nitric Acid	7
EDTA pH 3.2	Did not decalcify after 40 days
EDTA pH 7.0	40
EDTA pH 10.3	16

Table 32 Comparison of different solutions for immersion-based decalcification(373).

5.3.3 Imaging and analysis

Images were taken using a Nikon A1 confocal microscope at 60× optical magnification with a 1.55× digital magnification applied, using solid-state lasers to provide light at the following wavelengths 405, 488, 546 and 647 nm.

Image analysis was performed on Imaris image analysis software (Bitplane, v.8.4). Using the 405nm channel, the mitochondrial mass was identified in areas positive for the VDAC antibody in those cells which were positive for osteocalcin (546nm).

The software was then used to measure the average intensity value of these positive areas in the VDAC (405nm), Complex IV/MTCO1 (488 nm) and Complex I/NDUFB8 (647 nm) channels. No primary controls were used to calculate background signal intensity for the 405, 488 and 647nm wavelengths in osteocalcin-positive cells.

As expected, the samples that were decalcified in Formical showed increased levels of autofluorescence when compared to those using the EDTA decalcification technique. Although the EDTA decalcified specimens still showed significant levels of autofluorescence, it improved on the previous mouse work. This meant distinguishing osteoblasts that should be located at the endosteal and periosteal borders of cortical bone extremely difficult. Osteocytes which are mature osteoblasts

which have become embed and isolated in the secreted matrix were obvious and were able to be imaged but autofluorescence remained an issue. Cancellous bone taken from total knee replacements and used initially for analysis did not reveal significant numbers of osteocytes or blasts when viewed on the confocal microscope. As a result, and coinciding with the tissue culture results attention was turned to proximal femur samples and cortical bone from the femoral neck. These samples did show osteocytes but not definable osteoblasts.

Interestingly collaboration with an MRC fellow from the University of Nottingham looking at proximal tibia bone marrow lesions in total knee patients demonstrated osteoblasts and osteoclasts around these lesions and was more identifiable within surrounding cancellous bone see *Figure 92*. Non-cystic bone marrow lesions are associated with osteoarthritis and are present in 75% or more of total knee replacement patients. These lesions were identifiable on sections and so acted as targets to locate osteoblasts and osteoclasts.

Using data acquired from confocal imaging and Imaris analysis of average intensity levels of osteocytes from femoral neck samples and bone marrow lesion samples showed no clear trend as would be expected reviewing the previous mouse model and published data by Dobson et al. Here a clear relationship was seen between COX-I and NDUFB8 deficiencies in the mutated mouse. As can be seen in *Figure 92* there is no clear relationship between mitochondrial mass (VDAC) and COX-I or NDUFB8. There is also no clear relationship between COX-I and NDUFB8, as mitochondrial DNA mutations accumulate phenotypical protein expression of the respiratory chain would occur. it would, therefore, be expected as complex I mutations accumulate so too should complex IV mutations. In the samples as below, no such relationship was seen. Fundamentally, the issues are twofold. There are no control samples from young patients who would not have accumulated mitochondrial mutations as in the mouse model. The levels of autofluorescence seen in human bone exceed those of the mouse and sample collection and processing differs making imaging more difficult. As can be seen in

Figure 93 when the average background fluorescence from the no primary controls for each section was subtracted (matched samples) from the stained sections some background fluorescent intensity signals exceeded the specific signal resulting in negative results.

Discussion with the authors of the paper on the mouse quadruple immunofluorescence assay (Dobson et al.,) felt the assay was optimised and could provide no further alteration to reduce the levels of autofluorescence.

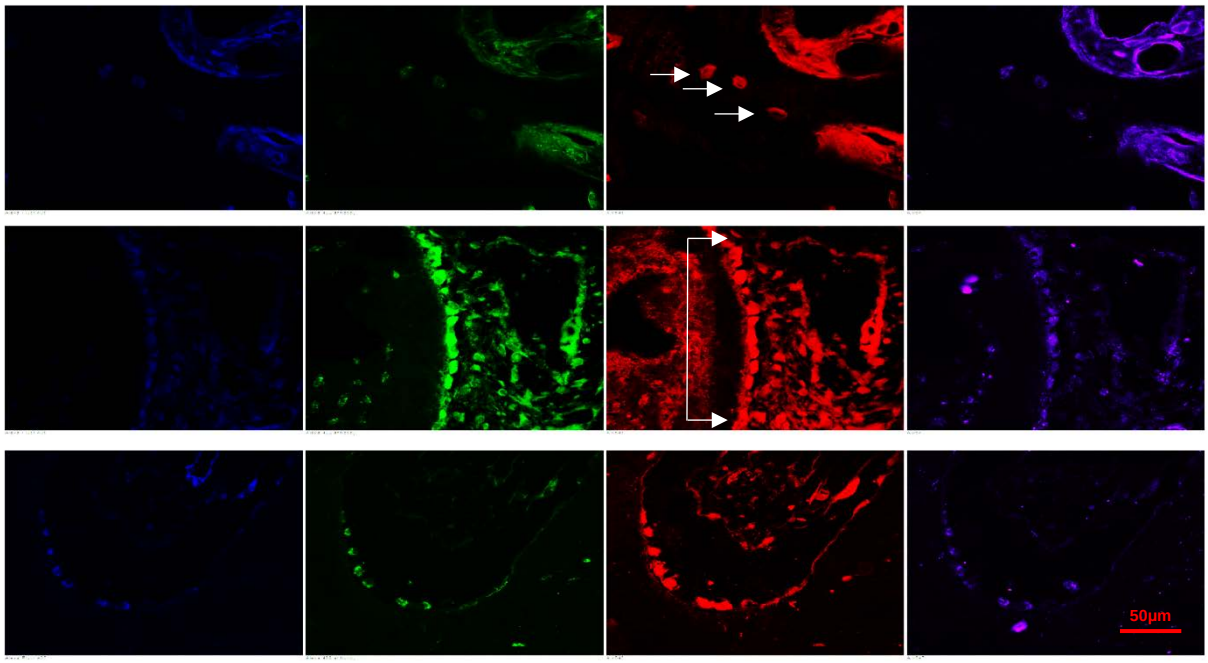

Figure 92 Application of quadruple immunofluorescence assay to human bone 90x magnification: First-row Osteoblast imaging in the hip. Second-row osteoblast imaging in bone marrow lesion of the proximal tibia. Third-row osteoclast imaging in bone marrow lesion of the proximal tibia (Osteocalcin substituted for cathepsin K). Cells marked by the white arrows. Auto fluorescent signal and background levels are high despite imaging configuration optimisation.

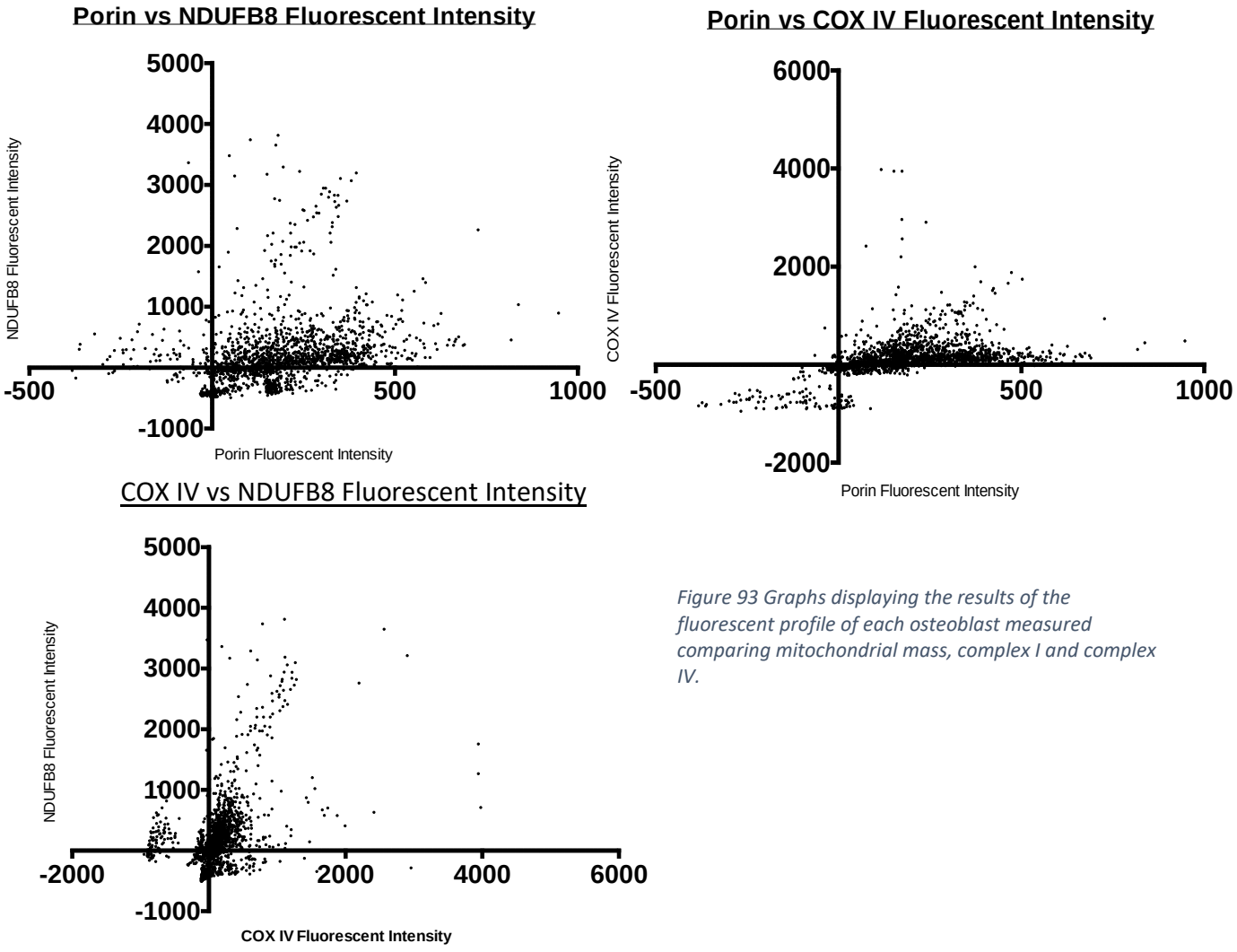

Figure 93 Graphs displaying the results of the fluorescent profile of each osteoblast measured comparing mitochondrial mass, complex I and complex IV.

Autofluorescence in bone is a well-documented issue (359-362). As documented before in the discussion of chapter 4 there are a number of factors preventing adequate imaging on bone using quadruple immunofluorescence. Such as the autofluorescence of collagen and varying autofluorescent profile dependent on mineralisation and metabolic activity or bone remodelling.

Analysing whole organ tissue with more than five markers is extremely difficult in skeletal tissue as most preparation methods lead to disruption of tissue architecture and cause autofluorescence (359). There are also issues in the presentation of specimens for analysis. Thicker sections lead to more light scatter and autofluorescence and uniformly cutting sections with the same thickness also can prove more difficult than softer tissues (359).

These unpredictable characteristics of human bone make meaningful analysis and detection of osteoblasts and mitochondrial deficiency unreliable and difficult. After trialling several steps to improve the background autofluorescence signal in the bone a more suitable technique was sought out.

Imaging mass cytometry is a method for measuring protein abundance in single cells, much like quadruple immunofluorescence, but is based on mass cytometry instead of immunofluorescence and so autofluorescence is avoided entirely. Imaging mass cytometry (IMC) is a recently developed technique which uses laser ablation of cells on sections combined with Time-of-Flight Inductively Coupled Plasma mass spectrometry (ICP-MS) technology to measure the ions from each cell. Mass cytometry relies on the use of stable non-radioactive isotopes of rare-earth metals, typically lanthanide metals which are coupled to antibodies instead of fluorescent probes. The other major advantage of the mass cytometry technique is that it allows for the simultaneous measurement of a greatly increased number of antibody targets in a single section compared to conventional immunofluorescent techniques (374).

Proteomics is also a recently emerging field of bone investigation over the last 10 years. Osteoproteomics techniques have initially focused on extracellular matrix proteins, MSC renewal and the processes of osteoblastogenesis and osteoclastogenesis (375-377). More recently there has been further research into intracellular signalling via microvesicles or exomes from osteoblasts again this has been related to osteoblastogenesis signalling pathways (378). Proteomics has allowed the discovery of new proteins relating to bone turnover, linking hormones and cytokines to the activity and proliferation of osteoblasts and osteoclasts. More specifically work relating to mitochondria has shown links to osteoblastogenesis and mineralisation but not directly to age-related respiratory chain deficiency in osteoblasts. Michaletti et al. (379) related mitochondrial respiratory chain dysfunction and osteoblast dysfunction due to microgravity. This work was performed concerning induced osteoporosis experienced by astronauts due to a lack of physiological loading. Whereas Baroncelli et al., (380) showed MSCs treated with osteogenic inducers depositing extracellular matrix related to osteoblastogenesis were shown to have upregulated mitochondrial proteins, suggesting the process of osteogenic differentiation is a high energy demanding process.

Whilst proteomics does allow multiple protein analysis, in comparison to IMC, there are drawbacks. There is no spatial component to the output of the data, in IMC proteins are detected in relation to their position within the tissue and intensity values enable post-analysis tissue differentiation. IMC,

therefore, creates an unbiased proteomics technique by not requiring pre-orientation of the analysis (381). Some proteomic techniques analysing bone have been based upon laser microdissection analysing nanoscale 5µm sections at a time (375), but are largely based upon homogenised tissue limiting the structural analysis of the tissue. IMC as highlighted able to analyse tissue at 1mm2 per hour from ablation of tissue. This allows single-cell analysis and the potential to quantify the heterogeneity within a tissue, which for stochastic processes like ageing and mitochondrial disease progression can be an informative component of the phenotype.

Imaging mass cytometry would prove to be the logical solution moving the research forward.

5.3.4 Hyperion Imaging Mass Cytometry

Imaging mass cytometry using the Hyperion module in addition to the Helios mass cytometer allows the analysis and imaging of bone without the issues of autofluorescence which has been such a significant factor in imaging-based studies of bone in this research and prior immunofluorescence investigation in the bone. DAB and other immunohistochemical stains not based upon fluorescence only allow single antibody staining.

5.3.4.1 Hyperion Antibodies

Unlike the antibodies used in the quadruple immunofluorescence assay antibodies used in mass cytometry were conjugated so there was no primary-secondary antibody step. Although there are conjugated antibodies available the majority of these are targeted and immunology-based cells and proteins. To target mitochondrial proteins and osteo-lineage cells antibodies therefore had to be conjugated to the metal lanthanides.

Concurrently in the Wellcome Centre for mitochondrial research, Dr Charlotte Warren was preparing samples of muscle to test the suitability of the Hyperion imaging mass cytometry system to assess mitochondrial protein deficiencies. The antibodies conjugated for the study of osteo-lineage cells and protocol optimisation are listed below:

Anti-cathepsin K IgG rabbit	Santa-Cruz
Anti-Osteocalcin IgG rabbit	Santa-Cruz
Anti-MT1-MMP mouse	Merck

The antibodies conjugated by Dr Charlotte Warren were:

Anti-SDHA IgG1 mouse	Abcam
Anti-TOM20 IgG mouse	Abcam
Anti-NDUFB8 IgG1 mouse	Abcam
Anti-OSCP IgG1 mouse	Abcam
Anti-NDUFA13 IgG2b mouse	Abcam
Anti-VDAC1 IgG2b mouse	Abcam
Anti-COX4+4L2 Ig2a mouse	Abcam
Anti-MTCO1 IgG2a goat anti-mouse	Abcam
Anti-UQCRC2 IgG1 goat anti-mouse	Abcam

5.3.4.2 Antibody conjugation

The mitochondrial antibodies were conjugated by Dr Charlotte Warren and the osteo specific antibodies were conjugated by myself. The process of conjugation was performed using the MAXPAR X8 antibody labelling kit from Fluidigm this included the reagents: R-Buffer, C-Bugger, L-Buffer, W-Buffer, MAXPAR® polymer, Lanthanide solution, BondBreaker™TCEP solution, antibody stabilizer. 5kDa filter, 50kDa filter tubes were also required as part of the conjugation protocol.

The Fluidigm protocol (241) was followed with some slight modification. Antibodies suitable for conjugation had to be serum-free and only suspended in PBS although the addition of azide was not an issue. Steps were taken before commencing the protocol were to check the antibody concentration on the nanodrop. The MAXPAR polymer is moisture sensitive and so is kept a -20°C, this had to be equilibrated room temperature to avoid moisture condensation when opening.
The polymer was first pulse spun to ensure the reagent was at the bottom of the tube before 95µl of the L-buffer were added and mixed with a pipette. 5µl of the designated lanthanide metal was then added giving a final concentration of 2.5mM in 100µl. This combined solution was incubated in a heat block at 37°C for 40 minutes.

The antibody to be conjugated was then prepared and partially reduced. The concentration of the antibody had to be at least 100µg for the conjugation to take place. 300µl of R-buffer was added to the antibody stock in a 50kDa filter tube. This was then spun at 12000g for 10 minutes at room temperature. Whilst the antibody was been centrifuged the 0.5M TCEP stock was diluted to 4mM by adding 992µl of R-buffer to 8µl of the TCEP. After centrifugation, the supernatant flow through from the filter tube was discarded and 100µl of the diluted TCEP/R-buffer solution added to the filter column and mixed with a pipette. This then was incubated in a heat block for 30 minutes at 37°C.

Whilst the antibody was being reduced the combined lanthanide and polymer had to be purified. This was done by adding 200µl of the L-buffer to a 5kDa filter tube. Then the lanthanide-polymer mixture was added to the filter tube and the combined mixture was centrifuged at 12000g for 25 minutes at room temperature. A further was performed after discarding the flow-through by adding 400µl of L-buffer and centrifuging again at 12000g for 30 minutes at RT.

Once the antibody was removed from the heat block it also needed to be purified. 300µl of C-buffer was added to the 50kDa filter tube as a wash step and the tube was centrifuged for 10 minutes at

12000g at room temperature. The flow-through of the filter was discarded and a second wash was performed by adding 400µl of C-buffer and repeating the centrifugation step. The antibody could then be conjugated with the lanthanide polymer. To do this the polymer in the 5kDa filter column was resuspended in 100µl of C-buffer and this solution was transferred to the 50kDa filter column containing the antibody the two were mixed with a pipette and the filter sides washed to resuspend the antibody in the solution. This combined solution was then incubated for 1hr 30 minutes in the heat block at 37°C. Following this the combined mixture was washed 3 times using first 300µl of the W-buffer and centrifuging at 12000g for 10 minutes at room temperature, the flow-through was discarded and followed by 2 further washes using 400µl of W-buffer each time.

Recovery of the lanthanide conjugated antibody to place by adding 50µl of the W-buffer to the 50kDa filter and using a pipette to rinse the filter sides thoroughly. The filter was then inverted in a new tube and centrifuged at 1000g for 2 minutes. A further 50µl of W-buffer was then added to the filter again rinsing the sides and the process repeated.

The process of testing the conjugation is covered in the *Materials and Methods chapter 2.8.3.* This was done using ABC compensation beads and the Helios mass cytometer the results are demonstrated in *Figure 94.*

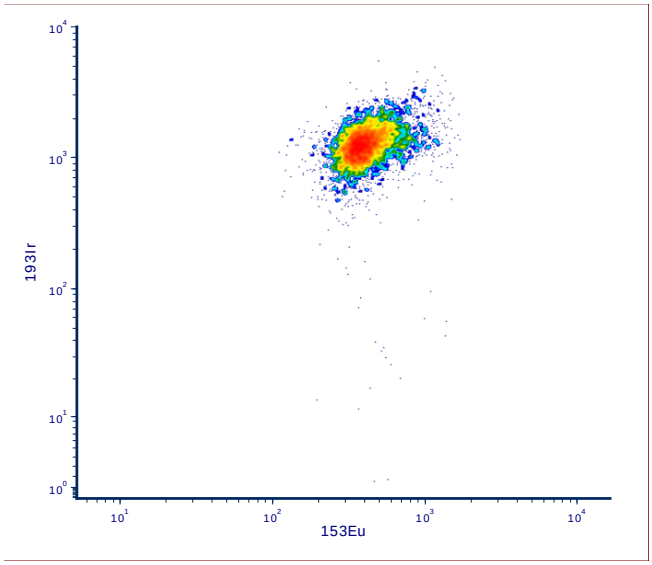

Figure 94 Binding of MT1-MMP antibody conjugated with 153 Europium in comparison to 193 Iridium binding on AbC compensation beads, both channels displaying positive signal intensities.

5.3.4.3 Antibody Panel Design

The mitochondrial antibody targets were conjugated by Dr Charlotte Warren, the design of this panel had to take into consideration the abundance of the antigen and the "brightness or signal intensity of the metal conjugate. The Helios/Hyperion mass cytometer can detect up to 90+ isotopes but the ion

optics for detection of ions by mass are tuned between the 153-176 Daltons range. Therefore, antibodies targets with low abundance were best suited to fall into the middle of this range.

Steps were taken by Dr Charlotte Warren in the design of the panel in conjunction with Dr Roberto Spada (Fluidigm). Mitochondrial antibodies were all tested on muscle sections at a concentration of 1/100. They were then conjugated with an Alexa Fluor 488 secondary antibody. Images were then taken at the same optical settings and the signal intensity was measured and quantified as in *Figure 95*. The basis of these results allowed the conjugation of the antibodies with the lowest abundance to the metal lanthanides which gave the best signal. Care was taken to space the antibodies out to limit spectral overlap due to impurities within the lanthanide conjugate, the reference for this cross over can be seen in *Table 37* in the appendix of this chapter.

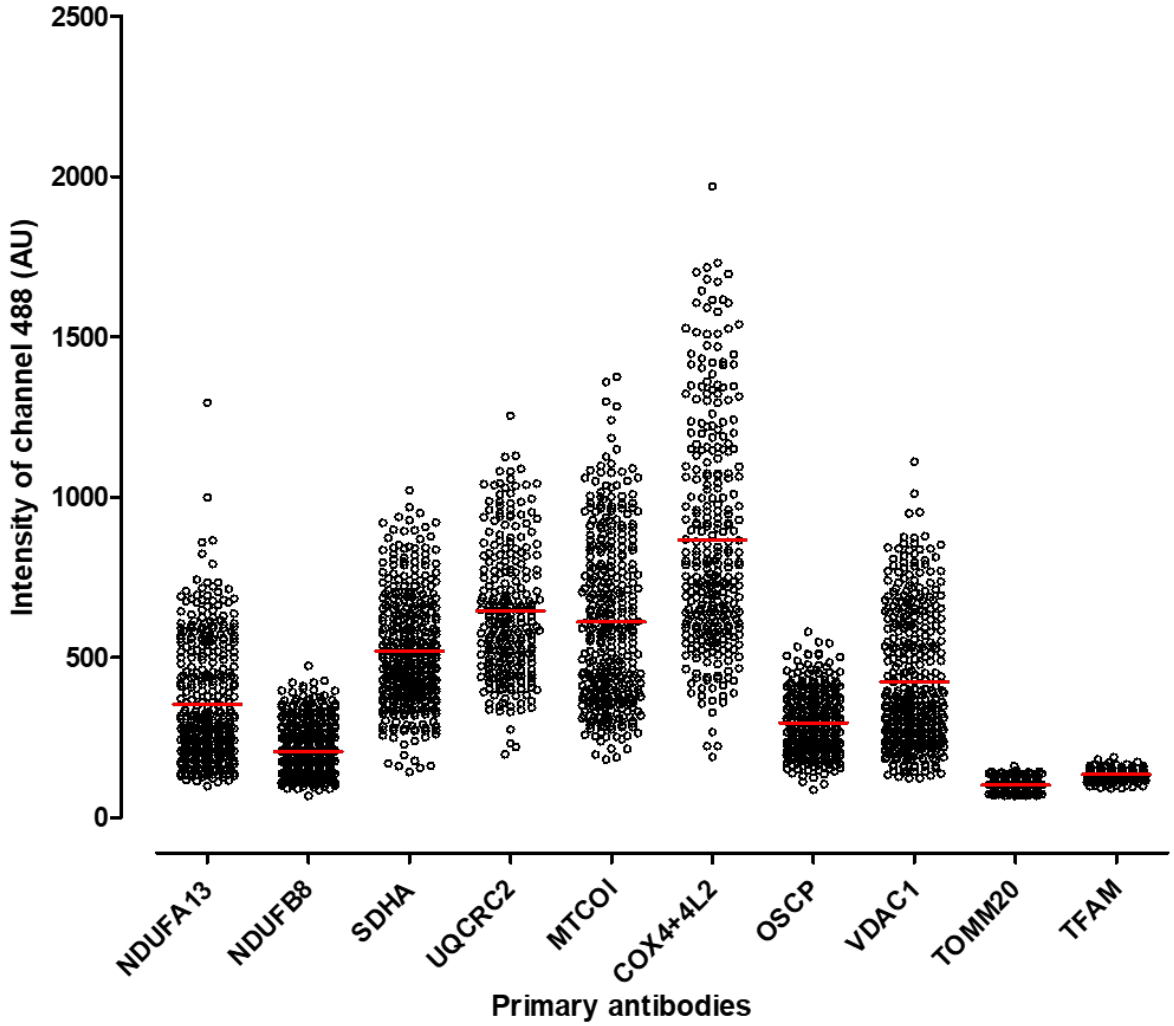

Figure 95 Expression level of each antibody in the IMC panel. Graph displaying expression of each protein by measurement of the intensity of the 488 channel. Each antibody is displayed as a separate strip and each dot represents an individual fibre. Red bars show the mean intensity for the given antibody. (a) non-metal bound antibodies and (b) metal-bound antibodies. Figure courtesy of Dr Charlotte Warren.

Mitochondrial Antibodies were conjugated to the following metals

Anti-SDHA IgG1	153Eu
Anti-TOM22 IgG	158Gd
Anti-NDUFB8 IgG1	160Gd
Anti-OSCP IgG1	161Dy
Anti-GRIM19 IgG1	164Dy
Anti-VDAC1 IgG2b	166Er
Anti-COX4+4L2 Ig2a	168Er
Anti-MTCO1 IgG2a	172Yb
Anti-UQCRC2 IgG1	174Yb

Osteo-lineage markers were conjugated as below

Anti-cathepsin K IgG	170Er
Anti-Osteocalcin IgG	176Yb
Anti-MT1 MMP	153Eu

(not used in conjunction with SDHA)

Intercalator-Ir (Fluidigm 201192A) is a cationic nucleic acid intercalator. It contains a natural abundance of the iridium isotopes 191Ir and 193Ir and was used as a nucleus marker at a concentration of 1:400 (0.3125µM).

Further testing and validation of the mitochondrial antibodies were performed by Dr Charlotte Warren comparing signal intensities of the metal and non-metal conjugated antibodies with a secondary Alexa Fluor 488 antibody. This revealed that the metal tagged antibodies had a lower channel intensity and as a result using them at a concentration of 1:50 would be more appropriate.

5.3.4.4 3,3′-Diaminobenzidine (DAB) staining

Due to the issues of autofluorescence and difficulty in imaging bone as highlighted above it was not possible to optimise the above antibodies using immunofluorescent imaging. As a result, DAB staining was used.

Decalcified samples were first cut into 4µm sections on to Leica X-tra, these were left to air dry for one week and then dewaxed at 60°C for 30 minutes. Deparaffinisation was performed with two

histoclear washes before rehydration in graded alcohol concentrations. Following this antigen retrieval was performed by incubating sections in 1mM EDTA pH 8 80°C for 35 minutes followed by a rinse in cold $_{di}H_2O$. Sections were then encircled using a PAP pen before blocking with 10% NGS PBS solution for 1 hour and avidin/biotin blocking steps as per Vector protocol (15mins avidin followed by 2 x5 minute wash steps, then 15 minutes biotin followed by 2 x5 minute wash steps). Antibody staining was performed at 1:50, 1:100, 1:200 concentrations initially but due to the fact of biotin amplification, 1:200 was suitable to demonstrate antibody binding. Sections were left in a humidified chamber at 4°C overnight.

After primary antibody incubation, 2 PBS washes were performed followed by endogenous peroxidase blocking using a 0.3% hydrogen peroxide in PBS solution for 10 minutes followed by 2 PBS washes.

For mouse-based antibodies, the slides were incubated with 1:200 of mouse biotin secondary for 1 hour at room temperature in the humidified chamber followed by 2X7 minute PBS washes before a secondary incubation with ABC buffer for 30 minutes. After these slides were rinsed three times with PBS. DAB solution was then made up and applied to the slides which were developed for around 10 minutes. This time was variable, and completion was checked under the microscope.

For rabbit-based antibodies the Dako kit was used after the peroxidase blocking step for 30 minutes. After these slides were rinsed three times with PBS. DAB solution was then made up and applied to the slides which were developed for around 10 minutes. This time was variable, and completion was checked under the microscope.

Both the mouse and rabbit antibody slides were then stained with haematoxylin before been run through a dehydration gradient and mounted using DPX medium.

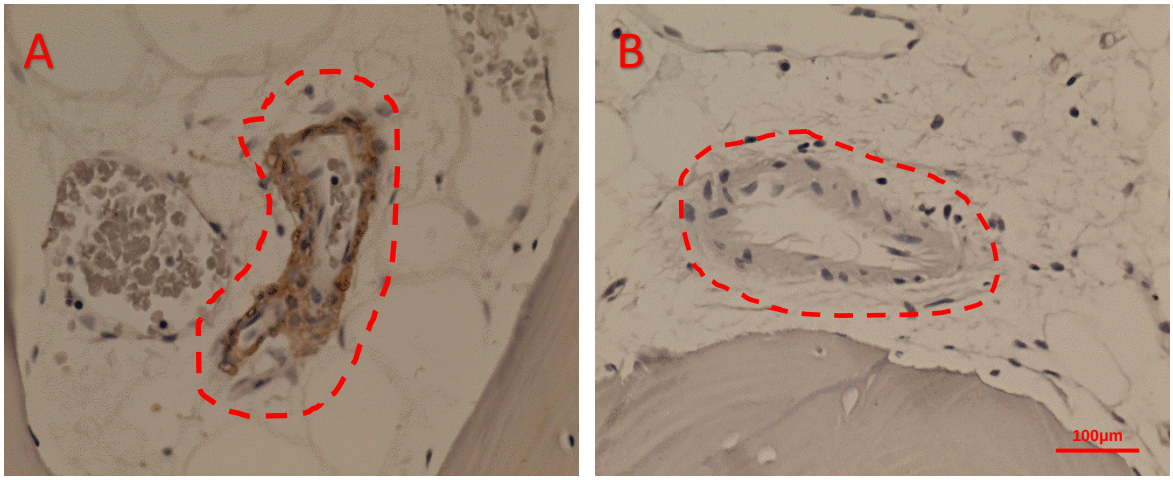

Figure 96 DAB staining of osteoblasts (circled in red) using Osteocalcin (1:200) at 20x magnification (A) compared with no primary antibody control (B).

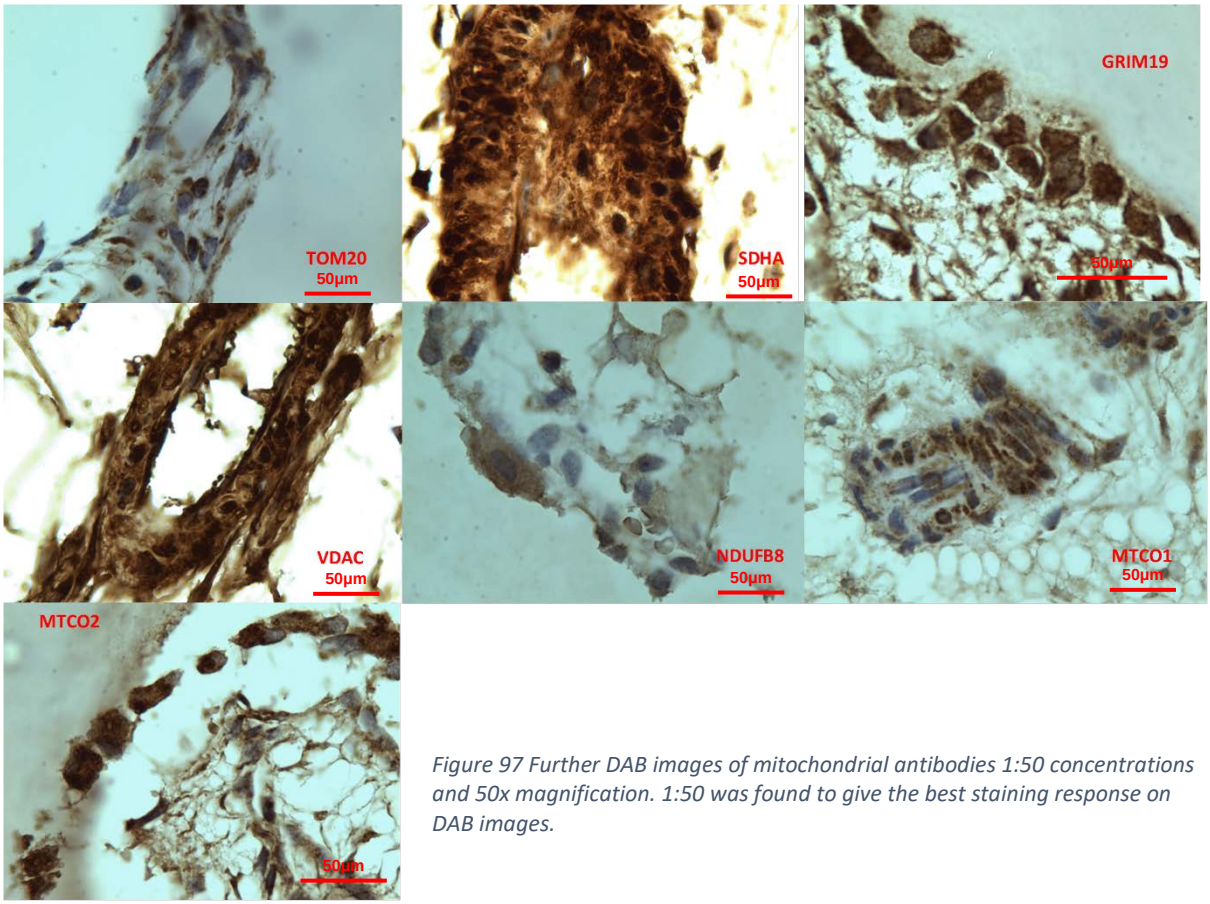

Figure 97 Further DAB images of mitochondrial antibodies 1:50 concentrations and 50x magnification. 1:50 was found to give the best staining response on DAB images.

5.3.4.5 Mass cytometry protocol development.

Fluidgim has their own published protocol for formalin-fixed paraffin-embedded tissue (241), but they also advocate the adaption of the normal IHC methods usually employed in the specific tissue types, as not all tissues and antibodies can be tested. With this in mind, a combination of the protocol by Dobson et al.,(205) and the Fluidigm protocol was developed.

After decalcified sections were cut onto Leica X-tra slides they were left to oven-dry for 48 hours and then air dry for one week. They were then dewaxed for 30 minutes at 60°C. Residual paraffin was then cleared with two five-minute clearing steps in Histoclear before graded rehydration through an alcohol gradient. Antigen retrieval was performed in the same fashion to Dobson et al., using 1mM EDTA at pH 8.0 at 80°C for 35 minutes. Sections were then rinsed in cold ddH_2O. A PAP pen was then used to encircle the sections before blocking with a 10%NGS PBS solution for one hour at room temperature. Sections were then once again rinsed in cold ddH_2O before staining with the antibodies.

Antibodies were made up at a 1:50 concentration cocktail in 10%NGS and PBS (based upon the work by Dr Charlotte Warren) and placed upon the slides to incubate in a humidified chamber at 4°C overnight. This was followed initially PBS with 0.1% Triton X100 washes x2 for 7 minutes on the rocker as per the Fluidigm protocol. As in the previous optimisation of the immunohistochemistry assays deviation from the use of Leica X-tra slides or use of detergents led to the loss of tissue from the slide surface. As a result, this was replaced with PBS only washes for 7 minutes on the rocker at room temperature. Iridium-intercalator was then used at a concentration of 0.3125µM in PBS for 30 minutes at room temperature to stain the nuclear regions. This was followed by a further wash step in $_{di}H_2O$ for 7 minutes. Slides were then air-dried at room temperature for 20 minutes before been stored in a box ready for ablation.

5.3.4.6 Optimisation with Histocyte control sections and osteosarcoma mouse models.

When optimising the Hyperion imaging mass spectrometry running full sections or large sections is simply not feasible in terms of time or economics. The Hyperion laser ablation module ablates tissue at around the 0.75mm^2 per hour (240). So, to cover a full bone section would not be feasible; instead, target areas need to be selected.

The first method used to create target lesions was employing Histocyte a spin-off company within Newcastle University. They process cultured cells to create embedded sections which can be cut and placed on slides for the purpose of on slide controls in histopathology. These small sections or dots provided a small target area of ablation which would allow ablation in a feasible and timely manner.

Control wild type fibroblasts (M456) and deficient fibroblast (M304) cell lines were grown up as well as cells derived from a paediatric ACL reconstruction and elderly total hip replacement patient. Existing blocks with sarcoma cell lines used at the Northern Institute for Cancer Research were also used whilst the cells were cultured in preparation.

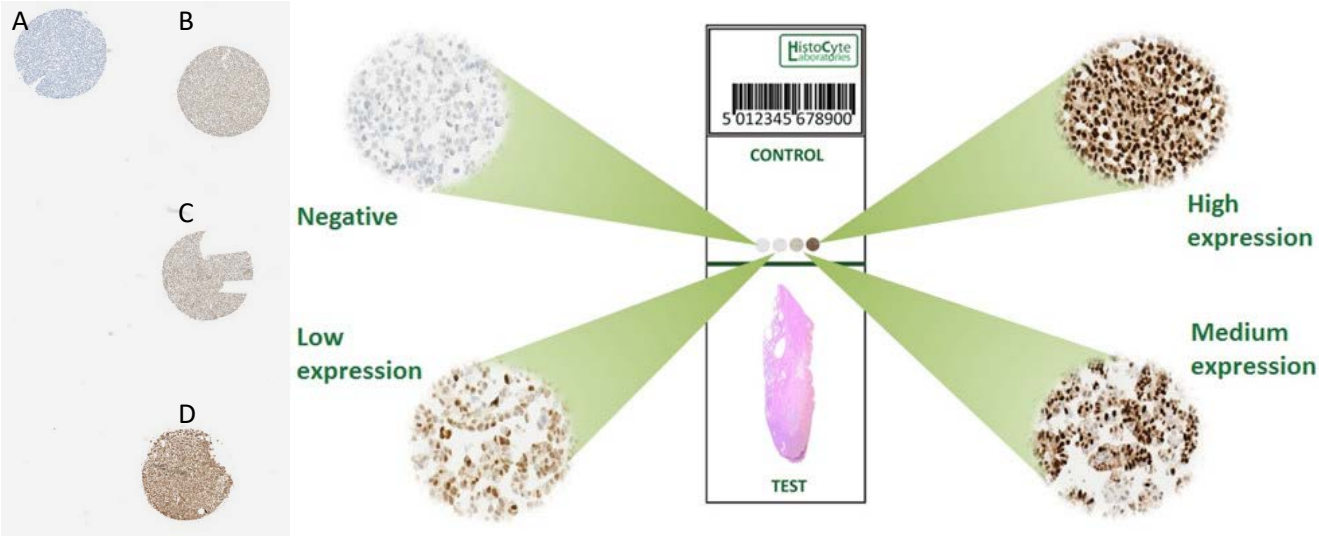

Figure 98 Histocyte control sections created for MT1-MMP antibody showing incremental DAB staining: A)Breast Carcinoma cell lines, B) Ewing's Sarcoma, C) High-grade osteosarcoma, D) High grade differentiated chondrosarcoma. On the left aspect Histocyte example use.

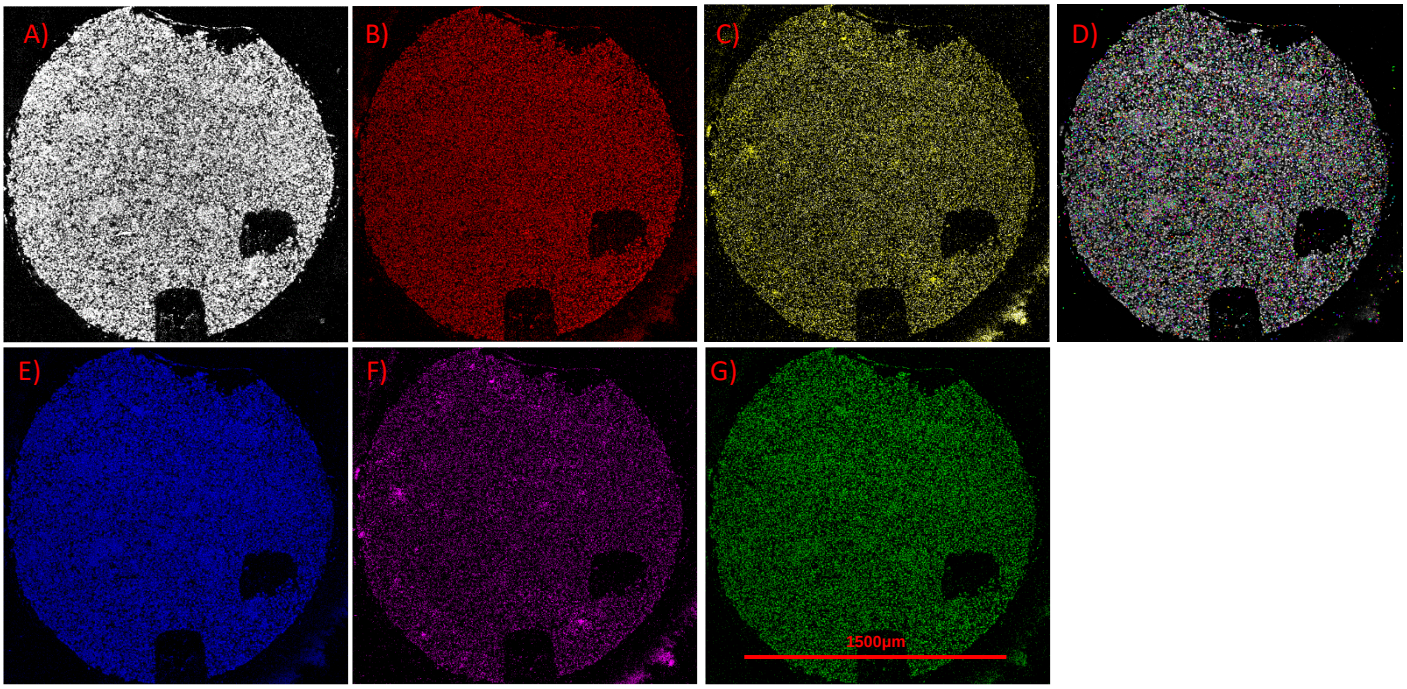

Figure 99 Mass cytometry results showing A) DNA staining, B) Osteocalcin staining, C) MT1-MMP staining, D) Cell profiling result, E) VDAC1 staining, F) Complex I am staining, G) Complex IV staining.

Image reconstructions can be seen in *Figure 99.* The raw data from these images were then processed using the Fluidigm MCD viewer. TIFF files were then exported and analysed using cell profiler. Currently, only around 60% of the cells were selected based on nuclear staining (image A and image D – cell profiling). The resolution of the Hyperion is not sufficient to allow cell profiler to distinguish the artificially tightly packed cells of the control blocks.

Whilst the potential of the cultured cell line blocks represents good methods to check the efficacy of histochemical staining the resolution of the Hyperion made the analysis of these blocks difficult in terms of single-cell segregation. The Northern Institute for Cancer Research also uses a mouse model based upon the work of Vormoor et al., for modelling osteosarcoma (382). Essentially human sarcoma cell lines were transplanted by intrafemoral injection into severe combined immunodeficient mice. This created malignant osteosarcoma tumour tissue within the mouse femur. The advantage of this is it allows whole mouse leg sections to be analysed on one slide with the implanted human osteosarcoma cell lines. These readily identifiable areas proved useful in trials of the mass cytometry protocol and antibody optimisation.

Figure 100 shows the details of the best antibody staining across the panel although there is a fold in the section which accounts for the abnormal staining across the muscle section of the images. Other antibodies were also trialled, these included TOM20 (158Gd), NDUFB8 (160Gd) and UqCRC2 (174Yb). The signal from these antibodies was poor and followed a non-specific pattern suggest that the staining had failed. Dr Charlotte Warren had also encountered issues with muscle tissue when using the TOM20 antibodies whilst TOM20 is poor the NDUFB8 and UqCRC2 work well in muscle tissue and there is some tissue-specific variation.

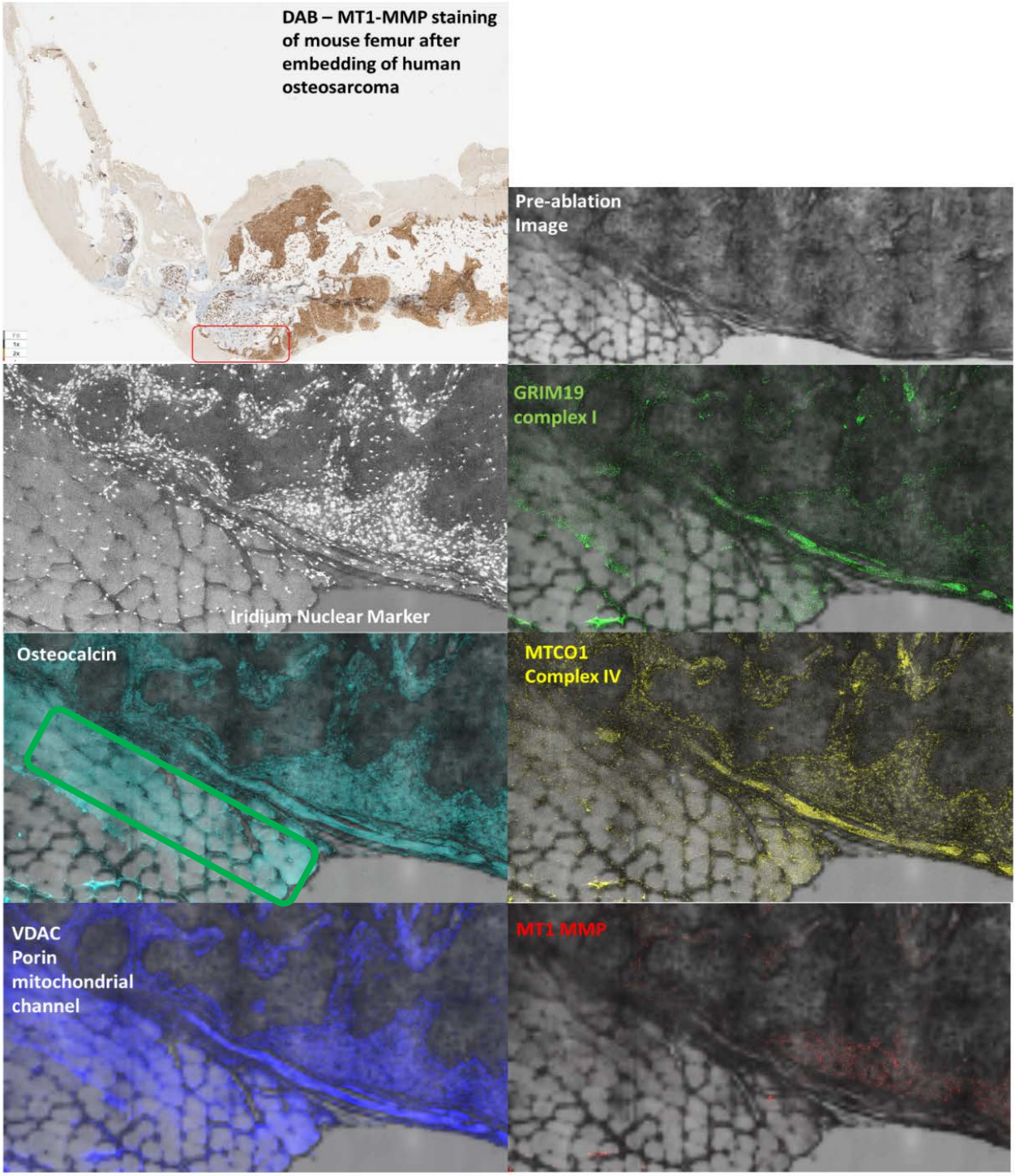

Figure 100 Immune-deficient Mouse leg with human osteosarcoma development following implantation. Imaging Mass cytometry results – area ablated highlighted by the red circle and shown in pre ablation image. The green area as highlighted on Osteocalcin is a fold in the section hence the abnormal staining profile seen within the muscle.

5.3.4.7 Optimisation using human bone marrow lesions

The same bone marrow lesion sections used in the immunofluorescence experiments and collaboration with an MRC fellow from the University of Nottingham were available for analysis and to run the IMC protocol on and image. First H and E and DAB serial sections were stained and scanned using the Aperio scanner unit. The aperio system is a digital pathology slide scanner capable of doing whole slide z-stacking in RGB channels with the capability of up to 20x zoom. It is accessible through a web-based server. This allowed direct comparison of DAB-stained sections with Osteocalcin and location of these areas on the slides to compare with the panoramas taken of the slides prepared for IMC. By taking this approach it enables the location of appropriately sized target areas to be scanned in a timely and efficient manner. This is a similar technique employed as Chang et al., although due to the nature of tissue they were using they were able to use immunofluorescent images to help locate areas of interest and a template from which to choose ablation areas (370).

Targeting these areas of bone marrow lesions can be seen adjacent in an example lesion. There is a clear number of cells marked in the Osteocalcin channel surrounded by the green dashed line. In terms of mitochondrial markers, the VDAC1 performed better in terms of the image produced than the TOM20 as with the mouse sections. The trend also was the same for COX4 vs MTCO1 and GRIM19 vs NDUFB8 for complex IV and complex I respectively.

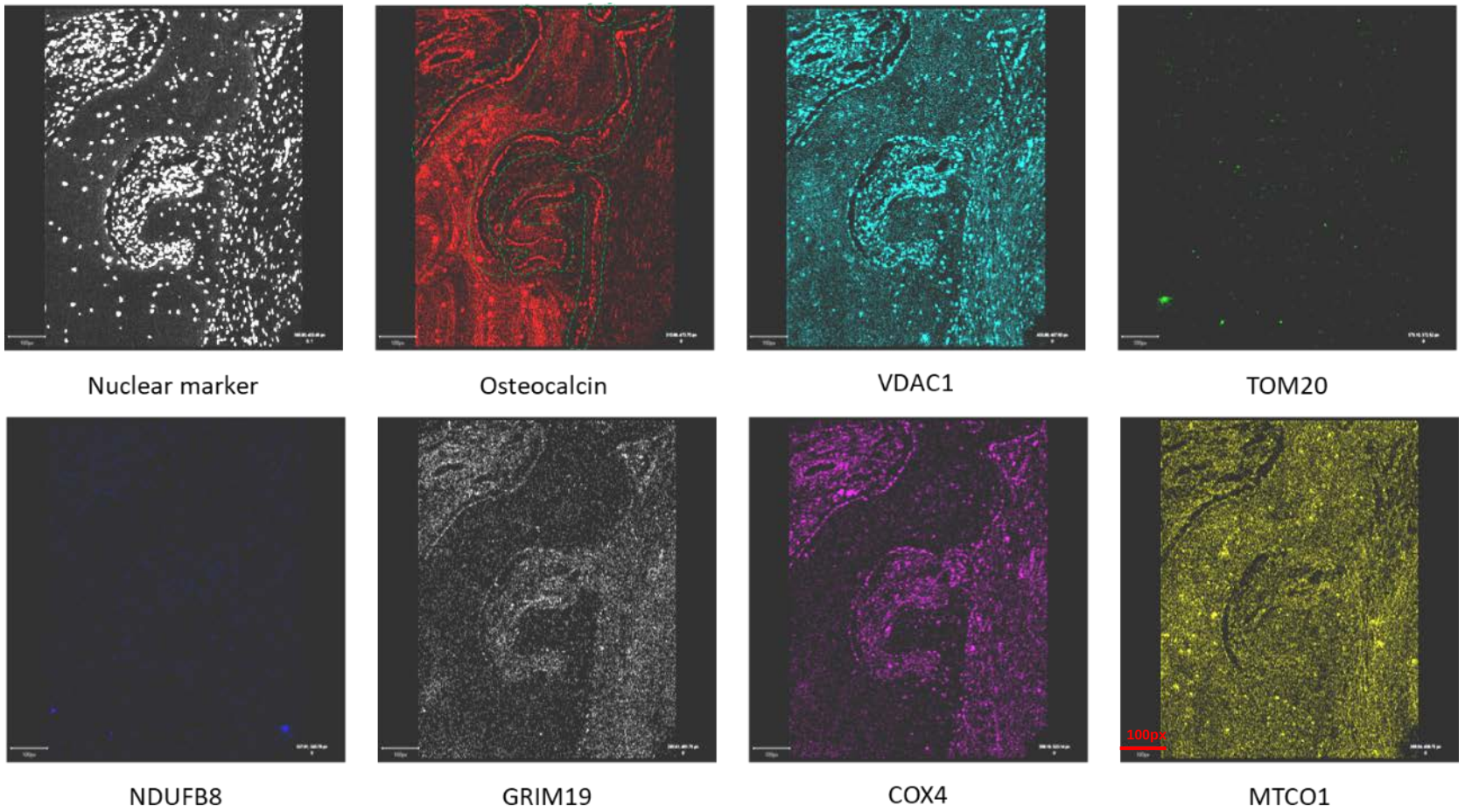

Figure 101 Imaging mass cytometry images of a bone marrow lesion from a proximal tibia showing osteoblasts and mitochondrial marker signal. Osteoblasts highlighted by the green dashed line.

5.3.5 Final samples

Sections of bone were taken at the time of routine orthopaedic surgery where they were surplus to requirements. The vast proportion of bone samples were femoral neck from older patients however there were samples of the femur, iliac crest and distal tibia from young and paediatric control patients also used. Demographics of the patients can be seen in *Table 33.*

At the time of routine orthopaedic surgery, samples were taken and if required they were cut to fit into standard size tissue cassettes. Samples were then were fixed in 4% PFA (Santa Cruz) for 72 hours followed by a dH_2O wash. A 14%, tetra EDTA buffered to pH 7.4 was used for decalcification of the bone blocks to allow cutting with the microtome. This took place at 4°C on a rocker to ensure even decalcification. The samples were then paraffin-embedded before 4-micron sections were cut using the microtome and placed on to Leica X-tra clipped corner slide.

Serial sections of the samples were then used, from the first two sections H and E staining and DAB staining for Osteocalcin were performed. The results of these slides were loaded into the Aperio scanner and viewer software.

The IMC slides were loaded into the Hyperion imaging module of the Helios mass cytometer (Fluidigm). A provisional image was taken and loaded into the software. From this image and with comparisons to the DAB-stained image on Aperio, “panoramas” were created containing areas with osteoblasts. These panoramas were then scanned with the Hyperion which allowed the creation of regions of interest (ROI) or areas which would be ablated. The resolution of these scanned images is lower than the Aperio scanned slides therefore the tissue architecture was used as a reference point to identify the appropriate areas to ablate. The major drawback to imaging mass cytometry is the time to ablate tissue, this is around $1mm^2$ per hour. Due to the amount of time taken to image sections target areas or ROIs were used rather than imaging the whole slide. In comparison to other soft tissues, the solid-state laser settings needed to be at their maximum intensity to ensure adequate ablation of the bone tissue.

Sample	Age (years)	Sex	Surgery	Date of Surgery	Indication	Co-morbidities	Osteoporotic preventive/causative medication
Hip 1	53	f	Total hip replacement	16/01/2019	Osteoarthritis	hypertension	Omeprazole/lisinopril
Hip 2	84	f	Total hip replacement	12/03/2019	Osteoarthritis	ischaemic heart disease, type II diabetes mellitus, asthma, hypertension, peripheral neuropathy, venothromboembolism, vitamin D deficiency, B12 and folate deficiency	Atorvastatin, Metformin, Warfarin
Hip 3	88	f	Total hip replacement	13/03/2019	Osteoarthritis	type II diabetes mellitus, chronic kidney disease, atrial fibrillation, diverticular disease, hypertension	Furosemide, Atorvastatin
Hip 4	83	f	Total hip replacement	01/04/2019	Failed Fixation	hypothyroid, hypertension, osteoarthritis	Calcichew d3,cholecalciferoll, furosemide, levothyroxine, risedronate
Hip 5	66	f	Total hip replacement	02/04/2019	Osteoarthritis	hypothyroid, raised cholesterol, hypertension,	Lansoprazole, Levothyroxine, losartan, simvastatin
Hip 6	45	f	Total hip replacement	02/04/2019	Osteoarthritis		
Hip 7	82	m	Total hip replacement	03/04/2019	Osteoarthritis	chronic obstructive pulmonary disease, gastro-oesophageal reflux disease, iron-deficiency anaemia	Omeprazole, steroid inhalers - tiotropium, fluticasone, Seretide
Hip 8	74	f	Total hip replacement	11/04/2019	Osteoarthritis	atrial fibrillation, pulmonary hypertension, iron-deficiency anaemia	Omeprazole, Bisoprolol, Rivaroxaban
Hip 9	64	m	Total hip replacement	11/04/2019	Osteoarthritis	chronic kidney disease, type II diabetes mellitus	Dialysis, Atorvastatin, Diltiazem, Furosemide,
Hip 10	62	m	Total hip replacement	02/05/2019	Osteoarthritis	type II diabetes mellitus, hypertension	Lisinopril, metformin atorvastatin, Adalat
Femur 1	22	m	Intramedullary nail and bone graft	27/03/2019	Leg length discrepancy after trauma		
Paediatric 1	13	m	Excision of a bone bridge and fat graft	29/11/2018	Physeal injury and growth arrest		
Paediatric 2	1.5	f	Open reduction and pelvic osteotomy	18/04/2019	Developmental dysplasia of the hip		

Table 33 Adult and paediatric patient cohort of samples used in CyToF experiments.

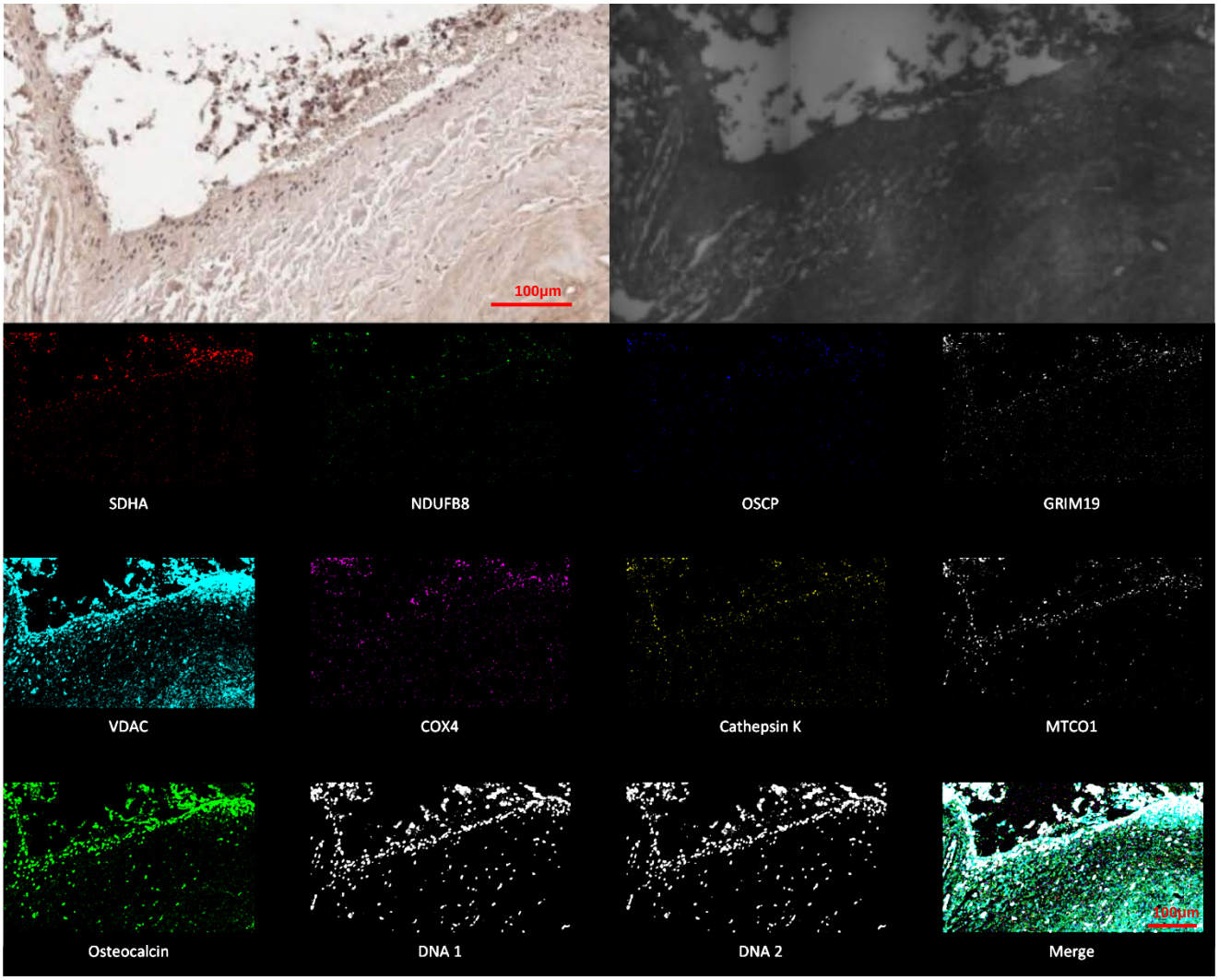

Figure 102: TOP LEFT - DAB staining of osteocalcin positive cells, TOP RIGHT - Pre ablation image of the slide as scanned by the Hyperion, BOTTOM ROWS - various channels of the ablated image after processing with the Hyperion mass cytometer.5.3.5 Analysis development.

5.3.5.1 MCD Viewer

MCD viewer is the coupled program to the Hyperion created by Fluidgim. It allows base visualisation of the channels some alteration of thresholds and colours. It also shows the pre-ablation and post-ablation images of each slide as well as information related to the panoramas and regions of interest created in the Hyperion running software CyToF 6.7 system control. This software is utilised to create the panoramas of the slide or area of the slide in question from which the smaller regions of interest or ROI can then be selected.

The main function of the MCD viewer is for exporting the Hyperion data into TIFF image files. Two options are present either 16 bit or 32 bit. Initial exports using 16 bit gave signal intensities that were too low for visualisation and subsequent segmentation analysis steps. However, 32 bit was improved.

5.3.5.2 Cell profiler

The Bodenmiller group who have pioneered early IMC work used cell profiler for image segmentation which would provide data to the feed into histoCAT. HistoCAT is an open-source computational histology topography cytometry analysis toolbox developed by the Bodenmiller group(383). With the data acquired from the Hyperion, the aim was to load this into histocat, but first, a cell profile pipeline would need to be built. This was based upon a Fluidigm cell profiler guide. However full pipelines are now available to download from the Bodenmiller group (https://github.com/BodenmillerGroup/ImcSegmentationPipeline).

To construct the pipeline for analysis, images were first loaded into cell profiler as single-channel TIFFs (32 bit required at this point onwards). Within these images, different channels were then used to identify cells. The iridium nuclear stain channel was used to recognise the nuclei of individual cells for this step an ImageMath function was added to amplify the signal. The pipeline would then proceed to identify the cells and finally the cytoplasm. This would allow object intensity measurement of the mitochondria and direct comparison of the signal intensities of mitochondrial mass VDAC1 with GRIM19 (complex I) and COX4 (complex IV).

Unfortunately, the pipeline developed by Bodenmillar and publicised by Fluidigm was developed for relatively homogenous tissue and not the extremely heterogeneous tissue of bone. Segmentation of single osteoblast cells proved difficult. Adding a manual segmentation step did work but the image generated by cell profiler was random and only represented a small section of each image and so not suitable to manually segment.

Discussion with Fluidigm and the flow cytometry department were unable to advance on this issue and a further method was required.

5.3.5.3 Fiji and QuPath analysis

The Fiji software is an open-source version of ImageJ it allows the incorporation of different bundles, java and plugins to suit the users need in a more convenient package than ImageJ. It still retains the core components of ImageJ which is a java-based image processing program which reads multiple formats files and also allows the modification of bundles by users to suit their needs.

QuPath is an open-source digital pathology analysis tool. It was originally developed by the Centre for Cancer Research & Cell Biology at Queen's University Belfast. It is also open source and allows users to develop new algorithms and scripts to analyse complex tissue.

Dr Ashwin Sachdeva had utilised both Fiji and QuPath in the analysis of tissue microarrays when investigating the role mitochondria play in prostate cancer. In doing so he adapted and wrote a script which would allow the combining of the TIFFs exported in MCD viewer into a multichannel TIFF which could then be imported into QuPath. A further script was written to adapt QuPath to meet the needs of IMC analysis.

Following export of the 32-bit TIFF IMC files from MCD viewer for each region of interest they were combined into a multichannel image with Fiji and then imported into QuPath. In QuPath the second script was run. The thresholds for each antibody were then adjusted before selecting areas or cells of interest within the image. The cell detection tool within the analysis function of QuPath was then used to first detect the nucleus then the cytoplasm. The signal intensities for each channel could then be recorded for each antibody channel for only the Osteocalcin positive cells of interest. This data could then be exported as CSV file for use in Excel, Spotfire or Prizm.

The issue with using Qupath is that the cell detection was based on nucleus detection then an arbitrary grow out or expansion region determined by the software and user to define the cytoplasm. When the results were analysed, the incorporation of pixels with zero values and no signal in any channel within the arbitrary cell reduced all the signals intensities measured for the cell see *Figure 105* for visual details.

Options to create a script and mask to the VDAC signal were explored but did not offer a feasible or logical method to isolate the cells and measure the true mitochondrial signal masked to VDAC within the cytoplasm without analysing dead pixels (zero values).

The use of Fiji and Qupath to generate data from the CyToF images was not an appropriate method and could not be used moving forward. Across the five slides bone marrow lesion slides, there were no clear identifiable trends and what was noise and meaningful results were not distinguishable from the background signal. The signal intensities detected using Qupath were extremely low, and the intensity of true signal and background were within close proximity the use of Qupath and Fiji in terms of analysis is not suitable in analysing CyToF images in bone. This can be demonstrated in the preliminary bone marrow lesion work in 5.3.5.4 Bone Marrow Lesion Results and the visual representation of the process of cell segmentation can be seen in *Figure 105.*

5.3.5.4 Bone Marrow Lesion Results

From the bone marrow lesion blocks, 5 were chosen for the analysis. These samples were chosen as it was felt that the bone marrow lesions within these cells were the most pronounced of the sample group and therefore easily identifiable. Following imaging and analysis, there were almost 5000 cells available to analyse. This data was generated using the Qupath analysis step based on cell identification by expansion step from nuclear detection to define the cell body rather than defining cell body based upon Osteocalcin signal. The five slides' demographics can be seen below in *Table 34*

Slide	Sex	Age (years)
1	Female	61
2	Female	65.5
3	Female	65
4	Male	63.3
5	Female	73

Table 34 Demographics of the bone marrow lesions samples selected for the trial CyToF run.

The data generated from the Qupath analysis can be seen in *Figure 103*. The values of the data points from the cells were all extremely low and difficult to distinguish from what could be background noise. There were no obvious clear correlations or patterns.

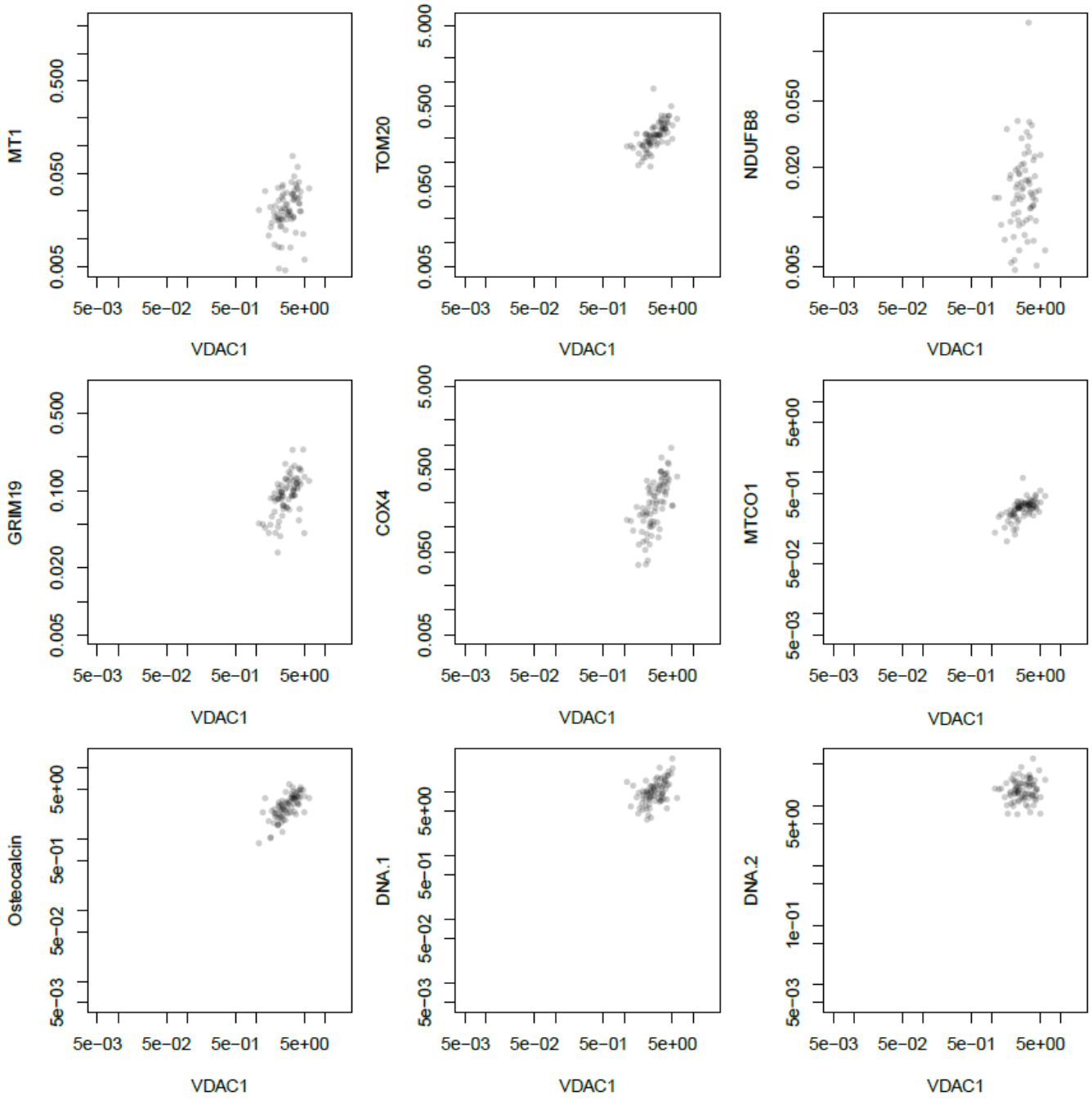

Figure 103 Scatter plots of cell signals vs VDAC signals for slide one using a logarithmic scale. No clear pattern is seen, and values are low across the plots. This pattern is repeated across the five slides. Below can be seen the corresponding images generated from the CyToF data from which the analysis has been performed in Figure 104.

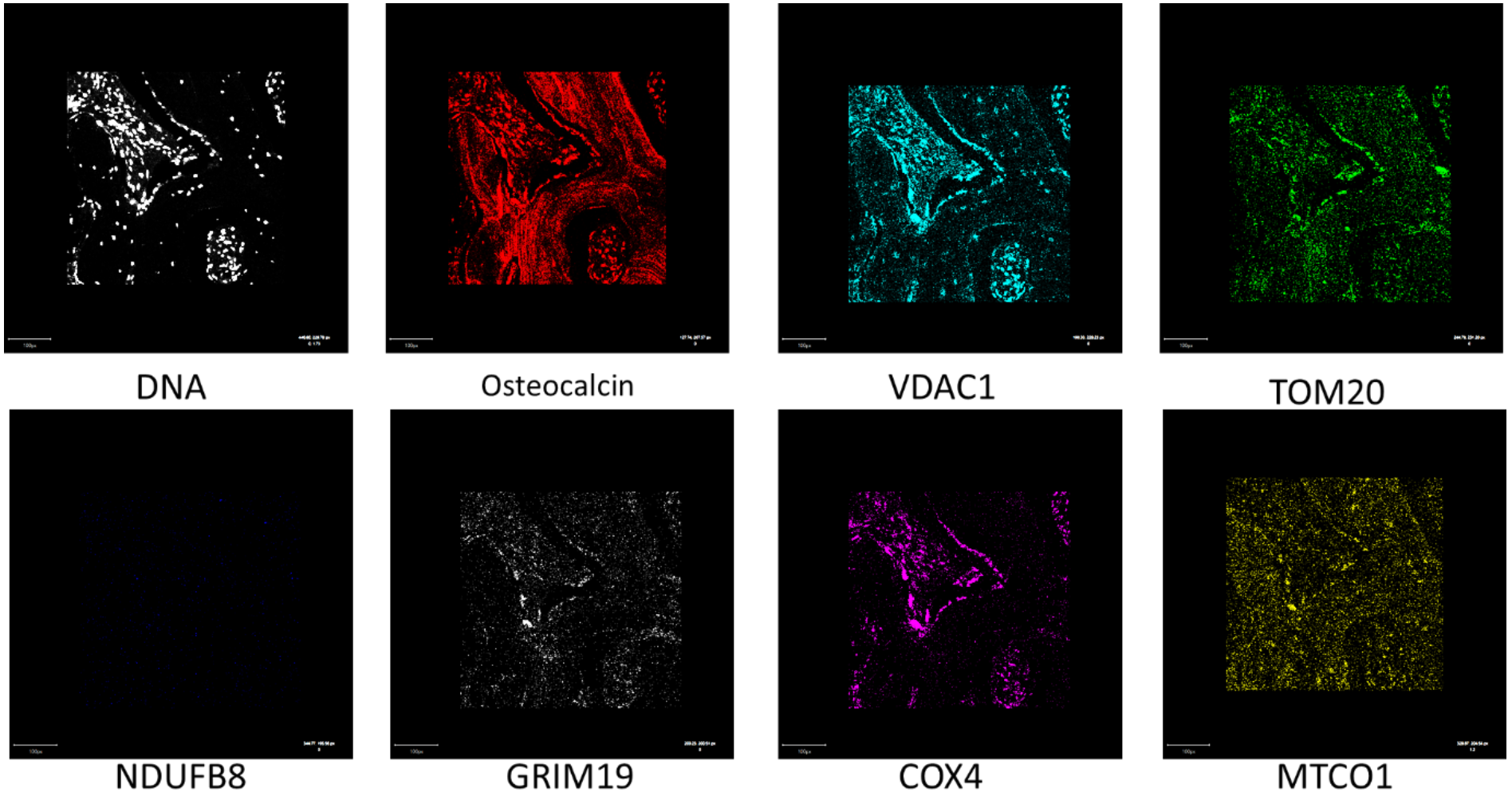

Figure 104 Images of a bone marrow lesion generated from MCD viewer TIFFs and viewed in QuPath to demonstrate the different channels.

Figure 105 Using Qupath to segment and separate the osteoblasts from the selected region on nuclear markers and cell detection using expansion algorithm.

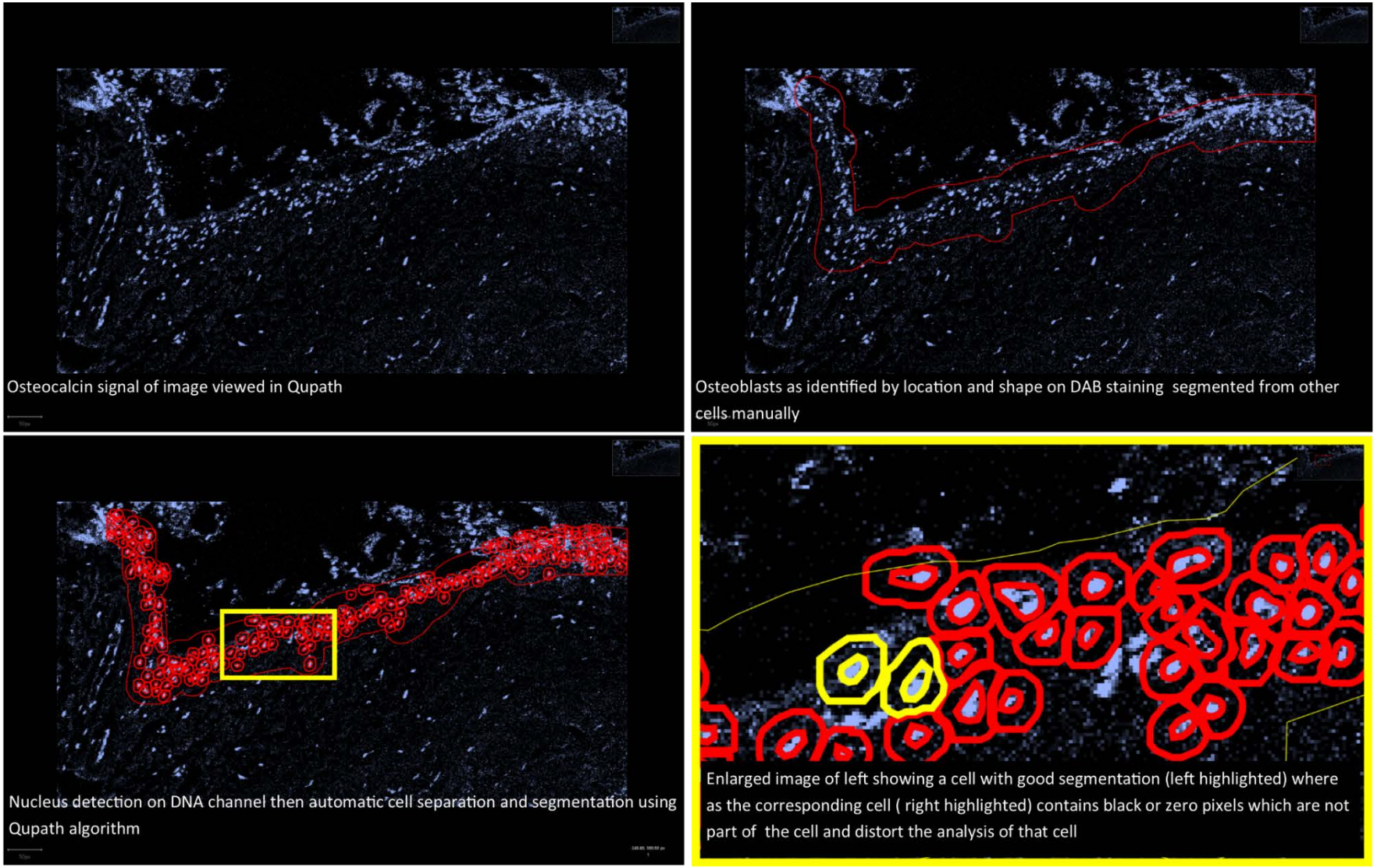

5.3.5.4 Mitocyto

Mitocyto (384) was also trialled but this failed to detect all the cells of images as can be seen in *Figure 106.* Mitocyto is a software developed for mitochondrial analysis both in fluorescent and CyToF images. It creates a cell map based upon the dystrophin channel of muscle sections. Individual fibres within each of these segmented areas can then be analysed. The heterogeneity of the sections of bone prevented mitocyto been employed for the analysis of CyToF images. It was unable to recognise the cells consistently and define them based upon the osteocalcin signal.

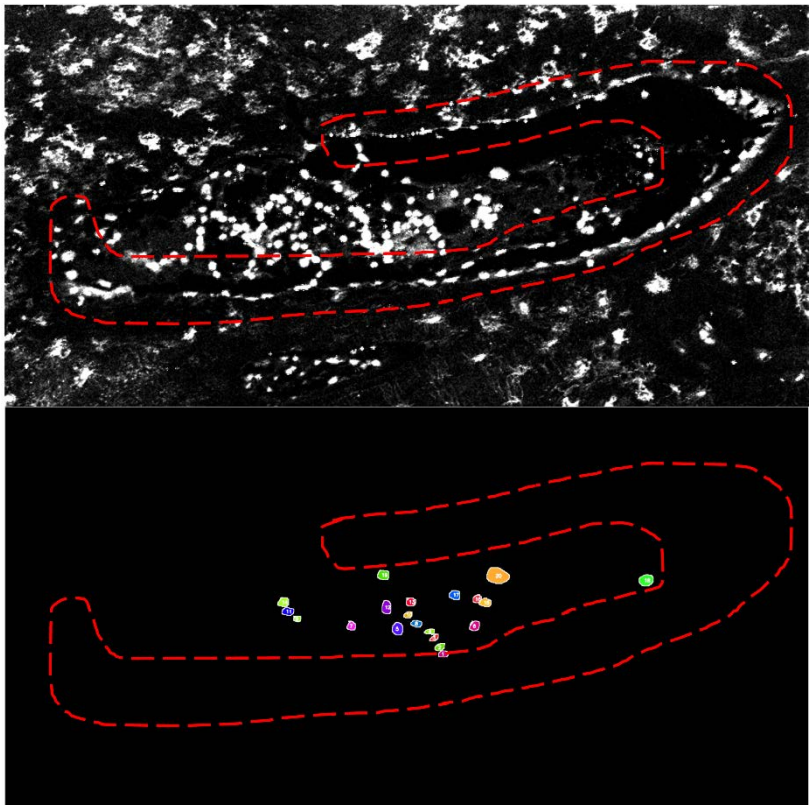

Figure 106 Cells of interest marked on nuclear channel TIFF in red dashed area. Cells identified and segmented using mitocyto software highlighted in colours - not corresponding to the red dashed area.

5.3.5.5 Nikon Elements and Volocity.

Work was undertaken with the Bio-Imaging unit at Newcastle University to find a method of analysing the images from an imaging perspective rather than a cytometry perspective.

First TIFFs were exported from MCD viewer in 16-bit format. Each channel of each ROI analysed is exported as a separate TIFF file. The TIFFs were combined in Nikon Elements. This converted the multiple channel TIFFs into a single ND2 Nikon Elements file. By combining these TIFFs into one single ND2 file with multiple “wavelengths” or in the case of mass cytometry, channels, the files could be imported into the Perkins Elmer software Volocity. Volocity is software produced by Perkins Elmer which allows restoration, visualisation and quantification. It also can be used to perform batch

analysis. The summary of the volocity pipeline created for analysis can be seen in *Figure 107* and is detailed below.

To quantify the now combined TIFF files exported from MCD viewer in Volocity; first images were cropped to the areas of interest based upon the previously acquired DAB-stained osteocalcin Aperio acquired images. The cells were then identified using the nuclear marker (channel 191), an exclusion based on size and a split of touching objects was then applied. The cell cytoplasm was then identified by using the Osteocalcin cell marker (channel 176). A mask was then created to highlight each cell by combining the Osteocalcin signal associated with a nucleus identified from the first step. Within this area, a further mask was created by identifying only the VDAC positive pixels indicated areas of mitochondrial mass. Masks were then used to quantify protein expression in individual cells. A noise reduction filter was also applied to limit background signal.

R based analysis was performed by Dr Conor Lawless. To estimate the proportion of cells deficient in one or more proteins, the workflow of Rocha et al., 2015 (235) was adapted replacing their linear regression model of the variation of e.g. NDUFB8 with mitochondrial mass (e.g. VDAC). Instead, using a non-parametric 2D kernel estimate of the density of cells from healthy patients in NDUFB8-VDAC space generated using the `kde2d` function from the `MASS` package in R (385, 386). Specifically, this calculated the level from the KDE which contains 95% of the control cells. Then, for each patient, any cell which lies outside that 95% contour was annotated as being “different” from controls. The further label of cells lying “above” (e.g., with NDUFB8 values vertically above the contour) or “below” (e.g., with NDUFB8 values vertically below the contour). Code and data for calculating proportions can be found here: (https://github.com/CnrLwlss/Hipps_2020).

The volocity pipeline for analysis is summarised on the following page.

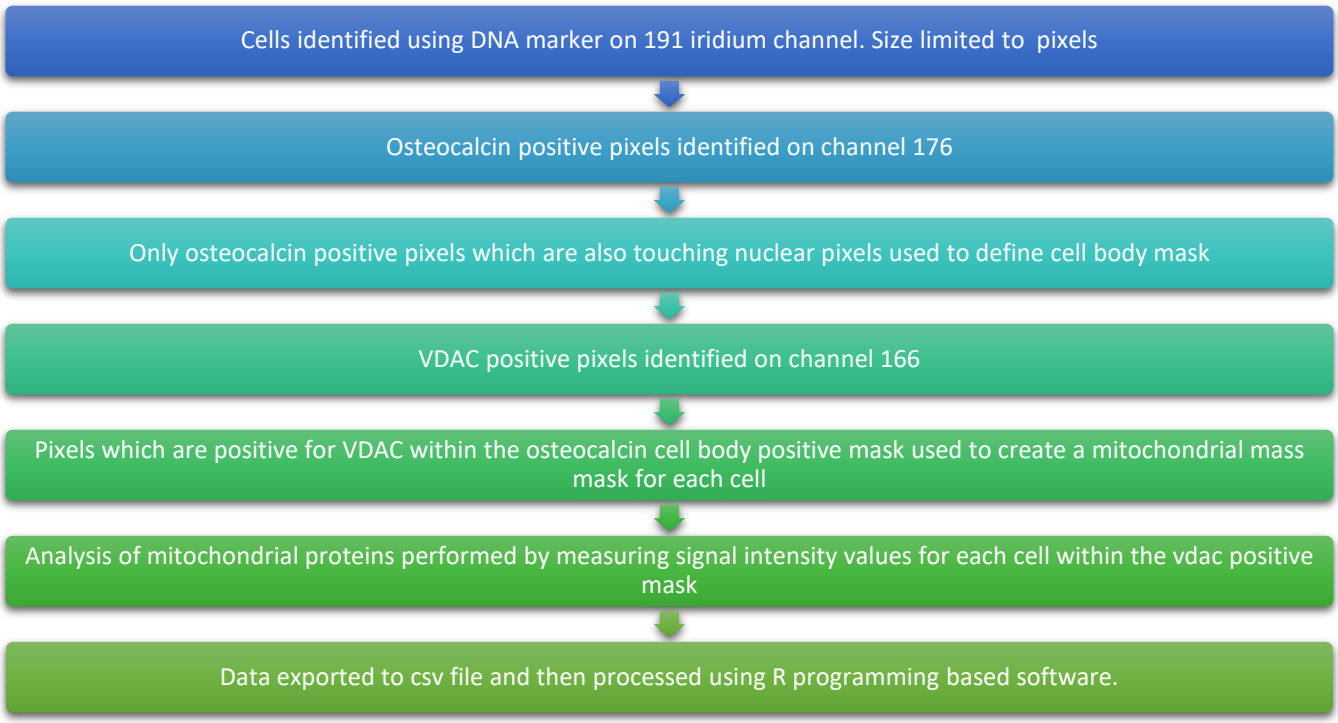

Figure 107 Summary of volocity analysis pipeline.

5.4 Results

5.4.1 Final experiment results and analysis using Volocity, and R based algorithms.

I have optimised the use of imaging mass cytometry to analyse and assess respiratory chain protein levels within bone at the single-cell osteoblast level. Using metal labelled antibodies, I was able to target multiple proteins beyond the limits (number of parameters) of a fluorescent-based assay and without the issues of autofluorescence. Something which is a significant and limiting factor in the analysis of bone-based parameters.

For this assay, I aimed to show a link with age and accumulated mitochondrial respiratory chain protein deficiency in osteoblasts. The antibody targets chosen were those of the mitochondrial oxidative phosphorylation subunits.

Samples of bone were obtained from 13 patients undergoing elective routine orthopaedic surgery using the ethics as highlighted in Chapter 2. There was a spread in terms of ages from 1.5 years to 88 years of age with three paediatric/young control patients (1.5, 13 and 22 years of age). There was a split of 8 to 5 in terms of female to male patients. The majority of the patients were undergoing elective total hip replacement for arthritis. The paediatric/young patients were having surgery for a variety of different reasons as detailed in *Table 33* above.

For the final experiment embedded sections of all the patients as in *Table 33* were used and stained as per the protocol covered in the material and methods chapter. Following ablation on the Hyperion and the data acquisition steps using Volocity, the data could be prepared for presentation.

First log plots of mean antibody signal intensity were created for each ROI of each patient. These log plots allowed the identification of anomaly slides were there had been an error in readings with values disproportionate to the corresponding slides an example of this can be seen in *Figure 108.* The list of excluded clear outlying anomalies is listed in *Table 35*. From the raw images, it was not clear why these ROIs were such outliers compared to other images. Whilst in early optimisation there had been a noticeable drop off in signal due to laser power falling this wasn't the case for the ROIs identified in *Table 35*. The data contained over these ROIs were created in continuum with the rest of the data between 8/7/19 and 22/7/19 with no observed drop off in signal within this time frame. The signal profile of these images was not in keeping with the rest of the data and so they were removed from the analysis stages.

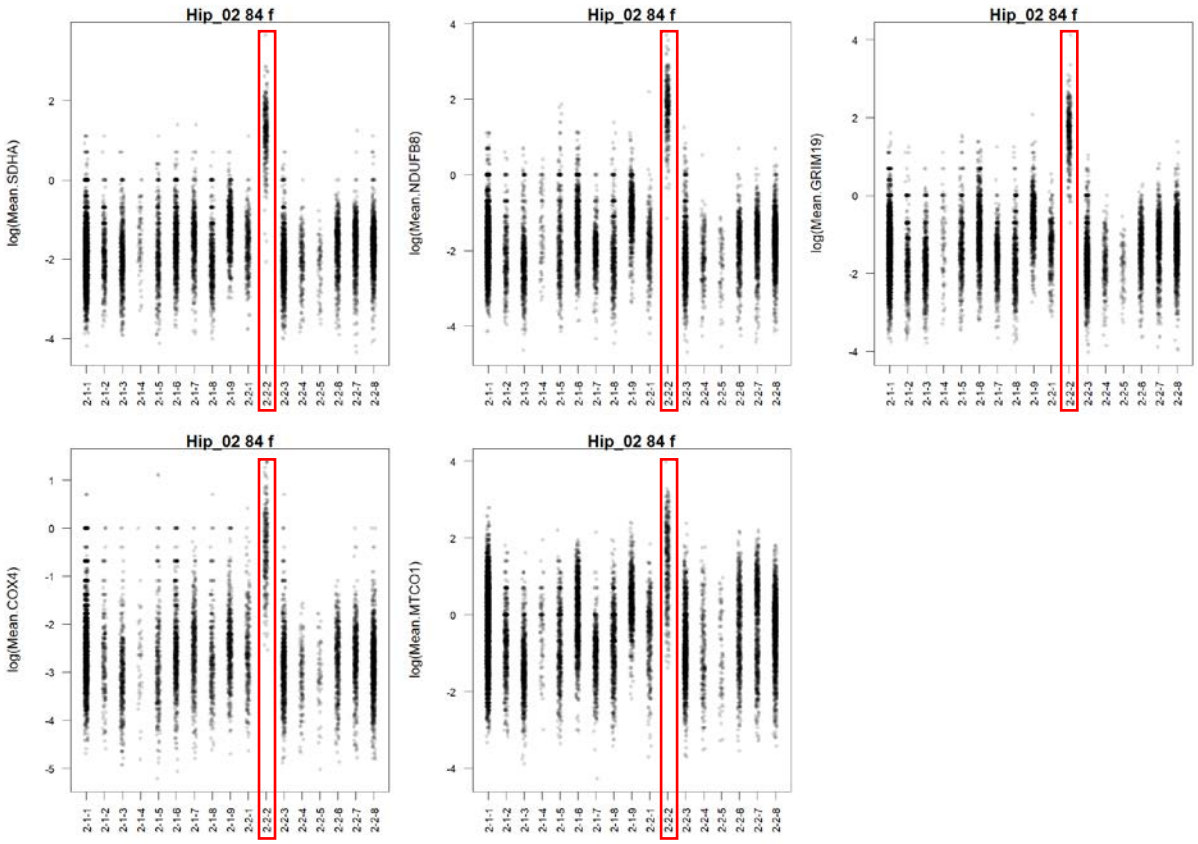

Figure 108 Log plots of mean IMC signal intensity for Hip 2, an 84-year-old female patient. Slide 2-2-2 was a clear outlier and excluded.

Sample	Slide	ROI
Hip 2	2	2
Hip 3	3	1
Hip 3	3	2
Hip 3	3	3
Hip 3	3	4
Hip 3	3	5
Hip 3	3	6
Hip 3	3	7
Hip 3	3	8
Hip 3	3	9
Hip 5	1	8
Hip 6	1	6
Hip 6	1	7
Hip 7	1	1

Table 35 Regions of interest identified as anomalies and excluded from the analysis. With similar variance as seen in 2-2-2 compared to the rest of a samples data.

5.4.1.1 Data for the patient "Hip 1"

Hip 1 samples were taken from a 53-year-old female patient undergoing a total hip replacement for arthritis. In total 6 ROIs (regions of interest) on one slide or section was analysed and this totalled 4809 osteoblasts. There were no anomaly ROIs and signals were all within a comparable range to each other.

As can be seen in *Figure 109* the Contour lines represent the kernel density estimate levels containing 95% and 50% of the control population for each pairwise comparison. The grey points are from patient cells that lie within the 95% contour from controls. Red points are from patient cells lying outside the 95% contour from controls. There is only a small proportion of cells deficient for complex I (0.96% NDUFB8 and 0.69% GRIM19) lying outside the 0.95 contour mass and below the vertical value of the 0.95 contour. SDHA or complex II showed deficiency in 0.52% of cells outside and below the 0.95 confidence interval. Complex IV has an even lower level of deficiency (0.27% MTCO1 and 0.35% COX4). OSCP - oligomycin sensitivity conferral protein is part of the mitochondrial ATPase or complex V were deficient in only 1% of osteoblasts.

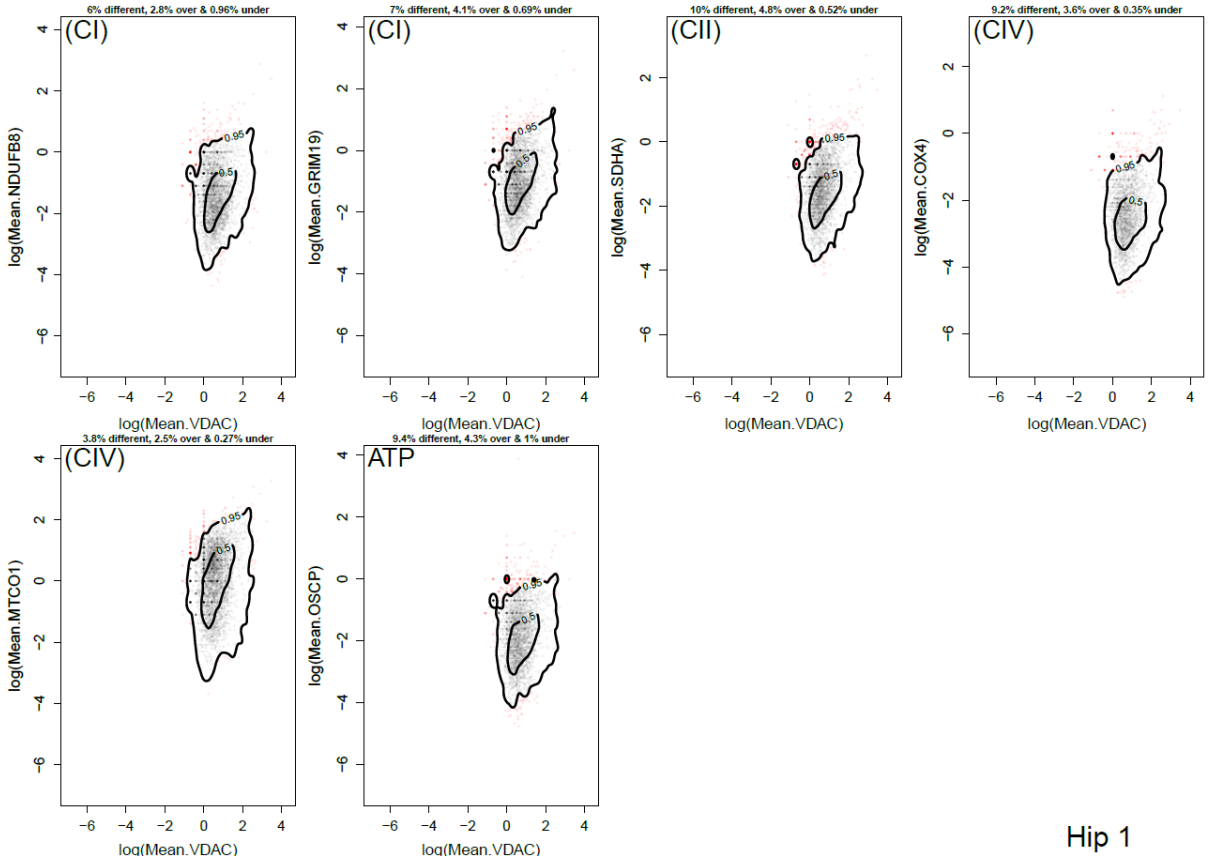

Figure 109 Estimating deficiency in Complex I, Complex II, Complex IV and Complex V Data from Hip 1: Contour lines represent the kernel density estimate levels containing 95% and 50% of the control population for each pairwise comparison. Grey points are from patient cells that lie within the 95% contour from controls. Red points are from patient cells lying outside the 95% contour from controls. The proportion of cells different from, vertically above and vertically below the 95% contour from controls written above each panel.

5.4.1.2 Data for the patient "Hip 2"

Hip 2 samples were taken from an 84-year-old female undergoing a total hip replacement for arthritis. In total 16 ROIs across 2 sections or slides were analysed, this totalled 18571 individual osteoblasts. As highlighted in *Figure 108* ROI 2 on slide/section 2 (2-2-2) had an unusually high signal across all antibodies in comparison to the rest of the sections and as a result, this was excluded from the analysis.

As can be seen in *Figure 110* the proportion of cells deficient cells for complex I lying outside and below the 0.95% contour is 1.9% NDUFB8 and 1.8% GRIM19. SDHA deficiency was evident in just in 0.95% of the cells analysed. For Complex IV the level of deficient cells is less pronounced 1.1% MTCO1 and 0.69% COX4. OSCP values were also low at 1.6%.

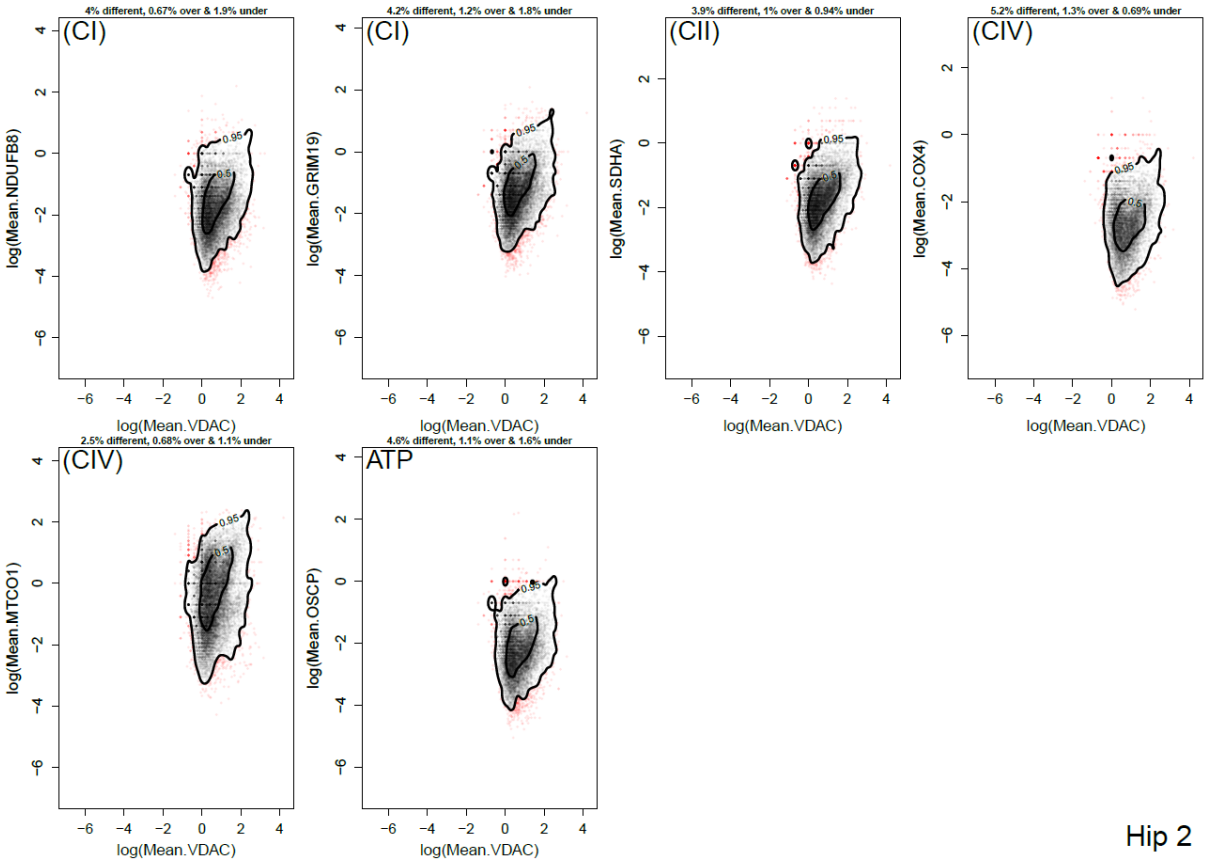

Figure 110 Estimating deficiency in Complex I, Complex II, Complex IV and Complex V Data from Hip 2: Contour lines represent the kernel density estimate levels containing 95% and 50% of the control population for each pairwise comparison. Grey points are from patient cells that lie within the 95% contour from controls. Red points are from patient cells lying outside the 95% contour from controls. The proportion of cells different from, vertically above and vertically below the 95% contour from controls written above each panel.

5.4.1.3 Data for the patient "Hip 3"

Hip 3 samples were taken from an 88-year-old female undergoing a total hip replacement for arthritis. In total 17 ROIs were analysed across 2 sections or slides (1 and 2). The ROIs on slide number 3 – hip 3-3 had abnormally high signal across all data points in comparison with the other slides from hip 3 for this reason it was excluded. In total 18749 osteoblasts were analysed.

As can be seen in *Figure 111* the proportion of cells deficient cells for complex I is significant in comparison to the other samples with 9.9% NDUFB8 and 5.1% for GRIM19 values lying outside and below the 0.95% contour. SDHA deficiency was evident in just in 4.5% of the cells analysed. For Complex IV the level of deficient cells is less pronounced 7.1% MTCO1 and 2.1% COX4. OSCP was deficient in 5.1% of the cells.

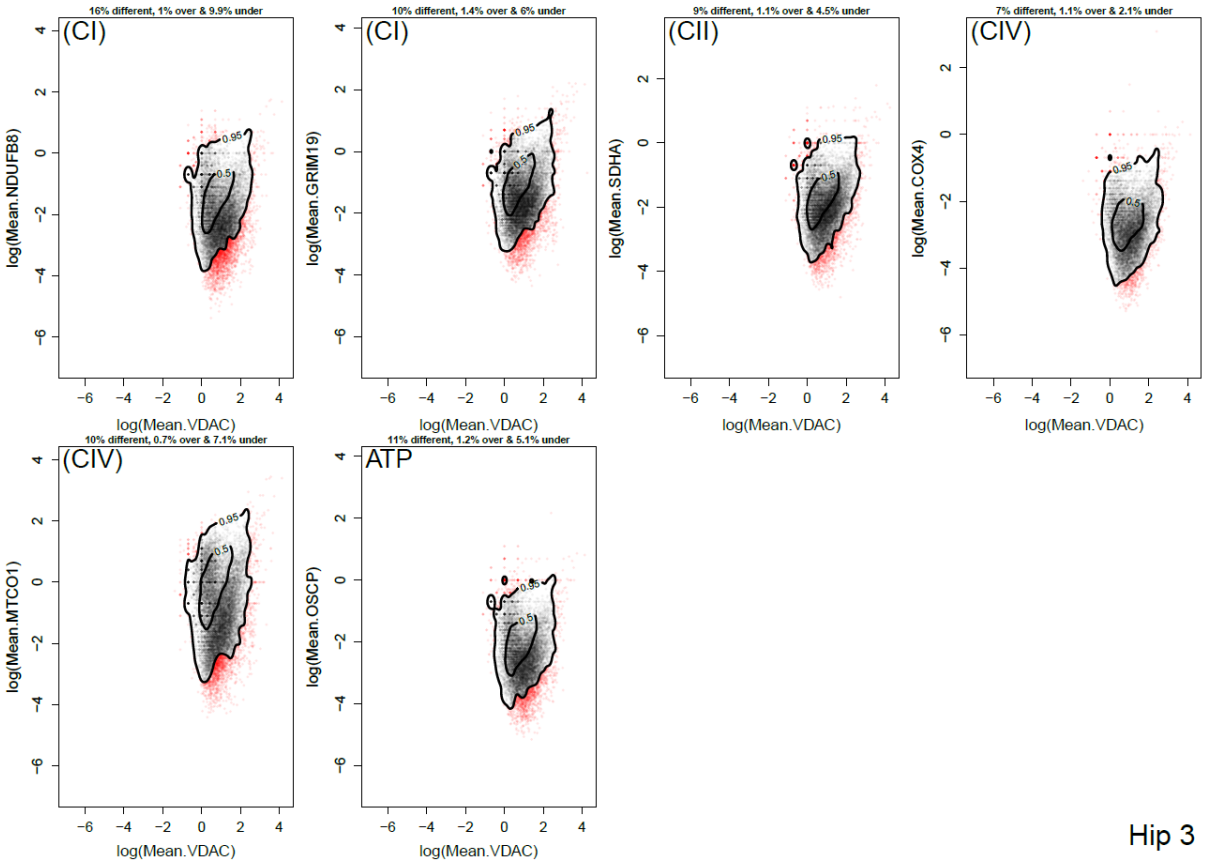

Figure 111 Estimating deficiency in Complex I, Complex II, Complex IV and Complex V Data from Hip 3: Contour lines represent the kernel density estimate levels containing 95% and 50% of the control population for each pairwise comparison. Grey points are from patient cells that lie within the 95% contour from controls. Red points are from patient cells lying outside the 95% contour from controls. The proportion of cells different from, vertically above and vertically below the 95% contour from controls written above each panel.

5.4.1.4 Data for the patient "Hip 4"

Hip 4 samples were taken from an 83-year-old female undergoing a total hip replacement for the failure of fixation following a fractured neck of femur. In total 6 ROIs from 1 section/slide were analysed. This totalled 7867 osteoblasts. There were no abnormal ROIs in terms of signal profile to be filtered out.

As can be seen in *Figure 112* the proportion of deficient cells for complex I compared to the control contours is 2.2% NDUFB8 and 1.9% for GRIM19. SDHA protein deficiency was evident in just in 1% of the cells analysed. For Complex IV the level of deficient cells is less pronounced 0.75% MTCO1 and 1.2% COX4. There were also low levels of deficiency in OSCP 1.9%.

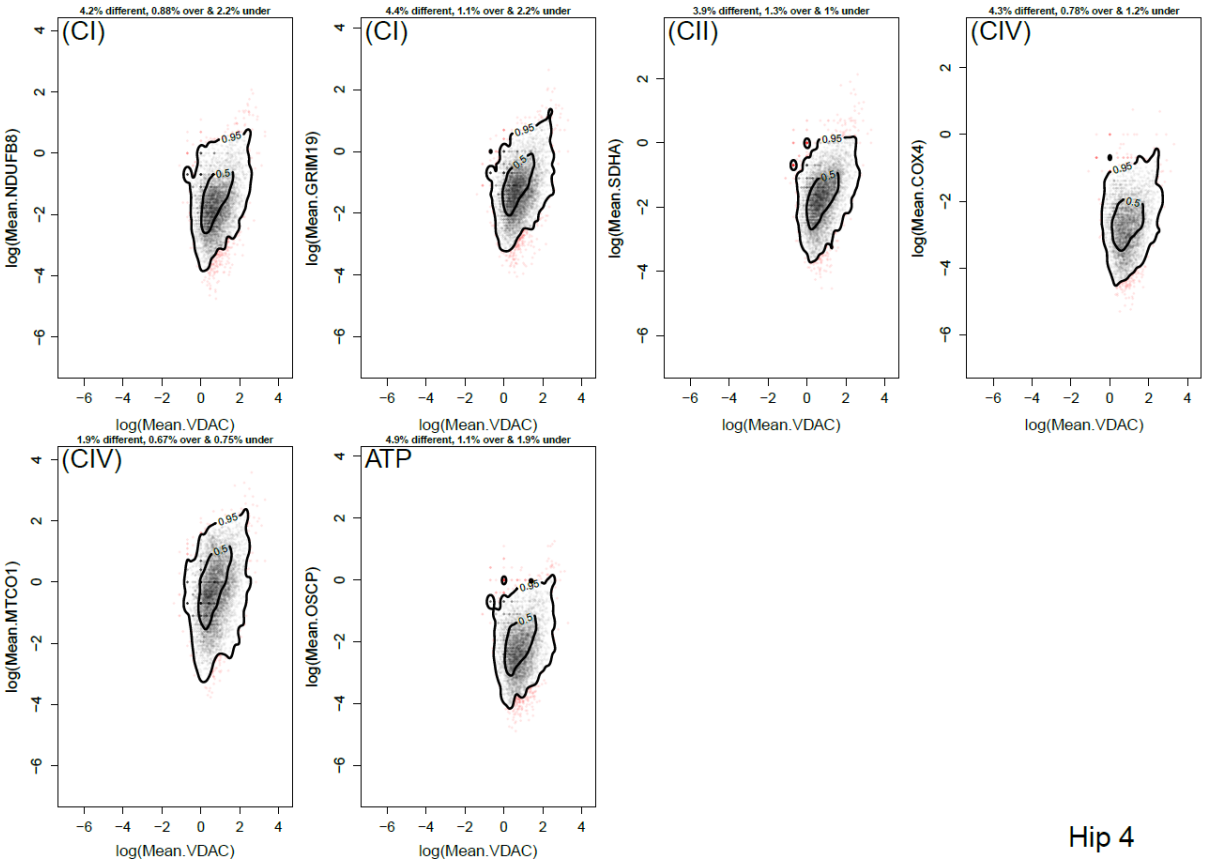

Figure 112 Estimating deficiency in Complex I, Complex II, Complex IV and Complex V Data from Hip 4: Contour lines represent the kernel density estimate levels containing 95% and 50% of the control population for each pairwise comparison. Grey points are from patient cells that lie within the 95% contour from controls. Red points are from patient cells lying outside the 95% contour from controls. The proportion of cells different from, vertically above and vertically below the 95% contour from controls written above each panel.

5.4.1.5 Data for the patient "Hip 5"

Hip 5 samples were taken from a 66-year-old female undergoing a total hip replacement for osteoarthritis. 7 ROIs were analysed from one section/slide. This totalled 3071 osteoblasts. One ROI was removed due to abnormal signal in comparison to the other 7 ROIs (5-1-8).

As can be seen in *Figure 113* there was a raised proportion of deficient cells for complex I compared to the control contours is 6.6% NDUFB8 and 4.5% for GRIM19. SDHA protein deficiency was evident in just in 1.3% of the cells analysed. For Complex IV the level of deficient cells is less pronounced 0.59% MTCO1 and 1.9% COX4. OSCP also showed a raised proportion of deficient cells of 4.5%.

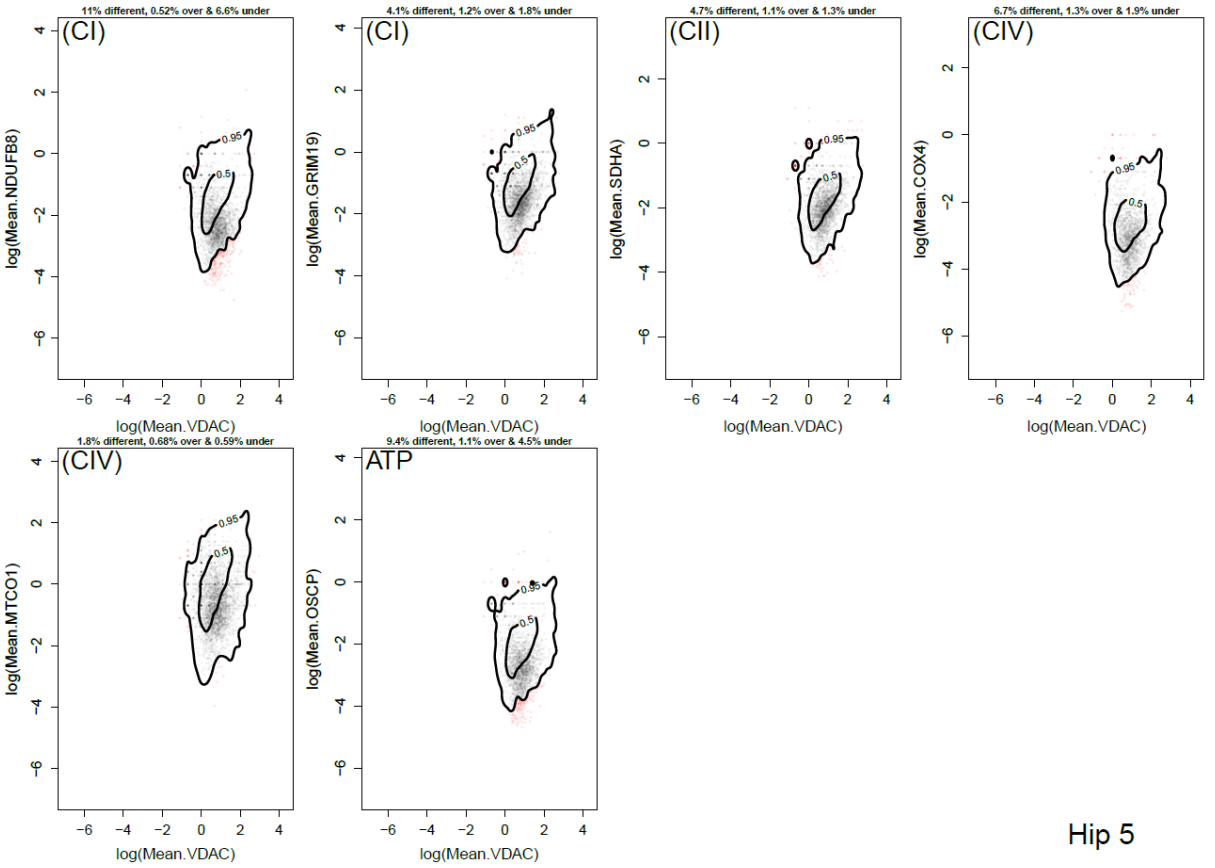

Figure 113 Estimating deficiency in Complex I, Complex II, Complex IV and Complex V Data from Hip 5: Contour lines represent the kernel density estimate levels containing 95% and 50% of the control population for each pairwise comparison. Grey points are from patient cells that lie within the 95% contour from controls. Red points are from patient cells lying outside the 95% contour from controls. The proportion of cells different from, vertically above and vertically below the 95% contour from controls written above each panel.

5.4.1.6 Data for the patient "Hip 6"

Hip 6 samples were taken from a 45-year-old female undergoing a total hip replacement osteoarthritis. 5 ROIs were analysed from one section or slide. This totalled 2407 osteoblasts analysed. ROIs 6-1-7 and 6-1-8 were removed from further analysis for abnormal signals across all antibody targets when in comparison to the other ROIs

As can be seen in *Figure 114* the level of deficient cells seen was elevated compared to other patients. Complex I deficiency was 6.4% for NDUFB8 and 1.2% for GRIM19. SDHA deficiency was also lower than the complex I deficiency seen only 1.5%. Complex IV deficiency was less pronounced 2.7% MTCO1 and 1.2% COX4. OSCP deficiency was only present in 2.4% of osteoblasts.

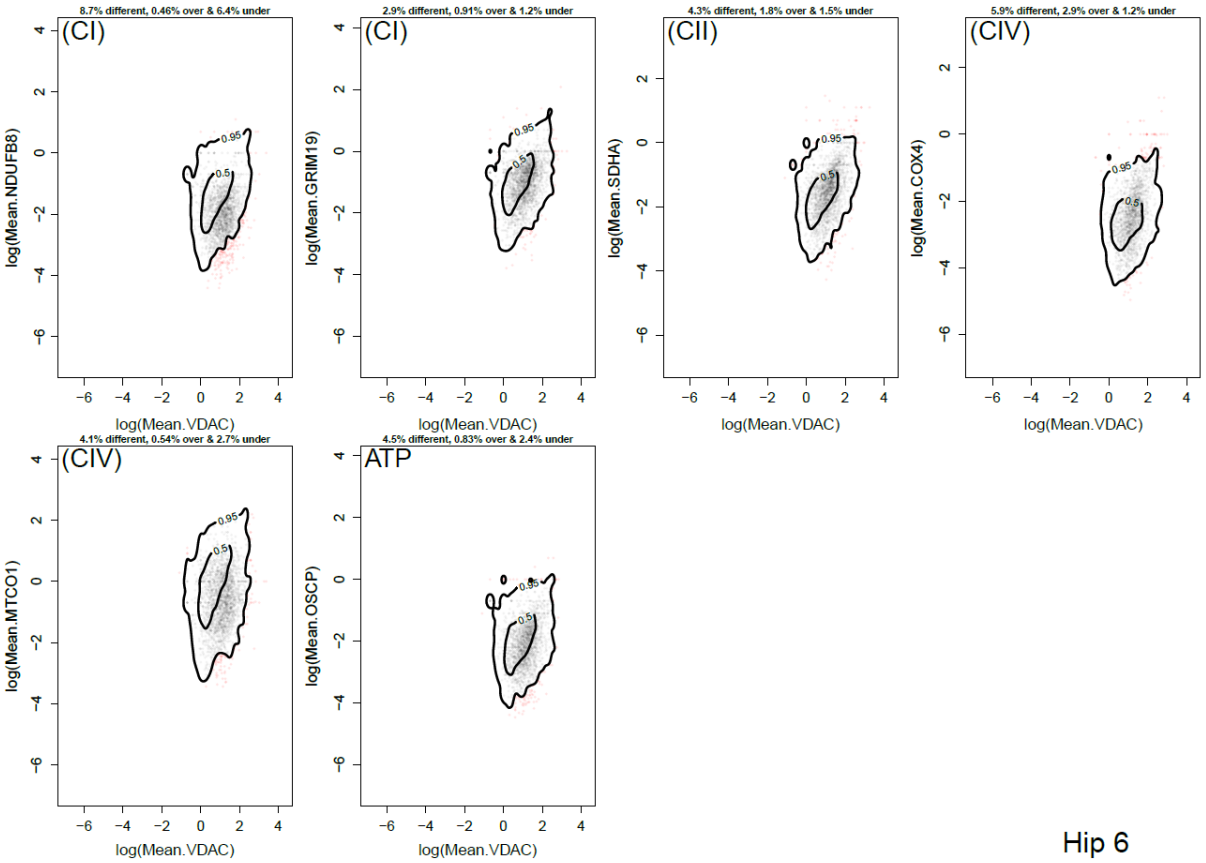

Figure 114 Estimating deficiency in Complex I, Complex II, Complex IV and Complex V Data from Hip 6: Contour lines represent the kernel density estimate levels containing 95% and 50% of the control population for each pairwise comparison. Grey points are from patient cells that lie within the 95% contour from controls. Red points are from patient cells lying outside the 95% contour from controls. The proportion of cells different from, vertically above and vertically below the 95% contour from controls written above each panel.

5.4.1.7 Data for the patient "Hip 7"

Hip 7 samples were taken from an 82-year-old female undergoing a total hip replacement osteoarthritis. 4 ROIs on one slide were analysed, this totalled 4743 osteoblasts. ROI 1 was excluded due to abnormal signal.

As can be seen in Figure 115 the level of deficient cells seen was significantly elevated compared to other patients. Complex I deficiency was 16% for NDUFB8 and 5.8% for GRIM19. SDHA II deficiency was also lower than the complex I deficiency seen only 3.7%. Complex IV deficiency was less pronounced 4.1% MTCO1 and 1.9% COX4. OSCP deficiency was seen in 5.7% of osteoblasts.

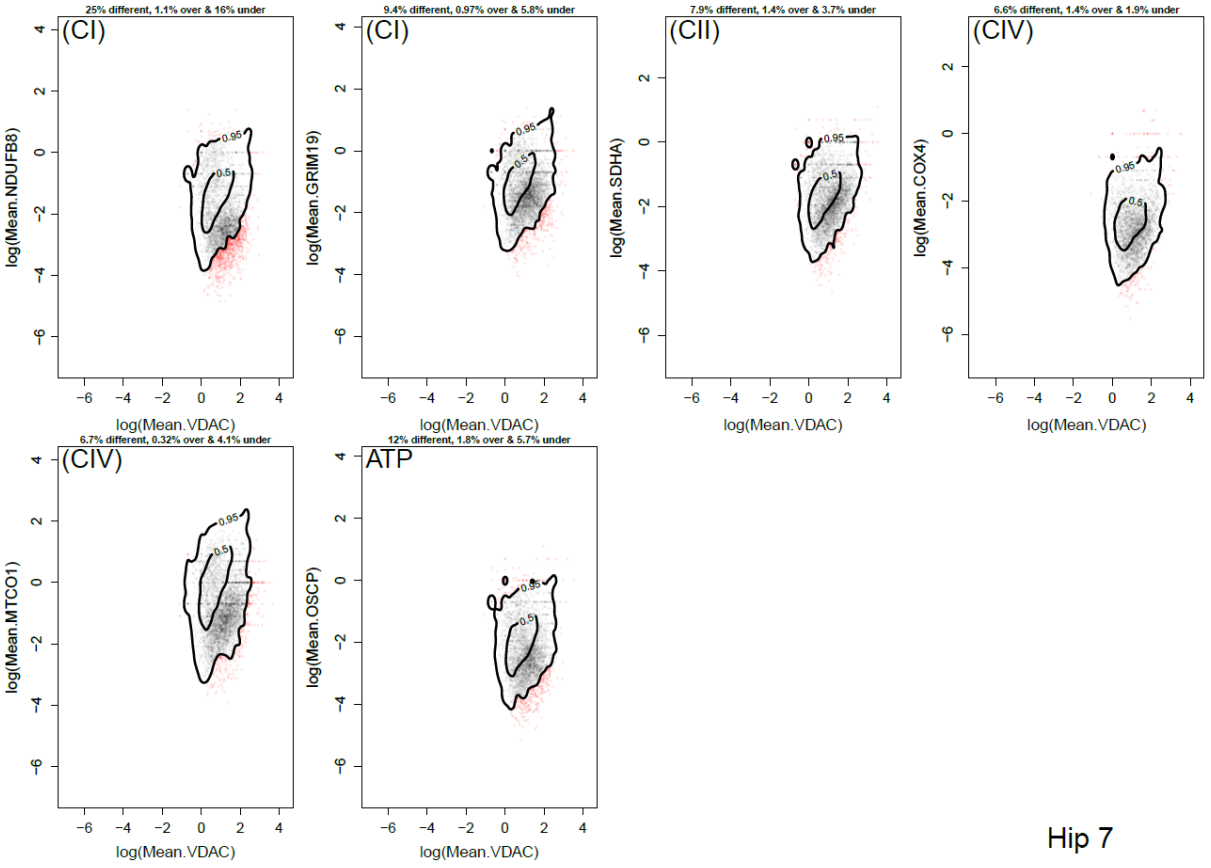

Figure 115 Estimating deficiency in Complex I, Complex II, Complex IV and Complex V Data from Hip 7: Contour lines represent the kernel density estimate levels containing 95% and 50% of the control population for each pairwise comparison. Grey points are from patient cells that lie within the 95% contour from controls. Red points are from patient cells lying outside the 95% contour from controls. The proportion of cells different from, vertically above and vertically below the 95% contour from controls written above each panel.

5.4.1.8 Data for the patient "Hip 8"

Hip 8 samples were taken from a 74-year-old female undergoing a total hip replacement osteoarthritis. 6 ROIs from 1 section were analysed, this totalled 4820 osteoblasts. No ROIs had to be excluded for an abnormal signal.

As can be seen in *Figure 116* complex I deficiency was seen in 9.5% of NDUFB8 measurements and 6.9% of GRIM19 data points. Complex II deficiency was also raised in comparison to the rest of the patient cohort at 5.7% for SDHA. Complex IV deficiency was less pronounced but still elevated in comparison to the rest of the patient cohort: with MTCO1 showing 7.1% and COX4 2.1% deficiency. OSCP deficiency was present in 6.7% of the osteoblasts.

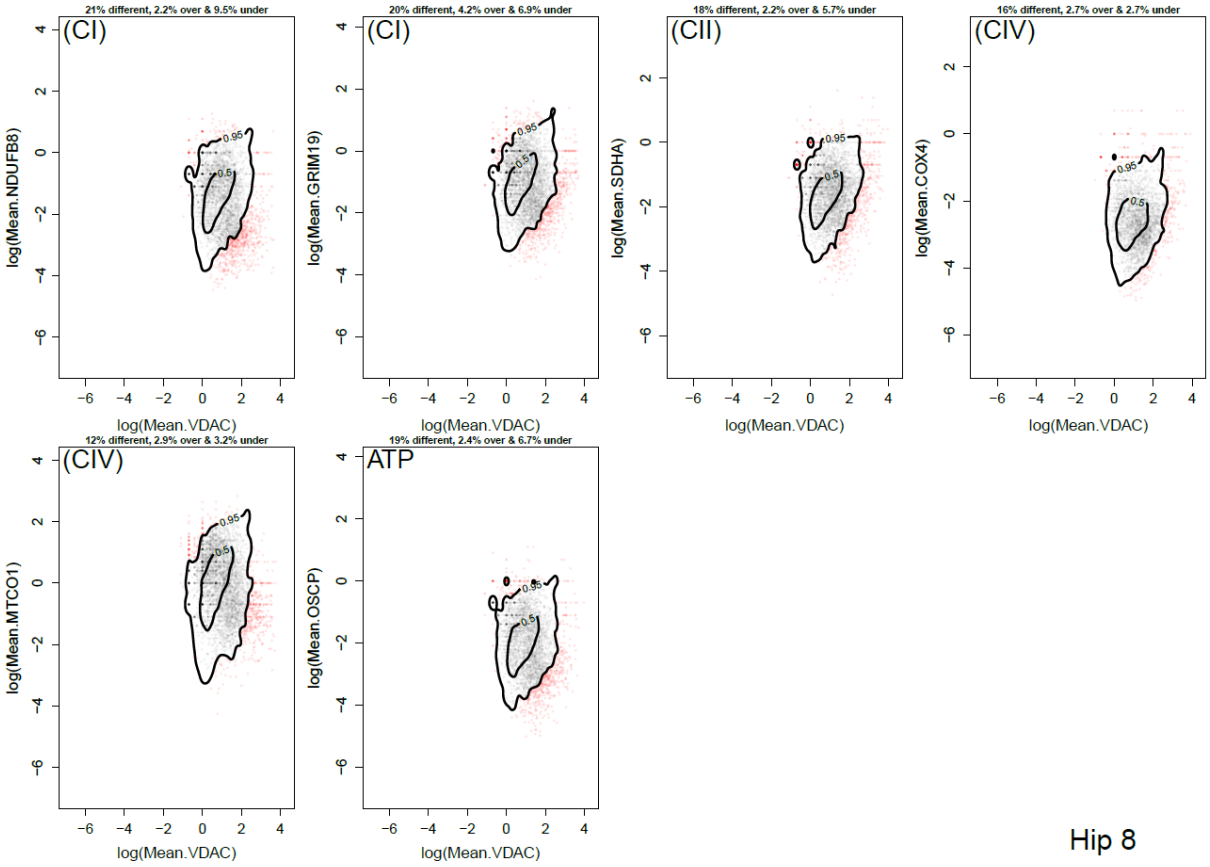

Figure 116 Estimating deficiency in Complex I, Complex II, Complex IV and Complex V Data from Hip 8: Contour lines represent the kernel density estimate levels containing 95% and 50% of the control population for each pairwise comparison. Grey points are from patient cells that lie within the 95% contour from controls. Red points are from patient cells lying outside the 95% contour from controls. The proportion of cells different from, vertically above and vertically below the 95% contour from controls written above each panel.

5.4.1.9 Data for the patient "Hip 9"

Hip 9 samples were taken from a 64-year-old male undergoing a total hip replacement osteoarthritis. 10 ROIs were analysed across two different sections/slides. There was no anomaly signal ROIs seen. In total 15446 osteoblasts were analysed across the 10 ROIs.

As can be seen in *Figure 117* of the 15446 osteoblasts analysed 3.4% showed deficiency in NDUFB8 and 3.1% for GRIM19. Complex II or SDHA levels showed a deficiency in 1.3% of the osteoblasts analysed. With regards to complex IV deficiency, MTCO1 values were deficient in 1.5% of osteoblasts with comparable figures of 1.4% seen in COX4. Complex V deficiency in terms of OSCP expression was also not significantly reduced at 2.4% of osteoblasts showing deficiency.

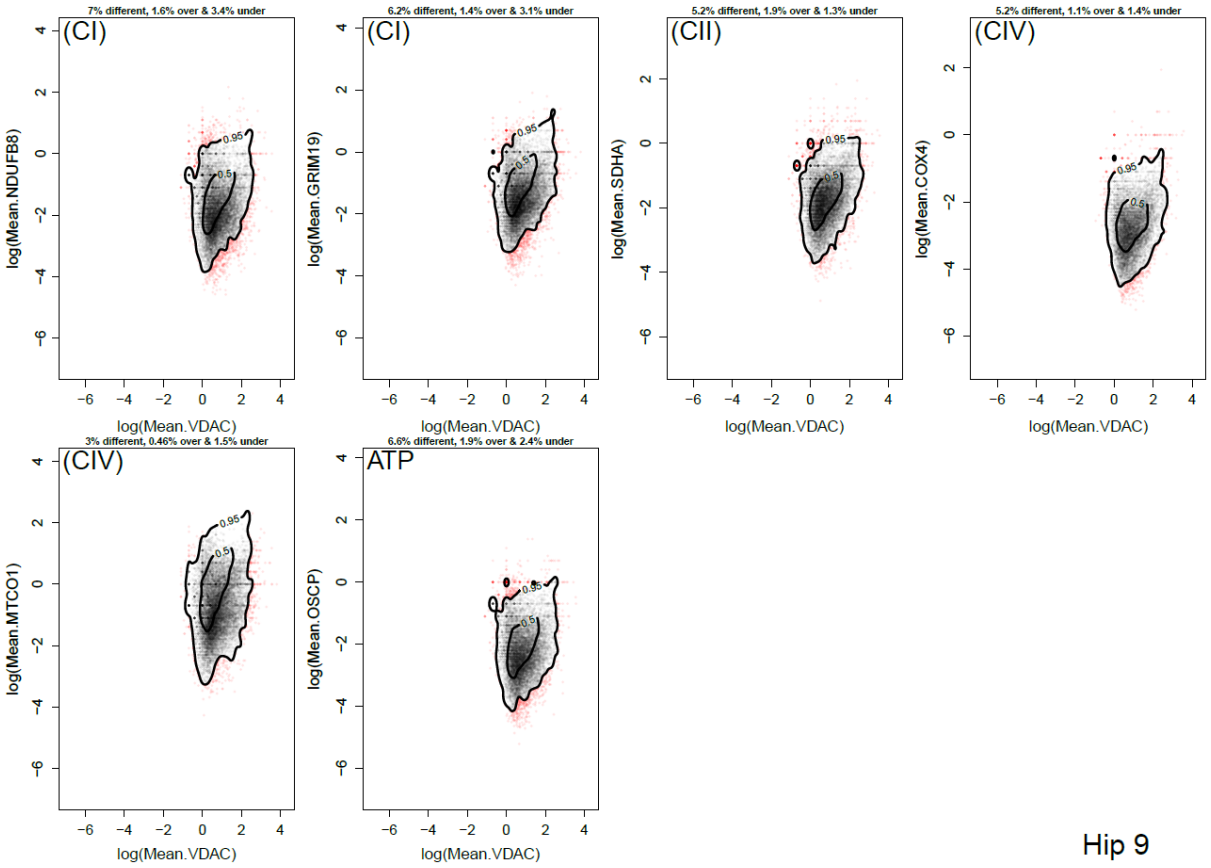

Figure 117 Estimating deficiency in Complex I, Complex II, Complex IV and Complex V Data from Hip 9: Contour lines represent the kernel density estimate levels containing 95% and 50% of the control population for each pairwise comparison. Grey points are from patient cells that lie within the 95% contour from controls. Red points are from patient cells lying outside the 95% contour from controls. The proportion of cells different from, vertically above and vertically below the 95% contour from controls written above each panel.

5.4.1.10 Data for the patient "Hip 10"

Hip 10 samples were taken from a 62-year-old male undergoing a total hip replacement osteoarthritis. 13 ROIs were analysed across 2 sections or slides. No ROIs needed to be excluded for abnormal signal profiles. In total 7503 osteoblasts were analysed.

As can be seen in *Figure 118* a relatively large proportion of deficiency is seen in the complex I proteins of the osteoblasts analysed (13% for NDUFB8 and 12% for GRIM19). SDHA/complex II levels were deficient in 8.4% of the osteoblasts. Whereas complex IV levels of deficiency were less pronounced (4.7% of MTCO1 and 3% deficiency is COX4). OSCP also was deficient in 8.3% of osteoblasts.

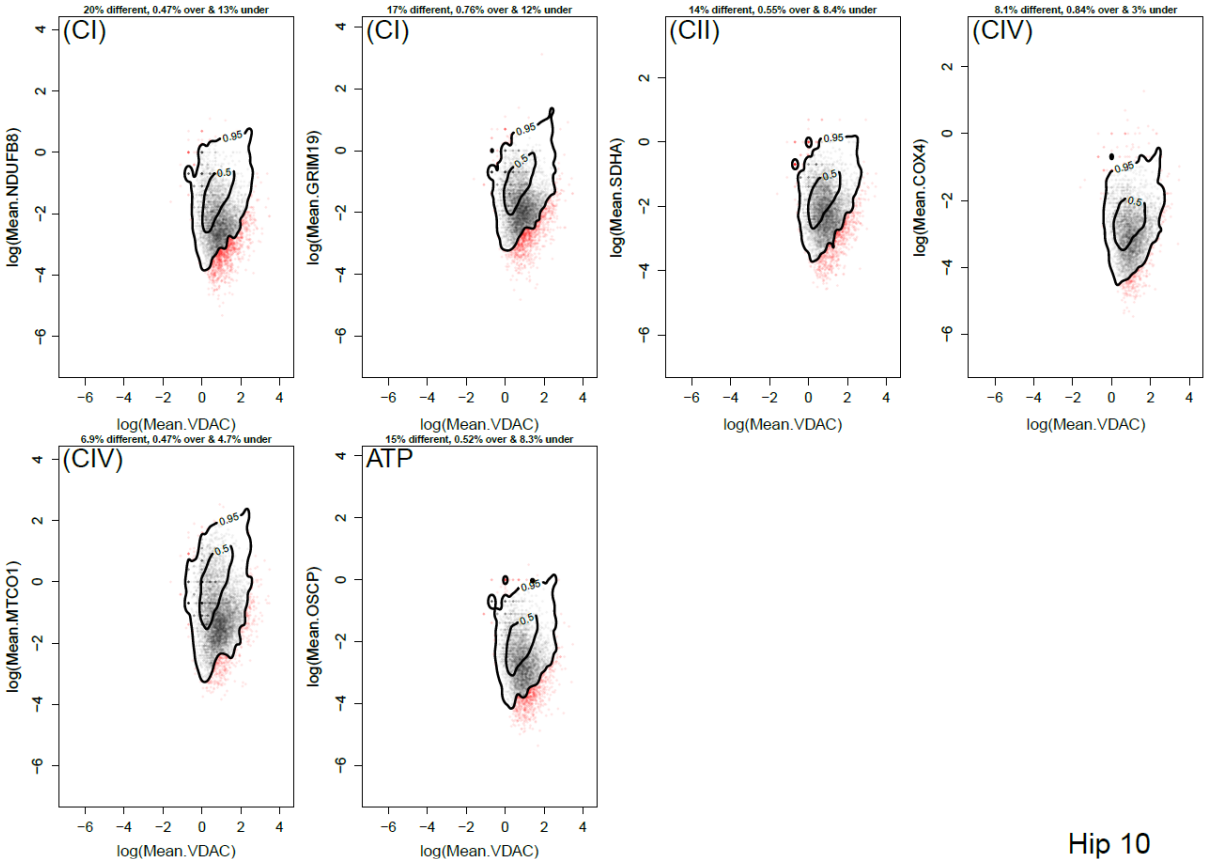

Figure 118 Estimating deficiency in Complex I, Complex II, Complex IV and Complex V Data from Hip 10: Contour lines represent the kernel density estimate levels containing 95% and 50% of the control population for each pairwise comparison. Grey points are from patient cells that lie within the 95% contour from controls. Red points are from patient cells lying outside the 95% contour from controls. The proportion of cells different from, vertically above and vertically below the 95% contour from controls written above each panel.

5.4.1.11 Data for the patient "Femur 1"

Femur 1 is the first of the control patients. Femur 1 samples were taken from a 22-year-old male having an intramedullary nailing procedure to address a leg length discrepancy. Samples were taken from the osteotomy site before insertion of the nail to lengthen and stabilise the femur. 11 ROIs from 1 section/slide were analysed and this totalled to 5053 osteoblasts. No ROIs needed to be removed from analysis due to abnormal signal values.

As expected in the paediatric and younger patient controls the levels of deficiency were low for complex I, II and IV. Complex I deficiency was only seen in 1.8% of osteoblasts for NDUFB8 and 1.7% of GRIM19. Complex II deficiency was present in 1.4% of cells. Complex IV deficiency was seen in 2.4% of cells (MTCO1) and 0.99% of cells (COX4). Only 1.4% of osteoblasts were deficient for OSCP.

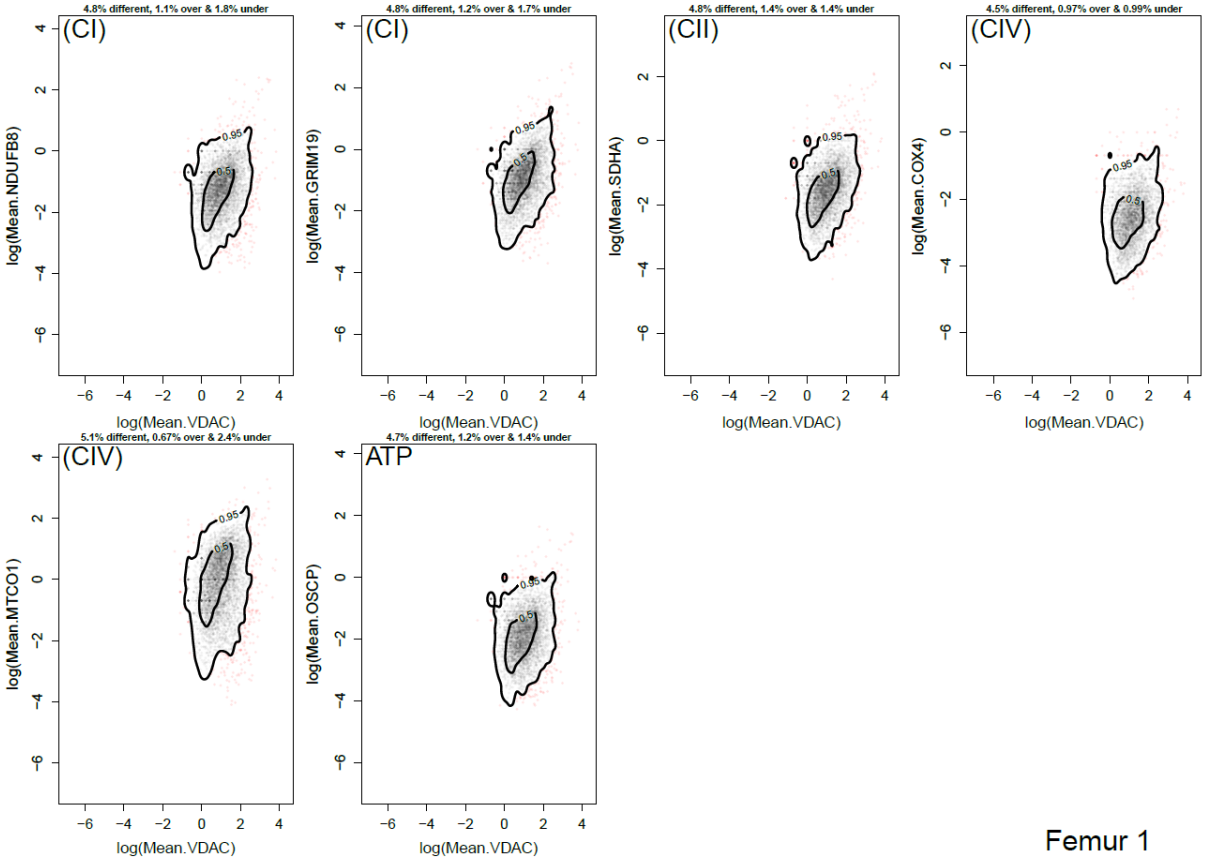

Figure 119 Estimating deficiency in Complex I, Complex II, Complex IV and Complex V Data from Femur 1: Contour lines represent the kernel density estimate levels containing 95% and 50% of the control population for each pairwise comparison. Grey points are from patient cells that lie within the 95% contour from controls. Red points are from patient cells lying outside the 95% contour from controls. The proportion of cells different from, vertically above and vertically below the 95% contour from controls written above each panel.

5.4.1.12 Data for the patient "Paediatric 1"

Paediatric 1 is a 13-year-old male who had suffered an ankle injury or triplanar injury. This had caused a bony bridge to grow across the physis or growth plate causing deformity. This needed to be excised to restore correct alignment and restore growth potential. 5 ROIs were analysed from 1 section/slide. In total this accounted for 3827 osteoblasts.

Again, as seen in "Femur 1" the levels of deficiency seen here are much less than in the rest of the patient cohort. Complex I NDUFB8 expression only showed deficiency in 0.84% of osteoblasts analysed. GRIM19 deficient cells accounted for just 0.73%. Complex II deficiency was evident in just 0.68% of osteoblasts. Complex IV deficiency was seen in 0.68% and 0.29% of osteoblasts for MTCO1 and COX4 respectively. There were also limited levels of OSCP deficiency just 0.52% of osteoblasts.

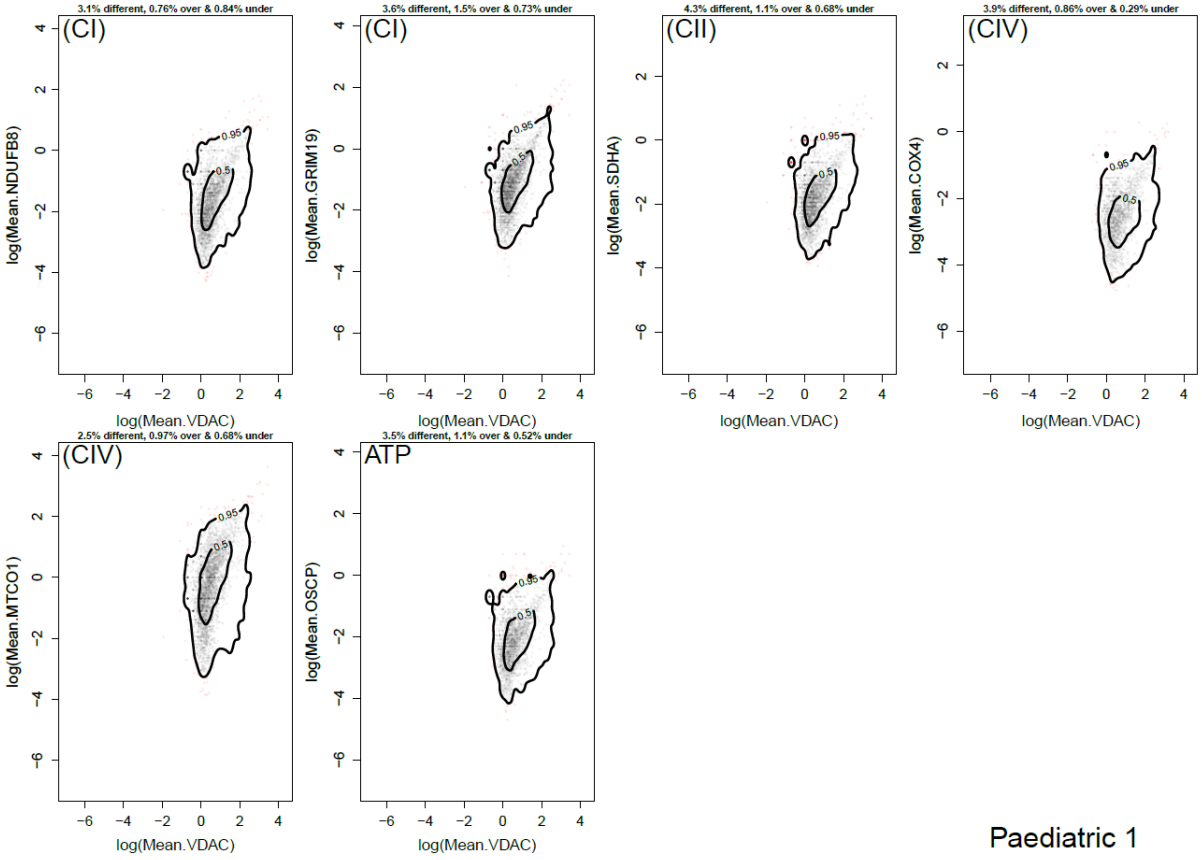

Figure 120 Estimating deficiency in Complex I, Complex II, Complex IV and Complex V Data from Paediatric 1: Contour lines represent the kernel density estimate levels containing 95% and 50% of the control population for each pairwise comparison. Grey points are from patient cells that lie within the 95% contour from controls. Red points are from patient cells lying outside the 95% contour from controls. The proportion of cells different from, vertically above and vertically below the 95% contour from controls written above each panel.

5.4.1.13 Data for the patient "Paediatric 2"

Paediatric 2 is a sample taken from an 18-month-old female who was undergoing a pelvic osteotomy for developmental dysplasia of the hip. This would re-orientate her acetabulum to restore normal anatomy and future growth of the femoral head and acetabulum. 13 ROIs were analysed from 2 sections/slides. No ROIs needed to be removed due to abnormal signal. In total 7378 osteoblasts were analysed.

As can be seen in *Figure 121* again as with the other young control patients, femur 1 and paediatric 1 low levels of deficiency were seen in complex I (NDUFB8 deficiency in 0.92% of osteoblasts and 0.53% deficiency of GRIM19 in osteoblasts). Complex II had a deficiency in just 0.52% of osteoblasts, with complex IV also following a similar trend of just 0.38% and 0.39% for MTCO1 and COX4 respectively. OSCP also had relatively little deficiency present in the osteoblasts analysed just 0.70%.

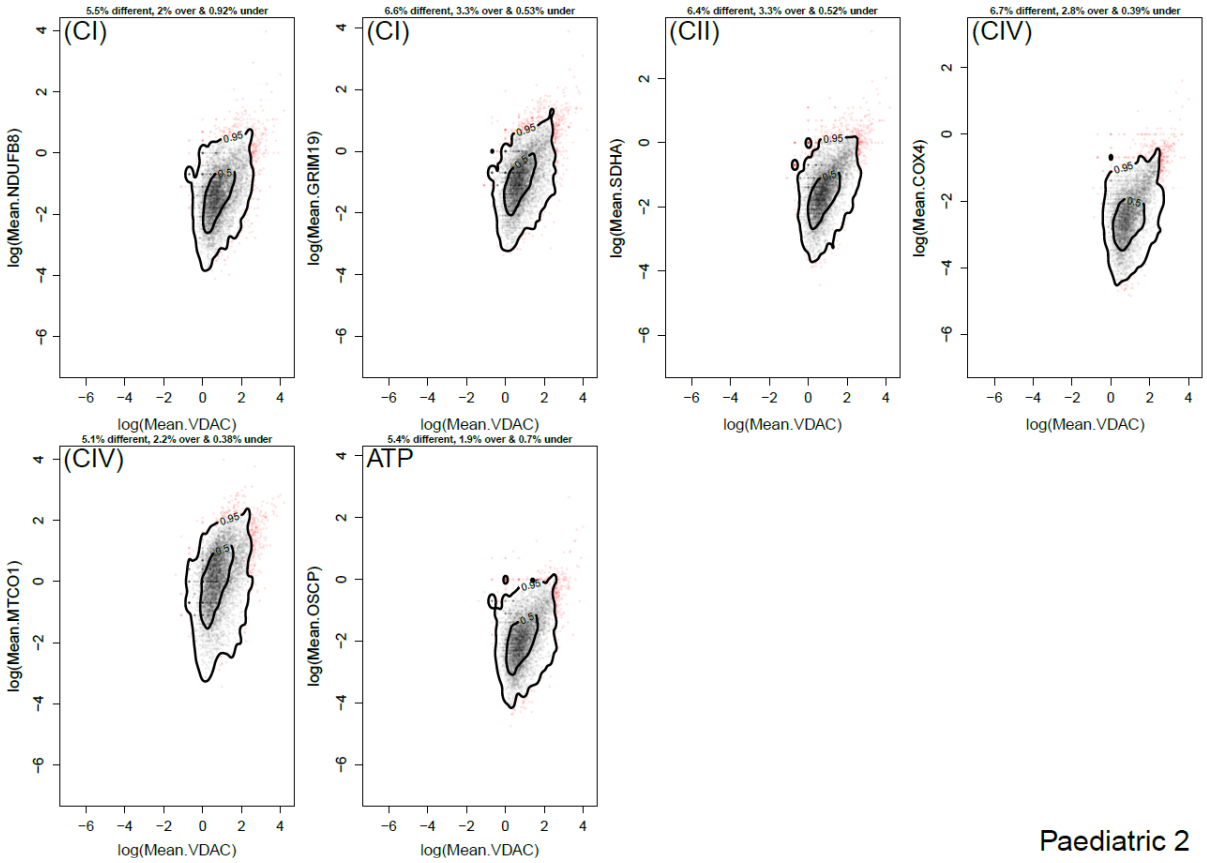

Figure 121 Estimating deficiency in Complex I, Complex II, Complex IV and Complex V Data from Paediatric 2: Contour lines represent the kernel density estimate levels containing 95% and 50% of the control population for each pairwise comparison. Grey points are from patient cells that lie within the 95% contour from controls. Red points are from patient cells lying outside the 95% contour from controls. The proportion of cells different from, vertically above and vertically below the 95% contour from controls written above each panel.

5.4.1.14 Results Summary

The proportion of deficient cells observed was calculated in each patient and plotted against age as in *Figure 122*. This analysis demonstrates a clear increase in NDUFB8 deficiency with age, a less pronounced increase with age for an alternative CI subunit GRIM19 and only minor changes in complex II, Complex IV and complex V. Complex II and IV deficiency levels were generally around the 5% expected variation cut off. There is a very slight increase in the prevalence of OSCP deficiency with age but this is much less pronounced than that of complex I. Evidence of complex I deficiency is in line with previous research in other human tissues (19) and the PolgA^{mut}/PolgA^{mut} mouse model (205).

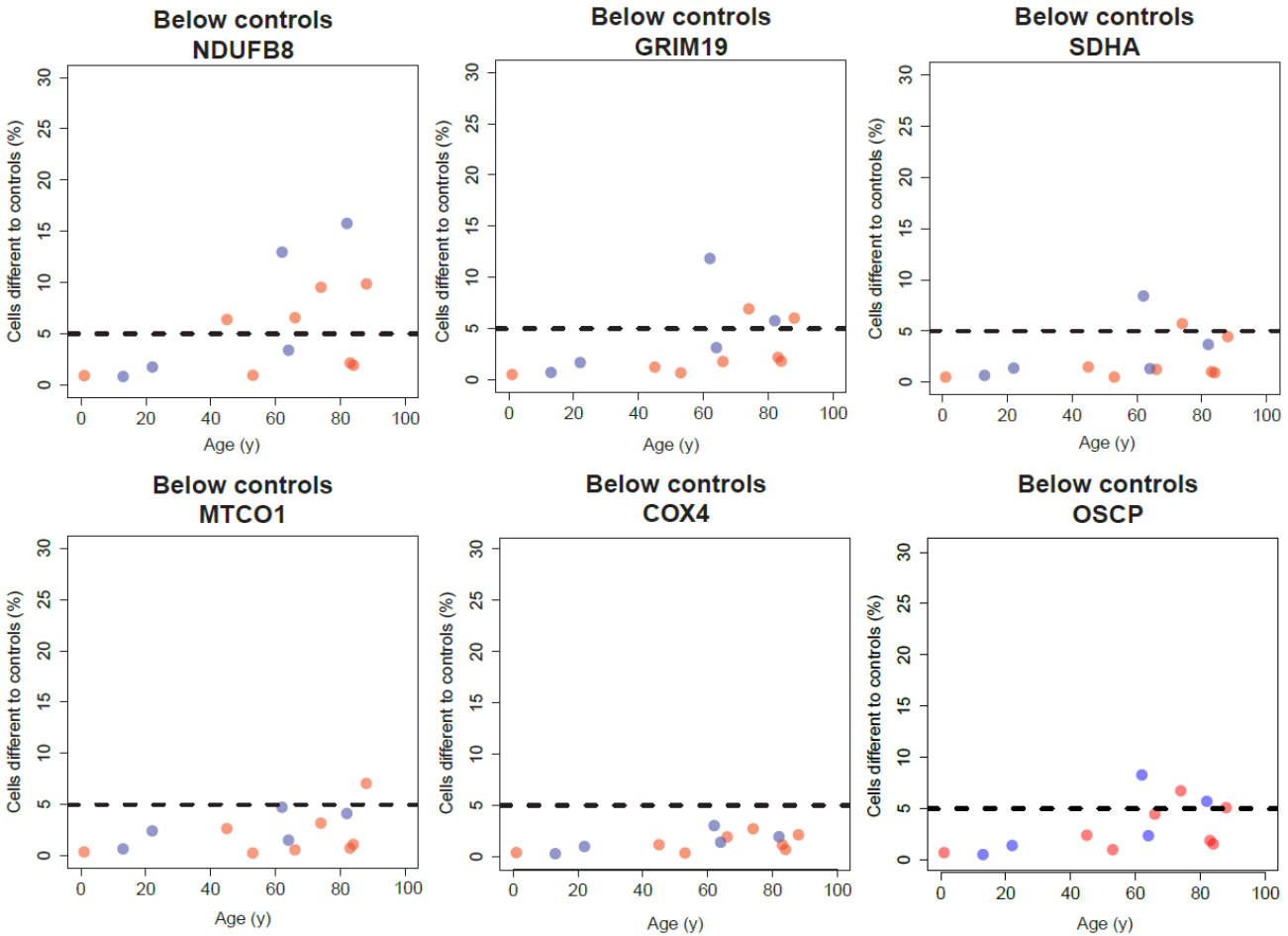

Figure 122 Variation in Complex I, Complex II & CIV deficiency with age. *The proportion of cells lying vertically below the 95% contour from controls in all patients presented in Table 33. Blue points represent proportions from male patients and red points from female patients. The horizontal dashed line represents the proportion of differences from control patients that we might expect to see by chance i.e., 0.05.*

Patient	Age (years)	Sex	Male / Female	ɔtein deficiency on CyToF - cells below 0.95 contour						Osteoblast protein upregulation on CyToF - cells above 0.95 contour					
				iRIM19	SDHA	MTCO1	COX4	OSCP		NDUFB8	GRIM19	SDHA	MTCO1	COX4	OSCP
Hip 1	53	Female		0.96%	0.69%	0.52%	0.27%	0.35%	1.00%	2.80%	4.10%	4.80%	2.50%	3.60%	4.30%
Hip 2	84	Female		1.90%	1.80%	0.95%	1.10%	0.69%	1.60%	0.67%	1.20%	1.00%	0.72%	0.68%	1.10%
Hip 3	88	Female		9.90%	5.10%	4.50%	7.10%	2.10%	5.10%	1.00%	1.40%	1.10%	0.70%	1.10%	1.20%
Hip 4	83	Female		2.20%	1.90%	1.00%	0.75%	1.20%	1.90%	0.88%	1.10%	1.30%	0.67%	0.78%	1.10%
Hip 5	66	Female		6.60%	4.50%	1.30%	0.59%	1.90%	4.50%	0.52%	1.20%	1.10%	0.68%	1.30%	1.10%
Hip 6	45	Female		6.40%	1.20%	1.50%	2.70%	1.20%	2.40%	0.46%	0.91%	1.80%	0.54%	2.90%	0.83%
Hip 7	82	Female		16.00%	5.80%	3.70%	4.10%	1.90%	5.70%	1.10%	0.97%	1.40%	0.32%	1.40%	1.80%
Hip 8	74	Female		9.50%	6.90%	5.70%	3.20%	2.70%	6.70%	2.20%	4.20%	2.20%	2.90%	2.70%	2.40%
Hip 9	64	Male		3.40%	3.10%	1.30%	1.50%	1.40%	2.40%	1.60%	1.40%	1.90%	0.46%	1.10%	1.90%
Hip 10	61	Male		13.00%	12.00%	8.40%	4.70%	3.00%	8.30%	0.47%	0.76%	0.55%	0.47%	0.84%	0.52%
Femur 1	19	Male		1.80%	1.70%	1.40%	2.40%	0.99%	1.40%	1.10%	1.20%	1.40%	0.67%	0.97%	1.20%
Paediatric 1	13	Male		0.84%	0.73%	0.68%	0.68%	0.29%	0.52%	0.76%	1.50%	1.10%	0.97%	0.86%	1.10%
Paediatric 2	1.5	Female		0.92%	0.53%	0.52%	0.38%	0.39%	0.70%	2.00%	3.30%	3.30%	2.20%	2.80%	1.90%

Table 36: A summary table showing the percentage of osteoblasts above and below the 0.95 contour for complex I, complex II, complex IV and complex V across the patient cohort. Values greater than 5% (deemed level of background outliers) are highlighted in red.

Looking specifically hip 3, 7, 8 and 10 had more of a global mitochondrial deficiency seen in some cells with evidence of deficiency in complexes I, IV and V. All patients that showed deficiency for MTCO1 had reciprocal high levels of complex 1 deficiency. Hip 8 and 10 also had a deficiency in SDHA which does not have any mtDNA coded proteins and suggest a more global respiratory chain issue within those cells. There was no significant upregulation of any of the other complexes in response to complex I deficiency with the levels of cells above the 0.95 contour remaining relatively constant throughout the cohort.

5.5 Discussion

Complex I deficiency is the most frequently observed mitochondrial respiratory chain disorder and this is in part due to its structure. It is the most complicated of the complexes in terms of its components and assembly. It is coded for both by nuclear and mitochondrial DNA, consisting of 45 subunits of which 7 are encoded by mtDNA (286). All 7 of these mtDNA coded proteins have reported pathological variants as do 21 of the nuclear-encoded proteins and 10 of the assembly factors (287, 288).

Mitochondrial DNA is prone to mutations with age with *de novo* mutations arising at a rate up to 10x greater than nucleic mutations (289). Mitochondrial DNA encodes for 7 proteins (ND1-6, ND4L) of complex I, compared to just 3 proteins of complex IV (COI-III). This accounts for 56% of the DNA accounting for complex I compared to 27% of complex IV (290). Not only is there more mtDNA accounting for complex I proteins but age-related mtDNA mutations frequently affect the area between the heavy and light strand origins of replication (291). This frequently affects the ND3, ND4, ND4L and ND5 proteins affecting complex I. Overall mutations affecting complex I are around twice as likely to occur than those affecting complex IV (290). There are no mtDNA encoded proteins in complex II instead it is made from 4 subunits which are nuclear-encoded (161). It is the rarest of the complexes to show mitochondrial deficiency or defect (387). Documented mutations have been associated with Leigh Syndrome and mutations in the flavoprotein and assembly proteins of complex II (388). These mutations are germline rather than acquired and tend to be associated with consanguinity (389) and deficiency is inherited in autosomal recessive fashion (390).

Changes in complex IV in previous studies are not detectable below the age of 35 and only detectable in one-third of colonocytes in patients over 70 (20). We did not detect significant levels of complex IV deficiency in the osteoblasts of our aged patients. Complex IV tends to be less affected by sporadic mtDNA mutations, possibly due to the lower number of CIV genes encoded by mtDNA. The threshold for deficiency is also higher for complex IV than complex I (391) which may explain the limited evidence of deficiency in this small sample population. The antibody targets for complex IV were COX4 and MTCO1. Anti-COX4+4L2 targets the nuclear-encoded subunits COX4+COX4L2. Anti-MTCO1 is primarily targeted at the mitochondrial encoded COX1 gene. Complex IV has 2 other mitochondrial encoded genes COX2 and COX3. The rest of complex IV is encoded by 10 nuclear proteins, these ten subunits are much smaller than the mtDNA encoded COX 1-3 (392), mutations are more likely to be in the mtDNA encoded proteins which would explain the elevated deficiency levels in MTCO1 when in comparison to the COX4 levels. Although there are syndromes and

pathology associated with the nuclear encoded COX subunits there are relatively fewer recognised DNA mutations in the nuclear-encoded subunits compared to the mtDNA encoded COX1-3 which is in part due to their size and mtDNA's predisposition for mutation (392).

Although the data shows significant differences in the complex I protein, NDUFB8 between young and old patients, the effect is not so apparent with GRIM19 in the limited sample population. GRIM19 or NDUFA13 is part of the P module of complex I and is among the first proteins assembled as part of the Q/Pp-a intermediate and only contains 1 mtDNA encoded protein (ND1). NDUFB8 is part of the PD-b module which is made up of the mitochondrially encoded proteins ND2, ND3, ND4-L, ND5 and ND6 (393). Thus, issues affecting the assembly and incorporation of NDUFB8 into complex I have a greater chance of causing deficiency than those of GRIM19 due to the presence of more mtDNA encoded proteins in each individual intermediate's assembly.

The data also did not show any upregulation of complexes in response to deficiency of complex I. Work by Warren et al., (394) has shown upregulation of complex II, III, IV and V although this was in patients with an established complex I deficiency rather than an age-related acquired deficiency as seen here.

5.6 Conclusion

Through this work, I have shown the potential of IMC to investigate protein expression levels in bone in particular singular osteoblasts, where we were able to analyse over 130,000 cells across the 13 sample patients. Although after exclusion of some ROIs/slides the final number of osteoblasts analysed was 104,244. Six proteins and two DNA markers were detected in the antibody panel we used but IMC has the scope for many more antibodies to be detected synchronously on the same slide. This forgoes the need for further multiplexed staining methods requiring further slide preparation or sequential staining steps which can affect the integrity of the tissue. Along with antibody data, IMC also has the scope to provide spatial data for the selected antibodies with the x/y coordinates of each signal recorded and reconstructed into an image. Analysis of fixed FFPE and snap-frozen tissue allows flexibility and the retrospective analysis of archived samples (395, 396). Whilst proteomics may compete or exceed the possible number of parameters to be measured it does not give a spatial component and image reconstruction in the same way as imaging mass cytometry. IMC would provide options to analyse population densities as Dobson et al., has in the PolgA^{mut}/PolgA^{mut} *model* which showed reduced osteoblast population densities associated with accelerated bone loss (206).

The staining protocol developed is relatively simple and based upon the established quadruple immunofluorescent assay used by Dobson et al., (205). This translation from immunofluorescence to imaging mass cytometry is relatively straightforward and could be replicated for further assays.

The method of analysis developed here is a clear pathway which can be used in heterogeneous tissue with some degree of automation once the parameters to determine cell and protein detection are appropriately defined. Most IMC data generated thus far has been on relatively homogenous cellular soft tissue such as tumours and immune system tissues (396, 397). Here it has been utilised to discover the link between cell and disease (395). The significant advantage of imaging mass cytometry over conventional techniques and even mass cytometry is that it allows the analysis of multiple parameters of multiple cells and interaction between cells, all within their microenvironment without disruption of tissue architecture.

The protocol and image analysis pathway presented here paves a new era for discovery in bone. With no autofluorescence the ability to analyse many more proteins and individual cells with disturbing the structure of mineralised bone now possible. Along with the relationship of the proteins and cells to one another within the tissue sample.

Whilst IMC represents a potential new era of discovery there are limitations. To date, most conjugated antibodies available are targeted towards cancer and immunology targets. For more specific targets outside of these areas of investigation, antibodies must be conjugated. Conjugation relies on the possibility to get the required antibody target in a protein-free solution, although this is possible and purification kits or independent purification is an option. As alluded to by Warren et al., (394) there is a potential issue in conjugating antibodies in the fact batches may vary in terms of concentration from experiment to experiment and would need validation from one batch to another to quantify this (394). The results here were not affected as all sections were stained with the same batch of antibodies.

The other limiting factor is the resolution this is around 1μm^2. Whilst, on the whole, this does allow subcellular imaging the resolution is poor in comparison to microscopy and visualising subcellular detail such as mitochondrial shape and morphology is not possible, especially in smaller cells like osteoblasts. This also introduces more issues in regard to errors on small cells as the signal is a digital value per pixel or average for that pixel it is not continuous so borders of cells could on average be lower values than expected due to overlap with the background in smaller cells, this is less of an issue with larger cells, however.

Whilst autofluorescence is not an issue we did identify issues with the signal and there is a background signal. Subjectively we found the laser intensities required for the ablation of bone to be much higher than that of other soft tissue and in prior experiments, a gradual loss of power was noted requiring laser replacement. In terms of specificity of the signal as in fluorescent-based techniques, non-specific binding of antibodies can be an issue. For this reason, we based the protocol upon validated and tested techniques employed in fluorescent-based analysis before conjugation with heavy metals. Successful conjugation was also clarified using compensation beads and the Helios mass cytometer.

In terms of background signal, this was addressed on two fronts. Noise reduction steps were carried out as part of the Volocity pipeline analysis. Signal was also only recorded for areas identified by the various masks created through volocity. Other authors have taken their own steps to address the issues of background. A standardised method is currently not clear and is image tissue dependent. Wang et al., utilised a 5 × 5 μm^2 median filter to account for horizontal streaking. This means for each pixel if the value exceeds the median filter area and lies in the top 2% of pixels it was removed (398). Keren et al., use a “no primary antibody” type control step measuring the background signal of a

channel not associated with antibody signal. The signal intensity was then used as a threshold to remove background signal intensity. Keren et al. also noted areas of isolated low signal intensity were associated with noise whereas true signal was clustered. They also filtered out the isolated pixels (399).

Whilst there is not one clear method to address background with regards to variability in terms of tissue type and architecture it should be acknowledged and accounted for in regard to the assembly of an experimental and analysis protocol.

This work highlights the correlation between accumulating mitochondrial respiratory chain deficiency and age in human osteoblasts. Previous work with the PolgA^{mut}/PolgA^{mut} mouse model showed evidence of premature osteoporosis with respiratory chain deficiency (181). Dobson et al. confirmed that respiratory chain deficiency in osteoblasts was evident and related to osteoporosis in the PolgA^{mut}/PolgA^{mut} mouse model. The in vitro assays demonstrated significant defects in bone mineralisation by osteoblasts with increased resorption in osteoclasts related to an increase in mtDNA mutation load and respiratory chain deficiency.

The new discovery in terms of quantifying the increasing presence of respiratory chain deficiency in human osteoblasts offers an insight into the pathology and cause of age-related osteoporosis at a protein-based and cellular level. This mirrors the findings of the PolgA^{mut}/PolgA^{mut} mouse model and offers an insight into the pathogenesis of osteoporosis where increased bone resorption and decreases bone formation occurs. This also relates age acquired osteoporosis pathology and the implications of mitochondrial respiratory deficiency inline with the mitochondrial theory of ageing which affects cells almost universally (289).

In conclusion, I have optimised and developed the first use of an IMC assay on human bone assessing multiple proteins in osteoblasts. This work has demonstrated the suitability of IMC to analyse highly heterogeneous tissue and bone across a range of ages, assessing respiratory chain deficiencies present in human osteoblasts. This has further potential to build upon the work of Dobson et al., and their work with the PolgA^{mut}/PolgA^{mut} mouse model linking mitochondrial respiratory chain deficiency with the pathogenesis of osteoporosis (205).

Further development of the use of IMC in bone has the potential to unlock the combination of assays which were previously limited to single antibody measurements or the constraints and issues of

fluorescent-based analysis in bone. There is potential to analyse multiple pathways and cell interactions within bone which influence osteoporosis and other bone pathology.

5.7 Appendix

Table 37 Matrix displaying percentage crosstalk for metal tags. The signal overlap is indicated: blue boxes ≥ 0.5%, clear boxes ≤ 0.5%. Mass Channels are in columns and Mass Tag probes are in rows. For Mass Tags: Colour indicates probes that contribute ≥ 0.5% crosstalk into no channels (green), one or two channels (yellow), or more than two channels (orange). For Mass Channels: Colour indicates channels receiving ≥ 0.5% crosstalk from no probes (green), one or two channels (yellow), or more than two channels (orange). Images adapted from Fluidigm with extra information courtesy of FCCF Newcastle."

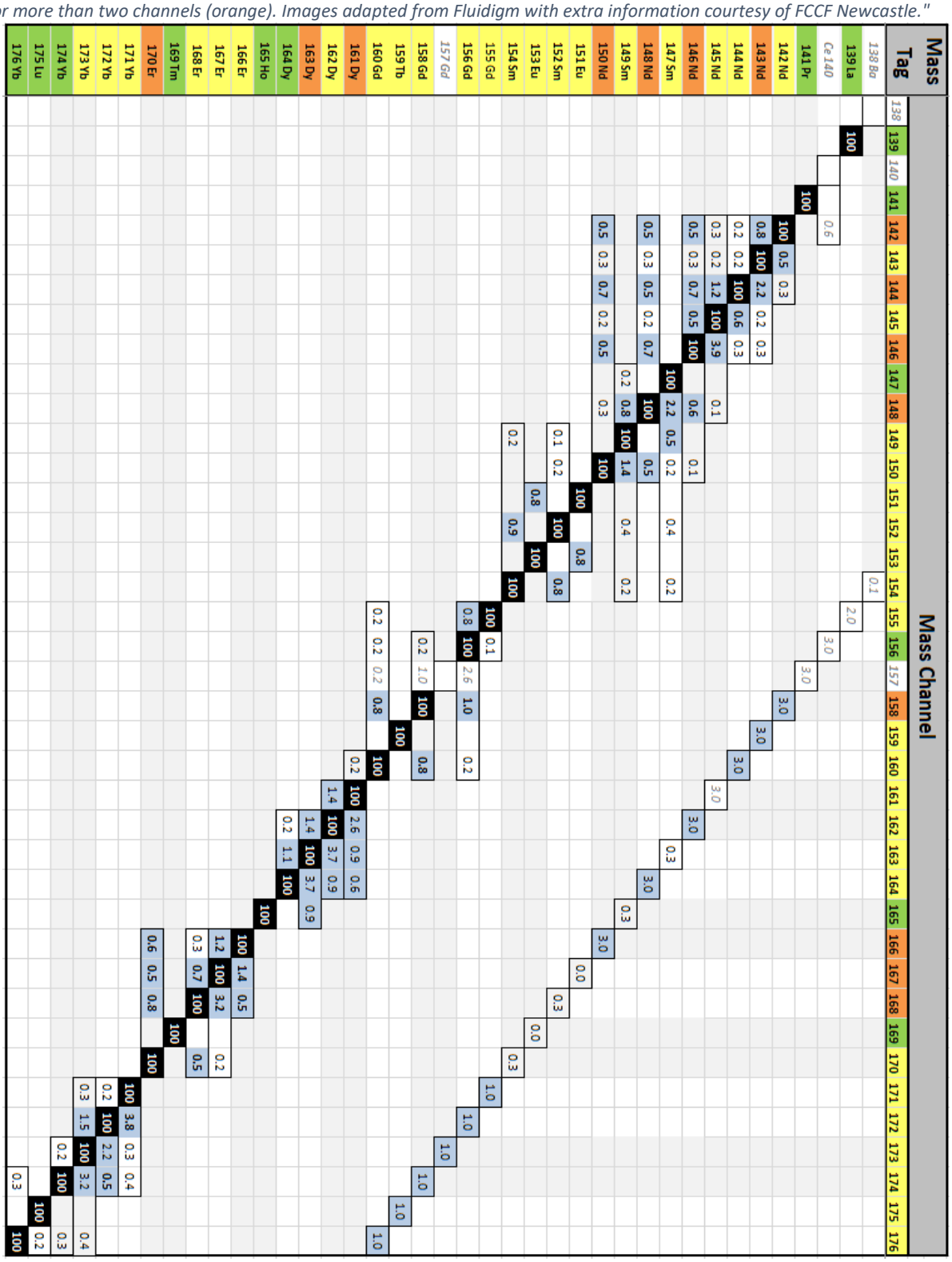

Chapter 6 Final discussion and conclusion

6.1 Current understanding of osteoporosis

Levels of osteoporosis are on the increase globally, the age-related deterioration in bone microarchitecture with increasing porosity and reduced mineralisation levels affects men and women universally and has an increased risk of fracture with age (4, 5). Prevalence in Western countries ranges from 9-38% for women and 1-8% of men (6).

Associated fragility fractures cause significant morbidity, mortality and huge costs to healthcare economies worldwide (8-10). Hip fracture alone costs the NHS £2 billion per year and is associated with a high 30-day (7.1%) and 1-year mortality (12).

The current overview of the literature regarding the pathogenesis of osteoporosis is multifactorial (3, 13, 14) with implications of diet and exercise (400, 401). There is also significant evidence suggesting a hormonal pathology related to increased endogenous glucocorticoids (402, 403), insulin-like growth factor (404) and of course the significant role of declining sex hormones in men as well as women experiencing the menopause(405-408). However, this does not fully account for the decline in bone mineral density from around the age of 30 onwards in both men and women (3). At this point, the menopause, altered hormonal profiles and activity levels should not have a significant impact as in later life. This point in life does however correlate with the age-related appearance of mitochondrial mutations and respiratory chain deficiency (19).

The PolgA^{mut}/PolgA^{mut} mouse model first stated an observational finding of premature osteoporosis in conjunction with increased mitochondrial DNA mutation load (181). Further work by Dobson et al., (205, 206) showed first the presence of respiratory chain deficiency in PolgA^{mut}/PolgA^{mut} osteoblasts but also the osteoblasts of naturally aged mice. Additional work then demonstrated decreases in osteoblasts populations' density, reduced bone formation and increased osteoclast activity all associated with increased respiratory chain deficiency. Ultimately the work by Dobson et al., was able to demonstrate the role mitochondrial dysfunction plays in impaired osteogenesis and accelerated bone loss with age.

The work by Dobson et al., in particular with regards to osteoporosis backed up by previous work on the role of mitochondrial pathology and ageing leads to the question of are reciprocal changes seen in human osteoblasts and stem cells with advancing age and ultimately contribute to osteoporosis pathogenesis?

6.2 Summary of results and further discussion

6.2.1 Results summary evidence of the role mitochondrial pathology plays in osteoporosis.

In the results chapters 3-5 this work has demonstrated 3 novel techniques and protocols to demonstrate the presence of pathogenic single nucleotide polymorphisms with increasing age in mesenchymal stem cells. The presence of mitochondrial respiratory chain deficiency within mesenchymal stem cells and a protocol and framework to investigate this further. Finally, this work has confirmed the presence of mitochondrial respiratory chain deficiency in osteoblasts and shown a positive correlation with increasing age.

As in *Table 38* the results from the PCR and CyToF chapters are summarised below. The non-synonymous SNP mutation rate increased with age this was particularly pronounced for the low-level mutations. There was also an increase of deleterious mutations with age. The Pearson correlation coefficient for deleterious mutations and age was 0.45.

This work has also shown the presence of mitochondrial respiratory chain deficiency in osteoblasts, there were positive correlations for age and deficiency for complex I (NDUFB8) and Complex IV (MTCO1), for NDUFB8 deficiency the Pearson correlation coefficient was 0.52 and for MTCO1 it was 0.43 These positive correlations are scored on a low to moderate correlation but this may be due in part to the limited sample size of the data as well as the multiple variables in human study compared to a murine based study.

When analysing the results as a whole combining the PCR data and CyToF data it is unsurprising that high levels of mutations in complex I, IV or V do not necessarily lead to a reciprocal deficiency in CyToF analysis. Unlike the work by Fellous or Greaves (320, 324), there is no established relationship between the mesenchymal stem cell and subsequent osteoblasts analysed. The data from each merely acts as a sample and potentially limited overview of the prevalence of either MSC mutation load or osteoblast respiratory chain deficiency. Equally had the high throughput experiment been fully successful again this would only highlight an overview of deficiency within the sample population and correlate this with the findings of the CyToF and PCR chapters. The method outlined in the high throughout chapter did however show the presence of detectable respiratory chain deficiency in MSCs without the potential impact of cell culture.

6.2.2 The effect of mitochondria pathology on mesenchymal stem cell functions

With these new findings in terms of the presence of both respiratory chain deficiency and mitochondrial DNA mutations further exploration of the current literature highlights several interesting points.

In the case of progressive supranuclear palsy (part of atypical parkinsonism) it was shown that mesenchymal stem cells with mitochondrial dysfunction and reduced mitochondrial mass had a significant drop off in terms of ability to differentiate into adipocytes (409) whether the same is true for osteoblasts and if differentiation would be affected is not clear but mitochondria play an important role in the differentiation of MSCs.

Dobson et al., found reduced osteoblast populations within their data relating this to acquired mitochondrial dysfunction in the $PolgA^{mut}/PolgA^{mut}$ mouse model. In patients with ankylosing spondylitis oxidative stress-mediated mitochondrial dysfunction leads to mesenchymal stem cell senescence. Ye et al., also showed that MSCs cultured with ankylosing spondylitis serum had decreased mitochondrial membrane potential, decreased ATP production and respiratory rate as well as the increased levels of senescence (410). Subjectively in cell culture aspects of this research elderly patients' MSCs did not divide at the same rate and reached senescence at an earlier passage than the paediatric controls. With increased levels of senescence due to mitochondrial dysfunction would this explain the reduced osteoblast population densities seen in the $PolgA^{mut}/PolgA^{mut}$ mouse model? Would the likelihood of reduced population densities in human bone also be present given the proven mitochondrial DNA mutations and respiratory deficiency seen in the results chapters and subsequently contribute to osteoporosis?

Further evidence of the important role mitochondrial dysfunction plays in osteogenesis can be determined by the fact MSC populations are more reliant on glycolytic energy production than OXPHOS mitochondrial-mediated energy production than their progeny cells (411, 412). At the time of differentiation activation of the mitochondria and a switch, OXPHOS glycolysis becomes an important factor although the mechanism is not understood (412). This switch in respiration is an important factor in osteogenic differentiation (413). Further factors also affect osteogenic differentiation relating to mitochondrial fusion proteins (414). At the time of osteogenic differentiation, MSC mitochondria elongate and increased Mfn1 and Mfn2 (Mitofusin-1 and 2) expression are correlated with osteogenesis. Direct knockdown of Mfn2 has shown to cause defective differentiation and osteogenesis as a result (415).

In summary, the findings of the PCR and high throughput chapter directly demonstrated the presence of mtDNA pathogenic mutations and the presence of detectable respiratory chain deficiency in MSCs. Reviewing the evidence above there is a strong correlation with mitochondrial dysfunction and osteogenesis. A reduced number of osteoblasts and an imbalance in the osteoblast/osteoclast axis would lead to increased bone resorption and fundamentally lead to osteoporosis (15-17). This is further evidence to support the findings of Dobson et al., and show the same is likely to be true in human study with regards to the reduced levels of osteoblasts in the PolgA^{mut}/PolgA^{mut} mouse model and subsequent premature onset of osteoporosis.

6.2.3 Mitochondrial respiratory chain deficiency in Osteoblasts.

Through this work, I have shown evidence of respiratory chain deficiency in osteoblasts and the association of complex I and complex IV deficiency with age. To date, a vast sum of the literature concerning mitochondrial pathology impact on the function of osteoblasts relates to apoptotic pathways (416-418) or osteogenic differentiation of mesenchymal stem cells (245, 412, 414, 415, 419-421). Komarova et al., looked more specifically at the number and activity of mitochondria, they showed an increasing number of mitochondria and metabolic activity coincide with differentiation into mature osteoblasts in response to the metabolic demands of producing mineralised matrix (420). Other studies consider the impact of long-term antibiotics in the case of septic arthritis treatment and their effect upon osteoblast mitochondria (422).

There are of course the mouse models as listed in the introduction chapter, Miyazaki et al. (217) investigated the effect of Tfam deficiency on osteoclast survival and bone resorption finding increased bone-resorbing activity in knockout mice and concluding that ATP depletion leads to osteoclastic bone resorption. There is also the Sod2 – mitochondrial superoxide dismutase 2 mouse model (109, 419). Relating the importance of Sod2 to osteoblast differentiation by regulating mitochondrial stress and Sod2 deficiency causing suppressed bone formation by upregulation of sclerostin and RANKL. Equally the work by Zhou et al., found that impaired regulation of oxidative stress in mitochondria by a knockout of Stat3 (Signal transducers and activators of transcription 3) also had the same corresponding effect on osteoblasts and osteocyte bone formation (423).

However, there are only two papers by Dobson et al., (205, 206) that consider the role mitochondrial respiratory chain deficiency would play on osteoblast function. Fundamentally they showed that in the PolgA^{mut}/PolgA^{mut} mouse model:

- Decreased cortical bone compared to wildtype mice
- Reduced bone formation rate and osteoblast populations with concurrent increases in osteoclast populations and activity
- Decreased levels of mineralisation with mitochondrial dysfunction and age and in comparison, to wild type young mice.

All of these changes were shown in conjunction with increased respiratory chain dysfunction and deficiency both in the aged mice and at a premature rate in the PolgA^{mut}/PolgA^{mut} mouse model. It would be a logical conclusion to follow that the increasing respiratory chain deficiency and mitochondrial dysfunction found through this work in osteoblasts with increasing age would have significant effects upon the osteogenic potential of the osteoblasts. The production of bone requires substantial amounts of energy (420) and any deficiency in the capability of osteoblasts to produce and utilise the energy would likely lead to osteoporosis as it has done in the PolgA^{mut}/PolgA^{mut} mouse model.

6.2.4 Future Work

Ultimately the outcomes of this research are limited by the sample size and steps required to develop three novel investigative experiments within the scope of the research period. The conclusions are limited by population size and distribution. Physical restrictions in terms of accessing young paediatric controls are more of an issue than aged patients. The frequency at which scheduled elective surgery from where it would be possible to get both paediatric bone and marrow samples is limited, this limits the capacity of the “young control” population. There is more scope to get a greater spread and number of aged samples from elective total hip procedures to analyse in the established experimental investigations within this research.

The timing of running experiments becomes the next significant issue. To transport cells from the operating theatre to the lab and then perform the high throughput assay and mtDNA sequencing to a lesser effect is time sensitive. The issue of freeze storage of MSCs was significant and prevented analysis by high throughput unless done fresh and as soon as physically possible. Whilst cell culture and then the analysis would be an option. Cultured MSCs could either be identified on physical parameters or by the flow cytometry separation assay. However, what effect on mitochondrial biology culture would have would introduce significant variables and potential for non-deficient cells to proliferate at a greater level than those with deficiency.

Whilst amplicons were generated for all the patients those samples which had been frozen longer were more prone to sequence drop off and sequencing errors. The numbers of MSCs extracted and efficiency of cell sorts were also affected by the length of time the cells were frozen and time from collection as well as age. Freezing was found to have effects on both cellular function and viability of MSCs harvested from umbilical cord Wharton's jelly (350).

In another function of timing but less of an issue is the time taken to analyse cells via CyToF in terms of ablation speed. This does however bypass the issues of autofluorescence which have been discussed extensively in the prior chapters that prevent the use of simpler and quicker immunofluorescent based assays.

With the issues in the timing of experiments, it would be important to use a control population for instance in the high throughput assay as it is not feasible to run all the patients together. Surrounding PCR this should be less of an issue as MSC separation could take place at the same time as the high throughput separation with the preparation of the amplicons ready for sequencing done at the time of marrow collection and then stored. Throughout this research the development of the protocol meant some samples were stored for significant periods until all samples were available to start sequencing. The CyToF experiment is unaffected by time to the experiment but merely is constrained by the time taken to get results.

The other obvious limitation are the vast variables in human study compared to murine experiments and the influence those many other variables can have upon osteoporosis such as diet, exercise, comorbidities, genetics and medication.

6.3 Final conclusion

This work builds on the work of Dobson et al., by showing for the first time that mitochondrial dysfunction is present in both human mesenchymal stem cells and osteoblasts with increasing deficiency and mutation load with age. These findings would suggest that mitochondrial pathology may have a major role in human osteoporosis based on the mouse model findings.

Reducing bone mineral density from the age of 30 as well as a concurrent increase in mitochondrial DNA mutation load and deficiency in humans has been linked to several ageing diseases. Osteoporosis remains poorly understood and deemed to be multifactorial. There is increasing evidence that mitochondria have a role to play in relation to osteogenic differentiation as well as a

functional role within osteoblasts to providing adequate energy levels for the excretion of the mineralised bone matrix.

Significant milestones have been made in establishing three experiments and protocols for investigating mitochondrial pathology in MSCs and osteoblasts. Further work would look to clarify the results of these assays across a larger population and correlating them with functional osteoblast assays and potential for bone mineral density investigation. The pursuit of samples from patients with established osteoporosis or hip fractures which are defined as fragility fractures due to osteoporosis could help to clarify this but the logistics, patient suitability and capacity to consent combined with the unpredictability of trauma presentation and operating would mean that this would require significant planning and experimental flexibility.

Table 38 Summary of results from the PCR and CyToF chapters for each patient. When samples were not available or used in each experiment these are represented by blanks.

			mtDNA sequencing results												Osteoblast protein deficiency on CyToF					
			SIFT scores for all mutations						Complex I mutations	Complex IV mutations	Complex V mutations	Complex I mutations	Complex IV mutations	Complex V mutations						
									All mutations			>50% and non-synonymous								
Patient	**Age**	**Sex**	No score	Deleterious	Deleterious low confidence	Tolerated	Tolerated low confidence	Grand Total							NDUFB8	GRIM19	SDHA	MTCO1	COX4	OSCP
Hip 4	83	Female	61	3	28	10	6	108	26	39	4	2	4	0	2.20%	1.90%	1.00%	0.75%	1.20%	1.90%
Hip 5	66	Female													6.60%	4.50%	1.30%	0.59%	1.90%	4.50%
Hip 6	45	Female	41	2	15	1	5	64	10	24	1	0	0	0	6.40%	1.20%	1.50%	2.70%	1.20%	2.40%
Hip 7	82	Female	46	3	24		6	79	16	28	4	0	0	0	16.00 %	5.80%	3.70%	4.10%	1.90%	5.70%
Hip 8	74	Female	85	10	28	13	5	141	28	50	7	1	1	0	9.50%	6.90%	5.70%	3.20%	2.70%	6.70%
Hip 9	64	Male	80	3	42	8	14	147	33	50	3	4	0	0	3.40%	3.10%	1.30%	1.50%	1.40%	2.40%
Hip 10	62	Male	59	9	27	9	19	123	25	49	4	2	1	0	13.00 %	12.00 %	8.40%	4.70%	3.00%	8.30%
Hip 11	61	Female	77	8	30	5	13	133	15	47	5	1	1	1						
Hip 12	78	Female	262	18	75	22	17	394	66	150	17	6	0	1						
Hip 13	25	Male	91	5	34	4	11	145	29	51	6	2	1	0						
Femur 1	19	Male	87	4	38	3	12	144	31	53	3	2	0	1	1.80%	1.70%	1.40%	2.40%	0.99%	1.40%
Paediatric 1	13	Male													0.84%	0.73%	0.68%	0.68%	0.29%	0.52%
Paediatric 2	1.5	Female													0.92%	0.53%	0.52%	0.38%	0.39%	0.70%

List of Figures

FIGURE 1 ENDOCHONDRAL OSSIFICATION ADAPTED FROM SALAZAR ET AL., (29). 14
FIGURE 2 THE STRUCTURE AND SUBSTRUCTURE OF BONE ADAPTED FROM RHO ET AL., (30). 15
FIGURE 3 DIFFERENTIATION OF OSTEOBLASTS, OSTEOCLAST AND THEIR PRECURSORS. 19
FIGURE 4 SKELETAL HOMEOSTASIS AND BONE MASS. NEGATIVE FACTORS ON RESORPTION AND FORMATION ARE SHOWN IN RED WHEREAS POSITIVE FACTORS ARE SHOWN IN GREEN. PHARMACOLOGICAL FACTORS ARE MARKED IN ITALICS. THE RELATIVE IMPACT, WHERE KNOWN, IS REPRESENTED BY THE THICKNESS OF THE ARROWS. SOLID LINES ARE CURRENT THERAPIES AND DOTTED LINES PUTATIVE ONES. ABBREVIATIONS: BMP, BONE MORPHOGENETIC PROTEIN(S); SOST, SCLEROSTIN; LRP5, LOW-DENSITY LIPOPROTEIN (LDL)-RECEPTOR-RELATED PROTEIN 5; PTH, PARATHYROID HORMONE; SERM, SELECTIVE OESTROGEN-RECEPTOR MODULATOR. ADAPTED FROM (104). 28
FIGURE 5 THE WNT PATHWAY (57) THE FRIZZLED/LRP5 COMPLEX IS BOUND BY THE WNT PROTEIN. THIS INDUCES A SIGNAL TO INTRACELLULAR PROTEINS PREVENTING THE BREAKDOWN OF B-CATENIN. AN ABUNDANCE B-CATENIN WITHIN THE CELL AND NUCLEUS INTERACTS WITH TRANSCRIPTION FACTORS AND THE ACTIVATION OF CERTAIN GENES TARGETED BY THE WNT SIGNALLING PATHWAY. 32
FIGURE 6: OSTEOCLAST PROLIFERATION AND DIFFERENTIATION ARE UNDER THE CONTROL OF CYTOKINES SUCH AS MACROPHAGE COLONY STIMULATING FACTOR (MCSF) BINDING TO THE MACROPHAGE COLONY-STIMULATING FACTOR 1 RECEPTOR (C-FMS) AND RECEPTOR ACTIVATOR OF NUCLEAR FACTOR KAPPA-B LIGAND (RANKL). THE RANK RECEPTOR ON OSTEOCLASTS IS BOUND BY RANKL SECRETED FROM OSTEOBLASTS OR BOUND TO THE OSTEOBLAST CELL MEMBRANE. RANKL EXPRESSION IS INHIBITED BY THE SEX HORMONES OESTRADIOL AND TESTOSTERONE; IN CONTRAST, PARATHYROID HORMONE (PTH) INCREASES RANK EXPRESSION. INTERLEUKINS 1 AND 6 AS WELL AS TISSUE NECROSIS FACTOR IL-1A, IL-6 AND TNFA ALSO PLAY A ROLE IN OSTEOCLAST DIFFERENTIATION (49). 34
FIGURE 7 SCHEMATIC REPRESENTATION OF THE HUMAN MTDNA GENOME, THE GENOME CODES FOR 13 PROTEINS, 22 TRNAS AND 2 RRNAS ARE MAPPED. THE TWO STRANDS OF THE MTDNA ARE DESIGNATED HEAVY AND LIGHT (142). 37
FIGURE 8 THE OXIDATIVE PHOSPHORYLATION PATHWAY OF THE MITOCHONDRIAL RESPIRATORY CHAIN. NADH IS UTILISED AS A PRODUCT OF THE KREBS CYCLE, SERIAL REDOX REACTIONS GENERATE A PROTON GRADIENT WHICH CAN BE USED TO CONVERT ADP TO ATP AND BIOLOGICAL ENERGY (151). 39
FIGURE 9 DISORDERS ASSOCIATED WITH MUTATIONS IN THE PROTEINS OF THE RESPIRATORY CHAIN. (MITOCHONDRIAL DNA ENCODED PROTEINS (YELLOW) NUCLEAR DNA ENCODED PROTEINS (BLUE) (161). 41
FIGURE 10 A) BONE MINERAL DENSITY AND BONE MINERAL CONTENT MEASURED BY X-RAY DENSITOMETRY OF DISSECTED FEMUR FROM $POLGA^{MUT}/POLGA^{MUT}$ MICE (RED BARS) AND WILD-TYPE MICE (BLUE BARS) AT 20 WEEKS AND 40 WEEKS OLD. B) THE AGEING-RELATED PHENOTYPE SEEN IN $POLGA^{MUT}/POLGA^{MUT}$ MICE (181). 47
FIGURE 11 QUADRUPLE IMMUNOFLUORESCENCE ASSAY OF MOUSE FEMUR, 90X MAGNIFICATION OSTEOBLASTS TARGETED WITH AN ANTIBODY TO OSTEOCALCIN. $POLGA^{MUT}/POLGA^{MUT}$ MOUSE IN COMPARISON WITH AGE-MATCHED WILD-TYPE CONTROL MICE TOP ROW, NDUFB8 (COMPLEX I) AND COX-I (COMPLEX IV) MITOCHONDRIAL RESPIRATORY CHAIN DEFICIENCIES ARE SEEN AT 11 MONTHS IN $POLGA^{MUT}/POLGA^{MUT}$ (LOWER ROW) RELATIVE TO MITOCHONDRIAL MASS (PORIN) (205). 48
FIGURE 12 FLOW ANALYSIS OF THE CD105-PE POSITIVE CELLS, THE CD90-FITC POSITIVE CELLS, CD73-APC POSITIVE CELLS AND PERCP POSITIVE CELLS (219). 64
FIGURE 13 FLOW CYTOMETRY SORT OF MSCS FROM FRESH BONE MARROW. THE MSC POPULATION IS CIRCLED IN RED. THE MSC POPULATION IS FIRST DEFINED THE SIDE SCATTER (SSC-A) REPRESENTING GRANULARITY AND FORWARD SCATTER (FSA-A) REPRESENTING SIZE. FURTHER DELINEATION IS THEN MADE USING POSITIVE EXPRESSION OF CD73, CD90, AND CD105, AND THESE CELLS MUST LACK EXPRESSION OF CD34, CD45, AND CD14. 65

FIGURE 14 SCHEMATIC REPRESENTATION OF A FLOW CYTOMETER, WITH THE LASER BEAM, THE SHEATH STREAM CONTAINING THE INDIVIDUAL CELLS, AND THE LENSES FOR THE COLLECTION OF FORWARD SCATTER AND SIDE SCATTER/FLUORESCENCE ALL AT ORTHOGONAL ANGLES TO EACH OTHER. THE OBSCURATION BAR ENSURES ONLY LIGHT THAT HAS HIT A PARTICLE AND BEEN REFRACTED ACCOUNTS FOR FORWARD SCATTER (227). 76
FIGURE 15 RESULTS OF FIXATION AND LYSIS BUFFER ADDITION TO K562 CELLS. THE DEAD CELLS AND DEBRIS ARE IN THE RED CIRCLE, THE UNFIXED IN THE GREEN CIRCLE AND FIXED IN THE BLUE CIRCLE. AFTER THE ADDITION OF A LYSIS BUFFER, THERE IS LITTLE CHANGE IN THE BLUE CIRCLE POPULATIONS COMPARED TO THE GREEN POPULATION WHICH DISAPPEARS WITH CONCURRENT CHANGE IN THE DEAD CELL POPULATION (RED). 78
FIGURE 16 SCHEMATIC REPRESENTATION OF MASS CYTOMETRY IN SUSPENSION (HELIOS) AND IMAGING MODES (HYPERION) BASED UPON ATKURI ET AL.,(239). 81
FIGURE 17 ELECTROPHORESIS GEL SHOWING POSITIVE AMPLICON PRODUCTS UTILISING THE PRIMERS 29F:5R, 4F:13R, 12F:21R AND 20F:28R FROM A SINGLE MSC CELL FROM THE 25-YEAR-OLD PATIENT. 95
FIGURE 18 COMPARISON OF USING THE PRIMERS AS IN TABLE 7 COMPARED TO MOVING EACH PRIMER PAIR BY 1 PRIMER SET FURTHER ALONG THE GENOME AS ON THE REFERENCE TABLE 18. USING THE SAME PATIENTS (4 AND 5) DNA AND CELL SAMPLES (1-12). PRIMER PAIRING CHANGES 20F:28R TO 21F:29R (TOP IMAGE) AND 28F:D4R TO 29F:1R (BOTTOM IMAGE). 98
FIGURE 19 OUTPUT FROM THE BIOANALYZER DEMONSTRATING DNA PEAK AT AROUND 4000BP WITH THE TWO MARKER REFERENCE PEAKS AT EITHER END OF THE OUTPUT. 100
FIGURE 20 A VIRTUAL ELECTROPHORESIS GEL PRODUCED BY THE BIOANALYZER. THE MARKER DNA IS REPRESENTED BY THE PURPLE AND GREEN BARS WITH THE SAMPLE AMPLICONS REPRESENTED BY THE BLACK/GREY BARS IN LANES C, G, K,19, D, H, L, P, 56, 4, 16, 26. AGAIN THESE RESIDE AROUND THE 4000BP MARK. 101
FIGURE 21 OUTPUT FROM MTDNA SERVER: HETEROPLASMY LEVELS FOR EACH PATIENT (2 CELLS PER PATIENT EXCEPT THE 61-YEAR-OLD PATIENT) DEMONSTRATED THROUGH A BOXPLOT. 102
FIGURE 22 HETEROPLASMY PER REGION ACROSS ALL SAMPLES (AMOUNT OF HETEROPLASMIC SITES GROUPED ACCORDING TO THEIR LOCI ON THE MITOCHONDRIAL GENOME). 103
FIGURE 23 SUMMARY OF MISEQ ANALYSIS PROCESS. 106
FIGURE 24 TOTAL MITOCHONDRIAL DNA MUTATIONS DISTRIBUTION BY HETEROPLASMY PERCENTAGE AND PATIENT. 109
FIGURE 25 PIE CHART DEMONSTRATING THE MUTATION TYPE ENCOUNTERED WITHIN THE PATIENT COHORT. 110
FIGURE 26 MUTATION DISTRIBUTION ACROSS THE MITOCHONDRIAL GENOME FOR THE WHOLE SAMPLE GROUP (SEQUENCE ERROR CELLS REMOVED), FURTHER DELINEATION OF EACH GENE BY PATIENT. 111
FIGURE 27 AVERAGE MITOCHONDRIAL DNA MUTATIONS PER PATIENT PER CELL COMPARING AGE ACROSS THE PATIENT COHORT TO MUTATION RATE. SAMPLE SPLIT BASED UPON HETEROPLASMY PERCENTAGE OF EACH MUTATION. 113
FIGURE 28 TOTAL MITOCHONDRIAL DNA MUTATIONS PER CELL OF EACH PATIENT SHOWING THE DISTRIBUTION OF MUTATION COUNTS BETWEEN INDIVIDUAL CELLS FOR EACH PATIENT. 114
FIGURE 29 NON-SYNONYMOUS MUTATIONS ARRANGED BY SIFT OUTCOME COMPARED TO AGE. 116
FIGURE 30 NON-SYNONYMOUS MUTATIONS OF EACH PATIENT - HETEROPLASMY RATES FOR EACH MUTATION DEFINED FOR EACH SIFT SCORE CATEGORY. DATA ARRANGED BY PATIENTS' AGES. 118
FIGURE 31 COVERAGE GRAPHS FOR HIP 1 - READ DEPTH OF EACH BASE AND 500 READ DEPTH THRESHOLD DEMONSTRATED. 124
FIGURE 32 HIP 1 HETEROPLASMIC SINGLE NUCLEOTIDE MUTATIONS GREATER THAN 50% HETEROPLASMY...125
FIGURE 33 COVERAGE GRAPHS FOR HIP 2 - READ DEPTH OF EACH BASE AND 500 READ DEPTH THRESHOLD DEMONSTRATED. 127
FIGURE 34 HIP 2 HETEROPLASMIC SINGLE NUCLEOTIDE MUTATIONS GREATER THAN 50% HETEROPLASMY...128

FIGURE 35 COVERAGE GRAPHS FOR HIP 3 - READ DEPTH OF EACH BASE AND 500 READ DEPTH THRESHOLD DEMONSTRATED. 131
FIGURE 36 HIP 3 HETEROPLASMIC SINGLE NUCLEOTIDE MUTATIONS GREATER THAN 50% HETEROPLASMY. . 132
FIGURE 37 COVERAGE GRAPHS FOR HIP 4 - READ DEPTH OF EACH BASE AND 500 READ DEPTH THRESHOLD DEMONSTRATED. 135
FIGURE 38 HIP 4 HETEROPLASMIC SINGLE NUCLEOTIDE MUTATIONS GREATER THAN 50% HETEROPLASMY. THE TOP GRAPH INCLUDES ALL CELLS, THE BOTTOM GRAPH HAS CELL 3 REMOVED AS THERE WAS A CONCERN OF SEQUENCE ERROR. 136
FIGURE 39 COVERAGE GRAPHS FOR HIP 6 - READ DEPTH OF EACH BASE AND 500 READ DEPTH THRESHOLD DEMONSTRATED. 140
FIGURE 40 HIP 6 HETEROPLASMIC SINGLE NUCLEOTIDE MUTATIONS GREATER THAN 50% HETEROPLASMY. THE TOP GRAPH INCLUDES ALL CELLS, THE BOTTOM GRAPH HAS CELLS 1,2,7,8,10 REMOVED AS THERE WAS A CONCERN OF SEQUENCE ERROR. 142
FIGURE 41 COVERAGE GRAPHS FOR HIP 7 - READ DEPTH OF EACH BASE AND 500 READ DEPTH THRESHOLD DEMONSTRATED. 146
FIGURE 42 HIP 7 HETEROPLASMIC SINGLE NUCLEOTIDE MUTATIONS GREATER THAN 50% HETEROPLASMY. . 147
FIGURE 43 COVERAGE GRAPHS FOR HIP 8 - READ DEPTH OF EACH BASE AND 500 READ DEPTH THRESHOLD DEMONSTRATED. 151
FIGURE 44 HIP 8 HETEROPLASMIC SINGLE NUCLEOTIDE MUTATIONS GREATER THAN 50% HETEROPLASMY. . 152
FIGURE 45 COVERAGE GRAPHS FOR HIP 9 - READ DEPTH OF EACH BASE AND 500 READ DEPTH THRESHOLD DEMONSTRATED. 154
FIGURE 46 HIP 9 HETEROPLASMIC SINGLE NUCLEOTIDE MUTATIONS GREATER THAN 50% HETEROPLASMY. . 155
FIGURE 47 COVERAGE GRAPHS FOR HIP 10 - READ DEPTH OF EACH BASE AND 500 READ DEPTH THRESHOLD DEMONSTRATED. 157
FIGURE 48 HIP 10 HETEROPLASMIC SINGLE NUCLEOTIDE MUTATIONS GREATER THAN 50% HETEROPLASMY. 158
FIGURE 49 COVERAGE GRAPHS FOR HIP 11 - READ DEPTH OF EACH BASE AND 500 READ DEPTH THRESHOLD DEMONSTRATED. 161
FIGURE 50 HIP 11 HETEROPLASMIC SINGLE NUCLEOTIDE MUTATIONS GREATER THAN 50% HETEROPLASMY. 162
FIGURE 51 COVERAGE GRAPHS FOR HIP 12 - READ DEPTH OF EACH BASE AND 500 READ DEPTH THRESHOLD DEMONSTRATED. 165
FIGURE 52 HIP 12 HETEROPLASMIC SINGLE NUCLEOTIDE MUTATIONS GREATER THAN 50% HETEROPLASMY. 166
FIGURE 53 COVERAGE GRAPHS FOR HIP 13 - READ DEPTH OF EACH BASE AND 500 READ DEPTH THRESHOLD DEMONSTRATED. 169
FIGURE 54 HIP 13 HETEROPLASMIC SINGLE NUCLEOTIDE MUTATIONS GREATER THAN 50% HETEROPLASMY. 170
FIGURE 55 COVERAGE GRAPHS FOR FEMUR 1 - READ DEPTH OF EACH BASE AND 500 READ DEPTH THRESHOLD DEMONSTRATED. 173
FIGURE 56 FEMUR 1 HETEROPLASMIC SINGLE NUCLEOTIDE MUTATIONS GREATER THAN 50% HETEROPLASMY. 174
FIGURE 57 CARTOON REPRESENTATION OF THE ANTIBODY CONJUGATION PROCESS WITH A FLUORESCENT LABEL (YELLOW CIRCLE) (332). 185
FIGURE 58 COMPARISON OF FIXATION BUFFERS USING K562 CELL LINE AS A CONTROL POPULATION. K562 CELL LINE SHOWN FROM LEFT TO RIGHT IN PBS, THERMO PFA 4%, CHEMCRUZ PFA 4% AND TAAB PFA 4%. THE TOP ROW COMPARES FSC AND SSC CELLULAR PROFILE BEFORE THE ADDITION OF THE PERMEABILISATION AGENT TRITON X-100. THE MIDDLE ROW SHOWS THE CELLULAR PROFILE AFTER 1 MINUTE OF EXPOSURE TO TRITON X-100 AND THE BOTTOM ROW SHOWS THE PROFILE AFTER 5 MINUTES OF TRITON X-100 EXPOSURE. 186
FIGURE 59 FLOW CYTOMETRY OUTPUT REPRESENTED BY FLUORESCENT SIGNAL INTENSITY PROFILE OF THE K562 CELLS IN DIFFERENT PERMEABILISATION BUFFERS AND STAINED WITH THE MTCO2 ANTIBODY CONJUGATED TO ALEXA 647. 188

FIGURE 60 PROTOCOL DEVELOPMENT SUMMARY. 189
FIGURE 61 BLOCKING BUFFER OPTIMISATION USING K562 CELLS AND MTCO2 ANTIBODY AND ISOTYPE CONTROL CONJUGATED WITH THE ALEXA 647 FLUOROPHORE. EACH LINE REPRESENTS THE SIGNAL INTENSITY OF THE CELLS ANALYSED USING THE BD SYMPHONY FLOW CYTOMETER IN COMPARISON TO EACH BLOCKING AGENT. THE DATA IS ALSO SHOWN IN TABLE 8. 192
FIGURE 62 ANTIBODY TITRATION IN K562 CELLS USING THE TOM20, MTCO2, NDUFB8 AND TFAM CONJUGATE ANTIBODIES AND ISOTYPES. 193
FIGURE 63 UPDATED PROTOCOL DEVELOPMENT SUMMARY. 194
FIGURE 64 THE COMPARISON OF SIGNAL INTENSITY PROFILES OF K562 CELLS PASSED THROUGH THE BD SYMPHONY FLOW CYTOMETER. ISOTYPE ANTIBODY CONTROL BATCHES AND MTCO2 ANTIBODY CONJUGATED TO ALEXA 647. 195
FIGURE 65 MEAN SIGNAL INTENSITY VALUES FOR TFAM AND NDUFB8 COMPARED TO ISOTYPE CONTROLS FOR THE COMPLEX I DEFICIENT FIBROBLASTS AND WILD TYPE NON-COMPLEX I DEFICIENT FIBROBLASTS. 196
FIGURE 66 NON-SPECIFIC STAINING OF K562 CELLS COMPARING TOM20 SPECIFIC MITOCHONDRIAL PUNCTATE STAINING WITH NDUFB8 AND MTCO1 NON-SPECIFIC STAINING WITHIN THE NUCLEUS AND CELL. ALL ANTIBODIES BOUND WITH AN ALEXA FLUOR 488 SECONDARY ANTIBODY 60X ZOOM ON NIKON TIE CONFOCAL MICROSCOPE. 199
FIGURE 67 FLOW CYTOMETRY RESULT OF USING PERFINGO LYSIS AGENT, THE GATED AREA IN RED DEMONSTRATES LYSED CELLS AND CELLULAR DEBRIS. 199
FIGURE 68 IMMUNOFLUORESCENT IMAGES USING THE ZEISS LMS8000 AIRYSCANNER AT 20X MAGNIFICATION DEMONSTRATING THE VARIABLE IMPROVEMENT WHEN USING A DIGITONIN STEP TO IMPROVE K562 PERMEABILISATION AND MITOCHONDRIAL STAINING. 201
FIGURE 69 K562 CELLS STAINED WITH NDUFB8, MTCO1, TOM20 AND DAPI FOLLOWING A 10 MINUTE AND 5-MINUTE FIXATION STEP USING THE ZEISS AXIO-OBSERVER LSM800/SDI MICROSCOPE AT 63X MAGNIFICATION 205
FIGURE 70 PERMEABILISATION OF THE WILDTYPE CONTROL FIBROBLAST CELL LINE USING A METHANOL GRADIENT. COMPLEX I, COMPLEX IV AND MITOCHONDRIAL MASS VISUALISED USING CONFOCAL MICROSCOPY (ZEISS AXIO-OBSERVER LSM800 20X LENS). 206
FIGURE 71 SCHEMATIC REPRESENTATION OF THE USE OF BIOTINYLATED SECONDARY ANTIBODIES AND STREPTAVIDIN SIGNAL AMPLIFICATION. 207
FIGURE 72 QUADRUPLE IMMUNOFLUORESCENCE STAINING OF TOM20, MTCO1, DAPI AND NDUFB8 USING A BIOTINYLATED SECONDARY AND STANDARD FLUORESCENT SECONDARY ANTIBODY. CD7 MICROSCOPE AT 20X MAGNIFICATION. 209
FIGURE 73 IMMUNOFLUORESCENCE IMAGES TAKEN USING THE ZEISS AXIO-OBSERVER LSM800 CONFOCAL MICROSCOPE TO IMAGE WILD TYPE FIBROBLASTS AFTER A SINGLE AND DOUBLE BIOTIN BLOCKING REGIME CD7 MICROSCOPE AT 20X MAGNIFICATION. 210
FIGURE 74 OVERVIEW TILED IMAGES USING THE ZEISS CD7 MICROSCOPE AT 5X MAGNIFICATION SHOWING 1000 CELLS (DAPI STAINING) SORTED INTO A 96 AND 384 WELL PLATE. 211
FIGURE 75 QUADRUPLE IMMUNOFLUORESCENCE ASSAY OF FIBROBLASTS AFTER CELL SORTING USING THE CD7 MICROSCOPE AT 20X MAGNIFICATION. 212
FIGURE 76 NON-SPECIFIC BINDING SEEN IN THE TOM20 AND NDUFB8 CHANNELS CAUSED BY NON-SPECIFIC BINDING OF SECONDARY ANTIBODIES TO THE FLOW CYTOMETRY SORTING ANTIBODIES. 213
FIGURE 77 COMPARISON OF ANTIBODY STAINING PROFILE ON FLOW CYTOMETRY SORTED MSCS, TOP ROW - ORIGINAL ANTIBODY PANEL WITH EXTRA ALEXA FLUOR 750 FOLLOWED BY ALEXA FLUOR 488, SECOND-ROW ALTERED PANEL OF ANTIBODIES WITH PRIOR IGG1 488 ANTIBODY BLOCK, THE THIRD-ROW ALTERNATIVE PANEL OF ANTIBODIES WITHOUT BLOCK, FOURTH ROW NO PRIMARY CONTROLS FOR THE ALTERNATIVE PANEL OF ANTIBODIES. 214

FIGURE 78 IMMUNOFLUORESCENT IMAGING AT 20X MAGNIFICATION USING THE CD7 MICROSCOPE ON WILDTYPE FIBROBLASTS DEMONSTRATING BIOTINYLATED RABBIT AND MOUSE NDUFB8 SIGNAL VS RABBIT NDUFB8 SIGNAL. 215
FIGURE 79 HUMAN MUSCLE VIEWED AT 20X MAGNIFICATION USING THE CD7 MICROSCOPE. SERIAL SECTIONS COMPARING BIOTINYLATED ANTI-MOUSE NDUFB8 AND BIOTINYLATED ANTI-RABBIT NDUFB8. SERIAL SECTION AREAS MARKED BY THE GREEN DASHED LINE. WITHIN THIS AREA, EACH INDIVIDUAL FIBRE WAS ANALYSED. 217
FIGURE 80 DEMONSTRATING THE RATIO OF NDUFB8 AND VDAC SIGNALS FOR INDIVIDUAL HUMAN MUSCLE FIBRES. COMPARISON OF ANTI-RABBIT NDUFB8 AND ANTI-MOUSE NDUFB8. 218
FIGURE 81 DIRECT COMPARISON OF ANTI-RABBIT NDUFB8 AND ND4 ANTIBODIES ON WILD TYPE AND DEFICIENT FIBROBLASTS. 219
FIGURE 82 20X IMAGE OF WILDTYPE FIBROBLASTS TAKEN ON CD7 MICROSCOPE. THE COMPARISON OF THE CLEAR PUNCTATE (TYPICAL) MITOCHONDRIAL STAINING CAN BE SEEN IN CLEAR COMPARISON TO THE HIGH LEVELS OF BACKGROUND SEEN IN THE ND4 ANTIBODY. 219
FIGURE 83 COMPARISON OF BIOTINYLATED AND UNBIOTINYLATED ANTI-RABBIT NDUFB8 AND VDAC SIGNAL USING WILDTYPE AND DEFICIENT CELL LINES. 220
FIGURE 84 FINAL TEST OF COMBINED FLOW CYTOMETRY SORTING ASSAY AND IMMUNOFLUORESCENCE ASSAY ON CULTURED MSCS FROM 25-YEAR-OLD MALE PATIENT. 222
FIGURE 85 SCHEMATIC REPRESENTATION OF THE SORTING PROCESS USING THE BD FACSARIA FUSION SORTER: TOP LEFT CELLS ARE SORTED ON THE BASIS OF SIDE AND FORWARD SCATTER DEAD CELLS AND DEBRIS ARE ELIMINATED. THESE CELLS THEN PASS TO THE TOP RIGHT WHERE CELLS ARE SORTED USING FORWARD SCATTER HEIGHT AND AREA, CELLS JOINED TOGETHER ARE EXCLUDED. THE SORTED SINGLE CELLS ARE THEN ANALYSED ON THE BOTTOM LEFT GRAPH, CELLS ARE SORTED BASED ON ANTIBODIES CONJUGATED WITH FLUOROPHORES: CELLS POSITIVE FOR CD105 AND NEGATIVE FOR 14/20/34/45 SELECTED AND PROCESSED ON THE BOTTOM RIGHT GRAPH WHICH SELECTS ONLY THOSE CELLS POSITIVE FOR CD73 AND CD90. THE SORTER THEN SORTS SINGLE LIVE CELLS WHICH ARE POSITIVE FOR CD73/90/105 AND NEGATIVE FOR CD14/20/34/45 ON TO THE 96 WELL PLATES. 224
FIGURE 86 OVERVIEW SCAN RESULTS SHOWING SINGLE SORTED MSC CELLS AS WELL AS CELLULAR DEBRIS IN A SINGLE WELL OF A 96 WELL PLATE - TAKEN WITH THE ZEISS CD7 CELLDISCOVERER MICROSCOPE AT 2.5X. 229
FIGURE 87 IMAGES OF SINGLE SORTED MSCS TAKEN AT 40X USING THE ZEISS AXIO-OBSERVER LSM800. TOP TWO ROWS DEPICT MSCS, AND THE BOTTOM ROW SHOW A NO PRIMARY CONTROL CELL STAINED WITH ONLY VDAC AND DAPI PRIMARIES. 230
FIGURE 88 IMAGES OF WILDTYPE AND COMPLEX I DEFICIENT FIBROBLASTS USED AS CONTROLS AT THE SAME TIME AS THE MSC EXPERIMENT AS SEEN IN FIGURE 87. 231
FIGURE 89 LINEAR REGRESSION MODEL SHOWING VDAC MEAN VALUES COMPARE TO COMPLEX I AND COMPLEX IV MEAN VALUES. MSCS WHICH LIE OUTSIDE THE 95% PREDICTIVE INTERVALS ARE HIGHLIGHTED. 233
FIGURE 90 RESULTS OF THE COMPLEX 1 DEFICIENT FIBROBLASTS CLEARLY DEMONSTRATING A DEFICIENT POPULATION IN RED FOR COMPLEX 1 NDUFB8 SIGNAL COMPARED TO THE SIMILAR DISTRIBUTION OF COMPLEX 4 (MTCO1) WHEN COMPARED TO THE WILDTYPE FIBROBLASTS. 233
FIGURE 91 OSTEOCYTES IMAGED AT 60X MAGNIFICATION ON THE NIKON TIE CONFOCAL MICROSCOPE. OSTEOCALCIN PRIMARY ANTIBODY USED WITH ALEXA 546 SECONDARY. ON THE LEFT-HAND IMAGE TAKEN FROM DEEPER WITHIN THE SECTION OSTEOCYTES WITHIN LACUNA ARE VISIBLE AS MARKED IN THE GREEN OVAL. THE TRABECULAR LINES ARE ALSO CLEARER WHEREAS ON THE RIGHT-HAND IMAGE TAKEN FROM THE SURFACE OF THE TISSUE SECTION THERE ARE EMPTY LACUNA (GREEN OVAL) AND DISRUPTION OF THE TISSUE ARCHITECTURE WITH DISCONTINUITY BETWEEN THE TRABECULAR LINES. 239
FIGURE 92 APPLICATION OF QUADRUPLE IMMUNOFLUORESCENCE ASSAY TO HUMAN BONE 90X MAGNIFICATION: FIRST-ROW OSTEOBLAST IMAGING IN THE HIP. SECOND-ROW OSTEOBLAST IMAGING IN

BONE MARROW LESION OF THE PROXIMAL TIBIA. THIRD-ROW OSTEOCLAST IMAGING IN BONE MARROW LESION OF THE PROXIMAL TIBIA (OSTEOCALCIN SUBSTITUTED FOR CATHEPSIN K). CELLS MARKED BY THE WHITE ARROWS. AUTO FLUORESCENT SIGNAL AND BACKGROUND LEVELS ARE HIGH DESPITE IMAGING CONFIGURATION OPTIMISATION. 242
FIGURE 93 GRAPHS DISPLAYING THE RESULTS OF THE FLUORESCENT PROFILE OF EACH OSTEOBLAST MEASURED COMPARING MITOCHONDRIAL MASS, COMPLEX I AND COMPLEX IV. 243
FIGURE 94 BINDING OF MT1-MMP ANTIBODY CONJUGATED WITH 153 EUROPIUM IN COMPARISON TO 193 IRIDIUM BINDING ON ABC COMPENSATION BEADS, BOTH CHANNELS DISPLAYING POSITIVE SIGNAL INTENSITIES. 248
FIGURE 95 EXPRESSION LEVEL OF EACH ANTIBODY IN THE IMC PANEL. GRAPH DISPLAYING EXPRESSION OF EACH PROTEIN BY MEASUREMENT OF THE INTENSITY OF THE 488 CHANNEL. EACH ANTIBODY IS DISPLAYED AS A SEPARATE STRIP AND EACH DOT REPRESENTS AN INDIVIDUAL FIBRE. RED BARS SHOW THE MEAN INTENSITY FOR THE GIVEN ANTIBODY. (A) NON-METAL BOUND ANTIBODIES AND (B) METAL-BOUND ANTIBODIES. FIGURE COURTESY OF DR CHARLOTTE WARREN. 249
FIGURE 96 DAB STAINING OF OSTEOBLASTS (CIRCLED IN RED) USING OSTEOCALCIN (1:200) AT 20X MAGNIFICATION (A) COMPARED WITH NO PRIMARY ANTIBODY CONTROL (B). 252
FIGURE 97 FURTHER DAB IMAGES OF MITOCHONDRIAL ANTIBODIES 1:50 CONCENTRATIONS AND 50X MAGNIFICATION. 1:50 WAS FOUND TO GIVE THE BEST STAINING RESPONSE ON DAB IMAGES. 252
FIGURE 98 HISTOCYTE CONTROL SECTIONS CREATED FOR MT1-MMP ANTIBODY SHOWING INCREMENTAL DAB STAINING: A)BREAST CARCINOMA CELL LINES, B) EWING'S SARCOMA, C) HIGH-GRADE OSTEOSARCOMA, D) HIGH GRADE DIFFERENTIATED CHONDROSARCOMA. ON THE LEFT ASPECT HISTOCYTE EXAMPLE USE. 254
FIGURE 99 MASS CYTOMETRY RESULTS SHOWING A) DNA STAINING, B) OSTEOCALCIN STAINING, C) MT1-MMP STAINING, D) CELL PROFILING RESULT, E) VDAC1 STAINING, F) COMPLEX I AM STAINING, G) COMPLEX IV STAINING. 254
FIGURE 100 IMMUNE-DEFICIENT MOUSE LEG WITH HUMAN OSTEOSARCOMA DEVELOPMENT FOLLOWING IMPLANTATION. IMAGING MASS CYTOMETRY RESULTS – AREA ABLATED HIGHLIGHTED BY THE RED CIRCLE AND SHOWN IN PRE ABLATION IMAGE. THE GREEN AREA AS HIGHLIGHTED ON OSTEOCALCIN IS A FOLD IN THE SECTION HENCE THE ABNORMAL STAINING PROFILE SEEN WITHIN THE MUSCLE. 256
FIGURE 101 IMAGING MASS CYTOMETRY IMAGES OF A BONE MARROW LESION FROM A PROXIMAL TIBIA SHOWING OSTEOBLASTS AND MITOCHONDRIAL MARKER SIGNAL. OSTEOBLASTS HIGHLIGHTED BY THE GREEN DASHED LINE. 258
FIGURE 102: TOP LEFT - DAB STAINING OF OSTEOCALCIN POSITIVE CELLS, TOP RIGHT - PRE ABLATION IMAGE OF THE SLIDE AS SCANNED BY THE HYPERION, BOTTOM ROWS - VARIOUS CHANNELS OF THE ABLATED IMAGE AFTER PROCESSING WITH THE HYPERION MASS CYTOMETER.5.3.5 ANALYSIS DEVELOPMENT. 261
FIGURE 103 SCATTER PLOTS OF CELL SIGNALS VS VDAC SIGNALS FOR SLIDE ONE USING A LOGARITHMIC SCALE. NO CLEAR PATTERN IS SEEN, AND VALUES ARE LOW ACROSS THE PLOTS. THIS PATTERN IS REPEATED ACROSS THE FIVE SLIDES. BELOW CAN BE SEEN THE CORRESPONDING IMAGES GENERATED FROM THE CYTOF DATA FROM WHICH THE ANALYSIS HAS BEEN PERFORMED IN FIGURE 104. 265
FIGURE 104 IMAGES OF A BONE MARROW LESION GENERATED FROM MCD VIEWER TIFFS AND VIEWED IN QUPATH TO DEMONSTRATE THE DIFFERENT CHANNELS. 266
FIGURE 105 USING QUPATH TO SEGMENT AND SEPARATE THE OSTEOBLASTS FROM THE SELECTED REGION ON NUCLEAR MARKERS AND CELL DETECTION USING EXPANSION ALGORITHM. 267
FIGURE 106 CELLS OF INTEREST MARKED ON NUCLEAR CHANNEL TIFF IN RED DASHED AREA. CELLS IDENTIFIED AND SEGMENTED USING MITOCYTO SOFTWARE HIGHLIGHTED IN COLOURS - NOT CORRESPONDING TO THE RED DASHED AREA. 268
FIGURE 107 SUMMARY OF VOLOCITY ANALYSIS PIPELINE. 270
FIGURE 108 LOG PLOTS OF MEAN IMC SIGNAL INTENSITY FOR HIP 2, AN 84-YEAR-OLD FEMALE PATIENT. SLIDE 2-2-2 WAS A CLEAR OUTLIER AND EXCLUDED. 272

FIGURE 109 ESTIMATING DEFICIENCY IN COMPLEX I, COMPLEX II, COMPLEX IV AND COMPLEX V DATA FROM HIP 1: CONTOUR LINES REPRESENT THE KERNEL DENSITY ESTIMATE LEVELS CONTAINING 95% AND 50% OF THE CONTROL POPULATION FOR EACH PAIRWISE COMPARISON. GREY POINTS ARE FROM PATIENT CELLS THAT LIE WITHIN THE 95% CONTOUR FROM CONTROLS. RED POINTS ARE FROM PATIENT CELLS LYING OUTSIDE THE 95% CONTOUR FROM CONTROLS. THE PROPORTION OF CELLS DIFFERENT FROM, VERTICALLY ABOVE AND VERTICALLY BELOW THE 95% CONTOUR FROM CONTROLS WRITTEN ABOVE EACH PANEL. 273
FIGURE 110 ESTIMATING DEFICIENCY IN COMPLEX I, COMPLEX II, COMPLEX IV AND COMPLEX V DATA FROM HIP 2: CONTOUR LINES REPRESENT THE KERNEL DENSITY ESTIMATE LEVELS CONTAINING 95% AND 50% OF THE CONTROL POPULATION FOR EACH PAIRWISE COMPARISON. GREY POINTS ARE FROM PATIENT CELLS THAT LIE WITHIN THE 95% CONTOUR FROM CONTROLS. RED POINTS ARE FROM PATIENT CELLS LYING OUTSIDE THE 95% CONTOUR FROM CONTROLS. THE PROPORTION OF CELLS DIFFERENT FROM, VERTICALLY ABOVE AND VERTICALLY BELOW THE 95% CONTOUR FROM CONTROLS WRITTEN ABOVE EACH PANEL. 274
FIGURE 111 ESTIMATING DEFICIENCY IN COMPLEX I, COMPLEX II, COMPLEX IV AND COMPLEX V DATA FROM HIP 3: CONTOUR LINES REPRESENT THE KERNEL DENSITY ESTIMATE LEVELS CONTAINING 95% AND 50% OF THE CONTROL POPULATION FOR EACH PAIRWISE COMPARISON. GREY POINTS ARE FROM PATIENT CELLS THAT LIE WITHIN THE 95% CONTOUR FROM CONTROLS. RED POINTS ARE FROM PATIENT CELLS LYING OUTSIDE THE 95% CONTOUR FROM CONTROLS. THE PROPORTION OF CELLS DIFFERENT FROM, VERTICALLY ABOVE AND VERTICALLY BELOW THE 95% CONTOUR FROM CONTROLS WRITTEN ABOVE EACH PANEL. 275
FIGURE 112 ESTIMATING DEFICIENCY IN COMPLEX I, COMPLEX II, COMPLEX IV AND COMPLEX V DATA FROM HIP 4: CONTOUR LINES REPRESENT THE KERNEL DENSITY ESTIMATE LEVELS CONTAINING 95% AND 50% OF THE CONTROL POPULATION FOR EACH PAIRWISE COMPARISON. GREY POINTS ARE FROM PATIENT CELLS THAT LIE WITHIN THE 95% CONTOUR FROM CONTROLS. RED POINTS ARE FROM PATIENT CELLS LYING OUTSIDE THE 95% CONTOUR FROM CONTROLS. THE PROPORTION OF CELLS DIFFERENT FROM, VERTICALLY ABOVE AND VERTICALLY BELOW THE 95% CONTOUR FROM CONTROLS WRITTEN ABOVE EACH PANEL. 276
FIGURE 113 ESTIMATING DEFICIENCY IN COMPLEX I, COMPLEX II, COMPLEX IV AND COMPLEX V DATA FROM HIP 5: CONTOUR LINES REPRESENT THE KERNEL DENSITY ESTIMATE LEVELS CONTAINING 95% AND 50% OF THE CONTROL POPULATION FOR EACH PAIRWISE COMPARISON. GREY POINTS ARE FROM PATIENT CELLS THAT LIE WITHIN THE 95% CONTOUR FROM CONTROLS. RED POINTS ARE FROM PATIENT CELLS LYING OUTSIDE THE 95% CONTOUR FROM CONTROLS. THE PROPORTION OF CELLS DIFFERENT FROM, VERTICALLY ABOVE AND VERTICALLY BELOW THE 95% CONTOUR FROM CONTROLS WRITTEN ABOVE EACH PANEL. 277
FIGURE 114 ESTIMATING DEFICIENCY IN COMPLEX I, COMPLEX II, COMPLEX IV AND COMPLEX V DATA FROM HIP 6: CONTOUR LINES REPRESENT THE KERNEL DENSITY ESTIMATE LEVELS CONTAINING 95% AND 50% OF THE CONTROL POPULATION FOR EACH PAIRWISE COMPARISON. GREY POINTS ARE FROM PATIENT CELLS THAT LIE WITHIN THE 95% CONTOUR FROM CONTROLS. RED POINTS ARE FROM PATIENT CELLS LYING OUTSIDE THE 95% CONTOUR FROM CONTROLS. THE PROPORTION OF CELLS DIFFERENT FROM, VERTICALLY ABOVE AND VERTICALLY BELOW THE 95% CONTOUR FROM CONTROLS WRITTEN ABOVE EACH PANEL. 278
FIGURE 115 ESTIMATING DEFICIENCY IN COMPLEX I, COMPLEX II, COMPLEX IV AND COMPLEX V DATA FROM HIP 7: CONTOUR LINES REPRESENT THE KERNEL DENSITY ESTIMATE LEVELS CONTAINING 95% AND 50% OF THE CONTROL POPULATION FOR EACH PAIRWISE COMPARISON. GREY POINTS ARE FROM PATIENT CELLS THAT LIE WITHIN THE 95% CONTOUR FROM CONTROLS. RED POINTS ARE FROM PATIENT CELLS LYING OUTSIDE THE 95% CONTOUR FROM CONTROLS. THE PROPORTION OF CELLS DIFFERENT FROM, VERTICALLY ABOVE AND VERTICALLY BELOW THE 95% CONTOUR FROM CONTROLS WRITTEN ABOVE EACH PANEL. 279

FIGURE 116 ESTIMATING DEFICIENCY IN COMPLEX I, COMPLEX II, COMPLEX IV AND COMPLEX V DATA FROM HIP 8: CONTOUR LINES REPRESENT THE KERNEL DENSITY ESTIMATE LEVELS CONTAINING 95% AND 50% OF THE CONTROL POPULATION FOR EACH PAIRWISE COMPARISON. GREY POINTS ARE FROM PATIENT CELLS THAT LIE WITHIN THE 95% CONTOUR FROM CONTROLS. RED POINTS ARE FROM PATIENT CELLS LYING OUTSIDE THE 95% CONTOUR FROM CONTROLS. THE PROPORTION OF CELLS DIFFERENT FROM, VERTICALLY ABOVE AND VERTICALLY BELOW THE 95% CONTOUR FROM CONTROLS WRITTEN ABOVE EACH PANEL. 280
FIGURE 117 ESTIMATING DEFICIENCY IN COMPLEX I, COMPLEX II, COMPLEX IV AND COMPLEX V DATA FROM HIP 9: CONTOUR LINES REPRESENT THE KERNEL DENSITY ESTIMATE LEVELS CONTAINING 95% AND 50% OF THE CONTROL POPULATION FOR EACH PAIRWISE COMPARISON. GREY POINTS ARE FROM PATIENT CELLS THAT LIE WITHIN THE 95% CONTOUR FROM CONTROLS. RED POINTS ARE FROM PATIENT CELLS LYING OUTSIDE THE 95% CONTOUR FROM CONTROLS. THE PROPORTION OF CELLS DIFFERENT FROM, VERTICALLY ABOVE AND VERTICALLY BELOW THE 95% CONTOUR FROM CONTROLS WRITTEN ABOVE EACH PANEL. 281
FIGURE 118 ESTIMATING DEFICIENCY IN COMPLEX I, COMPLEX II, COMPLEX IV AND COMPLEX V DATA FROM HIP 10: CONTOUR LINES REPRESENT THE KERNEL DENSITY ESTIMATE LEVELS CONTAINING 95% AND 50% OF THE CONTROL POPULATION FOR EACH PAIRWISE COMPARISON. GREY POINTS ARE FROM PATIENT CELLS THAT LIE WITHIN THE 95% CONTOUR FROM CONTROLS. RED POINTS ARE FROM PATIENT CELLS LYING OUTSIDE THE 95% CONTOUR FROM CONTROLS. THE PROPORTION OF CELLS DIFFERENT FROM, VERTICALLY ABOVE AND VERTICALLY BELOW THE 95% CONTOUR FROM CONTROLS WRITTEN ABOVE EACH PANEL. 282
FIGURE 119 ESTIMATING DEFICIENCY IN COMPLEX I, COMPLEX II, COMPLEX IV AND COMPLEX V DATA FROM FEMUR 1: CONTOUR LINES REPRESENT THE KERNEL DENSITY ESTIMATE LEVELS CONTAINING 95% AND 50% OF THE CONTROL POPULATION FOR EACH PAIRWISE COMPARISON. GREY POINTS ARE FROM PATIENT CELLS THAT LIE WITHIN THE 95% CONTOUR FROM CONTROLS. RED POINTS ARE FROM PATIENT CELLS LYING OUTSIDE THE 95% CONTOUR FROM CONTROLS. THE PROPORTION OF CELLS DIFFERENT FROM, VERTICALLY ABOVE AND VERTICALLY BELOW THE 95% CONTOUR FROM CONTROLS WRITTEN ABOVE EACH PANEL. 283
FIGURE 120 ESTIMATING DEFICIENCY IN COMPLEX I, COMPLEX II, COMPLEX IV AND COMPLEX V DATA FROM PAEDIATRIC 1: CONTOUR LINES REPRESENT THE KERNEL DENSITY ESTIMATE LEVELS CONTAINING 95% AND 50% OF THE CONTROL POPULATION FOR EACH PAIRWISE COMPARISON. GREY POINTS ARE FROM PATIENT CELLS THAT LIE WITHIN THE 95% CONTOUR FROM CONTROLS. RED POINTS ARE FROM PATIENT CELLS LYING OUTSIDE THE 95% CONTOUR FROM CONTROLS. THE PROPORTION OF CELLS DIFFERENT FROM, VERTICALLY ABOVE AND VERTICALLY BELOW THE 95% CONTOUR FROM CONTROLS WRITTEN ABOVE EACH PANEL. 284
FIGURE 121 ESTIMATING DEFICIENCY IN COMPLEX I, COMPLEX II, COMPLEX IV AND COMPLEX V DATA FROM PAEDIATRIC 2: CONTOUR LINES REPRESENT THE KERNEL DENSITY ESTIMATE LEVELS CONTAINING 95% AND 50% OF THE CONTROL POPULATION FOR EACH PAIRWISE COMPARISON. GREY POINTS ARE FROM PATIENT CELLS THAT LIE WITHIN THE 95% CONTOUR FROM CONTROLS. RED POINTS ARE FROM PATIENT CELLS LYING OUTSIDE THE 95% CONTOUR FROM CONTROLS. THE PROPORTION OF CELLS DIFFERENT FROM, VERTICALLY ABOVE AND VERTICALLY BELOW THE 95% CONTOUR FROM CONTROLS WRITTEN ABOVE EACH PANEL. 285
FIGURE 122 VARIATION IN COMPLEX I, COMPLEX II & CIV DEFICIENCY WITH AGE. THE PROPORTION OF CELLS LYING VERTICALLY BELOW THE 95% CONTOUR FROM CONTROLS IN ALL PATIENTS PRESENTED IN TABLE 33. BLUE POINTS REPRESENT PROPORTIONS FROM MALE PATIENTS AND RED POINTS FROM FEMALE PATIENTS. THE HORIZONTAL DASHED LINE REPRESENTS THE PROPORTION OF DIFFERENCES FROM CONTROL PATIENTS THAT WE MIGHT EXPECT TO SEE BY CHANCE I.E., 0.05. 286

List of tables

TABLE 1 MAIN CHARACTERISTICS OF MESENCHYMAL STEM CELLS: EXPRESSION OF SPECIFIC ANTIGENS, CYTOKINE RECEPTORS, ADHESION MOLECULES, AND PRODUCTION OF CYTOKINES AND MATRIX MOLECULES (47). 20
TABLE 2: CAUSES OF SECONDARY OSTEOPOROSIS IN PREMENOPAUSAL WOMEN (110). 30
TABLE 3: PATIENT DEMOGRAPHICS AND DETAILS FROM WHICH SAMPLES WERE USED IN THIS RESEARCH..... 62
TABLE 4: NUMBERING BASED ON ANDERSON ET AL. SEQUENCE AND ORGANIZATION OF THE HUMAN MITOCHONDRIAL GENOME (220). AND ANDREWS ET AL. REANALYSIS AND REVISION OF THE CAMBRIDGE REFERENCE SEQUENCE FOR HUMAN MITOCHONDRIAL DNA (221) THESE PRIMERS ARE PUBLISHED IN TUPPEN ET AL BRAIN 2010, 133(10): 2952 (222). 73
TABLE 5 COMMON LASERS USED IN FLOW CYTOMETRY AND THEIR EMISSION PROFILES (226) 77
TABLE 6 COMPARISON OF MASS CYTOMETRY AND FLOW CYTOMETRY (239). 82
TABLE 7 PATIENTS' WHOSE SAMPLES WERE USED IN THE MTDNA SEQUENCING EXPERIMENTS. 90
TABLE 8: INITIAL SETUP OF THE THERMOCYCLER FOR LONG-RANGE PCR. 94
TABLE 9 PRIMER DETAILS FOR ≈4500BP AMPLICONS. 94
TABLE 10: INITIAL THERMOCYCLER SETTINGS FOR GOTAQ MASTER MIX. 95
TABLE 11: 2 STAGE STEP 2 SETUP OF THE THERMOCYCLER FOR USE WITH GOTAQ LONG PCR MASTER MIX. 95
TABLE 12 3 STAGE STEP 2 SETUP OF THE THERMOCYCLER FOR USE WITH GOTAQ LONG PCR MASTER MIX. 96
TABLE 13 SETUP OF THE THERMOCYCLER AS USED FOR SAMPLE GENERATION FOR SEQUENCING. 96
TABLE 14 SETUP OF THE THERMOCYCLER WITH THE ADDITIONAL ANNEALING/EXTENSION STEP..... 96
TABLE 15 FINAL PRIMER PAIRINGS USED FOR THE AMPLIFICATION OF THE MITOCHONDRIAL GENOME IN SINGLE MESENCHYMAL STEM CELLS. 97
TABLE 16 TECHNICAL SPECIFICATIONS OF NEXT GENERATION SEQUENCING PLATFORMS UTILISED IN QUAIL ET AL. 2012 (279) 104
TABLE 17 DEMONSTRATING THE OUTPUT FROM THE MUTPRED SCORED FOR THE 13 NON-SYNONYMOUS MUTATIONS SEEN IN THE MSC POPULATION COMPARED TO THE CONSENSUS SEQUENCE OF HIP 12 ON THE INITIAL MISEQ EXPERIMENT. 107
TABLE 18 PRIMERS FOR PCR AMPLIFICATION OF THE MITOCHONDRIAL GENOME. NUMBERING BASED ON ANDERSON ET AL. SEQUENCE AND ORGANIZATION OF THE HUMAN MITOCHONDRIAL GENOME (220). AND ANDREWS ET AL. REANALYSIS AND REVISION OF THE CAMBRIDGE REFERENCE SEQUENCE FOR HUMAN MITOCHONDRIAL DNA (221) THESE PRIMERS ARE PUBLISHED IN TUPPEN ET AL BRAIN 2010, 133(10): 2952 (222). 176
TABLE 19 DEMOGRAPHICS AND DETAILS OF PATIENTS' WHOSE SAMPLES WERE USED IN THE HIGH THROUGHPUT ASSAY. 181
TABLE 20 ANTIBODY SUMMARY TABLE: RABMAB – RABBIT MONOCLONAL ANTIBODIES, MSMAB – MOUSE MONOCLONAL ANTIBODIES. 184
TABLE 21 RESULTS OF VARYING FIXATION TIME USING TAAB 4% PFA SOLUTION ON THE MTCO2 FLUORESCENT INTENSITY, ALTHOUGH SPECIFIC BINDING WAS POOR. 187
TABLE 22 TWEEN 20 PBS VS TWEEN 20 TBS AS A PERMEABILISATION AND STAINING BUFFER DEMONSTRATING THE DIFFERENCE IN SIGNAL INTENSITY BETWEEN THE ISOTYPE CONTROL AND MTCO2 ANTIBODY AT DIFFERENT CONCENTRATIONS. 189
TABLE 23 DURATION OF BLOCKING STEP USING 10% NGS SOLUTION ON NON-SPECIFIC BINDING MTCO2 VS ISOTYPE CONTROL. 190
TABLE 24 HUMAN IGG BLOCK DURATION USING MTCO2 ANTIBODY AND ISOTYPE CONTROL AND THE EFFECT ON NON-SPECIFIC BINDING. 190
TABLE 25 RESULTS OF USING BD FC RECEPTOR BLOCK ON SIGNAL INTENSITY USING THE MTCO2 ANTIBODY AND ISOTYPE CONTROL CONJUGATED TO THE ALEXA FLUOR 647 MOLECULE..... 191
TABLE 26 RESULTS OF VARIABLE BLOCKING AGENTS ON A NON-SPECIFIC BINDING FLUORESCENT SIGNAL WHEN USING THE MTCO2 ANTIBODY AND ISOTYPE CONTROL..... 191

TABLE 27 INITIAL FLOW CYTOMETRY PROTOCOL FOR MEASURING MITOCHONDRIAL RESPIRATORY CHAIN PROTEIN DEFICIENCIES. 194
TABLE 28 MEAN SIGNAL INTENSITY VALUES OF K562 CELLS USING PRIMARY SECONDARY ANTIBODY INCUBATION STEPS ON THE BD SYMPHONY FLOW CYTOMETER. 197
TABLE 29 SUMMARY TABLE OF PERMEABILISATION AND FIXATION METHODS FOR ASSESSING MITOCHONDRIA PROTEIN TARGETS USING IMMUNOHISTOCHEMISTRY. 202
TABLE 30 RESULTS OF MSC CELL SORTING ON BD FACSARIA FUSION. 225
TABLE 31 FURTHER SORTING RESULTS OF MSCS USING THE BD FACSARIA FUSION. 226
TABLE 32 COMPARISON OF DIFFERENT SOLUTIONS FOR IMMERSION-BASED DECALCIFICATION(372). 240
TABLE 33 ADULT AND PAEDIATRIC PATIENT COHORT OF SAMPLES USED IN CYTOF EXPERIMENTS. 260
TABLE 34 DEMOGRAPHICS OF THE BONE MARROW LESIONS SAMPLES SELECTED FOR THE TRIAL CYTOF RUN. 264
TABLE 35 REGIONS OF INTEREST IDENTIFIED AS ANOMALIES AND EXCLUDED FROM THE ANALYSIS. WITH SIMILAR VARIANCE AS SEEN IN 2-2-2 COMPARED TO THE REST OF A SAMPLES DATA. 272
TABLE 36: A SUMMARY TABLE SHOWING THE PERCENTAGE OF OSTEOBLASTS ABOVE AND BELOW THE 0.95 CONTOUR FOR COMPLEX I, COMPLEX II, COMPLEX IV AND COMPLEX V ACROSS THE PATIENT COHORT. VALUES GREATER THAN 5% (DEEMED LEVEL OF BACKGROUND OUTLIERS) ARE HIGHLIGHTED IN RED. 287
TABLE 37 MATRIX DISPLAYING PERCENTAGE CROSSTALK FOR METAL TAGS. THE SIGNAL OVERLAP IS INDICATED: BLUE BOXES ≥ 0.5%, CLEAR BOXES ≤ 0.5%. MASS CHANNELS ARE IN COLUMNS AND MASS TAG PROBES ARE IN ROWS. FOR MASS TAGS: COLOUR INDICATES PROBES THAT CONTRIBUTE ≥ 0.5% CROSSTALK INTO NO CHANNELS (GREEN), ONE OR TWO CHANNELS (YELLOW), OR MORE THAN TWO CHANNELS (ORANGE). FOR MASS CHANNELS: COLOUR INDICATES CHANNELS RECEIVING ≥ 0.5% CROSSTALK FROM NO PROBES (GREEN), ONE OR TWO CHANNELS (YELLOW), OR MORE THAN TWO CHANNELS (ORANGE). IMAGES ADAPTED FROM FLUIDIGM WITH EXTRA INFORMATION COURTESY OF FCCF NEWCASTLE." 294
TABLE 38 SUMMARY OF RESULTS FROM THE PCR AND CYTOF CHAPTERS FOR EACH PATIENT. WHEN SAMPLES WERE NOT AVAILABLE OR USED IN EACH EXPERIMENT THESE ARE REPRESENTED BY BLANKS. 302

References:

1. Law MR, Wald NJ, Meade TW. Strategies for prevention of osteoporosis and hip fracture. BMJ: British Medical Journal. 1991;303(6800):453.
2. World Health O. Assessment of fracture risk and its application to screening for postmenopausal osteoporosis: report of a WHO study group [meeting held in Rome from 22 to 25 June 1992]. 1994.
3. Hendrickx G, Boudin E, Van Hul W. A look behind the scenes: the risk and pathogenesis of primary osteoporosis. Nature Reviews Rheumatology. 2015;11(8):462-74.
4. Riggs BL, Wahner HW, Dunn WL, Mazess RB, Offord KP, Melton 3rd LJ. Differential changes in bone mineral density of the appendicular and axial skeleton with aging: relationship to spinal osteoporosis. Journal of Clinical Investigation. 1981;67(2):328.
5. Riggs BL, Wahner HW, Seeman E, Offord KP, Dunn WL, Mazess RB, et al. Changes in bone mineral density of the proximal femur and spine with aging: differences between the postmenopausal and senile osteoporosis syndromes. Journal of Clinical Investigation. 1982;70(4):716.
6. Wade SW, Strader C, Fitzpatrick LA, Anthony MS, O'Malley CD. Estimating prevalence of osteoporosis: examples from industrialized countries. Archives of Osteoporosis. 2014;9(1):182.
7. Ljiii M. How many women have osteoporosis now. J Bone Miner Res1995. 1995;10:175-7.
8. Johnell O. The socioeconomic burden of fractures: today and in the 21st century. The American journal of medicine. 1997;103(2):S20-S6.

9. Braithwaite RS, Col NF, Wong JB. Estimating hip fracture morbidity, mortality and costs. Journal of the American Geriatrics Society. 2003;51(3):364-70.
10. Harvey N, Dennison E, Cooper C. Osteoporosis: impact on health and economics. Nature Reviews Rheumatology. 2010;6(2):99-105.
11. Melton LJ, Chrischilles EA, Cooper C, Lane AW, Riggs BL. How many women have osteoporosis? Journal of bone and mineral research. 2005;20(5):886-92.
12. Royal College of Physicians. National Hip Fracture Database (NHFD) annual report 2016. Royal College of Physicians,; 2016.
13. Almeida M. Aging mechanisms in bone. BoneKEy reports. 2012;1(7).
14. Rosen CJ, Bouxsein ML. Mechanisms of disease: is osteoporosis the obesity of bone? Nature clinical practice Rheumatology. 2006;2(1):35-43.
15. Bolander ME. Regulation of fracture repair by growth factors. Experimental Biology and Medicine. 1992;200(2):165-70.
16. Bruder SP, Fink DJ, Caplan AI. Mesenchymal stem cells in bone development, bone repair, and skeletal regenaration therapy. Journal of cellular biochemistry. 1994;56(3):283-94.
17. Einhorn TA. The cell and molecular biology of fracture healing. Clinical orthopaedics and related research. 1998;355:S7-S21.
18. Zhang Q, Riddle RC, Clemens TL. Bone and the regulation of global energy balance. Journal of internal medicine. 2015;277(6):681-9.
19. Taylor RW, Barron MJ, Borthwick GM, Gospel A, Chinnery PF, Samuels DC, et al. Mitochondrial DNA mutations in human colonic crypt stem cells. The Journal of clinical investigation. 2003;112(9):1351-60.
20. Taylor RW, Turnbull DM. Mitochondrial DNA mutations in human disease. Nature Reviews Genetics. 2005;6(5):389-402.
21. Tuppen HAL, Blakely EL, Turnbull DM, Taylor RW. Mitochondrial DNA mutations and human disease. Biochimica et Biophysica Acta (BBA)-Bioenergetics. 2010;1797(2):113-28.
22. Kujoth GC, Hiona A, Pugh TD, Someya S, Panzer K, Wohlgemuth SE, et al. Mitochondrial DNA mutations, oxidative stress, and apoptosis in mammalian aging. Science. 2005;309(5733):481-4.
23. Linnane A, Ozawa T, Marzuki S, Tanaka M. Mitochondrial DNA mutations as an important contributor to ageing and degenerative diseases. The Lancet. 1989;333(8639):642-5.
24. Trifunovic A, Larsson NG. Mitochondrial dysfunction as a cause of ageing. J Intern Med. 2008;263(2):167-78.
25. Miller MD, Thompson SR, Hart J. Review of Orthopaedics E-Book: Elsevier Health Sciences; 2012.
26. Rodan GA. Bone homeostasis. Proceedings of the National Academy of Sciences. 1998;95(23):13361-2.
27. Zhao Q, Eberspaecher H, Lefebvre V, De Crombrugghe B. Parallel expression of Sox9 and Col2a1 in cells undergoing chondrogenesis. Developmental dynamics. 1997;209(4):377-86.
28. Kronenberg HM. Developmental regulation of the growth plate. Nature. 2003;423(6937):332.
29. Salazar VS, Gamer LW, Rosen V. BMP signalling in skeletal development, disease and repair. Nature Reviews Endocrinology. 2016;12(4):203.
30. Rho J-Y, Kuhn-Spearing L, Zioupos P. Mechanical properties and the hierarchical structure of bone. Medical engineering & physics. 1998;20(2):92-102.
31. Weiner S, Traub W. Bone structure: from angstroms to microns. The FASEB journal. 1992;6(3):879-85.
32. Landis W. The strength of a calcified tissue depends in part on the molecular structure and organization of its constituent mineral crystals in their organic matrix. Bone. 1995;16(5):533-44.
33. Hodge AJ. Recent studies with the electron microscope on ordered aggregates of the tropocollagen macromolecule. Aspects of protein structure. 1963:289-300.
34. Marotti G. A new theory of bone lamellation. Calcified Tissue International. 1993;53(1):S47-S56.

35. Giraud-Guille M-M. Twisted plywood architecture of collagen fibrils in human compact bone osteons. Calcified tissue international. 1988;42(3):167-80.
36. Weiner S, Wagner HD. The material bone: structure-mechanical function relations. Annual Review of Materials Science. 1998;28(1):271-98.
37. Dudley HR, Spiro D. The fine structure of bone cells. The Journal of Cell Biology. 1961;11(3):627-49.
38. Gorski JP. Is all bone the same? Distinctive distributions and properties of non-collagenous matrix proteins in lamellar vs. woven bone imply the existence of different underlying osteogenic mechanisms. Critical Reviews in Oral Biology & Medicine. 1998;9(2):201-23.
39. Rubin R, Strayer DS, Rubin E. Rubin's pathology: clinicopathologic foundations of medicine: Lippincott Williams & Wilkins; 2008.
40. Wilson A, Trumpp A. Bone-marrow haematopoietic-stem-cell niches. Nature Reviews Immunology. 2006;6(2):93.
41. Lin GL, Hankenson KD. Integration of BMP, Wnt, and notch signaling pathways in osteoblast differentiation. Journal of cellular biochemistry. 2011;112(12):3491-501.
42. Short B, Brouard N, Occhiodoro-Scott T, Ramakrishnan A, Simmons PJ. Mesenchymal stem cells. Archives of medical research. 2003;34(6):565-71.
43. Kopen GC, Prockop DJ, Phinney DG. Marrow stromal cells migrate throughout forebrain and cerebellum, and they differentiate into astrocytes after injection into neonatal mouse brains. Proceedings of the National Academy of Sciences. 1999;96(19):10711-6.
44. Caplan AI. The mesengenic process. Clinics in plastic surgery. 1994;21(3):429-35.
45. Kuznetsov SA, Friedenstein AJ, Robey PG. Factors required for bone marrow stromal fibroblast colony formation in vitro. British journal of haematology. 1997;97(3):561-70.
46. Prockop DJ. Marrow stromal cells as stem cells for nonhematopoietic tissues. Science. 1997;276(5309):71-4.
47. Minguell JJ, Erices A, Conget P. Mesenchymal stem cells. Experimental biology and medicine. 2001;226(6):507-20.
48. Kulterer B, Friedl G, Jandrositz A, Sanchez-Cabo F, Prokesch A, Paar C, et al. Gene expression profiling of human mesenchymal stem cells derived from bone marrow during expansion and osteoblast differentiation. BMC genomics. 2007;8(1):70.
49. Mosekilde L, Vestergaard P, Rejnmark L. The pathogenesis, treatment and prevention of osteoporosis in men. Drugs. 2013;73(1):15-29.
50. Simonet W, Lacey D, Dunstan C, Kelley M, Chang M-S, Lüthy R, et al. Osteoprotegerin: a novel secreted protein involved in the regulation of bone density. Cell. 1997;89(2):309-19.
51. Baud'huin M, Duplomb L, Teletchea S, Lamoureux F, Ruiz-Velasco C, Maillasson M, et al. Osteoprotegerin: multiple partners for multiple functions. Cytokine & growth factor reviews. 2013;24(5):401-9.
52. Fortner RT, Sarink D, Schock H, Johnson T, Tjønneland A, Olsen A, et al. Osteoprotegerin and breast cancer risk by hormone receptor subtype: a nested case-control study in the EPIC cohort. BMC medicine. 2017;15(1):26.
53. Sordillo EM, Pearse RN. RANK-Fc: A therapeutic antagonist for RANK-L in myeloma. Cancer: Interdisciplinary International Journal of the American Cancer Society. 2003;97(S3):802-12.
54. Kato H, Han X, Yamaza H, Masuda K, Hirofuji Y, Sato H, et al. Direct effects of mitochondrial dysfunction on poor bone health in Leigh syndrome. Biochemical and biophysical research communications. 2017;493(1):207-12.
55. Chen CT, Shih YRV, Kuo TK, Lee OK, Wei YH. Coordinated changes of mitochondrial biogenesis and antioxidant enzymes during osteogenic differentiation of human mesenchymal stem cells. Stem Cells. 2008;26(4):960-8.
56. Fujii M, Takeda K, Imamura T, Aoki H, Sampath TK, Enomoto S, et al. Roles of bone morphogenetic protein type I receptors and Smad proteins in osteoblast and chondroblast differentiation. Molecular biology of the cell. 1999;10(11):3801-13.

57. Logan CY, Nusse R. The Wnt signaling pathway in development and disease. Annu Rev Cell Dev Biol. 2004;20:781-810.
58. Boyden LM, Mao J, Belsky J, Mitzner L, Farhi A, Mitnick MA, et al. High bone density due to a mutation in LDL-receptor–related protein 5. New England Journal of Medicine. 2002;346(20):1513-21.
59. Qiu W, Andersen TE, Bollerslev J, Mandrup S, Abdallah BM, Kassem M. Patients with high bone mass phenotype exhibit enhanced osteoblast differentiation and inhibition of adipogenesis of human mesenchymal stem cells. Journal of Bone and Mineral Research. 2007;22(11):1720-31.
60. Gong Y, Slee RB, Fukai N, Rawadi G, Roman-Roman S, Reginato AM, et al. LDL receptor-related protein 5 (LRP5) affects bone accrual and eye development. Cell. 2001;107(4):513-23.
61. Holmen SL, Zylstra CR, Mukherjee A, Sigler RE, Faugere M-C, Bouxsein ML, et al. Essential role of β-catenin in postnatal bone acquisition. Journal of Biological Chemistry. 2005;280(22):21162-8.
62. Bennett CN, Longo KA, Wright WS, Suva LJ, Lane TF, Hankenson KD, et al. Regulation of osteoblastogenesis and bone mass by Wnt10b. Proceedings of the National Academy of Sciences. 2005;102(9):3324-9.
63. Boland GM, Perkins G, Hall DJ, Tuan RS. Wnt 3a promotes proliferation and suppresses osteogenic differentiation of adult human mesenchymal stem cells. Journal of cellular biochemistry. 2004;93(6):1210-30.
64. St-Jacques B, Hammerschmidt M, McMahon AP. Indian hedgehog signaling regulates proliferation and differentiation of chondrocytes and is essential for bone formation. Genes & development. 1999;13(16):2072-86.
65. Plaisant M, Fontaine C, Cousin W, Rochet N, Dani C, Peraldi P. Activation of hedgehog signaling inhibits osteoblast differentiation of human mesenchymal stem cells. Stem Cells. 2009;27(3):703-13.
66. Hanada K, Dennis JE, Caplan AI. Stimulatory effects of basic fibroblast growth factor and bone morphogenetic protein-2 on osteogenic differentiation of rat bone marrow-derived mesenchymal stem cells. Journal of Bone and Mineral Research. 1997;12(10):1606-14.
67. Nakashima K, Zhou X, Kunkel G, Zhang Z, Deng JM, Behringer RR, et al. The novel zinc finger-containing transcription factor osterix is required for osteoblast differentiation and bone formation. Cell. 2002;108(1):17-29.
68. Kaback LA, Soung DY, Naik A, Smith N, Schwarz EM, O'Keefe RJ, et al. Osterix/Sp7 regulates mesenchymal stem cell mediated endochondral ossification. Journal of cellular physiology. 2008;214(1):173-82.
69. Lapunzina P, Aglan M, Temtamy S, Caparrós-Martín JA, Valencia M, Letón R, et al. Identification of a frameshift mutation in Osterix in a patient with recessive osteogenesis imperfecta. The American Journal of Human Genetics. 2010;87(1):110-4.
70. Hall BK. Bones and cartilage: developmental and evolutionary skeletal biology: Elsevier; 2005.
71. Norris DO, Carr JA. Chapter 14 - Regulation of Calcium and Phosphate Homeostasis in Vertebrates. In: Norris DO, Carr JA, editors. Vertebrate Endocrinology (Fifth Edition). San Diego: Academic Press; 2013. p. 501-27.
72. Lee NK, Sowa H, Hinoi E, Ferron M, Ahn JD, Confavreux C, et al. Endocrine regulation of energy metabolism by the skeleton. Cell. 2007;130(3):456-69.
73. Boskey AL, Robey PG. The regulatory role of matrix proteins in mineralization of bone. Osteoporosis (Fourth Edition): Elsevier; 2013. p. 235-55.
74. Chapurlat RD, Genant HK. Chapter 69 - Osteoporosis. In: Jameson JL, De Groot LJ, de Kretser DM, Giudice LC, Grossman AB, Melmed S, et al., editors. Endocrinology: Adult and Pediatric (Seventh Edition). Philadelphia: W.B. Saunders; 2016. p. 1184-213.e6.
75. Friedman PA, Przysiecki CT. Vitamin K-dependent carboxylation. International Journal of Biochemistry. 1987;19(1):1-7.
76. Ducy P, Desbois C, Boyce B, Pinero G, Story B, Dunstan C, et al. Increased bone formation in osteocalcin-deficient mice. Nature. 1996;382(6590):448.

77. Murshed M, Schinke T, McKee MD, Karsenty G. Extracellular matrix mineralization is regulated locally; different roles of two gla-containing proteins. The Journal of cell biology. 2004;165(5):625-30.
78. Zoch ML, Clemens TL, Riddle RC. New insights into the biology of osteocalcin. Bone. 2016;82:42-9.
79. Sommerfeldt DW, Rubin CT. Biology of bone and how it orchestrates the form and function of the skeleton. European spine journal : official publication of the European Spine Society, the European Spinal Deformity Society, and the European Section of the Cervical Spine Research Society. 2001;10 Suppl 2:S86-95.
80. Golub EE, editor Biomineralization and matrix vesicles in biology and pathology. Seminars in immunopathology; 2011: Springer.
81. Bandyopadhyay A, Tsuji K, Cox K, Harfe BD, Rosen V, Tabin CJ. Genetic Analysis of the Roles of BMP2, BMP4, and BMP7 in Limb Patterning and Skeletogenesis. PLoS Genet. 2006;2(12):e216.
82. Boonrungsiman S, Gentleman E, Carzaniga R, Evans ND, McComb DW, Porter AE, et al. The role of intracellular calcium phosphate in osteoblast-mediated bone apatite formation. Proceedings of the National Academy of Sciences of the United States of America. 2012;109(35):14170-5.
83. McHugh KP, Hodivala-Dilke K, Zheng M-H, Namba N, Lam J, Novack D, et al. Mice lacking β3 integrins are osteosclerotic because of dysfunctional osteoclasts. Journal of Clinical Investigation. 2000;105(4):433-40.
84. Ek-Rylander B, Flores M, Wendel M, Heinegård D, Andersson G. Dephosphorylation of osteopontin and bone sialoprotein by osteoclastic tartrate-resistant acid phosphatase. Modulation of osteoclast adhesion in vitro. Journal of Biological Chemistry. 1994;269(21):14853-6.
85. Lemma S, Sboarina M, Porporato PE, Zini N, Sonveaux P, Di Pompo G, et al. Energy metabolism in osteoclast formation and activity. The International Journal of Biochemistry & Cell Biology. 2016;79:168-80.
86. Oursler MJ, Bradley EW, Elfering SL, Giulivi C. Native, not nitrated, cytochrome c and mitochondria-derived hydrogen peroxide drive osteoclast apoptosis. American Journal of Physiology-Cell Physiology. 2005;288(1):C156-C68.
87. Jin Z, Wei W, Yang M, Du Y, Wan Y. Mitochondrial complex I activity suppresses inflammation and enhances bone resorption by shifting macrophage-osteoclast polarization. Cell metabolism. 2014;20(3):483-98.
88. Cornish J, MacGibbon A, Lin J-M, Watson M, Callon KE, Tong P, et al. Modulation of osteoclastogenesis by fatty acids. Endocrinology. 2008;149(11):5688-95.
89. Ishii K-a, Fumoto T, Iwai K, Takeshita S, Ito M, Shimohata N, et al. Coordination of PGC-1β and iron uptake in mitochondrial biogenesis and osteoclast activation. Nature medicine. 2009;15(3):259.
90. Srinivasan S, Koenigstein A, Joseph J, Sun L, Kalyanaraman B, Zaidi M, et al. Role of mitochondrial reactive oxygen species in osteoclast differentiation. Annals of the New York Academy of Sciences. 2010;1192(1):245-52.
91. Darden AG, Ries WL, Wolf WC, Rodriguiz RM, Key Jr LL. Osteoclastic superoxide production and bone resorption: stimulation and inhibition by modulators of NADPH oxidase. Journal of Bone and Mineral Research. 1996;11(5):671-5.
92. Steinbeck MJ, Appel WH, Verhoeven AJ, Karnovsky MJ. NADPH-oxidase expression and in situ production of superoxide by osteoclasts actively resorbing bone. The Journal of Cell Biology. 1994;126(3):765-72.
93. Yang S, Ries W, Key Jr L. Nicotinamide adenine dinucleotide phosphate oxidase in the formation of superoxide in osteoclasts. Calcified tissue international. 1998;63(4):346-50.
94. Garrett IR, Boyce BF, Oreffo R, Bonewald L, Poser J, Mundy GR. Oxygen-derived free radicals stimulate osteoclastic bone resorption in rodent bone in vitro and in vivo. The Journal of clinical investigation. 1990;85(3):632-9.
95. Fraser J, Helfrich M, Wallace H, Ralston S. Hydrogen peroxide, but not superoxide, stimulates bone resorption in mouse calvariae. Bone. 1996;19(3):223-6.

96. Ha H, Kwak HB, Lee SW, Jin HM, Kim H-M, Kim H-H, et al. Reactive oxygen species mediate RANK signaling in osteoclasts. Experimental cell research. 2004;301(2):119-27.
97. Wu X, McKenna MA, Feng X, Nagy TR, McDonald JM. Osteoclast apoptosis: the role of Fas in vivo and in vitro. Endocrinology. 2003;144(12):5545-55.
98. Berenson JR. Antitumor effects of bisphosphonates: from the laboratory to the clinic. Current opinion in supportive and palliative care. 2011;5(3):233-40.
99. Reszka AA, Rodan GA. Mechanism of action of bisphosphonates. Current osteoporosis reports. 2003;1(2):45-52.
100. Jiang Y, Proteau P, Poulter D, Ferro-Novick S. BTS1 encodes a geranylgeranyl diphosphate synthase in Saccharomyces cerevisiae. Journal of Biological Chemistry. 1995;270(37):21793-9.
101. Kawahara I, Koide M, Tadokoro O, Udagawa N, Nakamura H, Takahashi N, et al. The relationship between calcium accumulation in osteoclast mitochondrial granules and bone resorption. Bone. 2009;45(5):980-6.
102. Giorgi C, Baldassari F, Bononi A, Bonora M, De Marchi E, Marchi S, et al. Mitochondrial Ca2+ and apoptosis. Cell calcium. 2012;52(1):36-43.
103. Solomon LW, D. Nayagam, S. Apley's system of Orthopaedics and Fractures. Ninth ed2010.
104. Harada S-i, Rodan GA. Control of osteoblast function and regulation of bone mass. Nature. 2003;423(6937):349.
105. Poole KE, Reeve J. Parathyroid hormone—a bone anabolic and catabolic agent. Current opinion in pharmacology. 2005;5(6):612-7.
106. Potts JT. Parathyroid hormone: past and present. The Journal of endocrinology. 2005;187(3):311-25.
107. Erdogan M, Gursoy A, Kulaksizoglu M. Long-term effects of elevated gastrin levels on calcitonin secretion. Journal of endocrinological investigation. 2006;29(9):771-5.
108. Nicholson G, Moseley J, Sexton P, Mendelsohn F, Martin T. Abundant calcitonin receptors in isolated rat osteoclasts. Biochemical and autoradiographic characterization. The Journal of clinical investigation. 1986;78(2):355-60.
109. Kobayashi K, Nojiri H, Saita Y, Morikawa D, Ozawa Y, Watanabe K, et al. Mitochondrial superoxide in osteocytes perturbs canalicular networks in the setting of age-related osteoporosis. Sci Rep. 2015;5:9148.
110. Martinez-Morillo M, Grados D, Holgado S. Premenopausal osteoporosis: how to treat? Reumatol Clin. 2012;8(2):93-7.
111. Deng H-W, Chen W-M, Recker S, Stegman MR, Li J-L, Davies KM, et al. Genetic Determination of Colles' Fracture and Differential Bone Mass in Women With and Without Colles' Fracture. Journal of Bone and Mineral Research. 2000;15(7):1243-52.
112. Richards JB, Zheng H-F, Spector TD. Genetics of osteoporosis from genome-wide association studies: advances and challenges. Nat Rev Genet. 2012;13(8):576-88.
113. Ralston SH. Genetics of osteoporosis. Annals of the New York Academy of Sciences. 2010;1192(1):181-9.
114. Weiner S, Traub W, Wagner HD. Lamellar Bone: Structure–Function Relations. Journal of Structural Biology. 1999;126(3):241-55.
115. Grant SFA, Reid DM, Blake G, Herd R, Fogelman I, Ralston SH. Reduced bone density and osteoporosis associated with a polymorphic Sp1 binding site in the collagen type I [alpha] 1 gene. Nat Genet. 1996;14(2):203-5.
116. Mann V, Hobson EE, Li B, Stewart TL, Grant SF, Robins SP, et al. A COL1A1 Sp1 binding site polymorphism predisposes to osteoporotic fracture by affecting bone density and quality. J Clin Invest. 2001;107(7):899-907.
117. Stewart TL, Roschger P, Misof BM, Mann V, Fratzl P, Klaushofer K, et al. Association of COLIA1 Sp1 alleles with defective bone nodule formation in vitro and abnormal bone mineralization in vivo. Calcif Tissue Int. 2005;77(2):113-8.

118. Gong Y, Slee RB, Fukai N, Rawadi G, Roman-Roman S, Reginato AM, et al. LDL receptor-related protein 5 (LRP5) affects bone accrual and eye development. Cell. 2001;107(4):513-23.
119. MacDonald BT, Tamai K, He X. Wnt/β-catenin signaling: components, mechanisms, and diseases. Developmental cell. 2009;17(1):9-26.
120. Williams BO, Insogna KL. Where Wnts went: the exploding field of Lrp5 and Lrp6 signaling in bone. J Bone Miner Res. 2009;24(2):171-8.
121. Clarke BL. Anti-sclerostin antibodies: utility in treatment of osteoporosis. Maturitas. 2014;78(3):199-204.
122. Sun J, Zhang C, Xu L, Yang M, Yang H. The Transforming Growth Factor-β1 (TGF-β1) Gene Polymorphisms (TGF-β1 T869C and TGF-β1 T29C) and Susceptibility to Postmenopausal Osteoporosis: A Meta-Analysis. Medicine. 2015;94(4):e461.
123. Khosla S, Amin S, Orwoll E. Osteoporosis in men. Endocrine reviews. 2008;29(4):441-64.
124. Clarke BL, Khosla S. Androgens and bone. Steroids. 2009;74(3):296-305.
125. Khosla S. Update in male osteoporosis. The Journal of Clinical Endocrinology & Metabolism. 2010;95(1):3-10.
126. Eghbali-Fatourechi G, Khosla S, Sanyal A, Boyle WJ, Lacey DL, Riggs BL. Role of RANK ligand in mediating increased bone resorption in early postmenopausal women. J Clin Invest. 2003;111(8):1221-30.
127. Adachi JD. Glucocorticoid-induced osteoporosis. Osteoporosis international. 2009;20(3):239-40.
128. Manolagas SC. From estrogen-centric to aging and oxidative stress: a revised perspective of the pathogenesis of osteoporosis. Endocr Rev. 2010;31(3):266-300.
129. Kawano Y, Kypta R. Secreted antagonists of the Wnt signalling pathway. Journal of Cell Science. 2003;116(13):2627-34.
130. Ohnaka K, Tanabe M, Kawate H, Nawata H, Takayanagi R. Glucocorticoid suppresses the canonical Wnt signal in cultured human osteoblasts. Biochemical and Biophysical Research Communications. 2005;329(1):177-81.
131. Nicodemus KK, Folsom AR. Type 1 and Type 2 Diabetes and Incident Hip Fractures in Postmenopausal Women. Diabetes Care. 2001;24(7):1192-7.
132. Bain J. Testosterone and the aging male: to treat or not to treat? Maturitas. 2010;66(1):16-22.
133. Thrailkill KM, Lumpkin CK, Jr., Bunn RC, Kemp SF, Fowlkes JL. Is insulin an anabolic agent in bone? Dissecting the diabetic bone for clues. Am J Physiol Endocrinol Metab. 2005;289(5):E735-45.
134. Holick MF. Vitamin D Deficiency. New England Journal of Medicine. 2007;357(3):266-81.
135. Ferder M, Inserra F, Manucha W, Ferder L. The world pandemic of vitamin D deficiency could possibly be explained by cellular inflammatory response activity induced by the renin-angiotensin system. Am J Physiol Cell Physiol. 2013;304(11):C1027-39.
136. Rizzoli R, Boonen S, Brandi ML, Bruyère O, Cooper C, Kanis JA, et al. Vitamin D supplementation in elderly or postmenopausal women: a 2013 update of the 2008 recommendations from the European Society for Clinical and Economic Aspects of Osteoporosis and Osteoarthritis (ESCEO). Current medical research and opinion. 2013;29(4):305-13.
137. Lemann Jr J, Litzow JR, Lennon EJ. The effects of chronic acid loads in normal man: further evidence for the participation of bone mineral in the defense against chronic metabolic acidosis. Journal of Clinical Investigation. 1966;45(10):1608.
138. Kraut JA, Mishler DR, Singer FR, Goodman WG. The effects of metabolic acidosis on bone formation and bone resorption in the rat. Kidney international. 1986;30(5):694-700.
139. Wiederkehr M, Krapf R. Metabolic and endocrine effects of metabolic acidosis in humans. Swiss Medical Weekly. 2001;131(9-10):127-32.
140. Gray MW, Burger G, Lang BF. Mitochondrial Evolution. Science. 1999;283(5407):1476-81.
141. Mokranjac D, Neupert W. Protein import into mitochondria. Portland Press Limited; 2005.

142. Asin-Cayuela J, Gustafsson CM. Mitochondrial transcription and its regulation in mammalian cells. Trends in biochemical sciences. 2007;32(3):111-7.
143. Sjöstrand FS. The ultrastructure of cells as revealed by the electron microscope. International Review of Cytology. 1956;5:455-533.
144. Palade GE. The fine structure of mitochondria. The Anatomical Record. 1952;114(3):427-51.
145. Frey TG, Renken CW, Perkins GA. Insight into mitochondrial structure and function from electron tomography. Biochimica et Biophysica Acta (BBA)-Bioenergetics. 2002;1555(1):196-203.
146. Zalman LS, Nikaido H, Kagawa Y. Mitochondrial outer membrane contains a protein producing nonspecific diffusion channels. Journal of Biological Chemistry. 1980;255(5):1771-4.
147. Mohamad N, Gutiérrez A, Núñez M, Cocca C, Martín G, Cricco G, et al. Mitochondrial apoptotic pathways. Biocell. 2005;29(2):149-61.
148. Hatefi Y. The mitochondrial electron transport and oxidative phosphorylation system. Annual review of biochemistry. 1985;54(1):1015-69.
149. Sun F, Huo X, Zhai Y, Wang A, Xu J, Su D, et al. Crystal structure of mitochondrial respiratory membrane protein complex II. Cell. 2005;121(7):1043-57.
150. Balaban RS. Regulation of oxidative phosphorylation in the mammalian cell. American Journal of Physiology-Cell Physiology. 1990;258(3):C377-C89.
151. Kühlbrandt W. Structure and function of mitochondrial membrane protein complexes. BMC biology. 2015;13(1):89.
152. Vinothkumar KR, Zhu J, Hirst J. Architecture of mammalian respiratory complex I. Nature. 2014;515(7525):80.
153. Sazanov LA. The mechanism of coupling between electron transfer and proton translocation in respiratory complex I. Journal of bioenergetics and biomembranes. 2014;46(4):247-53.
154. Sazanov LA. Respiratory complex I: mechanistic and structural insights provided by the crystal structure of the hydrophilic domain. Biochemistry. 2007;46(9):2275-88.
155. Anderson S, Bankier AT, Barrell BG, de Bruijn MH, Coulson AR, Drouin J, et al. Sequence and organization of the human mitochondrial genome. Nature. 1981;290(5806):457.
156. Hägerhäll C. Succinate: quinone oxidoreductases: variations on a conserved theme. Biochimica et Biophysica Acta (BBA)-Bioenergetics. 1997;1320(2):107-41.
157. Iwata S, Lee JW, Okada K, Lee JK, Iwata M, Rasmussen B, et al. Complete structure of the 11-subunit bovine mitochondrial cytochrome bc1 complex. Science. 1998;281(5373):64-71.
158. Tsukihara T, Aoyama H, Yamashita E, Tomizaki T, Yamaguchi H, Shinzawa-Itoh K, et al. The whole structure of the 13-subunit oxidized cytochrome c oxidase at 2.8 Å. Science. 1996;272(5265):1136-44.
159. Balsa E, Marco R, Perales-Clemente E, Szklarczyk R, Calvo E, Landázuri MO, et al. NDUFA4 is a subunit of complex IV of the mammalian electron transport chain. Cell metabolism. 2012;16(3):378-86.
160. Watt IN, Montgomery MG, Runswick MJ, Leslie AG, Walker JE. Bioenergetic cost of making an adenosine triphosphate molecule in animal mitochondria. Proceedings of the National Academy of Sciences. 2010;107(39):16823-7.
161. DiMauro S, Schon EA. Mitochondrial respiratory-chain diseases. New England Journal of Medicine. 2003;348(26):2656-68.
162. Roy SS, Hajnóczky G. Calcium, mitochondria and apoptosis studied by fluorescence measurements. Methods. 2008;46(3):213-23.
163. Carafoli E. Intracellular calcium homeostasis. Annual review of biochemistry. 1987;56(1):395-433.
164. Kroemer G, Galluzzi L, Brenner C. Mitochondrial membrane permeabilization in cell death. Physiological reviews. 2007;87(1):99-163.
165. Gaspari M, Falkenberg M, Larsson NG, Gustafsson CM. The mitochondrial RNA polymerase contributes critically to promoter specificity in mammalian cells. The EMBO journal. 2004;23(23):4606-14.

166. Taanman J-W. The mitochondrial genome: structure, transcription, translation and replication. Biochimica et Biophysica Acta (BBA)-Bioenergetics. 1999;1410(2):103-23.
167. Scarpulla RC. Transcriptional paradigms in mammalian mitochondrial biogenesis and function. Physiological reviews. 2008;88(2):611-38.
168. Montoya J, Gaines GL, Attardi G. The pattern of transcription of the human mitochondrial rRNA genes reveals two overlapping transcription units. Cell. 1983;34(1):151-9.
169. Koene S, Smeitink JAM, Hirano M. Mitochondrial Medicine: A Clinical Guideline: Khondrion; 2011.
170. Wang TSF. Eukaryotic DNA polymerases. Annual Review of Biochemistry. 1991;60:513-52.
171. Chang DD, Clayton DA. Priming of human mitochondrial DNA replication occurs at the light-strand promoter. Proceedings of the National Academy of Sciences. 1985;82(2):351-5.
172. Weber K, Wilson JN, Taylor L, Brierley E, Johnson MA, Turnbull DM, et al. A new mtDNA mutation showing accumulation with time and restriction to skeletal muscle. American journal of human genetics. 1997;60(2):373.
173. Elson JL, Samuels DC, Turnbull DM, Chinnery PF. Random intracellular drift explains the clonal expansion of mitochondrial DNA mutations with age. The American Journal of Human Genetics. 2001;68(3):802-6.
174. De Grey AD. A proposed refinement of the mitochondrial free radical theory of aging. Bioessays. 1997;19(2):161-6.
175. Yoneda M, Chomyn A, Martinuzzi A, Hurko O, Attardi G. Marked replicative advantage of human mtDNA carrying a point mutation that causes the MELAS encephalomyopathy. Proceedings of the National Academy of Sciences. 1992;89(23):11164-8.
176. Kowald A, Kirkwood TB. Transcription could be the key to the selection advantage of mitochondrial deletion mutants in aging. Proceedings of the National Academy of Sciences. 2014;111(8):2972-7.
177. Vincent AE, Rosa HS, Pabis K, Lawless C, Chen C, Grünewald A, et al. Subcellular origin of mitochondrial DNA deletions in human skeletal muscle. Annals of neurology. 2018;84(2):289-301.
178. Lawless C, Greaves L, Reeve AK, Turnbull DM, Vincent AE. The rise and rise of mitochondrial DNA mutations. Open biology. 2020;10(5):200061.
179. Alexeyev MF. Is there more to aging than mitochondrial DNA and reactive oxygen species? Febs Journal. 2009;276(20):5768-87.
180. Jang YC, Van Remmen H. The mitochondrial theory of aging: insight from transgenic and knockout mouse models. Experimental gerontology. 2009;44(4):256-60.
181. Trifunovic A, Wredenberg A, Falkenberg M, Spelbrink JN, Rovio AT, Bruder CE, et al. Premature ageing in mice expressing defective mitochondrial DNA polymerase. Nature. 2004;429(6990):417-23.
182. Cottrell DA, Blakely EL, Johnson MA, Ince PG, Borthwick GM, Turnbull DM. Cytochrome c oxidase deficient cells accumulate in the hippocampus and choroid plexus with age. Neurobiology of aging. 2001;22(2):265-72.
183. Fayet G, Jansson M, Sternberg D, Moslemi A-R, Blondy P, Lombès A, et al. Ageing muscle: clonal expansions of mitochondrial DNA point mutations and deletions cause focal impairment of mitochondrial function. Neuromuscular Disorders. 2002;12(5):484-93.
184. Müller-Höcker J. Cytochrome-c-oxidase deficient cardiomyocytes in the human heart--an age-related phenomenon. A histochemical ultracytochemical study. The American journal of pathology. 1989;134(5):1167.
185. Hansen AB, Griner NB, Anderson JP, Kujoth GC, Prolla TA, Loeb LA, et al. Mitochondrial DNA integrity is not dependent on DNA polymerase-β activity. DNA repair. 2006;5(1):71-9.
186. Loeb LA, Wallace DC, Martin GM. The mitochondrial theory of aging and its relationship to reactive oxygen species damage and somatic mtDNA mutations. Proceedings of the National Academy of Sciences of the United States of America. 2005;102(52):18769-70.
187. Harman D. Aging: a theory based on free radical and radiation chemistry. 1955.

188. Wanrooij S, Fusté JM, Stewart JB, Wanrooij PH, Samuelsson T, Larsson NG, et al. In vivo mutagenesis reveals that OriL is essential for mitochondrial DNA replication. EMBO reports. 2012;13(12):1130-7.
189. Kukat C, Larsson N-G. mtDNA makes a U-turn for the mitochondrial nucleoid. Trends in cell biology. 2013;23(9):457-63.
190. Hansford RG, Hogue BA, Mildaziene V. Dependence of H 2 O 2 formation by rat heart mitochondria on substrate availability and donor age. Journal of bioenergetics and biomembranes. 1997;29(1):89-95.
191. Kauppila TES, Kauppila JHK, Larsson N-G. Mammalian Mitochondria and Aging: An Update. Cell Metabolism. 2016.
192. Fukui H, Moraes CT. Mechanisms of formation and accumulation of mitochondrial DNA deletions in aging neurons. Human molecular genetics. 2009;18(6):1028-36.
193. Gandhi SS, Muraresku C, McCormick EM, Falk MJ, McCormack SE. Risk factors for poor bone health in primary mitochondrial disease. Journal of inherited metabolic disease. 2017;40(5):673-83.
194. Miyazaki T, Iwasawa M, Nakashima T, Mori S, Shigemoto K, Nakamura H, et al. Intracellular and extracellular ATP coordinately regulate the inverse correlation between osteoclast survival and bone resorption. Journal of Biological Chemistry. 2012:jbc. M112. 385369.
195. Varanasi SS, Francis RM, Berger CE, Papiha SS, Datta HK. Mitochondrial DNA deletion associated oxidative stress and severe male osteoporosis. Osteoporos Int. 1999;10(2):143-9.
196. Guo Y, Yang TL, Liu YZ, Shen H, Lei SF, Yu N, et al. Mitochondria-wide association study of common variants in osteoporosis. Annals of human genetics. 2011;75(5):569-74.
197. Guo Y, Yang TL, Liu YZ, Shen H, Lei SF, Yu N, et al. Mitochondria-wide association study of common variants in osteoporosis. Ann Hum Genet. 2011;75(5):569-74.
198. Choi EM, Suh KS, Lee YS. Liquiritigenin restores osteoblast damage through regulating oxidative stress and mitochondrial dysfunction. Phytotherapy research. 2014;28(6):880-6.
199. HO WP, CHEN TL, CHIU WT, TAI YT, CHEN RM. Nitric oxide induces osteoblast apoptosis through a mitochondria-dependent pathway. Annals of the New York Academy of Sciences. 2005;1042(1):460-70.
200. Yang Y-H, Li B, Zheng X-F, Chen J-W, Chen K, Jiang S-D, et al. Oxidative damage to osteoblasts can be alleviated by early autophagy through the endoplasmic reticulum stress pathway—implications for the treatment of osteoporosis. Free Radical Biology and Medicine. 2014;77:10-20.
201. Bartell SM, Kim H-N, Ambrogini E, Han L, Iyer S, Ucer SS, et al. FoxO proteins restrain osteoclastogenesis and bone resorption by attenuating H 2 O 2 accumulation. Nature communications. 2014;5:3773.
202. Kha HT, Basseri B, Shouhed D, Richardson J, Tetradis S, Hahn TJ, et al. Oxysterols regulate differentiation of mesenchymal stem cells: Pro-bone and anti-fat. Journal of Bone and Mineral Research. 2004;19(5):830-40.
203. Liu H, Yuan L, Xu S, Wang K, Zhang T. Cholestane-3β,5α,6β-triol inhibits osteoblastic differentiation and promotes apoptosis of rat bone marrow stromal cells. Journal of Cellular Biochemistry. 2005;96(1):198-208.
204. Baines HL, Turnbull DM, Greaves LC. Human stem cell aging: do mitochondrial DNA mutations have a causal role? Aging cell. 2014;13(2):201-5.
205. Dobson PF, Rocha MC, Grady JP, Chrysostomou A, Hipps D, Watson S, et al. Unique quadruple immunofluorescence assay demonstrates mitochondrial respiratory chain dysfunction in osteoblasts of aged and PolgA−/− mice. Scientific reports. 2016;6(1):1-10.
206. Dobson PF, Dennis EP, Hipps D, Reeve A, Laude A, Bradshaw C, et al. Mitochondrial dysfunction impairs osteogenesis, increases osteoclast activity, and accelerates age related bone loss. Scientific reports. 2020;10(1):1-14.
207. Bonewald LF. The amazing osteocyte. Journal of Bone and Mineral Research. 2011;26(2):229-38.

208. Dunstan CR, Somers NM, Evans RA. Osteocyte death and hip fracture. Calcified tissue international. 1993;53:S113-S7.
209. Busse B, Djonic D, Milovanovic P, Hahn M, Püschel K, Ritchie RO, et al. Decrease in the osteocyte lacunar density accompanied by hypermineralized lacunar occlusion reveals failure and delay of remodeling in aged human bone. Aging cell. 2010;9(6):1065-75.
210. Almeida M, Han L, Martin-Millan M, Plotkin LI, Stewart SA, Roberson PK, et al. Skeletal involution by age-associated oxidative stress and its acceleration by loss of sex steroids. Journal of Biological Chemistry. 2007;282(37):27285-97.
211. Almeida M, Ambrogini E, Han L, Manolagas SC, Jilka RL. Increased lipid oxidation causes oxidative stress, increased peroxisome proliferator-activated receptor-γ expression, and diminished pro-osteogenic Wnt signaling in the skeleton. Journal of Biological Chemistry. 2009;284(40):27438-48.
212. Nojiri H, Saita Y, Morikawa D, Kobayashi K, Tsuda C, Miyazaki T, et al. Cytoplasmic superoxide causes bone fragility owing to low-turnover osteoporosis and impaired collagen cross-linking. Journal of Bone and Mineral Research. 2011;26(11):2682-94.
213. Almeida M, O'Brien CA. Basic biology of skeletal aging: role of stress response pathways. The Journals of Gerontology Series A: Biological Sciences and Medical Sciences. 2013:glt079.
214. Larsson N-G, Wang J, Wilhelmsson H, Oldfors A, Rustin P, Lewandoski M, et al. Mitochondrial transcription factor A is necessary for mtDNA maintenance and embryogenesis in mice. Nature genetics. 1998;18(3):231-6.
215. Pikó L, Chase DG. Role of the mitochondrial genome during early development in mice: effects of ethidium bromide and chloramphenicol. The Journal of cell biology. 1973;58(2):357.
216. Pikó L, Matsumoto L. Number of mitochondria and some properties of mitochondrial DNA in the mouse egg. Developmental biology. 1976;49(1):1-10.
217. Miyazaki T, Iwasawa M, Nakashima T, Mori S, Shigemoto K, Nakamura H, et al. Intracellular and extracellular ATP coordinately regulate the inverse correlation between osteoclast survival and bone resorption. Journal of Biological Chemistry. 2012;287(45):37808-23.
218. Kang S, Fernandes-Alnemri T, Alnemri ES. A novel role for the mitochondrial HTRA2/OMI protease in aging. Autophagy. 2013;9(3):420-1.
219. Miltenyi Biotec. MSC Phenotyping Kit human. http://www.miltenyibiotec.com/en/products-and-services/macs-flow-cytometry/reagents/kits-and-assays/msc-phenotyping-kit-human.aspx2011.
220. Anderson RE, Bankier A, Barrell B. Get al. Nature. 1981;290:457-65.
221. Andrews RM, Kubacka I, Chinnery PF, Lightowlers RN, Turnbull DM, Howell N. Reanalysis and revision of the Cambridge reference sequence for human mitochondrial DNA. Nature genetics. 1999;23(2):147.
222. Tuppen HA, Hogan VE, He L, Blakely EL, Worgan L, Al-Dosary M, et al. The p. M292T NDUFS2 mutation causes complex I-deficient Leigh syndrome in multiple families. Brain. 2010;133(10):2952-63.
223. Promega. GoTaq® Long PCR Master Mix Instructions for Use of Product M4021,. 2017.
224. Thermo Fisher Scientific. Prepare Amplicon Libraries Requiring Fragmentation Using the Ion Xpress™ Plus Fragment Library Kit,. 2016.
225. Invitrogen. Qubit® dsDNA HS Assay Kits,. 2015.
226. Givan AL. Flow Cytometry: An Introduction. In: Hawley TS, Hawley RG, editors. Flow Cytometry Protocols. Totowa, NJ: Humana Press; 2011. p. 1-29.
227. Bio-Rad. How Does a Flow Cytometer Work? 2020 [Available from: https://www.bio-rad.com/featured/en/flow-cytometer.html.
228. Moldavan A. Photo-electric technique for the counting of microscopical cells. Science. 1934;80(2069):188-9.
229. Graham JK, Kunze E, Hammerstedt RH. Analysis of sperm cell viability, acrosomal integrity, and mitochondrial function using flow cytometry. Biology of reproduction. 1990;43(1):55-64.

230. Ronot X, Benel L, Adolphe M, Mounolou JC. Mitochondrial analysis in living cells: the use of rhodamine 123 and flow cytometry. Biology of the Cell. 1986;57(1):1-7.
231. Skowronek P, Krummeck G, Haferkamp O, Rödel G. Flow cytometry as a tool to discriminate respiratory-competent and respiratory-deficient yeast cells. Current genetics. 1990;18(3):265-7.
232. Mukhopadhyay P, Rajesh M, Haskó G, Hawkins BJ, Madesh M, Pacher P. Simultaneous detection of apoptosis and mitochondrial superoxide production in live cells by flow cytometry and confocal microscopy. Nature protocols. 2007;2(9):2295.
233. Pham NA, Robinson BH, Hedley DW. Simultaneous detection of mitochondrial respiratory chain activity and reactive oxygen in digitonin-permeabilized cells using flow cytometry. Cytometry Part A. 2000;41(4):245-51.
234. Ricci J-E, Muñoz-Pinedo C, Fitzgerald P, Bailly-Maitre B, Perkins GA, Yadava N, et al. Disruption of mitochondrial function during apoptosis is mediated by caspase cleavage of the p75 subunit of complex I of the electron transport chain. Cell. 2004;117(6):773-86.
235. Rocha MC, Grady JP, Grünewald A, Vincent A, Dobson PF, Taylor RW, et al. A novel immunofluorescent assay to investigate oxidative phosphorylation deficiency in mitochondrial myopathy: understanding mechanisms and improving diagnosis. Scientific reports. 2015;5:15037.
236. Filby A, Perucha E, Summers H, Rees P, Chana P, Heck S, et al. An imaging flow cytometric method for measuring cell division history and molecular symmetry during mitosis. Cytometry Part A. 2011;79(7):496-506.
237. Bandura DR, Baranov VI, Ornatsky OI, Antonov A, Kinach R, Lou X, et al. Mass cytometry: technique for real time single cell multitarget immunoassay based on inductively coupled plasma time-of-flight mass spectrometry. Analytical chemistry. 2009;81(16):6813-22.
238. Di Palma S, Bodenmiller B. Unraveling cell populations in tumors by single-cell mass cytometry. Current opinion in biotechnology. 2015;31:122-9.
239. Atkuri KR, Stevens JC, Neubert H. Mass cytometry: a highly multiplexed single-cell technology for advancing drug development. Drug Metabolism and Disposition. 2015;43(2):227-33.
240. Chang Q, Ornatsky OI, Siddiqui I, Loboda A, Baranov VI, Hedley DW. Imaging mass cytometry. Cytometry part A. 2017.
241. Fluidigm. Imaging Mass Cytometry Staining Protocol for FFPE Sections,. 2018.
242. Helfrich MH. Bone research protocols: Springer Science & Business Media; 2003.
243. Taylor SEB, Shah M, Orriss IR. Generation of rodent and human osteoblasts. BoneKEy reports. 2014;3.
244. Harry I. Nutrition Needs of Mammali Cells in Tissue Cultu. 1955.
245. Jaiswal N, Haynesworth SE, Caplan AI, Bruder SP. Osteogenic differentiation of purified, culture-expanded human mesenchymal stem cells in vitro. Journal of cellular biochemistry. 1997;64(2):295-312.
246. Orriss IR, Hajjawi MOR, Huesa C, MacRae VE, Arnett TR. Optimisation of the differing conditions required for bone formation in vitro by primary osteoblasts from mice and rats. International journal of molecular medicine. 2014;34(5):1201-8.
247. Kartsogiannis V, Ng KW. Cell lines and primary cell cultures in the study of bone cell biology. Molecular and cellular endocrinology. 2004;228(1):79-102.
248. Conget PA, Minguell JJ. Phenotypical and functional properties of human bone marrow mesenchymal progenitor cells. Journal of cellular physiology. 1999;181(1):67-73.
249. Bellows CG, Aubin JE, Heersche JNM, Antosz ME. Mineralized bone nodules formedin vitro from enzymatically released rat calvaria cell populations. Calcified tissue international. 1986;38(3):143-54.
250. Chen TL, Cone CM, Feldman D. Glucocorticoid modulation of cell proliferation in cultured osteoblast-like bone cells: differences between rat and mouse. Endocrinology. 1983;112(5):1739-45.
251. Schwarz RI. Procollagen secretion meets the minimum requirements for the rate-controlling step in the ascorbate induction of procollagen synthesis. Journal of Biological Chemistry. 1985;260(5):3045-9.

252. Aronow MA, Gerstenfeld LC, Owen TA, Tassinari MS, Stein GS, Lian JB. Factors that promote progressive development of the osteoblast phenotype in cultured fetal rat calvaria cells. Journal of cellular physiology. 1990;143(2):213-21.
253. Graves SE, Francis MJO, Gundle R, Beresford JN. P69. Primary culture of human trabecular bone: effects of L-ascorbate-2-phosphate. Bone. 1994;15(1):132-3.
254. Elson J, Samuels D, Turnbull D, Chinnery P. Random intracellular drift explains the clonal expansion of mitochondrial DNA mutations with age. The American Journal of Human Genetics. 2001;68(3):802-6.
255. Brierley EJ, Johnson MA, Lightowlers RN, James OF, Turnbull DM. Role of mitochondrial DNA mutations in human aging: implications for the central nervous system and muscle. Annals of Neurology: Official Journal of the American Neurological Association and the Child Neurology Society. 1998;43(2):217-23.
256. Schon EA, Bonilla E, DiMauro S. Mitochondrial DNA mutations and pathogenesis. Journal of bioenergetics and biomembranes. 1997;29(2):131-49.
257. Hayashi J, Ohta S, Kikuchi A, Takemitsu M, Goto Y-i, Nonaka I. Introduction of disease-related mitochondrial DNA deletions into HeLa cells lacking mitochondrial DNA results in mitochondrial dysfunction. Proceedings of the National Academy of Sciences. 1991;88(23):10614-8.
258. Sacconi S, Salviati L, Nishigaki Y, Walker WF, Hernandez-Rosa E, Trevisson E, et al. A functionally dominant mitochondrial DNA mutation. Human molecular genetics. 2008;17(12):1814-20.
259. Cortopassi GA, Arnheim N. Detection of a specific mitochondrial DNA deletion in tissues of older humans. Nucleic acids research. 1990;18(23):6927-33.
260. Corral-Debrinski M, Horton T, Lott MT, Shoffner JM, Beal MF, Wallace DC. Mitochondrial DNA deletions in human brain: regional variability and increase with advanced age. Nature genetics. 1992;2(4):324.
261. Corral-Debrinski M, Shoffner J, Lott M, Wallace D. Association of mitochondrial DNA damage with aging and coronary atherosclerotic heart disease. Mutation Research/DNAging. 1992;275(3-6):169-80.
262. Shadel GS, Clayton DA. Mitochondrial DNA maintenance in vertebrates. Annual review of biochemistry. 1997;66(1):409-35.
263. Wallace DC. Mitochondrial genetics: a paradigm for aging and degenerative diseases? Science. 1992;256(5057):628-32.
264. Wallace DC. Mitochondrial diseases in man and mouse. Science. 1999;283(5407):1482-8.
265. Coller HA, Khrapko K, Bodyak ND, Nekhaeva E, Herrero-Jimenez P, Thilly WG. High frequency of homoplasmic mitochondrial DNA mutations in human tumors can be explained without selection. Nature genetics. 2001;28(2):147-50.
266. Coller HA, Khrapko K, Bodyak ND, Nekhaeva E, Herrero-Jimenez P, Thilly WG. High frequency of homoplasmic mitochondrial DNA mutations in human tumors can be explained without selection. Nature genetics. 2001;28(2):147.
267. Nicholas A, Kraytsberg Y, Guo X, Khrapko K. On the timing and the extent of clonal expansion of mtDNA deletions: evidence from single-molecule PCR. Experimental neurology. 2009;218(2):316-9.
268. Pak JW, Herbst A, Bua E, Gokey N, McKenzie D, Aiken JM. Mitochondrial DNA mutations as a fundamental mechanism in physiological declines associated with aging. Aging cell. 2003;2(1):1-7.
269. Michikawa Y, Mazzucchelli F, Bresolin N, Scarlato G, Attardi G. Aging-dependent large accumulation of point mutations in the human mtDNA control region for replication. Science. 1999;286(5440):774-9.
270. Greaves LC, Nooteboom M, Elson JL, Tuppen HA, Taylor GA, Commane DM, et al. Clonal expansion of early to mid-life mitochondrial DNA point mutations drives mitochondrial dysfunction during human ageing. PLoS genetics. 2014;10(9):e1004620.

271. Smith AL, Whitehall JC, Bradshaw C, Gay D, Robertson F, Blain AP, et al. Age-associated mitochondrial DNA mutations cause metabolic remodeling that contributes to accelerated intestinal tumorigenesis. Nature Cancer. 2020;1(10):976-89.
272. Dominici M, Le Blanc K, Mueller I, Slaper-Cortenbach I, Marini F, Krause D, et al. Minimal criteria for defining multipotent mesenchymal stromal cells. The International Society for Cellular Therapy position statement. Cytotherapy. 2006;8(4):315-7.
273. Wexler SA, Donaldson C, Denning-Kendall P, Rice C, Bradley B, Hows JM. Adult bone marrow is a rich source of human mesenchymal 'stem'cells but umbilical cord and mobilized adult blood are not. British journal of haematology. 2003;121(2):368-74.
274. Ganguly P, El-Jawhari JJ, Giannoudis PV, Burska AN, Ponchel F, Jones EA. Age-related changes in bone marrow mesenchymal stromal cells: a potential impact on osteoporosis and osteoarthritis development. Cell transplantation. 2017;26(9):1520-9.
275. Promega. GoTaq® Long PCR Master Mix, 2019 [Available from: https://www.promega.co.uk/products/pcr/endpoint-pcr/gotaq-long-pcr-master-mix/?catNum=M4021.
276. Agilent Technologies. Agilent DNA 7500 and DNA 12000 Kit Quick Start Guide,. 2018.
277. Agilent Technologies. Agilent High Sensitivity DNA Kit Quick Start Guide,. 2018.
278. Weissensteiner H, Forer L, Fuchsberger C, Schöpf B, Kloss-Brandstätter A, Specht G, et al. mtDNA-Server: next-generation sequencing data analysis of human mitochondrial DNA in the cloud. Nucleic acids research. 2016;44(W1):W64-W9.
279. Quail MA, Smith M, Coupland P, Otto TD, Harris SR, Connor TR, et al. A tale of three next generation sequencing platforms: comparison of Ion Torrent, Pacific Biosciences and Illumina MiSeq sequencers. BMC genomics. 2012;13(1):341.
280. Lott MT, Leipzig JN, Derbeneva O, Xie HM, Chalkia D, Sarmady M, et al. mtDNA Variation and Analysis Using Mitomap and Mitomaster. Current protocols in bioinformatics. 2013;44:1.23.1-6.
281. Castellana S, Rónai J, Mazza T. MitImpact: An exhaustive collection of pre-computed pathogenicity predictions of human mitochondrial non-synonymous variants. Human mutation. 2015;36(2):E2413-E22.
282. Greaves LC, Preston SL, Tadrous PJ, Taylor RW, Barron MJ, Oukrif D, et al. Mitochondrial DNA mutations are established in human colonic stem cells, and mutated clones expand by crypt fission. Proceedings of the National Academy of Sciences. 2006;103(3):714-9.
283. Sim N-L, Kumar P, Hu J, Henikoff S, Schneider G, Ng PC. SIFT web server: predicting effects of amino acid substitutions on proteins. Nucleic acids research. 2012;40(W1):W452-W7.
284. Chan CKF, Gulati GS, Sinha R, Tompkins JV, Lopez M, Carter AC, et al. Identification of the Human Skeletal Stem Cell. Cell. 2018;175(1):43-56.e21.
285. Park J, Lee Y, Shin J, Lee H-J, Son Y-B, Park B-W, et al. Mitochondrial genome mutations in mesenchymal stem cells derived from human dental induced pluripotent stem cells. BMB reports. 2019;52(12):689.
286. Swalwell H, Kirby DM, Blakely EL, Mitchell A, Salemi R, Sugiana C, et al. Respiratory chain complex I deficiency caused by mitochondrial DNA mutations. European Journal of Human Genetics. 2011;19(7):769-75.
287. Alston CL, Rocha MC, Lax NZ, Turnbull DM, Taylor RW. The genetics and pathology of mitochondrial disease. The Journal of pathology. 2017;241(2):236-50.
288. Craven L, Alston CL, Taylor RW, Turnbull DM. Recent advances in mitochondrial disease. Annual review of genomics and human genetics. 2017;18:257-75.
289. Haas RH. Mitochondrial dysfunction in aging and diseases of aging. Multidisciplinary Digital Publishing Institute; 2019.
290. Cortopassi G, Wang E. Modelling the effects of age-related mtDNA mutation accumulation; complex I deficiency, superoxide and cell death. Biochimica et Biophysica Acta (BBA)-Molecular Basis of Disease. 1995;1271(1):171-6.

291. Katayama M, Tanaka M, Yamamoto H, Ohbayashi T, Nimura Y, Ozawa T. Deleted mitochondrial DNA in the skeletal muscle of aged individuals. Biochemistry international. 1991;25(1):47-56.
292. Sherry ST, Ward M-H, Kholodov M, Baker J, Phan L, Smigielski EM, et al. dbSNP: the NCBI database of genetic variation. Nucleic acids research. 2001;29(1):308-11.
293. Adzhubei IA, Schmidt S, Peshkin L, Ramensky VE, Gerasimova A, Bork P, et al. A method and server for predicting damaging missense mutations. Nature methods. 2010;7(4):248-9.
294. Tate JG, Bamford S, Jubb HC, Sondka Z, Beare DM, Bindal N, et al. COSMIC: the catalogue of somatic mutations in cancer. Nucleic acids research. 2019;47(D1):D941-D7.
295. Gasparetto M, Gentry T, Sebti S, O'Bryan E, Nimmanapalli R, Blaskovich MA, et al. Identification of compounds that enhance the anti-lymphoma activity of rituximab using flow cytometric high-content screening. Journal of immunological methods. 2004;292(1-2):59-71.
296. Wang Y, Yoshihara T, King S, Le T, Leroy P, Zhao X, et al. Automated High-Throughput Flow Cytometry for High-Content Screening in Antibody Development. SLAS DISCOVERY: Advancing Life Sciences R&D. 2018;23(7):656-66.
297. Peluso J, Tabaka-Moreira H, Taquet N, Dumont S, Muller CD, Reimund JM. Can flow cytometry play a part in cell based high-content screening? Cytometry Part A: The Journal of the International Society for Analytical Cytology. 2007;71(11):901-4.
298. Edwards BS, Kuckuck FW, Prossnitz ER, Ransom JT, Sklar LA. HTPS flow cytometry: a novel platform for automated high throughput drug discovery and characterization. Journal of biomolecular screening. 2001;6(2):83-90.
299. Edwards BS, Young SM, Saunders MJ, Bologa C, Oprea TI, Ye RD, et al. High-throughput flow cytometry for drug discovery. Expert opinion on drug discovery. 2007;2(5):685-96.
300. Black CB, Duensing TD, Trinkle LS, Dunlay RT. Cell-based screening using high-throughput flow cytometry. Assay and drug development technologies. 2011;9(1):13-20.
301. Old SL, Johnson MA. Methods of microphotometric assay of succinate dehydrogenase and cytochromec oxidase activities for use on human skeletal muscle. The Histochemical journal. 1989;21(9-10):545-55.
302. Macarron R, Banks MN, Bojanic D, Burns DJ, Cirovic DA, Garyantes T, et al. Impact of high-throughput screening in biomedical research. Nature reviews Drug discovery. 2011;10(3):188.
303. Edwards BS, Oprea T, Prossnitz ER, Sklar LA. Flow cytometry for high-throughput, high-content screening. Current opinion in chemical biology. 2004;8(4):392-8.
304. Abraham VC, Taylor DL, Haskins JR. High content screening applied to large-scale cell biology. Trends in biotechnology. 2004;22(1):15-22.
305. Huang S-G. Development of a high throughput screening assay for mitochondrial membrane potential in living cells. Journal of biomolecular screening. 2002;7(4):383-9.
306. Maitra A, Cohen Y, Gillespie SE, Mambo E, Fukushima N, Hoque MO, et al. The Human MitoChip: a high-throughput sequencing microarray for mitochondrial mutation detection. Genome research. 2004;14(5):812-9.
307. Leonard J, Schapira AH. Mitochondrial respiratory chain disorders I: mitochondrial DNA defects. The Lancet. 2000;355(9200):299-304.
308. Bourgeron T, Rustin P, Chretien D, Birch-Machin M, Bourgeois M, Viegas-Péquignot E, et al. Mutation of a nuclear succinate dehydrogenase gene results in mitochondrial respiratory chain deficiency. Nature genetics. 1995;11(2):144.
309. Parfait B, Chretien D, Rötig A, Marsac C, Munnich A, Rustin P. Compound heterozygous mutations in the flavoprotein gene of the respiratory chain complex II in a patient with Leigh syndrome. Human genetics. 2000;106(2):236-43.
310. Ma Y-Y, Wu T-F, Liu Y-P, Wang Q, Song J-Q, Xiao J-X, et al. Leigh syndrome due to mitochondrial respiratory chain complex II deficiency. Zhongguo Dang dai er ke za zhi= Chinese Journal of Contemporary Pediatrics. 2011;13(7):569-72.

311. Visapää I, Fellman V, Vesa J, Dasvarma A, Hutton JL, Kumar V, et al. GRACILE syndrome, a lethal metabolic disorder with iron overload, is caused by a point mutation in BCS1L. The American Journal of Human Genetics. 2002;71(4):863-76.
312. Zeviani M, editor The expanding spectrum of nuclear gene mutations in mitochondrial disorders. Seminars in cell & developmental biology; 2001: Elsevier.
313. Keightley JA, Anitori R, Burton MD, Quan F, Buist NR, Kennaway NG. Mitochondrial encephalomyopathy and complex III deficiency associated with a stop-codon mutation in the cytochrome b gene. The American Journal of Human Genetics. 2000;67(6):1400-10.
314. Blakely EL, Mitchell AL, Fisher N, Meunier B, Nijtmans LG, Schaefer AM, et al. A mitochondrial cytochrome b mutation causing severe respiratory chain enzyme deficiency in humans and yeast. The FEBS journal. 2005;272(14):3583-92.
315. Keightley JA, Hoffbuhr KC, Burton MD, Salas VM, Johnston WS, Penn AM, et al. A microdeletion in cytochrome c oxidase (COX) subunit III associated with COX deficiency and recurrent myoglobinuria. Nature genetics. 1996;12(4):410-6.
316. Hanna M, Nelson I, Rahman S, Lane R, Land J, Heales S, et al. Cytochrome c oxidase deficiency associated with the first stop-codon point mutation in human mtDNA. The American Journal of Human Genetics. 1998;63(1):29-36.
317. Bruno C, Martinuzzi A, Tang Y, Andreu AL, Pallotti F, Bonilla E, et al. A stop-codon mutation in the human mtDNA cytochrome c oxidase I gene disrupts the functional structure of complex IV. The American Journal of Human Genetics. 1999;65(3):611-20.
318. Jaksch M, Hofmann S, Kleinle S, Liechti-Gallati S, Pongratz DE, Müller-Höcker J, et al. A systematic mutation screen of 10 nuclear and 25 mitochondrial candidate genes in 21 patients with cytochrome c oxidase (COX) deficiency shows tRNA (Ser)(UCN) mutations in a subgroup with syndromal encephalopathy. Journal of medical genetics. 1998;35(11):895-900.
319. Ware SM, El-Hassan N, Kahler S, Zhang Q, Miller E, Wong B, et al. Infantile cardiomyopathy caused by a mutation in the overlapping region of mitochondrial ATPase 6 and 8 genes. Journal of medical genetics. 2009;46(5):308-14.
320. Greaves LC, Barron MJ, Plusa S, Kirkwood TB, Mathers JC, Taylor RW, et al. Defects in multiple complexes of the respiratory chain are present in ageing human colonic crypts. Experimental gerontology. 2010;45(7-8):573-9.
321. Müller-Höcker J. Cytochrome c oxidase deficient fibres in the limb muscle and diaphragm of man without muscular disease: an age-related alteration. Journal of the neurological sciences. 1990;100(1-2):14-21.
322. Cottrell D, Blakely E, Johnson M, Ince P, Borthwick G, Turnbull D. Cytochrome c oxidase deficient cells accumulate in the hippocampus and choroid plexus with age. Neurobiology of aging. 2001;22(2):265-72.
323. Cottrell D, Ince P, Wardell T, Turnbull D, Johnson M. Accelerated ageing changes in the choroid plexus of a case with multiple mitochondrial DNA deletions. Neuropathology and applied neurobiology. 2001;27(3):206-14.
324. Fellous TG, Islam S, Tadrous PJ, Elia G, Kocher HM, Bhattacharya S, et al. Locating the stem cell niche and tracing hepatocyte lineages in human liver. Hepatology. 2009;49(5):1655-63.
325. Tuppen HAL, Hogan VE, He L, Blakely EL, Worgan L, Al-Dosary M, et al. The p. M292T NDUFS2 mutation causes complex I-deficient Leigh syndrome in multiple families. Brain. 2010;133(10):2952-63.
326. Klein E, Ben-Bassat H, Neumann H, Ralph P, Zeuthen J, Polliack A, et al. Properties of the K562 cell line, derived from a patient with chronic myeloid leukemia. Int J Cancer. 1976;18(4):421-31.
327. Abe Y, Shodai T, Muto T, Mihara K, Torii H, Nishikawa S-i, et al. Structural basis of presequence recognition by the mitochondrial protein import receptor Tom20. Cell. 2000;100(5):551-60.

328. Shoshan-Barmatz V, Zalk R, Gincel D, Vardi N. Subcellular localization of VDAC in mitochondria and ER in the cerebellum. Biochimica et Biophysica Acta (BBA)-Bioenergetics. 2004;1657(2-3):105-14.
329. Camara AK, Zhou Y, Wen P-C, Tajkhorshid E, Kwok W-M. Mitochondrial VDAC1: a key gatekeeper as potential therapeutic target. Frontiers in physiology. 2017;8:460.
330. Kang D, Kim SH, Hamasaki N. Mitochondrial transcription factor A (TFAM): roles in maintenance of mtDNA and cellular functions. Mitochondrion. 2007;7(1-2):39-44.
331. Takamatsu C, Umeda S, Ohsato T, Ohno T, Abe Y, Fukuoh A, et al. Regulation of mitochondrial D-loops by transcription factor A and single-stranded DNA-binding protein. EMBO reports. 2002;3(5):451-6.
332. Emahazion T, Brookes A. Mapping of the NDUFA2, NDUFA6, NDUFA7, NDUFB8, and NDUFS8, electron transport chain genes by intron based radiation hybrid mapping. Cytogenetic and Genome Research. 1998;82(1):114.
333. Abcam. ab102859 APC/Cy7®Conjugation Kit Protocol,. 2019.
334. Abcam. Immunocytochemistry and immuoflurorescence protocol. www.abcam.com,: Abcam.
335. Kun E, Kirsten E, Piper WN. [14] Stabilization of mitochondrial functions with digitonin. Methods in enzymology. 55: Elsevier; 1979. p. 115-8.
336. Scorrano L, Ashiya M, Buttle K, Weiler S, Oakes SA, Mannella CA, et al. A distinct pathway remodels mitochondrial cristae and mobilizes cytochrome c during apoptosis. Developmental cell. 2002;2(1):55-67.
337. Zorkau M, Proctor-Kent Y, Berlinguer-Palmini R, Hamilton A, Chrzanowska-Lightowlers ZM, Lightowlers RN. Visualizing Mitochondrial Ribosomal RNA and Mitochondrial Protein Synthesis in Human Cell Lines. Mitochondrial Gene Expression: Springer; 2021. p. 159-81.
338. Amidzadeh Z, Behbahani AB, Erfani N, Sharifzadeh S, Ranjbaran R, Moezi L, et al. Assessment of different permeabilization methods of minimizing damage to the adherent cells for detection of intracellular RNA by flow cytometry. Avicenna journal of medical biotechnology. 2014;6(1):38.
339. Grünewald A, Lax NZ, Rocha MC, Reeve AK, Hepplewhite PD, Rygiel KA, et al. Quantitative quadruple-label immunofluorescence of mitochondrial and cytoplasmic proteins in single neurons from human midbrain tissue. Journal of neuroscience methods. 2014;232:143-9.
340. Hanson BJ, Capaldi RA, Marusich MF, Sherwood SW. An immunocytochemical approach to detection of mitochondrial disorders. Journal of Histochemistry & Cytochemistry. 2002;50(10):1281-8.
341. Murphy JL, Ratnaike TE, Shang E, Falkous G, Blakely EL, Alston CL, et al. Cytochrome c oxidase-intermediate fibres: importance in understanding the pathogenesis and treatment of mitochondrial myopathy. Neuromuscular Disorders. 2012;22(8):690-8.
342. Russell OM, Fruh I, Rai PK, Marcellin D, Doll T, Reeve A, et al. Preferential amplification of a human mitochondrial DNA deletion in vitro and in vivo. Scientific reports. 2018;8(1):1799.
343. Schmid I, Uittenbogaart CH, Giorgi JV. A gentle fixation and permeabilization method for combined cell surface and intracellular staining with improved precision in DNA quantification. Cytometry: The Journal of the International Society for Analytical Cytology. 1991;12(3):279-85.
344. Oliver C, Jamur MC. Immunocytochemical methods and protocols: Springer; 2010.
345. Abcam. Detect low-abundance proteins with biotinylated antibodies,. 2019.
346. . !!! INVALID CITATION !!! .
347. Zhou S, Greenberger JS, Epperly MW, Goff JP, Adler C, LeBoff MS, et al. Age-related intrinsic changes in human bone-marrow-derived mesenchymal stem cells and their differentiation to osteoblasts. Aging cell. 2008;7(3):335-43.
348. Heng BC, Ye CP, Liu H, Toh WS, Rufaihah AJ, Yang Z, et al. Loss of viability during freeze–thaw of intact and adherent human embryonic stem cells with conventional slow-cooling protocols is predominantly due to␣ apoptosis rather than cellular necrosis. Journal of biomedical science. 2006;13(3):433-45.

349. Pollock K, Sumstad D, Kadidlo D, McKenna DH, Hubel A. Clinical mesenchymal stromal cell products undergo functional changes in response to freezing. Cytotherapy. 2015;17(1):38-45.
350. Chatzistamatiou TK, Papassavas AC, Michalopoulos E, Gamaloutsos C, Mallis P, Gontika I, et al. Optimizing isolation culture and freezing methods to preserve W harton's jelly's mesenchymal stem cell (MSC) properties: an MSC banking protocol validation for the H ellenic C ord B lood B ank. Transfusion. 2014;54(12):3108-20.
351. Lopez P, Bergeron A, Box A, Brundage K, Chittur S, Cochran M, et al. Evaluating Effects of Cell Sorting on Cellular Integrity. Journal of Biomolecular Techniques: JBT. 2014;25(Suppl):S1.
352. Kissner M. Increase Cell Viability With These 3 Flow Cytometry Experimental Research Design Tips 2015 [Available from: https://expertcytometry.com/increase-cell-viability-3-flow-cytometry-experimental-research-design-tips/.
353. Basu S, Campbell HM, Dittel BN, Ray A. Purification of specific cell population by fluorescence activated cell sorting (FACS). JoVE (Journal of Visualized Experiments). 2010(41):e1546.
354. Munn S. Flow cytometry separation of X and Y spermatozoa could be detrimental for human embryos. Mutat Res. 1994;228:125-31.
355. Gross A, Schoendube J, Zimmermann S, Steeb M, Zengerle R, Koltay P. Technologies for single-cell isolation. International journal of molecular sciences. 2015;16(8):16897-919.
356. Bellantuono I, Aldahmash A, Kassem M. Aging of marrow stromal (skeletal) stem cells and their contribution to age-related bone loss. Biochimica et Biophysica Acta (BBA)-Molecular Basis of Disease. 2009;1792(4):364-70.
357. Baker N, Boyette LB, Tuan RS. Characterization of bone marrow-derived mesenchymal stem cells in aging. Bone. 2015;70:37-47.
358. Rygiel KA, Grady JP, Turnbull DM. Respiratory chain deficiency in aged spinal motor neurons. Neurobiology of aging. 2014;35(10):2230-8.
359. Coutu DL, Kokkaliaris KD, Kunz L, Schroeder T. Multicolor quantitative confocal imaging cytometry. Nature methods. 2018;15(1):39.
360. Prentice A. Bone autofluorescence and mineral content. Nature. 1965;206(4989):1167.
361. Yova D, Hovhannisyan V, Theodossiou T. Photochemical effects and hypericin photosensitized processes in collagen. Journal of biomedical optics. 2001;6(1):52-7.
362. Prentice A. Autofluorescence of bone tissues. Journal of clinical pathology. 1967;20(5):717-9.
363. Troyan MB, Gilman VR, Gay CV. Mitochondrial membrane potential changes in osteoblasts treated with parathyroid hormone and estradiol. Experimental cell research. 1997;233(2):274-80.
364. Chattopadhyay PK, Roederer M. Cytometry: today's technology and tomorrow's horizons. Methods. 2012;57(3):251-8.
365. Bendall SC, Nolan GP, Roederer M, Chattopadhyay PK. A deep profiler's guide to cytometry. Trends in immunology. 2012;33(7):323-32.
366. Simoni Y, Chng MHY, Li S, Fehlings M, Newell EW. Mass cytometry: a powerful tool for dissecting the immune landscape. Current opinion in immunology. 2018;51:187-96.
367. Newell EW, Sigal N, Bendall SC, Nolan GP, Davis MM. Cytometry by time-of-flight shows combinatorial cytokine expression and virus-specific cell niches within a continuum of CD8+ T cell phenotypes. Immunity. 2012;36(1):142-52.
368. Matos TR, Liu H, Ritz J. Research techniques made simple: mass cytometry analysis tools for decrypting the complexity of biological systems. Journal of Investigative Dermatology. 2017;137(5):e43-e51.
369. Giesen C, Wang HA, Schapiro D, Zivanovic N, Jacobs A, Hattendorf B, et al. Highly multiplexed imaging of tumor tissues with subcellular resolution by mass cytometry. Nature methods. 2014;11(4):417.
370. Chang Q, Ornatsky OI, Siddiqui I, Loboda A, Baranov VI, Hedley DW. Imaging mass cytometry. Cytometry part A. 2017;91(2):160-9.

371. James TP, Chang G, Micucci S, Sagar A, Smith EL, Cassidy C. Effect of applied force and blade speed on histopathology of bone during resection by sagittal saw. Medical engineering & physics. 2014;36(3):364-70.
372. Skinner RA. PRACTICAL APPROACHES TO PROCESSING BONE: A CLINICAL / RESEARCH COMPARATIVE OVERVIEW,. National Society for Histotechnology Annual Symposium,; Cincinnati, Ohio2011.
373. Callis G, Sterchi D. Decalcification of bone: Literature review and practical study of various decalcifying agents. Methods, and their effects on bone histology. Journal of histotechnology. 1998;21(1):49-58.
374. Giesen C, Wang H, Schapiro D, Zivanovic N, Jacobs A, Hattendorf B, et al. Highly multiplexed imaging of tumor tissues with subcellular resolution by mass cytometry2014.
375. Sroga GE, Karim L, Colón W, Vashishth D. Biochemical characterization of major bone-matrix proteins using nanoscale-size bone samples and proteomics methodology. Molecular & Cellular Proteomics. 2011;10(9).
376. Zhang H, Recker R, Lee W-NP, Xiao GG. Proteomics in bone research. Expert review of proteomics. 2010;7(1):103-11.
377. Zhang A-X, Yu W-H, Ma B-F, Yu X-B, Mao FF, Liu W, et al. Proteomic identification of differently expressed proteins responsible for osteoblast differentiation from human mesenchymal stem cells. Molecular and cellular biochemistry. 2007;304(1-2):167-79.
378. Ge M, Ke R, Cai T, Yang J, Mu X. Identification and proteomic analysis of osteoblast-derived exosomes. Biochemical and biophysical research communications. 2015;467(1):27-32.
379. Michaletti A, Gioia M, Tarantino U, Zolla L. Effects of microgravity on osteoblast mitochondria: a proteomic and metabolomics profile. Scientific reports. 2017;7(1):1-12.
380. Baroncelli M, van der Eerden BC, Kan YY, Alves RD, Demmers JA, van de Peppel J, et al. Comparative proteomic profiling of human osteoblast-derived extracellular matrices identifies proteins involved in mesenchymal stromal cell osteogenic differentiation and mineralization. Journal of Cellular Physiology. 2018;233(1):387-95.
381. MacAleese L, Stauber J, Heeren RM. Perspectives for imaging mass spectrometry in the proteomics landscape. Proteomics. 2009;9(4):819-34.
382. Vormoor B, Knizia HK, Batey MA, Almeida GS, Wilson I, Dildey P, et al. Development of a preclinical orthotopic xenograft model of ewing sarcoma and other human malignant bone disease using advanced in vivo imaging. PLoS One. 2014;9(1):e85128.
383. Schapiro D, Jackson HW, Raghuraman S, Fischer JR, Zanotelli VR, Schulz D, et al. histoCAT: analysis of cell phenotypes and interactions in multiplex image cytometry data. Nature methods. 2017;14(9):873.
384. Lawless C. Mitocyto 2019 [Available from: https://github.com/CnrLwlss/mitocyto.
385. Venables W, Ripley B. Modern applied statistics with S fourth edition. World. 2002.
386. Team RC. R Core Team (2017). R: A language and environment for statistical computing. R Found Stat Comput Vienna, Austria URL http://www R-project org/, page R Foundation for Statistical Computing. 2017.
387. Darryl C, Paradas C, DiMauro S. Mitochondrial Encephalomyopathies. Neuromuscular Disorders of Infancy, Childhood, and Adolescence: Elsevier; 2015. p. 796-833.
388. Delonlay P, Rötig A, Sarnat HB. Pediatric Neurology Part III: Chapter 168. Respiratory chain deficiencies: Elsevier Inc. Chapters; 2013.
389. Darryl C, DiMauro S. Mitochondrial Diseases. Swaiman's Pediatric Neurology: Elsevier; 2017. p. 334-46.
390. Jackson CB, Nuoffer J-M, Hahn D, Prokisch H, Haberberger B, Gautschi M, et al. Mutations in SDHD lead to autosomal recessive encephalomyopathy and isolated mitochondrial complex II deficiency. Journal of medical genetics. 2014;51(3):170-5.
391. Rocha MC, Rosa HS, Grady JP, Blakely EL, He L, Romain N, et al. Pathological mechanisms underlying single large-scale mitochondrial DNA deletions. Annals of neurology. 2018;83(1):115-30.

392. Rak M, Bénit P, Chrétien D, Bouchereau J, Schiff M, El-Khoury R, et al. Mitochondrial cytochrome c oxidase deficiency. Clinical Science. 2016;130(6):393-407.
393. Guerrero-Castillo S, Baertling F, Kownatzki D, Wessels HJ, Arnold S, Brandt U, et al. The assembly pathway of mitochondrial respiratory chain complex I. Cell metabolism. 2017;25(1):128-39.
394. Warren C, McDonald D, Capaldi R, Deehan D, Taylor RW, Filby A, et al. Decoding mitochondrial heterogeneity in single muscle fibres by imaging mass cytometry. Scientific Reports. 2020;10(1):1-14.
395. Baharlou H, Canete NP, Cunningham AL, Harman AN, Patrick E. Mass Cytometry Imaging for the Study of Human Diseases—Applications and Data Analysis Strategies. Frontiers in Immunology. 2019;10.
396. Ijsselsteijn ME, van der Breggen R, Farina Sarasqueta A, Koning F, de Miranda NF. A 40-Marker Panel for High Dimensional Characterization of Cancer Immune Microenvironments by Imaging Mass Cytometry. Frontiers in immunology. 2019;10:2534.
397. Giesen C, Wang HA, Schapiro D, Zivanovic N, Jacobs A, Hattendorf B, et al. Highly multiplexed imaging of tumor tissues with subcellular resolution by mass cytometry. Nature methods. 2014;11(4):417-22.
398. Wang YJ, Traum D, Schug J, Gao L, Liu C, Atkinson MA, et al. Multiplexed in situ imaging mass cytometry analysis of the human endocrine pancreas and immune system in type 1 diabetes. Cell metabolism. 2019;29(3):769-83. e4.
399. Keren L, Bosse M, Marquez D, Angoshtari R, Jain S, Varma S, et al. A structured tumor-immune microenvironment in triple negative breast cancer revealed by multiplexed ion beam imaging. Cell. 2018;174(6):1373-87. e19.
400. Prince RL, Smith M, Dick IM, Price RI, Webb PG, Henderson NK, et al. Prevention of postmenopausal osteoporosis: a comparative study of exercise, calcium supplementation, and hormone-replacement therapy. New England journal of medicine. 1991;325(17):1189-95.
401. Heinonen A, Kannus P, Sievänen H, Oja P, Pasanen M, Rinne M, et al. Randomised controlled trial of effect of high-impact exercise on selected risk factors for osteoporotic fractures. The Lancet. 1996;348(9038):1343-7.
402. O'Brien CA, Jia D, Plotkin LI, Bellido T, Powers CC, Stewart SA, et al. Glucocorticoids act directly on osteoblasts and osteocytes to induce their apoptosis and reduce bone formation and strength. Endocrinology. 2004;145(4):1835-41.
403. Chiodini I, Mascia ML, Muscarella S, Battista C, Minisola S, Arosio M, et al. Subclinical hypercortisolism among outpatients referred for osteoporosis. Annals of internal medicine. 2007;147(8):541-8.
404. Kurland ES, Rosen CJ, Cosman F, McMahon D, Chan F, Shane E, et al. Insulin-like growth factor-I in men with idiopathic osteoporosis. The Journal of Clinical Endocrinology & Metabolism. 1997;82(9):2799-805.
405. Fink HA, Ewing SK, Ensrud KE, Barrett-Connor E, Taylor BC, Cauley JA, et al. Association of testosterone and estradiol deficiency with osteoporosis and rapid bone loss in older men. The Journal of Clinical Endocrinology & Metabolism. 2006;91(10):3908-15.
406. Baran DT, Bergfeld MA, Teitelbaum SL, Avioli LV. Effect of testosterone therapy on bone formation in an osteoporotic hypogonadal male. Calcified tissue research. 1978;26(1):103-6.
407. Aitken J, Armstrong E, Anderson J. Osteoporosis after oophorectomy in the mature female rat and the effect of oestrogen and/or progestogen replacement therapy in its prevention. Journal of Endocrinology. 1972;55(1):79-87.
408. Lindsay R, Aitken J, Anderson L, Hart D, MacDonald E, Clarke A. Long-term prevention of postmenopausal osteoporosis by oestrogen: evidence for an increased bone mass after delayed onset of oestrogen treatment. The Lancet. 1976;307(7968):1038-41.
409. Angelova PR, Barilani M, Lovejoy C, Dossena M, Viganò M, Seresini A, et al. Mitochondrial dysfunction in Parkinsonian mesenchymal stem cells impairs differentiation. Redox biology. 2018;14:474-84.

410. Ye G, Xie Z, Zeng H, Wang P, Li J, Zheng G, et al. Oxidative stress-mediated mitochondrial dysfunction facilitates mesenchymal stem cell senescence in ankylosing spondylitis. Cell Death & Disease. 2020;11(9):1-13.
411. Zhang H, Menzies KJ, Auwerx J. The role of mitochondria in stem cell fate and aging. Development. 2018;145(8).
412. Li Q, Gao Z, Chen Y, Guan M-X. The role of mitochondria in osteogenic, adipogenic and chondrogenic differentiation of mesenchymal stem cells. Protein & cell. 2017;8(6):439-45.
413. Tahara EB, Navarete FD, Kowaltowski AJ. Tissue-, substrate-, and site-specific characteristics of mitochondrial reactive oxygen species generation. Free Radical Biology and Medicine. 2009;46(9):1283-97.
414. Seo BJ, Yoon SH, Do JT. Mitochondrial dynamics in stem cells and differentiation. International journal of molecular sciences. 2018;19(12):3893.
415. Forni MF, Peloggia J, Trudeau K, Shirihai O, Kowaltowski AJ. Murine mesenchymal stem cell commitment to differentiation is regulated by mitochondrial dynamics. Stem Cells. 2016;34(3):743-55.
416. Lee SJ, Kim MS, Park JY, Woo JS, Kim YK. 15-Deoxy-Δ12, 14-prostaglandin J2 induces apoptosis via JNK-mediated mitochondrial pathway in osteoblastic cells. Toxicology. 2008;248(2-3):121-9.
417. Chang CC, Liao YS, Lin YL, Chen RM. Nitric oxide protects osteoblasts from oxidative stress-induced apoptotic insults via a mitochondria-dependent mechanism. Journal of orthopaedic research. 2006;24(10):1917-25.
418. Duque G, El Abdaimi K, Henderson JE, Lomri A, Kremer R. Vitamin D inhibits Fas ligand-induced apoptosis in human osteoblasts by regulating components of both the mitochondrial and Fas-related pathways. Bone. 2004;35(1):57-64.
419. Gao J, Feng Z, Wang X, Zeng M, Liu J, Han S, et al. SIRT3/SOD2 maintains osteoblast differentiation and bone formation by regulating mitochondrial stress. Cell Death & Differentiation. 2018;25(2):229-40.
420. Komarova SV, Ataullakhanov FI, Globus RK. Bioenergetics and mitochondrial transmembrane potential during differentiation of cultured osteoblasts. American Journal of Physiology-Cell Physiology. 2000;279(4):C1220-C9.
421. Esen E, Chen J, Karner CM, Okunade AL, Patterson BW, Long F. WNT-LRP5 signaling induces Warburg effect through mTORC2 activation during osteoblast differentiation. Cell metabolism. 2013;17(5):745-55.
422. Duewelhenke N, Krut O, Eysel P. Influence on mitochondria and cytotoxicity of different antibiotics administered in high concentrations on primary human osteoblasts and cell lines. Antimicrobial agents and chemotherapy. 2007;51(1):54-63.
423. Zhou H, Newnum AB, Martin JR, Li P, Nelson MT, Moh A, et al. Osteoblast/osteocyte-specific inactivation of Stat3 decreases load-driven bone formation and accumulates reactive oxygen species. Bone. 2011;49(3):404-11.